PROTEIN DYNAMICS AND MEMBRANE TRAFFIC IN SYNAPTIC TRANSMISSION AND SYNAPTIC PLASTICITY

EDITED BY: Cong Ma, Zhitao Hu and Wei Liu
PUBLISHED IN: Frontiers in Cell and Developmental Biology

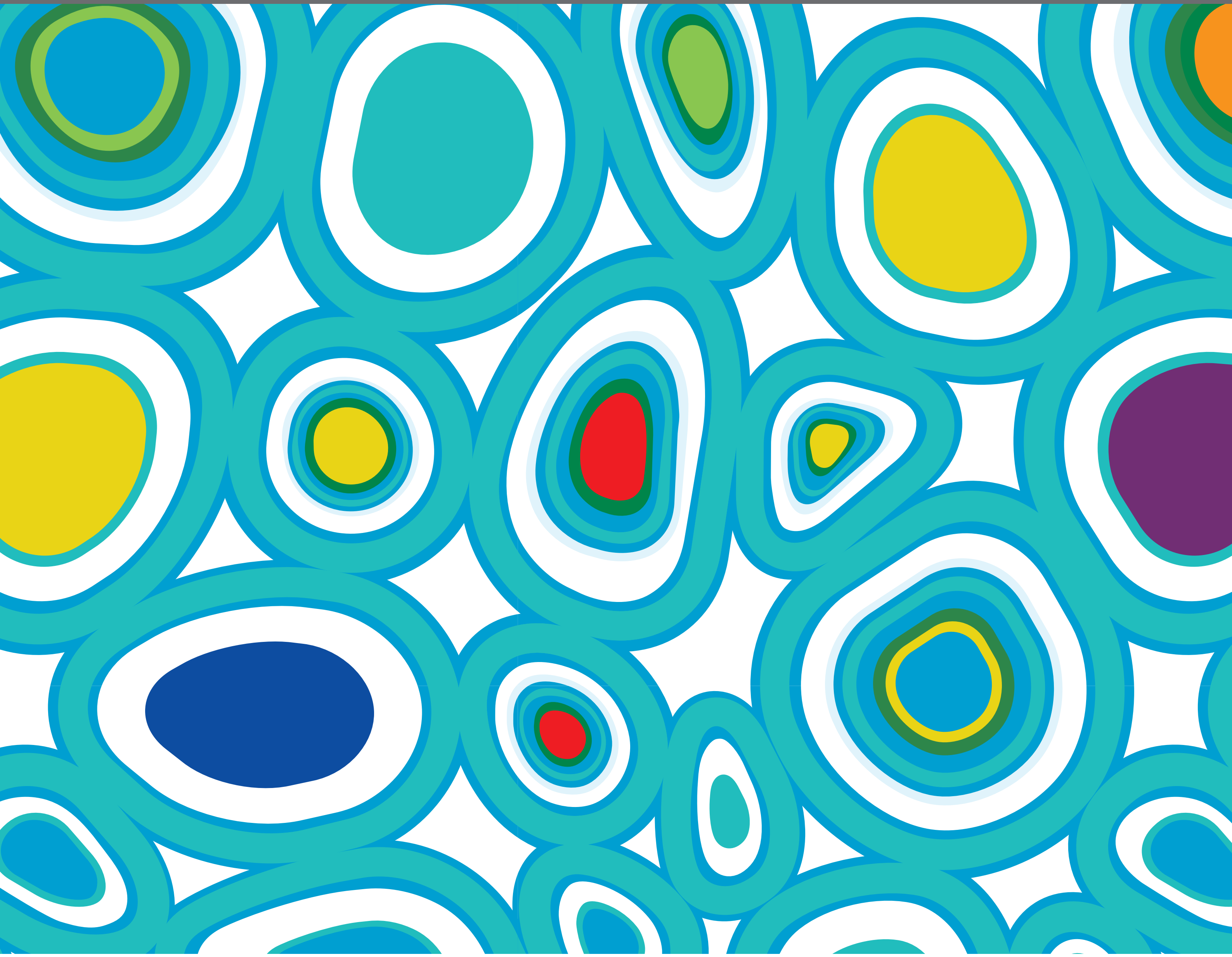

frontiers Research Topics

ISSN 1664-8714
ISBN 978-2-88974-365-0
DOI 10.3389/978-2-88974-365-0

About Frontiers

Frontiers is more than just an open-access publisher of scholarly articles: it is a pioneering approach to the world of academia, radically improving the way scholarly research is managed. The grand vision of Frontiers is a world where all people have an equal opportunity to seek, share and generate knowledge. Frontiers provides immediate and permanent online open access to all its publications, but this alone is not enough to realize our grand goals.

Frontiers Journal Series

The Frontiers Journal Series is a multi-tier and interdisciplinary set of open-access, online journals, promising a paradigm shift from the current review, selection and dissemination processes in academic publishing. All Frontiers journals are driven by researchers for researchers; therefore, they constitute a service to the scholarly community. At the same time, the Frontiers Journal Series operates on a revolutionary invention, the tiered publishing system, initially addressing specific communities of scholars, and gradually climbing up to broader public understanding, thus serving the interests of the lay society, too.

Dedication to Quality

Each Frontiers article is a landmark of the highest quality, thanks to genuinely collaborative interactions between authors and review editors, who include some of the world's best academicians. Research must be certified by peers before entering a stream of knowledge that may eventually reach the public - and shape society; therefore, Frontiers only applies the most rigorous and unbiased reviews.
Frontiers revolutionizes research publishing by freely delivering the most outstanding research, evaluated with no bias from both the academic and social point of view.
By applying the most advanced information technologies, Frontiers is catapulting scholarly publishing into a new generation.

What are Frontiers Research Topics?

Frontiers Research Topics are very popular trademarks of the Frontiers Journals Series: they are collections of at least ten articles, all centered on a particular subject. With their unique mix of varied contributions from Original Research to Review Articles, Frontiers Research Topics unify the most influential researchers, the latest key findings and historical advances in a hot research area! Find out more on how to host your own Frontiers Research Topic or contribute to one as an author by contacting the Frontiers Editorial Office: frontiersin.org/about/contact

PROTEIN DYNAMICS AND MEMBRANE TRAFFIC IN SYNAPTIC TRANSMISSION AND SYNAPTIC PLASTICITY

Topic Editors:
Cong Ma, Huazhong University of Science and Technology, China
Zhitao Hu, The University of Queensland, Australia
Wei Liu, Shenzhen Peking University Hong Kong University of Science and Technology Medical Center, China

Citation: Ma, C., Hu, Z., Liu, W., eds. (2022). Protein Dynamics and Membrane Traffic in Synaptic Transmission and Synaptic Plasticity. Lausanne: Frontiers Media SA. doi: 10.3389/978-2-88974-365-0

Table of Contents

frontiers
in Cell and Developmental Biology

ORIGINAL RESEARCH
published: 25 August 2020
doi: 10.3389/fcell.2020.00829

PORCN Negatively Regulates AMPAR Function Independently of Subunit Composition and the Amino-Terminal and Carboxy-Terminal Domains of AMPARs

Mengping Wei[1,2], Meng Wang[2], Jue Wang[2], Feng Su[2,3], Yangzhen Wang[2,4], Meng Sun[2], Shanshan Wang[1,2], Mengna Liu[1,2], Hongyi Wang[2], Mingyang Lu[2], Wei Li[2], Yutian Gong[2], Lei Yang[2]* and Chen Zhang[1,2]*

[1] PKU-IDG/McGovern Institute for Brain Research, School of Life Sciences, Peking University, Beijing, China, [2] Beijing Key Laboratory of Neural Regeneration and Repair, School of Basic Medical Sciences, Advanced Innovation Center for Human Brain Protection, Capital Medical University, Beijing, China, [3] Peking-Tsinghua Center for Life Sciences, Academy for Advanced Interdisciplinary Studies, Peking University, Beijing, China, [4] School of Life Sciences, Tsinghua University, Beijing, China

Edited by:
Cong Ma,
Huazhong University of Science and Technology, China

Reviewed by:
Jaewon Ko,
Daegu Gyeongbuk Institute of Science and Technology (DGIST), South Korea
Xiaoke Chen,
Stanford University, United States

***Correspondence:**
Lei Yang
yangleivet@sina.com
Chen Zhang
ch.zhang@pku.edu.cn

Specialty section:
This article was submitted to Membrane Traffic, a section of the journal Frontiers in Cell and Developmental Biology

Received: *15 June 2020*
Accepted: *04 August 2020*
Published: *25 August 2020*

Citation:
Wei M, Wang M, Wang J, Su F, Wang Y, Sun M, Wang S, Liu M, Wang H, Lu M, Li W, Gong Y, Yang L and Zhang C (2020) PORCN Negatively Regulates AMPAR Function Independently of Subunit Composition and the Amino-Terminal and Carboxy-Terminal Domains of AMPARs. Front. Cell Dev. Biol. 8:829. doi: 10.3389/fcell.2020.00829

Most fast excitatory synaptic transmissions in the mammalian brain are mediated by α-amino-3-hydroxy-5-methylisoxazole-4-propionic acid receptors (AMPARs), which are ligand-gated cation channels. The membrane expression level of AMPARs is largely determined by auxiliary subunits in AMPAR macromolecules, including porcupine O-acyltransferase (PORCN), which negatively regulates AMPAR trafficking to the plasma membrane. However, whether PORCN-mediated regulation depends on AMPAR subunit composition or particular regions of a subunit has not been determined. We systematically examined the effects of PORCN on the ligand-gated current and surface expression level of GluA1, GluA2, and GluA3 AMPAR subunits, alone and in combination, as well as the PORCN-GluA interaction in heterologous HEK293T cells. PORCN inhibited glutamate-induced currents and the surface expression of investigated GluA AMPAR subunits in a subunit-independent manner. These inhibitory effects required neither the amino-terminal domain (ATD) nor the carboxy-terminal domain (CTD) of GluA subunits. In addition, PORCN interacted with AMPARs independently of their ATD or CTD. Thus, the functional inhibition of AMPARs by PORCN in transfected heterologous cells was independent of the ATD, CTD, and subunit composition of AMPARs.

Keywords: AMPA receptor, PORCN, receptor trafficking, glutamate-induced currents, protein-protein interactions

INTRODUCTION

Most fast excitatory synaptic transmissions in the mammalian brain are mediated by α -amino-3-hydroxy-5-methylisoxazole-4-propionic acid receptors (AMPARs), which are ligand-gated cation channels. Dynamic changes in AMPAR properties serve as a major mechanism governing many forms of synaptic plasticity, including homeostatic scaling and long-term depression and potentiation (Malenka, 2003; Kessels and Malinow, 2009; Huganir and Nicoll, 2013; Diering and Huganir, 2018). AMPAR dysfunction results in neuropsychiatric diseases, such as Alzheimer's disease (Madsen et al., 1994; Whitehead et al., 2017), schizophrenia (Danysz, 2002; Barkus et al., 2014; Ward et al., 2015), and autism (Sudhof, 2008; Lee et al., 2016; Cheng et al., 2017). Mature AMPARs are tetramers comprising different combinations of four pore-forming subunits, which are as follows: GluA1, GluA2, GluA3, and GluA4 (Wu et al., 1996; Rosenmund et al., 1998; Dingledine et al., 1999; Greger and Mayer, 2019). Each GluA subunit comprises a large extracellular amino-terminal domain (ATD), three transmembrane domains (M1, M3, and M4), one reentrant loop (M2), a ligand-binding domain (LBD), and a carboxy-terminal domain (CTD). In addition, the endogenous AMPAR complex contains multiple auxiliary subunits that, together with the GluA tetramer, form a 0.6 to 1 MDa macromolecule (Schwenk et al., 2012). Genetic and proteomic studies have revealed more than a dozen auxiliary subunits, including transmembrane AMPAR regulatory proteins [TARPs; (Chen et al., 1999, 2000; Hashimoto et al., 1999; Tomita et al., 2003; Rouach et al., 2005)], cornichon homolog 2/3 [CNIH-2/3; (Schwenk et al., 2009; Kato et al., 2010; Herring et al., 2013)], germ cell-specific gene 1-like protein [GSG1L; (Shanks et al., 2012; McGee et al., 2015; Gu et al., 2016)], abhydrolase domain containing 6 [ABHD6; (Wei et al., 2016, 2017)], and porcupine O-acyltransferase [PORCN; (Erlenhardt et al., 2016)]. These auxiliary subunits modulate membrane localization, synaptic targeting, interorganelle trafficking, and the channel kinetics of AMPARs [reviewed in Jackson and Nicoll (2011), Cheng et al. (2012), Straub and Tomita (2012), Bettler and Fakler (2017), Bissen et al. (2019)].

As transmembrane receptors, AMPARs are transported to the plasma membrane, where they bind glutamate transmitters to transmit signals from the presynaptic neuron to the postsynaptic neuron. The auxiliary subunits of AMPARs are important mediators of AMPAR cell surface localization. Auxiliary subunits, including TARPS, CNIH-2/3, GSG1L, ABHD6, and PORCN, have been shown to have a role in the AMPAR trafficking process. Some auxiliary subunits, like stargazin and other type-I TARPS (Chen et al., 2000; Rouach et al., 2005; Straub and Tomita, 2012; Ben-Yaacov et al., 2017), promote AMPAR trafficking to the membrane and consequent synaptic transmission, whereas other auxiliary subunits, like GSG1L (Shanks et al., 2012; McGee et al., 2015; Gu et al., 2016) and ABHD6 (Wei et al., 2016, 2017), reduce the surface level of AMPARs and, hence, AMPAR-mediated excitatory neurotransmission. The auxiliary subunit PORCN serves as a negative regulator for AMPAR function in both neuronal cells and transfected heterologous cells (Erlenhardt et al., 2016). In this study, the inactivation of PORCN in hippocampal neurons reduced the amplitude but accelerated the decay kinetics of AMPAR-mediated synaptic transmission. Additionally, biochemistry analysis revealed a significant reduction in GluA1 and GluA2/3 levels in crude extracts and intracellular membrane fractions. However, there was a significant reduction in GluA2/3 but not GluA1 expression levels in the postsynaptic density (PSD) fraction. Finally, in HEK293T cells that lacked expression of AMPARs, PORCN overexpression decreased glutamate-induced currents when exogenously expressing GluA1 homologous AMPARs (Erlenhardt et al., 2016). Whether the inhibitory effects of PORCN on AMPAR function involve interactions with a specific AMPAR subunit or particular regions of an AMPAR subunit has not been determined.

In the present study, we examined the AMPAR subunit requirement for PORCN-mediated inhibition of AMPAR function in transfected heterologous cells. We showed that PORCN inhibits glutamate-induced currents and AMPAR surface expression in an AMPAR subunit-independent manner in heterologous cells. Furthermore, the ATD and CTD of AMPARs were not required to mediate the inhibitory effect of PORCN. We used immunoprecipitation assays to show that PORCN associated with all AMPAR subunits independently of the ATD and CTD. This was consistent with the functional data. Thus, our observations strongly supported the hypothesis that PORCN regulates AMPAR trafficking to the plasma membrane through protein-protein interactions.

MATERIALS AND METHODS

HEK293T Cell Culture and Transfection

In this study, stargazin, PORCN, full-length GluA subunits, and GluA deletion constructs were expressed in HEK293T cells (CRL-11268, ATCC). First, cells were cultured in a 37°C incubator supplied with 5% CO_2. Then, cells were dissociated with 0.05% trypsin and plated on dishes at a density of 800,000 cells per 35 mm dish (counted with a μScope CellCounter Basic; C.E.T.) 24 h before transfection. A 2:3 ratio of GluA:stargazin cDNA and a 3:1 ratio of GluA-stargazin:PORCN cDNA was used as previously reported (Shi et al., 2009; Wei et al., 2017). A cDNA ratio of 3:2 was used for the coexpression of GluA1 and GluA2 as well as GluA2 and GluA3 as previously reported (Shi et al., 2009; Wei et al., 2017). In control groups, the same amount of empty vector was used instead of PORCN cDNA. Transfection was performed using polyethylenimine (Polysciences, United States) reagents. Transfected HEK293T cells were dissociated with 0.05% trypsin and plated on pretreated coverslips that were 8 mm diameter and coated with poly-D-lysine. Electrophysiological recording or immunostaining analyses were performed on cells transfected with 4 μg of total cDNA per 35 mm dish 24–36 h after transfection. For Western blotting, cells were transfected with 6.75 μg of full-length GluA subunit or GluA deletion plasmids together with 2.25 μg of myc-PORCN or control plasmids in 60 mm dishes and harvested 48 h after transfection.

Electrophysiological Recording

Electrophysiological recording was conducted on coverslips seeded with transfected HEK293T cells maintained in an external solution of 144 mM NaCl, 10 mM KCl, 2 mM $CaCl_2$, 1 mM $MgCl_2$, 10 mM HEPES, and 10 mM D-glucose (pH 7.3–7.4, Osm 315 mOsm/kg). For whole-cell patches, microelectrodes (3–5 MΩ, World Precision Instruments) were filled with an internal solution of 145 mM KCl, 5 mM NaCl, 5 mM EGTA, 4 mM MgATP, 0.3 mM Na_2GTP, and 10 mM HEPES (pH 7.2, Osm 305 mOsm/kg). Series resistance was compensated to 60–70%, and recordings with series resistance values greater than 20 MΩ were rejected. Glutamate-induced currents were elicited through the local administration of external solution containing 10 mM L-glutamate acid (Sigma, G8415) for 2 s using an MPS-2 perfusion instrument [Inbio Life Science Instrument Co., Ltd.; (Wu et al., 2005)]. Whole-cell voltage clamp recordings were taken with an EPC10 patch clamp amplifier (HEKA, Lambrecht, Germany). Data were analyzed using the following software packages: Clampfit 10.0 (pClamp), Prism 5 (GraphPad Prism), and Igor 6.02 (WaveMetrics).

Hippocampal Culture and Calcium-Phosphate Transfection

Hippocampi were dissected from P0 pups and digested with 0.25% trypsin (Gibco, 25200072) at 37°C for 15 min. Neurons were plated on poly-D-lysine-coated glass coverslips and maintained at 37°C in 5% CO_2 for 14 days before the experiment. The calcium-phosphate transfection method was used for the transfection of cultured neurons at 10 days *in vitro*. The DNA (0.5 μg per well in a 48 well plate) and Ca^{2+} were mixed and added to HBS drop by drop with a gentle vortex. After keeping the DNA/Ca^{2+}/HBS mixture at room temperature for 30 min, it was added to the culture and incubated for 40 min at 37°C. Then, the culture was washed with culture medium two to three times and kept in the incubator.

Immunostaining

Immunostaining analyses were performed as previously described (Jiang et al., 2017). In brief, transfected HEK293T cells were washed once with phosphate-buffered saline (PBS; Thermo Scientific), fixed with 4% paraformaldehyde in PBS for 10 min at room temperature, and washed three times with PBS. Then, cells were permeabilized with 0.2% Triton X-100 for 5 min at room temperature for total protein analysis or were left unpermeabilized for surface protein analysis. After blocking with PBS containing 5% milk and 3% goat serum for 30 min at room temperature, cells were incubated with a primary antibody (anti-HA, 1:1000, Abmart; anti-Flag, 1:1000, Abmart) for 2 h at room temperature, washed three times with PBS, and incubated with the secondary antibody (donkey anti-mouse Alexa Fluor 546-conjugated secondary antibody, Life Technologies) for 30 min at room temperature. Fluoromount-G (Southern Biotech) was used to mount the cells on microscope slides. Images were acquired with a laser scanning confocal microscope (Olympus, FV3000) using a 60× objective lens (Olympus) and were further analyzed using the National Institutes of Health ImageJ program and Prism 5 software (GraphPad Prism).

Immunoblotting and co-IP Assay

Transfected HEK293T cells were washed once with PBS and incubated in 360 μL of cell lysis buffer comprising 50 mM Tris–HCl, 1 mM EDTA, 150 mM NaCl, and 1% CA-630 for 15 min at 4°C. Then, cell lysates were collected and centrifuged at 12,000 × *g* for 10 min at 4°C to remove the insoluble fraction. The supernatant was collected, and 10 μL was used as the input, while 350 μL was used for co-IP. Anti-myc magnetic beads (40 μL, 88843, Thermo Scientific) were added to the samples and rotated for 12 h at 4°C then washed four times with cell lysis buffer comprising 50 mM Tris–HCl, 1 mM EDTA, 150 mM NaCl, 1% Igepal CA-630, pH 7.4. Input and pulldown beads were heated at 70°C in sample buffer comprising 4× lithium dodecyl sulfate sample buffer and 10× sample reducing buffer. Then, they were subjected to SDS-PAGE (10% Bis-Tris gels, Life Technology) for 45 min at 200 V and transferred to nitrocellulose membranes. After blocking in SuperBlock T20 blocking buffer (37516, Thermo Scientific), membranes were incubated overnight at 4°C with primary antibodies against GluA1 (AB1504, Millipore, 1:2000), GluA2 (13607, CST, 1:2000), and flag (AE004, Abclonal, 1:1000). After three washes, membranes were incubated with the secondary antibody (IRDye 680LT goat anti-mouse IgG and 800CW goat anti-rabbit IgG, Odyssey) for 1 h at room temperature. Signals were detected with an infrared imaging system (Odyssey) and analyzed using the National Institutes of Health ImageJ program and Prism 5 software (GraphPad Prism).

RESULTS

PORCN Suppressed Glutamate-Induced Currents in HEK293T Cells Expressing GluA1, A2, or A3 With or Without Stargazin

To investigate whether the functional inhibition of AMPARs by PORCN depended on AMPAR subunit composition, we measured glutamate-induced currents via the whole-cell patch clamping of HEK293T cells transfected with various AMPAR subunits alone or in combination with stargazin and/or PORCN. Stargazin was used to promote AMPAR cell surface localization (Chen et al., 2000). Glutamate-induced currents were undetectable in HEK293T cells without transfection, because such cells do not normally express AMPAR subunits (Wei et al., 2016). In this study, PORCN expression significantly suppressed glutamate-induced currents mediated by GluA1 (**Figure 1A**), GluA2 (**Figure 1B**), and GluA3 (**Figure 1C**). The coexpression of stargazin with GluA2 or GluA3 significantly increased glutamate-induced currents compared with GluA2 or GluA3 expression alone but did not abolish the PORCN-mediated inhibition of AMPAR-mediated currents (**Figures 1D–F**). PORCN expression inhibited the peak amplitude of glutamate-induced currents in GluA1, GluA2, and GluA3 overexpressing cells with stargazin coexpression by 74.14 ± 14.79%, 95.39 ± 18.52%, and 70.99 ± 18.34%, respectively, and without stargazin coexpression by 60.45 ± 15.65%, 53.85 ± 20.45%, and 58.55 ± 19.44%, respectively. PORCN had similar effects on the plateau amplitude of glutamate-induced currents. In this case, percentage inhibition with stargazin coexpression was 75.39 ± 18.88%, 96.13 ± 18.72%, and 63.90 ± 30.36%, and without stargazin coexpression, it was 56.00 ± 15.30%, 68.14 ± 25.46%, and 76.37 ± 25.70%.

Most endogenous AMPARs in the brain exist in complexes comprising GluA1/A2 or GluA2/A3 (Wenthold et al., 1996; Lu et al., 2009). To account for this, we transfected HEK293T cells

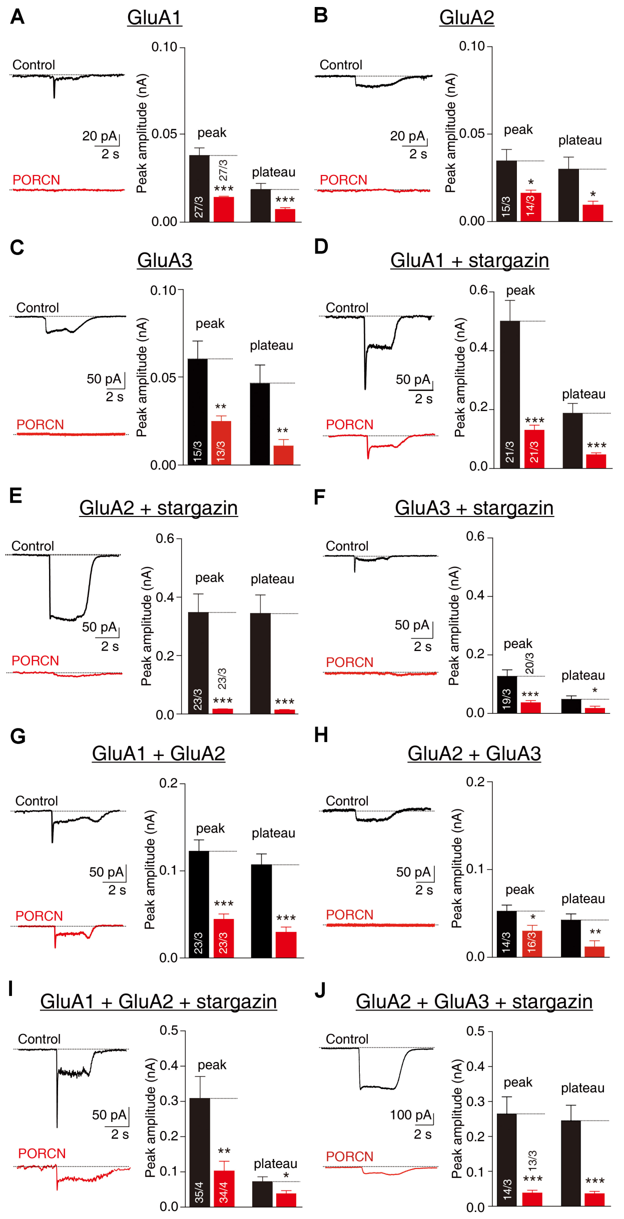

FIGURE 1 | The overexpression of PORCN suppressed glutamate-induced currents mediated by GluA2 and GluA3 in HEK293T cells with or without stargazin coexpression. **(A)** Representative traces (left) and summary graphs (right) of the peak amplitudes and plateaus of 10 mM glutamate-induced currents in HEK293T cells transfected with GluA1 and either PORCN or a control plasmid. **(B)** Representative traces (left) and summary graphs (right) of the peak amplitudes and plateaus of 10 mM glutamate-induced currents in HEK293T cells transfected with GluA2 and either PORCN or a control plasmid. **(C)** Representative traces (left) and summary graphs (right) of the peak amplitudes and plateaus of 10 mM glutamate-induced currents in HEK293T cells transfected with GluA3 and either PORCN or a control plasmid. **(D)** Representative traces and summary graphs of the peak amplitudes and plateaus of 10 mM glutamate-induced currents in HEK293T cells transfected with GluA1, stargazin, and either PORCN or a control plasmid. **(E)** Representative traces and summary graphs of the peak amplitudes and plateaus of 10 mM glutamate-induced currents in HEK293T cells transfected with GluA2, stargazin, and either PORCN or a

(Continued)

FIGURE 1 | Continued

control plasmid. **(F)** Representative traces and summary graphs of the peak amplitudes and plateaus of 10 mM glutamate-induced currents in HEK293T cells transfected with GluA3, stargazin, and either PORCN or a control plasmid. **(G)** Representative traces and summary graphs of the peak amplitudes and plateaus of 10 mM glutamate-induced currents in HEK293T cells transfected with GluA1 and GluA2 and either PORCN or a control plasmid. **(H)** Representative traces and summary graphs of the peak amplitudes and plateaus of 10 mM glutamate-induced currents in HEK293T cells transfected with GluA2 and GluA3 and either PORCN or a control plasmid. **(I)** Representative traces and summary graphs of the peak amplitudes and plateaus of 10 mM glutamate-induced currents in HEK293T cells transfected with GluA1, GluA2, and stargazin and either PORCN or a control plasmid. **(J)** Representative traces and summary graphs of the peak amplitudes and plateaus of 10 mM glutamate-induced currents in HEK293T cells transfected with GluA2, GluA3, and stargazin and either PORCN or a control plasmid. In all panels, the black traces and bars represent the control condition (no PORCN expression), while the red traces and bars represent PORCN overexpression. All summary graphs show means ± SEMs; statistical comparisons were performed with a student's *t*-test ($^{*}p < 0.05$; $^{**}p < 0.01$; $^{***}p < 0.001$).

with a combination of GluA1/A2 or GluA2/A3 at a ratio of 3:2. PORCN inhibited glutamate-induced currents in HEK293T cells expressing GluA1/A2 (**Figure 1G**) and GluA2/A3 (**Figure 1H**) by 67.88 ± 23.54% and 85.80 ± 19.71%, respectively. The coexpression of stargazin together with GluA1/A2 and GluA2/A3 was not associated with a PORCN-related inhibitory effect, as percentage inhibition was 64.55 ± 12.99% for GluA1/A2 and 42.87 ± 18.56% for GluA2/A3 (**Figures 1I,J**). Thus, PORCN inhibited glutamate-induced currents in a subunit- and stargazin-independent manner in transfected HEK293T cells.

PORCN Suppressed the Surface Delivery of GluA1, GluA2, and GluA3 in Transfected HEK293T Cells and Cultured Hippocampal Neurons

To investigate whether the PORCN-mediated inhibition of AMPAR-mediated currents was due to a reduction in surface AMPAR levels, we used quantitative immunocytochemistry to measure total and cell surface GluA protein levels in permeabilized and non-permeabilized transfected HEK293T cells, respectively. PORCN overexpression significantly reduced surface expression levels of GluA1, GluA2, and GluA3 in cells cotransfected with stargazin as indicated by decreased signals for the antibody against an extracellular epitope in non-permeabilized HEK293T cells. Signals decreased by 42.75 ± 11.09%, 59.30 ± 11.05%, and 82.11 ± 20.47%, respectively (**Figures 2A1–A3**). In contrast, immunostaining signals in permeabilized HEK293T cells for total GluA1, GluA2, and GluA3 levels were significantly higher in PORCN-transfected cells than in corresponding control cells (**Figures 2B1–B3**). This finding ruled out the possibility that the PORCN-mediated inhibition of surface GluA expression was due to a reduction in the expression of total AMPAR proteins. Thus, PORCN appeared to inhibit the plasma membrane delivery of AMPAR subunits (GluA1, GluA2, and GluA3) while increasing the total expression of these subunits in transfected HEK293T cells.

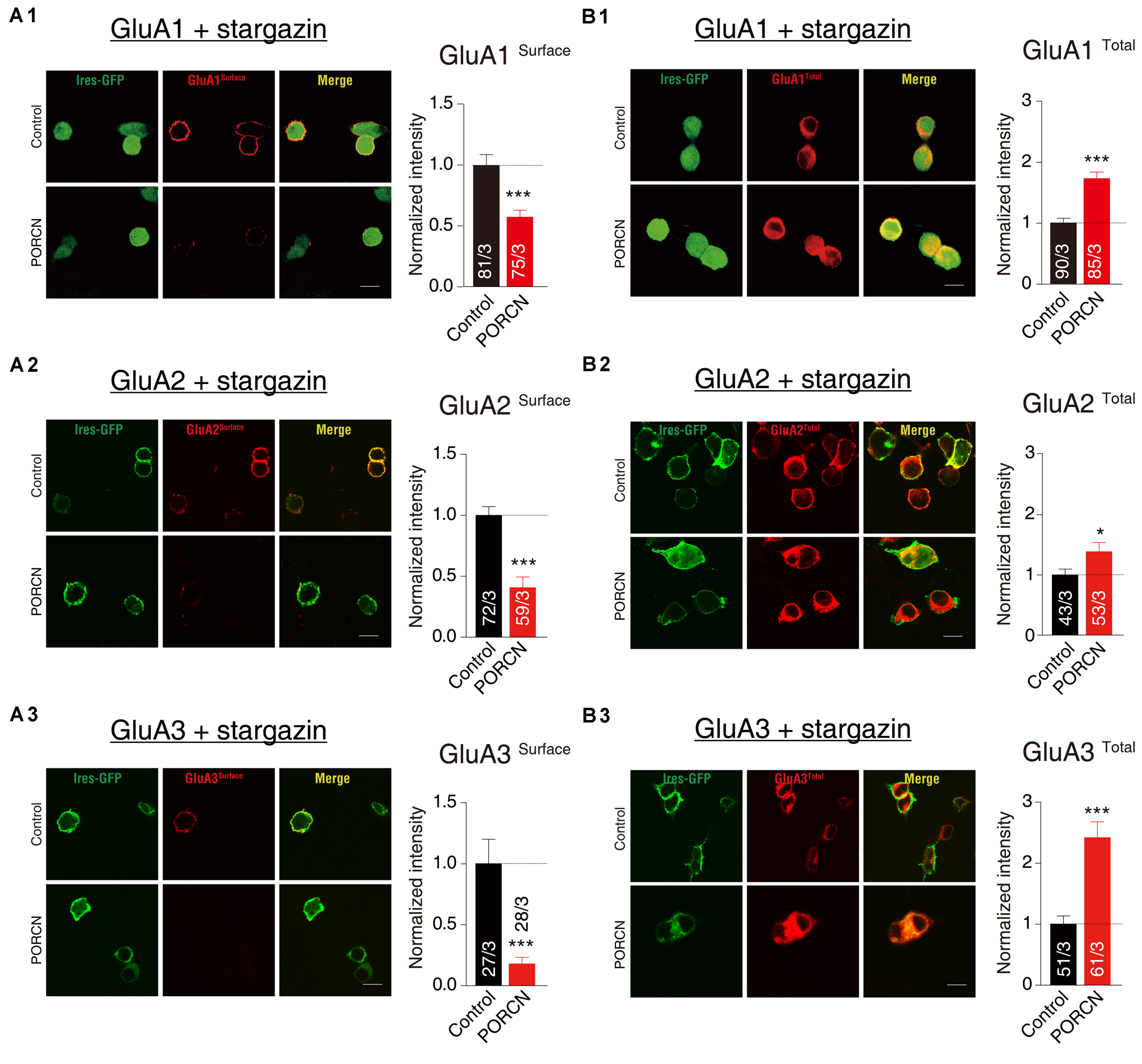

FIGURE 2 | The overexpression of PORCN suppressed the surface expression of GluA1, GluA2, and GluA3 in transfected HEK293T cells. **(A)** Representative images (left) and quantification of the puncta intensity (right) of the surface expression of GluAs in HEK293T cells expressing GluA1 and stargazin **(A1)**, GluA2 and stargazin **(A2)**, or GluA3 and stargazin **(A3)** and transfected with either PORCN or a control plasmid. **(B)** Representative images (left) and quantification of the puncta intensity (right) of the total expression of GluAs in HEK293T cells expressing GluA1 and stargazin **(B1)**, GluA2 and stargazin **(B2)**, or GluA3 and stargazin **(B3)** and transfected with either PORCN or a control plasmid. The white lines in the images represent scale bars (scale bars = 10 μm). All summary graphs show means ± SEMs; statistical comparisons were performed with a student's *t*-test ($^*p < 0.05$; $^{***}p < 0.001$).

To further determine whether PORCN suppressed the surface expression of GluA subunits of AMPARs in cultured neurons, we transfected hippocampal neurons with plasmid encoding PORCN together with plasmid encoding GFP plasmids. Then, we labeled surface GluA1 and GluA2 subunits using the antibody against extracellular epitopes in transfected neurons and measured surface GluA1 and GluA2 levels using quantitative immunocytochemistry. The intensity of surface GluA1 and GluA2 puncta in non-permeabilized neurons decreased by 67.32 ± 15.92% and 51.12 ± 10.15%, respectively, while their density decreased by 33.94 ± 8.224% and 34.26 ± 7.720%, respectively (**Figures 3A,B**). Thus, the overexpression of PORCN significantly reduced surface GluA1 and GluA2 levels. As there were no antibodies suitable for labeling surface GluA3 levels in neurons, so we transfected the hippocampus neurons with GluA3 with a flag tag in the N terminal and labeled the surface signal using the antibody against the flag tag. The intensity of GluA3-transfected hippocampus neurons decreased by 39.44 ± 19.70%, while their density decreased by 66.95 ± 18.33% (**Figure 3C**). Thus, as was the case with GluA1 and GluA2, the overexpression of PORCN significantly decreased surface GluA3 levels. Overall, our data suggested that PORCN suppressed the surface expression of GluA1, GluA2, and GluA3 subunits of AMPARs in cultured neurons.

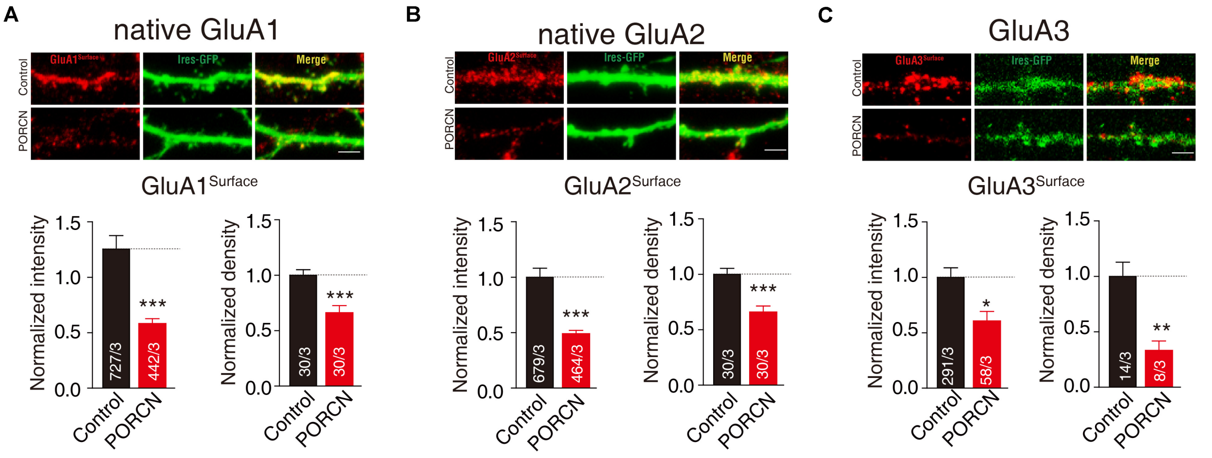

FIGURE 3 | PORCN suppressed the surface expression of GluA subunits of AMPARs in cultured neurons. **(A)** Representative images and quantification of the intensity and density of the surface expression of native GluA1. **(B)** Representative images and quantification of the intensity and density of the surface expression of native GluA2. **(C)** Representative images and quantification of the intensity and density of the surface expression of GluA3 in neurons transfected with N-flag tagged GluA3. The white lines in the images represent scale bars (scale bars = 10 μm). All summary graphs show means ± SEMs; statistical comparisons were performed with a student's t-test ($^{*}p < 0.05$; $^{**}p < 0.01$; $^{***}p < 0.001$).

The ATD and CTD of AMPAR Subunits Are Not Required for the PORCN-Mediated Inhibition of AMPAR Delivery to the Plasma Membrane

Next, we investigated which AMPAR regions were required for the PORCN-mediated inhibition of AMPAR plasma membrane delivery. The removal of the LBD or transmembrane domain of AMPARs results in a complete loss of receptor function, so we focused the analysis on the ATD and CTD regions of AMPARs. To this end, we constructed thirteen plasmids expressing full or mutated versions of GluA1, GluA2, or GluA3. These plasmids had the ATD and various CTDs or the amino acid 824 from the CTD deleted. To delete the amino acid 824 from the CTD, we removed two serine phosphorylation sites and the PDZ-binding domain (Granger et al., 2013). In addition, we constructed a mutated version of GluA3 with KSRAESKRMKLTK (MPR) deleted, as this is known to disrupt the palmitoylation site and abolish the interaction with N4.1 in GluA1 (Lin et al., 2009; **Supplementary Figure S1A**). We generated GluA2-ΔATD and GluA3-ΔATD deletion constructs according to our previously reported protocol for GluA1-ΔATD construction (Wei et al., 2016, 2017). We generated CTD deletion constructs using strategies similar to those adopted previously for GluA1 (Sheng et al., 2018). We fused all GluA-ΔATD constructs with a flag tag immediately downstream from the signal peptide separated by a GQG spacer, and we fused GluA CTD deletion constructs with an HA tag at the extreme C-terminus separated by a GQG spacer. Then, we measured the ligand-gated currents of cells expressing these GluA mutants. As expected, glutamate elicited detectable inward currents in all cells coexpressing GluA and stargazin, except for HEK293T cells expressing GluA3-ΔC with four other amino acids, leaving only "EFCY" remaining in the AMPAR's cytoplasmic tail (**Supplementary Figure S1B**). To analyze the contribution of the GluA3 CTD, we used the GluA3-ΔMPR deletion construct to complement the GluA3-Δ824 mutant in the following function assay.

Our results demonstrated that glutamate-induced currents were significantly higher in control cells expressing stargazin and GluA1/2/3-ΔATD constructs and in control cells expressing the GluA1/2/3 CTD deletion constructs GluA1/2-ΔC, GluA1/2/3-Δ824, and GluA3-ΔMPR than in corresponding cells coexpressing PORCN. Percentage inhibitions for GluA1-ΔATD (69.87 ± 15.46%), GluA1-Δ824 (65.66 ± 15.35%), GluA1-ΔC (89.81 ± 19.65%), GluA2-ΔATD (79.53 ± 17.53%), GluA2-Δ824 (83.63 ± 19.53%), GluA2-ΔC (81.52 ± 31.68%), GluA3-ΔATD (82.47 ± 25.50%), GluA3-Δ824 (86.10 ± 18.90%), and GluA3-ΔMPR (67.98 ± 15.30%) have been shown in **Figures 4A–C**. Consistent with these results, the surface expression of AMPARs in non-permeabilized HEK293T cells transfected with GluA1/2/3-ΔATD or CTD deletion constructs was significantly suppressed by the overexpression of PORCN. Percentage inhibitions for GluA1-ΔATD (45.22 ± 8.90%), GluA1-Δ824 (50.15 ± 8.97%), GluA1-ΔC (80.55 ± 14.46%), GluA2-ΔATD (84.74 ± 10.79%), GluA2-Δ824 (85.62 ± 11.50%), GluA2-ΔC (82.23 ± 12.84%), GluA3-ΔATD (50.73 ± 10.06%), GluA3-Δ824 (52.84 ± 16.18%), and GluA3-ΔMPR (47.09 ± 13.62%) have been given in **Figures 5A–C**.

To determine whether PORCN suppressed the surface expression of the various fragments of AMPARs employed in cultured neurons, we transfected neurons with plasmid encoding PORCN, together with GluA1-ΔATD, GluA1-ΔC, GluA2-ΔATD, GluA2-ΔC, GluA3-ΔATD, GluA3-Δ824, or GluA3-ΔMPR and labeled the surface signal using the antibody against the flag tag in the N terminal of deletion constructs. Quantitative immunocytochemistry showed that the overexpression of PORCN suppressed the surface expression of all deletion constructs. Decreases in the intensity of

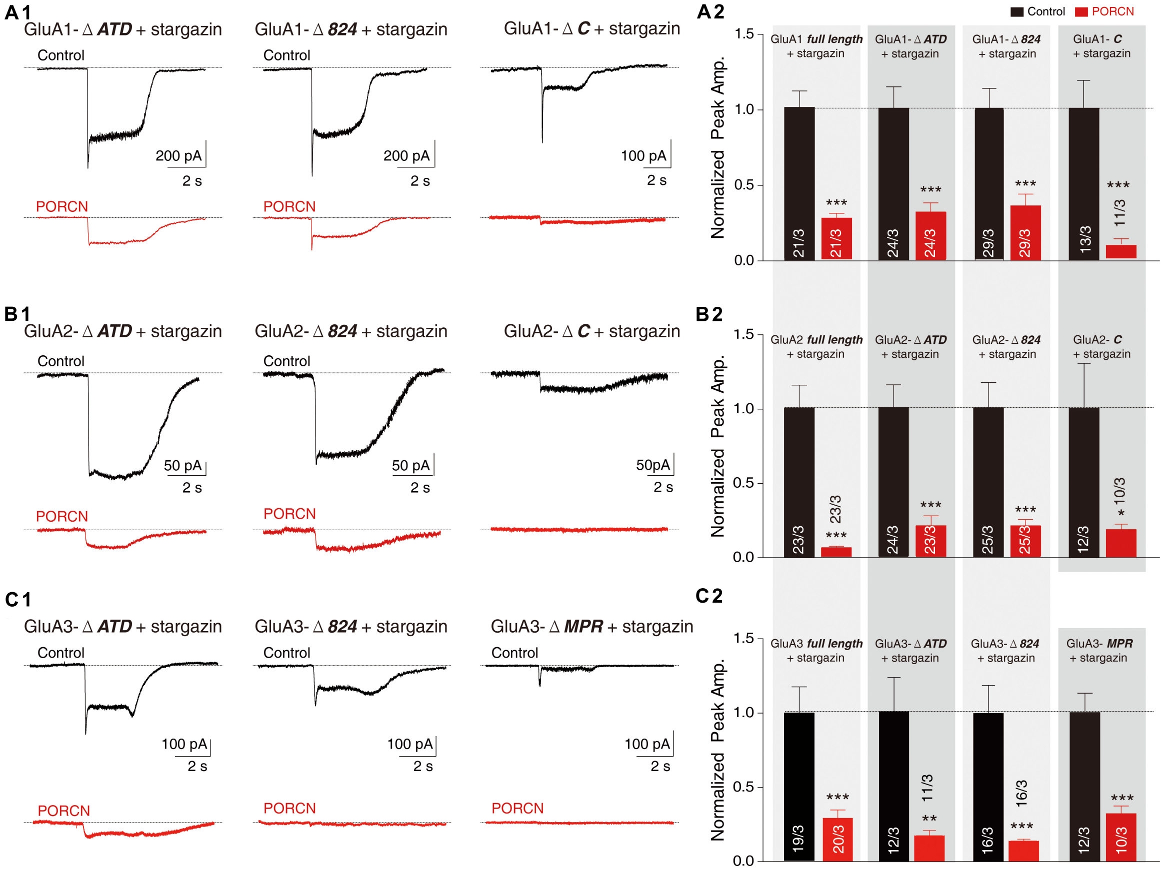

FIGURE 4 | The ATD and CTD of GluAs are not required for the inhibitory effect of PORCN on glutamate-induced currents. **(A)** Representative traces **(A1)** and summary graphs **(A2)** of the normalized peak amplitudes of 10 mM glutamate-induced currents in HEK293T cells transfected with full-length GluA1 or GluA1 deletion constructs (GluA1-ΔATD, GluA1-Δ824, and GluA1-ΔC), stargazin, and either PORCN or a control plasmid. **(B)** Representative traces **(B1)** and summary graphs **(B2)** of the normalized peak amplitudes of 10 mM glutamate-induced currents in HEK293T cells transfected with full-length GluA2 or GluA2 deletion constructs (GluA2-ΔATD, GluA2-Δ824, or GluA2-ΔC), stargazin, and either PORCN or a control plasmid. **(C)** Representative traces **(C1)** and summary graphs **(C2)** of the normalized peak amplitudes of 10 mM glutamate-induced currents in HEK293T cells transfected with full-length GluA3 or GluA3 deletion constructs (GluA3-ΔATD, GluA3-Δ824, and GluA3-ΔMPR), stargazin, and either PORCN or a control plasmid. All summary graphs show means ± SEMs; statistical comparisons were performed with a student's *t*-test (*$p < 0.05$; **$p < 0.01$; ***$p < 0.001$).

GluA1-ΔATD (66.47 ± 13.30%), GluA1-ΔC (83.47 ± 17.66%), GluA2-ΔATD (79.84 ± 13.89%), GluA2-ΔC (74.20 ± 11.99%), GluA3-ΔATD (75.61 ± 19.31%), GluA3-Δ824 (69.23 ± 14.05%), GluA3-ΔMPR (57.72 ± 13.44%) varied. Decreases in the density of GluA1-ΔATD (25.37 ± 11.17%), GluA1-ΔC (51.10 ± 11.19%), GluA2-ΔATD (40.54 ± 10.29%), GluA2-ΔC (26.60 ± 9.540%), GluA3-ΔATD (53.14 ± 10.26%), GluA3-Δ824 (50.29 ± 11.66%), GluA3-ΔMPR (62.02 ± 8.041%) also varied (**Figures 6A1,A2,B1,B2,C1–C3**). Taken together, our results demonstrated that neither the ATD nor the CTD of AMPAR subunits GluA1, GluA2, and GluA3 were required for the PORCN-mediated functional inhibition of AMPARs.

The Interaction of PORCN With AMPARs Was Independent of Their ATD or CTD

The PORCN-mediated functional inhibition of AMPARs is thought to be caused by an interaction of PORCN with these receptors (Schwenk et al., 2012; Erlenhardt et al., 2016). We used immunoprecipitation assays to search for regions in AMPAR subunits that interacted with PORCN. We used an anti-myc antibody to immunoprecipitate myc-PORCN in HEK293T cells transfected with PORCN and wild-type or deletion mutants of GluA1-3 subunits. First, we determined whether PORCN coimmunoprecipitated with full-length and mutant GluA1. To this end, we used anti-GluA1 to detect the wild-type and GluA1-ΔATD mutant and an anti-HA antibody to detect GluA1-CTD deletion proteins, because the anti-GluA1 antibody used in this study recognized CTD regions that were absent from GluA1-CTD deletion constructs. Findings showed that Myc-tagged PORCN coimmunoprecipitated with full-length GluA1 when both PORCN and GluA1 were expressed (**Figure 7A**). Furthermore, PORCN coimmunoprecipitated with GluA1-ΔATD and GluA1 CTD mutants GluA1-Δ824 and GluA1-ΔC in transfected HEK293T cells (**Figure 7A**).

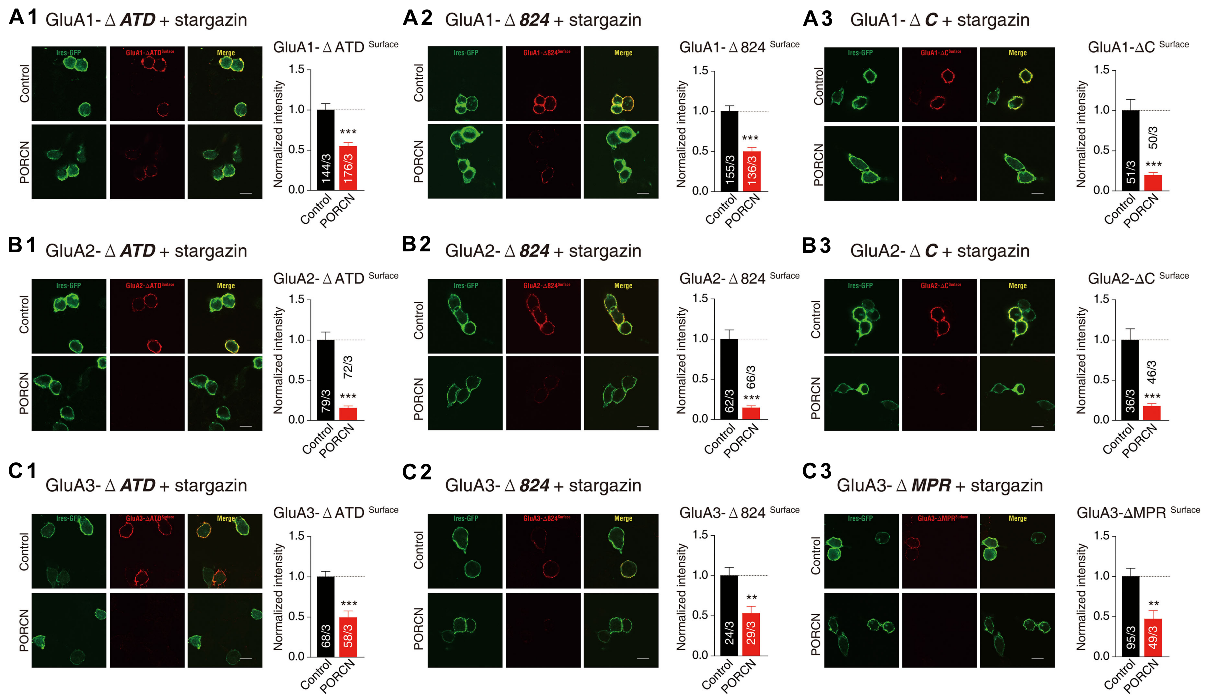

FIGURE 5 | The ATD and CTD of GluAs are not required for the inhibitory effect of PORCN on the membrane expression of AMPARs in transfected HEK cells. **(A)** Representative images and quantification of the puncta intensity of the surface expression of GluA1 deletion constructs in HEK293T cells expressing GluA1 deletion constructs (**A1**: GluA1-ΔATD, **A2**: GluA1-Δ824, **A3**: GluA1-ΔC) and stargazin and transfected with either PORCN or a control plasmid. **(B)** Representative images and quantification of the puncta intensity of the surface expression of GluA2 deletion constructs in HEK293T cells expressing GluA2 deletion constructs (**B1**: GluA2-ΔATD, **B2**: GluA2-Δ824, **B3**: GluA2-ΔC) and stargazin and transfected with either PORCN or a control plasmid. **(C)** Representative images and quantification of the puncta intensity of the surface expression of GluA3 deletion constructs in HEK293T cells expressing GluA3 deletion constructs (**C1**: GluA3-ΔATD, **C2**: GluA3-Δ824, **C3**: GluA3-ΔMPR) and stargazin and transfected with either PORCN or a control plasmid. All summary graphs show means ± SEMs; statistical comparisons were performed with a student's *t*-test ($^{**}p < 0.01$; $^{***}p < 0.001$).

We performed similar experiments with GluA2 using an anti-GluA2 antibody that recognized the transmembrane region of GluA2 present in all GluA2 deletion constructs. GluA2-Δ824, GluA2-ΔATD, GluA2-ΔC, and the full-length GluA2 protein bound to myc-PORCN (**Figure 7B**). The results of similar experiments performed with GluA3 using an anti-flag antibody revealed that GluA3-Δ824, GluA3-ΔATD, and GluA3-ΔMPR as well as the full-length GluA3 protein bound to myc-PORCN (**Figure 7C**). Collectively, our data indicated that neither the ATD nor the CTD were involved in the interaction of PORCN with AMPARs, which suggested that other regions in AMPARs, such as the LBD and transmembrane domains, might be involved.

DISCUSSION

The trafficking of AMPARs to the plasma membrane determines the synaptic strength at excitatory synapses, and auxiliary subunits are key regulators of the intracellular and membrane delivery of AMPARs. PORCN, an auxiliary subunit of AMPARs, controls surface AMPAR levels in both transfected heterologous cells and in neurons (Schwenk et al., 2012; Erlenhardt et al., 2016). Here, we demonstrated that PORCN inhibits the ligand-gated currents and surface expression levels of GluA1, GluA2, and GluA3 in transfected HEK293T cells. This finding of subunit independence supported the previous finding that the inactivation of PORCN in hippocampal neurons reduced the total levels of GluA1, GluA2, and GluA3 (Erlenhardt et al., 2016). This inhibition required neither the ATD nor the CTD of these AMPAR subunits. Moreover, the interaction of PORCN with AMPARs was independent of the ATD and CTD of these AMPAR subunits. Thus, PORCN inhibited the function of AMPARs in a subunit-independent manner that did not involve the ATD or CTD of AMPARs.

Similar to the inhibitory effect of ABHD6, another auxiliary subunit of AMPARs (Schwenk et al., 2012; Wei et al., 2016, 2017), the inhibitory effect of PORCN on cell surface levels of GluA1, GluA2, and GluA3 in transfected HEK293T cells does not require the presence of either stargazin (γ-2, **Figure 1C**) or γ-8 (Erlenhardt et al., 2016). In contrast, the expression of CNIH-2, another auxiliary AMPAR subunit, in HEK cells slows the deactivation of AMPARs comprising GluA1, A2, or their combination; however, γ-8 expression reverses the effect of CNIH-2 on GluA2-containing AMPARs but not GluA1 homomers (Herring et al., 2013). Thus, multiple classes of auxiliary AMPAR proteins can mediate AMPAR trafficking to the plasma membrane.

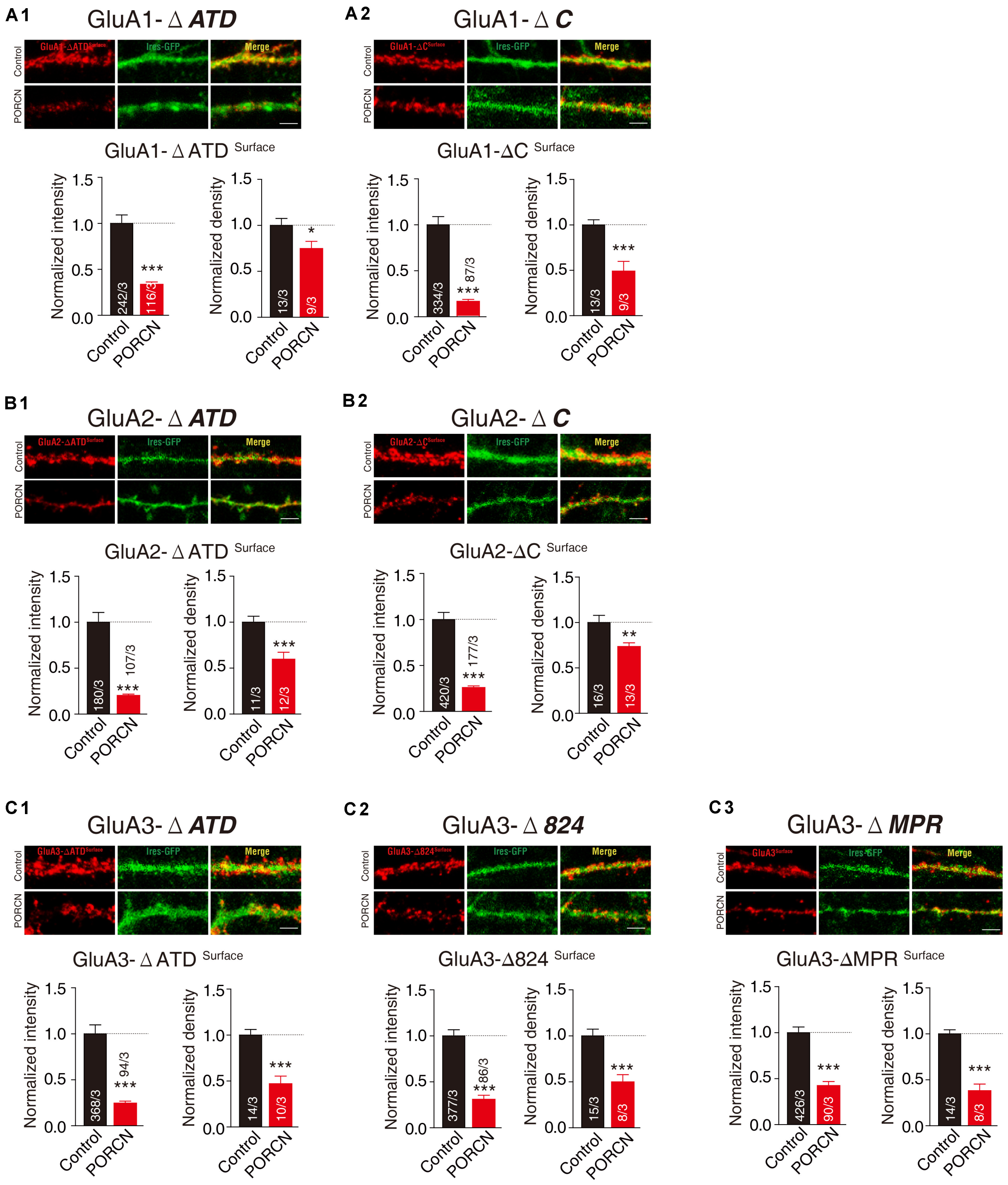

FIGURE 6 | The ATD and CTD of GluAs are not required for the inhibitory effect of PORCN on the surface expression of AMPARs in cultured neurons. **(A1,A2)** Representative images and quantification of the intensity and density of the surface expression of GluA1 deletion constructs (**A1**: GluA1-ΔATD, **A2**: GluA1-ΔC) in cultured neurons expressing GluA1 deletion constructs. **(B1,B2)** Representative images and quantification of the intensity and density of the surface expression of GluA2 deletion constructs (**B1**: GluA2-ΔATD, **B2**: GluA2-ΔC) in cultured neurons expressing GluA2 deletion constructs. **(C1–C3)** Representative images and quantification of the intensity and density of the surface expression of GluA3 full length and deletion constructs (**C1**: GluA3-ΔATD, **C1**: GluA1-Δ824, **C3**: GluA3-ΔMPR) in cultured neurons expressing GluA3 deletion constructs. The white lines in the images represent scale bars (scale bars = 5 μm). All summary graphs show means ± SEMs; statistical comparisons were performed with a student's *t*-test (*$p < 0.05$; **$p < 0.01$; ***$p < 0.001$).

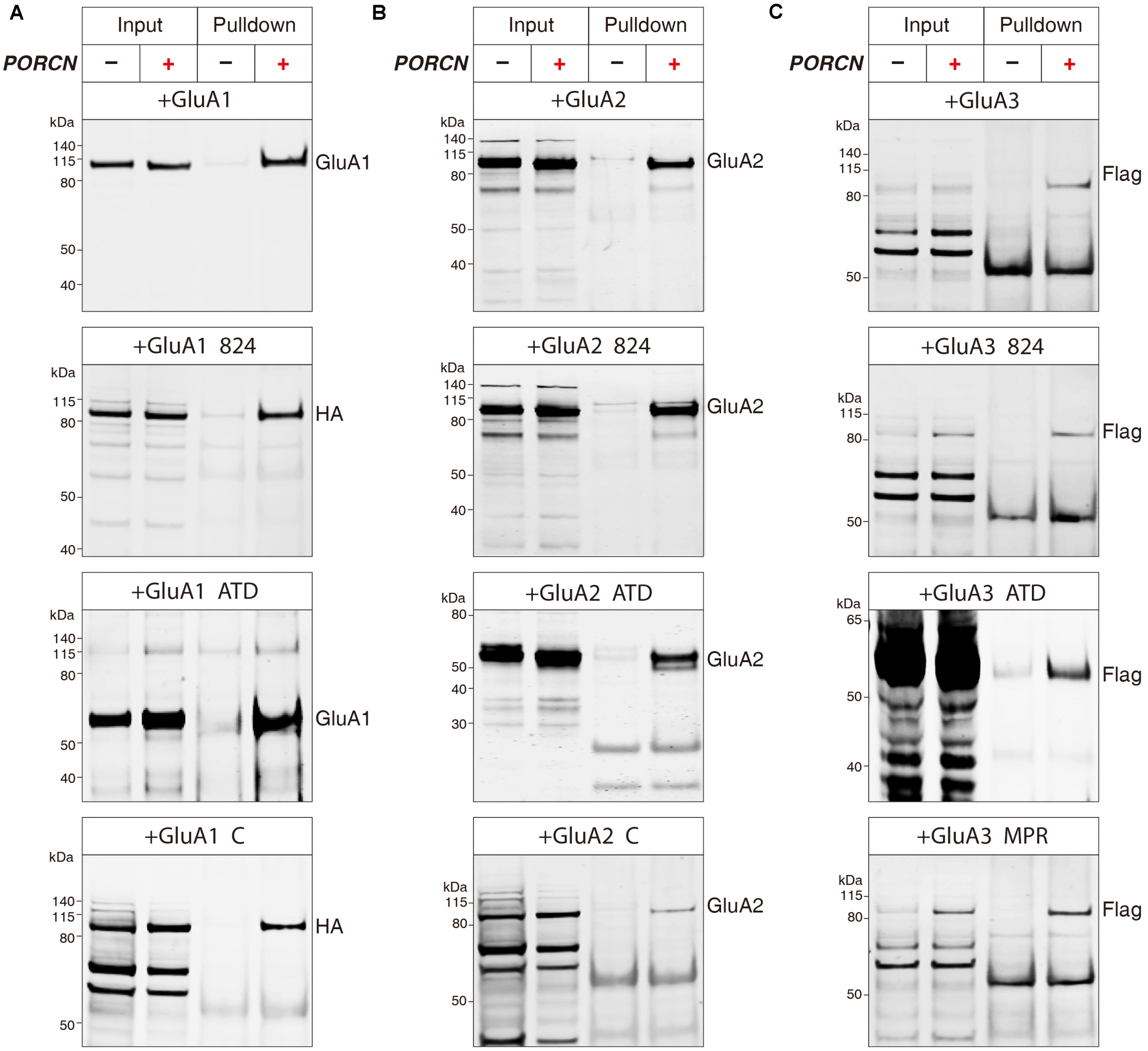

FIGURE 7 | The binding of PORCN to AMPARs is independent of the AMPAR ATD or CTD. **(A)** Pulldown of GluA1, GluA1-ΔATD, GluA1-Δ824, and GluA1-ΔC expressed in transfected HEK293T cells together with the pulldown of myc-tagged PORCN with an anti-myc antibody. **(B)** Pulldown of GluA2, GluA2-ΔATD, GluA2-Δ824, and GluA2-ΔC expressed in transfected HEK293T cells together with the pulldown of myc-tagged PORCN with an anti-myc antibody. **(C)** Pulldown of GluA3, GluA3-ΔATD, GluA3-Δ824, and GluA3-ΔMPR expressed in transfected HEK293T cells together with the pulldown of myc-tagged PORCN with an anti-myc antibody.

Our data demonstrated that the ATD and CTD of AMPAR subunits GluA1, GluA2, and GluA3 were not required for the PORCN-mediated inhibition of AMPAR function or for the PORCN–AMPAR interaction. The ATD and CTD of AMPARs play substantial roles in the membrane trafficking of this receptor (Xia et al., 2002; Granger et al., 2013). Notably, multiple sites or regions in the CTD of AMPARs undergo protein modifications, such as nitrosylation, palmitoylation, ubiquitination, and phosphorylation/dephosphorylation [see (Diering and Huganir, 2018) for a detailed review]. A sophisticated molecular replacement strategy has been used to show that the PDZ binding motif in the AMPAR CTD is crucial for the synaptic delivery of AMPARs to the postsynaptic plasma membrane during both the basal state and long-term potentiation (Sheng et al., 2018). The interaction of other auxiliary subunits with the AMPAR CTD is essential. For example, ABHD6 reduces the surface expression levels of AMPARs in heterologous cells by binding to their cytoplasmic region (Wei et al., 2016, 2017). Another recent report indicated that the AMPAR's ATD is involved in AMPAR trafficking. In the AMPAR complete knockout background, GluA1 or GluA2 expression resulted in the full or partial restoration of AMPAR-mediated synaptic transmission in Schaffer collateral pathways, while the expression of corresponding ATD deletion constructs did not rescue this transmission (Diaz-Alonso et al., 2017; Watson et al., 2017).

The exact molecules mediating this GluA-ATD interaction are unknown, but promising proteins associated with the GluA-ATD, including neuronal pentraxins, have been reported (O'Brien et al., 1999, 2002; Sia et al., 2007; Chang et al., 2010; Gu et al., 2013; Pelkey et al., 2015; Lee et al., 2017). In this study, AMPAR subunits, even in the absence of the ATD or CTD (for example, GluA-ΔC and GluA-ΔATD), constituted functional receptors in transfected HEK293T cells as indicated by their surface expression and capability to mediate glutamate-induced currents. Interestingly, PORCN inhibited the membrane expression of AMPARs and ligand-gated currents mediated by GluA CTD deletion constructs and GluA-ΔATD. This inhibition was not due to an effect on expression levels, because quantitative immunoblotting showed that the expression levels of these AMPAR mutants were not reduced to those of full-length AMPARs. This finding agreed with previous work, which showed that normal AMPAR-mediated synaptic transmission followed the replacement of endogenous AMPARs with various GluA1 CTD deletion mutants (Δ824, ΔMPR, or ΔC) in Cre-expressing Gria1-3fl/fl hippocampal CA1 neurons (Granger et al., 2013). Our data suggested that multiple mechanisms might act independently to regulate the processes through which AMPARs are delivered to the membrane.

Our patch clamp recording, immunostaining, and immunoprecipitation results indicated that the site at which AMPARs interact with PORCN was not located in the ATD or CTD and that it may be located in the LBD or transmembrane regions. Thus, the exact region in which PORCN and AMPAR subunits functionally interact remains to be identified. This issue must be addressed through further systematic molecular and cellular biology studies.

DATA AVAILABILITY STATEMENT

The original contributions presented in the study are included in the article/**Supplementary Material**, further inquiries can be directed to the corresponding authors.

AUTHOR CONTRIBUTIONS

MWe, LY, and CZ designed the research. MWe and LY performed the research. MWe, MWa, JW, FS, YW, MS, SW, MeL, HW, MiL, WL, and YG analyzed the data. CZ and LY wrote the manuscript. All authors contributed to the article and approved the submitted version.

FUNDING

This work was supported by grants from the National Basic Research Program of China (2017YFA0105201); the National Natural Science Foundation of China (31900698, 31670842, and 81925011); the China Postdoctoral Science Foundation (2019M650323); the Beijing Municipal Commission of Science, Technology, and Education (Z181100001518001, CIT&TCD20190334, and KZ201910025025); the Youth Beijing Scholars Program (015); and the Key Realm R&D Program of Guangdong Province (2019B030335001).

SUPPLEMENTARY MATERIAL

The Supplementary Material for this article can be found online at: https://www.frontiersin.org/articles/10.3389/fcell.2020.00829/full#supplementary-material

REFERENCES

Barkus, C., Sanderson, D. J., Rawlins, J. N., Walton, M. E., Harrison, P. J., and Bannerman, D. M. (2014). What causes aberrant salience in schizophrenia? A role for impaired short-term habituation and the GRIA1 (GluA1) AMPA receptor subunit. *Mol. Psychiatry* 19, 1060–1070. doi: 10.1038/mp.2014.91

Ben-Yaacov, A., Gillor, M., Haham, T., Parsai, A., Qneibi, M., and Stern-Bach, Y. (2017). Molecular mechanism of AMPA receptor modulation by TARP/Stargazin. *Neuron* 93, 1126.e4–1137.e4.

Bettler, B., and Fakler, B. (2017). Ionotropic AMPA-type glutamate and metabotropic GABA(B) receptors: determining cellular physiology by proteomes. *Curr. Opin. Neurobiol.* 45, 16–23. doi: 10.1016/j.conb.2017.02.011

Bissen, D., Foss, F., and Acker-Palmer, A. (2019). AMPA receptors and their minions: auxiliary proteins in AMPA receptor trafficking. *Cell Mol. Life Sci.* 76, 2133–2169. doi: 10.1007/s00018-019-03068-7

Chang, M. C., Park, J. M., Pelkey, K. A., Grabenstatter, H. L., Xu, D., Linden, D. J., et al. (2010). Narp regulates homeostatic scaling of excitatory synapses on parvalbumin-expressing interneurons. *Nat. Neurosci.* 13, 1090–1097. doi: 10.1038/nn.2621

Chen, L., Bao, S., Qiao, X., and Thompson, R. F. (1999). Impaired cerebellar synapse maturation in waggler, a mutant mouse with a disrupted neuronal calcium channel gamma subunit. *Proc. Natl. Acad. Sci. U.S.A.* 96, 12132–12137. doi: 10.1073/pnas.96.21.12132

Chen, L., Chetkovich, D. M., Petralia, R. S., Sweeney, N. T., Kawasaki, Y., Wenthold, R. J., et al. (2000). Stargazin regulates synaptic targeting of AMPA receptors by two distinct mechanisms. *Nature* 408, 936–943. doi: 10.1038/35050030

Cheng, G. R., Li, X. Y., Xiang, Y. D., Liu, D., McClintock, S. M., and Zeng, Y. (2017). The implication of AMPA receptor in synaptic plasticity impairment and intellectual disability in fragile X syndrome. *Physiol. Res.* 66, 715–727. doi: 10.33549/physiolres.933473

Cheng, J., Dong, J., Cui, Y. X., Wang, L. C., Wu, B., and Zhang, C. (2012). Interacting partners of AMPA-type glutamate receptors. *J. Mol. Neurosci.* 48, 441–447. doi: 10.1007/s12031-012-9724-6

Danysz, W. (2002). Positive modulators of AMPA receptors as a potential treatment for schizophrenia. *Curr. Opin. Investig Drugs* 3, 1062–1066.

Diaz-Alonso, J., Sun, Y. J., Granger, A. J., Levy, J. M., Blankenship, S. M., and Nicoll, R. A. (2017). Subunit-specific role for the amino-terminal domain of AMPA receptors in synaptic targeting. *Proc. Natl. Acad. Sci. U.S.A.* 114, 7136–7141. doi: 10.1073/pnas.1707472114

Diering, G. H., and Huganir, R. L. (2018). The AMPA receptor code of synaptic plasticity. *Neuron* 100, 314–329. doi: 10.1016/j.neuron.2018.10.018

Dingledine, R., Borges, K., Bowie, D., and Traynelis, S. F. (1999). The glutamate receptor ion channels. *Pharmacol. Rev.* 51, 7–61.

Erlenhardt, N., Yu, H., Abiraman, K., Yamasaki, T., Wadiche, J. I., Tomita, S., et al. (2016). Porcupine controls hippocampal AMPAR levels, composition, and synaptic transmission. *Cell Rep.* 14, 782–794. doi: 10.1016/j.celrep.2015.12.078

Granger, A. J., Shi, Y., Lu, W., Cerpas, M., and Nicoll, R. A. (2013). LTP requires a reserve pool of glutamate receptors independent of subunit type. *Nature* 493, 495–500. doi: 10.1038/nature11775

Greger, I. H., and Mayer, M. L. (2019). Structural biology of glutamate receptor ion channels: towards an understanding of mechanism. *Curr. Opin. Struct. Biol.* 57, 185–195. doi: 10.1016/j.sbi.2019.05.004

Gu, X. L., Mao, X., Lussier, M. P., Hutchison, M. A., Zhou, L., Hamra, F. K., et al. (2016). GSG1L suppresses AMPA receptor-mediated synaptic transmission and uniquely modulates AMPA receptor kinetics in hippocampal neurons. *Nat. Commun.* 7, 28–35. doi: 10.1152/jn.00307.2016

Gu, Y., Huang, S., Chang, M. C., Worley, P., Kirkwood, A., and Quinlan, E. M. (2013). Obligatory role for the immediate early gene NARP in critical period plasticity. *Neuron* 79, 335–346. doi: 10.1016/j.neuron.2013.05.016

Hashimoto, K., Fukaya, M., Qiao, X., Sakimura, K., Watanabe, M., and Kano, M. (1999). Impairment of AMPA receptor function in cerebellar granule cells of ataxic mutant mouse stargazer. *J. Neurosci.* 19, 6027–6036. doi: 10.1523/jneurosci.19-14-06027.1999

Herring, B. E., Shi, Y., Suh, Y. H., Zheng, C. Y., Blankenship, S. M., Roche, K. W., et al. (2013). Cornichon proteins determine the subunit composition of synaptic AMPA Receptors. *Neuron* 77, 1083–1096. doi: 10.1016/j.neuron.2013.01.017

Huganir, R. L., and Nicoll, R. A. (2013). AMPARs and synaptic plasticity: the last 25 years. *Neuron* 80, 704–717. doi: 10.1016/j.neuron.2013.10.025

Jackson, A. C., and Nicoll, R. A. (2011). The expanding social network of ionotropic glutamate receptors: TARPs and other transmembrane auxiliary subunits. *Neuron* 70, 178–199. doi: 10.1016/j.neuron.2011.04.007

Jiang, W., Wei, M., Liu, M., Pan, Y., Cao, D., Yang, X., et al. (2017). Identification of protein tyrosine phosphatase receptor type O (PTPRO) as a synaptic adhesion molecule that promotes synapse formation. *J. Neurosci.* 37, 9828–9843. doi: 10.1523/jneurosci.0729-17.2017

Kato, A. S., Gill, M. B., Ho, M. T., Yu, H., Tu, Y. A., Siuda, E. R., et al. (2010). Hippocampal AMPA receptor gating controlled by both TARP and cornichon proteins. *Neuron* 68, 1082–1096. doi: 10.1016/j.neuron.2010.11.026

Kessels, H. W., and Malinow, R. (2009). Synaptic AMPA receptor plasticity and behavior. *Neuron* 61, 340–350. doi: 10.1016/j.neuron.2009.01.015

Lee, K., Goodman, L., Fourie, C., Schenk, S., Leitch, B., and Montgomery, J. M. (2016). AMPA receptors as therapeutic targets for neurological disorders. *Adv. Protein Chem. Struct. Biol.* 103, 203–261. doi: 10.1016/bs.apcsb.2015.10.004

Lee, S. J., Wei, M. P., Zhang, C., Maxeiner, S., Pak, C., Botelho, S. C., et al. (2017). Presynaptic neuronal pentraxin receptor organizes excitatory and inhibitory synapses. *J. Neurosci.* 37, 1062–1080. doi: 10.1523/jneurosci.2768-16.2016

Lin, D. T., Makino, Y., Sharma, K., Hayashi, T., Neve, R., Takamiya, K., et al. (2009). Regulation of AMPA receptor extrasynaptic insertion by 4.1N, phosphorylation and palmitoylation. *Nat. Neurosci.* 12, 879–887. doi: 10.1038/nn.2351

Lu, W., Shi, Y., Jackson, A. C., Bjorgan, K., During, M. J., Sprengel, R., et al. (2009). Subunit composition of synaptic AMPA receptors revealed by a single-cell genetic approach. *Neuron* 62, 254–268. doi: 10.1016/j.neuron.2009.02.027

Madsen, U., Ebert, B., and Krogsgaard-Larsen, P. (1994). Modulation of AMPA receptor function in relation to glutamatergic abnormalities in Alzheimer's disease. *Biomed. Pharmacother.* 48, 305–311. doi: 10.1016/0753-3322(94)90176-7

Malenka, R. C. (2003). Synaptic plasticity and AMPA receptor trafficking. *Ann. N. Y. Acad. Sci.* 1003, 1–11. doi: 10.1196/annals.1300.001

McGee, T. P., Bats, C., Farrant, M., and Cull-Candy, S. G. (2015). Auxiliary subunit GSG1L acts to suppress calcium-permeable AMPA receptor function. *J. Neurosci.* 35, 16171–16179. doi: 10.1523/jneurosci.2152-15.2015

O'Brien, R., Xu, D., Mi, R., Tang, X., Hopf, C., and Worley, P. (2002). Synaptically targeted narp plays an essential role in the aggregation of AMPA receptors at excitatory synapses in cultured spinal neurons. *J. Neurosci.* 22, 4487–4498. doi: 10.1523/jneurosci.22-11-04487.2002

O'Brien, R. J., Xu, D., Petralia, R. S., Steward, O., Huganir, R. L., and Worley, P. (1999). Synaptic clustering of AMPA receptors by the extracellular immediate-early gene product Narp. *Neuron* 23, 309–323. doi: 10.1016/s0896-6273(00)80782-5

Pelkey, K. A., Barksdale, E., Craig, M. T., Yuan, X., Sukumaran, M., Vargish, G. A., et al. (2015). Pentraxins coordinate excitatory synapse maturation and circuit integration of parvalbumin interneurons. *Neuron* 85, 1257–1272. doi: 10.1016/j.neuron.2015.02.020

Rosenmund, C., Stern-Bach, Y., and Stevens, C. F. (1998). The tetrameric structure of a glutamate receptor channel. *Science* 280, 1596–1599. doi: 10.1126/science.280.5369.1596

Rouach, N., Byrd, K., Petralia, R. S., Elias, G. M., Adesnik, H., Tomita, S., et al. (2005). TARP gamma-8 controls hippocampal AMPA receptor number, distribution and synaptic plasticity. *Nat. Neurosci.* 8, 1525–1533. doi: 10.1038/nn1551

Schwenk, J., Harmel, N., Brechet, A., Zolles, G., Berkefeld, H., Muller, C. S., et al. (2012). High-resolution proteomics unravel architecture and molecular diversity of native AMPA receptor complexes. *Neuron* 74, 621–633. doi: 10.1016/j.neuron.2012.03.034

Schwenk, J., Harmel, N., Zolles, G., Bildl, W., Kulik, A., Heimrich, B., et al. (2009). Functional proteomics identify cornichon proteins as auxiliary subunits of AMPA receptors. *Science* 323, 1313–1319. doi: 10.1126/science.1167852

Shanks, N. F., Savas, J. N., Maruo, T., Cais, O., Hirao, A., Oe, S., et al. (2012). Differences in AMPA and kainate receptor interactomes facilitate identification of AMPA receptor auxiliary subunit GSG1L. *Cell Rep.* 1, 590–598. doi: 10.1016/j.celrep.2012.05.004

Sheng, N., Bemben, M. A., Diaz-Alonso, J., Tao, W., Shi, Y. S., and Nicoll, R. A. (2018). LTP requires postsynaptic PDZ-domain interactions with glutamate receptor/auxiliary protein complexes. *Proc. Natl. Acad. Sci. U.S.A.* 115, 3948–3953. doi: 10.1073/pnas.1800719115

Shi, Y., Lu, W., Milstein, A. D., and Nicoll, R. A. (2009). The stoichiometry of AMPA receptors and TARPs varies by neuronal cell type. *Neuron* 62, 633–640. doi: 10.1016/j.neuron.2009.05.016

Sia, G. M., Beique, J. C., Rumbaugh, G., Cho, R., Worley, P. F., and Huganir, R. L. (2007). Interaction of the N-terminal domain of the AMPA receptor GluR4 subunit with the neuronal pentraxin NP1 mediates GluR4 synaptic recruitment. *Neuron* 55, 87–102. doi: 10.1016/j.neuron.2007.06.020

Straub, C., and Tomita, S. (2012). The regulation of glutamate receptor trafficking and function by TARPs and other transmembrane auxiliary subunits. *Curr. Opin. Neurobiol.* 22, 488–495. doi: 10.1016/j.conb.2011.09.005

Sudhof, T. C. (2008). Neuroligins and neurexins link synaptic function to cognitive disease. *Nature* 455, 903–911. doi: 10.1038/nature07456

Tomita, S., Chen, L., Kawasaki, Y., Petralia, R. S., Wenthold, R. J., Nicoll, R. A., et al. (2003). Functional studies and distribution define a family of transmembrane AMPA receptor regulatory proteins. *J. Cell Biol.* 161, 805–816. doi: 10.1083/jcb.200212116

Ward, S. E., Pennicott, L. E., and Beswick, P. (2015). AMPA receptor-positive allosteric modulators for the treatment of schizophrenia: an overview of recent patent applications. *Future Med. Chem.* 7, 473–491. doi: 10.4155/fmc.15.4

Watson, J. F., Ho, H., and Greger, I. H. (2017). Synaptic transmission and plasticity require AMPA receptor anchoring via its N-terminal domain. *eLife* 6:e23024. doi: 10.7554/eLife.23024

Wei, M., Jia, M., Zhang, J., Yu, L., Zhao, Y., Chen, Y., et al. (2017). The inhibitory effect of alpha/beta-hydrolase domain-containing 6 (ABHD6) on the surface targeting of GluA2- and GluA3-containing AMPA receptors. *Front. Mol. Neurosci.* 10:55. doi: 10.3389/fnmol.2017.00055

Wei, M., Zhang, J., Jia, M., Yang, C., Pan, Y., Li, S., et al. (2016). Alpha/beta-Hydrolase domain-containing 6 (ABHD6) negatively regulates the surface delivery and synaptic function of AMPA receptors. *Proc. Natl. Acad. Sci. U.S.A.* 113, E2695–E2704.

Wenthold, R. J., Petralia, R. S., Blahos, J. II, and Niedzielski, A. S. (1996). Evidence for multiple AMPA receptor complexes in hippocampal CA1/CA2 neurons. *J. Neurosci.* 16, 1982–1989. doi: 10.1523/jneurosci.16-06-01982.1996

Whitehead, G., Regan, P., Whitcomb, D. J., and Cho, K. (2017). Ca(2+)-permeable AMPA receptor: a new perspective on amyloid-beta mediated pathophysiology of Alzheimer's disease. *Neuropharmacology* 112, 221–227. doi: 10.1016/j.neuropharm.2016.08.022

Wu, B., Wang, Y. M., Xiong, W., Zheng, L. H., Fu, C. L., Bruce, I. C., et al. (2005). Optimization of a multi-channel puffer system for rapid delivery of solutions during patch-clamp experiments. *Front. Biosci.Landmrk* 10:761–767. doi: 10.2741/1570

Wu, T. Y., Liu, C. I., and Chang, Y. C. (1996). A study of the oligomeric state of the alpha-amino-3-hydroxy-5-methyl-4-isoxazolepropionic acid-preferring glutamate receptors in the synaptic junctions of porcine brain. *Biochem. J.* 319(Pt 3), 731–739. doi: 10.1042/bj3190731

Xia, H., von Zastrow, M., and Malenka, R. C. (2002). A novel anterograde trafficking signal present in the N-terminal extracellular domain of ionotropic glutamate receptors. *J. Biol. Chem.* 277, 47765–47769. doi: 10.1074/jbc.m207122200

Conflict of Interest: The authors declare that the research was conducted in the absence of any commercial or financial relationships that could be construed as a potential conflict of interest.

frontiers
in Cell and Developmental Biology

ORIGINAL RESEARCH
published: 04 November 2020
doi: 10.3389/fcell.2020.591781

p.His16Arg of STXBP1 (MUNC18-1) Associated With Syntaxin 3B Causes Autosomal Dominant Congenital Nystagmus

Yulei Li[1,2†], Lei Jiang[1†], Lejin Wang[3], Cheng Wang[1], Chunjie Liu[1], Anyuan Guo[1], Mugen Liu[1], Luoying Zhang[1], Cong Ma[1], Xianqin Zhang[1*], Shangbang Gao[1] and Jing Yu Liu[4*]

[1] Key Laboratory of Molecular Biophysics of the Ministry of Education, College of Life Science and Technology, Huazhong University of Science and Technology, Wuhan, China, [2] School of Basic Medical Sciences, Hubei University of Medicine, Shiyan, China, [3] Department of Ophthalmology, Peking University People's Hospital, Beijing, China, [4] Institute of Neuroscience, State Key Laboratory of Neuroscience, CAS Center for Excellence in Brain Science and Intelligence Technology, Chinese Academy of Sciences, Shanghai, China

Edited by:
Mitsuo Tagaya,
Tokyo University of Pharmacy and Life Sciences, Japan

Reviewed by:
Fernando Calahorro,
University of Southampton,
United Kingdom
Shohei Mitani,
Tokyo Women's Medical University,
Japan

***Correspondence:**
Xianqin Zhang
xqzhang04@hust.edu.cn
Jing Yu Liu
liujy@ion.ac.cn

† These authors have contributed equally to this work

Specialty section:
This article was submitted to Membrane Traffic,
a section of the journal
Frontiers in Cell and Developmental Biology

Received: 05 August 2020
Accepted: 15 October 2020
Published: 04 November 2020

Citation:
Li Y, Jiang L, Wang L, Wang C, Liu C, Guo A, Liu M, Zhang L, Ma C, Zhang X, Gao S and Liu JY (2020) p.His16Arg of STXBP1 (MUNC18-1) Associated With Syntaxin 3B Causes Autosomal Dominant Congenital Nystagmus. Front. Cell Dev. Biol. 8:591781. doi: 10.3389/fcell.2020.591781

Congenital nystagmus (CN) is an ocular movement disorder manifested as involuntary conjugated binocular oscillation and usually occurs in early infancy. The pathological mechanism underlying CN is still poorly understood. We mapped a novel genetic locus 9q33.1-q34.2 in a larger Chinese family with autosomal dominant CN and identified a variant (c.47A>G/p.His16Arg) of *STXBP1* by exome sequencing, which fully co-segregated with the nystagmus phenotype in this family and was absent in 571 healthy unrelated individuals. The *STXBP1* encodes syntaxin binding protein 1 (also known as MUNC18-1), which plays a pivotal role in neurotransmitter release. In *unc-18* (nematode homolog of *MUNC18-1*) null *Caenorhabditis elegans*, we found that the p.His16Arg exhibits a compromised ability to rescue the locomotion defect and aldicarb sensitivity, indicating a functional defect in neurotransmitter release. In addition, we also found an enhanced binding of the p.His16Arg mutant to syntaxin 3B, which is a homolog of syntaxin 1A and specifically located in retinal ribbon synapses. We hypothesize that the variant p.His16Arg of STXBP1 is likely to affect neurotransmitter release in the retina, which may be the underlying etiology of CN in this family. Our results provide a new perspective on understanding the molecular mechanism of CN.

Keywords: autosomal dominant congenital nystagmus, STXBP1/MUNC18-1, syntaxin 3B, *Caenorhabditis elegans*, neurotransmitter release

INTRODUCTION

Congenital nystagmus (CN, OMIM 310700) is the involuntary oscillation of eyes, a common ocular disorder usually accompanied by reduced visual acuity, head nodding, strabismus and abnormal head position (Liu et al., 2007). It appears at birth or within the first few months of life, and often occurs in isolation or coupled with other visual diseases such as albinism, congenital cataracts, aniridia, or optic nerve hypoplasia (Gottlob and Proudlock, 2014). The directions of eye oscillations include horizontal, vertical, rotatory, or combinations of these directions, with horizontal being the most common. The prevalence of all forms of CN is estimated to be 0.14% in Western countries (Sarvananthan et al., 2009), while it is 0.025% in Chinese population (Hu, 1987). It is worth noting that CN is often recognized as a unique phenotype of patients with congenital stationary night blindness (CSNB) and foveal hypoplasia due to the lack of visual electrophysiological and optical coherence tomography (OCT) examinations (Roussi et al., 2011; Thomas et al., 2014).

The models of inheritance for CN are autosomal dominant, autosomal recessive, X-linked dominant and X-linked recessive. Of these, X-linked inheritance is the most common form. Up to now, three loci for X-linked CN have been mapped to Xq26.3-q27.1 (NYS1, OMIM 310700) (Kerrison et al., 1999), Xp11.4-p11.3 (NYS5, OMIM 300589) (Cabot et al., 1999) and Xp22 (NYS6, OMIM 300814) (Liu et al., 2007), and four loci for autosomal dominant congenital nystagmus (AD-CN) have been identified on 6p12 (NYS2, OMIM 164100) (Kerrison et al., 1996), 7p11.2 (NYS3, OMIM 608345) (Klein et al., 1998), 13q31-q33 (NYS4, OMIM 193003) (Ragge et al., 2003) and 1q31.3-q32.1 (NYS7, OMIM 614826) (Xiao et al., 2012). So far, only four pathogenic genes of CN have been identified. *FRMD7* (OMIM 300628) has been linked to NYS1 (Tarpey et al., 2006), and *GRP143* (OMIM 300808) has been associated to NYS6 (Liu et al., 2007). Recently, mutations in *MANBA* (OMIM 609489) and *AHR* (OMIM 600253) has been reported to cause autosomal dominant CN (Yu et al., 2015) and autosomal recessive CN (Mayer et al., 2019), respectively. Furthermore, structural variations in a non-coding region within the NYS7 locus have been linked to autosomal dominant CN (Sun et al., 2020). However, the role of these genes in CN is still largely unknown. Although several hypotheses have been proposed to elucidate the neurological mechanisms underlying CN, there is still no consensus on the pathogenesis of CN. Therefore, identification of more pathogenic genes and further exploration of their physiological function will advance our understanding of the etiology and pathogenesis of nystagmus.

STXBP1 (OMIM 602926) encodes syntaxin binding protein 1, commonly known as MUNC18-1, which plays a critical role in neurotransmitter release (Ma et al., 2013). Pathogenic variants in *STXBP1* have been reported to be mainly involved in epileptic encephalopathy, early infantile, 4 (EIEE4, OMIM 612164) with or without nystagmus (Saitsu et al., 2008; Stamberger et al., 2016). The interactions between MUNC18-1 and different syntaxin proteins are essential for membrane fusion and neurotransmitter release in various tissues. Syntaxin 1B is a syntaxin protein mostly expressed in central nervous system and pathogenic variants in which cause generalized epilepsy with febrile seizures plus, type 9 (OMIM 616172), with nystagmus symptom was noted in some patients (Vlaskamp et al., 2016). Epithelial cells and nervous system expressed *STX3* (OMIM 600876) has recently been reported as the pathogenic gene of microvillus inclusion disease (MVID) with or without nystagmus (Julia et al., 2019). Furthermore, gabapentin (analog of inhibitory neurotransmitter gamma-aminobutyric acid) and memantine (antagonist of excitatory neurotransmitters) were reported as effective drugs for the treatment of CN (McLean et al., 2007). These studies raised the question whether synaptic transmission plays a pivotal role in the pathogenesis of CN.

In this study, we mapped a novel genetic locus 9q31.3-q34.2 of AD-CN and identified a variant (c.47A>G/p.His16Arg) of *STXBP1* in a large Chinese family with CN and visual electrophysiological abnormalities. We found that the p.His16Arg mutant results in reduced locomotion and aldicarb sensitivity in *unc-18* (nematode homolog of *MUNC18-1*) null *Caenorhabditis elegans*, and exhibits a stronger binding to syntaxin 3B. We hypothesize that the variant p.His16Arg of MUNC18-1 may affect neurotransmitter secretion in the retina, which is the underlying etiology of CN. Our findings provide a new perspective on the significance of synaptic transmission underlying the pathological mechanism of nystagmus.

MATERIALS AND METHODS

Patients and Genomic DNA Extraction

A large Chinese family from Ningxia Autonomous Region with CN was identified and characterized at Peking University People's Hospital. The study was approved by the ethics committee of Huazhong University of Science and Technology (Wuhan, China) and conformed to the Declaration of Helsinki. Informed consents and 5 ml peripheral blood samples were obtained from eight affected and fifteen unaffected family members. Genomic DNA was extracted according to standard procedures using the Promega Wizard Genomic DNA Purification Kit (Promega, United States).

Linkage and Genotyping Analysis

Genome-wide linkage scan of this family was carried out with 382 fluorescent microsatellite markers from ABI Mapping Panel MD-10 (Applied Biosystems, United States). Microsatellite markers were genotyped using an ABI 3730 Genetic Analyzer (Applied Biosystems, United States). Genotypes were analyzed by the GeneMapper 2 Software (Applied Biosystems, United States). Two-point linkage analysis was performed as previously described (Dai et al., 2008). Microsatellite markers for fine mapping on chromosome 9 were obtained from the Marshfield Clinic Medical Genetics database.

Exome Sequencing and Sanger Sequencing

Exome sequencing was conducted by BGI Genomics (BGI, China). Detail methods were described previously (Zhang et al., 2013). The variants of candidate genes were verified by Sanger sequencing. Primers used to identify and analyze the *STXBP1* variant are listed in **Supplementary Table S2**.

Restriction Fragment Length Polymorphism (RFLP) Analysis

The c.47A>G variant of *STXBP1* would result in a loss of the *Nsi*I restriction site. Therefore, PCR primers designed for RFLP analysis are listed in **Supplementary Table S3**. The PCR products were digested with *Nsi*I (New England Biolabs, United States) overnight at 37°C and separated on 2% agarose gels to classify the wild-type and mutant alleles.

RT-PCR and Plasmid Construction

Total RNA was isolated from SH-SY5Y cell line or mouse tissue or worms with TRIzol reagent (Invitrogen, United States) according to the manufacturer's protocol. cDNA was generated using the M-MLV RT-PCR kit (Invitrogen, United States) with 1 μg of total RNA from each sample. Expression of mRNA in worms was analyzed with ABI 7900HT Real-Time PCR system (Applied Biosystems, United States) using SYBR Green mix (Roche Diagnostics, Germany). Primers used for qRT-PCR are listed in **Supplementary Table S3**.

The full-length coding sequence of human *STXBP1* (ENST00000373299) and *STX3B* (ENST00000633708) were obtained from SH-SY5Y cells cDNA, while the CDS of mouse *Stxbp1* (ENSMUST00000050000) and *Stx3B* (ENSMUST00000047698) were obtained from mouse retina cDNA. All the missense mutants were introduced by Overlap-PCR based on wild-type's sequence.

Cell Culture and Transfection

Neuro-2A cells, SH-SY5Y cells and HeLa cells were cultured in Dulbecco's modified Eagle medium (Gibco, United States) supplemented with 10% fetal bovine serum (Gibco, United States) at 37°C and 5% CO_2. Cells were transiently transfected using Lipofectamine 2000 (Invitrogen, United States) in Opti-MEM I Reduced Serum (Gibco, United States), according to the manufacturer's instructions. After transfection for 24 h or 36 h, cells were harvested for RNA/protein extraction or immunofluorescent labeling.

Western Blot, GST Pull-Down and Co-immunoprecipitation

Western blot, GST pull-down and co-immunoprecipitation assays were performed as previously described (Huang et al., 2015). Flag tagged human MUNC18-1, Flag tagged human syntaxin 1A (STX1A), Flag tagged human syntaxin 3B (STX3B), and Flag tagged mouse syntaxin 3B (Stx3B) were extracted from HeLa cells transfected with corresponding plasmids. GFP tagged human MUNC18-1 and GFP tagged worm UNC-64 were extracted from HeLa cells transfected with corresponding plasmids. GST tagged human MUNC18-1 was extracted from *Escherichia coli* Rosetta strain transformed with human MUNC18-1 cDNA plasmids. Mouse syntaxin 3 (Stx3) was extracted from mouse retina lysate. The primary antibodies were as follows: MUNC18-1 (1:500, mouse monoclonal antibody, BD Biosciences, Canada), Syntaxin 3 (1:1000, rabbit polyclonal antibody, Abcam, United Kingdom), GFP (1:5000, rabbit polyclonal antibody, Proteintech, United States), FLAG (1:5000, mouse monoclonal antibody, MBL, Japan), GPADH (1:3000, mouse monoclonal antibody, Proteintech, United States), GST (1:5000, rabbit polyclonal antibody, ABclonal, United States), beta-actin (1:3000, mouse monoclonal antibody, CST, United States). Quantitative analysis of protein bands was performed by the Image J software[1].

Preparation of Frozen Sections and Immunofluorescent Labeling

The mouse eyes were rapidly enucleated after cardiac perfusion and were incubated immediately in 4% paraformaldehyde for 30 min at room temperature. The eyes were equilibrated in 30% sucrose overnight followed by washing in PBS three times, and then embedded in optical cutting technology freezing medium and fast frozen. Sections were cut on Leica CM1950 cryostat (Leica, Germany) at 10 μm thickness and collected on the gelatin-coated slides.

Immunofluorescence assay was performed as previously described (Liu et al., 2015). The primary antibodies were as follows: MUNC18-1 (1:50, mouse monoclonal antibody, BD Biosciences, Canada), Syntaxin 3 (1:100, rabbit polyclonal antibody, Abcam, United Kingdom), FLAG (1:500, mouse monoclonal antibody, MBL, Japan).

Mice

This study was conducted using adult C57BL/6J mice. All animal procedures were approved by Institutional Animal Care and Use Committee at Huazhong University of Science and Technology.

Worm Assays

N2 (wild-type), CB81 [*unc-18* (*e81*)], CB234 [*unc-18* (*e234*)], NM204 [*snt-1* (*md290*)] and VC223 [*tom-1* (*ok285*)] strains were obtained from the Caenorhabditis Genetics Center (CGC, United States). All the worms were cultured at 22°C as described previously (Brenner, 1974).

Transgenic worms were generated according to the standard microinjection procedures (Mello et al., 1991). Human *STXBP1* cDNA and *C. elegans unc-18* cDNA were cloned into pPD95.75 vector which contains a 2.0 kb promoter of *snb-1* gene and a GFP tag. In co-expression experiments, wild-type human STXBP1 protein was fused with the GFP tag, while the p.His16Arg mutant STXBP1 protein was fused with the RFP tag. Expressing vectors were injected at 50 ng/μl together with P*lin44*::GFP (5 ng/μl) as a co-injection marker. Worms which showed green fluorescence in the neurons and tail (P*lin44*::GFP) were selected and bred into a non-integrated line. In wild-type and p.His16Arg mutant *STXBP1* co-expressing worms, only worms which showed both green and red fluorescence in the neurons were selected. At least five independent non-integrated lines were examined for rescue experiments.

Locomotion behavioral assay was performed as follows. Young adult nematodes were placed on nematode growth medium (NGM) plates contain OP50 *E. coli* lawn. The animals were allowed to rest and adapt to the new NGM plates for 10–15 min before recording. One-minute locomotion of worms was screened under a Zeiss Discovery V8 stereomicroscope (Carl Zeiss MicroImaging Gmbh, Germany), and the image sequences were captured with an Andor iXonEM + DV885K EMCCD

---

[1] http://imagej.nih.gov/ij/

camera (Andor, United Kingdom). The average movement rate (pix/s) were analyzed and calculated with Multi-Worm Tracker software (Swierczek et al., 2011).

Aldicarb stimulation assay was performed as follows. Aldicarb (Sigma Aldrich, United States) was dissolved in 70% ethanol to prepare 100 mM aldicarb stock solution and stored in −20°C. The 0.5 mM aldicarb NGM plates were prepared fresh two days before each experiment for appropriate moisture. Control and rescue lines were examined simultaneously under the same condition. Young adult worms were transferred to the 0.5 mM aldicarb NGM plates seeded with OP50 *E. coli* lawn. Worms were considered paralyzed if they failed to response to the stab of a platinum filament thrice. About 25 worms were picked up to aldicarb containing NGM plates in each individual assay, and the percentage of moving animals was measured every 15 min. The aldicarb stimulation assay was carried out double-blindedly, and was performed by one person for consistent standard of paralyzed worms.

Bioinformatics

The human homolog of mouse syntaxin 3B was searched by ensembl BLAST/BLAT search tool[2]. Protein sequences were aligned with Clustalw2 software[3]. The mouse and human syntaxin 3B protein's sequences were aligned and displayed by using the Boxshade program[4].

Statistical Analyses

All data are represented as the mean ± standard deviation (SD). Comparison of means was performed using SPSS v22 for Windows (IBM, United States) evaluated using unpaired two-tailed *t*-test. The asterisk indicates statistical significance (* means $p < 0.05$, ** means $p < 0.01$, *** means $p < 0.001$).

RESULTS

Clinical Characterization of the Patients With AD-CN

The proband (**Figure 1A**, IV-10) was a 30-year-old male patient who suffered from conjugated pendular nystagmus (**Supplementary Video S1**) accompanied with astigmatism and amblyopia. The nystagmus was intensified when he gazed at objects or followed with eye fatigue, and was diminished when he closed his eyes. His visual acuity of the right eye and left eye was 20/200 and 20/100, respectively. The ocular fundus revealed normal appearance of the optic nerve heads, blood vessel arrangement and retina pigmentation (**Figure 1B**). The well-formed fovea was shown by OCT (**Figure 1C**). The vestibular function of the proband was normal, with no photophobia, night blindness, color blindness or neurological symptoms observed (data not shown). Binocular flash electroretinograms (fERG) revealed that b wave is ahead with lower amplitude (**Figure 1D**). Pattern visual evoked potential (PVEP) showed delayed latency with low amplitude of P100 wave in the right optic nerve and shortened latency with low amplitude of P100 wave in the left optic nerve (**Figure 1E**).

Patient III-4 suffered from rotary nystagmus (**Supplementary Video S2**), and his visual acuity was 20/100 in both eyes. Patient III-6 showed horizontals jerk nystagmus (**Supplementary Video S3**) with orbicularis oculi muscle spasm, and patient III-8 had jerk horizontal nystagmus (**Supplementary Video S4**) with astigmatism and poor binocular visual acuity. Both eyes of patient IV-8 exhibited major jerk nystagmus (**Supplementary Video S5**) with restricted abduction of the right eye, and the visual acuity of both eyes were 20/200. Patient IV-14 displayed mixed pattern nystagmus (**Supplementary Video S6**) with low amplitude, poor binocular visual acuity and astigmatism. Patient V-3 exhibited pendular nystagmus (**Supplementary Video S7**) and poor binocular visual acuity. No patient showed progressive visual loss or aggravated oscillation of the eyes in the family, and no other ophthalmological or neurological abnormalities were observed.

Mapping of a Novel Genetic Locus for AD-CN on Chromosome 9q33.1-q34.2

At present, four genetic loci of AD-CN (6p12, 7p11.2, 13q31-q33, and 1q31.3-q32.1) have been reported. We therefore firstly genotyped the Chinese AD-CN family with twenty-one markers flanking above known AD-CN genetic loci. Linkage analysis showed negative LOD (log of the odds ratio) scores at a recombination fraction of zero for all twenty-one markers (data not shown), thus excluded the four known AD-CN loci. Recently, pathogenic variants of *MANBA* associated with AD-CN have been reported (Yu et al., 2015), so we performed direct sequencing analysis of *MANBA* gene in the proband, but no pathogenic variant was found.

To identify the pathogenic gene responsible for the Chinese family with AD-CN, we next undertook a genome-wide linkage scan with microsatellite markers in the family (including 8 patients and 15 unaffected individuals) as well as follow-up fine mapping. Our results showed a positive linkage with markers (*D9S1872, D9S1116, D9S1823, D9S1682, D9S290, D9S752, D9S1831,* and *D9S1861*) on chromosome 9 (**Figure 1A**). The LOD scores for the markers in chromosome 9 are shown in **Supplementary Table S1**. Patients IV-4 and V-3 displayed recombination events between markers *D9S1776* and *D9S1872*. Patients IV-4, V-3 and normal individual IV-12 showed recombination events between markers *D9S1861* and *D9S164*. Four markers (*D9S1872, D9S1116, D9S290,* and *D9S752*) generated LOD scores greater than 3, the cut-off LOD score for significant linkage. These results suggest that the gene responsible for AD-CN in this family lies between *D9S1776* and *D9S164* on chromosome 9q33.1-q34.2, a genomic region of 18.3 Mb (**Figure 1F**).

Identification of a Novel Variant c.47A>G/p.His16Arg of STXBP1 Responsible for AD-CN

The mapped interval spans 18.3 Mb and contains 202 protein-coding genes. Three genes involved in neural development and

---

[2] http://asia.ensembl.org/Multi/Tools/Blast?db=core

[3] http://www.ebi.ac.uk/Tools/msa/clustalw2

[4] https://embnet.vital-it.ch/software/BOX_form.html

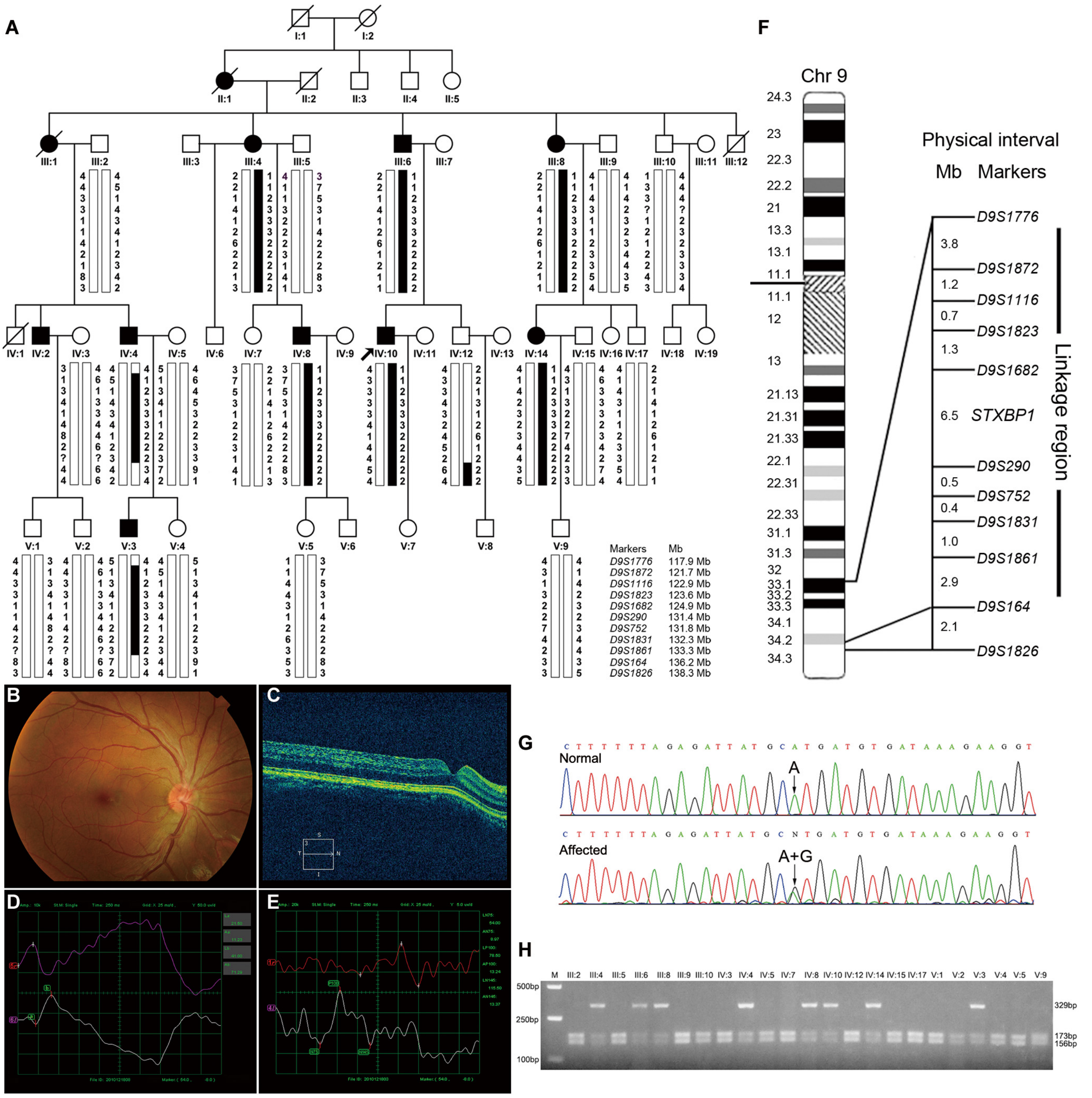

FIGURE 1 | Pedigree structure, clinical characteristics of the index case, genotypic analysis, diagram of chromosome 9, identification of *STXBP1* variant and RFLP analysis of the AD-CN family. **(A)** The pedigree structure and microsatellite haplotype analysis of the Chinese family with AD-CN. Individuals with CN are indicated by solid squares (males) or solid circles (females). Unaffected individuals are indicated by open symbols. Deceased individuals are indicated by slashes (/). The proband is indicated by an arrow. The disease haplotype is shown in black vertical bar; the variants of eight microsatellite markers (*D9S1872*, *D9S1116*, *D9S1823*, *D9S1862*, *D9S290*, *D9S752*, *D9S1831,* and *D9S1861*) are co-segregated with the clinical manifestation in the family. **(B,C)** Normal fundus **(B)** and normal foveal **(C)** of the proband. **(D)** The flash electroretinogram (fERG) of the proband. Both eyes show shortened latency and decreased amplitude of b-wave. The b-wave latency of right eye and left eye are 18.5 ms and 41.0 ms, respectively. The amplitudes of b-wave of right eye and left eye are 52.25 µV and 71.29 µV, respectively. **(E)** The pattern visual evoked potential (PVEP) of the proband. The amplitude of P100 wave in both eyes was decreased. The right eye shows a delayed latency of P100 wave, while the left eye shows a shortened latency of P100 wave. The amplitudes of P100 wave of right eye and left eye are 7.71 µV and 13.24 µV, respectively. The latency of P100 wave of right eye and left eye are 154 ms and 78.5 ms, respectively. **(F)** The linkage interval and flanking microsatellite markers are indicated. **(G)** DNA sequencing chromatograms show the heterozygous variant in *STXBP1* identified in this study. **(H)** The *Nsi*I restriction analysis showing full segregation of the c.47A>G variant with the disease phenotype in the family.

regulation of neural activity, *LHX2* (OMIM 603759), *LHX6* (OMIM 608215) and *FREQ* (OMIM 603315), were directly sequenced in the proband but failed to identify a pathogenic variant responsible for CN. To identify the pathogenic variants, genomic DNA from the proband was sent to BGI Genomics for exome sequencing. The summary of exome sequencing data is shown in **Supplementary Table S4**. Non-synonymous, splicing and indel variants with a minor allele frequency no more than 0.01 were filtered against dbSNP and gnomAD databases to exclude polymorphisms. Direct Sanger sequencing was performed on the exons of low coverage in the linked region (**Supplementary Table S5**), and the variants detected in the interval are listed in **Supplementary Table S6**.

After detailed analysis of all variants within the linked interval, a variant (c.47A > G) in *STXBP1* was identified (**Figure 1G**). This variant is predicted to result in a histidine to arginine substitution at amino acid residue 16 (p.His16Arg) located in domain 1 of STXBP1 (**Supplementary Figure S1A**). PCR-RFLP assay revealed that this variant fully segregated with the nystagmus phenotype in the family (**Figure 1H**), but was not found in 571 unrelated healthy Chinese Han individuals (data not shown). It is noteworthy that the variant c.47A>G is a polymorphism (rs571127140) in dbSNP database. Further analysis showed that such a polymorphism arises from Genome Aggregation Database (gnomAD), and its allele frequency is 1/251,356 in the database. The variation carrier came from the Human Genome Diversity Panel (HGDP), an anonymous collection of globally diverse DNA samples gathered many years ago (personal communication with the variation submitter), which cannot be traced at present, and it is impossible to ascertain whether the variation carrier was affected by CN. The p.His16Arg variant was predicted to be deleterious by MutationTaster (score at 29) and CADD (score at 23.2), demonstrating an evolutionally conserved His16 residue of MUNC18-1 from *Xenopus tropicalis* to *Homo sapiens* (**Supplementary Figure S1B**).

The Variant p.His16Arg of MUNC18-1 Impairs Neurotransmitter Release in *C. elegans*

STXBP1 encodes the syntaxin binding protein 1 MUNC18-1, pathogenic variants of which has been reported to be associated with EIEE4 (Saitsu et al., 2008). MUNC18-1 plays a pivotal role in soluble *N*-ethyl maleimide sensitive-factor attachment protein receptors attachment protein receptor (SNARE) complex assembly and synaptic transmission (Sudhof and Rizo, 2011; Ma et al., 2013). To analyze whether p.His16Arg affects the function of MUNC18-1 in neurotransmitter release (especially the excitatory neurotransmitter acetylcholine at neuromuscular junction), we set out to test this using *C. elegans* as a model organism, as there are high sequence conservation and functional homology between *C. elegans* UNC-18 and human MUNC18-1 (hMUNC18-1) proteins (The human MUNC18-1 protein shared an identity of 59% and a positivity of 75% with the *C. elegans* UNC-18 protein, while the corresponding position of human MUNC18-1 protein His16 residue in *C. elegans* UNC-18 protein is Asn13, which were showed in **Supplementary Figure S2**), and as that simple behavioral assays of *C. elegans* have facilitated the research of proteins involved in synaptic function (Gengyo-Ando et al., 1996). Our data revealed that the *unc-18* deficient worms exhibit severe uncoordination (**Figures 2A,B,G**), which is similar to the previous report (Weimer et al., 2003). *e81* worms expressing the *C. elegans* autologous *unc-18* showed similar locomotion rate as wild-type (N2) worms (**Figure 2A,C,G**), demonstrating a reliable approach. Both hMUNC18-1 WT and p.His16Arg mutant can partially rescue the locomotion defect of *e81* null worms, but the *e81* worms which expressing p.His16Arg mutant showed a weaker locomotion than those expressing WT (**Figures 2B,D,E,G**). We also conducted the locomotion assays in *e81* worms co-expressing wild-type hMUNC18-1 and p.His16Arg mutant at a 1:1 ratio. These worms exhibited a similar motor ability as *e81* worms expressing only the wild-type hMUNC18-1 (**Figures 2D,F,G**).The movements of individual worm in each strain (including N2, *e81*, *e81* + *unc-18*, *e81* + hMUNC18-1-WT, *e81* + hMUNC18-1-H16R and *e81* + hMUNC18-1-WT + hMUNC18-1-H16R) were recorded as shown in **Supplementary Videos S8–13**. Similar results were found in *e234* worms rescued by MUNC18-1 WT and p.His16Arg mutant (**Supplementary Figures S3A–E**). These findings suggest a potential effect of p.His16Arg mutant on synaptic function.

Exposing worms to aldicarb (acetylcholinesterase inhibitor) causes paralysis, due to the inability to turn off acetylcholine signaling at the neuromuscular junction which leads to hypercontraction (Mahoney et al., 2006). The hMUNC18-1 WT transgenic worms showed higher aldicarb sensitivity than p.His16Arg mutant expressing worms at 180 min (**Figures 2H,I**). *e81* worms co-expressing wild-type and p.His16Arg hMUNC18-1 showed no obvious difference on aldicarb resistance compared to *e81* worms expressing only the wild-type hMUNC18-1 (**Figures 2H,I**). Moreover, we obtained similar results when using *e234* worms. The only difference is that the p.His16Arg mutant transgenic *e234* worms have no obviously enhanced aldicarb sensitivity compared with *e234* worms (**Supplementary Figures S3F,G**). These data suggested that the p.His16Arg mutant might cause a decrease in the total amounts of acetylcholine release in *C. elegans*.

By q-PCR and Western blot assays, we observed hMUNC18-1 WT and p.His16Arg mutant exhibited similar expression levels of mRNA and protein in transgenic *e81* worms (**Figures 3A–C**), suggesting that the different ability to rescue locomotion defect and aldicarb resistance in *e81* worms are unrelated to hMUNC18-1 expression level.

To elucidate the potential molecular mechanism by which p.His16Arg mutant affects the acetylcholine release at neuromuscular junction in worms, we next explored whether this mutant alters the interaction with UNC-64 (the *C. elegans* homolog of human syntaxin), as the change of binding affinity between UNC-18 and UNC-64 often impacts neuronal exocytosis in *C. elegans*. Interestingly, co-immunoprecipitation assay showed a slightly enhanced interaction of MUNC18-1 p.His16Arg with UNC-64 in comparison with WT (**Figures 3D,E**). Based on these findings, we speculate that p.His16Arg compromises the ability of MUNC18-1 to rescue the

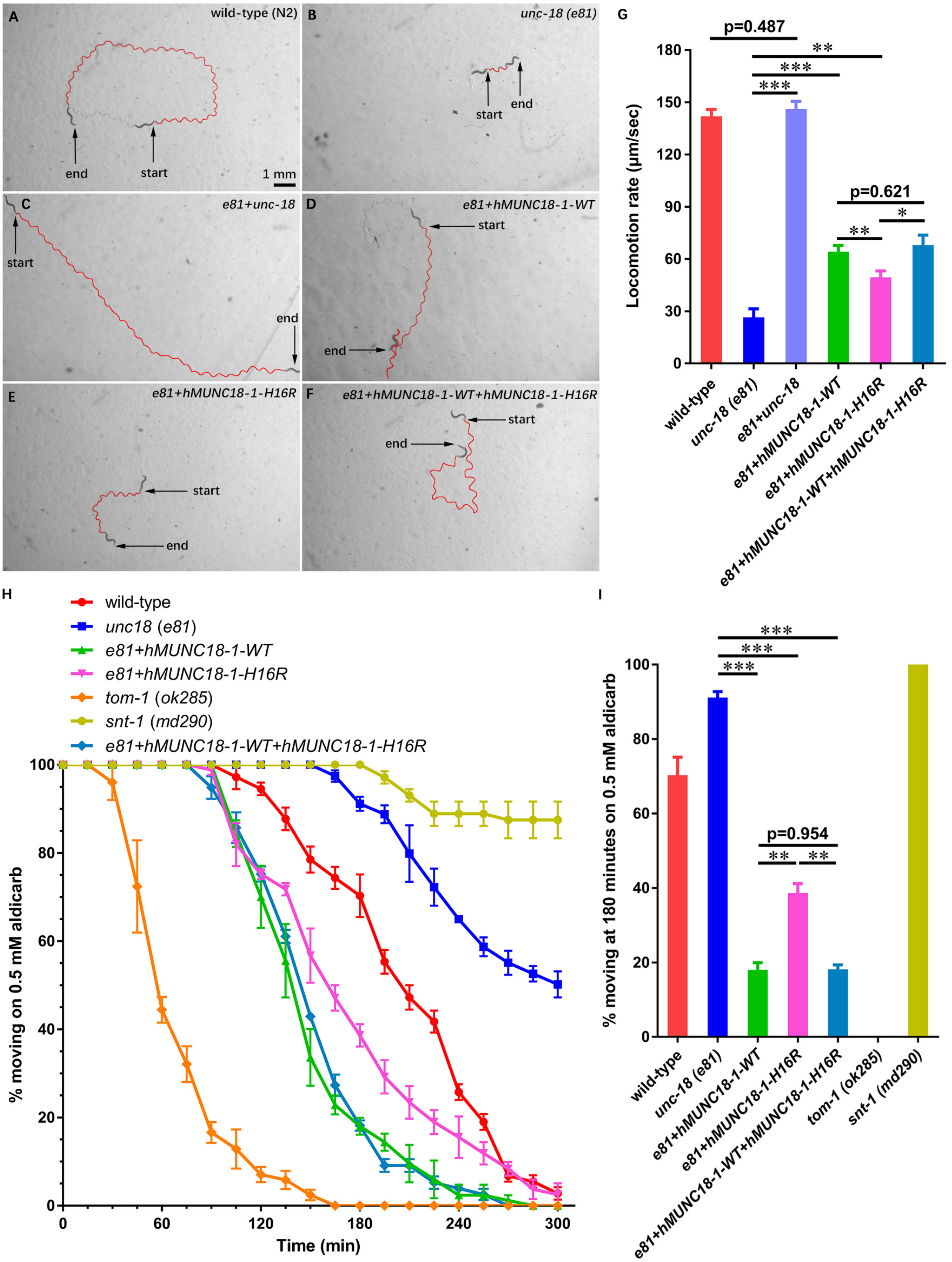

FIGURE 2 | Human MUNC18-1 transgenic *unc-18* (*e81*) *C. elegans* altered their locomotion and aldicarb resistance. **(A–F)** The locomotion trail of wild-type **(A)**, *unc-18* (*e81*) **(B)**, *e81* + *unc-18* **(C),** *e81* + *hMUNC18-1*-WT **(D),** *e81* + *hMUNC18-1*-H16R **(E)** and *e81* + *hMUNC18-1*-WT + *hMUNC18-1*-H16R **(F)** worms on NGM plate in 1 min. The traces of worms' locomotion in 1 min are outlined in red, start and end represent the start and end position of individual worm in 1-min recording, respectively. **(G)** The average locomotion rate (μm/sec) of wild-type (n = 16), *unc-18* (*e81*) (n = 15), *e81* + *unc-18* (n = 17), *e81* + *hMUNC18-1*-WT (n = 33), *e81* + *hMUNC18-1*-H16R (n = 35), and *e81* + *hMUNC18-1*-WT + *hMUNC18-1*-H16R (n = 19) strains. * means $p < 0.05$, ** means $p < 0.01$, *** means $p < 0.001$. **(H)** The paralysis time-course of *unc-18* (*e81*), *e81* + *unc-18, e81* + *hMUNC18-1*-WT, *e81* + *hMUNC18-1*-H16R and *e81* + *hMUNC18-1*-WT + *hMUNC18-1*-H16R worms on NGM plate containing 0.5 mM aldicarb (n = 3 repeats). *tom-1* (*ok285*) strain and *snt-1* (*md290*) strain are used as hypersensitivity control and super-resistance control, respectively. **(I)** The survival ratio of 7 worm strains on NGM plate containing 0.5 mM aldicarb at 180 min (n = 3 repeats), ** means $p < 0.01$, *** means $p < 0.001$.

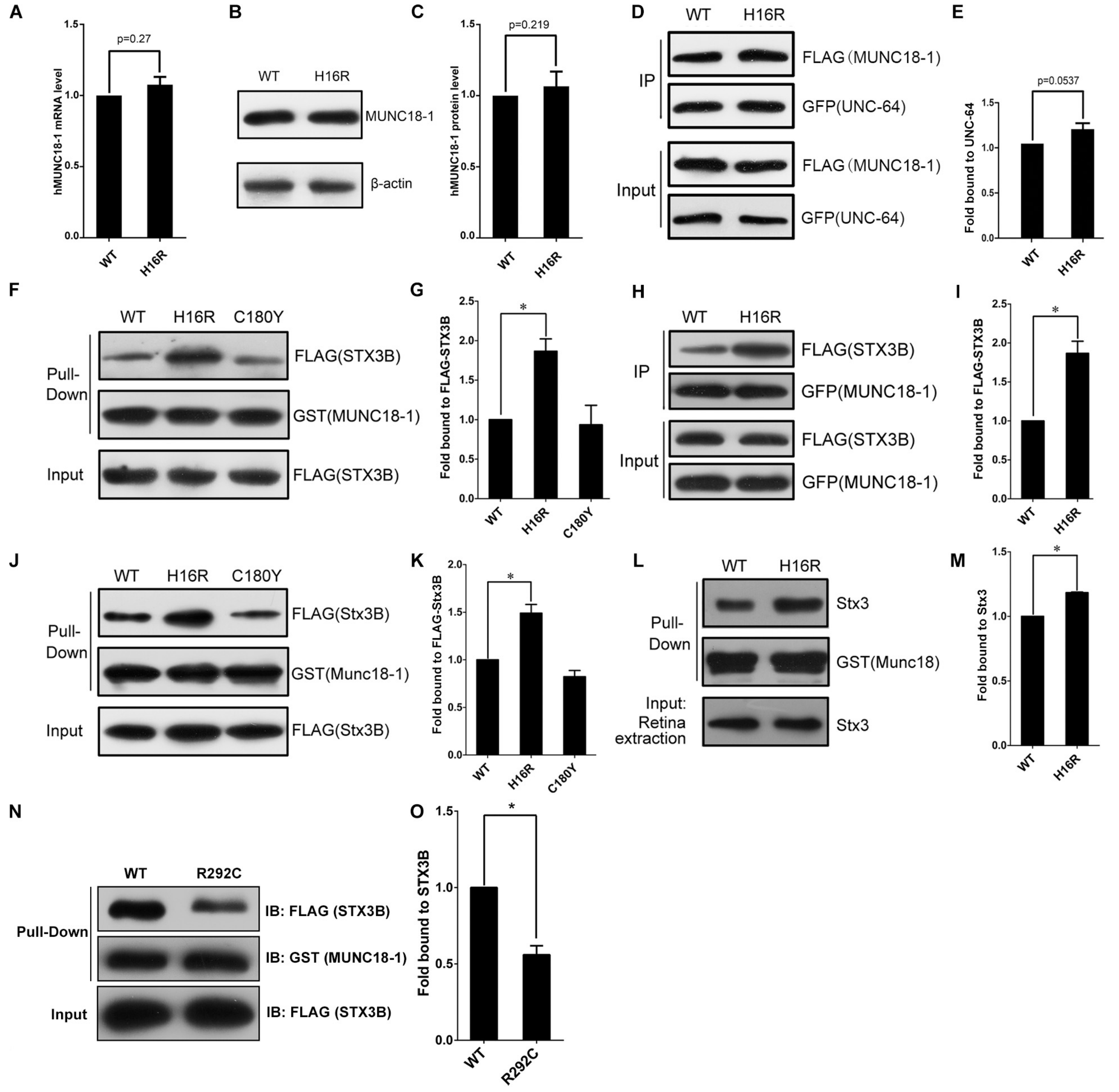

FIGURE 3 | The MUNC18-1 p.His16Arg mutant shows altered interaction with human and mouse syntaxin 3. **(A)** Wild-type and p.His16Arg mutant hMUNC18-1 transgenic *e81* worms show similar *hMUNC18-1* mRNA expression levels detected by RT-qPCR ($n = 3$, $p = 0.27$). **(B,C)** Western blot demonstrates similar levels of WT and p.His16Arg mutant hMUNC18-1-GFP fusion protein in transgenic *e81* worms ($n = 3$, $p = 0.219$). **(D,E)** Co-immunoprecipitation assay of FLAG-tagged WT and mutant MUNC18-1 with GFP-fused UNC-64, p.His16Arg mutant protein shows slight enhanced binding of to UNC-64 compared with WT ($n = 5$, $p = 0.0537$). The data are represented as the mean ± SD. Statistical significance was evaluated using two-tailed *t*-test. **(F,G)** GST pull-down assay of GST-tagged wild-type and mutant MUNC18-1 with the FLAG-tagged human STX3B. The p.His16Arg mutant exhibits obviously enhanced affinity for STX3B compared with WT, while the p.C180Y mutant shows similar affinity compared with WT. The experiments were repeated 3 times independently, * means $p < 0.05$. **(H,I)** GFP tagged wild-type and p.His16Arg mutant MUNC18-1 were co-transfected into HeLa cells with FLAG-tagged human STX3B. Cell extracts were immunoprecipitated with anti-GFP antibody and analyzed by immunoblotting with anti-FLAG antibody. The p.His16Arg mutant shows overt intensive interaction with human STX3B compared with WT. The assays were repeated 3 times independently, * means $p < 0.05$. **(J,L)** GST pull-down assay of GST-tagged mouse WT and mutant Munc18-1 with the FLAG-tagged mouse Stx3B or endogenous Stx3 (mouse retina extracts). **(K,M)** Quantitative analysis of the interaction between GST-Munc18-1 and FLAG-Stx3B or endogenous Stx3 based on the data shown in **(J,L)**, respectively, * means $p < 0.05$. **(N,O)** GST pull-down assays show that p.R292C mutant which cause EIEE4 associated with nystagmus exhibits decreased binding affinity to the FLAG-STX3B fusion protein compared to wild-type MUNC18-1, the assays were repeated 3 times independently, * means $p < 0.05$.

defects of locomotion and neurotransmitter release in *C. elegans* due to its slightly enhanced interaction with UNC-64.

The Variant p.His16Arg of MUNC18-1 Enhances the Interaction With Syntaxin 3B but Not Syntaxin 1A

Since there is a slightly enhanced interaction of MUNC18-1 p.His16Arg with UNC-64, we are interested in knowing whether this mutant affects the interaction with syntaxin 1A (encoded by *STX1A*, OMIM 186590), because it will help us to determine whether p.His16Arg mutant exerts an effect on synaptic vesicle secretion in mammalian cells (Han et al., 2011). The result showed that the p.His16Arg mutant does not affect interaction with the 'closed' or 'open' STX1A (**Supplementary Figures S4A–H**). We used the p.Cys180Tyr of MUNC18-1 (a pathogenic variant resulting in EIEE4) as a control and found that it showed a weak affinity to bind with the open form of STX1A (**Supplementary Figures S4A,B,E,F**), which is consistent with a previous report (Saitsu et al., 2008).

The attenuated amplitudes of b-wave of fERG and P100 wave of PVEP of the proband suggests a defect of neuronal signal transduction in the retina, therefore we focus on anther protein, syntaxin 3B (encoded by *STX3*), validated as the specific SNARE molecule responsible for the exocytosis of synaptic vesicles at ribbon synapses of the rodent and goldfish retina (Curtis et al., 2010). Since the research into the human homolog of mouse syntaxin 3B has not been reported, we first aligned the mouse Stx3B to human protein database and identified an alternative transcript of human syntaxin 3 (STX3B) with 99% identity (only three amino acids difference) to mouse Stx3B (**Supplementary Figure S5**). Unexpectedly, we observed an enhanced interaction between the p.His16Arg mutant and STX3B, whereas the p.C180Y mutant showed no effect on this interaction (**Figures 3F–I**). Likewise, we observed similar results by using mouse Munc18-1 (WT and p.His16Arg mutant) and Stx3B (**Figures 3J–M**). Furthermore, we observed significant signals of co-localization of Munc18-1 and Stx3B within the outer plexiform layer (OPL) where ribbon synapses exist, as well as within the inner plexiform layer (IPL) (**Supplementary Figure S6**).

Interestingly, Stamberger et al have reported a mutation c.874C>T/p.Arg292Cys of *STXBP1* to be associated with EIEE4 and rotatory nystagmus (Stamberger et al., 2016). We found that the p.Arg292Cys mutant significantly reduced the binding of MUNC18-1 to syntaxin 3B (**Figures 3N,O**) by GST pull-down assay. Collectively, these findings suggest that the altered interaction between MUNC18-1 and syntaxin 3B may be linked to CN.

DISCUSSION

In this study, we mapped a novel AD-CN genetic locus on 9q33.1-q34.2 in a five-generation Chinese family and identified a variant (c.47A>G/p.His16Arg) of *STXBP1* within this locus. *In vitro* function analysis showed that an obviously enhanced binding of the p.His16Arg mutant to syntaxin 3B, which is a homolog of syntaxin 1A and predominantly expressed in vertebrate retina. *In vivo*, the p.His16Arg mutant exhibits a reduced ability to rescue the locomotion defect and aldicarb sensitivity in *unc-18* (nematode homolog of *STXBP1*) null *C. elegans*.

STXBP1 (MUNC18-1) plays a pivotal role in synaptic vesicle exocytosis and neurotransmitter release (Ma et al., 2013). Pathogenic variants of *STXBP1* have been associated with EIEE4 (also known as Ohtahara syndrome), which is manifested as intractable epilepsy, severe developmental delay and mental retardation (Saitsu et al., 2008; Allen et al., 2016), while nystagmus was noted in a few cases (Stamberger et al., 2016). *STXBP1* heterozygous knockout neurons demonstrated reduced synaptic vesicle release due to haploinsufficiency of *STXBP1* (Patzke et al., 2015). To determine whether this variant has effects on neurotransmitter release, we use *C. elegans* as a model to explore this issue, but the genome-edited knock-in worm cannot be generated due to the low homology at the N-terminal region between STXBP1 and UNC-18 protein. Given the *unc-18* null worms showing uncoordinated locomotion and strong resistance to aldicarb due to the severe synaptic transmission defects (particularly the decreased acetylcholine release) (Weimer et al., 2003), our findings that p.His16Arg could weaken the ability of MUNC18-1 to restore locomotion and sensibility to aldicarb of the *unc-18* null worms suggests a compromised function of this mutant in neurotransmitter release, in particular the mutant might decrease acetylcholine release at neuromuscular junction of *C. elegans* (**Figures 2A–I** and **Supplementary Figures S3A–G**). The homologous protein of human syntaxin 1A in *C. elegans* is UNC-64, which is the main target protein of UNC-18, and UNC-18 regulates *C. elegans* neurotransmitter secretion mainly through interacting with UNC-64 (Ogawa et al., 1998). Besides, the interaction between UNC-18 and UNC-13 or RAB-3 also participates in the regulation of neurotransmitter secretion (Sassa et al., 1999; Johnson et al., 2013). We tested the interaction between STXBP1 and UNC-64 and found that the p.His16Arg mutation slightly enhanced the interaction between STXBP1 and UNC-64 (**Figures 3D,E**). We speculate that there may be other mechanisms leading to the altered neurotransmitter secretion between wild-type and p.His16Arg mutant transgenic *e81* worms, which may involve the interaction with UNC-13 or RAB-3. In addition, the results of nematode behavioral assays using worms that co-express WT and p.His16Arg mutant hMUNC18-1 suggest that the p.His16Arg mutation most likely exerts effect via haploinsufficiency rather than a dominant-negative manner (**Figures 2D,F-I**). It has been reported that the impaired interactions between MUNC18-1 and STX1A inhibit vesicle docking and membrane fusion at conventional synapses (Han et al., 2011; Martin et al., 2014). Previous research (Saitsu et al., 2008) had reported that some EIEE4-causing pathogenic variants of MUNC18-1 impair the ability of the protein to bind to the open form of STX1A rather than the closed form. In our study, the p.His16Arg mutant has little effect on the interaction with either closed or open form of STX1A (**Supplementary Figures S4A–H**), and this helps to explain why all the affected individuals have no other neurological dysfunction such as epilepsy.

The proband showed reduced amplitudes of b-wave of fERG and P100 wave of PVEP (**Figures 1D,E**), suggesting an impaired neural transduction in the retina, which was consistent with the decreased acetylcholine release at the neuromuscular junction of *C. elegans* (**Figures 2A–I** and **Supplementary Figures S3A–G**). There is a specialized type of synapse in photoreceptors and bipolar cells of vertebrate retina, which is known as ribbon synapse (Morgans, 2000). Unlike conventional synapses, the retinal ribbon synapses secrete neurotransmitters continuously, and the mechanism of neurotransmitter release in retinal ribbon synapses differ from that at conventional synapses (Morgans, 2000; Curtis et al., 2010). At conventional synapses, the core SNARE complexes including synaptic vesicle protein synaptobrevin 2/VAMP2, syntaxin 1 and SNAP-25 (Sudhof and Rizo, 2011), while at ribbon synapses, the core SNARE complexes contain syntaxin 3B instead of syntaxin 1A (Curtis et al., 2008, 2010). Recent researches showed that syntaxin 3B is predominantly expressed in the retina and plays a key role in ribbon synaptic vesicle exocytosis (Curtis et al., 2010). Furthermore, pathogenic variant in *STX3* (syntaxin 3) has been demonstrated to be associated with MVID and nystagmus (Julia et al., 2019), suggesting an important role of syntaxin3 in eye movement control, but detailed mechanism is still elusive. Syntaxin 3 has two major splice isoforms, syntaxin 3A (STX3A) and syntaxin 3B (STX3B) (Curtis et al., 2008). Syntaxin 3A was strongly expressed in the kidney but weakly expressed in the retina and brain, while syntaxin 3B showed strong signal in the retina, but weak signal in the cerebrum and cerebellum, and no signal in the kidney. Previous studies showed that syntaxin 3B is the major isoform of syntaxin 3 in the retina (Curtis et al., 2008, 2010), Interestingly, we found a significantly increased affinity of the binding of p.His16Arg mutant to syntaxin 3B (**Figures 3F–M**) and observed a significant co-localization of Munc18-1 and syntaxin 3B in mouse OPL and IPL (**Supplementary Figure S6**). Notably, a MUNC18-1 mutant p.R292C associated with EIEE4 and rotatory nystagmus (Stamberger et al., 2016) showed reduced interaction between MUNC18-1 and STX3B (**Figures 3N,O**). Based on the above, we speculate that the defect in retinal signal transduction may reflect the altered interaction between MUNC18-1 and syntaxin 3B, and this defect results in CN eventually. Further studies will be required to explore the effects of disrupted binding of MUNC18-1 to syntaxin 3B on the assembly of SNARE complexes and neurotransmitters secretion.

Given that the disrupted interaction between p.His16Arg mutant and syntaxin 3B may contribute to the impaired neurotransmission in retina, how the retinal defect in signal transduction causes congenital nystagmus? In fact, a large proportion of cases with congenital nystagmus is associated with various ophthalmology diseases, most of which are attributable to defects in visual signal transduction, such as achromatopsia (Trankner et al., 2004) and congenital amaurosis (Koenekoop, 2004), particularly the nystagmus in patients with congenital stationary night blindness was demonstrated to derive from abnormal nerve conduction in retina (Winkelman et al., 2019). In a previous study, our team also found that the FRMD7 associated CN is most likely caused by abnormal GABAergic synaptic transmission in the retina (Jiang et al., 2020). The impairment of visual transmission at infancy will impair early visual experience. It has been proposed that CN is a developmental process in which abnormal infant visual experience causes an adaptive oculomotor response that leads to nystagmus during a sensitive period of sensorimotor integration (Harris and Berry, 2006; Thomas et al., 2014). Therefore, we propose that, for the patients in this family, the impaired visual transduction since early infancy may cause abnormal visual experience that eventually results in sensorimotor integration defect and the development of nystagmus.

In summary, we identified a novel genetic locus for the AD-CN and demonstrated that the variant c.47A>G/p.His16Arg of *STXBP1*/MUNC18-1 affects neurotransmitter release in *C. elegans* and alters the interaction with syntaxin 3B. We propose that the altered interaction between MUNC18-1 and syntaxin 3B may impair neurotransmitter release at ribbon synapses, eventually leading to the abnormal retinal neurotransmission and nystagmus. Our results provide insights into the role of MUNC18-1-syntaxin 3B interaction in retinal function, and propose retina synaptic transmission as a novel target for treating these eye movement disorders.

DATA AVAILABILITY STATEMENT

The original contributions presented in the study are included in the article/**Supplementary Material**, further inquiries can be directed to the corresponding author/s.

ETHICS STATEMENT

The studies involving human participants were reviewed and approved by the ethics committee of Huazhong University of Science and Technology. Written informed consent to participate in this study was provided by the participants' legal guardian/next of kin. The animal study was reviewed and approved by Institutional Animal Care and Use Committee at Huazhong University of Science and Technology. Written informed consent was obtained from the individual(s), and minor(s)' legal guardian/next of kin, for the publication of any potentially identifiable images or data included in this article.

AUTHOR CONTRIBUTIONS

JYL, XZ, CM, LZ, and SG conceived the study and designed the experiments. JYL and YL obtained financial support. JYL and YL analyzed data and wrote the manuscript. YL and CW carried out the linkage analysis and mutation screening. JYL, YL, CW, and ML supported the genetic analyses. AG and CL performed the bioinformatics analysis. LW was responsible for clinical evaluation and sample collection. LJ and YL conducted the worm tests. LJ conducted the cell culture and transfection. LJ and YL carried out immunoprecipitation, GST pull-down, western blot, immunofluorescence and microscopic analysis. CM and LZ participated in the discussion and revision of the manuscript. All authors contributed to the article and approved the submitted version.

FUNDING

This study was mainly supported by the National Natural Science Foundation of China grants 31671301, 31871262 (JYL), and 31701083 (YL) and by the National Key R&D Program of China (2016YFC1306000) (JYL).

ACKNOWLEDGMENTS

We thank the affected individuals and the family members who participated in the study for their continuous support. We thank Dr. Yin Shen (Department of Ophthalmology, Renmin Hospital of Wuhan University, Wuhan, China) and Dr. Fagang Jiang (Department of Ophthalmology, Union Hospital of HUST, Wuhan, China) for clinical diagnosis to the affected individuals with nystagmus. We thank Dr. Shenglei Feng (School of Life Sciences and Technology, Huazhong University of Science and Technology) for cell culture and Western blot assays and Dr. Hongying Ma (School of Life Sciences and Technology, Huazhong University of Science and Technology) for pathogenic variants screening.

SUPPLEMENTARY MATERIAL

The Supplementary Material for this article can be found online at: https://www.frontiersin.org/articles/10.3389/fcell.2020.591781/full#supplementary-material

REFERENCES

Allen, N. M., Conroy, J., Shahwan, A., Lynch, B., Correa, R. G., Pena, S. D., et al. (2016). Unexplained early onset epileptic encephalopathy: exome screening and phenotype expansion. *Epilepsia* 57, e12–e17. doi: 10.1111/epi.13250

Brenner, S. (1974). The genetics of *Caenorhabditis elegans*. *Genetics* 77, 71–94.

Cabot, A., Rozet, J. M., Gerber, S., Perrault, I., Ducroq, D., Smahi, A., et al. (1999). A gene for X-linked idiopathic congenital nystagmus (NYS1) maps to chromosome Xp11.4-*p*11.3. *Am. J. Hum. Genet.* 64, 1141–1146. doi: 10.1086/302324

Curtis, L., Datta, P., Liu, X., Bogdanova, N., Heidelberger, R., and Janz, R. (2010). Syntaxin 3B is essential for the exocytosis of synaptic vesicles in ribbon synapses of the retina. *Neuroscience* 166, 832–841. doi: 10.1016/j.neuroscience.2009.12.075

Curtis, L. B., Doneske, B., Liu, X., Thaller, C., McNew, J. A., and Janz, R. (2008). Syntaxin 3b is a t-SNARE specific for ribbon synapses of the retina. *J. Comp. Neurol.* 510, 550–559. doi: 10.1002/cne.21806

Dai, X. H., Chen, W. W., Wang, X., Zhu, Q. H., Li, C., Li, L., et al. (2008). A novel genetic locus for familial febrile seizures and epilepsy on chromosome 3q26.2-*q*26.33. *Hum. Genet.* 124, 423–429. doi: 10.1007/s00439-008-0566-9

Gengyo-Ando, K., Kitayama, H., Mukaida, M., and Ikawa, Y. (1996). A murine neural-specific homolog corrects cholinergic defects in *Caenorhabditis elegans* unc-18 mutants. *J. Neurosci.* 16, 6695–6702. doi: 10.1523/JNEUROSCI.16-21-06695.1996

Gottlob, I., and Proudlock, F. A. (2014). Aetiology of infantile nystagmus. *Curr. Opin. Neurol.* 27, 83–91. doi: 10.1097/WCO.0000000000000058

Han, G. A., Malintan, N. T., Saw, N. M., Li, L., Han, L., Meunier, F. A., et al. (2011). Munc18-1 domain-1 controls vesicle docking and secretion by interacting with syntaxin-1 and chaperoning it to the plasma membrane. *Mol. Biol. Cell* 22, 4134–4149. doi: 10.1091/mbc.E11-02-0135

Harris, C., and Berry, D. (2006). A developmental model of infantile nystagmus. *Semin. Ophthalmol.* 21, 63–69. doi: 10.1080/08820530600613746

Hu, D. N. (1987). Prevalence and mode of inheritance of major genetic eye diseases in China. *J. Med. Genet.* 24, 584–588. doi: 10.1136/jmg.24.10.584

Huang, M., Li, D., Huang, Y., Cui, X., Liao, S., Wang, J., et al. (2015). HSF4 promotes G1/S arrest in human lens epithelial cells by stabilizing p53. *Biochim. Biophys. Acta Mol. Cell Res.* 1853, 1808–1817. doi: 10.1016/j.bbamcr.2015.04.018

Jiang, L., Li, Y., Yang, K., Wang, Y., Wang, J., Cui, X., et al. (2020). FRMD7 Mutations Disrupt the Interaction with GABRA2 and may result in infantile nystagmus syndrome. *Invest. Ophthalmol. Vis. Sci.* 61:41. doi: 10.1167/iovs.61.5.41

Johnson, J. R., Kashyap, S., Rankin, K., and Barclay, J. W. (2013). Rab-3 and unc-18 interactions in alcohol sensitivity are distinct from synaptic transmission. *PLoS One* 8:e81117. doi: 10.1371/journal.pone.0081117

Julia, J., Shui, V., Mittal, N., Heim-Hall, J., and Blanco, C. L. (2019). Microvillus inclusion disease, a diagnosis to consider when abnormal stools and neurological impairments run together due to a rare syntaxin 3 gene mutation. *J. Neonatal Perinatal Med.* 12, 313–319. doi: 10.3233/npm-1852

Kerrison, J. B., Arnould, V. J., Barmada, M. M., Koenekoop, R. K., Schmeckpeper, B. J., and Maumenee, I. H. (1996). A gene for autosomal dominant congenital nystagmus localizes to 6p12. *Genomics* 33, 523–526. doi: 10.1006/geno.1996.0229

Kerrison, J. B., Vagefi, M. R., Barmada, M. M., and Maumenee, I. H. (1999). Congenital motor nystagmus linked to Xq26-q27. *Am. J. Hum. Genet.* 64, 600–607. doi: 10.1086/302244

Klein, C., Vieregge, P., Heide, W., Kemper, B., Hagedorn-Greiwe, M., Hagenah, J., et al. (1998). Exclusion of chromosome regions 6p12 and 15q11, but not chromosome region 7p11, in a German family with autosomal dominant congenital nystagmus. *Genomics* 54, 176–177. doi: 10.1006/geno.1998.5535

Koenekoop, R. K. (2004). An overview of Leber congenital amaurosis: a model to understand human retinal development. *Surv. Ophthalmol.* 49, 379–398. doi: 10.1016/j.survophthal.2004.04.003

Liu, F., Chen, J., Yu, S., Raghupathy, R. K., Liu, X., Qin, Y., et al. (2015). Knockout of RP2 decreases GRK1 and rod transducin subunits and leads to photoreceptor degeneration in zebrafish. *Hum. Mol. Genet.* 24, 4648–4659. doi: 10.1093/hmg/ddv197

Liu, J. Y., Ren, X., Yang, X., Guo, T., Yao, Q., Li, L., et al. (2007). Identification of a novel GPR143 mutation in a large Chinese family with congenital nystagmus as the most prominent and consistent manifestation. *J. Hum. Genet.* 52, 565–570. doi: 10.1007/s10038-007-0152-3

Ma, C., Su, L., Seven, A. B., Xu, Y., and Rizo, J. (2013). Reconstitution of the vital functions of Munc18 and Munc13 in neurotransmitter release. *Science* 339, 421–425. doi: 10.1126/science.1230473

Mahoney, T. R., Luo, S., and Nonet, M. L. (2006). Analysis of synaptic transmission in *Caenorhabditis elegans* using an aldicarb-sensitivity assay. *Nat. Protoc.* 1, 1772–1777. doi: 10.1038/nprot.2006.281

Martin, S., Papadopulos, A., Tomatis, V. M., Sierecki, E., Malintan, N. T., Gormal, R. S., et al. (2014). Increased polyubiquitination and proteasomal degradation of a Munc18-1 disease-linked mutant causes temperature-sensitive defect in exocytosis. *Cell Rep.* 9, 206–218. doi: 10.1016/j.celrep.2014.08.059

Mayer, A. K., Mahajnah, M., Thomas, M. G., Cohen, Y., Habib, A., Schulze, M., et al. (2019). Homozygous stop mutation in AHR causes autosomal recessive foveal hypoplasia and infantile nystagmus. *Brain* 142, 1528–1534. doi: 10.1093/brain/awz098

McLean, R., Proudlock, F., Thomas, S., Degg, C., and Gottlob, I. (2007). Congenital nystagmus: randomized, controlled, double-masked trial of memantine/gabapentin. *Ann. Neurol.* 61, 130–138. doi: 10.1002/ana.21065

Mello, C. C., Kramer, J. M., Stinchcomb, D., and Ambros, V. (1991). Efficient gene transfer in C.elegans: extrachromosomal maintenance and integration of transforming sequences. *EMBO J.* 10, 3959–3970. doi: 10.1002/j.1460-2075.1991.tb04966.x

Morgans, C. W. (2000). Neurotransmitter release at ribbon synapses in the retina. *Immunol. Cell Biol.* 78, 442–446. doi: 10.1046/j.1440-1711.2000.00923.x

Ogawa, H., Harada, S., Sassa, T., Yamamoto, H., and Hosono, R. (1998). Functional properties of the unc-64 gene encoding a *Caenorhabditis elegans* syntaxin. *J. Biol. Chem.* 273, 2192–2198. doi: 10.1074/jbc.273.4.2192

Patzke, C., Han, Y., Covy, J., Yi, F., Maxeiner, S., Wernig, M., et al. (2015). Analysis of conditional heterozygous STXBP1 mutations in human neurons. *J. Clin. Invest.* 125, 3560–3571. doi: 10.1172/jci78612

Ragge, N. K., Hartley, C., Dearlove, A. M., Walker, J., Russell-Eggitt, I., and Harris, C. M. (2003). Familial vestibulocerebellar disorder maps to chromosome 13q31-q33: a new nystagmus locus. *J. Med. Genet.* 40, 37–41. doi: 10.1136/jmg.40.1.37

Roussi, M., Dalens, H., Marcellier, J. J., and Bacin, F. (2011). Congenital nystagmus and negative electroretinography. *Clin. Ophthalmol.* 5, 429–434. doi: 10.2147/OPTH.S14291

Saitsu, H., Kato, M., Mizuguchi, T., Hamada, K., Osaka, H., Tohyama, J., et al. (2008). De novo mutations in the gene encoding STXBP1 (MUNC18-1) cause early infantile epileptic encephalopathy. *Nat. Genet.* 40, 782–788. doi: 10.1038/ng.150

Sarvananthan, N., Surendran, M., Roberts, E. O., Jain, S., Thomas, S., Shah, N., et al. (2009). The prevalence of nystagmus: the Leicestershire nystagmus survey. *Invest. Ophthalmol. Vis. Sci.* 50, 5201–5206. doi: 10.1167/iovs.09-3486

Sassa, T., Harada, S., Ogawa, H., Rand, J. B., Maruyama, I. N., and Hosono, R. (1999). Regulation of the UNC-18-*Caenorhabditis elegans* syntaxin complex by UNC-13. *J. Neurosci.* 19, 4772–4777. doi: 10.1523/JNEUROSCI.19-12-04772.1999

Stamberger, H., Nikanorova, M., Willemsen, M. H., Accorsi, P., Angriman, M., Baier, H., et al. (2016). STXBP1 encephalopathy: a neurodevelopmental disorder including epilepsy. *Neurology* 86, 954–962. doi: 10.1212/wnl.0000000000002457

Sudhof, T. C., and Rizo, J. (2011). Synaptic vesicle exocytosis. *Cold Spring Harb. Perspect. Biol.* 3:a005637. doi: 10.1101/cshperspect.a005637

Sun, W., Li, S., Jia, X., Wang, P., Hejtmancik, J. F., Xiao, X., et al. (2020). Structural variations in a non-coding region at 1q32.1 are responsible for the NYS7 locus in two large families. *Hum. Genet.* 139, 1057–1064. doi: 10.1007/s00439-020-02156-0

Swierczek, N. A., Giles, A. C., Rankin, C. H., and Kerr, R. A. (2011). High-throughput behavioral analysis in C. elegans. *Nat. Methods* 8, 592–598. doi: 10.1038/nmeth.1625

Tarpey, P., Thomas, S., Sarvananthan, N., Mallya, U., Lisgo, S., Talbot, C. J., et al. (2006). Mutations in FRMD7, a newly identified member of the FERM family, cause X-linked idiopathic congenital nystagmus. *Nat. Genet.* 38, 1242–1244. doi: 10.1038/ng1893

Thomas, M. G., Crosier, M., Lindsay, S., Kumar, A., Araki, M., Leroy, B. P., et al. (2014). Abnormal retinal development associated with FRMD7 mutations. *Hum. Mol. Genet.* 23, 4086–4093. doi: 10.1093/hmg/ddu122

Trankner, D., Jagle, H., Kohl, S., Apfelstedt-Sylla, E., Sharpe, L. T., Kaupp, U. B., et al. (2004). Molecular basis of an inherited form of incomplete achromatopsia. *J. Neurosci.* 24, 138–147. doi: 10.1523/jneurosci.3883-03.2004

Vlaskamp, D. R., Rump, P., Callenbach, P. M., Vos, Y. J., Sikkema-Raddatz, B., van Ravenswaaij-Arts, C. M., et al. (2016). Haploinsufficiency of the STX1B gene is associated with myoclonic astatic epilepsy. *Eur. J. Paediatr. Neurol.* 20, 489–492. doi: 10.1016/j.ejpn.2015.12.014

Weimer, R. M., Richmond, J. E., Davis, W. S., Hadwiger, G., Nonet, M. L., and Jorgensen, E. M. (2003). Defects in synaptic vesicle docking in unc-18 mutants. *Nat. Neurosci.* 6, 1023–1030. doi: 10.1038/nn1118

Winkelman, B. H. J., Howlett, M. H. C., Holzel, M.-B., Joling, C., Fransen, K. H., Pangeni, G., et al. (2019). nystagmus in patients with congenital stationary night blindness (CSNB) originates from synchronously firing retinal ganglion cells. *PLoS Biol.* 17:e3000174. doi: 10.1371/journal.pbio.3000174

Xiao, X., Li, S., Guo, X., and Zhang, Q. (2012). A novel locus for autosomal dominant congenital motor nystagmus mapped to 1q31-q32.2 between *D*1S2816 and D1S2692. *Hum. Genet.* 131, 697–702. doi: 10.1007/s00439-011-1113-7

Yu, P., Cui, Y., Cai, W., Wu, H., Xiao, X., Shao, Q., et al. (2015). Lysosomal storage disease in the brain: mutations of the beta-mannosidase gene identified in autosomal dominant nystagmus. *Genet. Med.* 17, 971–979. doi: 10.1038/gim.2015.10

Zhang, X. Y., Wen, J., Yang, W., Wang, C., Gao, L., Zheng, L. H., et al. (2013). Gain-of-function mutations in SCN11A cause familial episodic pain. *Am. J. Hum. Genet.* 93, 957–966. doi: 10.1016/j.ajhg.2013.09.016

Conflict of Interest: The authors declare that the research was conducted in the absence of any commercial or financial relationships that could be construed as a potential conflict of interest.

frontiers
in Cell and Developmental Biology

ORIGINAL RESEARCH
published: 06 January 2021
doi: 10.3389/fcell.2020.609708

Structural Roles for the Juxtamembrane Linker Region and Transmembrane Region of Synaptobrevin 2 in Membrane Fusion

Yaru Hu, Le Zhu and Cong Ma*

Key Laboratory of Molecular Biophysics of the Ministry of Education, College of Life Science and Technology, Huazhong University of Science and Technology, Wuhan, China

Formation of the *trans*-SNARE complex is believed to generate a force transfer to the membranes to promote membrane fusion, but the underlying mechanism remains elusive. In this study, we show that helix-breaking and/or length-increasing insertions in the juxtamembrane linker region of synaptobrevin-2 exert diverse effects on liposome fusion, in a manner dependent on the insertion position relative to the two conserved tryptophan residues (W^{89}/W^{90}). Helical extension of synaptobrevin-2 to W^{89}/W^{90} is a prerequisite for initiating membrane merger. The transmembrane region of synaptobrevin-2 enables proper localization of W^{89}/W^{90} at the membrane interface to gate force transfer. Besides, our data indicate that the SNARE regulatory components Munc18-1 and Munc13-1 impose liposome fusion strong demand on tight coupling between the SNARE motif and the transmembrane region of synaptobrevin-2.

Keywords: synaptobrevin-2, SNARE complex assembly, membrane fusion, Munc18, Munc13

OPEN ACCESS

Edited by:
Mitsuo Tagaya,
Tokyo University of Pharmacy and Life Sciences, Japan

Reviewed by:
Erdem Karatekin,
Yale University, United States
Christopher Stroupe,
University of Virginia, United States
Binyong Liang,
University of Virginia, United States

***Correspondence:**
Cong Ma
cong.ma@hust.edu.cn

Specialty section:
This article was submitted to Membrane Traffic, a section of the journal Frontiers in Cell and Developmental Biology

Received: *24 September 2020*
Accepted: *09 December 2020*
Published: *06 January 2021*

Citation:
Hu Y, Zhu L and Ma C (2021) Structural Roles for the Juxtamembrane Linker Region and Transmembrane Region of Synaptobrevin 2 in Membrane Fusion. Front. Cell Dev. Biol. 8:609708. doi: 10.3389/fcell.2020.609708

INTRODUCTION

Neurotransmitter release mediated by synaptic exocytosis requires the fusion of synaptic vesicles with the plasma membrane of nerve cells. To accomplish fusion, membranes must overcome the energy barriers created by charge repulsing, local dehydration of polar phospholipid headgroups and membrane deformation. In synaptic exocytosis, the synaptic vesicle SNARE protein synaptobrevin-2 (R-SNARE) assembles with the plasma membrane SNARE proteins SNAP-25 and syntaxin-1 (both referred to as Q-SNAREs) to form the SNARE complex to catalyze the fusion of the two membranes (Südhof and Rizo, 2011; Jahn and Fasshauer, 2012; Han et al., 2017). In addition, a number of accessory proteins are required for the exquisite regulation of SNARE complex formation and SNARE-mediated membrane fusion (Rizo and Xu, 2015; Brunger et al., 2019).

SNARE complex assembly is characterized by the formation of a parallel four-helix bundle composed of four SNARE motifs, with synaptobrevin-2 and syntaxin-1 each contributing one motif whereas SNAP-25 contributes two (Fasshauer et al., 1998; Sutton et al., 1998). In synaptobrevin-2 and syntaxin-1, the SNARE motif is connected by juxtamembrane linker region

(JLR) to C-terminal transmembrane region (TMR) that anchor at the vesicles and the plasma membrane, respectively. SNAP-25 is anchored to the plasma membrane by palmitoyl chains bound to cysteine residues in a loop region connecting its two SNARE motifs. The assembly of a "*trans*" four-helix bundle upon an N- to C-zippering mode releases energy to bring the membranes into close proximity (Chen and Scheller, 2001; Jahn et al., 2003; Sørensen et al., 2006). Subsequent assembly proceeding over the JLR and TMR of synaptobrevin-2 and syntaxin-1 is believed to transmit the energy into the membrane interface, leading to a conversion from the "*trans*" complex into a "*cis*" complex in which the two TMRs are aligned in parallel in the same membrane (Han et al., 2017). This configuration transition is assumed to be functional at the final stage of exocytosis by facilitating membrane deformation and expansion of the fusion pore.

A variety of SNARE-based reconstitution experiments *in vitro* have demonstrated that efficient membrane fusion requires the SNARE motifs to support "*trans*" complex assembly, and the JLRs and TMRs to drive "*cis*" complex formation (Han et al., 2017). A solved crystal structure of the neuronal SNARE complex showed that assembly proceeds over the SNARE four-helix bundle, resulting in a continuous helical bundle extending to the end of the JLRs and TMRs (Stein et al., 2009). This study suggests a helical continuity model in which membrane fusion requires assembly of the SNARE complex all the way into the membranes. Although this model appears to be structurally and energetically attractive, a number of studies have challenged the model. For instance, helix-breaking mutations in the JLRs had little influence on fusion *in vitro* (Mcnew et al., 1999; Van Komen et al., 2005; Pieren et al., 2015) Similarly, a synaptobrevin-2 mutant carrying two helix-disrupting proline residues in the JLR enabled a nearly complete rescue of fusion in chromaffin cells (Kesavan et al., 2007). These results challenged the notion that the helical continuity model underlies the common nature of the general fusion mechanism. On the other hand, increasing length and flexibility of the JLRs by amino acid insertions gradually decrease fusion efficiency but does not eliminate fusion *in vitro* (Mcnew et al., 1999). Strikingly, synaptobrevin-2 with a 12-residue insertion or syntaxin-1 with a 7-residue insertion in the JLR was found to completely restore spontaneous release in cultured neurons (Deak et al., 2006; Zhou et al., 2013). Despite such mild effect on spontaneous fusion, synaptobrevin-2 or syntaxin-1 with a 3-residue (or 4-residue) insertion in the JLR were observed to dramatically reduce the RRP size and Ca^{2+}-evoked exocytosis in cultured neuronal and chromaffin cells (Kesavan et al., 2007; Guzman et al., 2010; Borisovska et al., 2012; Zhou et al., 2013). These data suggest that evoked fusion but not spontaneous fusion requires an extremely tight coupling between the SNARE motifs and the TMRs.

Although early studies have established the essential role of the TMRs in membrane fusion (Giraudo et al., 2005; Hofmann et al., 2006; Chang et al., 2016; Dhara et al., 2016; Chiang et al., 2018), this issue has become controversial. Previous work on yeast vacuolar fusion found that lipid-anchored R-SNARE Nyv1p, which lacks the TMR, supports fusion in the presence of the HOPS tethering complex that includes the Sec1/Munc18 (SM) protein Vps33p (Xu et al., 2011). Similarly, a more recent study on lytic granule exocytosis indicated that the SM protein Munc18-2 can assist lipid-anchored syntaxin-11 (without the TMR) to drive complete membrane fusion (Spessott et al., 2017). Consistent with these observations, it was found that lipid-anchored SNAREs (sytnaxin-1 and synaptobrevin-2) without the TMRs can totally rescue spontaneous and partially rescue Ca^{2+}-evoked release in neurons (Zhou et al., 2013). The dispensable role of the TMR in these studies challenged the helical continuity model, raising a possibility that SNARE complex assembly may be sufficient to destabilize the phospholipid membrane and induce full fusion, in a manner upon forcing the two opposing membrane into close proximity but without a need for the TMR. In this scenario, the contribution of the SNARE regulatory components (e.g., SM proteins and tethering factors that regulate SNARE complex assembly) in facilitating this process has been unclear and need to be investigated.

Indeed, in synaptic exocytosis, SNARE-mediated membrane fusion is highly regulated by the SM protein Munc18-1 and the tethering-related protein Munc13s (Rizo and Xu, 2015; Brunger et al., 2019). A wealth of evidence revealed that Munc18-1 and Munc13s cooperate to promote fusion via chaperoning proper SNARE assembly (Ma et al., 2013; Lai et al., 2017; Wang et al., 2019) and via protecting the assembled SNARE complex against NSF/α-SNAP disassembly (Ma et al., 2013; He et al., 2017; Jakhanwal et al., 2017). Besides, Munc18-1 and Munc13s have been reported to associate with the membranes via their intrinsic membrane-binding sites independent of the existence of the SNAREs (Xu et al., 2011; Quade et al., 2019). Despite these findings, it remains unclear whether Munc18-1 and Munc13s could act as force generators that exert direct force to induce membrane deformation and fusion, in addition to their regulatory role in SNARE complex assembly.

Here, we have systematically investigated the roles of the synaptobrevin-2 JLR and TMR in membrane fusion using *in-vitro* reconstitution systems with and without Munc18-1 and Munc13-1. Our data showed that helical extension of synaptobrevin-2 to the two consecutive tryptophan residues (W^{89}/W^{90}) in the JLR is absolutely required for initiating membrane merger, and helical extension beyond W^{89}/W^{90} is crucial for complete membrane fusion. Membrane-embedded TMR directs W^{89}/W^{90} to position at the membrane-water interface, enabling W^{89}/W^{90} to gate force transfer as a fusion barrier. Besides, our data indicate that Munc18-1 and Munc13-1 impose liposome fusion strong demand on tight coupling between the SNARE motifs and the TMR.

Abbreviations: JLR, Juxtamembrane Linker Region; TMR, transmembrane region; Syb2, Synaptobrevin-2; M18/Syx, Munc18-1/syntaxin-1; POPC, 1-Palmitoyl-2-oleoyl-sn-glycero-3-phosphocholine; POPE, 1-palmitoyl-2-oleoyl-sn-glycero-3-phosphoethanolamine; DOPS, 1,2-dioleoyl-sn-glycero-3-phospho-L-serine (sodium salt); rhodamine-PE, 1,2-dipalmitoyl-snglycero-3-phosphoethanolamine-N-[lissamine rhodamine B sulfonyl] ammonium salt; NBD-PE, 1,2-dipalmitoyl-sn-glycero-3-phosphoethanolamine-N-[7-nitro-2-1,3-benzoxadiazol-4-yl] ammonium salt; PI[4,5]P2, L-α-phosphatidylinositol-4,5-bisphosphate (Brain, Porcine) (ammonium salt); DAG, 1-2-dioleoyl-sn-glycerol; DGS-NTA, 1,2-dioleoyl-sn-glycero-3-[(N-(5-amino-1-carboxypentyl) iminodiacetic acid) succinyl] (nickel salt); BDPY, BODIPY FL N-(2-aminoethyl)-maleimide.

RESULTS

Fusion Affected by Disrupting Helical Continuity of Synaptobrevin-2

The JLR of synaptobrevin-2 contains two consecutive tryptophan residues (W^{89}/W^{90}), which are proposed to localize at the membrane-water interface and serve as a fusion barrier (Chen et al., 2004; Borisovska et al., 2012). Earlier studies showed that mutation or insertion of two helix-breaking proline residues in the JLR of synaptobrevin-2 has little effect on membrane fusion and exocytosis (Mcnew et al., 1999; Van Komen et al., 2005), at odds with the helical continuity model (Stein et al., 2009). However, it is noteworthy that these mutations or insertions were placed downstream of W^{89}/W^{90}, leading us to doubt whether insertion of helix-breaking residues upstream of W^{89}/W^{90} would exert more strong effect. Hence, we placed two proline residues symmetrically on either side of W^{89}/W^{90}, i.e., (K^{85}-PP) and (L^{93}-PP), respectively (**Figure 1A**), and examined their effects on membrane fusion.

First, we assayed fusion between liposomes harboring the syntaxin-1/SNAP-25 complex and liposomes bearing synaptobrevin-2 (wild type, WT) or its two mutations (K^{85}-PP and L^{93}-PP). Co-flotation assay confirmed that synaptobrevin-2 and its mutants were reconstituted on liposomes (**Supplementary Figures 1A,B**). To explore membrane fusion, we performed lipid-mixing and content-mixing assays (**Figures 1B,C**), as previously described (Weber et al., 1998; Wang et al., 2016). Note that the cytoplasmic fragment of synaptotagmin-1 (C_2AB) and Ca^{2+} were included to enhance fusion rate and extent throughout this study. As expected, WT synaptobrevin-2 supported efficient lipid mixing and content mixing (**Figures 1D,E**). As a control, the addition of the cytoplasmic fragment of synaptobrevin-2 (Syb^{29-96}) abolished both lipid mixing and content mixing (**Figures 1D,E**). L^{93}-PP designed to disrupt helical continuity downstream of W^{89}/W^{90} supported lipid mixing as effectively as WT synaptobrevin-2, but reduced content mixing by 55% compared to WT synaptobrevin-2 (**Figures 1D,E**). Intriguingly, K^{85}-PP proposed to break helical continuity upstream of W^{89}/W^{90} severely impaired both lipid and content mixing (**Figures 1D,E**). These data led to an idea that helical extension of synaptobrevin-2 to W^{89}/W^{90} in the JLR is essential for initiating membrane merger, and helical continuity beyond W^{89}/W^{90} contributes to drive complete membrane fusion.

To investigate whether the SNARE regulatory components Munc18-1 and Munc13-1 influence the dependence of SNARE-mediated liposome fusion on helical continuity of synaptobrevin-2, we exploited Munc18–Munc13-regulated fusion system wherein Munc13-1 catalyzes SNARE complex formation starting from the Munc18-1/syntaxin-1 complex (Ma et al., 2013). Hence, we assayed both lipid mixing and content mixing between liposomes bearing the Munc18-1/syntaxin-1 complex and liposomes containing synaptobrevin-2 and its mutations (K^{85}-PP and L^{93}-PP) in the presence of SNAP-25, C_1-C_2B-MUN (containing the priming activity of Munc13-1), C_2AB and Ca^{2+} (**Figures 1F,G**), as previous described (Ma et al., 2013; Yang et al., 2015). As a control, lipid mixing and content mixing were abolished when SNAP-25 was absent (**Figures 1H,I**). Intriguingly, K^{85}-PP abrogated both lipid mixing and content mixing, while L^{93}-PP effectively supported lipid mixing but reduced content mixing by 70% (**Figures 1H,I**), in line with the results obtained with the reconstitution system deficient in Munc18-1 and Munc13-1 (**Figures 1B–E**).

In addition to K^{85}-PP and L^{93}-PP, we introduced another two proline-insertion mutations that are more adjacent to W^{89}/W^{90} of synaptobrevin-2, referred to as Y^{88}-PP and W^{90}-PP, respectively (**Supplementary Figure 2A**). Co-flotation experiment confirmed that Y^{88}-PP and W^{90}-PP were reconstituted on liposomes as effective as WT synaptobrevin-2 (**Supplementary Figure 1B**). Consistently, using systems with and without Munc18-1 and Munc13-1, we observed that Y^{88}-PP and W^{90}-PP exhibited distinct effect on lipid and content mixing, in a manner similar to K^{85}-PP and L^{93}-PP, respectively (**Supplementary Figures 2B–E**). Notably, we verified that the content mixing assay in both systems reflects actual exchange of content between liposomes but not the leakage of sulforhodamine (**Supplementary Figures 2F,G**).

Taken together, the data obtained from both fusion systems with and without Munc18-1 and Munc13-1 suggest that helical continuity of synaptobrevin-2 extended to W^{89}/W^{90} in the JLR is an essential prerequisite to initiate membrane merger. The data indicate that W^{89}/W^{90} functions as a fusion landmark that gates force transmission into the membrane interface.

Fusion Affected by Substitution or Deletion of the Synaptobrevin-2 TMR

Next, we investigated for the importance of the synaptobrevin-2 TMR in membrane fusion with both fusion systems described above. In this respect, we generated a synaptobrevin-2 mutant that lacks its own TMR but bears the syntaxin-1 TMR, referred to as $Syb^{Syx-TMR}$, with the sequence following W^{89}/W^{90} (residues 95–116) in synaptobrevin-2 replaced with the TMR sequence (residues 267–288) of syntaxin-1 (**Figure 2A**). Co-flotation experiment confirmed that $Syb^{Syx-TMR}$ was reconstituted on liposomes as effectively as WT synaptobrevin-2 (**Supplementary Figure 1C**). In both fusion systems with and without Munc18-1 and Munc13-1, $Syb^{Syx-TMR}$ supported lipid mixing (**Figures 2B,C**) but obviously impaired content mixing by 50% and 55%, respectively (**Figures 2D,E**), implying that content mixing requires more precise sequence and topology structure of the TMR.

As the role of the TMR of synaptobrevin-2 in lipid mixing can be fully compensated by the TMR of syntaxin-1 (**Figures 2B,C**), we doubted whether the TMR is really required for initiating membrane merger. To explore this, we generated a TMR-deleted synaptobrevin-2 mutant (residues 23–93) and made this mutant attach the membrane surface upon introducing a 6-Histidine tag to its C-terminal end (after the residue L^{93}, referred to as $Syb^{\Delta TMR}$), and examined its activity in membrane fusion (**Figure 2F**). Five percentage molar ratio of DGS-NTA was accordingly included in liposomes (**Figure 2F**). Co-flotation assay verified efficient attachment of $Syb^{\Delta TMR}$ to liposomes (**Supplementary Figure 1C**). By using a Syb^{49-96}

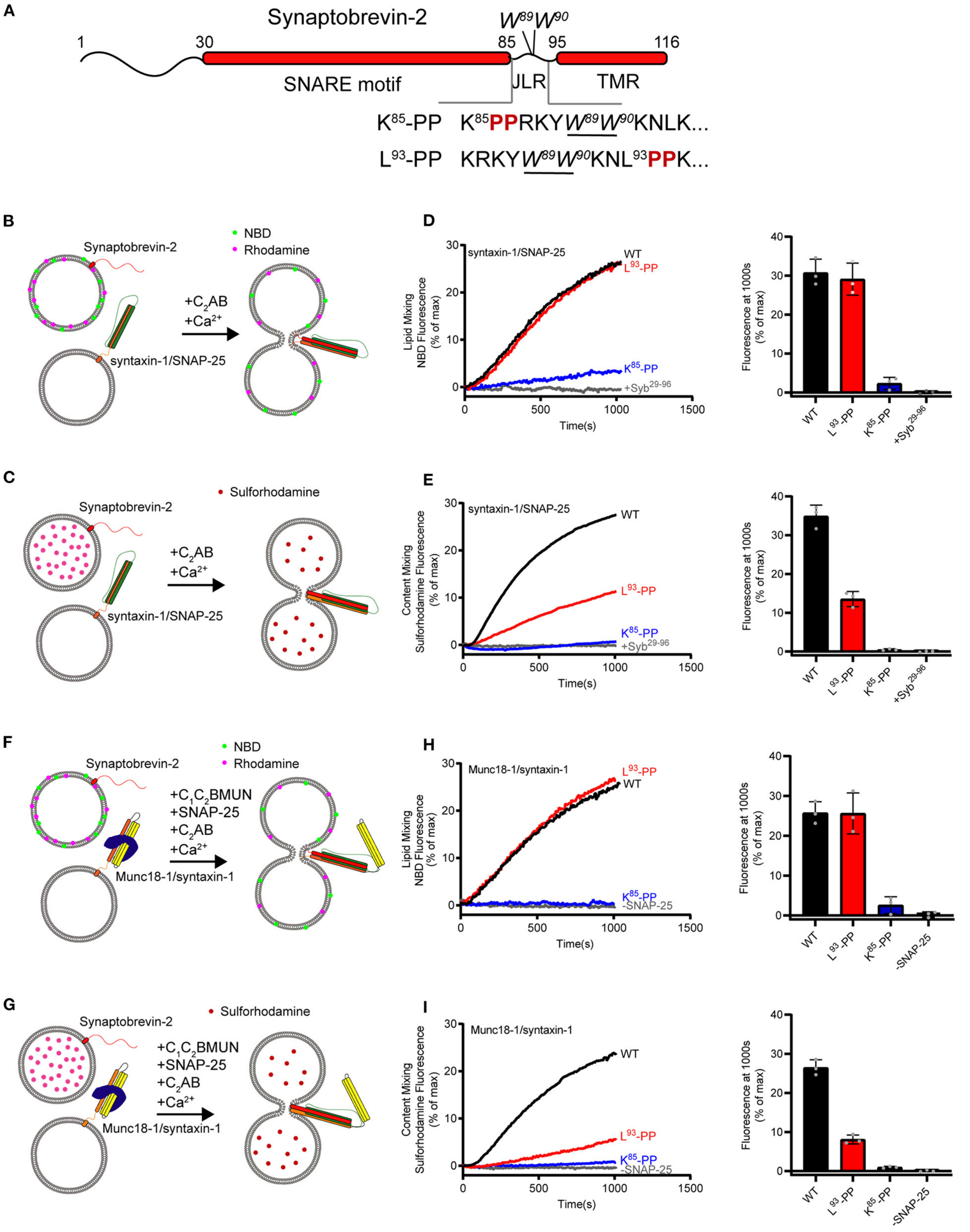

FIGURE 1 | Fusion affected by disrupting helical continuity of the synaptobrevin-2. **(A)** Domain structure of full length wild-type synaptobrevin-2 (WT) and its mutants with two-proline insertions after K^{85} (K^{85}-PP) or L^{93} (L^{93}-PP) in the JLR. **(B,C)** Scheme of lipid mixing **(B)** and content mixing assay **(C)** between syntaxin-1/SNAP-25 and synaptobrevin-2 liposomes in the presence of C_2AB fragment and 1 mM Ca^{2+}. Note that the syntaxin-1 SNARE motif (H3, residues 183–288) was used here to *(Continued)*

FIGURE 1 | form the syntaxin-1/SNAP-25 complex. **(D,E)** Lipid **(D)** and content mixing **(E)** of synaptobrevin-2 WT, K^{85}-PP, and L^{93}-PP liposomes with syntaxin-1/SNAP-25 liposomes. **(F,G)** Scheme of lipid mixing **(F)** and content mixing assay **(G)** between Munc18-1/syntaxin-1 (full length, residues 1–288) and synaptobrevin-2 liposomes in the presence of the Munc13-1 C_1-C_2B-MUN fragment, SNAP-25, C_2AB fragment, and 1 mM Ca^{2+}. **(H,I)** Lipid **(H)** and content mixing **(I)** of synaptobrevin-2 WT, K^{85}-PP, and L^{93}-PP liposomes with Munc18-1/syntaxin-1 liposomes. Representative traces came from one of three independent experiments. Bars on the right panel in **(D,E,H,I)** are means ± SDs, *n* = 3.

peptide displacement experiment (Pobbati et al., 2006), we found that $Syb^{\Delta TMR}$ was capable of forming *trans*-SNARE complexes with the syntaxin-1/SNAP-25 complex between the two membranes (**Supplementary Figure 3**). However, in comparison to WT synaptobrevin-2, $Syb^{\Delta TMR}$ failed to support lipid mixing (**Figures 2G,H**) in the absence and presence of Munc18-1 and Munc13-1. Hence, despite that $Syb^{\Delta TMR}$ can bring the membranes into close distance, the loss of lipid mixing by the lack of the TMR cannot be compensated by Munc18-1 and Munc13-1. These data, together with the results observed in **Figure 1**, indicate that even in a condition that the two membranes have reached to a close proximity, Munc18-1 and Munc13-1 execute no sufficient force or energy to induce membrane deformation and fusion, in addition to their important regulatory function in SNARE complex assembly.

Since the synaptobrevin-2 mutants described above, e.g., L^{93}-PP, W^{90}-PP, $Syb^{Syx-TMR}$, and $Syb^{\Delta TMR}$, are able to anchor on the liposomes and carry the W^{89}/W^{90} residues, how to interpret that only $Syb^{\Delta TMR}$ fails to support lipid mixing? It was suggested that precise insertion of the W^{89}/W^{90} residues at the membrane-water interface is essential for fusion (Borisovska et al., 2012). We thus examined the position of the W^{89}/W^{90} region of the mutants with respect to the membrane-water interface. To this aim, we applied brominated lipid into synaptobrevin-2-liposomes where bromines were attached to the acyl chain (4,5-Br_2-PC) (**Figure 3A**). In this case, tryptophan fluorescence (F) could be effectively quenched if the W^{89}/W^{90} residues were in contact with the acyl chain (Kweon et al., 2003). Indeed, a significant decrease in F was observed for WT synaptobrevin-2 with increased mole fraction of Br_2-PC (**Figures 3B,E**), confirming the close contact of the W^{89}/W^{90} residues with the membrane. Similar result was observed for $Syb^{Syx-TMR}$ (**Figures 3C,E**), indicating that substitution of the TMR of synaptobrevin-2 with that of syntaxin-1 retains the ability to bring the W^{89}/W^{90} residues at the membrane surface. However, little decrease in F was detected for $Syb^{\Delta TMR}$ (**Figures 3D,E**), suggesting that the two tryptophan residues are sequestered from the membrane-water phase owing to the lack of the TMR. Control experiments ruled out the possibilities that 5% molar ratio of DGS-NTA quenches tryptophan fluorescence (**Supplementary Figure 4A**) and that Ca^{2+} competes with DGS-NTA for $Syb^{\Delta TMR}$ binding (**Supplementary Figure 1C**). Moreover, based on brominated lipid tryptophan quenching assay, we found that the behaviors of the tryptophans of Y^{88}-PP, W^{90}-PP, K^{85}-9i, and L^{93}-9i are similar to that of WT synaptobrevin-2 (**Supplementary Figure 4B**). These data showed that tryptophan fluorescence is insensitive to the PP and Gly/Ser insertions, implying that the insertions do not change position or orientation of W^{89}/W^{90} with respect to the membrane.

Thus, we suggest that although $Syb^{\Delta TMR}$ retains the ability to attach on the membrane surface, improper position, or orientation of W^{89}/W^{90} with respect to the membrane caused by deletion of the TMR is expected to impair the force-transmission role of W^{89}/W^{90}.

Fusion Affected by Extension of the Length or Flexibility of the Synaptobrevin-2 JLR

Previous studies have found that extension of the length or flexibility of the synaptobrevin-2 JLR exerts milder effects on spontaneous release but severe impairment on Ca^{2+}-evoked release (Deak et al., 2006; Bretou et al., 2008; Guzman et al., 2010; Zhou et al., 2013), suggesting that a tight coupling between the SNARE motif and the TMR is required for highly regulated fusion events. We hence explored whether such tight coupling demand is imposed by the SNARE regulatory proteins.

We increased the length of the synaptobrevin-2 JLR via inserting 3, 7, and 9 amino acids following the residue K^{85}, referred to as K^{85}-3i, K^{85}-7i, and K^{85}-9i, respectively (**Figure 4A**). These insertions are expected to extend the length and flexibility of the JLR outside the membrane surface, as the insertion position is upstream of W^{89}/W^{90}. Co-flotation assay confirmed that the insertions were reconstituted on liposomes (**Supplementary Figure 1D**). First, we explored the fusion effects of these insertions using the fusion system without Munc18-1 and Munc13-1, as shown in **Figures 1B,C**. K^{85}-3i, K^{85}-7i, and K^{85}-9i gradually reduced lipid mixing and content mixing in a length-dependent manner (**Figures 4B,C**). However, in the fusion system dependent of Munc18-1 and Munc13-1, as shown in **Figures 1F,G**, K^{85}-3i, K^{85}-7i, and K^{85}-9i severely impaired lipid mixing and content mixing (**Figures 4D,E**), consistent with the data observed in neurons (Zhou et al., 2013). Hence, the tight coupling between the SNARE motif and the TMR that is specific for evoked fusion was reproduced in *in vitro* fusion system mediated by Munc18-1 and Munc13-1, reflecting that Munc18–Munc13-dependent membrane fusion represents the dominant route leading to evoked exocytosis.

The synaptobrevin-2 JLR sequence (^{86}RKYWW^{90}) was recently found to bind the Munc13-1 MUN domain, and this interaction is required for the MUN domain to drive N-terminal SNARE complex assembly when starting from the Munc18-1/syntaxin-1 complex (Wang et al., 2019). Given that K^{85}-3i, K^{85}-7i, and K^{85}-9i all retain the RKYWW sequence as an entirety (**Figure 4A**), we assume that the three insertions do not influence MUN activity in promoting N-terminal SNARE

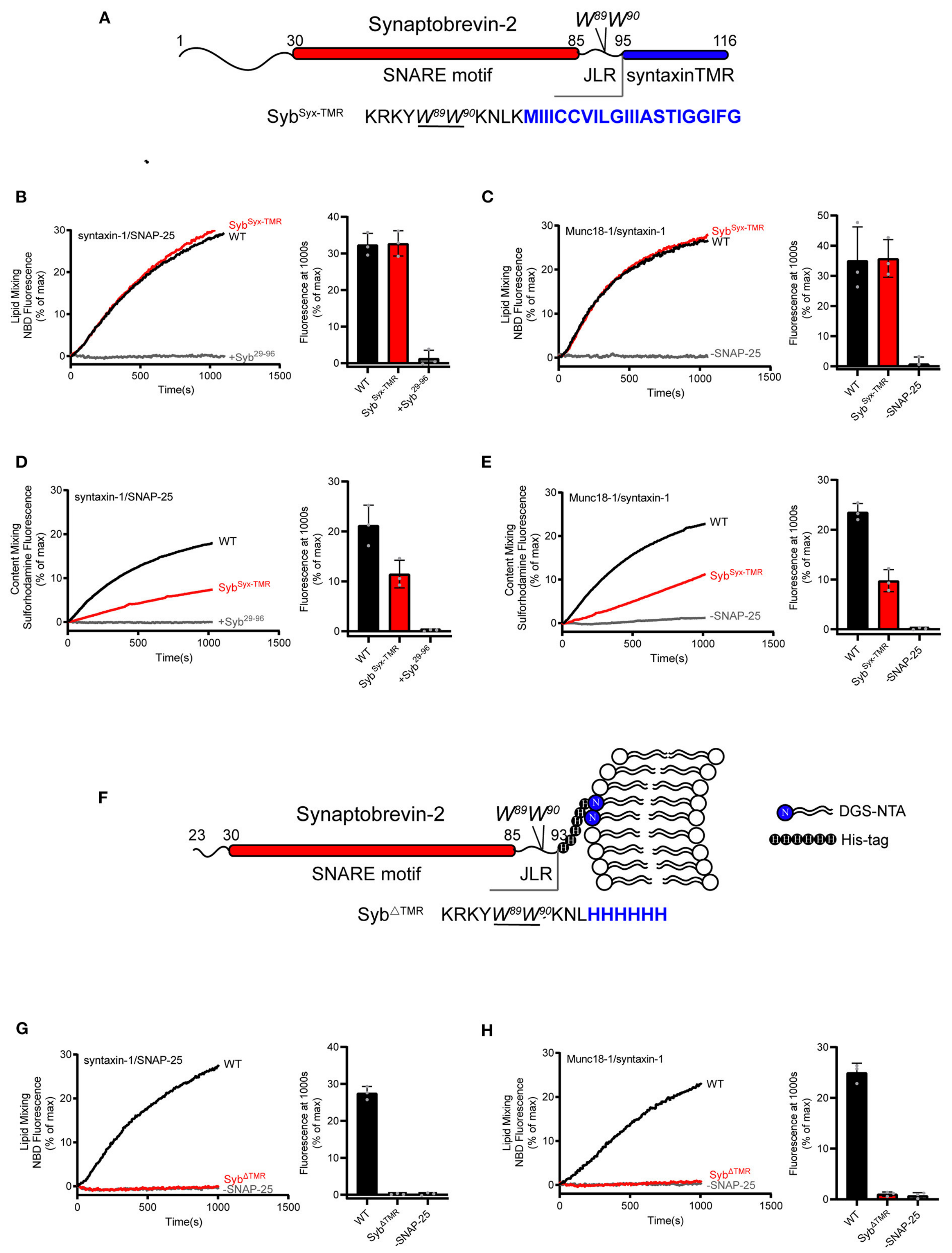

FIGURE 2 | Fusion affected by substitution or deletion of the synaptobrevin-2 TMR. **(A)** Domain structure of chimeric synaptobrevin-2 with TMR substituted by syntaxin-1 TMR (residues 267–288) ($Syb^{Syx-TMR}$). **(B,C)** Lipid mixing between synaptobrevin-2 WT, $Syb^{Syx-TMR}$ liposomes and liposomes reconstituted with syntaxin-1/SNAP-25 **(B)** or Munc18-1/syntaxin-1 **(C)**. **(D,E)** Content mixing between synaptobrevin-2 WT, $Syb^{Syx-TMR}$ liposomes, and liposomes reconstituted with *(Continued)*

FIGURE 2 | syntaxin-1/SNAP-25 (**D**) or Munc18-1/syntaxin-1 **(E)**. **(F)** Domain structure of TMR deletion mutant (Syb$^{\Delta TMR}$) with C-teminal 6-Histidine tag linked to DGS-NTA-containing liposome. **(G,H)** Lipid mixing between synaptobrevin-2 WT and Syb$^{\Delta TMR}$ liposomes and liposomes reconstituted with syntaxin-1/SNAP-25 **(G)** and Munc18-1/syntaxin-1 **(H)**. Representative traces came from one of three independent experiments. Bars on the right panel in **(B–E,G,H)** are Means ± SDs, $n = 3$.

assembly. To test this idea, we assessed MUN activity by using established native-gel assay (Yang et al., 2015; Wang et al., 2019). As expected, synaptobrevin-2 (residues 29–93) with K^{85}-3i, K^{85}-7i, and K^{85}-9i insertions all supported the transition from the Munc18-1/syntaxin-1 complex to the SNARE complex in the presence of the MUN domain and SNAP-25 (**Supplementary Figure 5**). Hence, these insertions seem unlikely to impair MUN–synaptobrevin-2 (JLR) interaction and MUN activity in N-terminal SNARE assembly. It is conceivable that the strongly impaired membrane fusion caused by K^{85}-3i, K^{85}-7i, and K^{85}-9i insertions arises likely from the uncooperative actions among the extended synaptobrevin-2 JLR, Munc13-1/Munc18-1, and phospholipids in C-terminal SNARE assembly and membrane merge.

In addition, similar insertions were placed downstream of W^{89}/W^{90}, i.e., following the residue L^{93}, referred to as L^{93}-3i, L^{93}-7i, and L^{93}-9i, respectively (**Figure 4F**). Co-flotation assay confirmed that the insertions were reconstituted on liposomes (**Supplementary Figure 1D**). These insertions are assumed to increase the length and flexibility of the TMR inside the membrane. Intriguingly, these insertions had little effect on lipid mixing (**Figures 4G,I**), but exerted more remarkable influence on content mixing (**Figures 4H,J**), regardless of using the fusion systems with or without Munc18-1 and Munc13-1. These data suggest that the precise sequence length upstream of W^{89}/W^{90}, but not that downstream of W^{89}/W^{90}, accounts for the tight coupling between the SNARE motif and the TMR.

Taken together, these data suggest that Munc18-1 and Munc13-1 cooperate to impose a tight coupling demand between the SNARE motif and the TMR on membrane fusion upon specifically sensing the length of the synaptobrevin-2 JLR, leading to a notion that the JLR of synaptobrevin-2 constitutes an essential structure element determining not only force transmission but also precise regulation demanded by fast exocytosis.

DISCUSSION

Aromatic and charged residues are highly conserved in the juxtamembrane linker regions (JLR) of synaptobrevins and play a role in membrane fusion (Maximov et al., 2009; Williams et al., 2009; Borisovska et al., 2012; Demill et al., 2014). Two consecutive tryptophan residues (W89/W90) in the JLR of synaptobrevin-2 were reported to reside at the membrane-water interface and serve as a fusion barrier to regulate Ca2+-evoked exocytosis and membrane fusion (Kweon et al., 2003; Chen et al., 2004; Bowen and Brunger, 2006; Maximov et al., 2009; Borisovska et al., 2012). Here, we observed that helix-breaking and/or length-increasing insertions in synaptobrevin-2 exerts distinctive effects on membrane fusion, in a manner dependent on the insertion position relative to W^{89}/W^{90}. For the insertions downstream of W^{89}/W^{90}, e.g., W^{90}-PP, L^{93}-PP, L^{93}-3i, L^{93}-7i, and L^{93}-9i, they exhibited ignoring effects on lipid mixing; while, for those insertions upstream of W^{89}/W^{90}, e.g., K^{85}-PP, Y^{88}-PP, K^{85}-3i, K^{85}-7i, and K^{85}-9i, they exerted severe defects on lipid mixing. The striking differences on the influence of lipid mixing by the insertions indicates that perturbation of the sequence downstream of W^{89}/W^{90} seems to be better tolerated than that upstream of W^{89}/W^{90}. Upon analysis and comparison of studies published previously (Mcnew et al., 1999; Van Komen et al., 2005; Kesavan et al., 2007; Pieren et al., 2015), we notice that the insertions placed after W^{89}/W^{90} in the JLR indeed exhibit virtually little effect on SNARE-mediated lipid mixing, consistent well with our results. In line with the conception that W^{89}/W^{90} positions at the membrane-water interface, our results suggest that W^{89}/W^{90} functions as a landmark gating force transmission into the membrane interface. In our point of view, with membrane approaching by *trans*-formation of the SNARE motifs, further assembly of the JLR to W^{89}/W^{90} is strictly required to initiate membrane merger. Note that helical extension of the JLR to W^{89}/W^{90} is coupled with conformational change of the JLR.

Our study also examined the roles of the TMR of synaptobrevin-2 in membrane fusion. First, the observations that the insertions downstream of W^{89}/W^{90}, e.g., W^{90}-PP, L^{93}-PP, L^{93}-3i, L^{93}-7i, and L^{93}-9i, support lipid mixing but remarkably reduce (but not eliminate) content mixing suggest that helical continuity and rigid of the TMR spanning the lipid bilayer is crucial for inner membrane merger. Similarly, replacement of the synaptobrevin-2 TMR with that of syntaxin-1 displayed an asymmetric effect on lipid and content mixing. The strong defect on content mixing caused by the replacement of the TMR might arise because specific interactions between the two heterogeneous TMRs are crucial for effective inner membrane merger, in line with previous results that the TMRs of synaptobrevin-2 and syntaxin-1 form a heterodimer during fusion (Margittai et al., 1999; Laage et al., 2000; Stein et al., 2009). Strikingly, although membrane-attached synaptobrevin-2 lacking the TMR allows *trans*-SNARE complex formation docking liposomes (**Supplementary Figure 3**), it totally abrogates membrane fusion regardless of the existence of Munc18-1 and Munc13s (**Figures 2G,H**), owing to improper location of W^{89}/W^{90} with respect to the membrane caused by the deletion of the TMR (**Figures 3D,E**). Consistently, a recent NMR study also found that the W^{89}/W^{90} residues in soluble synaptobrevin-2 (residue 1–96) are sequestered from the membrane (Lakomek et al., 2019). These data suggest that membrane proximity is not sufficient and that the TMR of synaptobrevin-2 drives membrane fusion via pulling W^{89}/W^{90} at the membrane interface so as to effectively transmit the force into the membrane. In addition to serving as a force-transmission element, the SNARE TMR has been implicated in fusion pore

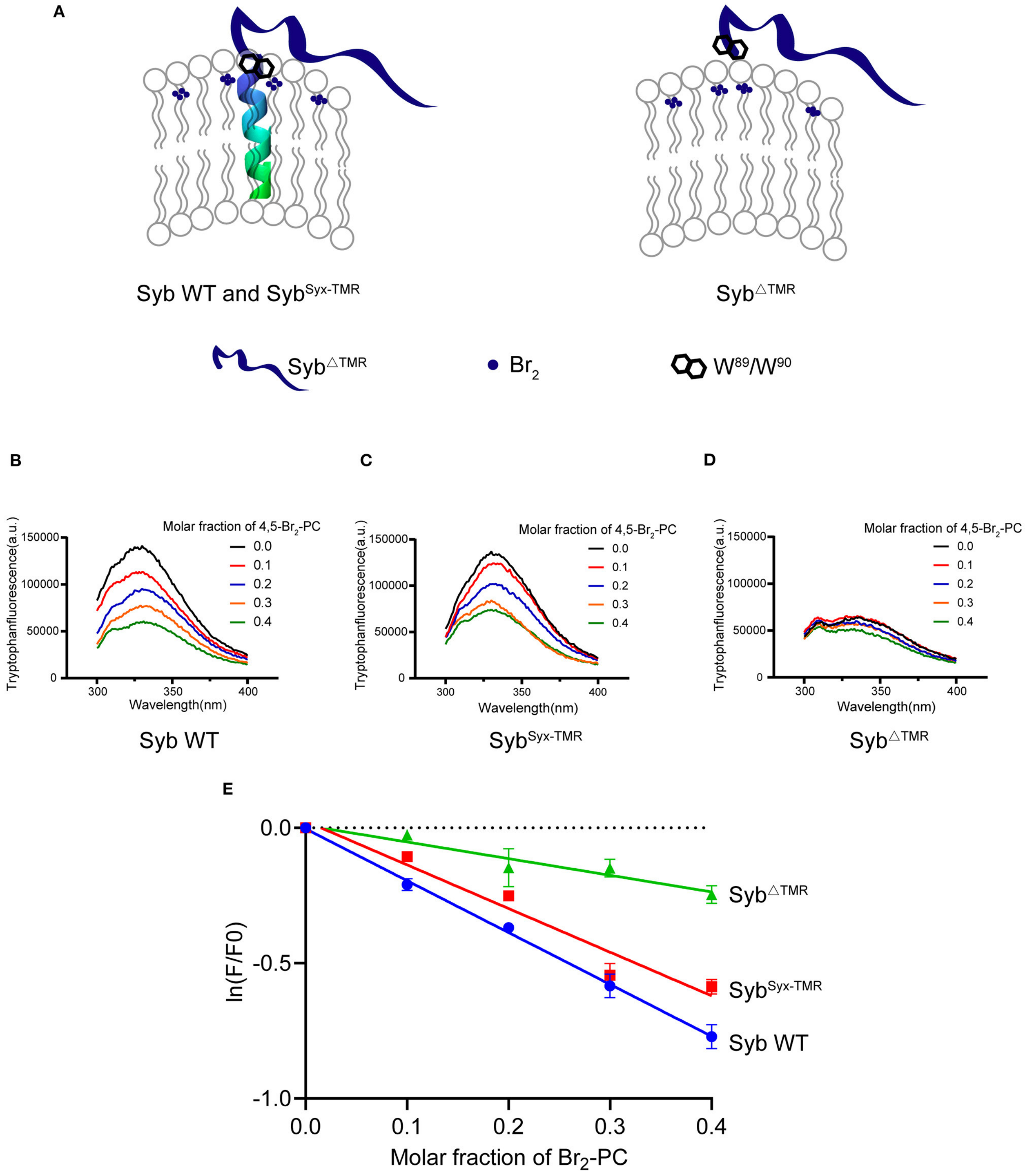

FIGURE 3 | W^{89}/W^{90} of TMR anchored synaptobrevin-2 are resided at the membrane-water interface. **(A)** Schematic diagrams of lipid quenching assay showing that fluorescence of embedded tryptophans in TMR anchored synaptobrevin-2 were quenched by lipid quencher 4,5-Br_2-PC. **(B–D)** Quenching of tryptophan fluorescence by different molar fraction of 4,5-Br_2-PC in synaptobrevin-2 WT **(B)**, $\mathrm{Syb}^{\mathrm{Syx-TMR}}$ **(C)**, and $\mathrm{Syb}^{\Delta\mathrm{TMR}}$ **(D)** liposomes. The samples were excited at 285 nm, and the emission spectra were collected in the range of 300–400 nm. **(E)** Quantification of the fluorescent intensities in **(B–D)** of synaptobrevin-2 WT (solid blue circles), $\mathrm{Syb}^{\mathrm{Syx-TMR}}$ (solid red squares), and $\mathrm{Syb}^{\Delta\mathrm{TMR}}$ (solid green triangles) liposome. The total fluorescence intensity (*F*) was calculated by integrating the intensity in the emission spectral range. (F_0) represents the fluorescent intensity in the absence of 4,5-Br_2-PC, ln (F/F_0) is plotted against the 4,5-Br_2-PC molar fraction. Linear regression was performed by Prism 6.01. Bars in **(E)** are presented as Means ± SDs, $n = 3$.

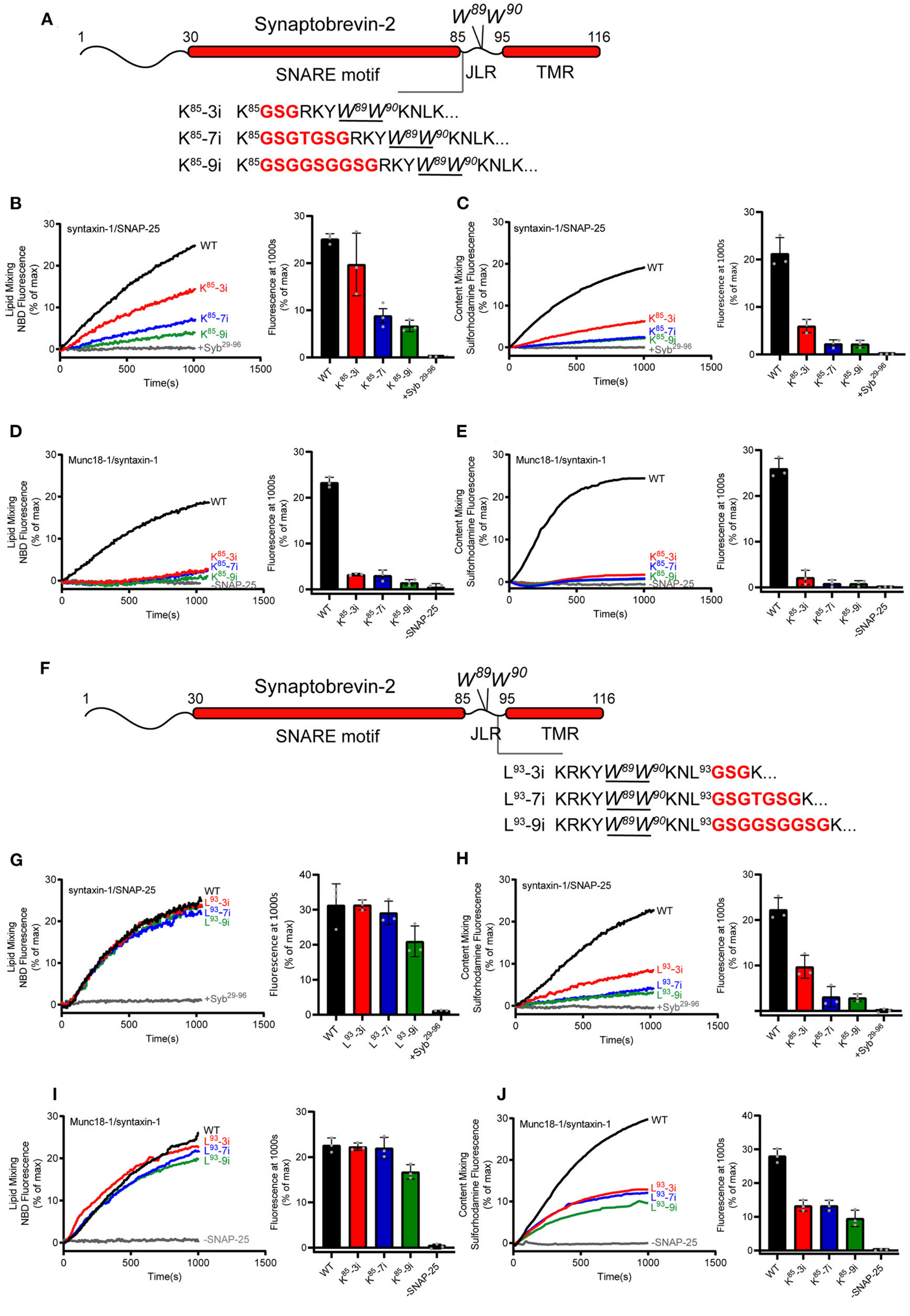

FIGURE 4 | Fusion affected by extension of the length or flexibility of the synaptobrevin-2 JLR. **(A)** Domain structure of full length synaptobrevin-2 with 3, 7, 9 GSG insertions after K^{85} (K^{85}-3i, K^{85}-7i, K^{85}-9i) in the JLR. **(B,C)** Lipid mixing **(B)** and content mixing **(C)** between synaptobrevin-2 WT, K^{85}-3i, K^{85}-7i, and K^{85}-9i liposomes and syntaxin-1/SNAP-25 liposome. **(D,E)** Lipid mixing **(D)** and content mixing **(E)** between synaptobrevin-2 WT, K^{85}-3i, K^{85}-7i, and K^{85}-9i liposomes and

(Continued)

FIGURE 4 | Munc18-1/syntaxin-1 liposome. **(F)** Domain structure of full-length synaptobrevin-2 with 3, 7, 9 GSG insertions after L^{93} (L^{93}-3i, L^{93}-7i, L^{93}-9i) in the JLR. **(G,H)** Lipid mixing **(G)** and content mixing **(H)** between synaptobrevin-2 WT, L^{93}-3i, L^{93}-7i, and L^{93}-9i liposomes and syntaxin-1/SNAP-25 liposome. **(I,J)** Lipid mixing **(I)** and content mixing **(J)** between synaptobrevin-2 WT, L^{93}-3i, L^{93}-7i, and L^{93}-9i liposomes and Munc18-1/syntaxin-1 liposome. Representative traces came from one of three independent experiments. Bars on the right panel in **(B–E,G–J)** are Means ± SDs, *n* = 3.

formation (Han et al., 2004; Ngatchou et al., 2010; Chang et al., 2015; Bao et al., 2016; Sharma and Lindau, 2018; Weiss, 2019).

Notably, the observations that abrogation of fusion by helix-breaking insertions and/or by TMR deletion cannot be rescued by Munc18-1 and Munc13-1 suggest that the synaptobrevin-2 TMR is absolutely required for inducing full fusion and that Munc18-1 and Munc13-1 are unlikely to serve as independent force generators in membrane deformation and fusion. Our results are not in line with previous data that forcing lipid membranes close together suffices to induce synaptic vesicle fusion without a need for the TMR and that SM proteins Munc18-2 and SM protein-containing HOPS complex exert force to drive complete fusion regardless of the presence of the SNARE TMR (Xu et al., 2011; Zhou et al., 2013; Spessott et al., 2017). This discrepancy needs to be interpreted with caution because different lipid (protein) composition, membrane mobility and curvature, and protein concentrations, etc., were used in these studies. For instance, (i) in the presynaptic active zones, protein, and lipid components around the fusion pore are expected to be more complicate than that in *in-vitro* man-made proteoliposomes; and (ii) increasing local numbers of the SNARE complex might lead to a higher energetically favorable state that could be sufficient to destabilize the phospholipid bilayers even without other fusion components. Nevertheless, our results are consistent with a recent study showing that lipid-anchored synaptobrevin-2 provides little or no support for liposome fusion and exocytosis (Chang et al., 2016), which rationalize the virtually universal presence of a TMD in R-SNAREs (Weimbs et al., 1998; Jahn and Südhof, 1999).

Previous work has identified a tight coupling between the SNARE motif and the TMR that is specific for evoked exocytosis (Deak et al., 2006; Kesavan et al., 2007; Bretou et al., 2008; Guzman et al., 2010; Borisovska et al., 2012; Zhou et al., 2013). Our finding that Munc18-1 and Munc13-1 renders the fusion more sensitive to the length and flexibility of the synaptobrevin-2 JLR sequence upstream of W^{89}/W^{90} leads to a notion that the tight coupling demanded by evoked fusion might be imposed by Munc18-1 and Munc13-1, reflecting that Munc18–Munc13-regulated SNARE complex assembly serves likely as the dominant route to evoked fusion. Actually, both spontaneous and evoke fusion require Munc18-1 and Munc13-1. Although it is believed that spontaneous and evoke fusion share same fusion machinery, the underlying mechanism may differ. In contrast to evoked fusion that relies on Munc13-catalyzed transition from the Munc18-1/syntaxin-1 complex to the SNARE complex in the presence of SNAP-25 and synaptobrevin-2, spontaneous fusion might use a different route that involves Munc18-1-mediated syntaxin-1 N-peptide interaction and Munc13-1-mediated association of the two apposing membranes. We suggest that Munc18-1 and Munc13-1 highly regulate the whole process of SNARE complex assembly in evoked fusion, whereas their predominant roles in spontaneous fusion lie in vesicle docking and membrane association prior to SNARE assembly. Increasing evidence has indicated that the JLR of synaptobrevin-2 serves as an important element not only for force transmission but also for regulations by multiple fusion components such as calmodulin, Munc13s, and phospholipids (Quetglas et al., 2000; Kweon et al., 2003; Bowen and Brunger, 2006; Ellena et al., 2009; Brewer et al., 2011; Borisovska et al., 2012; Han et al., 2016; Rathore et al., 2019; Wang et al., 2019). Although length-increasing insertions in the synaptobrevin-2 JLR do not disturb Munc13-mediated N-terminal SNARE assembly (**Supplementary Figure 5**), structural perturbations in this region may affect cooperative interplay among the JLR, Munc13s, and phospholipids, therefore altering fusion competence. For instance, the crystal structure of synaptobrevin-2 bound to Munc13-1 reveals a rigid but non-typical α-helical conformation of the JLR (Wang et al., 2019), suggesting that kinetics and thermodynamics for the conformational change of the JLR from priming to fusion may differ between the two fusion system with and without Munc13-1. Interestingly, a recent study showed that vacuoles in yeast are connected by a metastable, non-expanding, nanoscopic fusion pore that does not allow passage of some cargo. This work suggests that this is the default state, from which full fusion is regulated and that the SNARE TMR and the SM protein-containing HOPS complex stabilize the pore against re-closure (D'Agostino et al., 2018). Hence, it is also likely that the tight coupling imposed by Munc18-1 and Munc13-1 in evoked fusion might be due to the existence of small and dynamic fusion pores whose expansion can be regulated and stabilized by interactions of the synaptobrevin-2 JLR with Munc13-1 and/or Munc18-1. These may account for differentiated demand of the tight coupling between spontaneous and evoked fusions. Finally, the effects of Munc18-1 and Munc13-1 found in present study might depend partly on interplay with the synaptotagmin-1 C_2AB and Ca^{2+}, because of their existence in all our reactions. Despite these speculations, future investigations need to test how the regulatory fusion components selectively manipulate the structure and function of the JLR in different types of exocytosis.

MATERIALS AND METHODS

Plasmids Construction

All full-length synaptobrevin-2 mutant constructs were generated by PCR using the overlap expansion method. For synaptobrevin-2 R^{86}-PP, Y^{88}-PP, W^{90}-PP, L^{93}-PP variants, forward and reverse overlap primer encoding 2 proline (CCTCCG) were inserted into the target site. The same procedure was used to create R^{85}-3i and L^{93}-3i (GSG), R85-7i and L^{93}-7i (GSGTGSG), R^{85}-9i and L^{93}-9i (GSGGSGGSG) insertion constructions and $\text{Syb}^{\text{Syx}-\text{TMR}}$. All above PCR fragments were cut by BamHI (5′) and EcoRI (3′) (all from Thermo Fisher Scientific; America) restriction enzyme and then ligated into pGEX-6P-1 vector (GE Healthcare; Piscataway, NJ). To create Syb$^{\Delta TMR}$, PCR amplification of synaptobrevin-2 (residues 23–93) with a stop primer encoding six Histidine at the C-terminal was subcloned into pET-28a (Novagen; Australia) by NcoI and XhoI.

Protein Purification

Full-length synaptobrevin-2 and its recombinant variants were expressed as N-terminal GST fusion proteins (pGEX-6P-1-vector) in the *E.coli* strain BL21-DE3 and purified using glutathione-agarose in 1% (w/v) n-octyl β-D-glucopyranoside (Amresco; Solon, OH). All column elutions were analyzed for integrity and purity of the expressed proteins by SDS-PAGE and Coomassie blue staining. Syntaxin-1 (residues 183–288, the SNARE motif, JLR and TMR), SNAP-25 (with its four cysteines mutated to serines), Munc18-1/syntaxin-1(residues 1–288, full-length), Munc13-1 (the C_1-C_2B-MUN fragment, residues 529–1407, EF, 1453–1531), and the synaptotagmin-1 cytoplasmic domain (C_2AB, residues 140–421) were expressed and purified as described previously (Sutton et al., 1998; Dulubova et al., 1999, 2007; Ma et al., 2011, 2013). Protein concentrations were determined by UV-visible spectrometer (SHIMADZU UV-2450).

Lipid Mixing Assay

Proteoliposomes were prepared using established procedures (Ma et al., 2013). Donor (synaptobrevin-2) liposomes contained 1-Palmitoyl-2-oleoyl-sn-glycero-3-phosphocholine (POPC), 1-palmitoyl-2-oleoyl-sn-glycero-3-phosphoethanolamine (POPE), 1,2-dioleoyl-sn-glycero-3-phospho-L-serine (sodium salt) (DOPS), 1,2-dipalmitoyl-snglycero-3-phosphoethanolamine-N-[lissamine rhodamine B sulfonyl] ammonium salt (rhodamine-PE), 1,2-dipalmitoyl-sn-glycero-3-phosphoethanolamine-N-[7-nitro-2-1,3-benzoxadiazol-4-yl] ammonium salt (NBD-PE). Acceptor liposome (syntaxin-1/SNAP-25) contained 60% POPC, 20% POPE, 20% DOPS, and the other acceptor liposome (Munc18-1/syntaxin-1) contained additional 2% L-α-phosphatidylinositol-4,5-bisphosphate (Brain, Porcine) (ammonium salt) (PI[4, 5]P2) and 5% 1-2-dioleoyl-sn-glycerol (DAG) (all from Avanti Polar Lipids; Alabaster, AL). Lipid mixtures were dried in glass tubes with nitrogen gas and followed by vacuum for at least 3 h. Lipid films were resuspended in buffer A [25 mM HEPES, pH 7.4, 150 mM KCl, 10 % glycerol (v/v)] and 1 mM DTT, 1% 3-[(3-Cholamidopropyl) dimethylammonio] propanesulfonate (CHAPS) (w/v, Amersco) and vortexed for 10 min. Purified proteins were added slowly to the micelle at a final concentration of 5 mM total lipids. Liposome was acquired with a constant protein/lipid ratio which acceptor liposome is 1:800 and donor liposome is 1:500. The liposome protein mixtures were incubated at room temperature for 30 min followed by dialyzing in buffer A and 1 mM DTT, 1 g/L Bio-beads SM2 (Bio-Rad) 3 times at 4°C in order to remove the detergent extensively. Lipid mixing assay was then taken up based on 7-nitrobenz-2-oxa-1,3-diazole (NBD) fluorescence dequenching assay which is emitted at 538 nm and excited at 460 nm. In brief, Donor liposomes (0.25 mM lipids) were mixed with acceptor liposomes (0.5 mM lipids) in the presence of 2 μM C_2AB fragment, 0.5 mM Ca^{2+} (syntaxin-1/SNAP-25) and extra 1 μM Munc13-1 C_1-C_2B-MUN, 5 μM SNAP-25 (Munc18-1/syntaxin-1) (as indicated in the figures) in a total volume of 60 ul. All experiments were performed at 30°C. At the end of each reaction, 1% w/v β-OG was added to solubilize the liposomes and obtain maximum fluorescence signal for normalizing.

Content Mixing Assay

Forty millimeters sulforhodamine B (Sigma) was loaded into synaptobrevin-2 liposome without lipid probes. Other experimental details were same as lipid mixing assays. leakiness control was performed with 40 mm sulforhodamine B both loaded into syntaxin-1/SNAP-25 or Munc18-1/syntaxin-1 liposome and synaptobrevin-2 liposomes. fluorescence was monitored on a PTI QM-40 fluorescence spectrophotometer with an excitation wavelength of 565 nm and an emission wavelength of 580 nm. Fluorescence normalization is the same as that used in the lipid-mixing assay. All experiments were carried out at 30°C. At the end of each reaction, 1% w/v β-OG was added to solubilize the liposomes and obtain maximum fluorescence signal for normalizing.

Liposome Co-flotation Assay

Lipid films were re-suspended in buffer A [25 mM HEPES, pH 7.4, 150 mM KCl, 1 mM DTT, 10% glycerol (v/v)] and vortexed for at least 5 min. The re-suspended lipid films were frozen and thawed five times, and then extruded through a 50 nm polycarbonate filter with an Avanti extruder for at least 29 times to make the final liposome. Syb$^{\Delta TMR}$ was purified as the C-terminal 6-Histidine tagged tail-anchored forms earing a DGS-NTA lipid 1,2-dioleoyl-sn-glycero-3-[(N-(5-amino-1-carboxypentyl) iminodiacetic acid) succinyl] (nickel salt) that can be attached to lipid membranes. Proteins were preincubated with liposomes made by Extruder with a protein to lipid ratio of 1:100 for 3 h at room temperature. Co-floatation assay was firstly taken with a Histodenz (Sigma Aldrich) gradient density gradients (40:30%) using a SW 55 Ti rotor (Beckman Coulter; Boulevard Brea, CA) at a speed of 48,000 rpm for 2 h in order to get rid of remaining unattached 6-Histidine tail-anchored proteins. Samples from the top and the bottom of the gradient (50 μl) were taken and analyzed by SDS-PAGE and Coomassie Blue staining.

Fluorescence Anisotropy Assay

Synaptobrevin-2 (residues 49–96, S61C) was purified and labeled with BODIPY FL N-(2-aminoethyl)-maleimide (BDPY) according to the manufacturer's instruction (Molecular Probes). Syntaxin-1 (residues 183–288), SNAP-25 and synaptobrevin-2 (residues 49–96, S61C) were first preincubated at a molar ratio of 1:1:1 at room temperature for 3 h. Liposome were acquired using dialysis method described above. Co-floatation assay was then conducted to get rid of excess fluorescence labeled synaptobrevin-2. Syntaxin-1/SNAP-25/synaptobrevin-2 49–96 S61C liposome (0.25 mM lipids) was mixed with Syb$^{\Delta TMR}$ liposome (0.5 mM lipids) and the fluorescence anisotropy assay was performed on PTI QM-40 fluorescence spectrophotometer equipped with a set of polarizers. The experiment was carried out at 25°C with excitation and emission wavelength of 485 and 513 nm, respectively.

Tryptophan Fluorescence Quenching Assays

To explore the location of tryptophan residues in synaptobrevin-2 WT and mutants, lipid quencher 1-palmitoyl-2-stearoyl-(4.5)-dibromo-sn-glycero-3-phosphocholine (4,5-Br_2-PC, 10 mg/ml) was added in replacement of part of POPC at 0.0, 0.1, 0.2, 0.3, 0.4 molar fraction, respectively. Solutions of POPC (14 mg/ml) and 4,5-Br_2-PC (10 mg/ml) in chloroform were codissolved at 5 mM total lipid. Proteins were reconstituted into the liposome with a molar lipid/protein ratio of 250 using dialysis method described above. The degree of quenching was determined as a function of the mole fraction of added brominated POPC. The samples were excited at 285 nm, and the emission spectra were collected in the range of 300–400 nm. The total fluorescence intensity F was obtained by integrating the intensity in this spectral range. Normalized statistics method was described elsewhere (Kweon et al., 2003).

Native Gel Assay

Munc18-1 and syntaxin-1 (residues 2–253) were first incubated with a protein/protein ratio of a 1.2:1 at 30°C for 3 h to form a stable Munc18-1/syntaxin-1 (M18/Syx) complex. Ten micrometre synaptobrevin-2 (residues 23–93) or its mutants, 10 μM SNAP-25, 25 μM MUN (residues 933–1407, EF, 1453–1531) were then added and incubated for another 3 h at 30°C. The samples were loaded into the non-denaturing [sodium dodecyl sulfate (SDS)-free] gel and the electrophoresis were performed in native electrophoresis buffer at 4°C as described before (Yang et al., 2015). The representative gel displayed is from one of three replicates.

Data Analysis

Prism 6.01 (GraphPad) was used for graphing and performing linear regression.

DATA AVAILABILITY STATEMENT

The original contributions presented in the study are included in the article/**Supplementary Materials**, further inquiries can be directed to the corresponding author/s.

AUTHOR CONTRIBUTIONS

YH and LZ generated all mutants and performed and analyzed *in vitro* fusion experiments. YH and CM wrote the manuscript. CM conceived the experiments and supervised the study. All authors contributed to the article and approved the submitted version.

FUNDING

This work was supported by grants from the National Natural Science Foundation of China (31670846, 31721002), and funds from Huazhong University of Science and Technology.

ACKNOWLEDGMENTS

We thank Yun Li for purifying Munc13-1 C1-C2B-MUN protein, Xiaoyu Yang and Xianping Wang for purifying Munc18-1/syntaxin-1 protein, Shen Wang for technical assistance.

SUPPLEMENTARY MATERIAL

The Supplementary Material for this article can be found online at: https://www.frontiersin.org/articles/10.3389/fcell.2020.609708/full#supplementary-material

REFERENCES

Bao, H., Goldschen-Ohm, M., Jeggle, P., Chanda, B., Edwardson, J. M., and Chapman, E. R. (2016). Exocytotic fusion pores are composed of both lipids and proteins. *Nat. Struct. Mol. Biol.* 23, 67–73. doi: 10.1038/nsmb.3141

Borisovska, M., Schwarz, Y. N., Dhara, M., Yarzagaray, A., Hugo, S., Narzi, D., et al. (2012). Membrane-proximal tryptophans of synaptobrevin II stabilize priming of secretory vesicles. *J. Neurosci.* 32, 15983–15997. doi: 10.1523/JNEUROSCI.6282-11.2012

Bowen, M., and Brunger, A. T. (2006). Conformation of the synaptobrevin transmembrane domain. *Proc. Natl. Acad. Sci. U.S.A.* 103, 8378–8383. doi: 10.1073/pnas.0602644103

Bretou, M., Anne, C., and Darchen, F. (2008). A fast mode of membrane fusion dependent on tight SNARE zippering. *J. Neurosci.* 28, 8470–8476. doi: 10.1523/JNEUROSCI.0860-08.2008

Brewer, K. D., Li, W., Horne, B. E., and Rizo, J. (2011). Reluctance to membrane binding enables accessibility of the synaptobrevin SNARE motif for SNARE complex formation. *Proc. Natl. Acad. Sci. U.S.A.* 108, 12723–12728. doi: 10.1073/pnas.1105128108

Brunger, A. T., Choi, U. B., Lai, Y., Leitz, J., White, K. I., and Zhou, Q. (2019). The pre-synaptic fusion machinery. *Curr. Opin. Struct. Biol.* 54, 179–188. doi: 10.1016/j.sbi.2019.03.007

Chang, C. W., Chiang, C. W., Gaffaney, J. D., Chapman, E. R., and Jackson, M. B. (2016). Lipid-anchored synaptobrevin provides little or no support for exocytosis or liposome fusion. *J. Biol. Chem.* 291, 2848–2857. doi: 10.1074/jbc.M115.701169

Chang, C. W., Hui, E., Bai, J., Bruns, D., Chapman, E. R., and Jackson, M. B. (2015). A structural role for the synaptobrevin 2 transmembrane domain in dense-core vesicle fusion pores. *J. Neurosci.* 35, 5772–5780. doi: 10.1523/JNEUROSCI.3983-14.2015

Chen, Y., Xu, Y., Zhang, F., and Shin, Y. K. (2004). Constitutive versus regulated SNARE assembly: a structural basis. *EMBO J.* 23, 681–689. doi: 10.1038/sj.emboj.7600083

Chen, Y. A., and Scheller, R. H. (2001). SNARE-mediated membrane fusion. *Nat. Rev. Mol. Cell Biol.* 2, 98–106. doi: 10.1038/35052017

Chiang, C. W., Chang, C. W., and Jackson, M. B. (2018). The transmembrane domain of synaptobrevin influences neurotransmitter flux through synaptic fusion pores. *J. Neurosci.* 38, 7179–7191. doi: 10.1523/JNEUROSCI.0721-18.2018

D'Agostino, M., Risselada, H. J., Endter, L. J., Comte-Miserez, V., and Mayer, A. (2018). SNARE-mediated membrane fusion arrests at pore expansion to regulate the volume of an organelle. *EMBO J.* 37, e99193. doi: 10.15252/embj.201899193

Deak, F., Shin, O. H., Kavalali, E. T., and Südhof, T. C. (2006). Structural determinants of synaptobrevin 2 function in synaptic vesicle fusion. *J. Neurosci.* 26, 6668–6676. doi: 10.1523/JNEUROSCI.5272-05.2006

Demill, C. M., Qiu, X., Kisiel, M., Bolotta, A., and Stewart, B. A. (2014). Investigation of the juxtamembrane region of neuronal-Synaptobrevin in synaptic transmission at the Drosophila neuromuscular junction. *J. Neurophysiol.* 112, 1356–1366. doi: 10.1152/jn.00474.2013

Dhara, M., Yarzagaray, A., Makke, M., Schindeldecker, B., Schwarz, Y., Shaaban, A., et al. (2016). v-SNARE transmembrane domains function as catalysts for vesicle fusion. *Elife* 5:e17571. doi: 10.7554/eLife.17571.019

Dulubova, I., Khvotchev, M., Liu, S., Huryeva, I., Südhof, T. C., and Rizo, J. (2007). Munc18-1 binds directly to the neuronal SNARE complex. *Proc. Natl. Acad. Sci. U.S.A.* 104, 2697–2702. doi: 10.1073/pnas.0611318104

Dulubova, I., Sugita, S., Hill, S., Hosaka, M., Fernandez, I., Südhof, T. C., et al. (1999). A conformational switch in syntaxin during exocytosis: role of munc18. *EMBO J.* 18, 4372–4382. doi: 10.1093/emboj/18.16.4372

Ellena, J. F., Liang, B., Wiktor, M., Stein, A., Cafiso, D. S., Jahn, R., et al. (2009). Dynamic structure of lipid-bound synaptobrevin suggests a nucleation-propagation mechanism for trans-SNARE complex formation. *Proc. Natl. Acad. Sci. U.S.A.* 106, 20306–20311. doi: 10.1073/pnas.0908317106

Fasshauer, D., Sutton, R. B., Brunger, A. T., and Jahn, R. (1998). Conserved structural features of the synaptic fusion complex: SNARE proteins reclassified as Q- and R-SNAREs. *Proc. Natl. Acad. Sci. U.S.A.* 95, 15781–15786. doi: 10.1073/pnas.95.26.15781

Giraudo, C. G., Hu, C., You, D., Slovic, A. M., Mosharov, E. V., Sulzer, D., et al. (2005). SNAREs can promote complete fusion and hemifusion as alternative outcomes. *J. Cell Biol.* 170, 249–260. doi: 10.1083/jcb.200501093

Guzman, R. E., Schwarz, Y. N., Rettig, J., and Bruns, D. (2010). SNARE force synchronizes synaptic vesicle fusion and controls the kinetics of quantal synaptic transmission. *J. Neurosci.* 30, 10272–10281. doi: 10.1523/JNEUROSCI.1551-10.2010

Han, J., Pluhackova, K., and Bockmann, R. A. (2017). The multifaceted role of SNARE proteins in membrane fusion. *Front. Physiol.* 8:5. doi: 10.3389/fphys.2017.00005

Han, J., Pluhackova, K., Bruns, D., and Bockmann, R. A. (2016). Synaptobrevin transmembrane domain determines the structure and dynamics of the SNARE motif and the linker region. *Biochim. Biophys. Acta* 1858, 855–865. doi: 10.1016/j.bbamem.2016.01.030

Han, X., Wang, C. T., Bai, J., Chapman, E. R., and Jackson, M. B. (2004). Transmembrane segments of syntaxin line the fusion pore of Ca2+-triggered exocytosis. *Science* 304, 289–292. doi: 10.1126/science.1095801

He, E., Wierda, K., Van Westen, R., Broeke, J. H., Toonen, R. F., Cornelisse, L. N., et al. (2017). Munc13-1 and Munc18-1 together prevent NSF-dependent de-priming of synaptic vesicles. *Nat. Commun.* 8:15915. doi: 10.1038/ncomms15915

Hofmann, M. W., Peplowska, K., Rohde, J., Poschner, B. C., Ungermann, C., and Langosch, D. (2006). Self-interaction of a SNARE transmembrane domain promotes the hemifusion-to-fusion transition. *J. Mol. Biol.* 364, 1048–1060. doi: 10.1016/j.jmb.2006.09.077

Jahn, R., and Fasshauer, D. (2012). Molecular machines governing exocytosis of synaptic vesicles. *Nature* 490, 201–207. doi: 10.1038/nature11320

Jahn, R., Lang, T., and Südhof, T. C. (2003). Membrane fusion. *Cell* 112, 519–533. doi: 10.1016/S0092-8674(03)00112-0

Jahn, R., and Südhof, T. C. (1999). Membrane fusion and exocytosis. *Annu. Rev. Biochem.* 68, 863–911. doi: 10.1146/annurev.biochem.68.1.863

Jakhanwal, S., Lee, C. T., Urlaub, H., and Jahn, R. (2017). An activated Q-SNARE/SM protein complex as a possible intermediate in SNARE assembly. *EMBO J.* 36, 1788–1802. doi: 10.15252/embj.201696270

Kesavan, J., Borisovska, M., and Bruns, D. (2007). v-SNARE actions during Ca(2+)-triggered exocytosis. *Cell* 131, 351–363. doi: 10.1016/j.cell.2007.09.025

Kweon, D. H., Kim, C. S., and Shin, Y. K. (2003). Regulation of neuronal SNARE assembly by the membrane. *Nat. Struct. Biol.* 10, 440–447. doi: 10.1038/nsb928

Laage, R., Rohde, J., Brosig, B., and Langosch, D. (2000). A conserved membrane-spanning amino acid motif drives homomeric and supports heteromeric assembly of presynaptic SNARE proteins. *J. Biol. Chem.* 275, 17481–17487. doi: 10.1074/jbc.M910092199

Lai, Y., Choi, U. B., Leitz, J., Rhee, H. J., Lee, C., Altas, B., et al. (2017). Molecular mechanisms of synaptic vesicle priming by Munc13 and Munc18. *Neuron* 95, 591–607 e510. doi: 10.1016/j.neuron.2017.07.004

Lakomek, N. A., Yavuz, H., Jahn, R., and Perez-Lara, A. (2019). Structural dynamics and transient lipid binding of synaptobrevin-2 tune SNARE assembly and membrane fusion. *Proc. Natl. Acad. Sci. U.S.A.* 116, 8699–8708. doi: 10.1073/pnas.1813194116

Ma, C., Li, W., Xu, Y., and Rizo, J. (2011). Munc13 mediates the transition from the closed syntaxin-Munc18 complex to the SNARE complex. *Nat. Struct. Mol. Biol.* 18, 542–549. doi: 10.1038/nsmb.2047

Ma, C., Su, L., Seven, A. B., Xu, Y., and Rizo, J. (2013). Reconstitution of the vital functions of Munc18 and Munc13 in neurotransmitter release. *Science* 339, 421–425. doi: 10.1126/science.1230473

Margittai, M., Otto, H., and Jahn, R. (1999). A stable interaction between syntaxin 1a and synaptobrevin 2 mediated by their transmembrane domains. *FEBS Lett.* 446, 40–44. doi: 10.1016/S0014-5793(99)00028-9

Maximov, A., Tang, J., Yang, X., Pang, Z. P., and Südhof, T. C. (2009). Complexin controls the force transfer from SNARE complexes to membranes in fusion. *Science* 323, 516–521. doi: 10.1126/science.1166505

Mcnew, J. A., Weber, T., Engelman, D. M., Sollner, T. H., and Rothman, J. E. (1999). The length of the flexible SNAREpin juxtamembrane region is a critical determinant of SNARE-dependent fusion. *Mol. Cell.* 4, 415–421. doi: 10.1016/S1097-2765(00)80343-3

Ngatchou, A. N., Kisler, K., Fang, Q., Walter, A. M., Zhao, Y., Bruns, D., et al. (2010). Role of the synaptobrevin C terminus in fusion pore formation. *Proc. Natl. Acad. Sci. U.S.A.* 107, 18463–18468. doi: 10.1073/pnas.1006727107

Pieren, M., Desfougeres, Y., Michaillat, L., Schmidt, A., and Mayer, A. (2015). Vacuolar SNARE protein transmembrane domains serve as nonspecific membrane anchors with unequal roles in lipid mixing. *J. Biol. Chem.* 290, 12821–12832. doi: 10.1074/jbc.M115.647776

Pobbati, A. V., Stein, A., and Fasshauer, D. (2006). N- to C-terminal SNARE complex assembly promotes rapid membrane fusion. *Science* 313, 673–676. doi: 10.1126/science.1129486

Quade, B., Camacho, M., Zhao, X., Orlando, M., Trimbuch, T., Xu, J., et al. (2019). Membrane bridging by Munc13-1 is crucial for neurotransmitter release. *Elife* 8:e42806. doi: 10.7554/eLife.42806.025

Quetglas, S., Leveque, C., Miquelis, R., Sato, K., and Seagar, M. (2000). Ca2+-dependent regulation of synaptic SNARE complex assembly via a calmodulin- and phospholipid-binding domain of synaptobrevin. *Proc. Natl. Acad. Sci. U.S.A.* 97, 9695–9700. doi: 10.1073/pnas.97.17.9695

Rathore, S. S., Liu, Y., Yu, H., Wan, C., Lee, M., Yin, Q., et al. (2019). Intracellular vesicle fusion requires a membrane-destabilizing peptide located at the Juxtamembrane region of the v-SNARE. *Cell Rep.* 29, 4583–4592 e4583. doi: 10.1016/j.celrep.2019.11.107

Rizo, J., and Xu, J. (2015). The synaptic vesicle release machinery. *Annu. Rev. Biophys.* 44, 339–367. doi: 10.1146/annurev-biophys-060414-034057

Sharma, S., and Lindau, M. (2018). Molecular mechanism of fusion pore formation driven by the neuronal SNARE complex. *Proc. Natl. Acad. Sci. U.S.A.* 115, 12751–12756. doi: 10.1073/pnas.1816495115

Sørensen, J. B., Wiederhold, K., Muller, E. M., Milosevic, I., Nagy, G., De Groot, B. L., et al. (2006). Sequential N- to C-terminal SNARE complex assembly drives priming and fusion of secretory vesicles. *EMBO J* .25, 955–966. doi: 10.1038/sj.emboj.7601003

Spessott, W. A., Sanmillan, M. L., McCormick, M. E., Kulkarni, V. V., and Giraudo, C. G. (2017). SM protein Munc18-2 facilitates transition of Syntaxin 11-mediated lipid mixing to complete fusion for T-lymphocyte cytotoxicity. *Proc. Natl. Acad. Sci. U.S.A.* 114, E2176–E2185. doi: 10.1073/pnas.16179 81114

Stein, A., Weber, G., Wahl, M. C., and Jahn, R. (2009). Helical extension of the neuronal SNARE complex into the membrane. *Nature* 460, 525–528. doi: 10.1038/nature08156

Südhof, T. C., and Rizo, J. (2011). Synaptic vesicle exocytosis. *Cold Spring Harb Perspect Biol.* 3:a005637. doi: 10.1101/cshperspect.a005637

Sutton, R. B., Fasshauer, D., Jahn, R., and Brunger, A. T. (1998). Crystal structure of a SNARE complex involved in synaptic exocytosis at 2.4 A resolution. *Nature* 395, 347–353. doi: 10.1038/26412

Van Komen, J. S., Bai, X., Rodkey, T. L., Schaub, J., and Mcnew, J. A. (2005). The polybasic juxtamembrane region of Sso1p is required for SNARE function in vivo. *Eukaryotic Cell.* 4, 2017–2028. doi: 10.1128/EC.4.12.2017-2028.2005

Wang, S., Li, Y., Gong, J., Ye, S., Yang, X., Zhang, R., et al. (2019). Munc18 and Munc13 serve as a functional template to orchestrate neuronal SNARE complex assembly. *Nat. Commun.* 10:69. doi: 10.1038/s41467-018-08028-6

Wang, S., Li, Y., and Ma, C. (2016). Synaptotagmin-1 C2B domain interacts simultaneously with SNAREs and membranes to promote membrane fusion. *Elife* 5:e14211. doi: 10.7554/eLife.14211

Weber, T., Zemelman, B. V., Mcnew, J. A., Westermann, B., Gmachl, M., Parlati, F., et al. (1998). SNAREpins: minimal machinery for membrane fusion. *Cell* 92, 759–772. doi: 10.1016/S0092-8674(00)81404-X

Weimbs, T., Mostov, K., Low, S. H., and Hofmann, K. (1998). A model for structural similarity between different SNARE complexes based on sequence relationships. *Trends Cell Biol.* 8, 260–262. doi: 10.1016/S0962-8924(98)01285-9

Weiss, A. N. (2019). Synaptobrevin-2 C-terminal flexible region regulates the discharge of catecholamine molecules. *Biophys. J.* 116, 921–929. doi: 10.1016/j.bpj.2019.01.028

Williams, D., Vicogne, J., Zaitseva, I., Mclaughlin, S., and Pessin, J. E. (2009). Evidence that electrostatic interactions between vesicle-associated membrane protein 2 and acidic phospholipids may modulate the fusion of transport vesicles with the plasma membrane. *Mol. Biol. Cell.* 20, 4910–4919. doi: 10.1091/mbc.e09-04-0284

Xu, H., Zick, M., Wickner, W. T., and Jun, Y. (2011). A lipid-anchored SNARE supports membrane fusion. *Proc. Natl. Acad. Sci. U.S.A.* 108, 17325–17330. doi: 10.1073/pnas.1113888108

Yang, X., Wang, S., Sheng, Y., Zhang, M., Zou, W., Wu, L., et al. (2015). Syntaxin opening by the MUN domain underlies the function of Munc13 in synaptic-vesicle priming. *Nat. Struct. Mol. Biol.* 22, 547–554. doi: 10.1038/nsmb.3038

Zhou, P., Bacaj, T., Yang, X., Pang, Z. P., and Südhof, T. C. (2013). Lipid-anchored SNAREs lacking transmembrane regions fully support membrane fusion during neurotransmitter release. *Neuron* 80, 470–483. doi: 10.1016/j.neuron.2013.09.010

Conflict of Interest: The authors declare that the research was conducted in the absence of any commercial or financial relationships that could be construed as a potential conflict of interest.

frontiers
in Cell and Developmental Biology

MINI REVIEW
published: 28 January 2021
doi: 10.3389/fcell.2021.635636

The p38^{MAPK}-MK2 Signaling Axis as a Critical Link Between Inflammation and Synaptic Transmission

*Edward Beamer and Sonia A. L. Corrêa**

Faculty of Science and Engineering, Department of Life Sciences, Manchester Metropolitan University Manchester, Manchester, United Kingdom

p38 is a mitogen-activated protein kinase (MAPK), that responds primarily to stress stimuli. p38 has a number of targets for phosphorylation, including MAPK-activated protein kinase 2 (MK2). MK2 primarily functions as a master regulator of RNA-binding proteins, indirectly controlling gene expression at the level of translation. The role of MK2 in regulating the synthesis of pro-inflammatory cytokines downstream of inflammation and cellular stress is well-described. A significant amount of evidence, however, now points to a role for the p38^{MAPK}-MK2 signaling axis in mediating synaptic plasticity through control of AMPA receptor trafficking and the morphology of dendritic spines. These processes are mediated through control of cytoskeletal dynamics via the activation of cofilin-1 and possibly control of the expression of Arc/Arg3.1. There is evidence that MK2 is necessary for group I metabotropic glutamate receptors long-term depression (mGluR-LTD). Disruption of this signaling may play an important role in mediating cognitive dysfunction in neurological disorders such as fragile X syndrome and Alzheimer's disease. To date, the role of neuronal MK2 mediating synaptic plasticity in response to inflammatory stimuli has not yet been investigated. In immune cells, it is clear that MK2 is phosphorylated following activation of a broad range of cell surface receptors for cytokines and other inflammatory mediators. We propose that neuronal MK2 may be an important player in the link between inflammatory states and dysregulation of synaptic plasticity underlying cognitive functions. Finally, we discuss the potential of the p38^{MAPK}-MK2 signaling axis as target for therapeutic intervention in a number of neurological disorders.

Keywords: MK2, p38^{MAPK}, synaptic plasticity, mGluR-LTD, neuroinflammation, cognition, hippocampus, AMPAR trafficking

Edited by:
Cong Ma,
Huazhong University of Science and Technology, China

Reviewed by:
Cecilia Bucci,
University of Salento, Italy
Geri Kreitzer,
City University of New York, United States

****Correspondence:***
Sonia A. L. Corrêa
s.correa-muller@mmu.ac.uk

Specialty section:
This article was submitted to Membrane Traffic, a section of the journal Frontiers in Cell and Developmental Biology

Received: *30 November 2020*
Accepted: *11 January 2021*
Published: *28 January 2021*

Citation:
Beamer E and Corrêa SAL (2021) The p38^{MAPK}-MK2 Signaling Axis as a Critical Link Between Inflammation and Synaptic Transmission. Front. Cell Dev. Biol. 9:635636. doi: 10.3389/fcell.2021.635636

INTRODUCTION

Over recent years, the importance of bidirectional cross-talk between the immune system and central nervous system has become increasingly clear. Immune responses are subject to neuroendocrine modulation (Taub, 2008), while inflammatory signals mediate the activity of neural networks (Schneider et al., 1998; Pickering et al., 2005; Clarkson et al., 2017). Molecules that were previously defined by their contribution to the functioning of the immune system, such as tumor necrosis factor α (TNFα), have been shown also to play important roles in regulating neuronal activity (Shatz, 2009). Conversely, a role in immune function has emerged for molecules, such as γ-Aminobutyric acid (GABA), defined by their role in neurotransmission (Kerage et al., 2019). The importance of an inflammatory contribution to neurological disorders has become increasingly clear and mechanisms through which inflammatory signaling is transduced into neuronal responses are of particular interest. The p38 mitogen-activated protein kinase (MAPK, p38^{MAPK}), phosphorylates MAPK-activated protein kinase 2 (MK2). The role of this p38^{MAPK}-MK2 signaling axis in cellular responses to stress and inflammatory signals, including control of the synthesis and release of inflammatory signaling molecules, has been delineated in detail, largely from immune cells (Gaestel, 2006; Menon and Gaestel, 2018). In neurons, however, the p38^{MAPK}-MK2 signaling axis is responsible for mediating neurotransmission in response to activation of perisynaptic group I metabotropic glutamate receptors (mGluR1/5) on dendritic spines. Expressed in neurons throughout the brain, activated in response to inflammatory cues and with a demonstrated role in mediating synaptic plasticity, the p38^{MAPK}-MK2 signaling axis is an attractive candidate for mediating crosstalk between inflammatory and neuronal signaling. Here, we will discuss what is known about activation of the p38^{MAPK}-MK2 axis in response to inflammatory stimuli, the role it plays in mediating synaptic plasticity, discuss the potential of this signaling pathway for mediating cross-talk between inflammatory signals and neurotransmission and discuss settings within which targeting this signaling system may prove efficacious.

THE p38^{MAPK}-MK2 SIGNALING AXIS

MAPK-signaling cascades are highly conserved intracellular signaling pathways that convert external stimuli, usually through cell-surface receptors, into a range of cellular responses (Seger and Krebs, 1995). These signaling pathways are ubiquitous across the eukaryotic domain (Avruch, 2007) and mediate a great diversity of cellular processes, such as proliferation, differentiation, or apoptosis (Qi and Elion, 2005; Keshet and Seger, 2010; Morrison, 2012). These processes largely control the expression of a network of regulatory genes (Whitmarsh, 2007). Each cascade of conventional MAPKs is composed of a set of three sequentially acting kinases: an MAPK, an MAPK kinase (MAP2K), and an MAP2K kinase (MAP3K) (Cargnello and Roux, 2011). The MAP3Ks, at the top of the cascade, are protein serine/threonine kinases, often activated through phosphorylation and/or as a result of their interaction with a small GTP-binding protein of the Ras/Rho family in response to extracellular stimuli (Chiariello et al., 2010). MAP3K activation leads to the phosphorylation and activation of a MAP2K, which then activates a MAPK through dual phosphorylation on threonine and tyrosine residues within a conserved threonine-X-tyrosine motif (Cargnello and Roux, 2011).

p38^{MAPK} is a MAPK, that in mammalian cells is expressed in four splice variants: p38α, p38β, p38γ, and p38δ, with differential phosphorylation of molecular targets (Cuadrado and Nebreda, 2010). P38^{MAPK} is activated by the MAP2Ks, MKK3, and MKK6 (Zarubin and Han, 2005), via dual phosphorylation on threonine-180 and tyrosine-182 (Raingeaud et al., 1995). The principal role of p38^{MAPK} is in co-ordinating molecular responses within the cell to stimuli associated with diverse stressors (Coulthard et al., 2009). Stressors can involve changes in the immediate extracellular microenvironment, such as osmotic (Westfall et al., 2004) or thermal (Li et al., 2018) stress, or the detection of pathogens (Cargnello and Roux, 2011). Alternatively, pathology at the level of organ or organism can be detected through intercellular signaling molecules, such as chemoattractants, cytokines, and chemokines (Menon and Gaestel, 2018). These signals are transduced into a p38^{MAPK}-mediated cellular response through receptors, generally at the cell surface and the subsequent initiation of MAPK signaling cascades, as described above. Through phosphorylation and activation of a range of targets, p38^{MAPK} co-ordinates a cellular response to these inputs, which can include the amplification of inflammatory responses though synthesis and release of pro-inflammatory cytokines (Ronkina et al., 2010; Menon and Gaestel, 2018) and altering the morphology or motility of the cell through changes in the actin cytoskeleton (Scharf et al., 2013). Many of these processes are co-ordinated by MK2.

MK2 is activated by the α and β isoforms of p38^{MAPK}, through phosphorylation at Thr-222, Ser-272 and Thr-334 (Freshney et al., 1994; Han et al., 1994; Rouse et al., 1994; Li et al., 2018). MK2 has multiple targets for phosphorylation, but its primary function is as a master regulator of RNA binding proteins (Culbert et al., 2006; Gaestel, 2006; Gais et al., 2010; Gurgis et al., 2014; Soni et al., 2019). Experimental evidence indicates that MK2 regulates the stability of genes that harbor adenine/uridine-rich elements (AREs) in their 3'-untranslated region (3'-UTRs). The control of mRNA stability and translation by MK2 is dependent on AU-rich elements in the 3' untranslated mRNA region, and on RNA-binding proteins. Deletion of MK2 leads to an impaired inflammatory response, which is mainly due to reduced *TNF*-mRNA stability or translation (Gaestel, 2006).

ACTIVATION OF p38^{MAPK}-MK2 SIGNALING AXIS IN RESPONSE TO INFLAMMATION

The p38^{MAPK}-MK2 signaling axis is embedded in a signaling cycle both downstream of receptors for inflammatory stimuli and upstream of the synthesis and release of pro-inflammatory signaling molecules, allowing it to function as an amplifier of inflammation (Menon and Gaestel, 2018). A broad variety of receptors for inflammatory stimuli and signaling molecules converging through shared pathways, unite at this signaling axis to produce a cellular response (**Figure 1**). The immune system uses pattern recognition receptors (PRRs) (Takeuchi and Akira, 2010; Amarante-Mendes et al., 2018) for the detection of molecules associated with pathogens (pathogen-associated molecular patterns (PAMPs) and damage (damage-associated molecular patters (DAMPs) (Tang et al., 2012). The receptor for advanced glycation end-products (RAGE) is a multi-ligand, cell-surface PRR, which initiates cellular responses to DAMPs. It binds advanced glycation end-products (AGEs)- proteins or

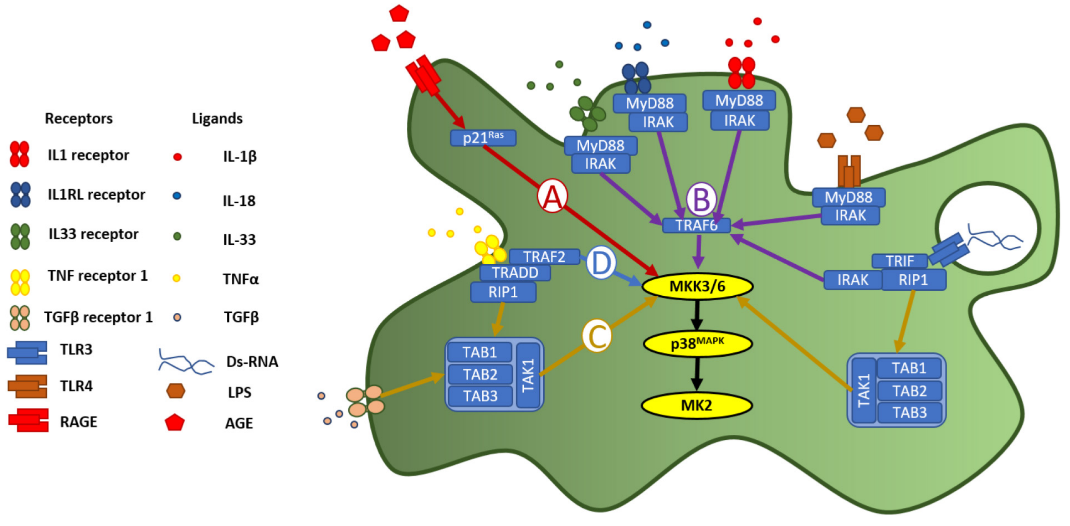

FIGURE 1 | $p38^{MAPK}$-MK2 axis is activated in response to diverse inflammatory stimuli. $p38^{MAPK}$ is a point of convergence for a wide diversity of intracellular signaling pathways triggered by pattern recognition receptors and receptors for cytokines and other inflammatory signaling molecules. Following activation of RAGE, **(A)** the $p38^{MAPK}$-MK2 signaling axis is activated downstream of $p21^{Ras}$, via MKK3/6 (Yeh et al., 2001; Ott et al., 2014). Activation of receptors in the IL1R superfamily **(B)**, including the toll-like receptors, signal through MyD88 and IRAK, to phosphorylate TRAF6, which in turn activates MKK3/6 and then $p38^{MAPK}$ (Martin and Wesche, 2002; Dunne and O'Neill, 2003). **(C)** Activation of TGFβR, meanwhile leads to activation of $p38^{MAPK}$, via TAK1 phosphorylation of MKK3/6 (Yu et al., 2002). This TAK1-dependent pathway is also activated downstream of TNFR1 and TLR3 activation, via RIP1 (Shin et al., 2009). **(D)** Activation of TNF receptor 1 activates $p38^{MAPK}$ via TRAF2 phosphorylation of MKK3/6.

lipids, which have become glycated after exposure to sugars—which accumulate in the extracellular space with increasing age, inflammation, oxidative stress, or as a consequence of ischemia-reperfusion or high glucose (Singh et al., 2001). As well as binding AGEs, RAGE is also activated by calgranulins (Hofmann et al., 1999), amyloid-beta (Aβ) peptides (Yan et al., 1996; Takuma et al., 2009; Piras et al., 2016), associated with Alzheimer's disease, and high-mobility group protein 1 (HMGB1) (Huebener et al., 2015), a chromatin protein which functions in the nucleus, but is released by immune cells as a leaderless cytokine (Klune et al., 2008). Activation of RAGE initiates, via $p21^{Ras}$ protein activator 1 (**Figure 1A**), a MAPK signaling cascade culminating in phosphorylation of MK2 by $p38^{MAPK}$ (Ott et al., 2014). In immune cells, the $p38^{MAPK}$-MK2 signaling axis is necessary for the synthesis and release of inflammatory cytokines in response to RAGE activation (Yeh et al., 2001).

Toll-like receptors (TLRs) are a family of archetypal PRRs, which detect molecular patterns associated with pathogens (Akira et al., 2001; Janeway and Medzhitov, 2002; **Figure 1B**). Lipopolysaccharide (LPS), the material from which the cell wall of gram positive bacteria is constructed, is a ligand for toll-like receptor 4 (TLR4) (Park and Lee, 2013), and can be used experimentally to induce an inflammatory response. Indeed, $p38^{MAPK}$ was first discovered through its activation, via tyrosine phosphorylation, in response to LPS-induced TLR4 activation (Han et al., 1993, 1994). Toll-like receptor 3 (TLR3) meanwhile, is expressed in the cytoplasm or in the membrane of endosomes (Chaturvedi and Pierce, 2009) where it detects strings of nucleotides indicative of a viral infection (Perales-Linares and Navas-Martin, 2013) (**Figure 1B**). Polyriboiosinic:polyribocytidylic acid [poly(I:C)] is a synthetic analog of double-stranded RNA, which can be used experimentally as an immunostimulant to induce an inflammatory response via activation of TLR3 (Farkas et al., 2019). Using Poly(I:C) to stimulate cells, it was demonstrated that the cellular response to activation of TLR3 is dependent on the $p38^{MAPK}$-MK2 signaling axis, through a pathway involving myeloid differentiation primary response 88 (myD88) and TIR-domain-containing adaptor-inducing interferon-β (TRIF) (Johnsen et al., 2012; **Figure 1B**). MK2, therefore functions an effector molecule in cellular responses to detection of both bacterial or viral pathogens.

The TLRs are part of a larger family of receptors, characterized by a toll-IL-1-receptor (TIR) domain (Boraschi et al., 2018). This group includes the interleukin-1 family of receptors, composed of interleukin receptor-1 (ILR1) [a receptor for the leaderless pro-inflammatory cytokines interleukin-1α and β (IL-1α and IL-1β)], interleukin receptor-18 (ILR18), interleukin receptor-like 1 (IL1RL1), receptors for interleukin-18 and interleukin-33, respectively (Dinarello, 2018). The IL-1 receptor family signal through MyD88 and interleukin-1 receptor associated kinase (IRAK) (Martin and Wesche, 2002). IRAK activates the classic MAPK-signaling pathway via tumor necrosis factor receptor associated factor 6 (TRAF6), leading, via MKK3 and MKK6 to activation of the $p38^{MAPK}$-MK2 signaling axis (Dunne and O'Neill, 2003; **Figure 1B**). Evidence for MK2 phosphorylation following activation of receptors in the IL-1R family includes in responses to IL-1β (Raingeaud et al., 1995; Dunne and O'Neill, 2003), IL-33 (Helbig et al., 2020; Petrova et al., 2020), and IL-18 (Dunne and O'Neill, 2003).

Transforming growth factor-β (TGF-β) is a multifunctional cytokine, released in latent form and activated by proteolysis by matrix metalloproteinases on the cell surface (Karsdal et al., 2002). Upon activation, TGFβ functions as a ligand for dimeric, single pass serine/threonine receptors made up of the subunits TGFβ receptor 1 (TGFβR1/ALK5) and TGFβ receptor 2 (TGFβR2). Binding of TGFβ to TGFβR1 activates a signaling cascade involving MKK3/6, p38^{MAPK} and MK2, through the phosphorylation of phosphorylation of TGFβ-activated kinase 1 (TAK1) (**Figure 1C**; Yu et al., 2002).

Tumor necrosis factor-α (TNFα) (Menon and Gaestel, 2018) is a pro-inflammatory cytokine released into the extracellular space, largely by leukocytes during the acute stage of inflammation (Parameswaran and Patial, 2010; Wajant and Siegmund, 2019), and functions as the ligand for two cell surface receptors: tumor necrosis factor receptor 1 and 2 (TNFR1 and TNFR2) (Idriss and Naismith, 2000). TNFR1 activates MAPK-signaling cascades via TNFR1-associated death domain (TRADD) and TNF receptor-associated factor 2 (TRAF2). TRAF2 phosphorylates MKK3/6 (Shi and Sun, 2018; **Figure 1D**). A separate pathway leading to phosphorylation of MKK3/6 is via receptor-interacting protein-1 (RIP1) phosphorylation of TAK1 (Shin et al., 2009) TAK1 phosphorylation is a point of confluence not only with signaling cascades downstream of TGFβR1 (described above), but also via RIP1 activated by TLR3 on endosomes (Kawasaki and Kawai, 2014).

The full range of inflammatory pathways, which lead to activation of the p38^{MAPK}-MK2 axis is broader than can be described within the scope of this review. Other receptors for inflammatory stimuli which have been demonstrated to activate the p38^{MAPK}-MK2 signaling axis include (but are not limited to): monocyte chemoattractant protein 1/chemotactic cytokine ligand 2 (MCP-1/CCL2) activation of chemotactic cytokine receptor 2 (CCR2) (Cho and Gruol, 2008), and interferon-γ activation of interferon-γ receptor (IFNGR) (Culbert et al., 2006).

p38^{MAPK}-MK2 SIGNALING AXIS IN NEURONS

All p38^{MAPK} isoforms are expressed in the mouse brain, with the p38α and β isoforms particularly prominent in the cerebral cortex and hippocampus, with p38α most abundant in neurons (Lee et al., 2000; Beardmore et al., 2005). MK2 is also constitutively expressed in neurons, where it is activated by p38α and β and plays an important role in mediating synaptic plasticity induced by group I metabotropic glutamate receptors (mGluR1/5) (Kemp and Bashir, 1997; Palmer et al., 1997; Moult et al., 2008; Gladding et al., 2009; Sanderson et al., 2016; Privitera et al., 2019; **Figure 2A**). In the hippocampus, activation of perisynaptic mGluR5 on excitatory neurons (Lujan et al., 1996) mediates a prolonged activity-dependent reduction in the synapse efficacy (long-term depression: mGluR-LTD) (Gladding et al., 2009). The mechanisms underlying mGluR-LTD have been extensively studied at hippocampal *Schaffer collateral*-CA1 synapses, where it can be induced through the application of paired-pulse low frequency stimulation (Kemp and Bashir, 1997) or with the mGluR5 agonist (S)-3,5-dihydroxyphenylglycine (DHPG) (Palmer et al., 1997).

The p38^{MAPK}-MK2 signaling axis (Thomas et al., 2008; Eales et al., 2014), activated downstream of mGluR5, controls the molecular machinery in dendritic spines necessary for induction of mGluR-LTD. This includes the molecular regulators of actin remodeling and trafficking of the α-Amino-3-hydroxy-5-methyl-4-isoxazoleproprionic acid receptor (AMPA-R) subunits, GluA1 and GluA2 (Corrêa and Eales, 2012; Eales et al., 2014; Wall et al., 2018; Privitera et al., 2019). The molecular mechanisms underlying synaptic plasticity often vary in different brain regions (Gladding et al., 2009). At CA1 dendrites, mGluR-LTD is mediated by Ca^{2+}-independent mechanisms dependent on a cascade triggered by mGluR5 activation leading to the sequential activation of repressor activator protein 1 (Rap1), MKK3/6, p38^{MAPK} and MK2 (Huang et al., 2004).

The morphology of dendritic spines, and GluA1/GluA2 trafficking is controlled through proteins which act to reorganize dynamic elements of the cytoskeleton. A principal target of MK2, in this regard, is LIM domain kinase 1 (LIMK1), which is phosphorylated at Ser-323 (Kobayashi et al., 2006) and regulates the activity of proteins involved in cytoskeletal remodeling. Cofilin1 is a target of LIMK1 (Meng et al., 2002) and, when activated coordinates the depolymerization of actin filaments (F-actin) into actin monomers (G-actin). The dynamic ratio between F-actin and G-actin is largely responsible for the structural changes of the dendritic spine. A switch toward G-actin, triggered through the p38^{MAPK}-MK2-LIMK-cofilin1 signaling cascade drives the spine toward decreased size and away from a mushroom-like morphology (Honkura et al., 2008; **Figure 2A**). These structural changes are associated with LTD and decreased neurotransmission through the synapse.

AMPA-R trafficking mediating mGluR-LTD is largely coordinated by the expression of the activity-dependent immediate early gene, Arc/Arg3.1 (Snyder et al., 2001; Bramham et al., 2008; Park et al., 2008; Waung et al., 2008; Smith-Hicks et al., 2010; Wall et al., 2018). Transcripts of Arc/Arg3.1 are rapidly transported to dendrites, enabling locally controlled translation at post-synaptic ribosomes (Bramham et al., 2008). Protein expression of Arc/Arg3.1 is regulated at individual dendritic spines through control of translational (Waung et al., 2008); polyubiquitination and targeting for proteolysis (Mabb and Ehlers, 2010; Mabb et al., 2014; Mabb and Ehlers, 2018; Wall et al., 2018). Translation and expression of Arc/Arg3.1 facilitates AMPA-R endocytosis via interaction with cytoskeletal elements (Chowdhury et al., 2006; Waung et al., 2008; DaSilva et al., 2016; Wall and Corrêa, 2018). Although the mechanism by which the MK2 cascade may control Arc/Arg3.1 expression is unclear, the Arc/Arg3.1 gene contains the serum response element (SRE), which may be directly phosphorylated by serum response factors (SRF) (Ronkina et al., 2011), under the control of MK2. Additionally, as a master regulator of RNA-binding proteins (Soni et al., 2019), MK2 may also control the phosphorylation state of proteins involved in regulating local translation and may regulate Arc/Arg3.1 expression both at the transcriptional and local translational level.

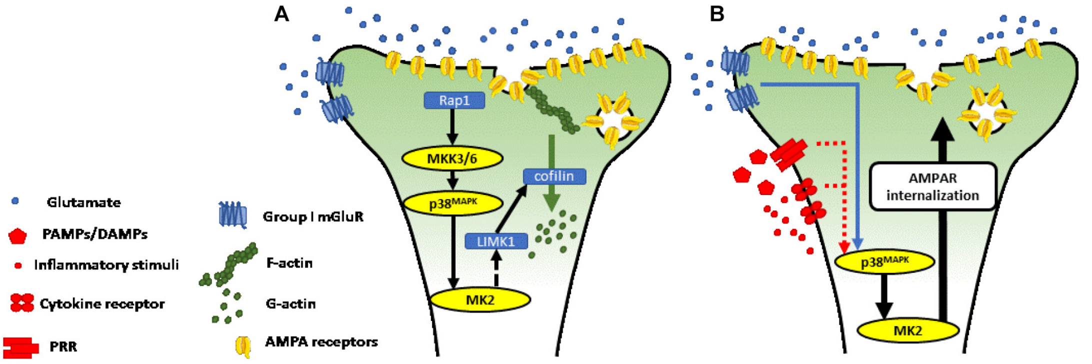

FIGURE 2 | (A) p38^{MAPK}-MK2 axis is necessary for mGluR-LTD at Schaffer collateral—CA1 synapses. Activation of perisynaptic group I mGluR induced long-term depression is dependent on activation of the p38^{MAPK}-MK2 axis. The p38^{MAPK}-MK2-LIMK1-cofilin signaling cascade leads to depolymerization of the actin cytoskeleton, with a decrease in ratio of filamentous (F-) to globular (G-) actin (Meng et al., 2002; Kobayashi et al., 2006; Honkura et al., 2008). **(B)** Putative mechanism through which p38^{MAPK}-MK2 signaling axis mediates neurotransmission in response to inflammatory stimuli. Pattern recognition receptors, receptors for cytokines, and receptors for other inflammatory signaling molecules trigger intracellular signaling cascades, which converge at the p38^{MAPK}-MK2 signaling axis (see section "Activation of p38^{MAPK}-MK2 Signaling Axis in Response to Inflammation" and **Figure 1** for more detail). MK2 controls cytoskeletal dynamics and receptor trafficking, as described in section "p38^{MAPK}-MK2 Signaling Axis in Neurons" and **A**). Through this mechanism, we propose that the p38^{MAPK}-MK2 signaling axis controls synapse strength in response to diverse inflammatory stimuli.

The molecular events controlled by the p38^{MAPK}-MK2 signaling axis mediate changes in synaptic strength that impact at cognitive and behavioral levels. Intact mGluR-LTD is necessary for maintaining cognitive flexibility (Eales et al., 2014), memory extinction (Lüscher and Huber, 2010), and setting the ground for functional long-term potentiation (LTP) at the synapse (Walsh et al., 2002), underlying the formation of new memories. The Barnes maze task, an assay for spatial learning, can be used to measure levels of cognitive flexibility, by adjusting the position of the exit hole after a period of training. While the initial spatial learning task was intact in MK2 knockout mice, they showed severe impairments in relearning the task, demonstrating a deficit in reversal learning (Privitera et al., 2019). These deficits resonate with impairments seen in Fragile-X syndrome (Bear et al., 2004) and Alzheimer's disease (Shankar et al., 2008), which involve dysfunction of mGluR-LTD.

p38^{MAPK}-MK2 SIGNALING AXIS AT CONFLUENCE OF INFLAMMATORY AND SYNAPTIC SIGNALING

Under inflammatory conditions, adaptive structural plasticity of dendritic spines is impaired (Zou et al., 2016) and AMPA-R internalization is increased (Park and Lee, 2013), though the mechanisms underlying these changes are not fully characterized. The p38^{MAPK}-MK2 signaling axis, embedded both in pathways downstream of receptors for a broad range of inflammatory mediators and a necessary effector of mGluR-LTD, is a prime candidate for mediating inflammation-induced changes in neurotransmission. Activated downstream of stress and inflammatory signals in other contexts, we propose that MK2, expressed in neurons, may be an important player in the dysregulation of cognitive and effective functions following injury, infection or as a consequence of autoimmune reactions (**Figure 2B**).

Central to this hypothesis is the neuronal expression of receptors for cytokines and/or chemokines, PRRs and other receptors that respond to inflammatory stimuli. Indeed, many of the receptors that activate the p38^{MAPK}-MK2 signaling axis in immune cells are also expressed in neurons, either constitutively, or induced under inflammatory conditions. Neurons constitutively express TNFR1 (Probert, 2015), while TNFR2 is largely restricted immune and glial cells. Neuronal TNFR1 can also be upregulated in response to insult (Pradillo et al., 2005), mediating processes involved in preconditioning. IL-1R, meanwhile, is expressed in neurons and, more specifically, in dendritic spines where it has been shown to influence synaptic plasticity (Prieto et al., 2015). Amongst other receptors in the IL-1R superfamily, the interleukin-18 receptor (IL-18R) is expressed in neurons, where it is involved in mediating neuronal responses to IL-18 (Alboni et al., 2010). Evidence for neuronal expression of interleukin-1 receptor like receptor (IL1RLR), also known as growth stimulation expressed gene 2 (ST2) is more limited. With expression in sensory neurons well characterized (Liu et al., 2016), but limited data supporting expression of this receptor in central neurons (Fairlie-Clarke et al., 2018).

Amongst the PRRs, there is strong evidence for both constitutive expression of TLR4 in neurons (Leow-Dyke et al., 2012), and upregulation of expression with aging and in pro-inflammatory conditions, such as high levels of extracellular Aβ (Calvo-Rodríguez et al., 2017). There is also strong evidence for endosomal TLR3 expression in neurons, where the receptor not only contributes to mediating cellular responses to pathogens, but also plays a role in regulation of neuronal morphology (Hung et al., 2018). Neuronal expression of RAGE is also well documented (Sasaki et al., 2001), with this receptor heavily implicated in the pathogenesis of neurodegenerative disorders, particularly Alzheimer's disease (Cai et al., 2016), and in contributing to neurological sequelae associated with diabetes (Toth et al., 2007) and other systemic pathologies with an inflammatory element (Gasparotto et al., 2019). Receptors for TGF-β are also expressed in neurons, where they have been implicated in mediating cell fate in response to insult (König et al., 2005).

As described in section "Activation of p38^{MAPK}-MK2 Signaling Axis in Response to Inflammation" above, these cytokine receptors and PRRs activate MAPK-signaling cascaded culminating in the p38^{MAPK}-MK2 axis. As described in section "p38^{MAPK}-MK2 Signaling Axis in Neurons," phosphorylated MK2 regulates synaptic plasticity through transcriptional, post-transcriptional and post-translational control of a suite of effector proteins, which lead to changes in the morphology of dendritic spines and endocytosis of AMPA receptors. While this has been demonstrated in response to activation of group I metabotropic glutamate receptors (mGluR-LTD) (Eales et al., 2014), we suggest that the importance of MK2 in effector pathways downstream of cytokine receptors and PRRs make this molecule a prime candidate in translating inflammatory stimuli into neuronal responses.

CONCLUSION AND FUTURE PERSPECTIVES

A key role for the p38^{MAPK}-MK2 signaling axis has been identified as an effector of cellular responses to inflammatory signals and stimuli. The same signaling axis has also been shown to be a key link in the processes mediating mGluR-LTD. Neuroinflammation is a ubiquitous or near ubiquitous feature of neurological disorders and we identify the p38^{MAPK}-MK2 signaling axis as a potentially important mechanistic link between neuroinflammation and synaptic dysregulation underlying cognitive impairments in neurological disorders, such as Alzheimer's disease. MK2-mediated mGluR-LTD is necessary for maintaining cognitive flexibility, the loss of which is an early clinical sign of Alzheimer's disease. Inhibitors of p38^{MAPK} have been trialed in a number of contexts where inflammation makes an important contribution to disease etiology (Lee and Kim, 2017). These inhibitors, however, have suffered from poor efficacy and a high burden of adverse effects (Hammaker and Firestein, 2010). Inhibitors which specifically target p38^{MAPK} mediated activation of MK2 or target the activity of MK2 itself may offer more promise, with a narrower focus. The p38^{MAPK}-MK2 signaling axis is a promising target for therapeutic intervention, where inflammation contributes to dysregulation of neuronal network activity. More evidence, however, is necessary to clarifying the contribution of this signaling axis.

AUTHOR CONTRIBUTIONS

EB and SALC conceived the review and shared in writing the manuscript. Both authors contributed to the article and approved the submitted version.

FUNDING

This work was funded by startup fund to SALC to setup laboratory at Manchester Metropolitan University.

REFERENCES

Akira, S., Takeda, K., and Kaisho, T. (2001). Toll-like receptors: critical proteins linking innate and acquired immunity. *Nat. Immunol.* 2, 675–680. doi: 10.1038/90609

Alboni, S., Cervia, D., Sugama, S., and Conti, B. (2010). Interleukin 18 in the CNS. *J. Neuroinflam.* 7:9. doi: 10.1186/1742-2094-7-9

Amarante-Mendes, G. P., Adjemian, S., Branco, L. M., Zanetti, L. C., Weinlich, R. Bortoluci, K. R. et al. (2018). Pattern recognition receptors and the host cell death molecular machinery. *Front. Immunol.* 9:2379. doi: 10.3389/fimmu.2018.02379

Avruch, J. (2007). MAP kinase pathways: the first twenty years. *Biochim. Biophys. Acta* 1773, 1150–1160. doi: 10.1016/j.bbamcr.2006.11.006

Bear, M. F., Huber, K. M., and Warren, S. T. (2004). The mGluR theory of fragile X mental retardation. *Trends Neurosci.* 27, 370–377. doi: 10.1016/j.tins.2004.04.009

Beardmore, V. A., Hinton, H. J., Eftychi, C., Apostolaki, M., Armaka, M., Darragh, J., et al. (2005). Generation and characterization of p38beta (MAPK11) gene-targeted mice. *Mol. Cell. Biol.* 25, 10454–10464. doi: 10.1128/mcb.25.23.10454-10464.2005

Boraschi, D., Italiani, P., Weil, S., and Martin, M. U. (2018). The family of the interleukin-1 receptors. *Immunol. Rev.* 281, 197–232. doi: 10.1111/imr.12606

Bramham, C. R., Worley, P. F., Moore, M. J., and Guzowski, J. F. (2008). The immediate early gene arc/arg3.1: regulation, mechanisms, and function. *J. Neurosci.* 28, 11760–11767. doi: 10.1523/jneurosci.3864-08.2008

Cai, Z., Liu, N., Wang, C., Qin, B., Zhou, Y., Xiao, M., et al. (2016). Role of RAGE in Alzheimer's Disease. *Cell. Mol. Neurobiol.* 36, 483–495. doi: 10.1007/s10571-015-0233-3

Calvo-Rodríguez, M., de la Fuente, C., García-Durillo, M., García-Rodríguez, C., Villalobos, C., and Núñez, L. (2017). Aging and amyloid β oligomers enhance TLR4 expression, LPS-induced Ca2+ responses, and neuron cell death in cultured rat hippocampal neurons. *J. Neuroinflam.* 14:24. doi: 10.1186/s12974-017-0802-0

Cargnello, M., and Roux, P. P. (2011). Activation and function of the MAPKs and their substrates, the MAPK-activated protein kinases. *Microbiol. Mol. Biol. Rev.* 75, 50–83. doi: 10.1128/mmbr.00031-10

Chaturvedi, A., and Pierce, S. K. (2009). How location governs toll-like receptor signaling. *Traffic* 10, 621–628. doi: 10.1111/j.1600-0854.2009.00899.x

Chiariello, M., Vaqué, J. P., Crespo, P., and Gutkind, J. S. (2010). Activation of Ras and Rho GTPases and MAP Kinases by G-protein-coupled receptors. *Methods Mol. Biol.* 661, 137–150. doi: 10.1007/978-1-60761-795-2_8

Cho, J., and Gruol, D. L. (2008). The chemokine CCL2 activates p38 mitogen-activated protein kinase pathway in cultured rat hippocampal cells. *J. Neuroimmunol.* 199, 94–103. doi: 10.1016/j.jneuroim.2008.05.011

Chowdhury, S., Shepherd, J. D., Okuno, H., Lyford, G., Petralia, R. S., Plath, N., et al. (2006). Arc/Arg3.1 interacts with the endocytic machinery to regulate AMPA receptor trafficking. *Neuron* 52, 445–459. doi: 10.1016/j.neuron.2006.08.033

Clarkson, B. D. S., Kahoud, R. J., McCarthy, C. B., and Howe, C. L. (2017). Inflammatory cytokine-induced changes in neural network activity measured by waveform analysis of high-content calcium imaging in murine cortical neurons. *Sci. Rep.* 7:9037. doi: 10.1038/s41598-017-09182-5

Corrêa, S. A., and Eales, K. L. (2012). The role of p38 MAPK and its substrates in neuronal plasticity and neurodegenerative disease. *J. Signal. Transduct.* 2012:649079. doi: 10.1155/2012/649079

Coulthard, L. R., White, D. E., Jones, D. L., McDermott, M. F., and Burchill, S. A. (2009). p38(MAPK): stress responses from molecular mechanisms to therapeutics. *Trends Mol. Med.* 15, 369–379. doi: 10.1016/j.molmed.2009.06.005

Cuadrado, A., and Nebreda, A. R. (2010). Mechanisms and functions of p38 MAPK signalling. *Biochem. J.* 429, 403–417. doi: 10.1042/BJ20100323

Culbert, A. A., Skaper, S. D., Howlett, D. R., Evans, N. A., Facci, L., Soden, P. E., et al. (2006). MAPK-activated protein kinase 2 deficiency in microglia inhibits pro-inflammatory mediator release and resultant neurotoxicity. Relevance to neuroinflammation in a transgenic mouse model of Alzheimer disease. *J. Biol. Chem.* 28, 23658–23667. doi: 10.1074/jbc.M513646200

DaSilva, L. L. P., Wall, M. J., de Almeida, L. P., Wauters, S. C., Januário, Y. C., Müller, J., et al. (2016). Activity-regulated cytoskeleton-associated protein controls AMPAR endocytosis through a direct interaction with clathrin-adaptor protein 2. *eNeuro* 3, 144–115. doi: 10.1523/ENEURO.0144-15.2016

Dinarello, C. A. (2018). Overview of the IL-1 family in innate inflammation and acquired immunity. *Immunol. Rev.* 281, 8–27. doi: 10.1111/imr.12621

Dunne, A., and O'Neill, L. A. (2003). The interleukin-1 receptor/Toll-like receptor superfamily: signal transduction during inflammation and host defense. *Sci. STKE* 2003:re3. doi: 10.1126/stke.2003.171.re3

Eales, K. L., Palygin, O., O'Loughlin, T., Rasooli-Nejad, S., Gaestel, M., Müller, J., et al. (2014). The MK2/3 cascade regulates AMPAR trafficking and cognitive flexibility. *Nat. Commun.* 5:4701. doi: 10.1038/ncomms5701

Fairlie-Clarke, K., Barbour, M., Wilson, C., Hridi, S. U., Allan, D., and Jiang, H. R. (2018). Expression and function of IL-33/ST2 Axis in the central nervous system under normal and diseased conditions. *Front. Immunol.* 9:2596. doi: 10.3389/fimmu.2018.02596

Farkas, D., Thompson, A. A. R., Bhagwani, A. R., Hultman, S., Ji, H., Kotha, N., et al. (2019). Toll-like Receptor 3 Is a therapeutic target for pulmonary hypertension. *Am. J. Respir. Crit. Care Med.* 199, 199–210. doi: 10.1164/rccm.201707-1370OC

Freshney, N. W., Rawlinson, L., Guesdon, F., Jones, E., Cowley, S., Hsuan, J., et al. (1994). Interleukin-1 activates a novel protein kinase cascade that results in the phosphorylation of Hsp27. *Cell* 78, 1039–1049. doi: 10.1016/0092-8674(94)90278-x

Gaestel, M. (2006). MAPKAP kinases — MKs — two's company, three's a crowd. *Nat. Rev. Mol. Cell. Biol.* 7, 120–130. doi: 10.1038/nrm1834

Gais, P., Tiedje, C., Altmayr, F., Gaestel, M., Weighardt, H., Holzmann, B. et al. (2010). TRIF signaling stimulates translation of TNF-alpha mRNA via prolonged activation of MK2. *J. Immunol.* 184, 5842–5848. doi: 10.4049/jimmunol.0902456

Gasparotto, J., Ribeiro, C. T., da Rosa-Silva, H. T., Bortolin, R. C., Rabelo, T. K., Peixoto, D. O., et al. (2019). Systemic inflammation changes the site of RAGE expression from endothelial cells to neurons in different brain areas. *Mol. Neurobiol.* 56, 3079–3089. doi: 10.1007/s12035-018-1291-6

Gladding, C. M., Fitzjohn, S. M., and Molnár, E. (2009). Metabotropic glutamate receptor-mediated long-term depression: molecular mechanisms. *Pharmacol. Rev.* 61, 395–412. doi: 10.1124/pr.109.001735

Gurgis, F. M., Ziaziaris, W., and Munoz, L. (2014). Mitogen-activated protein kinase-activated protein kinase 2 in neuroinflammation, heat shock protein 27 phosphorylation, and cell cycle: role and targeting. *Mol. Pharmacol.* 85, 345–356. doi: 10.1124/mol.113.090365

Hammaker, D., and Firestein, G. S. (2010). "Go upstream, young man": lessons learned from the p38 saga. *Ann. Rheum. Dis.* 69, 77–82. doi: 10.1136/ard.2009.119479

Han, J., Lee, J. D., Bibbs, L., and Ulevitch, R. J. (1994). A MAP kinase targeted by endotoxin and hyperosmolarity in mammalian cells. *Science* 265, 808–811. doi: 10.1126/science.7914033

Han, J., Lee, J. D., Tobias, P. S., and Ulevitch, R. J. (1993). Endotoxin induces rapid protein tyrosine phosphorylation in 70Z/3 cells expressing CD14. *J. Biol. Chem.* 268, 25009–25014.

Helbig, C., Weber, F., Andreas, N., Herdegen, T., Gaestel, M., Kamradt, T., et al. (2020). The IL-33-induced p38-/JNK1/2-TNFα axis is antagonized by activation of β-adrenergic-receptors in dendritic cells. *Sci. Rep.* 10:8152. doi: 10.1038/s41598-020-65072-3

Hofmann, M. A., Drury, S., Fu, C., Qu, W., Taguchi, A., Lu, Y., et al. (1999). RAGE mediates a novel proinflammatory axis: a central cell surface receptor for S100/calgranulin polypeptides. *Cell* 97, 889–901. doi: 10.1016/s0092-8674(00)80801-6

Honkura, N., Matsuzaki, M., Noguchi, J., Ellis-Davies, G. C., and Kasai, H. (2008). The subspine organization of actin fibers regulates the structure and plasticity of dendritic spines. *Neuron* 57, 719–729. doi: 10.1016/j.neuron.2008.01.013

Huang, C. C., You, J. L., Wu, M. Y., and Hsu, K. S. (2004). Rap1-induced p38 mitogen-activated protein kinase activation facilitates AMPA receptor trafficking via the GDI.Rab5 complex. Potential role in (S)-3,5-dihydroxyphenylglycene-induced long term depression. *J Biol. Chem.* 279, 12286–12292. doi: 10.1074/jbc.M312868200

Huebener, P., Pradere, J. P., Hernandez, C., Gwak, G. Y., Caviglia, J. M., Mu, X., et al. (2015). The HMGB1/RAGE axis triggers neutrophil-mediated injury amplification following necrosis. *J. Clin. Invest.* 125, 539–550. doi: 10.1172/jci76887

Hung, Y. F., Chen, C. Y., Shih, Y. C., Liu, H. Y., Huang, C. M., and Hsueh, Y. P. (2018). Endosomal TLR3, TLR7, and TLR8 control neuronal morphology through different transcriptional programs. *J. Cell. Biol.* 217, 2727–2742. doi: 10.1083/jcb.201712113

Idriss, H. T., and Naismith, J. H. (2000). TNF alpha and the TNF receptor superfamily: structure-function relationship(s). *Microsc. Res. Tech.* 50, 184–195. doi: 10.1002/1097-0029(20000801)50:3<184::aid-jemt2<3.0.co;2-h

Janeway, C. A., and Medzhitov, R. (2002). Innate immune recognition. *Ann. Rev. Immunol.* 20, 197–216. doi: 10.1146/annurev.immunol.20.083001.084359

Johnsen, I. B., Nguyen, T. T., Bergstrøm, B., Lien, E., and Anthonsen, M. W. (2012). Toll-like receptor 3-elicited MAPK activation induces stabilization of interferon-β mRNA. *Cytokine* 57, 337–346. doi: 10.1016/j.cyto.2011.11.024

Karsdal, M. A., Larsen, L., Engsig, M. T., Lou, H., Ferreras, M., Lochter, A., et al. (2002). Matrix metalloproteinase-dependent activation of latent transforming growth factor-beta controls the conversion of osteoblasts into osteocytes by blocking osteoblast apoptosis. *J. Biol. Chem.* 277, 44061–44067. doi: 10.1074/jbc.M207205200

Kawasaki, T., and Kawai, T. (2014). Toll-like receptor signaling pathways. *Front. Immunol.* 5:461. doi: 10.3389/fimmu.2014.00461

Kemp, N., and Bashir, Z. I. (1997). NMDA receptor-dependent and -independent long-term depression in the CA1 region of the adult rat hippocampus in vitro. *Neuropharmacology* 36, 397–399. doi: 10.1016/s0028-3908(96)90015-5

Kerage, D., Sloan, E. K., Mattarollo, S. R., and McCombe, P. A. (2019). Interaction of neurotransmitters and neurochemicals with lymphocytes. *J. Neuroimmunol.* 332, 99–111. doi: 10.1016/j.jneuroim.2019.04.006

Keshet, Y., and Seger, R. (2010). The MAP kinase signaling cascades: a system of hundreds of components regulates a diverse array of physiological functions. *Methods Mol. Biol.* 661, 3–38. doi: 10.1007/978-1-60761-795-2_1

Klune, J. R., Dhupar, R., Cardinal, J., Billiar, T. R., and Tsung, A. (2008). HMGB1: endogenous danger signaling. *Mol. Med.* 14, 476–484. doi: 10.2119/2008-00034.Klune

Kobayashi, M., Nishita, M., Mishima, T., Ohashi, K., and Mizuno, K. (2006). MAPKAPK-2-mediated LIM-kinase activation is critical for VEGF-induced actin remodeling and cell migration. *Embo. J.* 25, 713–726. doi: 10.1038/sj.emboj.7600973

König, H. G., Kögel, D., Rami, A., and Prehn, J. H. (2005). TGF-{beta}1 activates two distinct type I receptors in neurons: implications for neuronal NF-{kappa}B signaling. *J. Cell. Biol.* 168, 1077–1086. doi: 10.1083/jcb.200407027

Lee, J. K., and Kim, N. J. (2017). Recent advances in the inhibition of p38 MAPK as a potential strategy for the treatment of Alzheimer's Disease. *Molecules* 22:1287. doi: 10.3390/molecules22081287

Lee, S. H., Park, J., Che, Y., Han, P. L., and Lee, J. K. (2000). Constitutive activity and differential localization of p38alpha and p38beta MAPKs in adult mouse brain. *J. Neurosci. Res.* 60, 623–631. doi: 10.1002/(sici)1097-4547(20000601)60:5<623::aid-jnr7<3.0.co;2-4

Leow-Dyke, S., Allen, C., Denes, A., Nilsson, O., Maysami, S., Bowie, A. G., et al. (2012). Neuronal toll-like receptor 4 signaling induces brain endothelial activation and neutrophil transmigration in vitro. *J. Neuroinflam.* 9:230. doi: 10.1186/1742-2094-9-230

Li, H., Liu, Y., Gu, Z., Li, L., Wang, L., Su, L. et al. (2018). p38 MAPK-MK2 pathway regulates the heat-stress-induced accumulation of reactive oxygen species that mediates apoptotic cell death in glial cells. *Oncol. Lett.* 15, 775–782. doi: 10.3892/ol.2017.7360

Liu, B., Tai, Y., Achanta, S., Kaelberer, M. M., Caceres, A. I., Shao, X., et al. (2016). IL-33/ST2 signaling excites sensory neurons and mediates itch response in a mouse model of poison ivy contact allergy. *Proc. Natl. Acad. Sci. U S A.* 113, E7572–E7579. doi: 10.1073/pnas.1606608113

Lujan, R., Nusser, Z., Roberts, J. D., Shigemoto, R., and Somogyi, P. (1996). Perisynaptic location of metabotropic glutamate receptors mGluR1 and mGluR5 on dendrites and dendritic spines in the rat hippocampus. *Eur. J. Neurosci.* 8, 1488–1500. doi: 10.1111/j.1460-9568.1996.tb01611.x

Lüscher, C., and Huber, K. M. (2010). Group 1 mGluR-dependent synaptic long-term depression: mechanisms and implications for circuitry and disease. *Neuron* 65, 445–459. doi: 10.1016/j.neuron.2010.01.016

Mabb, A. M., and Ehlers, M. D. (2010). Ubiquitination in postsynaptic function and plasticity. *Ann. Rev. Cell. Dev. Biol.* 26, 179–210. doi: 10.1146/annurev-cellbio-100109-104129

Mabb, A. M., and Ehlers, M. D. (2018). Arc ubiquitination in synaptic plasticity. *Semin. Cell. Dev. Biol.* 77, 10–16. doi: 10.1016/j.semcdb.2017.09.009

Mabb, A. M., Je, H. S., Wall, M. J., Robinson, C. G., Larsen, R. S., Qiang, Y., et al. (2014). Triad3A regulates synaptic strength by ubiquitination of Arc. *Neuron* 82, 1299–1316. doi: 10.1016/j.neuron.2014.05.016

Martin, M. U., and Wesche, H. (2002). Summary and comparison of the signaling mechanisms of the Toll/interleukin-1 receptor family. *Biochim. Biophys. Acta* 1592, 265–280. doi: 10.1016/s0167-4889(02)00320-8

Meng, Y., Zhang, Y., Tregoubov, V., Janus, C., Cruz, L., Jackson, M., et al. (2002). Abnormal spine morphology and enhanced LTP in LIMK-1 knockout mice. *Neuron* 35, 121–133. doi: 10.1016/S0896-6273(02)00758-4

Menon, M. B., and Gaestel, M. (2018). MK2-TNF-signaling comes full circle. *Trends Biochem. Sci.* 43, 170–179. doi: 10.1016/j.tibs.2017.12.002

Morrison, D. K. (2012). MAP kinase pathways. *Cold Spring Harb. Perspect. Biol.* 4:a011254. doi: 10.1101/cshperspect.a011254

Moult, P. R., Corrêa, S. A., Collingridge G. L., Fitzjohn S. M., and Bashir Z. I. (2008). Co-activation of p38 mitogen-activated protein kinase and protein tyrosine phosphatase underlies metabotropic glutamate receptor-dependent long-term depression. *J. Physiol.* 15, 2499–2510. doi: 10.1113/jphysiol.2008.153122

Ott, C., Jacobs, K., Haucke, E., Navarrete Santos, A., Grune, T., and Simm, A. (2014). Role of advanced glycation end products in cellular signaling. *Redox. Biol.* 2, 411–429. doi: 10.1016/j.redox.2013.12.016

Palmer, M. J., Irving, A. J., Seabrook, G. R., Jane, D. E., and Collingridge, G. L. (1997). The group I mGlu receptor agonist DHPG induces a novel form of LTD in the CA1 region of the hippocampus. *Neuropharmacology* 36, 1517–1532. doi: 10.1016/s0028-3908(97)00181-0

Parameswaran, N., and Patial, S. (2010). Tumor necrosis factor-α signaling in macrophages. *Crit. Rev. Eukaryot. Gene Expr.* 20, 87–103. doi: 10.1615/critreveukargeneexpr.v20.i2.10

Park, B. S., and Lee, J.-O. (2013). Recognition of lipopolysaccharide pattern by TLR4 complexes. *Exp. Mol. Med.* 45:e66. doi: 10.1038/emm.2013.97

Park, S., Park, J. M., Kim, S., Kim, J. A., Shepherd, J. D., Smith-Hicks, C. L., et al. (2008). Elongation factor 2 and fragile X mental retardation protein control the dynamic translation of Arc/Arg3.1 essential for mGluR-LTD. *Neuron* 59, 70–83. doi: 10.1016/j.neuron.2008.05.023

Perales-Linares, R., and Navas-Martin, S. (2013). Toll-like receptor 3 in viral pathogenesis: friend or foe? *Immunology* 140, 153–167. doi: 10.1111/imm.12143

Petrova, T., Pesic, J., Pardali, K., Gaestel, M., and Arthur, J. S. C. (2020). p38 MAPK signalling regulates cytokine production in IL-33 stimulated Type 2 Innate Lymphoid cells. *Sci. Rep.* 10:3479. doi: 10.1038/s41598-020-60089-0

Pickering, M., Cumiskey, D., and O'Connor, J. J. (2005). Actions of TNF-alpha on glutamatergic synaptic transmission in the central nervous system. *Exp. Physiol.* 90, 663–670. doi: 10.1113/expphysiol.2005.030734

Piras, S., Furfaro, A. L., Domenicotti, C., Traverso, N., Marinari, U. M., Pronzato, M. A., et al. (2016). RAGE Expression and ROS generation in neurons: differentiation versus damage. *Oxid. Med. Cell. Longev.* 2016:9348651. doi: 10.1155/2016/9348651

Pradillo, J. M., Romera, C., Hurtado, O., Cárdenas, A., Moro, M. A., Leza, J. C., et al. (2005). TNFR1 upregulation mediates tolerance after brain ischemic preconditioning. *J. Cereb. Blood Flow Metab.* 25, 193–203. doi: 10.1038/sj.jcbfm.9600019

Prieto, G. A., Snigdha, S., Baglietto-Vargas, D., Smith, E. D., Berchtold, N. C., Tong, L., et al. (2015). Synapse-specific IL-1 receptor subunit reconfiguration augments vulnerability to IL-1β in the aged hippocampus. *Proc. Natl. Acad. Sci. U S A.* 112, E5078–E5087. doi: 10.1073/pnas.1514486112

Privitera, L., Hogg, E. L., Gaestel, M., Wall, M. J., and Corrêa, S. A. L. (2019). The MK2 cascade regulates mGluR-dependent synaptic plasticity and reversal learning. *Neuropharmacology* 155, 121–130. doi: 10.1016/j.neuropharm.2019.05.024

Probert, L. (2015). TNF and its receptors in the CNS: the essential, the desirable and the deleterious effects. *Neuroscience* 302, 2–22. doi: 10.1016/j.neuroscience.2015.06.038

Qi, M., and Elion, E. A. (2005). MAP kinase pathways. *J. Cell. Sci.* 118, 3569–3572. doi: 10.1242/jcs.02470

Raingeaud, J., Gupta, S., Rogers, J. S., Dickens, M., Han, J., Ulevitch, R. J., et al. (1995). Pro-inflammatory cytokines and environmental stress cause p38 mitogen-activated protein kinase activation by dual phosphorylation on tyrosine and threonine. *J. Biol. Chem.* 270, 7420–7426. doi: 10.1074/jbc.270.13.7420

Ronkina, N., Menon, M. B., Schwermann, J., Arthur, J. S., Legault, H., Telliez, J. B., et al. (2011). Stress induced gene expression: a direct role for MAPKAP kinases in transcriptional activation of immediate early genes. *Nucleic Acids Res.* 39, 2503–2518. doi: 10.1093/nar/gkq1178

Ronkina, N., Menon, M. B., Schwermann, J., Tiedje, C., Hitti, E., Kotlyarov, A., et al. (2010). MAPKAP kinases MK2 and MK3 in inflammation: complex regulation of TNF biosynthesis via expression and phosphorylation of tristetraprolin. *Biochem. Pharmacol.* 80, 1915–1920. doi: 10.1016/j.bcp.2010.06.021

Rouse, J., Cohen, P., Trigon, S., Morange, M., Alonso-Llamazares, A., Zamanillo, D., et al. (1994). A novel kinase cascade triggered by stress and heat shock that stimulates MAPKAP kinase-2 and phosphorylation of the small heat shock proteins. *Cell* 78, 1027–1037. doi: 10.1016/0092-8674(94)90277-1

Sanderson, T. M., Hogg, E. L., Collingridge, G. L., and Corrêa, S. A. (2016). Hippocampal metabotropic glutamate receptor long-term depression in health and disease: focus on mitogen-activated protein kinase pathways. *J. Neurochem.* 139, 200–214. doi: 10.1111/jnc.13592

Sasaki, N., Toki, S., Chowei, H., Saito, T., Nakano, N., Hayashi, Y., et al. (2001). Immunohistochemical distribution of the receptor for advanced glycation end products in neurons and astrocytes in Alzheimer's disease. *Brain Res.* 888, 256–262. doi: 10.1016/s0006-8993(00)03075-4

Scharf, M., Neef, S., Freund, R., Geers-Knörr, C., Franz-Wachtel, M., Brandis, A., et al. (2013). Mitogen-activated protein kinase-activated protein kinases 2 and 3 regulate SERCA2a expression and fiber type composition to modulate skeletal muscle and cardiomyocyte function. *Mol. Cell. Biol.* 33, 2586–2602. doi: 10.1128/mcb.01692-12

Schneider, H., Pitossi, F., Balschun, D., Wagner, A., del Rey, A., Besedovsky, H. O. et al. (1998). A neuromodulatory role of interleukin-1beta in the hippocampus. *Proc. Natl. Acad. Sci. U S A.* 95, 7778–7783. doi: 10.1073/pnas.95.13.7778

Seger, R., and Krebs, E. G. (1995). The MAPK signaling cascade. *Faseb. J.* 9, 726–735.

Shankar, G. M., Li, S., Mehta, T. H., Garcia-Munoz, A., Shepardson, N. E., Smith, I., et al. (2008). Amyloid-beta protein dimers isolated directly from Alzheimer's brains impair synaptic plasticity and memory. *Nat. Med.* 14, 837–842. doi: 10.1038/nm1782

Shatz, C. J. (2009). MHC class I: an unexpected role in neuronal plasticity. *Neuron* 64, 40–45. doi: 10.1016/j.neuron.2009.09.044

Shi, J.-H., and Sun, S.-C. (2018). Tumor necrosis factor receptor-associated factor regulation of nuclear factor κB and mitogen-activated protein kinase pathways. *Front. Immunol.* 9:1849. doi: 10.3389/fimmu.2018.01849

Shin, M. S., Shinghirunnusorn, P., Sugishima, Y., Nishimura, M., Suzuki, S., Koizumi, K., et al. (2009). Cross interference with TNF-alpha-induced TAK1 activation via EGFR-mediated p38 phosphorylation of TAK1-binding protein 1. *Biochim. Biophys. Acta* 1793, 1156–1164. doi: 10.1016/j.bbamcr.2009.04.005

Singh, R., Barden, A., Mori, T., and Beilin, L. (2001). Advanced glycation end-products: a review. *Diabetologia* 44, 129–146. doi: 10.1007/s001250051591

Smith-Hicks, C., Xiao, B., Deng, R., Ji, Y., Zhao, X., Shepherd, J. D., et al. (2010). SRF binding to SRE 6.9 in the Arc promoter is essential for LTD in cultured Purkinje cells. *Nat. Neurosci.* 13, 1082–1089. doi: 10.1038/nn.2611

Snyder, E. M., Philpot, B. D., Huber, K. M., Dong, X., Fallon, J. R., and Bear, M. F. (2001). Internalization of ionotropic glutamate receptors in response to mGluR activation. *Nat. Neurosci.* 4, 1079–1085. doi: 10.1038/nn746

Soni, S., Anand, P., and Padwad, Y. S. (2019). MAPKAPK2: the master regulator of RNA-binding proteins modulates transcript stability and tumor progression. *J. Exp. Clin. Cancer Res.* 38:121. doi: 10.1186/s13046-019-1115-1

Takeuchi, O., and Akira, S. (2010). Pattern recognition receptors and inflammation. *Cell* 140, 805–820. doi: 10.1016/j.cell.2010.01.022

Takuma, K., Fang, F., Zhang, W., Yan, S., Fukuzaki, E., Du, H., et al. (2009). RAGE-mediated signaling contributes to intraneuronal transport of amyloid-beta and neuronal dysfunction. *Proc. Natl. Acad. Sci U S A.* 106, 20021–20026. doi: 10.1073/pnas.0905686106

Tang, D., Kang, R., Coyne, C. B., Zeh, H. J., and Lotze, M. T. (2012). PAMPs and DAMPs: signal 0s that spur autophagy and immunity. *Immunol. Rev.* 249, 158–175. doi: 10.1111/j.1600-065X.2012.01146.x

Taub, D. D. (2008). Neuroendocrine interactions in the immune system. *Cell Immunol.* 252, 1–6. doi: 10.1016/j.cellimm.2008.05.006

Thomas, T., Hitti, E., Kotlyarov, A., Potschka, H., and Gaestel, M. (2008). MAP-kinase-activated protein kinase 2 expression and activity is induced after neuronal depolarization. *Eur. J. Neurosci.* 28, 642–654. doi: 10.1111/j.1460-9568.2008.06382.x

Toth, C., Martinez, J., and Zochodne, D. W. (2007). RAGE, diabetes, and the nervous system. *Curr. Mol. Med.* 7, 766–776. doi: 10.2174/156652407783220705

Wajant, H., and Siegmund, D. (2019). TNFR1 and TNFR2 in the control of the life and death balance of macrophages. *Front. Cell. Dev. Biol.* 7:91. doi: 10.3389/fcell.2019.00091

Wall, M. J., Collins, D. R., Chery, S. L., Allen, Z. D., Pastuzyn, E. D., George, A. J., et al. (2018). The temporal dynamics of arc expression regulate cognitive flexibility. *Neuron* 98, 1124–1132. doi: 10.1016/j.neuron.2018.05.012

Wall, M. J., and Corrêa, S. A. L. (2018). The mechanistic link between Arc/Arg3.1 expression and AMPA receptor endocytosis. *Semin. Cell. Dev. Biol.* 77, 17–24. doi: 10.1016/j.semcdb.2017.09.005

Walsh, D. M., Klyubin, I., Fadeeva, J. V., Cullen, W. K., Anwyl, R., Wolfe, M. S., et al. (2002). Naturally secreted oligomers of amyloid beta protein potently inhibit hippocampal long-term potentiation in vivo. *Nature* 416, 535–539. doi: 10.1038/416535a

Waung, M. W., Pfeiffer, B. E., Nosyreva, E. D., Ronesi, J. A., and Huber, K. M. (2008). Rapid translation of Arc/Arg3.1 selectively mediates mGluR-dependent LTD through persistent increases in AMPAR endocytosis rate. *Neuron* 59, 84–97. doi: 10.1016/j.neuron.2008.05.014

Westfall, P. J., Ballon, D. R., and Thorner, J. (2004). When the stress of your environment makes you go HOG wild. *Science* 306, 1511–1512. doi: 10.1126/science.1104879

Whitmarsh, A. J. (2007). Regulation of gene transcription by mitogen-activated protein kinase signaling pathways. *Biochim. Biophys. Acta* 1773, 1285–1298. doi: 10.1016/j.bbamcr.2006.11.011

Yan, S. D., Chen, X., Fu, J., Chen, M., Zhu, H., Roher, A., et al. (1996). RAGE and amyloid-β peptide neurotoxicity in Alzheimer's disease. *Nature* 382, 685–691. doi: 10.1038/382685a0

Yeh, C. H., Sturgis, L., Haidacher, J., Zhang, X. N., Sherwood, S. J., Bjercke, R. J., et al. (2001). Requirement for p38 and p44/p42 mitogen-activated protein kinases in RAGE-mediated nuclear factor-kappaB transcriptional activation and cytokine secretion. *Diabetes* 50, 1495–1504. doi: 10.2337/diabetes.50.6.1495

Yu, L., Hébert, M. C., and Zhang, Y. E. (2002). TGF-beta receptor-activated p38 MAP kinase mediates Smad-independent TGF-beta responses. *Embo. J.* 21, 3749–3759. doi: 10.1093/emboj/cdf366

Zarubin, T., and Han, J. (2005). Activation and signaling of the p38 MAP kinase pathway. *Cell. Res.* 15, 11–18. doi: 10.1038/sj.cr.7290257

Zou, C., Shi, Y., Ohli, J., Schüller, U., Dorostkar, M. M., and Herms, J. (2016). Neuroinflammation impairs adaptive structural plasticity of dendritic spines in a preclinical model of Alzheimer's disease. *Acta Neuropathol.* 131, 235–246. doi: 10.1007/s00401-015-1527-8

Conflict of Interest: The authors declare that the research was conducted in the absence of any commercial or financial relationships that could be construed as a potential conflict of interest.

frontiers
in Cell and Developmental Biology

ORIGINAL RESEARCH
published: 09 February 2021
doi: 10.3389/fcell.2021.634160

Flotillin-1 Interacts With and Sustains the Surface Levels of TRPV2 Channel

Juan Hu[1†], Yue Gao[1†], Qian Huang[1†], Yuanyuan Wang[1], Xiaoyi Mo[1], Peiyu Wang[1], Youjing Zhang[1], Chang Xie[1], Dongdong Li[2] and Jing Yao[1*]

[1] State Key Laboratory of Virology, Hubei Key Laboratory of Cell Homeostasis, College of Life Sciences, Frontier Science Center for Immunology and Metabolism, Wuhan University, Wuhan, China, [2] Institute of Biology Paris Seine, Neuroscience Paris Seine, CNRS UMR8246, INSERM U1130, Sorbonne Université, Paris, France

Transient receptor potential vanilloid subtype 2 (TRPV2) channel is a polymodal receptor regulating neuronal development, cardiac function, immunity and oncogenesis. The activity of TRPV2 is regulated by the molecular interactions in the subplasmalemmel signaling complex. Here by yeast two-hybrid screening of a cDNA library of mouse dorsal root ganglia (DRG) and patch clamp electrophysiology, we identified that flotillin-1, the lipid raft-associated protein, interacts with TRPV2 channel and regulates its function. The interaction between TRPV2 and flotillin-1 was validated through co-immuoprecipitation *in situ* using endogenous DRG neurons and the recombinant expression model in HEK 293T cells. Fluorescent imaging and bimolecular fluorescence complementation (BiFC) further revealed that flotillin-1 and TRPV2 formed a functional complex on the cell membrane. The presence of flotillin-1 enhanced the whole-cell current density of TRPV2 via increasing its surface expression levels. Using site-specific mapping, we also uncovered that the SPFH (stomatin, prohibitin, flotillin, and HflK/C) domain of flotillin-1 interacted with TRPV2 N-termini and transmembrane domains 1–4, respectively. Our findings therefore demonstrate that flotillin-1 is a key element in TRPV2 signaling complex and modulates its cellular response.

Keywords: TRPV2, flotillin-1, protein–protein interactions, protein stability, thermal sensation

Edited by:
Cong Ma,
Huazhong University of Science and Technology, China

Reviewed by:
Rui Xiao,
University of Florida, United States
Ye Yu,
China Pharmaceutical University, China
Yuko Iwata,
National Cerebral and Cardiovascular Center, Japan
Ritva Tikkanen,
University of Giessen, Germany

***Correspondence:**
Jing Yao
jyao@whu.edu.cn

[†] These authors have contributed equally to this work

Specialty section:
This article was submitted to Membrane Traffic, a section of the journal Frontiers in Cell and Developmental Biology

Received: 27 November 2020
Accepted: 20 January 2021
Published: 09 February 2021

Citation:
Hu J, Gao Y, Huang Q, Wang Y, Mo X, Wang P, Zhang Y, Xie C, Li D and Yao J (2021) Flotillin-1 Interacts With and Sustains the Surface Levels of TRPV2 Channel. Front. Cell Dev. Biol. 9:634160. doi: 10.3389/fcell.2021.634160

INTRODUCTION

Transient receptor potential vanilloid type 2 (TRPV2) was firstly identified in 1999. It has been proposed to mediate responses to noxious thermal (52°C) stimuli in medium- to large-diameter sensory neurons (Caterina et al., 1999). TRPV2 is a Ca^{2+}-permeable and polymodal channel modulated by mechanical stretch, heat, osmotic swelling, and endogenous and exogenous chemical modulators such as 2-aminoethoxydiphenyl borate (2-APB), cannabinoids, probenecid, amiloride and SKF96365 (Bang et al., 2007; Colton and Zhu, 2007; Juvin et al., 2007; Qin et al., 2008). TRPV2 is a well-conserved channel protein expressed in almost all tissues, such as the central and peripheral nervous systems, the immune system, and the muscular system. Structurally, mammalian TRPV2 consists of a 6 transmembrane (TM)-domain structure flanked by a large cytosolic N- and C-terminus with a pore-forming loop between the fifth and sixth TM domains (Huynh et al., 2016). Recent research on TRPV2 has made remarkable progress, especially in terms of the discovery of its physio-pathological functions. In addition to being a thermosensor for noxious heat, the widespread distribution of TRPV2 has been implicated in developing axon outgrowth

(Shibasaki et al., 2010), various osmo- or mechanosensation (Donate-Macian et al., 2019), physiological cardiac structure maintenance and function (Katanosaka et al., 2014), insulin secretion (Aoyagi et al., 2010), proinflammatory processes (Entin-Meer et al., 2017), immune activity (Link et al., 2010; Santoni et al., 2013).

TRPV2 channel is organized in signaling complexes, where its function is regulated by protein–protein interactions. For instance, TRPV2 channel biogenesis is associated with post-translational modification such as recombinase gene activator protein (RGA)-related glycosylation (Stokes et al., 2005) and protein kinase A (PKA)-mediated phosphorylation (Stokes et al., 2004). In addition, certain signaling molecules have been documented to regulate the channel expression. TRPV2 protein levels are upregulated by nerve growth factor (NGF) via the mitogen-activated protein kinase (MAPK) signaling pathway (Cohen et al., 2015). Antiaging gene Klotho enhances glucose-induced insulin secretion by increasing plasma membrane levels of TRPV2 and thus calcium influx (Lin and Sun, 2012). Other modulators have also been shown to affect TRPV2 function. For example, phosphatidylinositol 4,5-bisphosphate (PIP2) depletion contributes to Ca^{2+}-dependent desensitization of TRPV2 (Mercado et al., 2010). Inflammatory factors like TNF−α facilitate TRPV2 responses in human dental pulp cells (Liu et al., 2019). Further identification of binding partners will help to deepen the understanding of the regulatory mechanisms of TRPV2.

The flotillin (FLOT)/reggie protein family is integral membrane element and contains two isoforms: flotillin-1 (reggie-2) and flotillin-2 (reggie-1) (Schulte et al., 1997; Browman et al., 2007). Their C-terminal flotillin domains are required for the oligomerization, while the N-terminal SPFH (stomatin, prohibitin, flotillin, and HflK/C) domain is mainly responsible for membrane interactions (Solis et al., 2007; Bodin et al., 2014). Flotillin-1 is highly expressed in the nervous system and has been identified as an evolutionarily conserved protein involved in learning and memory (Monje et al., 2013). Flotillin-1 participates in various cellular functions, including cell adhesion, actin cytoskeleton reorganization, endocytosis, phagocytosis and the transduction of cellular signals (Langhorst et al., 2005). Moreover, flotillins are considered to be scaffolding proteins of lipid rafts and are preferentially associated with many other proteins. Flotillins interact with Src family kinase Fyn and contribute to the formation of signal transduction centers in adipocytes, T lymphocytes, and neurons (Stuermer et al., 2001; Liu et al., 2005). Flotillin-1 interacts with CAP, Vinexin α and ArgBP2, respectively, and regulates the organization of the actin cytoskeleton (Kimura et al., 2001). Cornfine et al. (2011) reported that flotillin-2 interacted with kinesin KIF9 and regulated matrix degradation by macrophage podosomes. In addition, flotillins have also been suggested to be associated with several ion channels, including the NR2A and NR2B subunits of NMDA receptors (Swanwick et al., 2009), Nav1.5 channels (Kessler et al., 2019), Kv2.1 channels (Liu et al., 2016), voltage-gated calcium channels (Robinson et al., 2010), calcium-activated chloride channels (Sones et al., 2010), aquaporin 5 (Wang et al., 2011), GABAA receptor (Nothdurfter et al., 2013), and the purinergic P2X3 receptor (Vacca et al., 2004) in different tissues. Nevertheless, the role of flotillins in regulating TRPV2 functions remains unaddressed.

Here combining yeast two-hybrid screening, immunoprecipitation and BiFC imaging, we demonstrate that flotillin-1 interacts with TRPV2 channel at the protein level. Heterologous co-expression of flotillin-1 increased the whole-cell current density of TRPV2 as a result of enhanced surface expression. Moreover, we show that the N-terminus and TM domains (1–4) of TRPV2 interact with the SPFH domain of flotillin-1 in the multiprotein assembly. Our findings thus indicate that flotillin-1 regulates TRPV2 channel cellular response by sustaining its surface stability.

MATERIALS AND METHODS

cDNA Constructs

The wild-type rat TRPV2 and TRPV1 cDNAs were kindly provided by Dr. Feng Qin (State University of New York at Buffalo, Buffalo). The pFlotillin-1-NsfGFP, pFlotillin-1-CsfGFP, pFlotillin-2-NsfGFP, pFlotillin-2-CsfGFP, pCsfGFP and pNsfGFP cDNAs were generously provided by Dr. Yu Ding (Fudan University, China). The full-length of flotillin-1 and flotillin-2 were cloned from the mouse dorsal root ganglion (DRG) cDNA library. For the expression in mammalian cells, the cDNAs of TRPV2, flotillin-1, and flotillin-2 were introduced into p3 × Flag-cmv-7.1, pEGFP-N1, or pcDNA5-HA, as indicated. The Flag-tags or HA-tags were fused to the N terminus of the target proteins, and EGFP was tagged to the C terminus of the proteins of interest. All recombinant constructs and mutations were carried out using the overlap-extension polymerase chain reaction (PCR) method. The resulting constructs and mutations were then verified by DNA sequencing. Oligo DNAs targeting flotillin-1 were synthesized, annealed and inserted into pLenti-GFP vector. The sequences of shRNA against flotillin-1 are as follows: #1, 5′- GGGACTATGAGCTGAAGAA-3′; #2, 5′-GCGTGGTTAGCTACACTTT-3′.

Cell Culture and Transfection

All mice were housed in the specific pathogen-free animal facility at Wuhan University and all animal experiments were in accordance with protocols approved by the Institutional Animal Care and Use Committee of Wuhan University (NO. WDSKY0201804). Primary culture of DRG neurons was established following enzymatically and mechanically dissociation of the ganglia as described before with minor modification (Tian et al., 2019). In brief, 6 to 8-week-old wild-type C57 BL/6 mice were deeply anesthetized and then decapitated. L3–L4 DRGs together with dorsal-ventral roots and attached spinal nerves were taken out from the spinal column. After removing the attached nerves and surrounding connective tissues, DRG neurons were rinsed with ice-cold phosphate buffer saline (PBS). Then total RNA was extracted from the intact DRG for yeast cDNA library construction using TRIzol (Life Technologies) following the manufacturer's instructions or directly homogenized DRG neurons for immunoprecipitation experiment.

HEK 293T and ND7/23 cells were cultured in Dulbecco's Modified Eagle's Medium (DMEM, Thermo Fisher Scientific, MA, United States) containing 4.5 mg/ml glucose, 10% heat-inactivated fetal bovine serum (FBS, Gibco, Thermo Fisher Scientific), 50 units/ml penicillin, and 50 μg/ml streptomycin, and were incubated at 37°C in a humidified incubator gassed with 5% CO_2. Cells grown into ~80% confluence were transfected with the desired DNA constructs using either the standard calcium phosphate precipitation method or Lipofectamine 2000 (Invitrogen) following the protocol provided by the manufacturer. Transfected HEK 293T cells were reseeded on 12 mm round glass coverslips coated by poly-L-lysine for electrophysiological experiments. Experiments took place usually 12–24 h after transfection.

Generation of TRPV2 Stable Cell Lines

For generation of stable cell lines, HEK 293T cells were transiently transfected with pHAGE-6tag-puro-TRPV2 using Lipofectamine 2000 (Invitrogen). Transfected cells were grown for 2 weeks in puromycin in order to select for stable expressing cells. Non-transfected cells were killed by additions of puromycin (2 μg/ml) 2 days after treatment. The surviving cells were resistant to puromycin, and these cells were successfully expressed with *Trpv2* gene. Medium was replaced every 2–3 days until single colonies were formed, then the stable cell lines were placed in a complete medium containing 1 μg/ml puromycin.

Yeast Two-Hybrid Assay

Yeast two-hybrid screen was conducted using the Matchmaker GAL4-based two-hybrid system (Clontech) as previously described (Wang et al., 2020). Briefly, the mouse DRG cDNA library was fused to the GAL4 activation domain of plasmid pGADT7 (Clontech). The titer of the primary cDNA library was calculated using the number of clones on plates. Colony PCR was used to verify the size of the inserted fragments in the library. Bait plasmid was constructed by introducing the N-terminal (aa 1–387) of TRPV2 into the GAL4 DNA binding domain of the pGBKT7 vector (Clontech). The pGBK-bait was transformed into the yeast strain Y187 and pGAD-preys into AH109. Cytotoxicity and self-activation activity were determined via observing yeast clone growth and size. Diploid yeast cells from yeast mating were selected on the triple dropout medium (TDO: SD/-His/-Leu/-Trp). Replica plate colonies were then transferred onto quadruple dropout medium (QDO: SD/-Ade/-His/-Leu/-Trp) containing *X*-α-Gal (4 mg/mL). X-α-gal was used as substrate for colorimetric detection of α-galactosidase activity. Plates were incubated at 30°C for 7 days. Plasmids extracted from the positive clones were transformed into *E. coli* cloning host DH5α to be amplified, and samples were then sequenced individually. BLAST comparisons and other bioinformatics methods were applied for sequence analysis. Thereafter, the bait and prey plasmids in different combinations were sequentially co-transformed into yeast stain AH109 and selected on double dropout medium (DDO: SD/-Leu/-Trp) and incubated at 30°C for 3–4 days. Then the positive clones were diluted and equally coated onto SD/-Leu/-Trp/-His/-Ade medium with *X*-α-gal and SD/-Leu/-Trp medium and cultured at 30°C for 3–4 days. In parallel, the combination of pGBKT7-53/pGADT7-T and pGBKT7-Lam/pGADT7-T were used as positive and negative controls, respectively.

Chemicals and Antibodies

Key antibodies and reagents used in this study were as bellow.

Antibodies or Reagents	Source	Identifier
Rabbit anti-TRPV2	Alomone labs	Cat#ACC-032
Rabbit anti-Flotillin-1	Thermo scientific	Cat#PA5-28118
Rabbit anti-Na^+/K^+ ATPase	Abcam	Cat#ab76020
Mouse anti-Flag	MBL	Cat#M185-3L
Rabbit anti-Flag	Proteintech	Cat#20543-1-AP
Mouse anti-GFP	Tianjin sungene biotech	Cat#KM8009
Rabbit anti-GFP	Solarbio life science	Cat#B1025F
Mouse anti-HA	MBL	Cat#M180-3
Rabbit anti-HA	Earthox	Cat#E02218002
Anti-Flag Affinity Gel	Bimake	Cat#B23100
Anti-HA Affinity Gel	Bimake	Cat#B23301
Goat anti-mouse IgG (H + L)	Jackson immunoresearch	Cat#115-035-003
Goat anti-rabbit IgG (H + L)	Jackson immunoresearch	Cat#111-005-003
EZ-Link Sulfo-NHS-LC-Biotin	Thermo fisher scientific	Cat#21335
High Capacity NeutrAvidin^{TM} Agarose	Thermo fisher scientific	Cat#29202
Cycloheximide	Merck	Cat#239763-M
Puromycin	Merck	Cat#P8833

Immunoprecipitation and Western Blot

Immunoprecipitation were performed as previously described (Wang et al., 2020). In brief, cells were harvested 24 h post-transfection and lysed in Non-idet P-40 lysis buffer containing 150 mM NaCl, 1 mM EDTA, 20 mM Tris–HCl, 1% Non-idet P-40, and 1% complete protease and phosphatase inhibitor cocktail (Bimake). Lysates were cleared of debris by centrifugation at 14,000 rpm for 10 min. The supernatants were collected and immunoprecipitated with the indicated antibodies and Protein G agarose beads for 2 h. The immunoprecipitants were washed with 1 ml lysis buffer containing 500 mM NaCl for three times followed by immunoblotting assay. Samples were loaded into 4–20% or 12% SDS-PAGE gels and electrophoretically separated according to the manufacturer's instructions (125 V for 60 min in Running Buffer).

Fluorescence Confocal Microscopy

HEK 293T cells transfected with the desired plasmids were fixed with 4% paraformaldehyde (Biosharp, BL539A) for 10 min at 4°C and the nuclei were counterstained with DAPI (Merck, D5492) for 15 min at room temperature in the dark, and washed three times with phosphate buffered saline (PBS). The cells were scanned and images were collected using a Leica SP8 confocal microscopy (63× oil objective NA 1.35).

Surface Biotinylation Assay

Surface biotinylation was performed following established protocols (Wang et al., 2018). Cells were firstly washed three times with the ice-cold PBS solution supplemented with 1 mM $MgCl_2$ and 2.5 mM $CaCl_2$ (pH 8.0). Then Sulfo-NHS-LC-Biotin (0.25 mg/ml; Thermo Scientific, Waltham, MA, United States) was added into the same solution and incubated with cells at 4°C for 30 min with gentle rocking. The unbound biotin group was quenched by the addition of 0.1 M glycine for 20 min at 4°C. Biotin-labeled proteins were isolated by incubating whole cell lysates with NeutrAvidin agarose beads (Thermo Fisher Scientific) overnight at 4°C with rocking. The beads were washed three times with PBS (pH 8.0) and bound proteins were eluted with the boiling SDS sample buffer and used for immunoblotting.

Electrophysiology

Conventional whole-cell patch-clamp recording methods was used. For the recombinant expressing system, green fluorescent from EGFP was used as a marker for gene expression. Currents were amplified using an Axopatch 200B amplifier (Molecular Devices, Sunnyvale, CA, United States) and recorded through a BNC-2090/MIO acquisition system (National Instruments, Austin, TX, United States) using QStudio developed by Dr. Feng Qin at State University of New York at Buffalo. Whole-cell recordings were typically sampled at 5 kHz and low-pass filtered at 1 kHz.

Bath solution for whole-cell recording consisted of (mM): 140 NaCl, 5 KCl, 3 EGTA, and 10 HEPES, pH 7.4 adjusted with NaOH. Electrodes were filled with (mM): 150 CsCl, 5 EGTA, 10 HEPES, pH 7.4 adjusted with CsOH. Recording pipettes were made from borosilicate glass capillaries (World Precision Instruments), and fire-polished to a resistance between 2 and 4 MΩ when filled with electrode saline. 2-Aminoethyl diphenylborinate (2-APB) was dissolved in DMSO to make a stock solution. All the stocks were diluted in the bath solution to the desired concentrations right before the experiment. Exchange of external solutions was performed using a gravity-driven local perfusion system. As determined by the conductance tests, the solution around a patch under study was fully controlled by the application of a solution with a flow rate of 100 μl/min or greater. All pharmacological experiments met this criterion. Unless otherwise noted, all chemicals were purchased from Sigma (Millipore Sigma, St. Louis, MO, United States). All patch-clamp recordings were made at room temperature (22–24°C) except for temperature stimulation.

Ultrafast Temperature Jump Achievement

A single emitter infrared laser diode (1,550 nm) was designed to produce temperature jumps as previously described (Yao et al., 2009). The laser diode was driven by a pulsed quasi-CW current power supply (Stone Laser, Beijing, China), and pulsing of the controller was controlled from a computer through BNC-2090/MIO data acquisition card, which was also responsible for patch-clamp recordings. The launched laser beam was transmitted by a multimode fiber with a core diameter of 100 μm. A blue laser line (460 nm) was coupled into the same fiber to aid alignment. Temperature was calibrated offline from the electrode current based on the temperature dependence of electrolyte conductivity. The temperature threshold for heat activation of TRPV2 was determined as the temperature at which the slow inward current was elicited.

Data Analysis

Densitometry was performed using ImageJ software for the quantitative analysis of the bands on the western blots. Electrophysiological data were analyzed offline with Qstudio developed by Dr. Feng Qin at State University of New York at Buffalo, Clampfit (Molecular Devices, Sunnyvale, CA, United States), IGOR (Wavemetrics, Lake Oswego, OR, United States), SigmaPlot (SPSS Science, Chicago, IL, United States) and OriginPro (OriginLab Corporation, MA, United States). For concentration response analysis, the modified Hill equation was used: $Y = \mathrm{A1} + (\mathrm{A2} - \mathrm{A1})/[1 + 10\ \hat{}\ (\log EC_{50} - X) * n_H]$, in which EC_{50} is the half maximal effective concentration, and n_H is the Hill coefficient. Unless stated otherwise, the summary data are presented as mean ± standard error (s.e.m.) or mean ± standard deviation (S.D.) as indicated, with statistical significance assessed using unpaired student *t*-test for two-group comparison. Significant difference is indicated by a *p*-value less than 0.05 ($^*p < 0.05$, $^{**}p < 0.01$, $^{***}p < 0.001$).

RESULTS

Flotillin-1 Physically Interacts With TRPV2 Channel

In an attempt to identify biomolecular partners directly interacting with TRPV2 channel, we embarked on a yeast two-hybrid approach. Specifically, we screened a cDNA library prepared from mouse DRG using the cytosolic N-terminus of mouse TRPV2 as a bait. In the screen, 36 positive clones were subjected to sequencing. One of the positive clones harbored a 747-bp cDNA fragment that corresponds to amino acid residues 1–249 of flotillin-1. We thus chose flotillin-1 as the target protein. To validate the interaction, flotillin-1-pGADT7 was co-transformed with TRPV2-Nt-pGBKT7 into the yeast reporter strain AH109, and the transformants at serial dilutions were cultured under a SD/-Ade/-His/-Leu/-Trp selective condition and subjected to *X*-α-gal assay. In addition, the 53-T and Lam-T were also expressed and served as positive and negative controls, respectively. As illustrated in **Figure 1A**, only cells containing both plasmids encoding flotillin-1 and TRPV2-Nt or the combination of pGBK-53 and pGAD-T, but not the control cells, were able to grow in the selective medium. This result indicates that flotillin-1 interacts with the N-terminus of TRPV2.

We next determined whether flotillin-1 interacted with TRPV2 in endogenous adult DRG neurons using coimmunoprecipitation (co-IP) strategy. As shown in **Figure 1B**, in primary cultures of mouse DRG neurons, flotillin-1 robustly coimmunoprecipitated with TRPV2 and vice versa. Further, in mammalian HEK 293T cells, flotillin-1-GFP was also co-immunoprecipitated by TRPV2-Flag with Flag beads, confirming

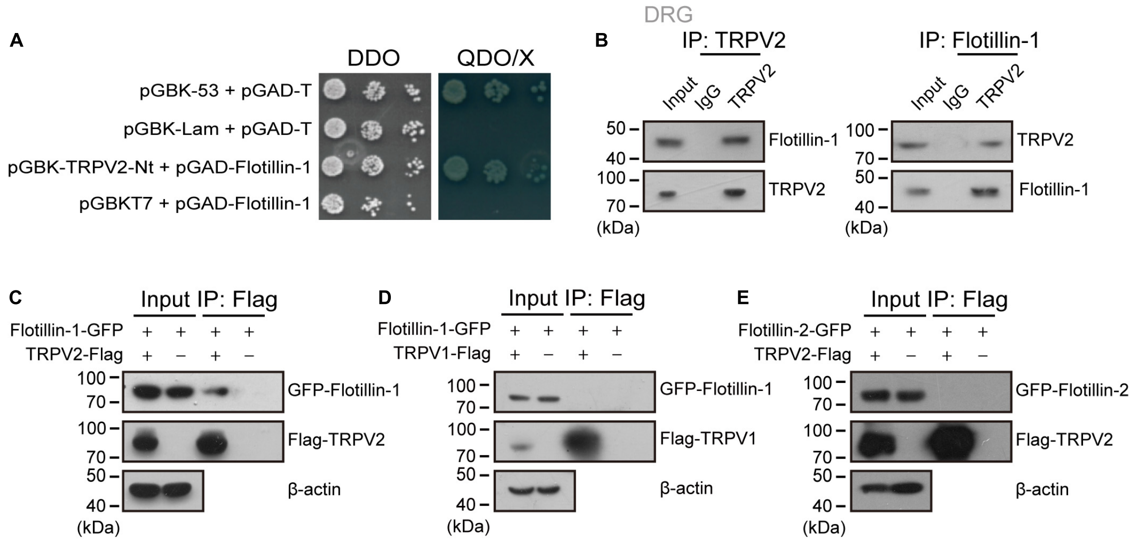

FIGURE 1 | Flotillin-1 physically interacts with TRPV2. **(A)** Yeast two-hybrid results showing the interaction between TRPV2 N-terminus (V2-Nt) and flotillin-1. The bait and prey constructs were co-transformed into yeast strain AH109, and the transformed yeast diploids were grown on DDO for 2 days and QDO for 5 days, respectively. The 53-T and Lam-T were served as positive and negative controls, respectively. DDO, SD-Leu/-Trp medium; QDO, SD-Leu/-Trp/-His/-Ade medium; X, *X*-α-gal. **(B)** Immunoprecipitation (with anti-TRPV2, anti-Flotillin-1, or IgG as a control) and immunoblot analysis (with anti-TRPV2 or anti-Flotillin-1) of the mouse DRG neurons. **(C)** Interaction between flotillin-1 and TRPV2. HEK 293T cells were transfected with plasmids as indicated. Immunoprecipitation (IP, with anti-Flag) and immunoblot analysis (with anti-GFP and anti-Flag) of the interaction between TRPV2 and flotillin-1. **(D)** No interaction between flotillin-1 and TRPV1. Immunoprecipitation (with anti-Flag) and immunoblot analysis (with anti-GFP and anti-Flag) of HEK 293T cells transfected with plasmids encoding Flag-tagged TRPV1 and GFP-tagged flotillin-1. **(E)** No interaction between TRPV2 and flotillin-2. Immunoprecipitation (with anti-Flag) and immunoblot analysis (with anti-GFP and anti-Flag) of HEK 293T cells transfected with plasmids encoding Flag-tagged TRPV2 and GFP-tagged flotillin-2. Data are representative of three independent experiments at least.

that flotillin-1 associated with the full length of TRPV2 (**Figure 1C**). However, TRPV1-Flag could not be precipitated by flotillin-1-GFP with Flag beads, implying that flotillin-1 does not interact with TRPV1 (**Figure 1D**).

Flotillin-1 and flotillin-2 usually form a heterodimer or oligomer complex (Liu et al., 2016; Gauthier-Rouvière et al., 2020). Thus, it is interesting to investigate whether flotillin-2 also interacted with TRPV2 channel. To this aim, co-immunoprecipitation was performed in HEK 293T cells with ectopically expressed flotillin-2 and full-length of TRPV2. As shown in **Figure 1E**, there was no interaction between flotillin-2 and TRPV2. Therefore, these observations imply that flotillin-1 physically interacts with TRPV2 channel.

Visualization of Flotillin-1-TRPV2 Complex by Immunofluorescent Imaging and BiFC

To further confirm the interaction between flotillin-1 and TRPV2, we co-expressed red fluorescent TRPV2-mcherry and green fluorescent flotillin-1-GFP in HEK 293T cells. Fluorescent imaging by confocal microscope showed apparent co-localization between TRPV2 and flotillin-1 (**Figure 2A**), as confirmed by quantitative analysis (Pearson's coefficient = 0.891, **Figures 2B,C**).

Next, we employed the high-throughput bimolecular fluorescence complementation (BiFC) technique that enables the direct visualization of molecular interactions in the cell. Briefly, GFP molecule is splitted into two fragments that individually lack fluorescence and then conjugated to different proteins. Only when the two conjugated proteins interact at the molecular level, GFP fluorescence could be reconstituted. Considering that flotillin-1 and flotillin-2 have been demonstrated to form both homo- and hetero-oligomeric complexes (Babuke et al., 2009), a pair of BiFC constructs (flotillin-2-NsfGFP and flotillin-1-CsfGFP) were co-transfected into HEK 293 cells as a positive control. As expected, this produced GFP green fluorescence on the cell membrane (**Figure 2D**). In contrast, in cells expressing the negative control constructs (flotillin-1-CsfGFP vs. NsfGFP or TRPV2-NsfGFP vs. CsfGFP), we observed no fluorescent signals (**Figure 2D**). Next, the similar approach was carried out to evaluate the interaction between flotillin-1 and TRPV2. Co-expression of TRPV2-NsfGFP and flotillin-1-CsfGFP in HEK 293T cells displayed significant green fluorescence on cell surface (**Figure 2D**), thus validating the molecular combination between flotillin-1 and TRPV2.

Flotillin-1 Increases Current Density of TRPV2

As having confirmed that flotillin-1 associates with TRPV2, we next evaluated the functional consequence by patch clamp electrophysiology. **Figure 3A** shows representative traces of whole-cell currents recorded from HEK 293T cells expressing TRPV2 alone or TRPV2 and flotillin-1. With the cells held at −60 mV, 2-APB-evoked whole-cell currents were recorded

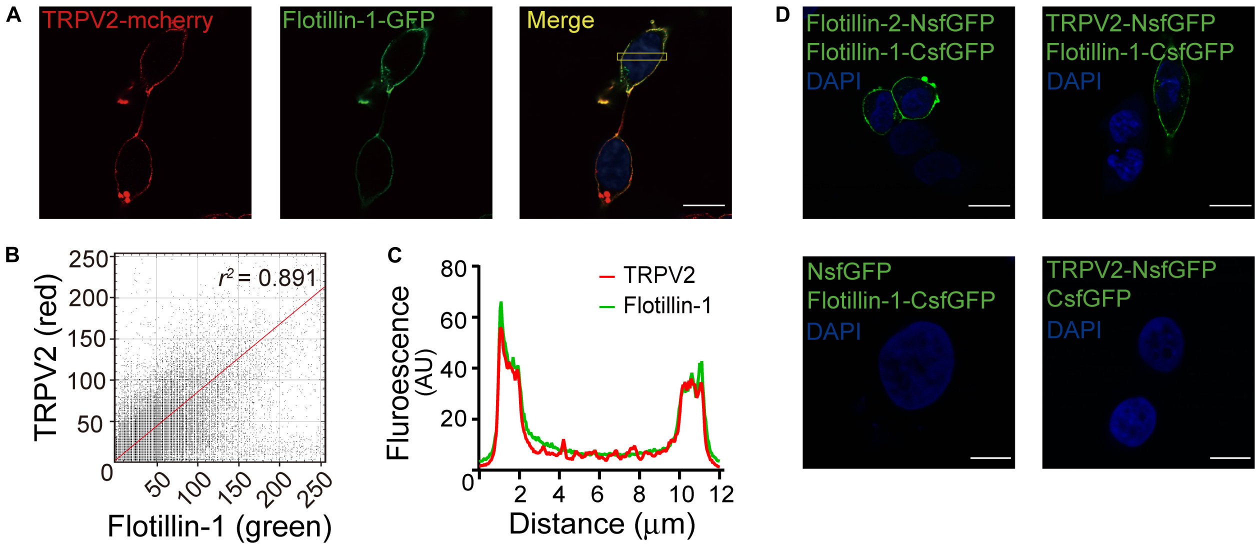

FIGURE 2 | Fluorescence images show co-localization of TRPV2 and flotillin-1. **(A)** Co-localization of TRPV2 and flotillin-1. HEK 293T cells were co-transfected with mcherry-TRPV2 (red) and GFP-flotillin-1 (green) and examined with confocal microscopy. In the merged images, the extensive co-localization of the two proteins was represented by yellow. **(B)** The fluorescence intensity scatterplot showed a clear linear relationship, with a Pearson's correlation coefficient value of 0.891. **(C)** The plot of fluorescence intensities between the red and green pixels along a section through the cell body as indicated in **(A)** indicated a well-correlated relationship between green and red. **(D)** Validation of the interaction between TRPV2 and flotillin-1 by bimolecular fluorescence complementation (BiFC) analysis. The confocal images of HEK 293T cells co-expressed with the indicated constructs, showing that strong fluorescence at the cell membrane region for that co-expressing TRPV2-NsfGFP and flotillin-1-CsfGFP, which is line with the green fluorescence observed from the BiFC complex formed by flotillin-1-CsfGFP and flotillin-2-NsfGFP. No detectable sfGFP fluorescence for HEK 293T cells co-expressed with NsfGFP and flotillin-1-CsfGFP or the combination of TRPV2-NsfGFP and CsfGFP. Nuclei were stained with DAPI. Scale bar: 10 μm. Data are representative of three independent experiments.

in response to different doses of 2-APB. The concentration-response curves to 2-APB were fitted with a Hill equation, and the corresponding EC_{50} values and Hill coefficients (n_H) for TRPV2 and TRPV2 co-expressed with flotillin-1 were not significantly changed by the presence of flotillin-1 (**Figure 3B**, $EC_{50} = 3.01 \pm 0.04$ mM, $n_H = 5.72 \pm 0.4$ for TRPV2 and $EC_{50} = 2.44 \pm 0.04$ mM, $n_H = 5.43 \pm 0.32$ for TRPV2 + flotillin-1). However, the TRPV2 current density calculated from steady-state currents yielded a remarkable increase in the presence of flotillin-1 as compared with recordings without flotillin-1, e.g., 361.4 ± 57.9 pA/pF ($n = 8$) versus 224.6 ± 30.7 pA/pF ($n = 8$) evoked by 5 mM 2-APB (**Figure 3C**).

TRPV2 channel is also a thermal sensor responding to noxious temperature for pain initiation. We next explored whether flotllin-1 modulates TRPV2 thermal responses. We used an infrared laser diode as a heat source to increase single cell temperatures under millisecond. HEK 293T cells expressing TRPV2 were held at −60 mV when the temperature jumps were delivered (**Figure 3D**). Plotting the relative responses against the step temperatures, we observed that the thermal activation profiles remained same for TRPV2 channels expressed with or without Flotillin-1 (**Figures 3E,F**). Using an Arrhenius plot of the amplitudes (**Figure 3G**), we determined the temperature coefficient (Q_{10}) for TRPV2 (**Figure 3H**) and found no change in the presence of flotillin-1 (**Figure 3F**). By calculating the current density, however, we observed that flotillin-1 co-expression led to a significant increase in TRPV2 current density evoked by temperature jumps (**Figure 3I**). Together, our data suggests that flotillin-1 upregulates the current density of TRPV2 without altering the sensitivity to agonistic or thermal activations.

Flotillin-1 Increases Membrane Expression of TRPV2

The increase in whole-cell current density suggests an enhanced surface expression levels of the ion channel. We then explored the influence of flotillin-1 on TRPV2 surface expression level. Flotillin-1-GFP and TRPV2-Flag were co-expressed in HEK 293T cells. The amounts of surface-expressed and total Flag-TRPV2 proteins were determined by surface biotinylation and western blotting, respectively. As revealed in **Figure 4A**, along with the amount of transfected flotillin-1 increased, the expression level of TRPV2 on the plasma membrane was proportionally upregulated. In this condition, however, the total amount of TRPV2 was unaffected. Since flotillin-1 is expressed on the inner side of the membrane, it cannot be directly biotinylated in the case of no TRPV2 expression (**Figure 4A**). Being co-expressed with TRPV2, flotillin-1 turned to be biotinylated as expected by their physical interaction (**Figure 4A**). With the sufficiently increased expression of flotillin-1, TRPV2 surface expression showed a nearly twofold increase compared with the control group (**Figure 4B**). In addition, we explored the effect of overexpressed flotinllin-1 on TRPV2 protein expression in ND7/23 cells, a hybridization line of mouse neuroblastoma and rat DRG neuron (Wood et al., 1990), that express endogenous TRPV2. As illustrated in **Figures 4C,D**, transfection of flotinllin-1 in ND7/23 cells proportionally increased the surface expression,

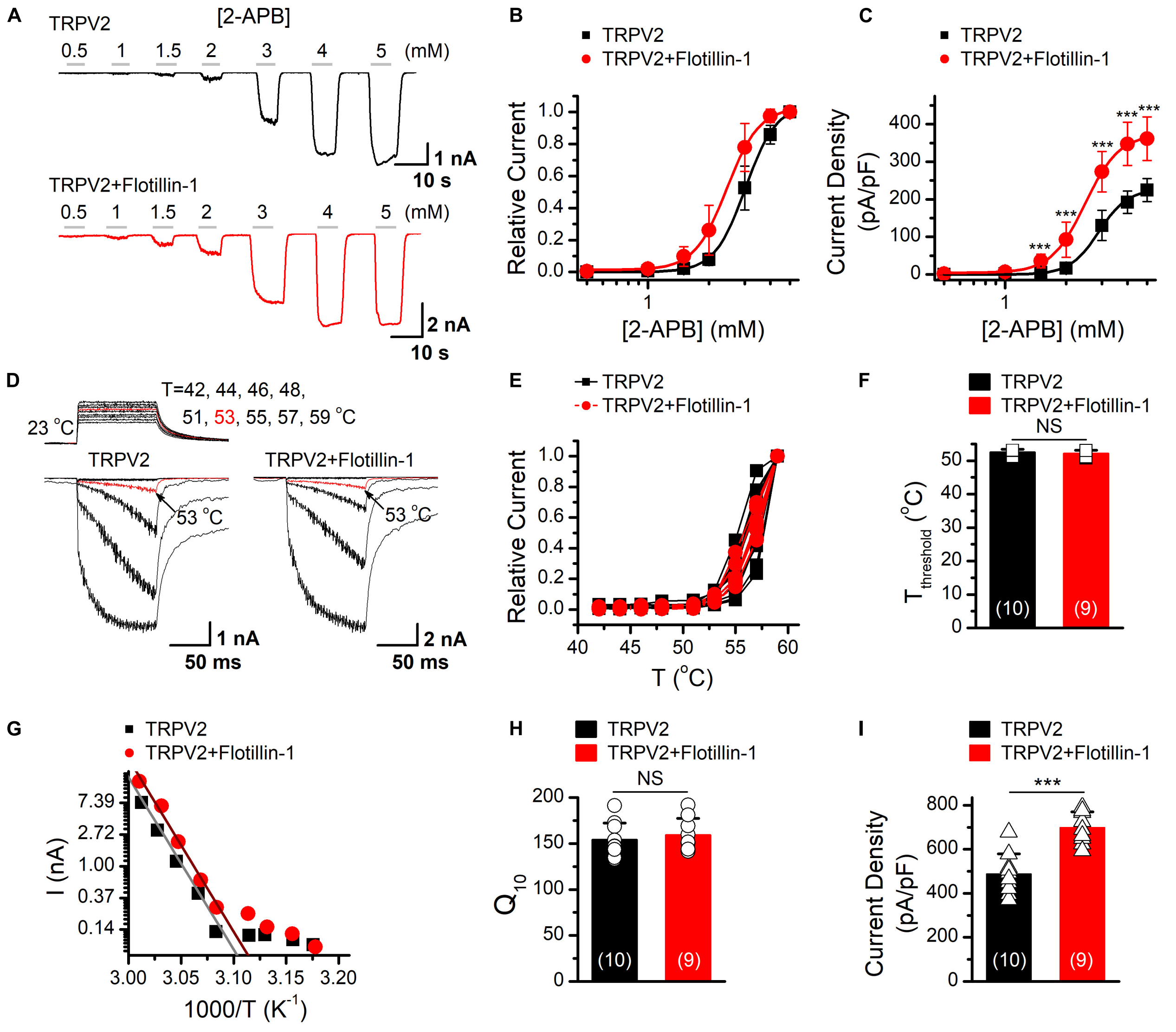

FIGURE 3 | Flotillin-1 enhances TRPV2 activity. **(A)** Representative whole-cell recording in HEK 293T cells expressed TRPV2 alone (*upper*), and TRPV2 + flotillin-1 (*lower*), showing that 2-APB activated TRPV2 channels in a dose-dependent manner. Holding potential was –60 mV. **(B)** Dose–response curves for 2-APB-evoked currents. Solid lines indicate fits with the Hill equation, which yielded EC_{50} = 3.01 ± 0.04 mM, n_H = 5.72 ± 0.4 for TRPV2 (n = 8); and EC_{50} = 2.44 ± 0.04 mM, n_H = 5.43 ± 0.32 for TRPV2 + flotillin-1 (n = 8). **(C)** Summary plot of current density. The current densities evoked by 2-APB were determined by normalizing the membrane peak current by membrane capacitance (n = 8). ***$P < 0.001$. **(D)** Representative responses to a family of temperature jumps ranging from 42 to 57°C for HEK 293T cells that expressed TRPV2 alone (left), and TRPV2 + flotillin-1 (right). Temperature pulses stepped from room temperature were generated by laser irradiation were 100 ms long and had a rise time of 2 ms. Temperatures were calibrated offline from the pipette current using the temperature dependence of electrolyte conductivity. The red traces indicate the response at 53°C. **(E)** Temperature response curves for TRPV2 (black), TRPV2 + flotillin-1 (red), measured from the maximal currents at the end of temperature steps. Each curve represents measurements from an individual cell and the responses were normalized to the maximum responses at 59°C. **(F)** Comparison of temperature threshold for heat activation of TRPV2. Different symbols represent individual data points. The mean temperature thresholds ($T_{threshold}$) of activation were 52.5 ± 0.8°C for TRPV2 (n = 10), 52.1 ± 0.9°C for TRPV2 + flotillin-1 (n = 9). P = 0.335. **(G)** Arrhenius plot of steady-state currents shown in **(D)**. The major component of the reflection that represents the strong temperature dependence was fitted to a linear equation. **(H)** Comparison of temperature dependence of TRPV2 and TRPV2 + flotillin-1. The values of Q10 derived from the linear fits in Arrhenius plot were as following, Q10 = 154.1 ± 18.2 for TRPV2 (n = 10), Q10 = 159.1 ± 18.2 for TRPV2 + flotillin-1 (n = 9). Colored symbols indicate individual data points. P = 0.566. **(I)** Summary of current density for temperature (59°C)-activated TRPV2 currents at –60 mV are shown. The current densities were 487.9 ± 90.8 pA/pF for TRPV2 (n = 10) and 697.9 ± 71.5 pA/pF for TRPV2 + flotillin-1 (n = 9); ***$p < 0.001$. Error bars represent SD.

but not the total amount of TRPV2 channel. These findings are consistent with the increased TRPV2 current density following flotillin-1 overexpression (**Figure 2**). Next, we evaluated the regulatory effect of endogenous flotillin-1 on TRPV2 expression using shRNA-mediated knockdown. As shown in **Figure 4E**, shFlotillin-1 #2 could remarkably inhibit the expression of endogenous flotillin-1, we used it for the following experiments. Then the surface biotinylation experiment was performed in

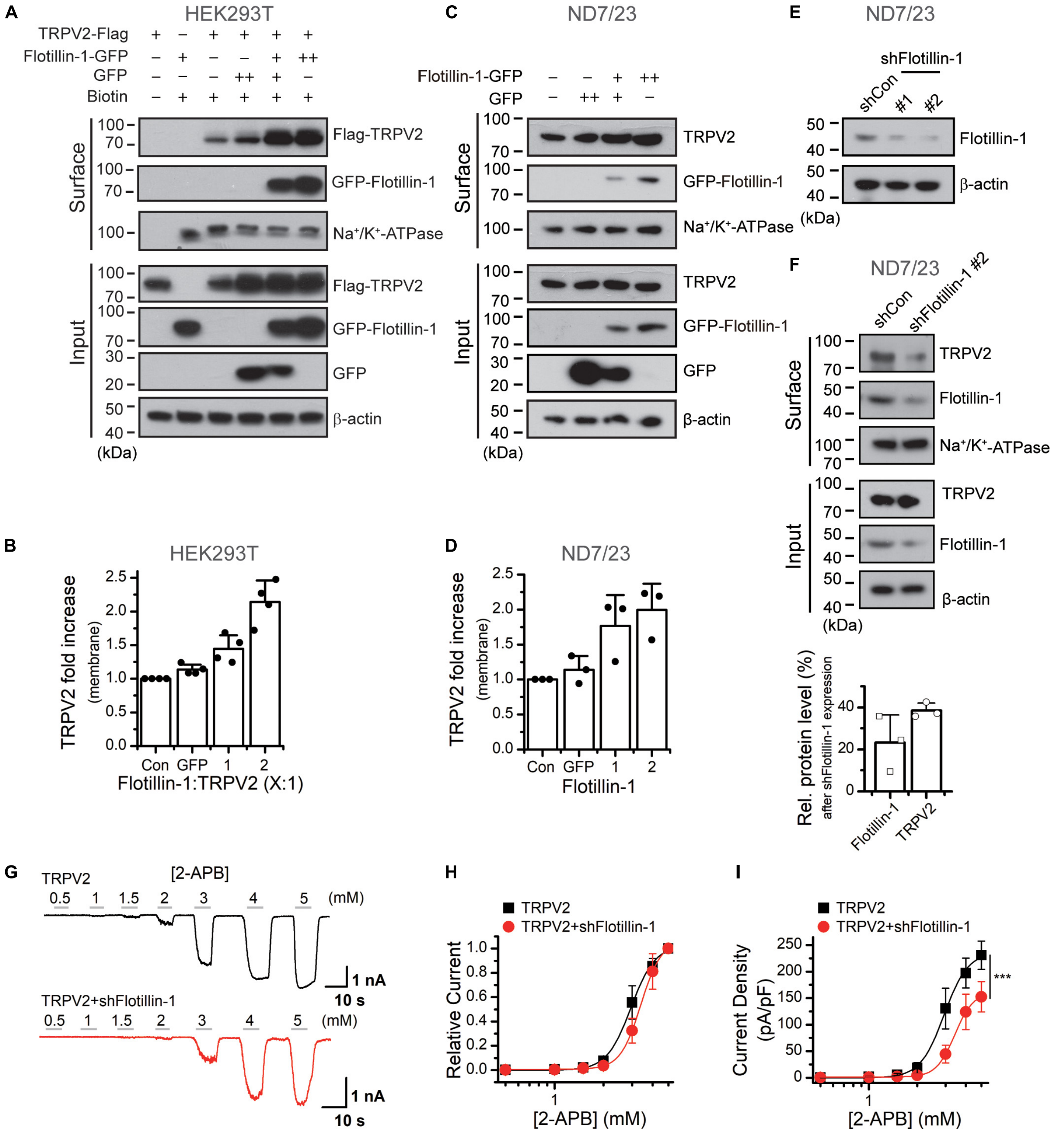

FIGURE 4 | Flotillin-1 enhances the surface expression levels of TRPV2. **(A)** Increased surface expression of TRPV2 by flotillin-1. HEK 293T cells were transiently transfected with TRPV2 with GFP or increased flotillin-1 as indicated. Surface levels of TRPV2 were measured by IB after plasma membrane proteins were biotinylated and purified with NeutrAvidin agarose beads. β-actin and Na^+/K^+ ATPase were used as controls for cytoplasmic and membrane proteins, respectively. **(B)** Quantitative analysis of the fold increase of TRPV2 on the plasma membrane by co-expression with flotillin-1 in HEK 293T cells ($n = 4$; means ± SD). **(C,D)** ND7/23 cells were transiently transfected with increasing amounts of flotillin-1-GFP cDNA. Similarly, surface levels of TRPV2 were measured by IB after plasma membrane proteins were biotinylated and purified with NeutrAvidin agarose beads. Blots are representatives of three independent experiments. Error bars represent SD. **(E)** Immunoblot analysis (with anti-flotillin-1) of ND7/23 cells transfected for 36 h with plasmids encoding flotillin-1-targeting shRNA (shFlotillin-1 #1, and shFlotillin-1 #2) or control shRNA (shCon) to test efficiency of shRNA. **(F)** Effect of knocking down flotillin-1 on the surface expression of TRPV2 in ND7/23 cells. The cell surface biotinylation assay was used to measure the surface levels of TRPV2 in ND7/23 cells that were stably transfected with shCon or shFlotillin-1 #2. Below showing the quantitative analysis of the relative protein levels of TRPV2 and flotillin-1 caused by shFlotillin-1 #2. Data are representative of three independent experiments. **(G)** Whole-cell recordings in HEK 293T cells expressed TRPV2 alone (*upper*), and TRPV2 + shFlotillin-1 (*lower*), showing that 2-APB dose-dependently activated TRPV2 channels. Holding potential was –60 mV. **(H)** Dose–response curves for 2-APB-evoked currents. Solid lines indicate fits with the Hill equation, which yielded $EC_{50} = 2.95 \pm 0.06$ mM, $n_H = 5.84 \pm 0.72$ for TRPV2 ($n = 8$); and $EC_{50} = 3.39 \pm 0.02$ mM, $n_H = 6.87 \pm 0.17$ for TRPV2 + shFlotillin-1 ($n = 8$). **(I)** Summary plot of current density. The current densities evoked by 2-APB were determined by normalizing the membrane peak current by membrane capacitance. ($n = 8$). $^{***}P < 0.001$.

ND7/23 cells to detect the shRNA impact on the total and surface expression of TRPV2. Quantitative analysis showing that ~80% reduction in flotillin-1 protein levels by transfection with shFlotillin-1 #2. As expected, the knockdown of endogenous flotillin-1 indeed reduced the surface expression of TRPV2 (**Figure 4F**). We further examined the effects of flotillin-1 knockdown on the electrophysiological activity of TRPV2. As illustrated in **Figures 4G,H**, we compared TRPV2 function by activating the channel with increasing concentrations of 2-APB at the holding potential of −60 mV. Fitting the dose-response curves with the Hill equation yielded similar EC50 values and Hill coefficients (n_H) for TRPV2 co-expressed with shFlotillin-1 #2 or not (EC50 = 2.95 ± 0.06 mM, n_H = 5.84 ± 0.72 for TRPV2, n = 8; and EC50 = 3.39 ± 0.02 mM, n_H = 6.87 ± 0.17 for TRPV2 + shFlotillin-1 #2, n = 8). The current density, however, showed a significant difference, e.g., 230.9 ± 26.8 pA/pF (n = 8) for TRPV2 and 152.6 ± 28.6 pA/pF (n = 8) for TRPV2 + shFlotillin-1 #2 evoked by 5 mM 2-APB, respectively (**Figure 4I**). Taken together, our results suggest that flotillin-1 exerts a role in regulating the surface expression levels of TRPV2, thereby its whole-cell current density.

Flotillin-1 Sustains the Surface Stability of TRPV2

To understand the effect of filotillin-1 on TRPV2 surface expression, we examined the steady-state protein level and the turnover rate. ND7/23 cells were transfected with flotillin-1-GFP or the GFP control vector. The stability of TRPV2 was measured by immunoblotting after treatment with the protein synthesis inhibitor cycloheximide (CHX, 100 μg/mL). In the absence of flotillin-1, TRPV2 is relatively unstable, showing a degradation kinetics that reaches ≥80% elimination upon 20 h translational arrest. On the contrary, in the presence of flotillin-1 the channel exhibited significantly slower elimination kinetics and reduced degradation rate, as only about half of TRPV2 faded away after 20 h (**Figures 5A,B**). We next sought to examine the degradation rate of surface-expressed TRPV2 following shRNA-mediated flotillin-1 knockdown. As expected, with flotillin-1 knockdown, the membrane TRPV2 exhibited a faster degradation rate (**Figures 5C,D**). Thus, flotillin-1 plays a role in sustaining TRPV2 protein stability and facilitates its surface expression.

Mapping of the Interaction Domains Between TRPV2 and Flotillin-1

Next, we determined which molecular regions of TRPV2 and flotillin-1 proteins were responsible for their interaction. Structurally, TRPV2 has six transmembrane (TM) domains flanked by intracellular N- and C-terminal domains, and a short pore-forming loop between the fifth (TM5) and sixth (TM6) transmembrane. In order to define the regions interacting with flotillin-1, we constructed various GFP-tagged deletions of TRPV2 as illustrate in **Figure 6A**. They were then individually co-expressed with FLAG-tagged-flotillin-1 in HEK 293T cells for co-IP evaluation. Flotillin-1 was strongly precipitated with TRPV2 N-terminus (aa 1–387) and transmembrane domains 1–4 (aa 388–520), respectively. In contrast, neither the pore region (aa 521–649) nor C-terminus (aa 650–762) showed interaction with flotillin-1, indicating N-termius and TM 1–4 of TRPV2 are required for the protein interaction (**Figure 6B**). Similarly, we further mapped the molecular domains of flotillin-1 that mediated its interaction with TRPV2. As shown in **Figure 6C**, two truncations of flotillin-1 were constructed, including SPFH domain (aa: 1–189), and Flotillin domain (aa: 190–427). **Figure 6D** shows that TRPV2-Flag could be precipitated by the SPFH domain, but not the Flotillin domain. These results thus indicate that the SPFH domain of flotillin-1 and the N-terminus and TM 1–4 of TRPV2 are required for their interaction.

DISCUSSION

The regulatory interactions between TRP channel and signaling molecules, and the formation of these protein complexes have a significant effect on their functions (Barnhill et al., 2004; Stokes et al., 2004; Zhang et al., 2008; Kim et al., 2011). Thus, the identification and characterization of TRPV2-interacting proteins are pivotal for a better understanding of the physiology of this thermo TRP channel. Here, we demonstrate that the scaffold protein flotillin-1 directly complexes with TRPV2 in both heterologous cell expression system and native DRG sensory neurons. The N-terminus (aa 1–387), the region spanning the first to fourth transmembrane domains (aa 388–520) of TRPV2 and the SPFH domains of flotillin-1 (aa 1–189) mediate their interaction. Functionally, flotillin-1 facilitates the cell surface expression levels of TRPV2, thereby enhancing the whole-cell current density. These findings broaden our understanding of the regulatory mechanisms of TRPV2 signaling complex.

Flotillin-1 is preferentially associated with flotillin-2 in hetero-oligomeric complexes, forms membrane microdomains that serve as scaffolds facilitating the assembly of multiprotein complexes at the membrane-cytosol interface (Zhao et al., 2011; Kwiatkowska et al., 2020). It was observed that flotillin-1 is associated with tyrosine-protein kinase Lyn and enhances its activity (Kato et al., 2006). The interaction between flotillin-1 and neuroglobin (Ngb) implied that flotillin-1 might play a crucial role in regulating neuronal death and proliferation (Wakasugi et al., 2004). As mentioned above, previous studies have shown that flotillins modulate several ion channels activity via the interplay between each of them. For instance, the reduction of potassium channel Kv2.1 current amplitude by flotillin-1 was suggested to be mainly due to the Kv2.1 clustering on the plasma membrane (Liu et al., 2016). In contrast, Kessler et al. (2019) reported that both protein expression and channel activity of Nav1.5 channel were significantly decreased in *flotillin-1* or *flotillin-1/2* deficient mice, thereby reducing cardiac excitation. Here we observed that the presence of flotillin-1 enhanced the stability of TRPV2 channels on the plasma membrane, thereby up-regulating their responsive current density.

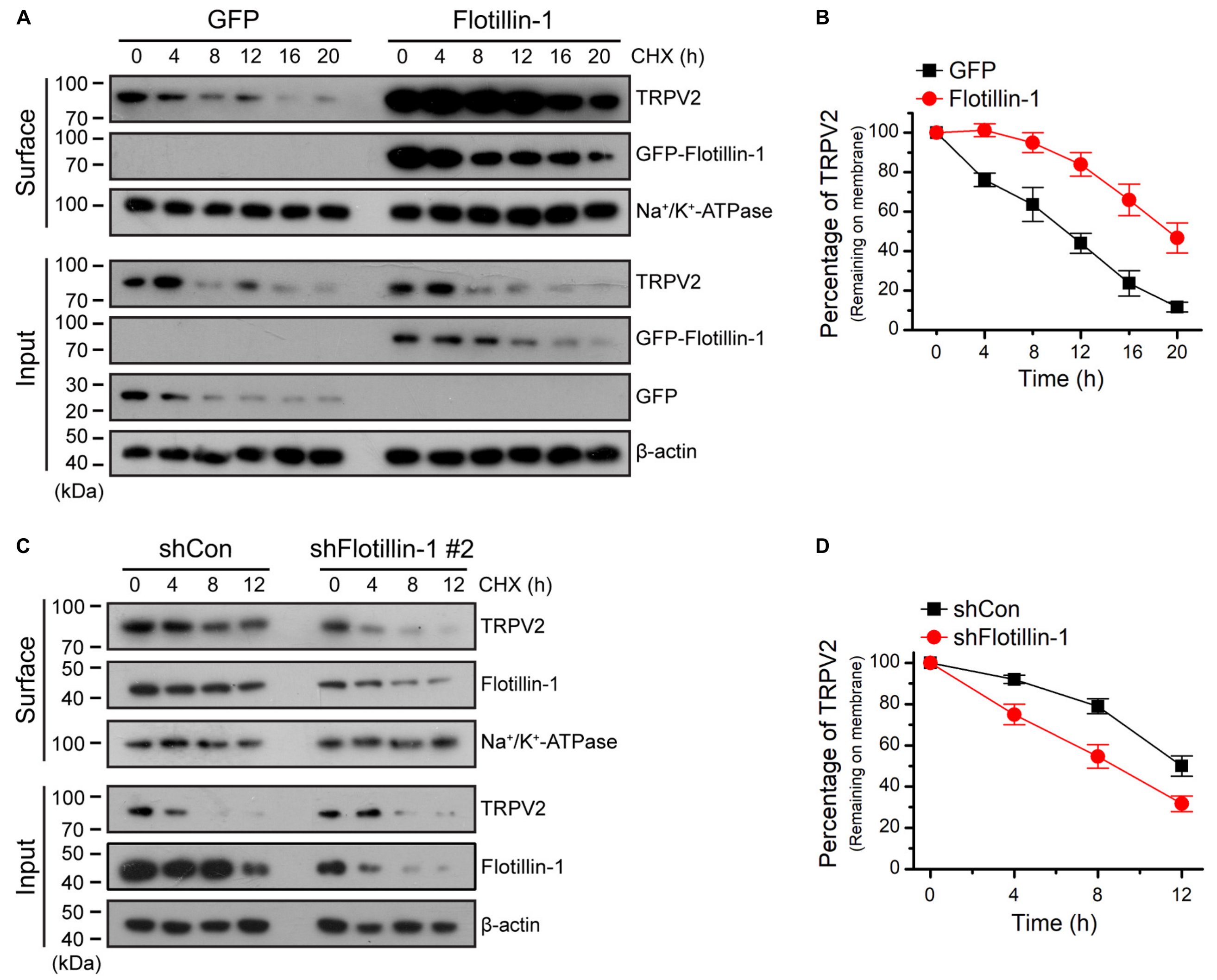

FIGURE 5 | Flotillin-1 sustains the surface stability of TRPV2. **(A)** Immunoblotting analysis of TRPV2 in ND7/23 cells time-dependently treated with the protein synthesis inhibitor cycloheximide (CHX, 100 μg/ml) after being transiently transfected with GFP-tagged flotillin-1 or GFP. After plasma membrane proteins were biotinylated and purified with streptavidin-agarose, the surface levels of TRPV2 were analyzed by IB. **(B)** Quantitation of the surface levels of TRPV2 after treatment using CHX. Quantitation was performed by digitizing the immunoblots. **(C)** CHX-chase experiment assessing the surface stability of TRPV2 in ND7/23 cells that expressed shCon or shFlotillin-1 #2. Cells were treated with 100 μg/ml of CHX for indicated times. **(D)** Quantification of the surface levels of TRPV2, showing a marked accelerate in endogenous TRPV2 degradation kinetics by knocking down flotillin-1 when compared to control cells. Data are representative of three independent experiments.

Flotillin-1 and flotillin-2 are two ubiquitous, highly conserved homologous proteins that assemble to form heterotetramers on the inner surface of cell membranes in cholesterol- and sphingolipid-enriched domains (Gauthier-Rouvière et al., 2020). The heterotetramers not only act as a skeleton to provide a platform for protein–protein interactions, but also are involved in signal transduction, nerve regeneration, endocytosis, and lymphocyte activation (Solis et al., 2010). Flotillins are composed of two domains: the N-terminal SPFH domain associated with the inner leaflet of cell membranes and the C-terminal domain is required for oligomerization (Morrow et al., 2002; Neumann-Giesen et al., 2004). The fact that TRPV2 shows no interaction with flotillin-2 but specifically interacts with the SPFH domain of flotillin-1, suggests that these two proteins might have distinct features in their SPFH domain or their C-terminal associations.

Studies have demonstrated that ankyrin repeat sequence motifs are common protein–protein recognition domains and, they are clearly important for the modulation of TRP channels. Moreover, the membrane proximal or pre-S1 domain of TRPV2 has been suggested to mediate protein–protein and lipid–protein interactions (Donate-Macian et al., 2019). Neeper et al. (2007) reported that deletion of 83 or more N-terminal residues greatly decreased TRPV2 expression levels. In addition to these observations, recently, it has

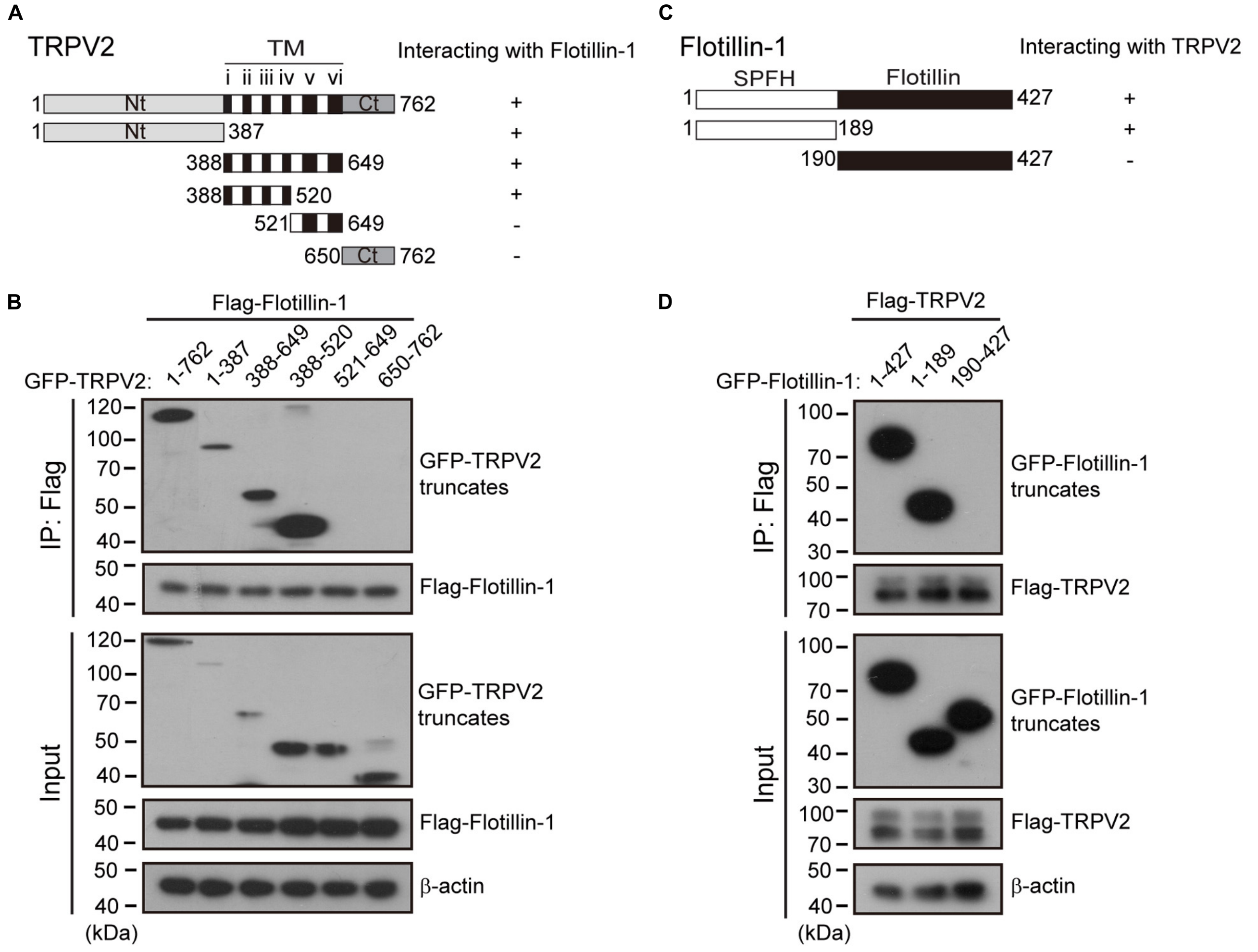

FIGURE 6 | Identification of interaction domains for the association between TRPV2 and flotillin-1. **(A)** A schematic representation of full-length TRPV2, its mutants that were studied, and their abilities to interact with flotillin-1. The number denotes the position of the amino acid residues. **(B)** N-terminal region and transmembrane domains 1–4 of TRPV2 are responsible for the interaction between TRPV2 and flotillin-1. HEK 293T cells were transiently transfected with different truncation mutants tagged with GFP and flotillin-1-Flag as indicated. Cell lysates were immunoprecipitated with anti-Flag agarose beads and analyzed by IB using anti-GFP and anti-Flag, respectively. Whole-cell lysates were also used for IB with anti-GFP and anti-Flag for input. **(C)** Schematic diagram of composition of mutant flotillin-1 including SPFH domain (aa 1–189), and flotillin domain (aa 190–427), and as well as their abilities to interact with TRPV2. **(D)** HEK 293T cells were transfected with TRPV2-Flag and different mutant flotillin-1 fused with GFP as indicated. Cell lysates were subjected to IP by anti-Flag, followed by IB for anti-GFP and anti-Flag, respectively. Note, molecular weight standards (in KD) are shown on the left. TM, transmembrane. Data are representative of three independent experiments.

been revealed that two structural motifs in transmembrane segments 2 and 4 of mTRPA1 regulates its interaction with cholesterol, which appears necessary for normal agonist sensitivity and plasma membrane localization (Startek et al., 2019). Consistent with these observations, we have shown here that the N-terminal and TM1–4 of TRPV2 are essential for the interactions between flotillin-1 and TRPV2. This observation parallels our finding that flotillin-1 helps to stabilize TRPV2 membrane expression.

It has been reported that flotillin-mediated endocytosis and ALIX–syntenin-1–mediated exocytosis protect the cell membrane from damage caused by necroptosis (Fan et al., 2019). Given the role of flotillin-1 in protein clustering and endocytosis, it is also plausible that flotillin-1 plays a role in maintaining the normal recycling of TRPV2 to the plasma membrane. This process would be important for refreshing the functional pool of TRPV2 on cell surface. We can not exclude the possibility that flotillin-1 may negatively regulate the intracellular degradation of TRPV2. This would also explain that an overexpression of flotillin-1 enhances TRPV2 membrane expression, and vice versa.

Since TRPV2 channel has been implicated in the processing of high intensity thermal pain, mechano-sensation, regulation of cardiovascular function, as well as many aspects of pathophysiology in different ways (Peralvarez-Marin et al., 2013; Shibasaki, 2016), our findings support that flotillin-1 is a key molecular element in TRPV2 signaling complex and exerts a regulatory effect on its cellular response.

Targeting flotillin-1 would offer an updated intervention strategy to manage TRPV2-mediated physio- and pathology responses.

CONCLUSION

We have characterized the role of flotillin-1 in mediating the membrane expression and cellular responses of TRPV2. This functional crosstalk between TRPV2 and lipid raft components may influence the cellular morphology and play critical roles in nociception and pain.

DATA AVAILABILITY STATEMENT

The original contributions generated for this study are included in the article/supplementary material, further inquiries can be directed to the corresponding author.

ETHICS STATEMENT

All mice were housed in the specific pathogen-free animal facility at Wuhan University and all animal experiments were in accordance with protocols approved by the Institutional Animal Care and Use Committee of Wuhan University (No. WDSKY0201804).

AUTHOR CONTRIBUTIONS

JY designed and supervised the study. JH, YG, QH, YW, XM, PW, YZ, CX, and JY carried out the experiments and analyzed the data. DL provided technical support and suggestions. JH and JY wrote the manuscript with inputs from all other authors. All authors discussed the results and commented on the manuscript.

FUNDING

This work was supported by grants from the National Natural Science Foundation of China (31830031, 31929003, 31871174, 31671209, and 31601864), Natural Science Foundation of Hubei Province (2017CFA063 and 2018CFA016), and the Fundamental Research Funds for the Central Universities.

ACKNOWLEDGMENTS

We are grateful to Drs. Bo Zhong, Jie Luo, and members of Yao lab for constructive comments and discussions, and we would also like to thank the core facilities of College of Life Sciences at Wuhan University for technical help.

REFERENCES

Aoyagi, K., Ohara-Imaizumi, M., Nishiwaki, C., Nakamichi, Y., and Nagamatsu, S. (2010). Insulin/phosphoinositide 3-kinase pathway accelerates the glucose-induced first-phase insulin secretion through TrpV2 recruitment in pancreatic beta-cells. *Biochem J.* 432, 375–386. doi: 10.1042/bj20100864

Babuke, T., Ruonala, M., Meister, M., Amaddii, M., Genzler, C., Esposito, A., et al. (2009). Hetero-oligomerization of reggie-1/flotillin-2 and reggie-2/flotillin-1 is required for their endocytosis. *Cell Signal* 21, 1287–1297. doi: 10.1016/j.cellsig.2009.03.012

Bang, S., Kim, K. Y., Yoo, S., Lee, S. H., and Hwang, S. W. (2007). Transient receptor potential V2 expressed in sensory neurons is activated by probenecid. *Neurosci. Lett.* 425, 120–125. doi: 10.1016/j.neulet.2007.08.035

Barnhill, J. C., Stokes, A. J., Koblan-Huberson, M., Shimoda, L. M., Muraguchi, A., Adra, C. N., et al. (2004). RGA protein associates with a TRPV ion channel during biosynthesis and trafficking. *J. Cell Biochem.* 91, 808–820. doi: 10.1002/jcb.10775

Bodin, S., Planchon, D., Rios Morris, E., Comunale, F., and Gauthier-Rouvière, C. (2014). Flotillins in intercellular adhesion - from cellular physiology to human diseases. *J. Cell Sci.* 127, 5139–5147. doi: 10.1242/jcs.159764

Browman, D. T., Hoegg, M. B., and Robbins, S. M. (2007). The SPFH domain-containing proteins: more than lipid raft markers. *Trends Cell Biol.* 17, 394–402. doi: 10.1016/j.tcb.2007.06.005

Caterina, M. J., Rosen, T. A., Tominaga, M., Brake, A. J., and Julius, D. (1999). A capsaicin-receptor homologue with a high threshold for noxious heat. *Nature* 398, 436–441. doi: 10.1038/18906

Cohen, M. R., Johnson, W. M., Pilat, J. M., Kiselar, J., Defrancesco-Lisowitz, A., Zigmond, R. E., et al. (2015). Nerve growth factor regulates transient receptor potential vanilloid 2 via extracellular signal-regulated kinase signaling to enhance neurite outgrowth in developing neurons. *Mol. Cell Biol.* 35, 4238–4252. doi: 10.1128/mcb.00549-15

Colton, C. K., and Zhu, M. X. (2007). 2-Aminoethoxydiphenyl borate as a common activator of TRPV1, TRPV2, and TRPV3 channels. *Handb Exp. Pharmacol.* 179, 173–187. doi: 10.1007/978-3-540-34891-7_10

Cornfine, S., Himmel, M., Kopp, P., El Azzouzi, K., Wiesner, C., Kruger, M., et al. (2011). The kinesin KIF9 and reggie/flotillin proteins regulate matrix degradation by macrophage podosomes. *Mol. Biol. Cell.* 22, 202–215. doi: 10.1091/mbc.e10-05-0394

Donate-Macian, P., Enrich-Bengoa, J., Degano, I. R., Quintana, D. G., and Peralvarez-Marin, A. (2019). Trafficking of stretch-regulated TRPV2 and TRPV4 channels inferred through interactomics. *Biomolecules* 9:791. doi: 10.3390/biom9120791

Entin-Meer, M., Cohen, L., Hertzberg-Bigelman, E., Levy, R., Ben-Shoshan, J., Keren, G. et al. (2017). TRPV2 knockout mice demonstrate an improved cardiac performance following myocardial infarction due to attenuated activity of peri-infarct macrophages. *PLoS One* 12:e0177132. doi: 10.1371/journal.pone.0177132

Fan, W., Guo, J., Gao, B., Zhang, W., Ling, L., Xu, T., et al. (2019). Flotillin-mediated endocytosis and ALIX-syntenin-1-mediated exocytosis protect the cell membrane from damage caused by necroptosis. *Sci. Signal.* 12:eaaw3423. doi: 10.1126/scisignal.aaw3423

Gauthier-Rouvière, C., Bodin, S., Comunale, F., and Planchon, D. (2020). Flotillin membrane domains in cancer. *Cancer Metastasis Rev.* 39, 361–374. doi: 10.1007/s10555-020-09873-y

Huynh, K. W., Cohen, M. R., Jiang, J., Samanta, A., Lodowski, D. T., Zhou, Z. H., et al. (2016). Structure of the full-length TRPV2 channel by cryo-EM. *Nat. Commun.* 7:11130.

Juvin, V., Penna, A., Chemin, J., Lin, Y. L., and Rassendren, F. A. (2007). Pharmacological characterization and molecular determinants of the activation of transient receptor potential V2 channel orthologs by 2-aminoethoxydiphenyl borate. *Mol. Pharmacol.* 72, 1258–1268. doi: 10.1124/mol.107.037044

Katanosaka, Y., Iwasaki, K., Ujihara, Y., Takatsu, S., Nishitsuji, K., Kanagawa, M., et al. (2014). TRPV2 is critical for the maintenance of cardiac structure and function in mice. *Nat. Commun.* 5:3932.

Kato, N., Nakanishi, M., and Hirashima, N. (2006). Flotillin-1 regulates IgE receptor-mediated signaling in rat basophilic leukemia (RBL-2H3) cells. *J Immunol* 177, 147–154. doi: 10.4049/jimmunol.177.1.147

Kessler, E. L., Van Stuijvenberg, L., Van Bavel, J. J. A., Van Bennekom, J., Zwartsen, A., Rivaud, M. R., et al. (2019). Flotillins in the intercalated disc are potential modulators of cardiac excitability. *J. Mol. Cell. Cardiol.* 126, 86–95. doi: 10.1016/j.yjmcc.2018.11.007

Kim, W., Bennett, E. J., Huttlin, E. L., Guo, A., Li, J., Possemato, A., et al. (2011). Systematic and quantitative assessment of the ubiquitin-modified proteome. *Mol. Cell.* 44, 325–340. doi: 10.1016/j.molcel.2011.08.025

Kimura, A., Baumann, C. A., Chiang, S. H., and Saltiel, A. R. (2001). The sorbin homology domain: a motif for the targeting of proteins to lipid rafts. *Proc. Natl. Acad. Sci. U S A.* 98, 9098–9103. doi: 10.1073/pnas.151252898

Kwiatkowska, K., Matveichuk, O. V., Fronk, J., and Ciesielska, A. (2020). Flotillins: at the intersection of protein S-palmitoylation and lipid-mediated signaling. *Int. J. Mol. Sci.* 21:2283. doi: 10.3390/ijms21072283

Langhorst, M. F., Reuter, A., and Stuermer, C. A. (2005). Scaffolding microdomains and beyond: the function of reggie/flotillin proteins. *Cell Mol. Life Sci.* 62, 2228–2240. doi: 10.1007/s00018-005-5166-4

Lin, Y., and Sun, Z. (2012). Antiaging gene Klotho enhances glucose-induced insulin secretion by up-regulating plasma membrane levels of TRPV2 in MIN6 β-cells. *Endocrinology* 153, 3029–3039. doi: 10.1210/en.2012-1091

Link, T. M., Park, U., Vonakis, B. M., Raben, D. M., Soloski, M. J., Caterina, M. J. et al. (2010). TRPV2 has a pivotal role in macrophage particle binding and phagocytosis. *Nat. Immunol.* 11, 232–239. doi: 10.1038/ni.1842

Liu, J., Deyoung, S. M., Zhang, M., Dold, L. H., and Saltiel, A. R. (2005). The stomatin/prohibitin/flotillin/HflK/C domain of flotillin-1 contains distinct sequences that direct plasma membrane localization and protein interactions in 3T3-L1 adipocytes. *J. Biol. Chem.* 280, 16125–16134. doi: 10.1074/jbc.m500940200

Liu, J., Zhao, Z., Wen, J., Wang, Y., Zhao, M., Peng, L., et al. (2019). TNF-α differently regulates TRPV2 and TRPV4 channels in human dental pulp cells. *Int. Endod. J.* 52, 1617–1628. doi: 10.1111/iej.13174

Liu, R., Yang, G., Zhou, M. H., He, Y., Mei, Y. A., Ding, Y. et al. (2016). Flotillin-1 downregulates K^+ current by directly coupling with Kv2.1 subunit. *Protein Cell* 7, 455–460. doi: 10.1007/s13238-016-0276-3

Mercado, J., Gordon-Shaag, A., Zagotta, W. N., and Gordon, S. E. (2010). Ca^{2+}-dependent desensitization of TRPV2 channels is mediated by hydrolysis of phosphatidylinositol 4,5-bisphosphate. *J. Neurosci.* 30, 13338–13347. doi: 10.1523/jneurosci.2108-10.2010

Monje, F. J., Divisch, I., Demit, M., Lubec, G., and Pollak, D. D. (2013). Flotillin-1 is an evolutionary-conserved memory-related protein up-regulated in implicit and explicit learning paradigms. *Ann. Med.* 45, 301–307. doi: 10.3109/07853890.2013.770637

Morrow, I. C., Rea, S., Martin, S., Prior, I. A., Prohaska, R., Hancock, J. F., et al. (2002). Flotillin-1/reggie-2 traffics to surface raft domains via a novel golgi-independent pathway. Identification of a novel membrane targeting domain and a role for palmitoylation. *J. Biol. Chem.* 277, 48834–48841. doi: 10.1074/jbc.m209082200

Neeper, M. P., Liu, Y., Hutchinson, T. L., Wang, Y., Flores, C. M., Qin, N. et al. (2007). Activation properties of heterologously expressed mammalian TRPV2: evidence for species dependence. *J. Biol. Chem.* 282, 15894–15902. doi: 10.1074/jbc.m608287200

Neumann-Giesen, C., Falkenbach, B., Beicht, P., Claasen, S., Lüers, G., Stuermer, C. A., et al. (2004). Membrane and raft association of reggie-1/flotillin-2: role of myristoylation, palmitoylation and oligomerization and induction of filopodia by overexpression. *Biochem. J.* 378, 509–518. doi: 10.1042/bj20031100

Nothdurfter, C., Tanasic, S., Di Benedetto, B., Uhr, M., Wagner, E. M., Gilling, K. E., et al. (2013). Lipid raft integrity affects GABAA receptor, but not NMDA receptor modulation by psychopharmacological compounds. *Int. J. Neuropsychopharmacol.* 16, 1361–1371. doi: 10.1017/s146114571200140x

Peralvarez-Marin, A., Donate-Macian, P., and Gaudet, R. (2013). What do we know about the transient receptor potential vanilloid 2 (TRPV2) ion channel? *FEBS J.* 280, 5471–5487. doi: 10.1111/febs.12302

Qin, N., Neeper, M. P., Liu, Y., Hutchinson, T. L., Lubin, M. L., and Flores, C. M. (2008). TRPV2 is activated by cannabidiol and mediates CGRP release in cultured rat dorsal root ganglion neurons. *J. Neurosci.* 28, 6231–6238. doi: 10.1523/jneurosci.0504-08.2008

Robinson, P., Etheridge, S., Song, L., Armenise, P., Jones, O. T., Fitzgerald, E. M. et al. (2010). Formation of N-type (Cav2.2) voltage-gated calcium channel membrane microdomains: lipid raft association and clustering. *Cell. Calcium* 48, 183–194. doi: 10.1016/j.ceca.2010.08.006

Santoni, G., Farfariello, V., Liberati, S., Morelli, M. B., Nabissi, M., Santoni, M., et al. (2013). The role of transient receptor potential vanilloid type-2 ion channels in innate and adaptive immune responses. *Front. Immunol.* 4:34. doi: 10.3389/fimmu.2013.00034

Schulte, T., Paschke, K. A., Laessing, U., Lottspeich, F., and Stuermer, C. A. (1997). Reggie-1 and reggie-2, two cell surface proteins expressed by retinal ganglion cells during axon regeneration. *Development* 124, 577–587.

Shibasaki, K. (2016). Physiological significance of TRPV2 as a mechanosensor, thermosensor and lipid sensor. *J. Physiol. Sci.* 66, 359–365. doi: 10.1007/s12576-016-0434-7

Shibasaki, K., Murayama, N., Ono, K., Ishizaki, Y., and Tominaga, M. (2010). TRPV2 enhances axon outgrowth through its activation by membrane stretch in developing sensory and motor neurons. *J. Neurosci.* 30, 4601–4612. doi: 10.1523/jneurosci.5830-09.2010

Solis, G. P., Hoegg, M., Munderloh, C., Schrock, Y., Malaga-Trillo, E., Rivera-Milla, E., et al. (2007). Reggie/flotillin proteins are organized into stable tetramers in membrane microdomains. *Biochem. J.* 403, 313–322. doi: 10.1042/bj20061686

Solis, G. P., Malaga-Trillo, E., Plattner, H., and Stuermer, C. A. (2010). Cellular roles of the prion protein in association with reggie/flotillin microdomains. *Front. Biosci (Landmark Ed)* 15:1075–1085. doi: 10.2741/3662

Sones, W. R., Davis, A. J., Leblanc, N., and Greenwood, I. A. (2010). Cholesterol depletion alters amplitude and pharmacology of vascular calcium-activated chloride channels. *Cardiovasc. Res.* 87, 476–484. doi: 10.1093/cvr/cvq057

Startek, J. B., Boonen, B., López-Requena, A., Talavera, A., Alpizar, Y. A., Ghosh, D., et al. (2019). Mouse TRPA1 function and membrane localization are modulated by direct interactions with cholesterol. *Elife* 8:e46084.

Stokes, A. J., Shimoda, L. M., Koblan-Huberson, M., Adra, C. N., and Turner, H. (2004). A TRPV2-PKA signaling module for transduction of physical stimuli in mast cells. *J. Exp. Med.* 200, 137–147. doi: 10.1084/jem.20032082

Stokes, A. J., Wakano, C., Del Carmen, K. A., Koblan-Huberson, M., and Turner, H. (2005). Formation of a physiological complex between TRPV2 and RGA protein promotes cell surface expression of TRPV2. *J. Cell Biochem.* 94, 669–683. doi: 10.1002/jcb.20331

Stuermer, C. A., Lang, D. M., Kirsch, F., Wiechers, M., Deininger, S. O., Plattner, H. et al. (2001). Glycosylphosphatidyl inositol-anchored proteins and fyn kinase assemble in noncaveolar plasma membrane microdomains defined by reggie-1 and -2. *Mol. Biol. Cell.* 12, 3031–3045. doi: 10.1091/mbc.12.10.3031

Swanwick, C. C., Shapiro, M. E., Yi, Z., Chang, K., and Wenthold, R. J. (2009). NMDA receptors interact with flotillin-1 and -2, lipid raft-associated proteins. *FEBS Lett.* 583, 1226–1230. doi: 10.1016/j.febslet.2009.03.017

Tian, Q., Hu, J., Xie, C., Mei, K., Pham, C., Mo, X., et al. (2019). Recovery from tachyphylaxis of TRPV1 coincides with recycling to the surface membrane. *Proc. Natl. Acad. Sci. U S A.* 116, 5170–5175. doi: 10.1073/pnas.1819635116

Vacca, F., Amadio, S., Sancesario, G., Bernardi, G., and Volonte, C. (2004). P2X3 receptor localizes into lipid rafts in neuronal cells. *J. Neurosci. Res.* 76, 653–661. doi: 10.1002/jnr.20069

Wakasugi, K., Nakano, T., Kitatsuji, C., and Morishima, I. (2004). Human neuroglobin interacts with flotillin-1, a lipid raft microdomain-associated protein. *Biochem. Biophys. Res. Commun.* 318, 453–460. doi: 10.1016/j.bbrc.2004.04.045

Wang, D., Yuan, Z., Inoue, N., Cho, G., Shono, M., Ishikawa, Y. et al. (2011). Abnormal subcellular localization of AQP5 and downregulated AQP5 protein in parotid glands of streptozotocin-induced diabetic rats. *Biochim. Biophys. Acta* 1810, 543–554. doi: 10.1016/j.bbagen.2011.01.013

Wang, Y., Gao, Y., Tian, Q., Deng, Q., Wang, Y., Zhou, T., et al. (2018). TRPV1 SUMOylation regulates nociceptive signaling in models of inflammatory pain. *Nat. Commun.* 9:1529.

Wang, Y., Mo, X., Ping, C., Huang, Q., Zhang, H., Xie, C., et al. (2020). Site-specific contacts enable distinct modes of TRPV1 regulation by the potassium channel Kvbeta1 subunit. *J. Biol. Chem.* 295, 17337–17348. doi: 10.1074/jbc.ra120.015605

Wood, J. N., Bevan, S. J., Coote, P. R., Dunn, P. M., Harmar, A., Hogan, P., et al. (1990). Novel cell lines display properties of nociceptive sensory neurons. *Proc. Biol. Sci.* 241, 187–194. doi: 10.1098/rspb.1990.0084

Yao, J., Liu, B., and Qin, F. (2009). Rapid temperature jump by infrared diode laser irradiation for patch-clamp studies. *Biophys. J.* 96, 3611–3619. doi: 10.1016/j.bpj.2009.02.016

Zhang, X., Li, L., and Mcnaughton, P. A. (2008). Proinflammatory mediators modulate the heat-activated ion channel TRPV1 via the scaffolding protein AKAP79/150. *Neuron* 59, 450–461. doi: 10.1016/j.neuron.2008.05.015

Zhao, F., Zhang, J., Liu, Y. S., Li, L., and He, Y. L. (2011). Research advances on flotillins. *Virol. J.* 8:479. doi: 10.1186/1743-422x-8-479

Conflict of Interest: The authors declare that the research was conducted in the absence of any commercial or financial relationships that could be construed as a potential conflict of interest.

frontiers
in Cell and Developmental Biology

ORIGINAL RESEARCH
published: 25 February 2021
doi: 10.3389/fcell.2020.627146

Deletion of *Mea6* in Cerebellar Granule Cells Impairs Synaptic Development and Motor Performance

Xin-Tai Wang[1†], Lin Zhou[1,2†], Xin-Yu Cai[1], Fang-Xiao Xu[1], Zhi-Heng Xu[3], Xiang-Yao Li[4*] and Ying Shen[1*]

[1] Department of Physiology, School of Medicine, Zhejiang University, Hangzhou, China, [2] Department of Psychiatry, Sir Run Run Shaw Hospital, School of Medicine, Zhejiang University, Hangzhou, China, [3] State Key Laboratory of Molecular Developmental Biology, CAS Center for Excellence in Brain Science and Intelligence Technology, Institute of Genetics and Developmental Biology, Chinese Academy of Sciences, Beijing, China, [4] Department of Neurobiology, School of Brain Science and Brain Medicine, Zhejiang University, Hangzhou, China

Edited by:
Cong Ma,
Huazhong University of Science and Technology, China

Reviewed by:
Zhenyu Gao,
Erasmus Medical Center, Netherlands
Haitao Wu,
Institute of Basic Medical Sciences, China
Pellegrino Lippiello,
University of Naples Federico II, Italy

***Correspondence:**
Ying Shen
yshen@zju.edu.cn
Xiang-Yao Li
lixiangy@zju.edu.cn

[†] These authors have contributed equally to this work

Specialty section:
This article was submitted to Membrane Traffic, a section of the journal Frontiers in Cell and Developmental Biology

Received: 08 November 2020
Accepted: 21 December 2020
Published: 25 February 2021

Citation:
Wang X-T, Zhou L, Cai X-Y, Xu F-X, Xu Z-H, Li X-Y and Shen Y (2021) Deletion of Mea6 in Cerebellar Granule Cells Impairs Synaptic Development and Motor Performance. Front. Cell Dev. Biol. 8:627146. doi: 10.3389/fcell.2020.627146

The cerebellum is conceptualized as a processor of complex movements. Many diseases with gene-targeted mutations, including Fahr's disease associated with the loss-of-function mutation of meningioma expressed antigen 6 (*Mea6*), exhibit cerebellar malformations, and abnormal motor behaviors. We previously reported that the defects in cerebellar development and motor performance of Nestin-Cre;*Mea6*$^{F/F}$ mice are severer than those of Purkinje cell-targeted pCP2-Cre;*Mea6*$^{F/F}$ mice, suggesting that Mea6 acts on other types of cerebellar cells. Hence, we investigated the function of Mea6 in cerebellar granule cells. We found that mutant mice with the specific deletion of *Mea6* in granule cells displayed abnormal posture, balance, and motor learning, as indicated in footprint, head inclination, balanced beam, and rotarod tests. We further showed that Math1-Cre;*Mea6*$^{F/F}$ mice exhibited disrupted migration of granule cell progenitors and damaged parallel fiber-Purkinje cell synapses, which may be related to impaired intracellular transport of vesicular glutamate transporter 1 and brain-derived neurotrophic factor. The present findings extend our previous work and may help to better understand the pathogenesis of Fahr's disease.

Keywords: Mea6, malformation, motor performance, vGluT1, granule cell, Fahr's syndrome

INTRODUCTION

The cerebellum has been conceptualized as a processor of complex movements and is also endowed with essential roles in cognitive and emotional behaviors (Su et al., 2020). In essence, the cerebellar cortex can be trained to run routine operations that result in skillful movements triggered by high-level commands from the cerebral cortex. The structure of the cerebellum is extremely conserved among species from rodents to human, and its development involves the integration of intrinsic and extrinsic events controlled by multiple genetic cascades. Many gene-targeted mutations cause cerebellar malformations and impair motor and non-motor behaviors (Su et al., 2020). For example, the patients with Fahr's disease (Lemos et al., 2011), a neurological inheritance disorder (Oliveira et al., 2007), exhibit unsteady gaits, and severe degeneration in brain regions controlling movements (Moskowitz et al., 1971; Geschwind et al., 1999; Saleem et al., 2013).

Meningioma expressed antigen 6 (Mea6), initially found in tumor tissues (Heckel et al., 1997; Comtesse et al., 2002; Kalniņa et al., 2008), is highly expressed in the central nervous system (CNS). Clinical evidence shows that a loss-of-function mutation of Mea6 might be associated with Fahr's syndrome (Lemos et al., 2011). Utilizing conditional knockout of *Mea6* driven by Nestin-Cre, Zhang et al. (2018) show that Mea6 is critical to neural development and dendrite outgrowth in the cerebral cortex. However, this study provides limited insights on how Mea6 plays roles in CNS development because Nestin-driven Cre recombinase inevitably affects all types of neural cells in the CNS. Instead, we report distinct cerebellar development and motor performance between Nestin-Cre;*Mea6*$^{F/F}$ and Purkinje cell-targeted pCP2-Cre;*Mea6*$^{F/F}$ mice (Wang et al., 2019). While Nestin-Cre;*Mea6*$^{F/F}$ mice have shrunken cerebellum and lobules, pCP2-Cre;*Mea6*$^{F/F}$ mice merely display extensive self-crossings of Purkinje cell dendrites without changing cyto-architecture of the cerebellum (Wang et al., 2019). These results suggest that Mea6 influences the development of other types of cerebellar cells beyond Purkinje cells.

Cerebellar granule cell, being the most numerous cell type, arises from the rhombic lip and forms a dense and distinct layers of cerebellar cortex. At the early developmental stage, granule precursor cells proliferate and differentiate to granule cells, which further migrate from the external granular layer (EGL) inwards to the internal granular layer (IGL). Granule cells receive afferent information from mossy fibers and innervate with Purkinje cells *via* parallel fibers. It has been established by physiological experiments and computational theories that granule cells are the ground of cerebellar circuitry and motor memories. Here, we investigated the contribution of Mea6 in cerebellar development and motor functions by deleting *Mea6* specifically in granule cells. Our results showed that the deletion of *Mea6* in granule cells led to severe motor symptoms during the posture, balance, and motor learning tests.

MATERIALS AND METHODS

Animals

All experiments were approved by the Animal Experimentation Ethics Committee of Zhejiang University. Mice were kept at the Experimental Animal Center of Zhejiang University under temperature-controlled condition on a 12:12 h light/dark cycle. *Mea6*$^{F/F}$ mice described previously (Wang et al., 2019). Math1-Cre;*Mea6*$^{F/F}$ mice were obtained by crossing *Mea6*$^{F/F}$ mice with Math1-Cre mice, which were obtained from Dr. Wei Mo (Xiamen University, Xiamen, China) (Kim et al., 2014). The resulting offspring were genotyped using PCR of genomic DNA (*Mea6* floxP fragment, F: 5′-GAC ACT TGA CCC CTC CTC TCC-3′; R: 5′-AAC GGC TCA TGC TTG CTA ACC-3′; Math1-cre, F: 5′-TGC AAC GAG TGA TGA GGT TC-3′; R: 5′-GCT TGC ATG ATC TCC GGT AT-3′). All experiments were performed blind to genotypes in age-matched littermates of either sex.

Antibodies and Reagents

Antibodies against GAPDH, GluA1, GluA2, NeuN, and synaptophysin were from Millipore (Billerica, MA, United States). Antibodies against Bip, Robo2, Sema6A, Synapsin-1, Munc18-1, and 5-bromo-2′-deoxyuridine (BrdU) were from Abcam (Cambridge, United Kingdom). Antibodies against γ-protocadherin (γ-pcdh), Rab3A, Rim1, and Munc13-1 were from Synaptic Systems (Gottingen, Germany). Antibody against Slit2 was from Proteintech (Rosemont, IL, United States). Antibody against TrkB was from Cell Signaling (Danvers, MA, United States). Anti-vesicular glutamate transporter 1 (vGluT1) antibody was a gift from Dr. Masahiko Watanabe (Hokkaido University, Sapporo, Japan). Antibodies against both Mea6 and calbindin were from Sigma-Aldrich (St. Louis, MO, United States). Antibodies to β-tubulin and brain-derived neurotrophic factor (BDNF) were from Santa Cruz Biotechnology (Dallas, TX, United States). Goat anti-mouse and anti-rabbit IgG horseradish peroxidase-conjugated were from Thermo Fisher (Waltham, MA, United States). DAPI and Alexa Fluor-conjugated secondary antibody was from Invitrogen (Carlsbad, CA, United States). Protease inhibitor cocktail was from Roche (Mannheim, Germany). Nissl was from Beyotime (Shanghai, China). Other chemicals were from Sigma unless stated otherwise.

Purification of Endoplasmic Reticulum (ER)

Endoplasmic reticulum fractions were purified according to previous work (Hammond et al., 2012; Wang et al., 2019). A centrifugation (700 × *g*; 10 min) was used to remove nuclei and large cellular debris from homogenized cerebellar tissues. A subsequent 15,000 × *g* (10 min) of supernatant was performed to pellet mitochondria. The resulting supernatant was loaded onto a three-layered sucrose gradient and centrifuged at 126,000 × *g* for 70 min on an ultracentrifuge. The white band between the top and 1.3 M-sucrose layers was collected, which was gently mixed by inversion with ice cold MTE solution supplemented with protease inhibitors. This mixture was centrifuged at 126,000 × *g* for 45 min resulting in a large and translucent pellet.

RT-PCR

The contents of individual granule cells (P21) were harvested as described in previous work (Zhou et al., 2017). The tip of a conventional patch-clamp pipette was placed tightly on the soma of a selected granule cell and a gentle suction was applied. After complete incorporation of the soma, the negative pressure was released and the pipette was quickly removed from the bath. The harvested contents were subjected to RT-PCR using OneStep Kit (Qiagen, Germany). Forward (F) and reverse (R) primers used for amplification were as follows: *Mea6*, F: 5′-GTT GAA GGA TCA CAA ATA TC-3′; R: 5′-TCC TTT TTG AAA TAT CAG CC-3′; *Math1*, F: 5′-GAG TGG GCT GAG GTA AAA GAG T-3′; R: 5′-GGT CGG TGC TAT CCA GGA G-3′; *Gapdh*, F: 5′-GGT GAA GGT CGG TGT GAA CG-3′; R: 5′-CTC GCT CCT GGA AGA TGG TG-3′.

Western Blot

The protein concentration was determined using BCA protein assay. Equal quantities of proteins were loaded and fractionated on SDS-PAGE, transferred to PVDF membrane (Immobilon-P, Millipore), immunoblotted with antibodies, and visualized by enhanced chemiluminescence (Thermo). The dilutions of antibodies were MEA6 (1:4,000), Slit2 (1:1,000), Robo2 (1:1,000), β-tubulin (1:2,000), GAPDH (1:20,000), γ-pcdh (1:2,000), BDNF (1:1,000), TrkB (1:1,000), Bip (1:5,000), Sema6A (1:1,000), vGluT1 (1:2000), Rab3A (1:2000), synapsin-1 (1:10000), Rim1 (1:1000), Munc18-1 (1:40000), synaptophysin (1:40000), Munc13-1 (1:1000), GluA1 (1:2000), GluA2 (1:2000), and secondary antibodies (1:10,000). Film signals were digitally scanned and quantitated using ImageJ 1.42q (NIH).

Immunohistochemistry

Frozen sagittal sections (30 μm) were cut and placed in blocking solution for 1 h at room temperature (RT). After washing with PBS, sections were incubated with primary antibodies overnight at 4°C and incubated with secondary antibodies for 3 h at RT. Primary antibody dilutions used for immunohistochemistry were calbindin (1:500), NeuN (1:500), BrdU (1:400), and Mea6 (1:250). Alexa Fluor 488-conjugated goat anti rat IgG, Alexa Fluor 488-conjugated goat anti mouse IgG, Alexa Fluor 594-conjugated goat anti-mouse IgG antibody, Alexa Fluor 488-conjugated goat anti-rabbit IgG antibody and Alexa Fluor 594-conjugated goat anti-rabbit IgG antibody were diluted at 1:1,000. All antibodies were diluted in PBS containing 1% BSA and 1% normal goat serum.

BrdU Labeling

Mice (P7) were injected intraperitoneally with 50 mg/kg BrdU and sacrificed for labeling observation after 5 days. After denaturing DNA (2 N HCl; 40°C; 30 min), brain sections (30 μm) were washed with sodium tetraborate (0.1 M). Sections were immunostained using BrdU and NeuN antibody.

Nissl Staining

Nissl staining was performed using Nissl staining Kit (Beyotime). Sagittal cerebellar slices (30 μm) were immersed in Nissl staining solution for 5 min, rinsed with distilled water, dehydrated in ethanol, and cleared in xylene. Images of cerebellar cortex were captured using a light microscope.

Transmission Electron Microscopy (TEM)

Mouse brains were removed and stored at 4°C for 2.5 h in fixative. Sagittal slices (300 μm) were prepared and rectangular molecular layer of lobules IV–V were separated. The slices were then rinsed six times with 0.1 M PB and post-fixed in 1% OsO_4 for 30 min. Slices were then rinsed three times with ddH_2O and stained with 2% uranyl acetate for 30 min at RT. After dehydrating, the samples were embedded in an epoxy resin. Ultrathin sections (90 nm) were cut using an ultra-microtome (Leica), stained with lead citrate solution, and mounted on grids. EM images were captured at 11,000× and 68,000× magnification using a TEM (FEI, Hillsboro, OR, United States). Parallel fiber-Purkinje cell synapses were identified by asymmetrical and short contacts, which were distinct from GABAergic or climbing fiber synapses (Ichikawa et al., 2016). ImageJ was used to count the numbers of synapse and vesicles per bouton.

Slice Preparation

Sagittal sections of cerebellar vermis (300 μm) were prepared from anesthetic mice (P20–21) using a vibrating tissue slicer (Leica VT1000S) and ice-cold standard artificial cerebrospinal fluid (aCSF) containing (in mM): 125 NaCl, 2.5 KCl, 1.25 NaH_2PO_4, 1 $MgCl_2$, 2 $CaCl_2$, 26 $NaHCO_3$, and 25 D-glucose, bubbled with 95% O_2/5% CO_2. After recovery for 30 min at 37°C, slices were placed in a submerged chamber that was perfused at 2 ml/min with aCSF. Patch clamp electrodes (3–5 MΩ) were filled with an intracellular solution composed of (in mM) 134 K-gluconate, 6 KCl, 4 NaCl, 10 HEPES, 0.2 EGTA, 4 Na_2ATP, 0.3 Na_3GTP, and 14 Na_2phosphocreatine (pH 7.3, OSM 290).

Whole-Cell Recording

Purkinje cells were visualized under an upright microscope (BX51, Olympus) with a 40× water-immersion objective and equipped with infrared differential interference contrast enhancement. Whole-cell recordings were obtained with an Axon MultiClamp 700B amplifier (Molecular Devices). Currents were digitized at 10 kHz and filtered at 3 kHz. Miniature excitatory synaptic currents (mEPSCs) was recorded in whole-cell configuration in the presence of tetrodotoxin (TTX, 0.5 μM) plus Gabazine (10 μM). To obtain parallel fiber-EPSCs, standard patch pipettes were filled with aCSF and placed in the middle third of the molecular layer. EPSCs were induced by above-threshold parallel fiber stimulation delivered in the presence Gabazine (10 μM). Paired-pulse facilitation (PPF) was examined by paired stimulations at different intervals. Offline analysis was conducted using a sliding template algorithm (ClampFit 10, Molecular Device).

Rotarod Test

Rotarod test was performed as previously described (Zhou et al., 2017). After the habituation to rotarod, mice (2 month) were tested twice a day at a time interval of 8 h for four consecutive days. In each session, the velocity of rotation increased at a constant acceleration of 9 rpm/min starting from 5 rpm.

Elevated Beam Test

This test was performed according to previous work (Hartmann et al., 2014; Zhou et al., 2017). The movement of mice on a round plastic beam (length 50 cm and diameter 1 cm) 40 cm above a surface with bedding was recorded and analyzed. The percentage of steps with hindpaw slips during runs on the beam was calculated.

Foot Print Test

To evaluate mice's walking gait we used footprint test according to previous work (Zhou et al., 2017; Wang et al., 2019). Mice hindpaws were painted with non-toxic ink, and they were allowed to freely traverse a clear plexiglass tunnel (100 cm × 10 cm × 10 cm), with a sheet of white absorbent paper (100 cm × 10 cm) placed at the bottom of the track and a darkened cage at the end of the tunnel to encourage the mouse to run toward a dark and safe environment. The resulting tracks provided the spatial relationship of consecutive footfalls, from which the stride length and stance width were measured. Measurements for three-step cycles were averaged, considering a cycle as the distance from one pair of hind prints to the next. Footprints at the start and the end of the tunnel were excluded from the analysis as they corresponded to the initiation and termination of the movement.

Measurement of Head Inclination

Mice were allowed to freely traverse a white plexiglass tunnel (100 cm × 10 cm × 10 cm) in front of a camera. The angle formed by the connection line of two eyes and horizontal plane was measured by Adobe Photoshop CS3.

Statistical Analysis

Data were analyzed using GraphPad Prism 6.0 (GraphPad Software, San Diego, CA, United States), Excel 2003 (Microsoft, Seattle, WA, United States), and Igor Pro 6.0 (Wavemetrics, Lake Oswego, OR, United States). Data analysts were blind to experimental conditions until the data were integrated. Standard deviations for controls were calculated from the average of all control data. Statistical difference was determined using two-sided unpaired Student's *t* test. The accepted level of significance was $p < 0.05$. *n* represents the number of preparations or cells. Data are presented as mean ± SEM.

RESULTS

Mea6 Was Specifically Deleted in Cerebellar Granule Cells in Math1-Cre;*Mea6*$^{F/F}$ Mice

Figure 1A shows that Mea6 was abundantly expressed in cell bodies and processes (parallel fibers) of cerebellar granule cells. Previous studies have shown that Mea6 is expressed in other brain regions besides the cerebellum (Zhang et al., 2018; Wang et al., 2019). Therefore, particular caution should be taken using Cre-loxp strategy to knock out *Mea6* in granule cells. We utilized the Math1-Cre mouse line (Kim et al., 2014), which targets to Math1+ neuronal precursors in developing rhombic lip that give rise to granule cells and unipolar brush cells (Englund et al., 2006; Schüller et al., 2008). To confirm the specificity, we crossed Math1-Cre and Ai9 lines and characterized the expression of Cre-recombinase by observing the tdTomato reporter in Math1-Cre;Ai9 mice. We found that tdTomato fluorescence was present merely in the cerebellum of these mice (**Figure 1B**), suggesting that the knockout mediated by Math1-recombinase is specific in the cerebellum. To examine whether Math1-recombination affects other cerebellar cells, we performed immunohistochemical staining using NeuN or calbindin antibodies and found that Math1-recombination was restricted to granule cell layer and parallel fibers (**Figure 1C**), suggesting that this recombination does not affect Purkinje cells and interneurons, which are located in Purkinje cell layer and molecular layer, respectively. Although Math1-recombination may affect unipolar brush cells as well, the influence should be marginal in our experiments because the number of these cells is very few compared to granule cells (Englund et al., 2006).

Next, we knock out *Mea6* gene in granule cells by mating *Mea6*$^{F/F}$ mice with Math1-Cre transgenic mice. The knockout efficiency was confirmed by patch-clamp-based RT-PCR assay (**Figure 1D**). Western blots also showed that Mea6 expression was significantly reduced in Math1-Cre;*Mea6*$^{F/F}$ mice (**Figure 1E**), which makes sense considering the great number of granule cells. We previously showed that both body weight and cerebellar size of Nestin-Cre;*Mea6*$^{F/F}$ mice are reduced (Wang et al., 2019). Differently, these phenotypes did not differ between Math1-Cre;*Mea6*$^{F/F}$ and *Mea6*$^{F/F}$ mice (**Figure 1F**). In addition, the lifetime of Math1-Cre;*Mea6*$^{F/F}$ mice was as long as that of *Mea6*$^{F/F}$ mice (**Figure 1G**), similar to mutant mice with the specific deletion of *Mea6* in Purkinje cells (Pcp2-Cre;*Mea6*$^{F/F}$) (Wang et al., 2019).

Mea6 Deletion in Granule Cells Impairs Motor Performance

We previous reported that Nestin-Cre;*Mea6*$^{F/F}$ mice displayed severe behavioral defects: they have abnormal limb-clasping reflex and foot prints, and perform poorly on elevated beam (Wang et al., 2019). In contrast, the behaviors of Pcp2-Cre;*Mea6*$^{F/F}$ mice are almost normal except motor learning (Wang et al., 2019). These results suggest that *Mea6* deletion driven by Nestin-Cre may affect the development and/or functions of other types of cells except Purkinje cells. Accordingly, we examined whether the deletion of *Mea6* in granule cells causes motor deficits. Indeed, we found that Math1-Cre;*Mea6*$^{F/F}$ mice walked abnormally with wider step stance of hindlimb without changing stride length (**Figure 2A**). Interestingly, Math1-Cre;*Mea6*$^{F/F}$ mice (19 out of 19) displayed unexpected head inclination: their heads always tilted to either left or right when they walked freely in the cages, while *Mea6*$^{F/F}$ mice did not (**Figure 2B**). To measure head tilt, mice were allowed to traverse a narrow plexiglass tunnel, where their free turning was limited. Through aligning ears and eyes, our results showed that average angels of head inclination were 1.2 ± 0.4° for *Mea6*$^{F/F}$ mice ($n = 16$) and 30.3 ± 0.9° Math1-Cre;*Mea6*$^{F/F}$ mice ($n = 19$). These experiments indicated abnormal walking gait of Math1-Cre;*Mea6*$^{F/F}$ mice. We also found that Math1-Cre;*Mea6*$^{F/F}$ mice were defective in other motor performances: They performed poorly when walking on an elevated beam with a higher number of hind-paw slips (**Figure 2C**) and spent

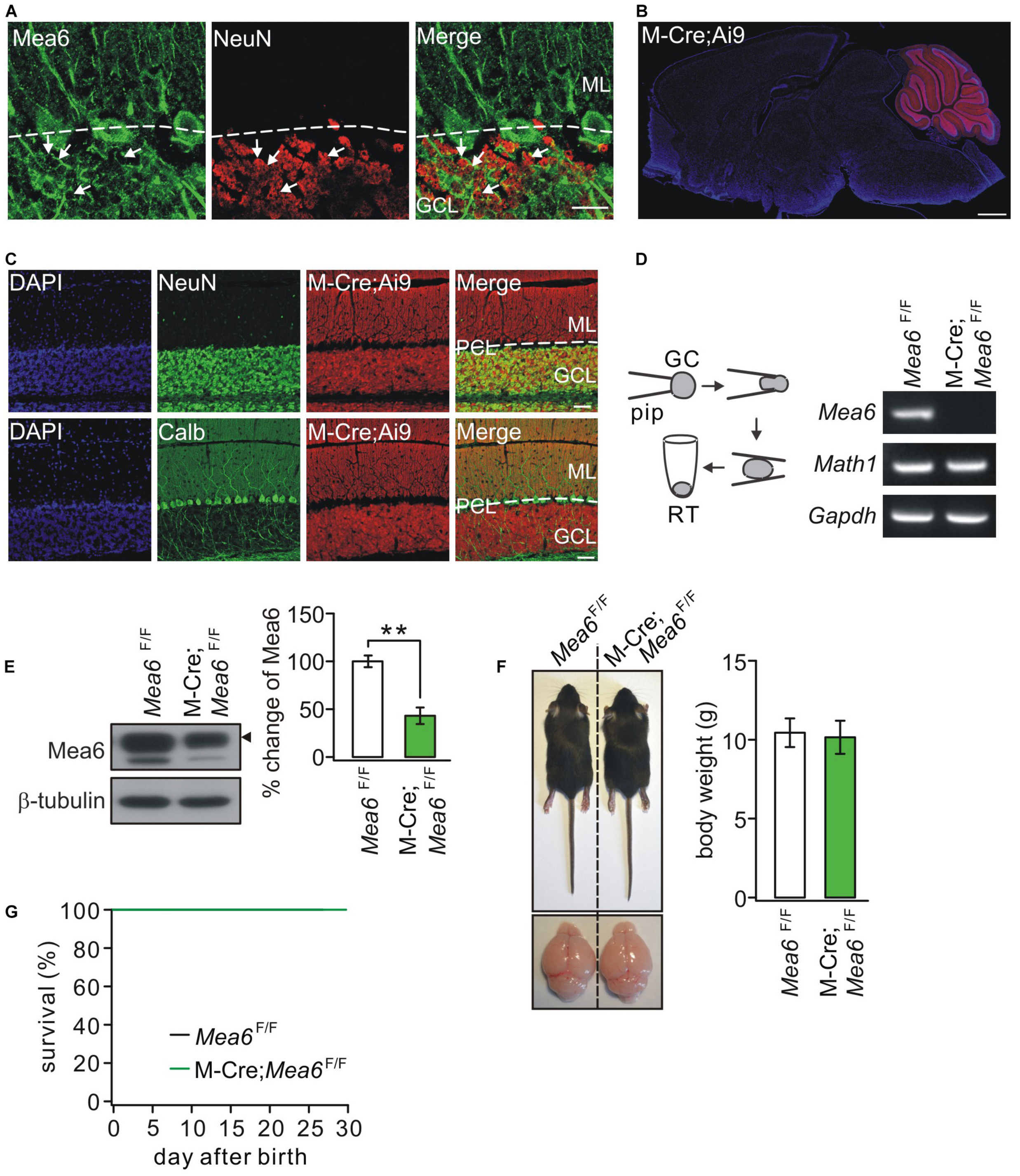

FIGURE 1 | The ablation of *Mea6* in Math1(M)-Cre;*Mea6*$^{F/F}$ mice. **(A)** The immunostaining of Mea6 (green) and NeuN (red) in mouse cerebellum. Arrows show Mea6-expressing granule cells. Scale bars: 20 µm. ML, molecular layer; GCL, granule cell layer. **(B)** Native tdTomato fluorescence in the whole brain from a Math1(M)-Cre;Ai9 mouse, indicating that Cre-recombinase is selectively expressed in the cerebellum. Scale bars: 1 mm. **(C)** Staining of NeuN or calbindin (Calb) with DAPI in the cerebellum of M-Cre;Ai9 mouse. Scale bars: 50 µm. **(D)** Granule cell contents of *Mea6*$^{F/F}$ and Math1-Cre;*Mea6*$^{F/F}$ mice (P21) were harvested using glass micropipettes (pip, OD 2 mm) and placed in a centrifuge tube. The contents collected from 10 cells were subjected to RT-PCR. A typical electrophoresis of *Mea6* (157 bp), *Math1* (151 bp), and *Gapdh* (233 bp) is show in the right ($n = 5$ trials). **(E)** Western blots of Mea6 in the cerebellum of *Mea6*$^{F/F}$ and Math1-Cre;*Mea6*$^{F/F}$ mice (P21), as indicated by the black triangle. The percentage changes of Mea6 were 100 ± 6% (*Mea6*$^{F/F}$; $n = 10$) and 44 ± 9% (Math1-Cre;*Mea6*$^{F/F}$; $n = 10$), $p = 0.001$ (unpaired *t* test). **(F)** The pictures of bodies and brains of *Mea6*$^{F/F}$ and Math1-Cre;*Mea6*$^{F/F}$ at P21. Average body weights were 10.4 ± 0.8 g (*Mea6*$^{F/F}$; $n = 10$) and 10.2 ± 1.0 g (Math1-Cre;*Mea6*$^{F/F}$; $n = 10$), $p = 0.78$ (unpaired *t* test). **(G)** Kaplan-Meier survival curves of *Mea6*$^{F/F}$ ($n = 59$ mice) and Math1-Cre;*Mea6*$^{F/F}$ mice ($n = 59$ mice). $^{**}p < 0.01$.

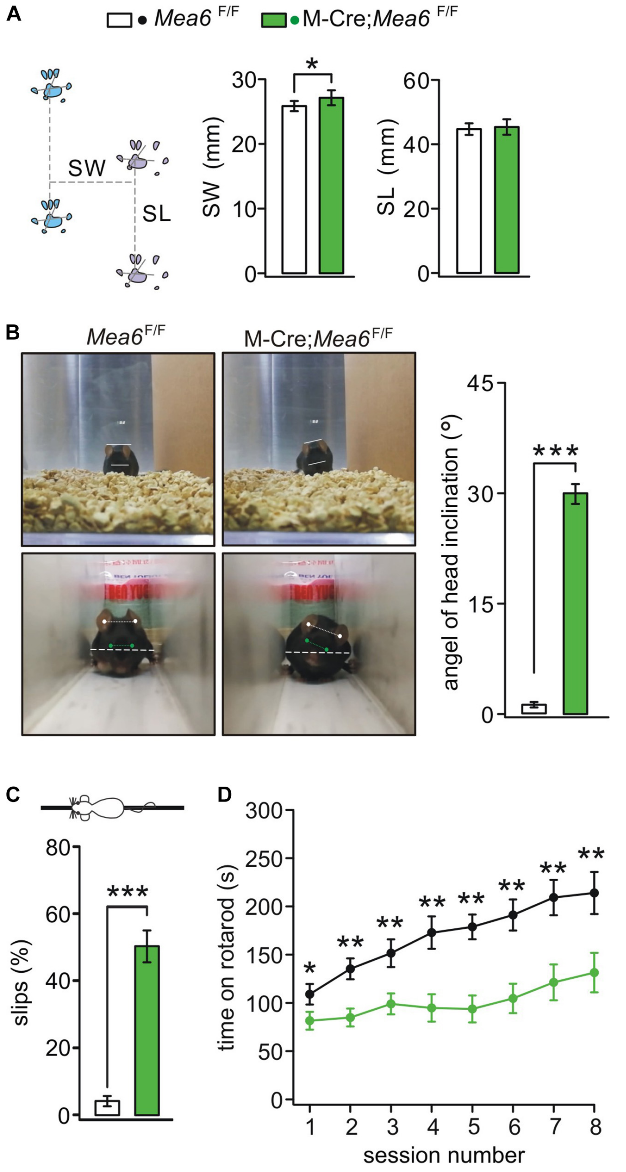

FIGURE 2 | Abnormal gait and motor learning in Math1(M)-Cre;*Mea6*$^{F/F}$ mice. **(A)** Footprints of *Mea6*$^{F/F}$ and Math1-Cre;*Mea6*$^{F/F}$ mice. Stride width (SW): 25.8 ± 0.8 mm (*Mea6*$^{F/F}$; $n = 16$) and 27.1 ± 1.1 mm (Math1-Cre;*Mea6*$^{F/F}$; $n = 17$), $p = 0.02$ (unpaired *t* test). Stance length (SL): 44.7 ± 1.8 mm (*Mea6*$^{F/F}$; $n = 16$) and 45.3 ± 2.4 mm (Math1-Cre;*Mea6*$^{F/F}$; $n = 17$), $p = 0.52$ (unpaired *t* test). **(B)** The upper panel shows a head inclination phenotype in a M-Cre;*Mea6*$^{F/F}$ mouse during the free moving in the cage. The lower panel shows the measurement of head inclination when *Mea6*$^{F/F}$ and M-Cre;*Mea6*$^{F/F}$ mice traversed a white plexiglass tunnel (100 cm × 10 cm × 10 cm). The white lines show the alignments of ears and eyes. The average angels of head inclination: 1.2 ± 0.4° (*Mea6*$^{F/F}$) and 30.0 ± 1.3° (Math1-Cre;*Mea6*$^{F/F}$), $p < 0.001$ (unpaired *t* test). **(C)** The percentages of hindpaw slips during runs on an elevated horizontal beam. *Mea6*$^{F/F}$: 4.1 ± 1.0% ($n = 24$). Math1-Cre;*Mea6*$^{F/F}$: 48.4 ± 4.5% ($n = 29$), $p < 0.001$ (unpaired *t* test). **(D)** Time spent on the accelerating rotarod for *Mea6*$^{F/F}$ ($n = 13$) and Math1-Cre;*Mea6*$^{F/F}$ mice ($n = 16$) at P90. Session 1: 108.9 ± 10.6 s (*Mea6*$^{F/F}$) and 81.5 ± 9.2 s (Math1-Cre;*Mea6*$^{F/F}$), $p = 0.04$ (unpaired *t* test); Session 2: 135.3 ± 10.9 s (*Mea6*$^{F/F}$) and 84.8 ± 9.3 s (Math1-Cre;*Mea6*$^{F/F}$), $p = 0.001$ (unpaired *t* test); Session 3: 151.5 ± 14.3 s

(Continued)

FIGURE 2 | Continued

(*Mea6*$^{F/F}$) and 98.9 ± 10.8 s (Math1-Cre;*Mea6*$^{F/F}$), $p = 0.004$ (unpaired *t* test); Session 4: 187.5 ± 16.8 s (*Mea6*$^{F/F}$) and 94.8 ± 14.2 s (Math1-Cre;*Mea6*$^{F/F}$), $p = 0.001$ (unpaired *t* test); Session 5: 178.8 ± 12.8 s (*Mea6*$^{F/F}$) and 93.7 ± 14.0 s (Math1-Cre;*Mea6*$^{F/F}$), $p = 0.001$ (unpaired *t* test); Session 6: 191.1 ± 16.1 s (*Mea6*$^{F/F}$) and 104.6 ± 15.2 s (Math1-Cre;*Mea6*$^{F/F}$), $p = 0.004$ (unpaired *t* test); Session 7: 209.2 ± 18.3 s (*Mea6*$^{F/F}$) and 121.25 ± 18.6 s (Math1-Cre;*Mea6*$^{F/F}$), $p = 0.002$ (unpaired *t* test); Session 8: 213.9 ± 21.8 s (*Mea6*$^{F/F}$) and 131.4 ± 20.5 s (Math1-Cre;*Mea6*$^{F/F}$), $p = 0.008$ (unpaired *t* test). $^{*}p < 0.05$, $^{**}p < 0.01$, $^{***}p < 0.001$.

much less time on rotating rod (**Figure 2D**). Taken together, our results indicated that Mea6 in granule cells is critical to motor behaviors.

Disrupted Migration of Granule Cell Progenitors in Math1-Cre;*Mea6*$^{F/F}$ Mice

The normal development of the cerebellum is essential to motor functions. The appearance of granule cell progenitors (G) in EGL and their migration to IGL are key features of cerebellar development (Alder et al., 1996). Having demonstrated motor deficits of Math1-Cre;*Mea6*$^{F/F}$ mice, a question was whether the development of granule cells is disrupted. To answer this, the production and migration of GCPs in EGL of control and mutant mice at P7, a peak stage for postnatal GCP proliferation (Leffler et al., 2016), were examined using anti-NeuN antibody and BrdU antibody (Yang et al., 2019). Our results showed that the density of BrdU+ cells in IGL was similar between *Mea6*$^{F/F}$ and Math1-Cre;*Mea6*$^{F/F}$ mice at P12, 5 days after BrdU injection (**Figure 3A**). In contrast, the density of BrdU+ cells in molecular layer and EGL significantly increased in Math1-Cre;*Mea6*$^{F/F}$ mice compared with *Mea6*$^{F/F}$ mice at P12. These results implicated that the deletion of *Mea6* disrupts the migration of GCPs in Math1-Cre;*Mea6*$^{F/F}$ mice.

The migration of GCPs is an intricate process that involves a number of secretary and cell-surface molecules, including cadherin (Horn et al., 2018), Slit2-Robo2 signaling (Xu et al., 2004; Guan et al., 2007; Geisen et al., 2008), BDNF-TrkB signaling (Borghesani et al., 2002; Wang et al., 2012), and semaphorin (Kerjan et al., 2005). Is the expression of these proteins changed by the deletion of *Mea6*? To answer this question, we measured the expression of Slit2, Robo2, γ-pcdh, BDNF, TrkB, and Sema6A. We found that the levels of Slit2, Robo2, γ-pcdh, TrkB, and Sema6A were not changed by specific deletion of *Mea6*, whereas the expression of BDNF significantly decreased in Math1-Cre;*Mea6*$^{F/F}$ mice compared with *Mea6*$^{F/F}$ mice (**Figure 3B**), implicating that the migration of GCPs is disrupted by BDNF down-regulation.

We continued to examine cerebellar cyto-architecture in adult mice. Using Nissl staining, we found that folia formation, lobular thickness, and GCL thickness of Math1-Cre;*Mea6*$^{F/F}$ mice were not changed compared to *Mea6*$^{F/F}$ mice (**Figure 3C**), indicating that cyto-architecture keeps intact in Math1-Cre;*Mea6*$^{F/F}$ mice. From these results, we concluded that the deletion of *Mea6* in granule cells may delay the migration of GCPs, but not

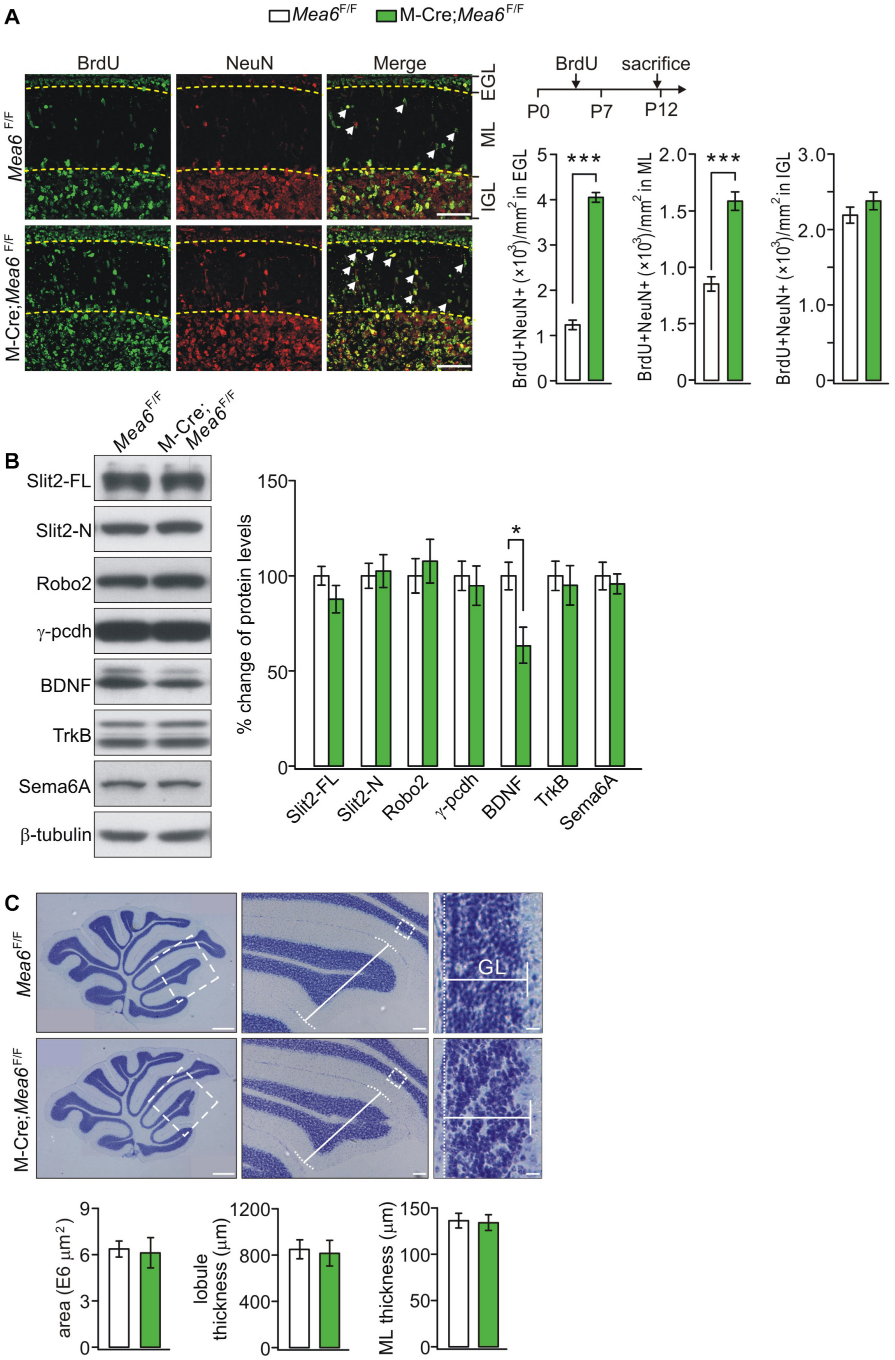

FIGURE 3 | Deficiency in GCP migration in Math1(M)-Cre;*Mea6*$^{F/F}$ mice. **(A)** Migrating GCPs in *Mea6*$^{F/F}$ and Math1-Cre;*Mea6*$^{F/F}$ cerebellum were treated with BrdU at P7 and labeled with anti-BrdU antibody after 5 days. White arrows show migrating GCPs in molecular layer (ML). Scale bars: 50 μm. The quantification of the numbers of NeuN+ and BrdU+ cells per 1 mm^2 is shown in bar graphs. BrdU+/NeuN+ cells in EGL: 1220.4 ± 106.5 (*Mea6*$^{F/F}$; $n = 13$) and 4061.7 ± 106.7 (Math1-Cre;*Mea6*$^{F/F}$; $n = 12$), $p < 0.001$ (unpaired *t* test). BrdU+/NeuN+ cells in ML: 854.3 ± 64.5 (*Mea6*$^{F/F}$; $n = 13$) and 1591.6 ± 81.8 (Math1-Cre;*Mea6*$^{F/F}$; $n = 12$), $p < 0.001$ (unpaired *t* test). BrdU+/NeuN+ cells in IGL: 2199.4 ± 106.3 (*Mea6*$^{F/F}$; $n = 13$) and 2388.8 ± 117.7 (Math1-Cre;*Mea6*$^{F/F}$; $n = 12$), $p = 0.24$ (unpaired *t* test). **(B)** Protein levels of Slit2, Robo2, γ-pcdh, BDNF, TrkB, and Sema6A in the cerebellum of *Mea6*$^{F/F}$ and Math1-Cre;*Mea6*$^{F/F}$ mice at P20 ($n = 6$ pairs). β-tubulin was used as the control. BDNF: 100 ± 7% (*Mea6*$^{F/F}$) and 63 ± 9% (Math1-Cre;*Mea6*$^{F/F}$), $p = 0.04$ (unpaired *t* test). **(C)** Nissl staining of sagittal cerebellar sections from *Mea6*$^{F/F}$ and Math1-Cre;*Mea6*$^{F/F}$ mice at P25. The middle panel (Scale bars: 100 μm) is the higher magnification of left panel (Scale bars: 200 μm) and the right panel (Scale bars: 10 μm) is the higher magnification of middle panel, as indicated by white dashed boxes. Cerebellar area: 6.4 ± 0.5 E6 μm^2 (*Mea6*$^{F/F}$; $n = 7$) and 6.1 ± 1.0 E6 μm^2 (Math1-Cre;*Mea6*$^{F/F}$; $n = 6$), $p = 0.13$ (unpaired *t* test). Lobule III thickness: 849 ± 81 μm (*Mea6*$^{F/F}$; $n = 7$) and 815 ± 109 μm (Math1-Cre;*Mea6*$^{F/F}$; $n = 7$), $p = 0.51$ (unpaired *t* test). Thickness of granule cell layer (GCL; lobule III): 136 ± 8 μm (*Mea6*$^{F/F}$; $n = 7$) and 134 ± 8 μm (Math1-Cre;*Mea6*$^{F/F}$; $n = 7$), $p = 0.43$ (unpaired *t* test). *$p < 0.05$, ***$p < 0.001$.

alter the structure of adult cerebellum. Hence, abnormal motor behaviors of Math1-Cre;*Mea6*$^{F/F}$ mice are not due to changed cyto-architecture.

Granule Cell Deletion of *Mea6* Damages Parallel Fiber-Purkinje Cell Synapse

Synaptogenesis and synaptic function between granule cells and Pukinje cells are also critical to the cerebellum-related motor behaviors (Su et al., 2020). We thereby used TEM to assess parallel fiber-Purkinje cell synapses identified by asymmetric synaptic contacts with Purkinje cell spines (**Figure 4A**; Peter et al., 2016). We found that the density of parallel fiber-Purkinje cell synapses was significantly reduced in Math1-Cre;*Mea6*$^{F/F}$ mice (12.7 ± 0.4 synapses per 100 μm^2; $n = 49$ slices of three mice) compared with *Mea6*$^{F/F}$ mice at P21 (16.4 ± 0.7 synapses per 100 μm^2; $n = 26$ slices of three mice; $p < 0.001$) (**Figure 4A**). Furthermore, the deletion of *Mea6* significantly decreased total number of vesicles at parallel fiber terminals (*Mea6*$^{F/F}$: 34.7 ± 2.9 vesicles, $n = 26$ boutons; Math1-Cre;*Mea6*$^{F/F}$: 15.0 ± 2.2 vesicles, $n = 27$ boutons; $p < 0.001$) (**Figure 4B**). These results suggest that the deletion of *Mea6* in granule cells impairs synaptic formation at parallel fiber-Purkinje cell synapses.

To further determine the effect of *Mea6* ablation on synaptic function, we recorded mEPSCs at parallel fiber-Purkinje cell synapses. Our results showed that mEPSC frequency was reduced in Math1-Cre;*Mea6*$^{F/F}$ mice (1.6 ± 0.1 Hz; $n = 19$ cells) compared with *Mea6*$^{F/F}$ mice (2.3 ± 0.2 Hz; $n = 15$ cells), whereas its mean amplitude did not differ between genotypes (*Mea6*$^{F/F}$: 20.8 ± 0.9 pA, $n = 15$ cells; Math1-Cre;*Mea6*$^{F/F}$: 23.7 ± 2.0 A, $n = 19$ cells) (**Figure 4C**). PPF of parallel fiber-Purkinje cell synapses was also examined using paired stimulations at different interstimulus intervals. Interleaved recordings indicated that average PPF recorded from Math1-Cre;*Mea6*$^{F/F}$ mice changed with stimulation intervals: it was smaller than that from *Mea6*$^{F/F}$ mice at intervals of <25 ms, but was unaltered at intervals larger than that (**Figure 4D**). Reduced PPF suggested a lower pre-synaptic release probability in Math1-Cre;*Mea6*$^{F/F}$ mice, consistent with reduced synapses and pre-synaptic vesicles (**Figure 4B**). Overall, these data indicated that neurotransmitter release at parallel fiber-Purkinje cell synapses is impaired by *Mea6* deletion.

Subcellular Transport of vGluT1 Is Interrupted in Math1-Cre;*Mea6*$^{F/F}$ Mice

We continued to examine whether *Mea6* ablation affects the expression of pre-synaptic proteins that are involved in synaptic release and transmission. A number of pre-synaptic proteins related to synaptic function, including vGluT1, Rab3, synapsin-1, Rim1, Munc18-1, synaptophysin, and Munc13-1, were selected to mark potential pre-synaptic changes by *Mea6* ablation. Unexpectedly, we found that only vGluT1 significantly decreased in Math1-Cre;*Mea6*$^{F/F}$ mice, while other pre-synaptic proteins were not changed (**Figure 5A**). The expression of vGluT1 was also detected at the synaptic level using different centrifugations (Zhou et al., 2015). Likewise, synaptic vGluT1 was significantly reduced in Math1-Cre;*Mea6*$^{F/F}$ mice (**Figure 5B**). In contrast, the expression of α-amino-3-hydroxy-5-methyl-4-isoxazolepropionic acid receptor (AMPAR) subunits, including GluA1 and GluA2, was unchanged at synaptic level (**Figure 5B**).

Previous work showed that Mea6 participates in the trafficking of exogenous protein (Zhang et al., 2018) and endogenous Slit2 (Wang et al., 2019) between ER and Golgi apparatus. We next investigated whether the subcellular trafficking of vGluT1 is affected by *Mea6* deletion taking advantage of a series of centrifugations to purify organelles (**Figure 5C**; Wang et al., 2019). The purification of ER fraction was confirmed with distinct organelle markers, PDI (ER), γ-adaptin (Golgi apparatus), YY1 (nuclei), PSD95 (synapse), VDAC (mitochondria), and Rab11 (endosome) (Wang et al., 2019). Our results indicated that Bip, a marker molecule for ER (Haefliger et al., 2011; Shimizu et al., 2017; McLelland et al., 2018), was not changed in Math1-Cre;*Mea6*$^{F/F}$ mice (**Figure 5D**), suggesting that ER is not affected by granule cell deletion of *Mea6*. Similar to Slit2 expression in pCP2-Cre;*Mea6*$^{F/F}$ mice (Wang et al., 2019), the expression of vGluT1 significantly increased in ER fraction of Math1-Cre;*Mea6*$^{F/F}$ mice compared to that in *Mea6*$^{F/F}$ mice (**Figure 5D**), indicating that the deletion of *Mea6* tethers vGluT1 in ER and then decreases its expression.

DISCUSSION

We previously reported that Mea6 is essential to cerebellar development and motor performance (Wang et al., 2019): Nestin-Cre-induced knockout of *Mea6* leads to defective adult cerebellum and impaired motor performance; Purkinje cell-specific deletion of *Mea6* does not change lobular formation, but causes self-crossings of Purkinje cell dendrites and impairs motor learning. The present findings extended previous work by demonstrating the function of Mea6 in granule cells. We found that Math1-Cre;*Mea6*$^{F/F}$ mice exhibited disrupted migration of GCPs, reduced synaptogenesis, and damaged parallel fiber-Purkinje cell synapses. These phenotypes may contribute to abnormal posture, balance, and motor learning of Math1-Cre;*Mea6*$^{F/F}$ mice, as indicated in footprint, head inclination, balanced beam, and rotarod tests. These abnormal behaviors are not surprising, because cerebellar granule cell, which is the most numerous neuronal type in the brain, encodes massive sensorimotor information and is the common denominator of cerebellar information processing in normal motor behaviors and motor symptoms. It is reported that *Mea6* mutations are associated with Fahr's syndrome (Lemos et al., 2011), which includes movement disorders (Oliveira et al., 2007). Therefore, the present work provides further insight into the roles of Mea6 in the development and function of the cerebellum and demonstrating Mea6 in granule cells may be more important to Fahr's syndrome, because Math1-Cre;*Mea6*$^{F/F}$ mice displayed severer movement phenotypes than Purkinje cell-targeted pCp2-Cre;*Mea6*$^{F/F}$ mice (Wang et al., 2019).

It is shown that Mea6 is vital to the secretion of proteins including collagen, low-density lipoprotein (VLDL), and insulin (Saito et al., 2011; Saito et al., 2014; Wang et al., 2016;

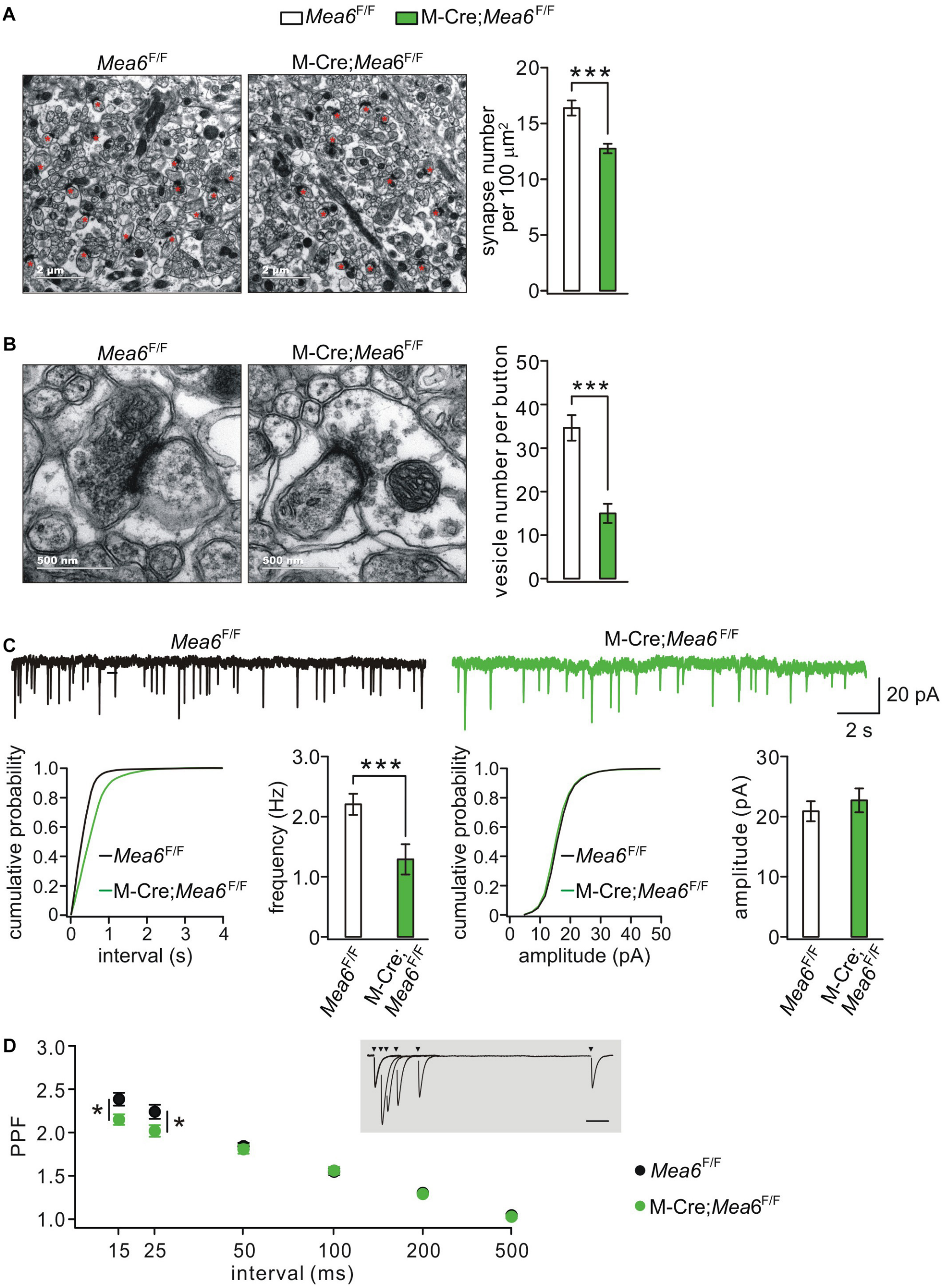

FIGURE 4 | Granule cell-specific deletion of *Mea6* impairs synaptic formation and function. **(A)** Representative EM (11,000×) of parallel fiber-Purkinje cell synapses from *Mea6*$^{F/F}$ and Math1(M)-Cre;*Mea6*$^{F/F}$ mice (P30). Synapses comprising of parallel fiber boutons opposed to Purkinje cell spines are marked with red asterisks. Scale bars: 2 µm. Bar graphs show average numbers of synapses per 100 µm^2 in *Mea6*$^{F/F}$ (16.4 ± 0.7; $n = 26$) and Math1-Cre;*Mea6*$^{F/F}$ mice (12.7 ± 0.4; $n = 49$), $p < 0.001$ (unpaired *t* test). **(B)** Representative EM (68,000×) of parallel fiber-Purkinje cell synapses from *Mea6*$^{F/F}$ and Math1-Cre;*Mea6*$^{F/F}$ mice (P30). Scale bars: 500 nm. Bar graphs show average numbers of total pre-synaptic vesicles per synapse in *Mea6*$^{F/F}$ (34.7 ± 2.9; $n = 26$) and Math1-Cre;*Mea6*$^{F/F}$ mice (15.0 ± 2.2; $n = 27$), $p < 0.001$ (unpaired *t* test). **(C)** Example Purkinje cell mEPSCs from *Mea6*$^{F/F}$ and Math1-Cre;*Mea6*$^{F/F}$ mice (P21–25). The lower panels show cumulative probabilities and statistics of frequency and amplitude of mEPSCs. Frequency: 2.3 ± 0.2 Hz (*Mea6*$^{F/F}$; $n = 15$) and 1.6 ± 0.1 Hz (Math1-Cre;*Mea6*$^{F/F}$; $n = 19$; $p = 0.006$), $p = 0.006$ (unpaired *t* test). Amplitude: 20.8 ± 0.9 pA (*Mea6*$^{F/F}$; n = 15) and 23.7 ± 2.0 pA (Math1-Cre;*Mea6*$^{F/F}$; $n = 19$), $p = 0.34$ (unpaired *t* test). **(D)** PPF as a function of interstimulus intervals in *Mea6*$^{F/F}$ and Math1-Cre;*Mea6*$^{F/F}$ mice (P21–23). The inset shows the superposition of PF-EPSCs evoked at different intervals in a WT cell. PPF ratios: 2.4 ± 0.1 (*Mea6*$^{F/F}$; $n = 12$) and 2.1 ± 0.1 (Math1-Cre;*Mea6*$^{F/F}$; $n = 16$) at 15 ms, $p = 0.03$ (unpaired *t* test); 2.2 ± 0.1 (*Mea6*$^{F/F}$; $n = 12$) and 2.0 ± 0.1 (Math1-Cre;*Mea6*$^{F/F}$; $n = 16$) at 25 ms, $p = 0.03$ (unpaired *t* test). $^{*}p < 0.05$, $^{***}p < 0.001$.

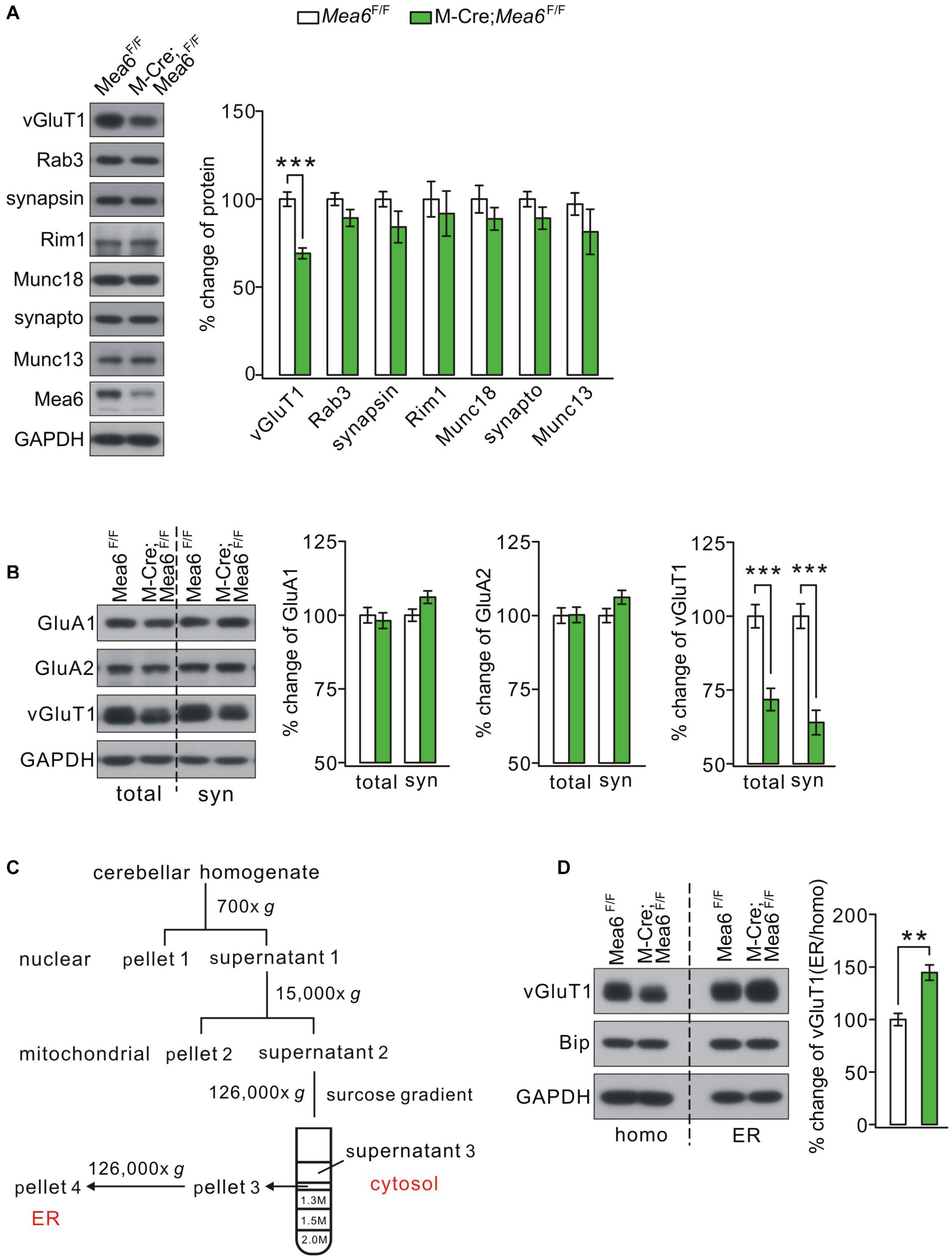

FIGURE 5 | Mea6 deficiency affects the transport of vGluT1 from ER to Golgi apparatus. **(A)** Protein levels of vGluT1, Rab3A (Rab3), synapsin-1 (synapsin), Rim1, Munc18-1 (Munc18), synaptophysin (synapto), Munc13-1 (Munc13), and Mea6 in *Mea6*$^{F/F}$ and Math1-Cre;*Mea6*$^{F/F}$ cerebellum at P21. The results were obtained from eight pairs of mice. GAPDH was used as the loading control. **(B)** Protein levels of GluA1, GluA2, and vGluT1 in the cerebellum from *Mea6*$^{F/F}$ and Math1-Cre;*Mea6*$^{F/F}$ mice at P21. Six independent replicates were performed. GAPDH was used as the loading control. vGluT1 in total cerebellum: 100 ± 4% (*Mea6*$^{F/F}$) and 72 ± 4% (Math1-Cre;*Mea6*$^{F/F}$), $p < 0.001$ (unpaired *t* test). vGluT1 in cerebellar synaptosome: 100 ± 4% (*Mea6*$^{F/F}$) and 64 ± 4% (Math1-Cre;*Mea6*$^{F/F}$), $p < 0.001$ (unpaired *t* test). **(C)** A cartoon illustrating the procedures for the purification of subcellular organelles. More details are given in Experimental Procedures. The purification of ER was confirmed by the Western blotting assay of marker proteins. **(D)** Western blotting assay of vGluT1 in ER purified from *Mea6*$^{F/F}$ and M-Cre;*Mea6*$^{F/F}$ mouse cerebella. Bip was used as the internal control. vGluT1: 100 ± 6% (*Mea6*$^{F/F}$) and 146 ± 7% (Math1-Cre;*Mea6*$^{F/F}$). The experiment was performed eight times. $p = 0.001$ (unpaired *t* test). $^{**}p < 0.01$, $^{***}p < 0.001$.

Fan et al., 2017). Further studies demonstrate that Mea6 regulates the sub-cellular transports of an exogenous component in cultured cortical neurons (Zhang et al., 2018) and endogenous proteins, including Slit2, BDNF, and semaphorin 3A, in Purkinje cells (Wang et al., 2019). The present work found that *Mea6* deletion in granule cells decreased the total and synaptic expressions of vGluT1 by detaining it in ER. Together, these studies suggest that Mea6 regulates the intracellular transport and maturation of proteins critical to neuronal development and function. In Purkinje cells, Mea6 regulates the expression of Slit2, BDNF, and semaphorin 3A, but not γ-pcdh, Robo2, and TrkB, all of which are critical to dendritic development (Wang et al., 2019). In granule cells, Mea6 regulates the expression of vGluT1 and BDNF, but not Rab3A, synapsin-1, Rim1, Munc18-1, synaptophysin, and Munc13-1, most of which are components of soluble N-ethyl-maleimide-sensitive fusion protein attachment protein receptor (SNARE) complex. These studies indicate a broad regulation capacity of Mea6 in neurons. Another point derived from the studies in Purkinje cells and granule cells is that Mea6 regulates part but not all proteins. From the study in Purkinje cells (Wang et al., 2019), we speculated that Mea6 influences secretary proteins but not membrane proteins. Similarly, Mea6 exhibits divergent roles in pre-synaptic proteins. However, the prevailing studies are not enough to answer a core question: What is the essence of divergent effects of Mea6 regulation of protein transport? Future study is needed to define the biological functions of Mea6 based on its structure and recognition capability.

Meningioma expressed antigen six ablation in Purkinje cells reduces Slit2 expression and thereby impairs the self-avoidance of Purkinje cell dendrites (Wang et al., 2019). Consequently, pCP2-Cre;*Mea6*$^{F/F}$ mice display defective motor learning, while their gait is not changed (Wang et al., 2019). On contrast, Math1-Cre;*Mea6*$^{F/F}$ mice exhibited more defects in posture, balance, and motor learning, indicating severer symptom in these mice. The difference between two types of mutants is an interesting question. Using biochemical, immunohistochemical, and electrophysiological assays, we demonstrated that Math1-Cre;*Mea6*$^{F/F}$ mice suffered from a delayed migration of GCPs and impaired formation and function of parallel fiber-Purkinje cell synapses. It appears that dysfunctional granule cells induce more motor disorders rather than Purkinje cells. Nevertheless, this speculation might be paradoxical, because both Purkinje cells and granule cells are essential to the plasticity occurring at their innervations, which is a classic theory for cerebellum-related movements. A possible explanation for the phenotype difference is that self-avoidance defect only occurs at distal sites of parallel fibers in pCP2-Cre;*Mea6*$^{F/F}$ mice (Wang et al., 2019) with the harm far milder than overall damage in Math1-Cre;*Mea6*$^{F/F}$ mice. Alternatively, Mea6 may affect the functions of granule cells undiscovered in the present work, for example, the activation of mossy fiber-to-granule cell synapses, which is crucial to behavioral states as well.

In summary, our present findings provide further evidence to manifest the functions of Mea6 in cerebellar development and motor behaviors. We showed that *Mea6* deletion in granule cells impairs the transport of vGluT1 from ER to Golgi apparatus and the formation and function of parallel fiber-Purkinje cell synapses, which might underlie the damaged motor performance in Math1-Cre;*Mea6*$^{F/F}$ mice. Last but not least, two caveats should be considered in the present work and need further studies: We had no clue to explain the cause of head inclination in Math1-Cre;*Mea6*$^{F/F}$ mice, a novel observation with dysfunctional granule cells; We did not answer why Mea6 delayed but not impeded the migration of GCPs.

CONCLUSION

The deletion of *Mea6* in cerebellar granule cells causes abnormal motor symptoms in footprint, head inclination, balanced beam, and rotarod tests. Math1-Cre;*Mea6*$^{F/F}$ mice exhibited disrupted migration of GCPs and damaged parallel fiber-Purkinje cell synapses, which may be related to disrupted intracellular transport of vGluT1 and BDNF.

DATA AVAILABILITY STATEMENT

The original contributions presented in the study are included in the article/supplementary material, further inquiries can be directed to the corresponding author/s.

ETHICS STATEMENT

The animal study was reviewed and approved by Animal Experimentation Ethics Committee of Zhejiang University.

AUTHOR CONTRIBUTIONS

X-TW and YS designed the research. X-TW, LZ, X-YC, and F-XX performed the research. Z-HX and X-YL provided the unpublished tools and techniques. X-TW, X-YC, and YS analyzed the data. X-TW, X-YL, and YS wrote the manuscript. All authors have read and approved the final manuscript.

FUNDING

This work was supported by the National Natural Science Foundation of China (31970923, 32000692, 81625006, 31900741, and 31820103005), China Postdoctoral Science Foundation (2019M662025), and the Natural Science Foundation of Zhejiang Province (LZ15C090001).

ACKNOWLEDGMENTS

We thank Dr. Wei Mo (Xiamen University) for kindly providing Math1-Cre mice and the Core Facility of Zhejiang University Institute of Neuroscience for technical assistance.

REFERENCES

Alder, J., Cho, N. K., and Hatten, M. E. (1996). Embryonic precursor cells from the rhombic lip are specified to a cerebellar granule neuron identity. *Neuron* 17, 389–399. doi: 10.1016/s0896-6273(00)80172-5

Borghesani, P. R., Peyrin, J. M., Klein, R., Rubin, J., Carter, A. R., Schwartz, P. M., et al. (2002). BDNF stimulates migration of cerebellar granule cells. *Development* 129, 1435–1442.

Comtesse, N., Niedermayer, I., Glass, B., Heckel, D., Maldener, E., Nastainczyk, W., et al. (2002). MGEA6 is tumor-specific overexpressed and frequently recognized by patient-serum antibodies. *Oncogene* 21, 239–247. doi: 10.1038/sj.onc.1205005

Englund, C., Kowalczyk, T., Daza, R. A., Dagan, A., Lau, C., Rose, M. F., et al. (2006). Unipolar brush cells of the cerebellum are produced in the rhombic lip and migrate through developing white matter. *J. Neurosci.* 26, 9184–9195. doi: 10.1523/JNEUROSCI.1610-06.2006

Fan, J., Wang, Y., Liu, L., Zhang, H., Zhang, F., Shi, L., et al. (2017). cTAGE5 deletion in pancreatic β cells impairs proinsulin trafficking and insulin biogenesis in mice. *J. Cell Biol.* 216, 4153–4164. doi: 10.1083/jcb.201705027

Geisen, M. J., Di Meglio, T., Pasqualetti, M., Ducret, S., Brunet, J. F., Chedotal, A., et al. (2008). Hox paralog group 2 genes control the migration of mouse pontine neurons through slit-robo signaling. *PLoS Biol.* 6:e0060142. doi: 10.1371/journal.pbio.0060142

Geschwind, D. H., Loginov, M., and Stern, J. M. (1999). Identification of a locus on chromosome 14q for idiopathic basal ganglia calcification (Fahr disease). *Am. J. Hum. Genet.* 65, 764–772. doi: 10.1086/302558

Guan, C. B., Xu, H. T., Jin, M., Yuan, X. B., and Poo, M. M. (2007). Long-range Ca2+ signaling from growth cone to soma mediates reversal of neuronal migration induced by slit-2. *Cell* 129, 385–395. doi: 10.1016/j.cell.2007.01.051

Haefliger, S., Klebig, C., Schaubitzer, K., Schardt, J., Timchenko, N., Mueller, B. U., et al. (2011). Protein disulfide isomerase blocks CEBPA translation and is up-regulated during the unfolded protein response in AML. *Blood* 117, 5931–5940. doi: 10.1182/blood-2010-08-304485

Hammond, J. C., Meador-Woodruff, J. H., Haroutunian, V., and McCullumsmith, R. E. (2012). AMPA receptor subunit expression in the endoplasmic reticulum in frontal cortex of elderly patients with schizophrenia. *PLoS One* 7:e39190. doi: 10.1371/journal.pone.0039190

Hartmann, J., Karl, R. M., Alexander, R. P., Adelsberger, H., Brill, M. S., Rühlmann, C., et al. (2014). STIM1 controls neuronal Ca2+ signaling, mGluR1-dependent synaptic transmission, and cerebellar motor behavior. *Neuron* 82, 635–644. doi: 10.1016/j.neuron.2014.03.027

Heckel, D., Brass, N., Fischer, U., Blin, N., Steudel, I., Türeci, O., et al. (1997). cDNA cloning and chromosomal mapping of a predicted coiled-coil proline-rich protein immunogenic in meningioma patients. *Hum. Mol. Genet.* 6, 2031–2041. doi: 10.1093/hmg/6.12.2031

Horn, Z., Behesti, H., and Hatten, M. E. (2018). N-cadherin provides a cis and trans ligand for astrotactin that functions in glial-guided neuronal migration. *Proc. Natl. Acad. Sci. U.S.A.* 115, 10556–10563. doi: 10.1073/pnas.1811100115

Ichikawa, R., Hashimoto, K., Miyazaki, T., Uchigashima, M., Yamasaki, M., Aiba, A., et al. (2016). Territories of heterologous inputs onto Purkinje cell dendrites are segregated by mGluR1-dependent parallel fiber synapse elimination. *Proc. Natl. Acad. Sci. U.S.A.* 113, 2282–2287. doi: 10.1073/pnas.1511513113

Kalniņa, Z., Siliņa, K., Meistere, I., Zayakin, P., Rivosh, A., Abols, A., et al. (2008). Evaluation of T7 and lambda phage display systems for survey of autoantibody profiles in cancer patients. *J. Immunol. Methods.* 334, 37–50. doi: 10.1016/j.jim.2008.01.022

Kerjan, G., Dolan, J., Haumaitre, C., Schneider-Maunoury, S., Fujisawa, H., Mitchell, K. J., et al. (2005). The transmembrane semaphorin Sema6A controls cerebellar granule cell migration. *Nat. Neurosci.* 8, 1516–1524. doi: 10.1038/nn1555

Kim, E., Wang, Y., Kim, S. J., Bornhorst, M., Jecrois, E. S., Anthony, T. E., et al. (2014). Transient inhibition of the ERK pathway prevents cerebellar developmental defects and improves long-term motor functions in murine models of neurofibromatosis type 1. *eLife* 3:e05151. doi: 10.7554/eLife.05151

Leffler, S. R., Legué, E., Aristizábal, O., Joyner, A. L., Peskin, C. S., and Turnbull, D. H. (2016). A mathematical model of granule cell generation during mouse cerebellum development. *Bull. Math Biol.* 78, 859–878. doi: 10.1007/s11538-016-0163-3

Lemos, R. R., Oliveira, D. F., Zatz, M., and Oliveira, J. R. (2011). Population and computational analysis of the MGEA6 P521A variation as a risk factor for familial idiopathic basal ganglia calcification (Fahr's disease). *J. Mol. Neurosci.* 43, 333–336. doi: 10.1007/s12031-010-9445-7

McLelland, G. L., Goiran, T., Yi, W., Dorval, G., Chen, C. X., Lauinger, N. D., et al. (2018). Mfn2 ubiquitination by PINK1/parkin gates the p97-dependent release of ER from mitochondria to drive mitophagy. *eLife* 20:e32866. doi: 10.7554/eLife.32866

Moskowitz, M. A., Winickoff, R. N., and Heinz, E. R. (1971). Familial calcification of the basal ganglions: a metabolic and genetic study. *N. Engl. J. Med.* 285, 72–77. doi: 10.1056/NEJM197107082850202

Oliveira, J. R., Sobrido, M. J., Spiteri, E., Hopfer, S., Meroni, G., Petek, E., et al. (2007). Analysis of candidate genes at the IBGC1 locus associated with idiopathic basal ganglia calcification ("Fahr" Disease'). *J. Mol. Neurosci.* 33, 151–154. doi: 10.1007/s12031-007-0030-7

Peter, S., Ten Brinke, M. M., Stedehouder, J., Reinelt, C. M., Wu, B., Zhou, H., et al. (2016). Dysfunctional cerebellar Purkinje cells contribute to autism-like behaviour in Shank2-deficient mice. *Nat. Commun.* 7:12627. doi: 10.1038/ncomms12627

Saito, K., Yamashiro, K., Ichikawa, Y., Erlmann, P., Kontani, K., Malhotra, V., et al. (2011). cTAGE5 mediates collagen secretion through interaction with TANGO1 at endoplasmic reticulum exit sites. *Mol. Biol. Cell* 22, 2301–2308. doi: 10.1091/mbc.E11-02-0143

Saito, K., Yamashiro, K., Shimazu, N., Tanabe, T., Kontani, K., and Katada, T. (2014). Concentration of Sec12 at ER exit sites via interaction with cTAGE5 is required for collagen export. *J. Cell Biol.* 206, 751–762. doi: 10.1083/jcb.201312062

Saleem, S., Aslam, H. M., Anwar, M., Anwar, S., Saleem, M., Saleem, A., et al. (2013). Fahr's syndrome: literature review of current evidence. *Orphanet J. Rare Dis.* 8:156. doi: 10.1186/1750-1172-8-156

Schüller, U., Heine, V. M., Mao, J., Kho, A. T., Dillon, A. K., Han, Y. G., et al. (2008). Acquisition of granule neuron precursor identity is a critical determinant of progenitor cell competence to form Shh-induced medulloblastoma. *Cancer Cell* 14, 123–134. doi: 10.1016/j.ccr.2008.07.005

Shimizu, A., Kaira, K., Yasuda, M., Asao, T., and Ishikawa, O. (2017). Clinical and pathological significance of ER stress marker (BiP/GRP78 and PERK) expression in malignant melanoma. *Pathol. Oncol. Res.* 23, 111–116. doi: 10.1007/s12253-016-0099-9

Su, L. D., Xu, F. X., Wang, X. T., Cai, X. Y., and Shen, Y. (2020). Cerebellar dysfunction, cerebro-cerebellar connectivity and autism spectrum disorders. *Neuroscience* 4522, 30323–30327. doi: 10.1016/j.neuroscience.2020.05.028

Wang, D., She, L., Sui, Y. N., Yuan, X. B., Wen, Y., and Poo, M. M. (2012). Forward transport of proteins in the plasma membrane of migrating cerebellar granule cells. *Proc. Natl. Acad. Sci. U.S.A.* 109, E3558–E3567. doi: 10.1073/pnas.1219203110

Wang, X. T., Cai, X. Y., Xu, F. X., Zhou, L., Zheng, R., Ma, K. Y., et al. (2019). MEA6 deficiency impairs cerebellar development and motor performance by tethering protein trafficking. *Front. Cell Neurosci.* 13:250. doi: 10.3389/fncel.2019.00250

Wang, Y., Liu, L., Zhang, H., Fan, J., Zhang, F., Yu, M., et al. (2016). Mea6 controls VLDL transport through the coordinated regulation of COPII assembly. *Cell Res.* 26, 787–804. doi: 10.1038/cr.2016.75

Xu, H. T., Yuan, X. B., Guan, C. B., Duan, S., Wu, C. P., and Feng, L. (2004). Calcium signaling in chemorepellant Slit2-dependent regulation of neuronal migration. *Proc. Natl. Acad. Sci. U.S.A.* 101, 4296–4301. doi: 10.1073/pnas.0303893101

Yang, H., Zhu, Q., Cheng, J., Wu, Y., Fan, M., Zhang, J., et al. (2019). Opposite regulation of Wnt/β-catenin and Shh signaling pathways by Rack1 controls mammalian cerebellar development. *Proc. Natl. Acad. Sci. U.S.A.* 116, 4661–4670. doi: 10.1073/pnas.1813244116

Zhang, F., Wang, Y., Wang, T., Yao, L., Lam, S. M., Huang, X., et al. (2018). cTAGE5/MEA6 plays a critical role in neuronal cellular components trafficking and brain development. *Proc. Natl. Acad. Sci. U.S.A.* 115, E9449–E9458. doi: 10.1073/pnas.1804083115

Zhou, J. H., Wang, X. T., Zhou, L., Zhou, L., Xu, F. X., Su, L. D., et al. (2017). Ablation of TFR1 in Purkinje cells inhibits mGlu1 trafficking and impairs motor coordination, but not autistic-like behaviors. *J. Neurosci.* 37, 11335–11352. doi: 10.1523/JNEUROSCI.1223-17.2017

Zhou, L., Yang, D., Wang, D. J., Xie, Y. J., Zhou, J. H., Zhou, L., et al. (2015). Numb deficiency in cerebellar Purkinje cells impairs synaptic expression of metabotropic glutamate receptor and motor coordination. *Proc. Natl. Acad. Sci. U.S.A.* 112, 15474–15479. doi: 10.1073/pnas.1512915112

Conflict of Interest: The authors declare that the research was conducted in the absence of any commercial or financial relationships that could be construed as a potential conflict of interest.

frontiers
in Cell and Developmental Biology

REVIEW
published: 19 March 2021
doi: 10.3389/fcell.2021.653381

Liprin-α-Mediated Assemblies and Their Roles in Synapse Formation

Xingqiao Xie[1,2†], Mingfu Liang[1†], Cong Yu[1,3] and Zhiyi Wei[1,4]*

[1] Department of Biology, Southern University of Science and Technology, Shenzhen, China, [2] Academy for Advanced Interdisciplinary Studies, Southern University of Science and Technology, Shenzhen, China, [3] Guangdong Provincial Key Laboratory of Cell Microenvironment and Disease Research, Shenzhen Key Laboratory of Cell Microenvironment, Shenzhen, China, [4] Brain Research Center, Southern University of Science and Technology, Shenzhen, China

Edited by:
Wei Liu,
Biomedical Research Institute,
Shenzhen Peking
University-Hong Kong University
of Science and Technology Medical
Center, China

Reviewed by:
Jaewon Ko,
Daegu Gyeongbuk Institute
of Science and Technology (DGIST),
South Korea
Adam C. Miller,
University of Oregon, United States
E. Anne Martin,
University of Oregon, United States,
in collaboration with reviewer AM

Correspondence:
Zhiyi Wei
weizy@sustech.edu.cn

†These authors have contributed equally to this work

Specialty section:
This article was submitted to
Membrane Traffic,
a section of the journal
Frontiers in Cell and Developmental
Biology

Received: *14 January 2021*
Accepted: *25 February 2021*
Published: *19 March 2021*

Citation:
Xie X, Liang M, Yu C and Wei Z
(2021) Liprin-α-Mediated Assemblies
and Their Roles in Synapse
Formation.
Front. Cell Dev. Biol. 9:653381.
doi: 10.3389/fcell.2021.653381

Brain's functions, such as memory and learning, rely on synapses that are highly specialized cellular junctions connecting neurons. Functional synapses orchestrate the assembly of ion channels, receptors, enzymes, and scaffold proteins in both pre- and post-synapse. Liprin-α proteins are master scaffolds in synapses and coordinate various synaptic proteins to assemble large protein complexes. The functions of liprin-αs in synapse formation have been largely uncovered by genetic studies in diverse model systems. Recently, emerging structural and biochemical studies on liprin-α proteins and their binding partners begin to unveil the molecular basis of the synaptic assembly. This review summarizes the recent structural findings on liprin-αs, proposes the assembly mechanism of liprin-α-mediated complexes, and discusses the liprin-α-organized assemblies in the regulation of synapse formation and function.

Keywords: SYD2, scaffold protein, presynaptic active zone, LLPS, protein structure, coiled coil, protein–protein interaction

INTRODUCTION

In the brain, neurons are connected and communicated with each other via highly specialized intercellular junctions, termed synapses. Chemical synapses are enriched with numerous proteins, including ion channels, receptors, enzymes, and scaffold proteins. These synaptic proteins are spatiotemporally orchestrated to control the release and receiving of neurotransmitter at the presynaptic and postsynaptic sites respectively to transmit neuronal signals (Broadie and Richmond, 2002; Sudhof, 2008, 2018; Chua et al., 2010; Harris and Weinberg, 2012; Missler et al., 2012; Ackermann et al., 2015). The precise signal response and transduction in synapse depend on the proper assemblies of presynaptic active zone and postsynaptic density, in which many scaffold proteins play essential roles to organize these assemblies through protein-protein interactions (Schoch and Gundelfinger, 2006; Feng and Zhang, 2009; Haucke et al., 2011; Sheng and Kim, 2011; Sudhof, 2012; Petzoldt et al., 2016; Biederer et al., 2017; Torres and Inestrosa, 2018; Zeng et al., 2018; Gramlich and Klyachko, 2019).

Liprin-α family proteins are core synaptic scaffolds and important for the assembly and maturation of synapses. By interacting with various synaptic proteins, liprin-αs participate in both presynaptic and postsynaptic functions, including active zone assembly, neurotransmitter release, and synaptic cargo transport (Zhen and Jin, 2004; Spangler and Hoogenraad, 2007; Stryker and Johnson, 2007; Sigrist, 2009; Ackermann et al., 2015; Wong et al., 2018) (**Table 1**). The liprin-α family contains four members (liprin-α1/2/3/4) in vertebrates and one member each in *C. elegans* and *Drosophila,* named SYD-2 and Dliprin-α, respectively (Serra-Pages et al., 1998;

Zhen and Jin, 1999; Kaufmann et al., 2002; Astigarraga et al., 2010). In mammals, while liprin-α1 is ubiquitously expressed, liprin-α2/3 are mainly expressed in the brain and liprin-α4 was found in both the brain and testis (Serra-Pages et al., 1998; Zurner and Schoch, 2009; Wong et al., 2018). Liprin-α2/3 proteins were shown to have both presynaptic and postsynaptic localization at excitatory synapses in both hippocampus and cultured neurons (Spangler et al., 2011; Zurner et al., 2011), indicating that liprin-αs have separate presynaptic and postsynaptic functions. The dysfunction or depletion of liprin-αs in worms and mice led to abnormal ultrastructure of the active zone and impaired synaptic transmission (Zhen and Jin, 1999; Patel et al., 2006; Kittelmann et al., 2013; Spangler et al., 2013; Wong et al., 2018). Notably, mammalian liprin-α1 was extensively characterized in non-neuronal cells by its functions in cell motility (de Curtis, 2011). Considering that liprin-α1 is the predominant liprin-α isoform in glial cells (Spangler et al., 2011), liprin-α1 may also contribute to the synapse development through glial-neuron interactions.

The sequence analysis shows that liprin-α proteins share an evolutionarily conserved domain organization, characterized by N-terminal coiled coils and C-terminal three tandem SAM (sterile-α-motif) domains (SAM123), which are the known regions for protein binding (Spangler and Hoogenraad, 2007) (**Figure 1** and **Table 1**). The similar domain organization was found in other liprin-type scaffold proteins, liprin-β1/2 and liprin-γ (Serra-Pages et al., 1998; Astigarraga et al., 2010). In addition, some isoform/species-specific regions found in liprin-αs endow additional interactions and functions (**Figure 1**). In this review, we focus on the synaptic assemblies that are organized and regulated by liprin-αs. To approach this topic, we describe the high-resolution structures of liprin-αs and their complexes, dissect the protein–protein interactions in these structures, and discuss the potential implications of these structural findings on the regulation of protein assemblies required for synaptogenesis and synaptic functions.

THE C-TERMINAL SAM123: PROVIDING MULTIPLE PROTEIN-BINDING SURFACES FOR SUPRAMOLECULAR ASSEMBLIES

Liprin-α was first identified as the binding protein of leukocyte common antigen-related receptor protein tyrosine phosphatases (LAR-RPTPs) that are cell surface receptors containing three members, LAR, PTPδ and PTPσ (Serrapages et al., 1995; Um and Ko, 2013; Han et al., 2016). The liprin-α/LAR-RPTP interaction is important for synaptogenesis as indicated by *in vitro* heterologous synapse-formation assays and *in vivo* characterizations of excitatory synaptic morphogenesis and electrophysiological function (Kaufmann et al., 2002; Dunah et al., 2005; Um and Ko, 2013; Han et al., 2018, 2019, 2020; Won and Kim, 2018). Biochemical analysis determined binding regions at the three SAM domains of liprin-α (also referred to as liprin homology domain or LHD) and the cytoplasmic phosphatase domains of LAR-RPTPs (Serra-Pages et al., 1998). The SAM domain is one of the most abundant protein-binding domains and consists of ∼70 amino acids folded as a five-helix bundle (Qiao and Bowie, 2005; Denay et al., 2017). Although the SAM domain appears once in most SAM-containing proteins, all liprin proteins contain three tandem SAM domains. To date, the SAM123 region of liprin-αs have been reported to mediate a diverse array of interactions with kinases (CASK and CAMKII), phosphatases (LAR-RPTPs), and other scaffolds (liprin-β1/2, mSYD1 and RSY-1) in spine formation and presynaptic assembly (Kaufmann et al., 2002; Olsen et al., 2005; Hoogenraad et al., 2007; Patel and Shen, 2009; Wentzel et al., 2013) (**Table 1**).

The first structural characterization of SAM123 in liprin-α2 revealed that the three SAM domains are integrated together as a structural module (Wei et al., 2011) (**Figure 2A**). This arrangement of the SAM domains creates several protein-binding surfaces across the SAM domains. Specifically, SAM123 was found to interact with the CaM kinase domain (CaMK) of CASK and SAM123 of liprin-β1 simultaneously, indicating that SAM123 mediates protein assemblies by using different interfaces (**Figures 2B,C**). This structural indication was further supported by two recent structural studies of liprin-α3 in complexes with the cytoplasmic phosphatase domains of two LAR-RPTP proteins, LAR and PTPδ (Wakita et al., 2020; Xie et al., 2020). The binding surface for LAR-RPTPs on SAM123 shows no overlap with that for either CASK or liprin-β (**Figures 2B,C**). Consistent with these structural findings, two ternary complexes of CASK/liprin-α2/liprin-β1 and CASK/liprin-α3/LAR mediated by SAM123 were formed in solution. To further dissect the reported protein-binding modes for SAM123, we analyzed each structural element in SAM123 contributing to the protein–protein interaction.

SAM1

Consistent with its high sequence conservation (**Figure 1**), the SAM1 domain is crucial for the SAM123-mediated liprin-α complexes with liprin-βs, LAR-RPTPs, and CASK (**Figure 2B**). The crystal structure of the liprin-α2_SAM123/liprin-β1_SAM123 complex and *in vitro* binding assays reveal that the binding of the liprin-α SAM1 domain to the liprin-β SAM3 domain is through the typical SAM/SAM interaction (Wei et al., 2011), which has been found in many SAM-containing proteins for homo-oligomerization (Qiao and Bowie, 2005). Although liprin-βs were much less studied than liprin-αs, the formation of the liprin-α/liprin-β heterodimer that involves the six SAM domains enlarges accessible surfaces on the SAM domains for protein binding and that extends the capacity of liprin-αs to assemble more supramolecular complexes. Indeed, *Drosophila* liprin-α and liprin-β were reported to interact with each other via their SAM domains and function together for normal synapse formation (Astigarraga et al., 2010). Compared with the other two SAM domains, SAM1 in liprin-α contains an additional helix (αN) at the N terminus (**Figure 2A**). The αN-helix in the LAR-bound liprin-α3_SAM123 structure shows a large rotation (**Figure 2D**). This rotational change of the αN-helix alters the available surface on the SAM1 domain, implying a regulation mechanism for the binding of an unknown partner to SAM1. Of note, the αN rotation is unlikely to be induced by its binding to LAR-RPTPs, as the αN-helix in the PTPδ-bound SAM1 domain does not show a similar rotation (**Figure 2D**).

Interestingly, despite that the LAR- and liprin-β1-binding surfaces on the SAM1 domain are not overlapped, the binding of liprin-α to LAR and to liprin-β1 is mutually exclusive (Xie et al., 2020). Structural comparison of the SAM1 structures bound to LAR-RPTPs and liprin-β1 shows that the LAR binding to liprin-α triggers a conformational propagation of several interacting residues in the SAM1 domain and leads to the steric inhibition of liprin-β1 binding (**Figure 2E**). Considering that the multiple roles of liprin-αs in the synapse, this allosteric regulation is likely to control the varied components in different protein assemblies mediated by liprin-αs.

SAM2

The liprin-α SAM2 domain is sandwiched by SAM1 and SAM3, which bury the typical protein-binding surfaces of the SAM2 domain. On the other hand, SAM1 and SAM2 together generate new binding surfaces for LAR-RPTPs and CASK (**Figures 2B,C**). Specifically, the phosphatase domains of LAR and PTPδ interact with a cleft between the two SAM domains, whereas a surface patch opposite to the cleft facilitates the binding of CASK to liprin-α.

TABLE 1 | Interactions meditated by liprin-α family members.

Interactor	Liprin-α family member	Interaction region	Cellular function	References
LAR, PTPδ, PTPσ Dlar PTP-3	α1, 2, 3, 4 Dliprin-α SYD2	SAM123	Synaptogenesis, neuron development, acrosome reaction	Serrapages et al., 1995; Serra-Pages et al., 1998; Kaufmann et al., 2002; Wyszynski et al., 2002; Ackley et al., 2005; Dunah et al., 2005; Astigarraga et al., 2010; Kiok et al., 2011; Joshi et al., 2014; Bomkamp et al., 2019; Wakita et al., 2020; Xie et al., 2020
CASK	α1, 2, 3, 4	SAM123	Neurotransmitter release	Olsen et al., 2005; Samuels et al., 2007; Wei et al., 2011; LaConte et al., 2016; Wu et al., 2016
Liprin-β1	α1, 2, 3 Dliprin-α SYD2	SAM123	Synaptogenesis, cell motility	Serra-Pages et al., 1998; Astigarraga et al., 2010; Wei et al., 2011; Chiaretti et al., 2016
mSYD1A SYD1	α2 SYD2	SAM123	Active zone formation	Chia et al., 2012; Owald et al., 2012; Wentzel et al., 2013; McDonald et al., 2020
RSY-1	SYD2	SAM123	Regulation of presynaptic assembly	Patel and Shen, 2009; Chia et al., 2013
CAMKIIα	α1	SAM123	Synapse morphogenesis	Hoogenraad et al., 2007
Unc13B	Dliprin-α	Coiled-coil region	Active zone formation	Bohme et al., 2016
Liprin-γ	Dliprin-α	Coiled-coil region	Synaptogenesis	Astigarraga et al., 2010
KIF1A Kinesin-3	α1,2, Dliprin-α SYD2	Coiled-coil region	Synaptic vesicles transport	Shin et al., 2003; Wagner et al., 2009; Stucchi et al., 2018
Tanc2	α2	Coiled-coil region	Postsynaptic development	Stucchi et al., 2018
Liprin-α	α1, 2, 3, 4 SYD2	Coiled-coil region	Presynaptic formation	Serra-Pages et al., 1998; Taru and Jin, 2011; Astro et al., 2016
RIM1	α3, 4	CC2	Neurotransmitter release	Schoch et al., 2002
ELKS, CAST	α1,2,3,4 SYD2	CC2	Active zone formation	Ko et al., 2003b; Dai et al., 2006; Kittelmann et al., 2013
GIT1	α1, 2, 3, 4 Dliprin-α SYD2	SAH	AMPA receptor targeting, cell spreading	Ko et al., 2003a,b; Totaro et al., 2007; Asperti et al., 2011; Liang et al., 2019; McDonald et al., 2020
mDia	α1, 3	LCR	Stress fiber formation	Sakamoto et al., 2012; Brenig et al., 2015
GRIP1	α1, 2, 3, 4	PBM	AMPA receptor targeting	Wyszynski et al., 2002; Im et al., 2003; Zurner and Schoch, 2009; Chatterjee and Roy, 2017
LNX1	α1,2,3	PBM	Ubiquitination of liprin-α	Lenihan et al., 2017a,b
PP2A B56γ	α1 Dliprin-α	PBBM	Regulation of synaptic materials in distal axons	Arroyo et al., 2008; Li et al., 2014
PP2Aα	α1	Unknown	Trafficking to the ciliary tip, Hedgehog signaling	Liu et al., 2014
Kinesin-1	Dliprin-α	Unknown	Synaptic vesicles transport	Miller et al., 2005
KIF7	α1	Unknown	Trafficking to the ciliary tip, Hedgehog signaling	Liu et al., 2014
ING4	α1	Unknown	Cell growth and motility	Unoki et al., 2006; Shen et al., 2007
α-Dystrobrevin-1	α1	Unknown	Neuromuscular junction development	Gingras et al., 2016; Bernadzki et al., 2017
PSD95	α1	Unknown	Postsynaptic organization	Huang et al., 2017
CDK5	α1	Unknown	Postsynaptic organization	Huang et al., 2017
PARP1	α1	Unknown	P65 transcriptional activation	Gu et al., 2019
EphA2	α1	Unknown	Cell motility	Buraschi et al., 2020

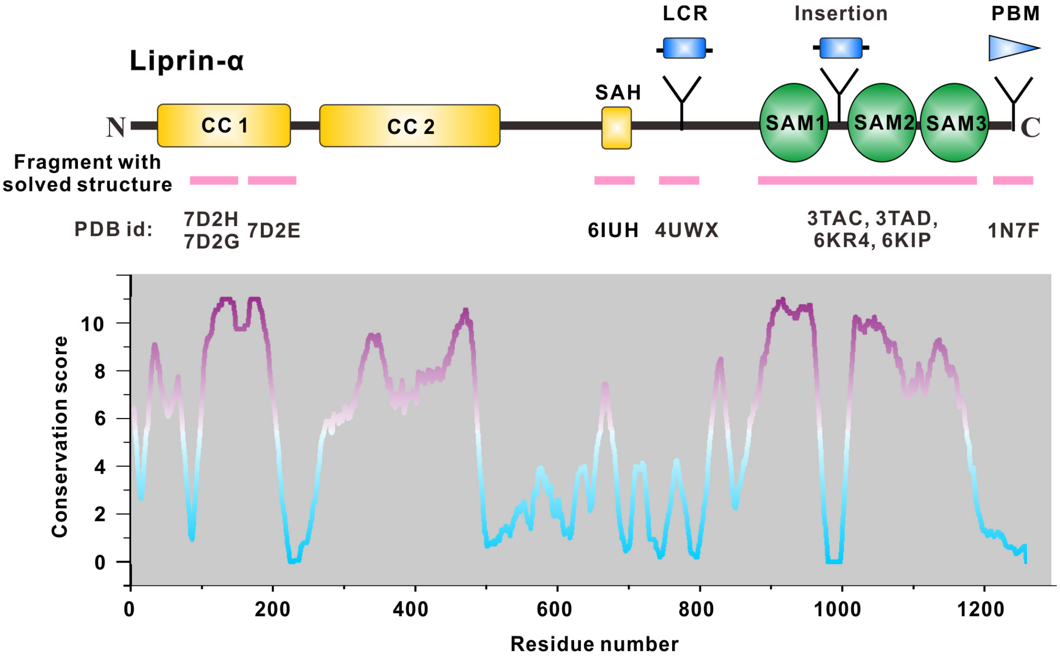

FIGURE 1 | Domain organization of liprin-α. The diagram depicts the domains or regions of liprin-α. CC, coiled-coil region; SAH, single alpha helix; SAM, sterile-α-motif domain. Isoform or species-specific regions were shown above the schematic diagram. LCR, a liprinα3 core region in liprin-α3; Insertion, an inserted loop region in liprin-α2/3/4; PBM, a PDZ binding motif in vertebrate liprin-αs. Regions of liprin-α with solved structure were highlighted by pink lines under the diagram. PDB ids were shown under the pink lines (7D2H and 7D2G for liprin-α2_H2, 7D2E for liprin-α2_H3; 6IUH for the liprin-α2_SAH/GIT1_PBD complex; 4UWX for the liprin-α3_LCR/mDia_DID complex; 3TAC, 3TAD, 6KR4, and 6KIP for the SAM123 structures in complex with CASK_CaMK, liprin-β1_SAM123, LAR_D1D2, and PTPδ_D2, respectively; 1N7F for the liprin-α1_PBM/GRIP1_PDZ6 complex). The value curve at the bottom panel indicates sequence conservation of liprin-α proteins. The conservation score for each residue was calculated in Jalview (Waterhouse et al., 2009) using the sequence alignment of liprin-α family members across species, including *Caenorhabditis elegans, Drosophila melanogaster, Danio rerio, Xenopus tropicalis, Gallus gallus, Mus musculus,* and *Homo sapiens*. The scores from 0 to 11 indicate the most variable to the most conserved state of each residue, colored from cyan to purple gradually.

SAM3

The liprin-α SAM3 domain has not been found to participate in the protein-target recognition. Considering that the SAM123-mediated interactions are not fully explored and the domain organization in liprin-αs requires the three SAM domains together, we propose that the SAM3 domain may also contribute its surface for the interactions with certain binding partners of liprin-αs (**Figure 2C**). Of note, although the liprin-β SAM3 binds to the liprin-α SAM1, the liprin-α SAM3 cannot interact with the liprin-α SAM1 to form oligomers, as the interface residues in the liprin-β SAM3 are not conserved in the liprin-α SAM3 (Wei et al., 2011).

Accessory Elements

In addition to the SAM domains, some accessory elements in the SAM123 region are required for the complex formation between liprin-α and its specific binding partners (**Figures 1**, **2A**). In both the crystal structures of liprin-α3_SAM123 in complex with the two tandem phosphatase domains (D1D2) of LAR and with the second phosphatase domain (D2) of PTPδ, a loop at the N-terminal to the αN-helix was found to provide a second binding site for the D2 phosphatase domains of LAR and PTPδ, suggesting a conserved two-site binding mode between liprin-αs and LAR-RPTPs (**Figure 2B**) (Wakita et al., 2020; Xie et al., 2020).

The liprin-α2/CASK interaction involves an insertion region between the SAM1 and SAM2 domains (**Figures 2A,B**), in which a valine-tryptophan-valine (“VWV”) motif is buried in a hydrophobic pocket on the CaMK domain of CASK (Wei et al., 2011). This insertion is conserved in neuronal specific liprin-αs, liprin-α2/3/4, but not in liprin-α1 and invertebrate liprin-αs. Notably, the insertion of human liprin-α2 is encoded by two exons (Zurner and Schoch, 2009), suggesting that the binding of CASK to liprin-α is an evolutionary gain and is regulated by alternative splicing.

Regulation Mechanisms of the SAM123-Mediated Interactions

The structural and biochemical characterizations of the SAM123-mediated interactions provide mechanistic insights into the understanding of liprin-α’s functions. Structure-guided mutagenesis study suggested that several X-linked mental retardation-associated mutations of CASK impair the binding of CASK to liprin-α2 (Najm et al., 2008; Tarpey et al., 2009; Wei et al., 2011). Because the VWV motif in the insertion of liprin-α2 is critical for the liprin-α/CASK interaction, Mint-1 and Caskin, which also bind to CASK using the similar VWV motif (Stafford et al., 2011; Wu et al., 2020), may interfere with this interaction. As the Veli/CASK/Mint-1 tripartite complex

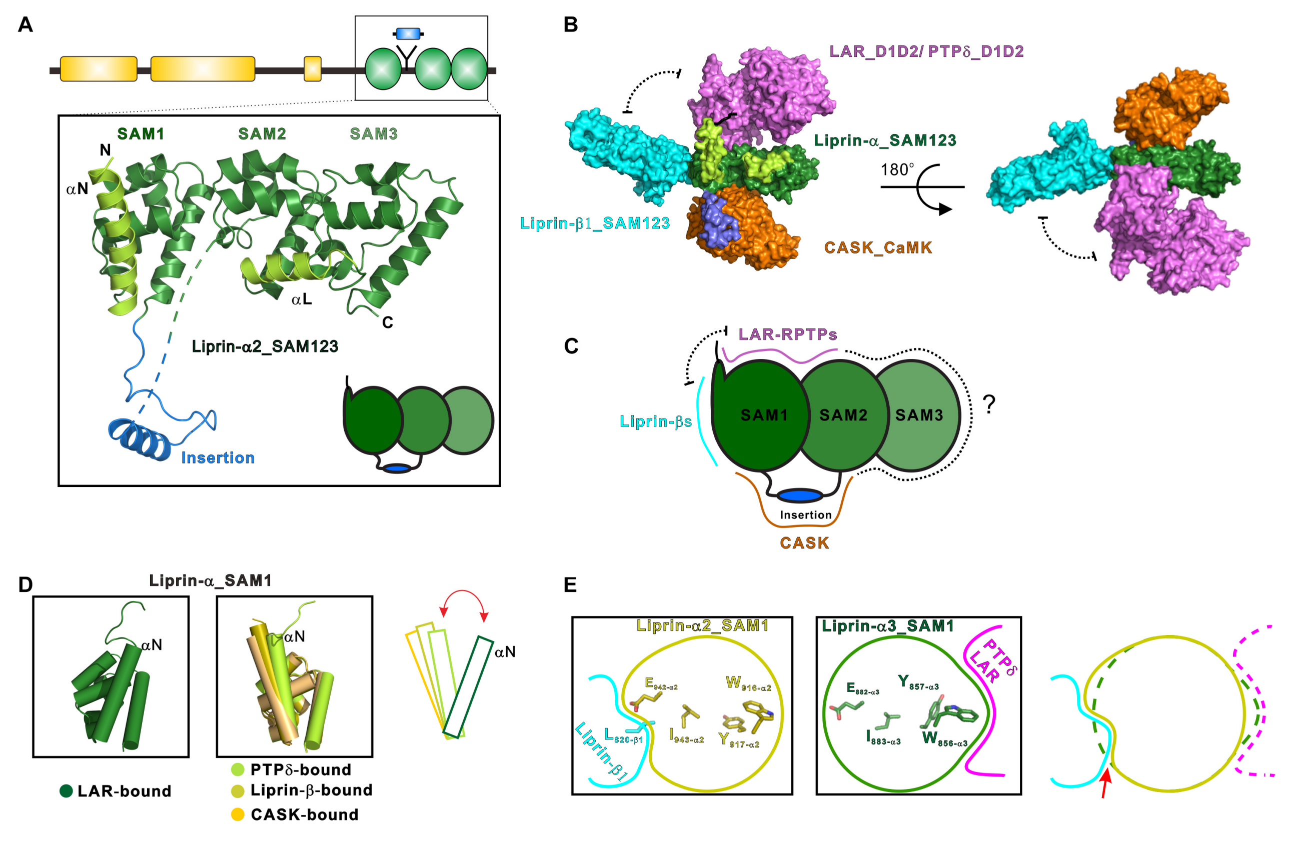

FIGURE 2 | Liprin-α SAM123 mediates supramolecular assemblies. **(A)** The structure of liprin-α SAM123. The SAM123 structure is derived from the liprin-α2/CASK complex (PDB id: 3TAC). **(B)** A structure model showing the SAM123-mediated protein assembly. The SAM123 structures in complex with CASK (PDB id: 3TAC), liprin-β1 (3TAD), and LAR (6KR4) are superimposed. **(C)** A schematic model indicates the target-binding surfaces of the liprin-α SAM123. Some surface patches on SAM2 and SAM3 may be also involved in protein binding. **(D)** Conformational dynamics of the αN-helix in the SAM1 domain. The rotational change of αN was indicated by a red bidirectional arrow. **(E)** Allosteric regulation of the binding of the liprin-α SAM123 to liprin-β1 and LAR-RPTPs. The SAM1 residues that are involved in the allosteric regulation were shown as sticks. The conformational propagation of these SAM1 residues upon LAR-RPTP binding leads to the clash (indicated by a red arrow) between the liprin-α SAM1 and liprin-β1 and thus blocks the liprin-α/β interaction.

is involved in neurotransmitter release (Olsen et al., 2005), the CASK-binding competition between liprin-αs and Mint-1 is likely a regulation mechanism for the distribution and composition of the presynaptic assemblies.

The highly conserved association between liprin-αs and LAR-RPTPs has been extensively characterized in the synapse initiation, assembly and maintenance (Kaufmann et al., 2002; Ackley et al., 2005; Dunah et al., 2005; Han et al., 2018; Ozel et al., 2019). Catalytically inactive mutants of LAR-RPTPs failed to control axon growth or synaptogenesis (Johnson et al., 2001; Dunah et al., 2005). The SAM123 regions of liprin-αs bind to the catalytically inactive D2 domains, instead of the active D1 domains of LAR-RPTPs (Serra-Pages et al., 1998; Astigarraga et al., 2010). However, the structural findings on the liprin-α3/LAR complex implied that by binding to liprin-α proteins, LAR forms clusters on the cell surface, which promotes the self-association of the LAR D1 domain, blocking its substrate binding (Xie et al., 2020). Thus, liprin-αs may regulate the synapse formation by attenuating LAR's activity via forming the large protein assembly. Importantly, the N-terminal coiled-coil regions of liprin-αs are also required for the cluster formation of the liprin-α/LAR complex by oligomerizing liprin-αs, which will be discussed in the next section.

THE N-TERMINAL COILED COILS: THE SELF-ASSEMBLY OF LIPRIN-α

The N-terminal coiled coils are essential for synaptic functions of liprin-αs. In *C. elagans*, the coiled-coil region of SYD2 is necessary and sufficient to suppress synaptic defects caused by a loss-of-function mutant of SYD2 (Dai et al., 2006; Taru and Jin, 2011) and to assemble functional synapses (Chia et al., 2013). The N-terminal conserved region of liprin-α contains three predicted coiled-coil segments, in which the first two segments are named CC1 and CC2 (**Figure 1**). The third one was recently characterized as a single α-helix (SAH) in solution (Liang et al., 2019), suggesting that only two coiled coils exist in liprin-α. The N-terminal region was suggested to organize self-assembly of liprin-αs (Serra-Pages et al., 1998; Astigarraga et al., 2010; Taru and Jin, 2011), presumably mediated by the coiled-coil formation despite lacking detailed investigations. In addition,

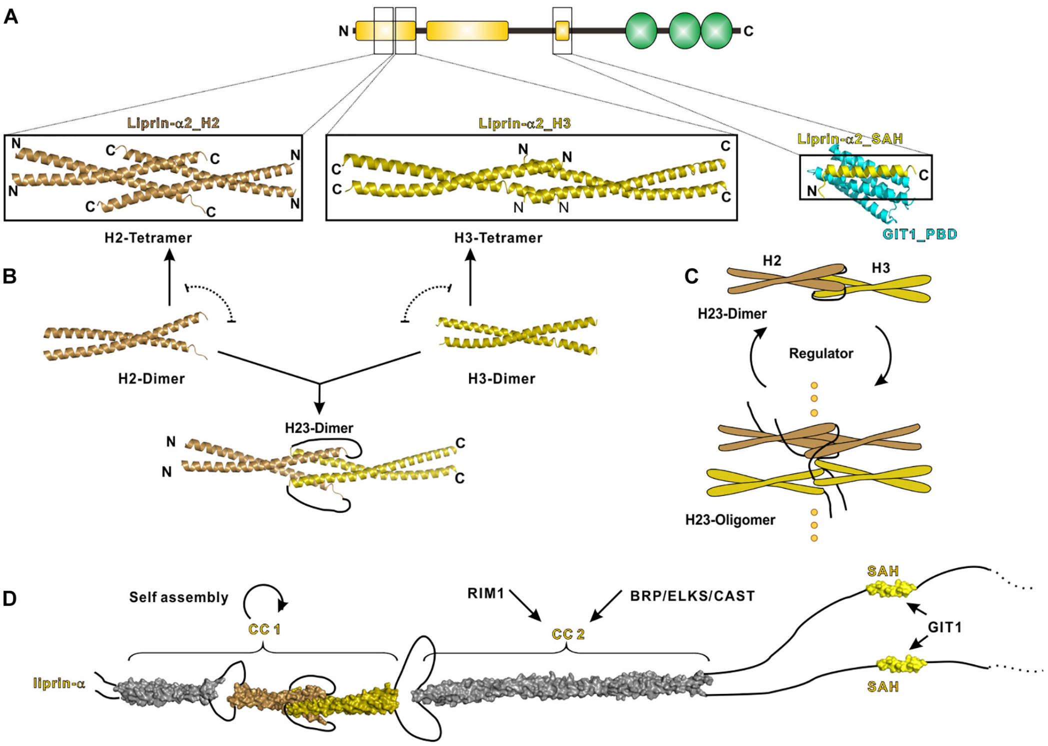

FIGURE 3 | N-terminal coiled coils mediate the self-assembly of liprin-α. **(A)** The solved structures of liprin-α N-terminus were indicated by black boxes. The H2 (PDB id: 7D2H), H3 (7D2E), and SAH (6IUH) segment structures of liprin-α2 were shown. **(B)** A model indicating that the dimeric H2 and H3 competitively transit between homo-tetramers and a H23-dimer. **(C)** A schematic cartoon showing the self-assembly mechanism of liprin-α CC1. The transition between dimers and higher oligomers may be controlled by unknown regulators. **(D)** A structure model showing the complete N-terminal structure of liprin-α. The H1 segment and CC2 was modeled as coiled coils and shown in gray.

several synaptic proteins (e.g., RIM, ELKS, GIT1, KIF1A, and TANC2) interact with liprin-αs via this coiled-coil region (Schoch et al., 2002; Ko et al., 2003b; Shin et al., 2003; Stucchi et al., 2018) (**Table 1**).

CC1

CC1 is the most conserved region among vertebrate liprin-αs and *C. elegans* SYD2 (**Figure 1**). In *C. elegans*, SYD2 functions together with SYD1, both of which are required for the synapse formation of hermaphrodite specific neurons (Dai et al., 2006). In mouse model, the depletion of liprin-α2, liprin-α3, or mSYD1A (a mammalian homolog of SYD1) led to the similar synaptic defects, including decreased vesicle docking and impaired synaptic transmission (Spangler et al., 2013; Wentzel et al., 2013; Wong et al., 2018). Interestingly, a single substitution of R184 with cysteine in the CC1 region of SYD2 was genetically identified as a gain-of-function mutation, which promote synaptic assembly even in the absence of SYD1 (Dai et al., 2006). An electron microscopic study demonstrated that the worm bearing the R184C mutation had highly enhanced protein-dense matrix at the presynaptic active zone (Kittelmann et al., 2013), suggesting the promoted active zone formation. Biochemical analysis indicated that the R184C mutation promotes the oligomerization of SYD2 (Taru and Jin, 2011; Kittelmann et al., 2013; Liang et al., 2020).

CC1 contains three α-helices termed H1, H2 and H3, respectively, connected by short loops. Recently, crystal structures of H2 and H3 in liprin-α2 were determined, which reveal the molecular mechanism underlying the self-assembly of liprin-αs (Liang et al., 2020). In these structures, the H2- and H3-helices are both homo-tetramerized yet through different assembly modes (**Figure 3A**). Combined with extensive biochemical characterizations, these structures suggest an assembly model of CC1, in which the dimeric coiled coils of H2 and H3 are either interacted with each other to form a H23 dimer or self-associated to form tetramers (**Figure 3B**). The gain-of-function mutation in CC1 diminishes the H2/H3 interaction and inhibits the H23 dimer formation, in return promoting H2 and H3 tetramerization and then CC1 oligomerization (Liang et al., 2020) (**Figure 3C**). Therefore, the mutation-promoted self-assembly of liprin-α/SYD2 provides multiple protein-binding sites and thus enhances the presynaptic recruitment of other synaptic proteins, such as ELKS for the active zone formation (Dai et al., 2006; Kittelmann et al., 2013).

This gain-of-function effect implies that the assembly of liprin-αs under the physiological condition is determined by unknown regulator(s). The regulator(s) may increase the self-assembly of liprin-αs through stabilizing the H23 dimer or vice versa (**Figure 3C**). SYD1 is a promising positive regulator in this regard, as the genetic analysis indicated that SYD1

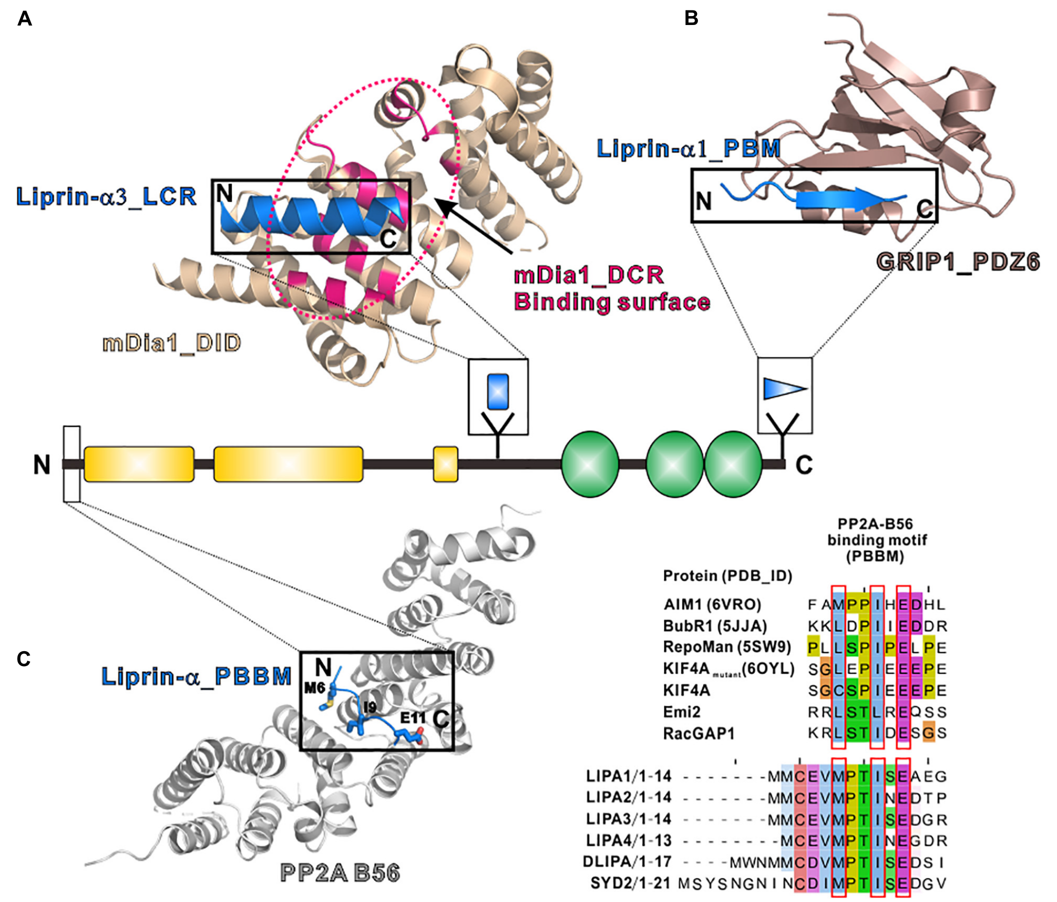

FIGURE 4 | Additional regions of liprin-α in protein–protein interactions. **(A)** The structure of the LCR in complex with mDia (PDB id: 4UWX). Base on another solved structure of mDia (PDB id: 2BAP), the surface on mDia that is involved in the autoinhibition formation was highlighted by a dotted hotpink circle, showing the two binding sites are largely overlapped. **(B)** The structure of the PBM in complex with the PDZ6 domain of GRIP1 (PDB id: 1N7F). **(C)** The manually modeled structure of the PP2A-B56/liprin-α_PBBM complex. The sequences of the PBBMs from different proteins in the solved structures were aligned with the PBBMs of liprin-αs. The residues that are involved in B56 binding were highlighted by red boxes.

acts as an upstream factor required for SYD2's activity on synaptogenesis (Dai et al., 2006). The coiled-coil region in SYD2 was suggested to associate with SAM123 to adopt an auto-inhibition conformation (Patel and Shen, 2009), presumably locking the H23 dimer to prevent the self-assembly of SYD2. As the mammalian homolog of SYD1 was reported to interact with liprin-α SAM123 (Wentzel et al., 2013), it is tempting to speculate that the SYD1 binding releases the auto-inhibition of liprin-α or SYD2 and thereby leads to the promoted self-assembly. The potential negative regulator is RSY-1 that inhibits the synapse formation in *C. elegans* (Patel and Shen, 2009). RSY-1 was found to associate with SYD2 and antagonize the pro-synaptic function of SYD2 (Patel and Shen, 2009).

CC2

The liprin-α CC2 is the binding region for ELKS and RIM, both of which participate in the ultrastructure organization and neurotransmitter release at the active zone (Ohtsuka et al., 2002; Schoch et al., 2002; Kittel et al., 2006; Wang et al., 2009, 2016; Held et al., 2016) (**Figure 3D**). Recent studies showed that liprin-α proteins undergo either phosphorylation-dependent phase transition or co-phase separation with ELKS (Emperador-Melero et al., 2020; Liang et al., 2020; McDonald et al., 2020). These findings indicate that the self-assembled liprin-αs act as a hub to dynamically recruit ELKS, RIM, and other binding partners to form the electron-dense protein aggregates in the presynaptic active zone observed by electron microscopy (Fouquet et al., 2009; Kittelmann et al., 2013; Spangler et al., 2013).

In addition to the liprin-α-mediated phase separation, RIM and RIM-binding protein (RIM-BP) co-phase separate and cluster calcium channels to form the active zone-like condensate *in vitro* (Wu et al., 2019). It is likely that the interplay between the two types of condensates, the liprin-α/ELKS condensate and the RIM/RIM-BP condensate, in the active zone contributes to the highly patterned distributions of the active zone proteins (Emperador-Melero and Kaeser, 2020). Consistently, the purified RIM and calcium channel proteins are differentially distributed in the two condensed phases in the presence of the self-assembled liprin-α (Liang et al., 2020), suggesting that liprin-α serves as a molecular sieve in protein condensates to facilitate the compartmentalization of synaptic proteins in the active zone.

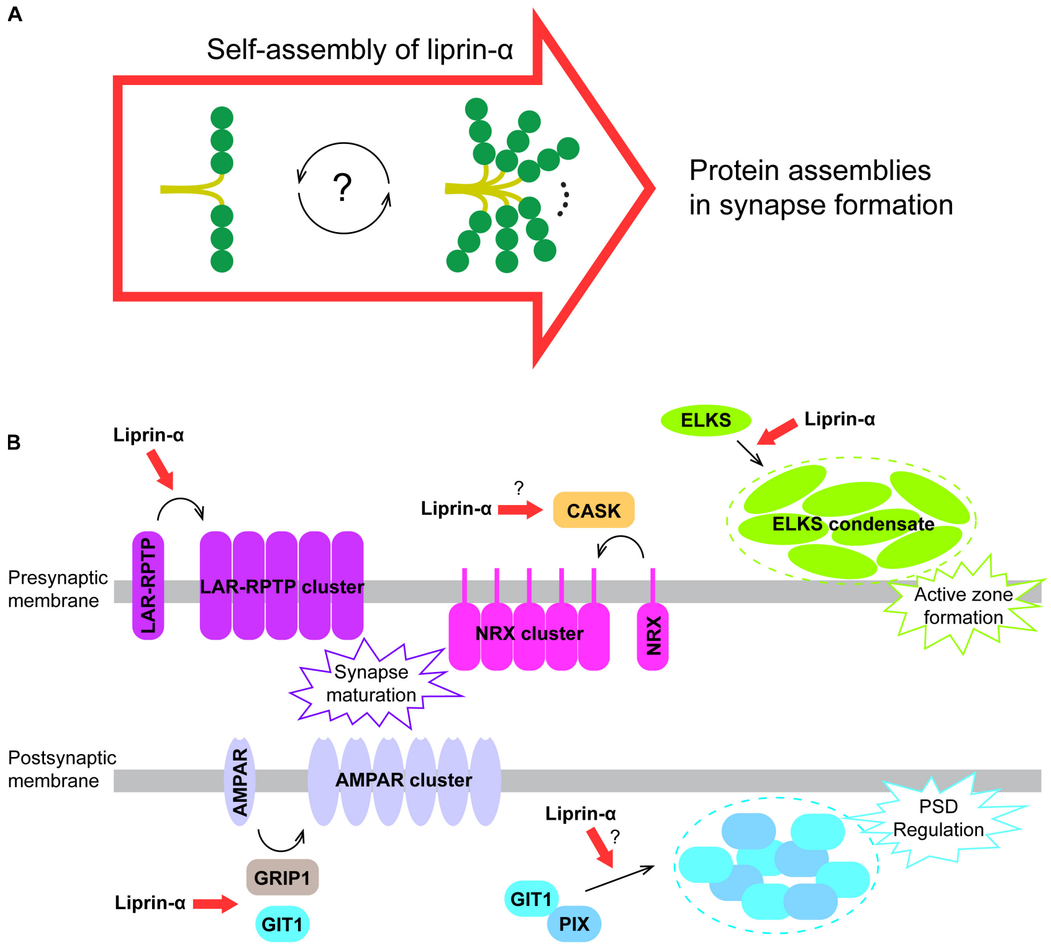

FIGURE 5 | A proposed model for liprin-α assembly in mediating protein accumulation in synapse development. **(A)** Liprin-α is self-assembled to form a large complex and to mediate protein assemblies. **(B)** The highly self-assembled liprin-α proteins, indicated by red arrows, organize different receptor clustering and protein condensates (indicated by dotted circles) on both presynaptic and postsynaptic membrane in synapse formation, although no direct evidence showing the involvement of liprin-α in the clustering of Neurexin and the condensation of the GIT1/PIX complex.

Single α-Helix

The SAH region of liprin-α contains a leucine/aspartate (LD)-like motif that binds to the C-terminal PBD domain of GIT1 (Ko et al., 2003a; Asperti et al., 2011). GIT1 is a GTPase-activating protein (GAP) that plays regulatory roles in neurotransmitter release and spine formation in mice (Zhang et al., 2003, 2005; Podufall et al., 2014; Hong and Mah, 2015). This liprin-α/GIT1 interaction was defined at the postsynapse specifically for AMPA receptor clustering (Wyszynski et al., 2002; Im et al., 2003). The crystal structure of the SAH/PBD complex reveals that the SAH interacts with the GIT1_PBD through a mode differing from the canonical LD binding mode (Liang et al., 2019) (**Figure 3A**). As the PBD domain of GIT1 interacts with other LD-containing proteins (Schmalzigaug et al., 2007; Zhang et al., 2008), the structural finding reveals how GIT1 specifically recognized liprin-α through the SAH-mediated interaction in the synapse.

Although liprin-αs and GIT1 are also enriched at the presynaptic site, the presynaptic function of the liprin-α/GIT1 complex remain unknown. In addition, because GIT1 interacts with Stonin2 and Piccolo for synaptic vesicle recycling (Kim et al., 2003; Podufall et al., 2014) and liprin-α regulates docking and exocytosis of synaptic vesicles (Wong et al., 2018), the liprin-α/GIT1 interaction may link the cycling synaptic vesicles to the presynaptic active zone.

OTHER PROTEIN-BINDING REGIONS IN LIPRIN-αs

Liprin-α3 Core Region (LCR)

The LCR, only found in liprin-α3, folds as a short α-helix and interacts with mDia, an actin nucleator, to regulate the dynamics of actin filaments (Sakamoto et al., 2012; Brenig et al., 2015). The structural study of the LCR/mDia complex showed that the LCR prevents mDia from adopting an auto-inhibited conformation (**Figure 4A**), therefore promoting actin polymerization in the cell (Brenig et al., 2015). Although the LCR sequence is not conserved in other liprin-α proteins, liprin-α1 was found to interact with mDia (Sakamoto et al., 2012). Whether liprin-α1 binds to mDia by using a similar sequence in other regions or a different sequence need further study.

PDZ Binding Motif (PBM)

PDZ binding motifs (PBMs) were found in the C-termini of vertebrate liprin-αs (Im et al., 2003; Zurner and Schoch, 2009) but not in their invertebrate homologs. The sixth PDZ domain of GRIP1 was identified to bind to the PBM of liprin-α (Wyszynski et al., 2002). The PBM-binding pocket of the dimeric GRIP1_PDZ6 is located at the distal sides of the dimer interface (**Figure 4B**). Dimeric PDZ6 domain mediates GRIP1 multimerization, which enhances the binding of the neighboring PDZ5 domain to receptors, clusters Glutamate receptor 2/3, and regulates AMPA receptor targeting in murine postsynapse (Wyszynski et al., 2002; Ko et al., 2003a). Alternative RNA splicing may generate some liprin-α protein products without the PBMs (Zurner and Schoch, 2009) and thus regulate the receptor binding for liprin-αs. As PBMs do not present in SYD2 or Dliprin-α, the PBM-mediated postsynaptic interaction is likely an evolutionary gain for vertebrate liprin-αs.

PP2A-B56 Binding Motif (PBBM)

In addition to tyrosine phosphatases, liprin-αs were found to interact with a serine/threonine phosphatase, protein phosphatase 2A (PP2A) (Arroyo et al., 2008; Li et al., 2014; Liu et al., 2014). Drosophila liprin-α, SYD1 and PP2A form a linear pathway for the presynapse formation (Li et al., 2014). In mammals, liprin-αs function together with PP2A in controlling the phosphorylation level of KIF7 and activating Hedgehog-target genes (Arroyo et al., 2008; Liu et al., 2014). The binding of liprin-α to the PP2A holoenzyme was mapped to the regulatory subunit of PP2A, B56 (Arroyo et al., 2008; Li et al., 2014). A systematic study of the PP2A-B56 binding motif (PBBM) uncovers a L/M-X-X-I-X-E consensus sequence motif (Hertz et al., 2016), which is also found in the very N-terminal parts of liprin-αs across different species (**Figure 4C**). Based on a previously solved structure of the B56/PBBM complex, the B56/liprin-α complex structure was modeled, showing that the PBBM sequence of liprin-α fits well to the typical PBBM-binding pocket of B56 (**Figure 4C**). Notably, as the phosphorylation of a threonine residue in the PBBM of Emi2 or RacGAP1 promotes their binding to B56 (Hertz et al., 2016), the strictly conserved threonine in the PBBM of liprin-α may be phosphorylated to regulate the liprin-α/PP2A interaction (**Figure 4C**).

CONCLUSION AND PERSPECTIVES

Liprin-αs are multiple-domains scaffold proteins mediating various synaptic protein assemblies through both their conserved N-terminal coiled coils and C-terminal SAM123. In these assemblies, each part of the liprin-α protein has its unique role. While SAM123 serves as a tunable hub to accommodate the different binding partners to form the large complexes, the coiled coils undergo regulated self-assembly to control the protein assemblies (**Figure 5A**).

The self-assembly of liprin-α not only accumulates many synaptic proteins essential for synapse formation, but also organizes these proteins on the presynaptic and postsynaptic membrane to regulate their functions. In addition to the promoting effect on LAR clustering (Xie et al., 2020) and the ELKS condensate formation in presynpase maturation (Liang et al., 2020; McDonald et al., 2020), liprin-αs are involved in several other protein assemblies in the synapse (**Figure 5B**). Through the interaction with CASK, the key binding partner of Neurexin in the presynapse (Butz et al., 1998; Tabuchi et al., 2002; Dean et al., 2003), liprin-αs may contribute to the presynaptic clustering of Neurexin, which plays a crucial role in the alignment of the presynaptic and postsynaptic machinery during presynaptic differentiation (Dean et al., 2003; Sudhof, 2017). Recently, two members of the LAR-RPTP family, PTPσ and PTPδ were reported to interact with Neurexin to coordinate the presynaptic assemblies (Han et al., 2020). Therefore, liprin-αs may also regulate the Neurexin-mediated assembly via LAR-RPTPs. At the postsynaptic terminal, the self-assembly of liprin-α may enhance the liprin-α/GIT1 interaction that is required for the AMPA receptor clustering (Wyszynski et al., 2002; Im et al., 2003). Finally, as the condensate formation of GIT1 and PIX was proposed to modulate the post-synaptic density (PSD) (Zhu et al., 2020), the self-assembled liprin-α may function as an upstream promoting factor for the regulation of PSD by binding to GIT1.

In support of the master scaffolding role of liprin-α, over 26 proteins have been identified to interact with liprin-αs for diverse functions (**Table 1**). For instance, liprin-αs assembles ELSK, RIM, and UNC13/Munc13 in the active zone for regulating synaptic vesicle release (Schoch et al., 2002; Deken et al., 2005; Bohme et al., 2016; Dong et al., 2018) and associates with KIF1A to regulate the axonal transport of vesicles (Shin et al., 2003; Hsu et al., 2011; Wu et al., 2016; Zhang et al., 2016; Stucchi et al., 2018). However, due to lacking structural and biochemical information, the molecular basis of these interactions remains elusive. The future structural research of liprin-α-mediated protein interactions will further advance our understanding of how proteins are spatiotemporally orchestrated to control neuron development and synaptic transmission.

AUTHOR CONTRIBUTIONS

XX and ML analyzed the structures and prepared the figures. XX and ZW drafted the manuscript. XX, ML, CY, and ZW revised and finalized the manuscript. All the authors contributed to the article and approved the submitted version.

FUNDING

This work was supported by the National Natural Science Foundation of China (Grant Nos. 31971131 and 31770791 to ZW, 31870757 to CY), Natural Science Foundation of Guangdong Province (2016A030312016), and Shenzhen-Hong Kong Institute of Brain Science, Shenzhen Fundamental Research Institutions (2021SHIB0002).

REFERENCES

Ackermann, F., Waites, C. L., and Garner, C. C. (2015). Presynaptic active zones in invertebrates and vertebrates. *Embo Rep.* 16, 923–938.

Ackley, B. D., Harrington, R. J., Hudson, M. L., Williams, L., Kenyon, C. J., Chisholm, A. D., et al. (2005). The two isoforms of the *Caenorhabditis elegans* leukocyte-common antigen related receptor tyrosine phosphatase PTP-3 function independently in axon guidance and synapse formation. *J. Neurosci.* 25, 7517–7528.

Arroyo, J. D., Lee, G. M., and Hahn, W. C. (2008). Liprin alpha1 interacts with PP2A B56gamma. *Cell Cycle* 7, 525–532.

Asperti, C., Astro, V., Pettinato, E., Paris, S., Bachi, A., and de Curtis, I. (2011). Biochemical and functional characterization of the interaction between liprin-alpha1 and GIT1: implications for the regulation of cell motility. *PLoS One* 6:e20757. doi: 10.1371/journal.pone.0020757

Astigarraga, S., Hofmeyer, K., Farajian, R., and Treisman, J. E. (2010). Three *Drosophila* liprins interact to control synapse formation. *J. Neurosci.* 30, 15358–15368.

Astro, V., Tonoli, D., Chiaretti, S., Badanai, S., Sala, K., Zerial, M., et al. (2016). Liprin-alpha1 and ERC1 control cell edge dynamics by promoting focal adhesion turnover. *Sci. Rep.* 6:33653.

Bernadzki, K. M., Gawor, M., Pezinski, M., Mazurek, P., Niewiadomski, P., Redowicz, M. J., et al. (2017). Liprin-alpha-1 is a novel component of the murine neuromuscular junction and is involved in the organization of the postsynaptic machinery. *Sci. Rep.* 7:9116.

Biederer, T., Kaeser, P. S., and Blanpied, T. A. (2017). Transcellular nanoalignment of synaptic function. *Neuron* 96, 680–696.

Bohme, M. A., Beis, C., Reddy-Alla, S., Reynolds, E., Mampell, M. M., Grasskamp, A. T., et al. (2016). Active zone scaffolds differentially accumulate Unc13 isoforms to tune Ca(2+) channel-vesicle coupling. *Nat. Neurosci.* 19, 1311–1320.

Bomkamp, C., Padmanabhan, N., Karimi, B., Ge, Y., Chao, J. T., Loewen, C. J. R., et al. (2019). Mechanisms of PTPsigma-Mediated presynaptic differentiation. *Front. Synaptic. Neurosci.* 11:17. doi: 10.3389/fnsyn.2019.00017

Brenig, J., de Boor, S., Knyphausen, P., Kuhlmann, N., Wroblowski, S., Baldus, L., et al. (2015). Structural and biochemical basis for the inhibitory effect of Liprin-alpha3 on mouse diaphanous 1 (mDia1) function. *J. Biol. Chem.* 290, 14314–14327.

Broadie, K. S., and Richmond, J. E. (2002). Establishing and sculpting the synapse in *Drosophila* and *C. elegans*. *Curr. Opin. Neurobiol.* 12, 491–498.

Buraschi, S., Neill, T., Xu, S. Q., Palladino, C., Belfiore, A., Iozzo, R. V., et al. (2020). Progranulin/EphA2 axis: a novel oncogenic mechanism in bladder cancer. *Matrix Biol.* 93, 10–24.

Butz, S., Okamoto, M., and Sudhof, T. C. (1998). A tripartite protein complex with the potential to couple synaptic vesicle exocytosis to cell adhesion in brain. *Cell* 94, 773–782.

Chatterjee, P., and Roy, D. (2017). Structural insight into GRIP1-PDZ6 in Alzheimer.s disease: study from protein expression data to molecular dynamics simulations. *J. Biomol. Struct. Dyn.* 35, 2235–2247.

Chia, P. H., Patel, M. R., and Shen, K. (2012). NAB-1 instructs synapse assembly by linking adhesion molecules and F-actin to active zone proteins. *Nat. Neurosci.* 15, 234–242.

Chia, P. H., Patel, M. R., Wagner, O. I., Klopfenstein, D. R., and Shen, K. (2013). Intramolecular regulation of presynaptic scaffold protein SYD-2/liprin-alpha. *Mol. Cell Neurosci.* 56, 76–84.

Chiaretti, S., Astro, V., Chiricozzi, E., and de Curtis, I. (2016). Effects of the scaffold proteins liprin-alpha1, beta1 and beta2 on invasion by breast cancer cells. *Biol. Cell* 108, 65–75.

Chua, J. J., Kindler, S., Boyken, J., and Jahn, R. (2010). The architecture of an excitatory synapse. *J. Cell Sci.* 123, 819–823.

Dai, Y., Taru, H., Deken, S. L., Grill, B., Ackley, B., Nonet, M. L., et al. (2006). SYD-2 Liprin-alpha organizes presynaptic active zone formation through ELKS. *Nat. Neurosci.* 9, 1479–1487.

de Curtis, I. (2011). Function of liprins in cell motility. *Exp. Cell Res.* 317, 1–8.

Dean, C., Scholl, F. G., Choih, J., DeMaria, S., Berger, J., Isacoff, E., et al. (2003). Neurexin mediates the assembly of presynaptic terminals. *Nat. Neurosci.* 6, 708–716.

Deken, S. L., Vincent, R., Hadwiger, G., Liu, Q., Wang, Z. W., and Nonet, M. L. (2005). Redundant localization mechanisms of RIM and ELKS in *Caenorhabditis elegans*. *J. Neurosci.* 25, 5975–5983.

Denay, G., Vachon, G., Dumas, R., Zubieta, C., and Parcy, F. (2017). Plant SAM-domain proteins start to reveal their roles. *Trends Plant Sci.* 22, 718–725.

Dong, W., Radulovic, T., Goral, R. O., Thomas, C., Suarez Montesinos, M., Guerrero-Given, D., et al. (2018). CAST/ELKS proteins control voltage-Gated Ca(2+) channel density and synaptic release probability at a mammalian central synapse. *Cell Rep.* 24, 284.e6–293.e6.

Dunah, A. W., Hueske, E., Wyszynski, M., Hoogenraad, C. C., Jaworski, J., Pak, D. T., et al. (2005). LAR receptor protein tyrosine phosphatases in the development and maintenance of excitatory synapses. *Nat. Neurosci.* 8, 458–467.

Emperador-Melero, J., and Kaeser, P. S. (2020). Assembly of the presynaptic active zone. *Curr. Opin. Neurobiol.* 63, 95–103.

Emperador-Melero, J., Wong, M. Y., Wang, S. S. H., de Nola, G., Kirchhausen, T., and Kaeser, P. S. (2020). Phosphorylation triggers presynaptic phase separation of Liprin-α3 to control active zone structure. *bioRxiv* [Preprint]. doi: 10.1101/2020.10.28.357574

Feng, W., and Zhang, M. (2009). Organization and dynamics of PDZ-domain-related supramodules in the postsynaptic density. *Nat. Rev. Neurosci.* 10, 87–99.

Fouquet, W., Owald, D., Wichmann, C., Mertel, S., Depner, H., Dyba, M., et al. (2009). Maturation of active zone assembly by *Drosophila* bruchpilot. *J. Cell Biol.* 186, 129–145.

Gingras, J., Gawor, M., Bernadzki, K. M., Grady, R. M., Hallock, P., Glass, D. J., et al. (2016). Alpha-Dystrobrevin-1 recruits Grb2 and alpha-catulin to organize neurotransmitter receptors at the neuromuscular junction. *J. Cell Sci.* 129, 898–911.

Gramlich, M. W., and Klyachko, V. A. (2019). Nanoscale organization of vesicle release at central synapses. *Trends Neurosci.* 42, 425–437.

Gu, C., Liu, Y., Yin, Z., Yang, J., Huang, G., Zhu, X., et al. (2019). Discovery of the Oncogenic Parp1, a target of bcr-abl and a potential therapeutic, in mir-181a/PPFIA1 signaling pathway. *Mol. Ther. Nucleic Acids* 16, 1–14.

Han, K. A., Jeon, S., Um, J. W., and Ko, J. (2016). Emergent synapse organizers: LAR-RPTPs and their companions. *Int. Rev. Cell Mol. Biol.* 324, 39–65.

Han, K. A., Kim, Y. J., Yoon, T. H., Kim, H., Bae, S., Um, J. W., et al. (2020). LAR-RPTPs directly interact with neurexins to coordinate bidirectional assembly of molecular machineries. *J. Neurosci.* 40, 8438–8462.

Han, K. A., Ko, J. S., Pramanik, G., Kim, J. Y., Tabuchi, K., Um, J. W., et al. (2018). PTPsigma drives excitatory presynaptic assembly via various extracellular and intracellular mechanisms. *J. Neurosci.* 38, 6700–6721.

Han, K. A., Um, J. W., and Ko, J. (2019). Intracellular protein complexes involved in synapse assembly in presynaptic neurons. *Adv. Protein Chem. Struct. Biol.* 116, 347–373.

Harris, K. M., and Weinberg, R. J. (2012). Ultrastructure of synapses in the mammalian brain. *Cold Spring Harb. Perspect. Biol.* 4:a005587.

Haucke, V., Neher, E., and Sigrist, S. J. (2011). Protein scaffolds in the coupling of synaptic exocytosis and endocytosis. *Nat. Rev. Neurosci.* 12, 127–138.

Held, R. G., Liu, C., and Kaeser, P. S. (2016). ELKS controls the pool of readily releasable vesicles at excitatory synapses through its N-terminal coiled-coil domains. *eLife* 5:e14862.

Hertz, E. P. T., Kruse, T., Davey, N. E., Lopez-Mendez, B., Sigurethsson, J. O., Montoya, G., et al. (2016). A conserved motif provides binding specificity to the PP2A-B56 phosphatase. *Mol. Cell* 63, 686–695.

Hong, S. T., and Mah, W. (2015). A critical role of GIT1 in vertebrate and invertebrate brain development. *Exp. Neurobiol.* 24, 8–16.

Hoogenraad, C. C., Feliu-Mojer, M. I., Spangler, S. A., Milstein, A. D., Dunah, A. W., Hung, A. Y., et al. (2007). Liprinalpha1 degradation by calcium/calmodulin-dependent protein kinase II regulates LAR receptor tyrosine phosphatase distribution and dendrite development. *Dev. Cell* 12, 587–602.

Hsu, C. C., Moncaleano, J. D., and Wagner, O. I. (2011). Sub-cellular distribution of UNC-104(KIF1A) upon binding to adaptors as UNC-16(JIP3), DNC-1(DCTN1/Glued) and SYD-2(Liprin-alpha) in *C. elegans* neurons. *Neuroscience* 176, 39–52.

Huang, H., Lin, X., Liang, Z., Zhao, T., Du, S., Loy, M. M. T., et al. (2017). Cdk5-dependent phosphorylation of liprinalpha1 mediates neuronal activity-dependent synapse development. *Proc. Natl. Acad. Sci. U.S.A.* 114, E6992–E7001.

Im, Y. J., Park, S. H., Rho, S. H., Lee, J. H., Kang, G. B., Sheng, M., et al. (2003). Crystal structure of GRIP1 PDZ6-peptide complex reveals the structural basis for class II PDZ target recognition and PDZ domain-mediated multimerization. *J. Biol. Chem.* 278, 8501–8507.

Johnson, K. G., McKinnell, I. W., Stoker, A. W., and Holt, C. E. (2001). Receptor protein tyrosine phosphatases regulate retinal ganglion cell axon outgrowth in the developing Xenopus visual system. *J. Neurobiol.* 49, 99–117.

Joshi, C. S., Khan, S. A., and Khole, V. V. (2014). Regulation of acrosome reaction by Liprin alpha3, LAR and its ligands in mouse spermatozoa. *Andrology* 2, 165–174.

Kaufmann, N., DeProto, J., Ranjan, R., Wan, H., and Van Vactor, D. (2002). *Drosophila* liprin-alpha and the receptor phosphatase Dlar control synapse morphogenesis. *Neuron* 34, 27–38.

Kim, S., Ko, J., Shin, H., Lee, J. R., Lim, C., Han, J. H., et al. (2003). The GIT family of proteins forms multimers and associates with the presynaptic cytomatrix protein Piccolo. *J. Biol. Chem.* 278, 6291–6300.

Kiok, K., Sun, H., Clancy, H., Bose, S., Kluz, T., Wu, F., et al. (2011). Liprin-alpha4 is required for nickel induced receptor protein tyrosine phosphatase-leukocyte antigen related receptor F (RPTP-LAR) activity. *PLoS One* 6:e22764. doi: 10.1371/journal.pone.0022764

Kittel, R. J., Wichmann, C., Rasse, T. M., Fouquet, W., Schmidt, M., Schmid, A., et al. (2006). Bruchpilot promotes active zone assembly. Ca2+ Channel clustering, and vesicle release. *Science* 312, 1051–1054.

Kittelmann, M., Hegermann, J., Goncharov, A., Taru, H., Ellisman, M. H., Richmond, J. E., et al. (2013). Liprin-alpha/SYD-2 determines the size of dense projections in presynaptic active zones in *C. elegans*. *J. Cell Biol.* 203, 849–863.

Ko, J., Kim, S., Valtschanoff, J. G., Shin, H. W., Lee, J. R., Sheng, M., et al. (2003a). Interaction between liprin-alpha and GIT1 is required for AMPA receptor targeting. *J. Neurosci.* 23, 1667–1677.

Ko, J., Na, M., Kim, S., Lee, J. R., and Kim, E. (2003b). Interaction of the ERC family of RIM-binding proteins with the liprin-alpha family of multidomain proteins. *J. Biol. Chem.* 278, 42377–42385.

LaConte, L. E., Chavan, V., Liang, C., Willis, J., Schonhense, E. M., Schoch, S., et al. (2016). CASK stabilizes neurexin and links it to liprin-alpha in a neuronal activity-dependent manner. *Cell Mol. Life Sci.* 73, 3599–3621.

Lenihan, J. A., Saha, O., Heimer-McGinn, V., Cryan, J. F., Feng, G., and Young, P. W. (2017a). Decreased anxiety-related behaviour but apparently unperturbed NUMB function in ligand of NUMB Protein-X (LNX) 1/2 double knockout mice. *Mol. Neurobiol.* 54, 8090–8109.

Lenihan, J. A., Saha, O., and Young, P. W. (2017b). Proteomic analysis reveals novel ligands and substrates for LNX1 E3 ubiquitin ligase. *PLoS One* 12:e0187352. doi: 10.1371/journal.pone.0187352

Li, L., Tian, X., Zhu, M., Bulgari, D., Bohme, M. A., Goettfert, F., et al. (2014). *Drosophila* Syd-1, liprin-alpha, and protein phosphatase 2A B' subunit Wrd function in a linear pathway to prevent ectopic accumulation of synaptic materials in distal axons. *J. Neurosci.* 34, 8474–8487.

Liang, M., Xie, X., Pan, J., Jin, G., Yu, C., and Wei, Z. (2019). Structural basis of the target-binding mode of the G protein-coupled receptor kinase-interacting protein in the regulation of focal adhesion dynamics. *J. Biol. Chem.* 294, 5827–5839.

Liang, M., Jin, G., Xie, X., Zhang, W., Li, K., Niu, F., et al. (2020). Oligomerized Liprin-α promotes phase separation of ELKS for compartmentalization of presynaptic active zone proteins. *Cell Rep.* [Preprint].

Liu, Y. C., Couzens, A. L., Deshwar, A. R., Ld, B. M.-C., Zhang, X., Puviindran, V., et al. (2014). The PPFIA1-PP2A protein complex promotes trafficking of Kif7 to the ciliary tip and Hedgehog signaling. *Sci. Signal.* 7:ra117.

McDonald, N. A., Fetter, R. D., and Shen, K. (2020). Assembly of synaptic active zones requires phase separation of scaffold molecules. *Nature* 588, 454–458.

Miller, K. E., DeProto, J., Kaufmann, N., Patel, B. N., Duckworth, A., and Van Vactor, D. (2005). Direct observation demonstrates that Liprin-alpha is required for trafficking of synaptic vesicles. *Curr. Biol.* 15, 684–689.

Missler, M., Sudhof, T. C., and Biederer, T. (2012). Synaptic cell adhesion. *Cold Spring Harb. Perspect. Biol.* 4:a005694.

Najm, J., Horn, D., Wimplinger, I., Golden, J. A., Chizhikov, V. V., Sudi, J., et al. (2008). Mutations of CASK cause an X-linked brain malformation phenotype with microcephaly and hypoplasia of the brainstem and cerebellum. *Nat. Genet.* 40, 1065–1067.

Ohtsuka, T., Takao-Rikitsu, E., Inoue, E., Inoue, M., Takeuchi, M., Matsubara, K., et al. (2002). Cast: a novel protein of the cytomatrix at the active zone of synapses that forms a ternary complex with RIM1 and munc13-1. *J. Cell Biol.* 158, 577–590.

Olsen, O., Moore, K. A., Fukata, M., Kazuta, T., Trinidad, J. C., Kauer, F. W., et al. (2005). Neurotransmitter release regulated by a MALS-liprin-alpha presynaptic complex. *J. Cell Biol.* 170, 1127–1134.

Owald, D., Khorramshahi, O., Gupta, V. K., Banovic, D., Depner, H., Fouquet, W., et al. (2012). Cooperation of Syd-1 with Neurexin synchronizes pre- with postsynaptic assembly. *Nat. Neurosci.* 15, 1219–1226.

Ozel, M. N., Kulkarni, A., Hasan, A., Brummer, J., Moldenhauer, M., Daumann, I. M., et al. (2019). Serial synapse formation through filopodial competition for synaptic seeding factors. *Dev. Cell* 50, 447.e8–461.e8.

Patel, M. R., Lehrman, E. K., Poon, V. Y., Crump, J. G., Zhen, M., Bargmann, C. I., et al. (2006). Hierarchical assembly of presynaptic components in defined *C. elegans* synapses. *Nat. Neurosci.* 9, 1488–1498.

Patel, M. R., and Shen, K. (2009). RSY-1 is a local inhibitor of presynaptic assembly in *C. elegans*. *Science* 323, 1500–1503.

Petzoldt, A. G., Lutzkendorf, J., and Sigrist, S. J. (2016). Mechanisms controlling assembly and plasticity of presynaptic active zone scaffolds. *Curr. Opin. Neurobiol.* 39, 69–76.

Podufall, J., Tian, R., Knoche, E., Puchkov, D., Walter, A. M., Rosa, S., et al. (2014). A presynaptic role for the cytomatrix protein GIT in synaptic vesicle recycling. *Cell Rep.* 7, 1417–1425.

Qiao, F., and Bowie, J. U. (2005). The many faces of SAM. *Sci. STKE* 2005:re7.

Sakamoto, S., Ishizaki, T., Okawa, K., Watanabe, S., Arakawa, T., Watanabe, N., et al. (2012). Liprin-alpha controls stress fiber formation by binding to mDia and regulating its membrane localization. *J. Cell Sci.* 125, 108–120.

Samuels, B. A., Hsueh, Y. P., Shu, T., Liang, H., Tseng, H. C., Hong, C. J., et al. (2007). Cdk5 promotes synaptogenesis by regulating the subcellular distribution of the MAGUK family member CASK. *Neuron* 56, 823–837.

Schmalzigaug, R., Garron, M. L., Roseman, J. T., Xing, Y., Davidson, C. E., Arold, S. T., et al. (2007). GIT1 utilizes a focal adhesion targeting-homology domain to bind paxillin. *Cell Signal.* 19, 1733–1744.

Schoch, S., Castillo, P. E., Jo, T., Mukherjee, K., Geppert, M., Wang, Y., et al. (2002). RIM1 alpha forms a protein scaffold for regulating neurotransmitter release at the active zone. *Nature* 415, 321–326.

Schoch, S., and Gundelfinger, E. D. (2006). Molecular organization of the presynaptic active zone. *Cell Tissue Res.*326, 379–391.

Serrapages, C., Kedersha, N. L., Fazikas, L., Medley, Q., Debant, A., and Streuli, M. (1995). The lar transmembrane protein-tyrosine-phosphatase and a coiled-coil lar-interacting protein co-localize at focal adhesions. *Embo J.* 14, 2827–2838.

Serra-Pages, C., Medley, Q. G., Tang, M., Hart, A., and Streuli, M. (1998). Liprins, a family of LAR transmembrane protein-tyrosine phosphatase-interacting proteins. *J. Biol. Chem.* 273, 15611–15620.

Shen, J. C., Unoki, M., Ythier, D., Duperray, A., Varticovski, L., Kumamoto, K., et al. (2007). Inhibitor of growth 4 suppresses cell spreading and cell migration by interacting with a novel binding partner, liprin alpha1. *Cancer Res.* 67, 2552–2558.

Sheng, M., and Kim, E. (2011). The postsynaptic organization of synapses. *Cold Spring Harb. Perspect. Biol.* 3:a005678.

Shin, H., Wyszynski, M., Huh, K. H., Valtschanoff, J. G., Lee, J. R., Ko, J., et al. (2003). Association of the kinesin motor KIF1A with the multimodular protein liprin-alpha. *J. Biol. Chem.* 278, 11393–11401.

Sigrist, S. J. (2009). The Yin and Yang of synaptic active zone assembly. *Sci. Signal.* 2, e32.

Spangler, S. A., and Hoogenraad, C. C. (2007). Liprin-alpha proteins: scaffold molecules for synapse maturation. *Biochem. Soc. Trans.* 35, 1278–1282.

Spangler, S. A., Jaarsma, D., De Graaff, E., Wulf, P. S., Akhmanova, A., and Hoogenraad, C. C. (2011). Differential expression of liprin-alpha family proteins in the brain suggests functional diversification. *J. Comp. Neurol.* 519, 3040–3060.

Spangler, S. A., Schmitz, S. K., Kevenaar, J. T., de Graaff, E., de Wit, H., Demmers, J., et al. (2013). Liprin-alpha2 promotes the presynaptic recruitment and turnover of RIM1/CASK to facilitate synaptic transmission. *J. Cell Biol.* 201, 915–928.

Stafford, R. L., Ear, J., Knight, M. J., and Bowie, J. U. (2011). The molecular basis of the Caskin1 and Mint1 interaction with CASK. *J. Mol. Biol.* 412, 3–13.

Stryker, E., and Johnson, K. G. (2007). LAR, liprin alpha and the regulation of active zone morphogenesis. *J. Cell Sci.* 120, 3723–3728.

Stucchi, R., Plucinska, G., Hummel, J. J. A., Zahavi, E. E., Guerra San Juan, I., Klykov, O., et al. (2018). Regulation of KIF1A-driven dense core vesicle transport: Ca(2+)/CaM Controls DCV binding and Liprin-alpha/TANC2 Recruits DCVs to postsynaptic sites. *Cell Rep.* 24, 685–700.

Sudhof, T. C. (2012). The presynaptic active zone. *Neuron* 75, 11–25.

Sudhof, T. C. (2017). Synaptic neurexin complexes: a molecular code for the logic of neural circuits. *Cell* 171, 745–769.

Sudhof, T. C. (2018). Towards an understanding of synapse formation. *Neuron* 100, 276–293.

Sudhof, T. C. (2008). Neurotransmitter release. *Handb. Exp. Pharmacol.* 184, 1–21.

Tabuchi, K., Biederer, T., Butz, S., and Sudhof, T. C. (2002). CASK participates in alternative tripartite complexes in which Mint 1 competes for binding with Caskin 1, a novel CASK-binding protein. *J. Neurosci.* 22, 4264–4273.

Tarpey, P. S., Smith, R., Pleasance, E., Whibley, A., Edkins, S., Hardy, C., et al. (2009). A systematic, large-scale resequencing screen of X-chromosome coding exons in mental retardation. *Nat. Genet.* 41, 535–543.

Taru, H., and Jin, Y. S. (2011). The liprin homology domain is essential for the homomeric interaction of SYD-2/Liprin-alpha protein in presynaptic assembly. *J. Neurosci.* 31, 16261–16268.

Torres, V. I., and Inestrosa, N. C. (2018). Vertebrate presynaptic active zone assembly: a role accomplished by diverse molecular and cellular mechanisms. *Mol. Neurobiol.* 55, 4513–4528.

Totaro, A., Paris, S., Asperti, C., and de Curtis, I. (2007). Identification of an intramolecular interaction important for the regulation of GIT1 functions. *Mol. Biol. Cell* 18, 5124–5138.

Um, J. W., and Ko, J. (2013). LAR-RPTPs: synaptic adhesion molecules that shape synapse development. *Trends Cell Biol.* 23, 465–475.

Unoki, M., Shen, J. C., Zheng, Z. M., and Harris, C. C. (2006). Novel splice variants of ING4 and their possible roles in the regulation of cell growth and motility. *J. Biol. Chem.* 281, 34677–34686.

Wagner, O. I., Esposito, A., Kohler, B., Chen, C. W., Shen, C. P., Wu, G. H., et al. (2009). Synaptic scaffolding protein SYD-2 clusters and activates kinesin-3 UNC-104 in *C. elegans*. *Proc. Natl. Acad. Sci. U.S.A.* 106, 19605–19610.

Wakita, M., Yamagata, A., Shiroshima, T., Izumi, H., Maeda, A., Sendo, M., et al. (2020). Structural insights into selective interaction between type IIa receptor protein tyrosine phosphatases and Liprin-alpha. *Nat. Commun.* 11:649.

Wang, S. S. H., Held, R. G., Wong, M. Y., Liu, C., Karakhanyan, A., and Kaeser, P. S. (2016). Fusion competent synaptic vesicles persist upon active zone disruption and loss of vesicle docking. *Neuron* 91, 777–791.

Wang, X., Hu, B., Zieba, A., Neumann, N. G., Kasper-Sonnenberg, M., Honsbein, A., et al. (2009). A protein interaction node at the neurotransmitter release site: domains of aczonin/piccolo, bassoon, CAST, and rim converge on the N-Terminal domain of Munc13-1. *J. Neurosci.* 29, 12584–12596.

Waterhouse, A. M., Procter, J. B., Martin, D. M. A., Clamp, M., and Barton, G. J. (2009). Jalview Version 2-a multiple sequence alignment editor and analysis workbench. *Bioinformatics* 25, 1189–1191.

Wei, Z., Zheng, S., Spangler, S. A., Yu, C., Hoogenraad, C. C., and Zhang, M. (2011). Liprin-mediated large signaling complex organization revealed by the liprin-alpha/CASK and liprin-alpha/liprin-beta complex structures. *Mol. Cell* 43, 586–598.

Wentzel, C., Sommer, J. E., Nair, R., Stiefvater, A., Sibarita, J. B., and Scheiffele, P. (2013). mSYD1A, a mammalian synapse-defective-1 protein, regulates synaptogenic signaling and vesicle docking. *Neuron* 78, 1012–1023.

Won, S. Y., and Kim, H. M. (2018). Structural Basis for LAR-RPTP-Mediated Synaptogenesis. *Mol. Cells* 41, 622–630.

Wong, M. Y., Liu, C., Wang, S. S. H., Roquas, A. C. F., Fowler, S. C., and Kaeser, P. S. (2018). Liprin-alpha3 controls vesicle docking and exocytosis at the active zone of hippocampal synapses. *Proc. Natl. Acad. Sci. U.S.A.* 115, 2234–2239.

Wu, G. H., Muthaiyan Shanmugam, M., Bhan, P., Huang, Y. H., and Wagner, O. I. (2016). Identification and characterization of LIN-2(CASK) as a regulator of kinesin-3 UNC-104(KIF1A) motility and clustering in neurons. *Traffic* 17, 891–907.

Wu, X., Cai, Q., Chen, Y., Zhu, S., Mi, J., Wang, J., et al. (2020). Structural Basis for the High-Affinity Interaction between CASK and Mint1. *Structure* 28, 664.e–673.e.

Wu, X., Cai, Q., Shen, Z., Chen, X., Zeng, M., Du, S., et al. (2019). RIM and RIM-BP form presynaptic active-zone-like condensates via phase separation. *Mol. Cell* 73, 971.e5–984.e5.

Wyszynski, M., Kim, E., Dunah, A. W., Passafaro, M., Valtschanoff, J. G., Serra-Pages, C., et al. (2002). Interaction between GRIP and liprin-alpha/SYD2 is required for AMPA receptor targeting. *Neuron* 34, 39–52.

Xie, X., Luo, L., Liang, M., Zhang, W., Zhang, T., Yu, C., et al. (2020). Structural basis of liprin-alpha-promoted LAR-RPTP clustering for modulation of phosphatase activity. *Nat. Commun.* 11:169.

Zeng, M., Chen, X., Guan, D., Xu, J., Wu, H., Tong, P., et al. (2018). Reconstituted postsynaptic density as a molecular platform for understanding synapse formation and plasticity. *Cell* 174, 1172.e16–1187.e16.

Zhang, H., Webb, D. J., Asmussen, H., and Horwitz, A. F. (2003). Synapse formation is regulated by the signaling adaptor GIT1. *J. Cell Biol.* 161, 131–142.

Zhang, H., Webb, D. J., Asmussen, H., Niu, S., and Horwitz, A. F. (2005). A GIT1/PIX/Rac/PAK signaling module regulates spine morphogenesis and synapse formation through MLC. *J. Neurosci.* 25, 3379–3388.

Zhang, Y. V., Hannan, S. B., Stapper, Z. A., Kern, J. V., Jahn, T. R., and Rasse, T. M. (2016). The *Drosophila* KIF1A homolog unc-104 Is important for site-specific synapse maturation. *Front. Cell Neurosci.* 10:207. doi: 10.3389/fncel.2016.00207

Zhang, Z. M., Simmerman, J. A., Guibao, C. D., and Zheng, J. J. (2008). GIT1 paxillin-binding domain is a four-helix bundle, and it binds to both paxillin LD2 and LD4 motifs. *J. Biol. Chem.* 283, 18685–18693.

Zhen, M., and Jin, Y. (1999). The liprin protein SYD-2 regulates the differentiation of presynaptic termini in *C. elegans*. *Nature* 401, 371–375.

Zhen, M., and Jin, Y. (2004). Presynaptic terminal differentiation: transport and assembly. *Curr. Opin. Neurobiol.* 14, 280–287.

Zhu, J., Zhou, Q., Xia, Y., Lin, L., Li, J., Peng, M., et al. (2020). GIT/PIX condensates are modular and ideal for distinct compartmentalized cell signaling. *Mol. Cell* 79, 782.e6–796.e6.

Zurner, M., Mittelstaedt, T., tom Dieck, S., Becker, A., and Schoch, S. (2011). Analyses of the spatiotemporal expression and subcellular localization of liprin-alpha proteins. *J. Comp. Neurol.* 519, 3019–3039.

Zurner, M., and Schoch, S. (2009). The mouse and human Liprin-alpha family of scaffolding proteins: genomic organization, expression profiling and regulation by alternative splicing. *Genomics* 93, 243–253.

Conflict of Interest: The authors declare that the research was conducted in the absence of any commercial or financial relationships that could be construed as a potential conflict of interest.

frontiers
in Cell and Developmental Biology

ORIGINAL RESEARCH
published: 09 April 2021
doi: 10.3389/fcell.2021.667412

Elevated Levels of miR-144-3p Induce Cholinergic Degeneration by Impairing the Maturation of NGF in Alzheimer's Disease

Lan-Ting Zhou[1,2]†, Juan Zhang[1,2]†, Lu Tan[1,2], He-Zhou Huang[1,2], Yang Zhou[1,2], Zhi-Qiang Liu[1,2], Youming Lu[2], Ling-Qiang Zhu[1,2], Chengye Yao[3]* and Dan Liu[2]*

[1] Department of Pathophysiology, School of Basic Medicine, Tongji Medical College, Huazhong University of Science and Technology, Wuhan, China, [2] Collaborative Innovation Center for Brain Science, The Institute of Brain Research, Huazhong University of Science and Technology, Wuhan, China, [3] Department of Neurology, Union Hospital, Tongji Medical College, Huazhong University of Science and Technology, Wuhan, China

OPEN ACCESS

Edited by:
Zhitao Hu,
The University of Queensland,
Australia

Reviewed by:
Zhifang Dong,
Chongqing Medical University, China
Quan-Hong Ma,
Soochow University, China
Elizabeth J. Coulson,
The University of Queensland,
Australia

***Correspondence:**
Chengye Yao
yaochebgye@hust.edu.cn
Dan Liu
liudan_echo@mail.hust.edu.cn

† These authors have contributed equally to this work

Specialty section:
This article was submitted to
Membrane Traffic,
a section of the journal
Frontiers in Cell and Developmental
Biology

Received: 13 February 2021
Accepted: 11 March 2021
Published: 09 April 2021

Citation:
Zhou L-T, Zhang J, Tan L,
Huang H-Z, Zhou Y, Liu Z-Q, Lu Y,
Zhu L-Q, Yao C and Liu D (2021)
Elevated Levels of miR-144-3p Induce
Cholinergic Degeneration by Impairing
the Maturation of NGF in Alzheimer's
Disease.
Front. Cell Dev. Biol. 9:667412.
doi: 10.3389/fcell.2021.667412

Cholinergic degeneration is one of the key pathological hallmarks of Alzheimer's disease (AD), a condition that is characterized by synaptic disorders and memory impairments. Nerve growth factor (NGF) is secreted in brain regions that receive projections from the basal forebrain cholinergic neurons. The trophic effects of NGF rely on the appropriate maturation of NGF from its precursor, proNGF. The ratio of proNGF/NGF is known to be increased in patients with AD; however, the mechanisms that underlie this observation have yet to be elucidated. Here, we demonstrated that levels of miR-144-3p are increased in the hippocampi and the medial prefrontal cortex of an APP/PS1 mouse model of AD. These mice also exhibited cholinergic degeneration (including the loss of cholinergic fibers, the repression of choline acetyltransferase (ChAT) activity, the reduction of cholinergic neurons, and an increased number of dystrophic neurites) and synaptic/memory deficits. The elevated expression of miR-144-3p specifically targets the mRNA of tissue plasminogen activator (tPA) and reduces the expression of tPA, thus resulting in the abnormal maturation of NGF. The administration of miR-144-3p fully replicated the cholinergic degeneration and synaptic/memory deficits observed in the APP/PS1 mice. The injection of an antagomir of miR-144-3p into the hippocampi partially rescued cholinergic degeneration and synaptic/memory impairments by restoring the levels of tPA protein and by correcting the ratio of proNGF/NGF. Collectively, our research revealed potential mechanisms for the disturbance of NGF maturation and cholinergic degeneration in AD and identified a potential therapeutic target for AD.

Keywords: Alzheimer's disease, NGF, miR-144-3p, cholinergic degeneration, synaptic disorder

INTRODUCTION

Alzheimer's disease (AD) is a progressive neurodegenerative disease and the most common cause of dementia (Alzheimer's Disease Facts and Figures, 2020). The main clinical symptoms of AD are progressive learning and memory deficits. Although researchers have revealed that the amyloid cascade and tauopathy play important roles in the pathogenesis of AD (Sotthibundhu et al., 2008;

Knowles et al., 2009; Ovsepian et al., 2014), related drug discovery strategies and clinical trials have yet to meet with success. Until now, only five drugs have been approved by the Food and Drug Administration (FDA) for the therapy of AD; three of these (donepezil, galantamine, and rivastigmine) are cholinesterase inhibitors, thus suggesting that cholinergic dysfunction plays a critical role in the progression of AD. Previous researchers also reported that in the early stages of AD, it is the cholinergic synapses that are particularly affected by an overload of Aβ, rather than other types of synapses (Wong et al., 1999; Bell et al., 2006). In line with this, it was demonstrated that cholinergic neurons in the basal nucleus of Meynert were selectively affected in patients with AD (Whitehouse et al., 1981). Moreover, the transcription of choline acetyltransferase (ChAT) was severely repressed in existing cholinergic neurons (Wilcock et al., 1982). In the brain of aged AD transgenic mice (Tg2576), researchers observed strong staining of acetylcholinesterase (AChE) associated with dystrophic fibers within cholinergic projections (Apelt et al., 2002). Collectively, all of these abnormalities in the cholinergic systems show strong correlations with impaired synaptic/memory in AD (Oda, 1999). Therefore, it is important to investigate the precise mechanisms that cause such cholinergic dysfunction.

Nerve growth factor (NGF) is a key neurotrophic factor that is involved in the regulation of growth, maintenance, proliferation, and survival of cholinergic neurons (Niewiadomska et al., 2011). Specifically, NGF has been reported to elevate the activity and promote the expression of ChAT (Pongrac and Rylett, 1998), thus increasing the synthesis and release of acetylcholine and the expression of vesicular acetylcholine transporter (Oosawa et al., 1999). Previous work has shown that endogenous NGF is mainly generated in the hippocampi, the neocortex, and other targets within the basal forebrain (Johnston et al., 1987; Koliatsos et al., 1990; Zhang et al., 2013). Secreted NGF can be trafficked in a retrograde manner to basal forebrain cholinergic neurons (BFCNs) and plays an important role in modulating cholinergic synaptic transmission and hippocampal plasticity (Conner et al., 2009). In the AD brain, the levels of proNGF, the precursor of NGF, are known to be increased (Fahnestock et al., 1996), thus leading to a change in the proNGF/NGF ratio. Previous researchers suggested that proNGF is neurotoxic because it can bind with the p75 receptor to activate apoptotic pathways (Ioannou and Fahnestock, 2017). Numerous lines of evidence have suggested that the increased ratio of proNGF/NGF in the AD brain is due to the defective processing of proNGF into the mature form of NGF (Cuello and Bruno, 2007; Bruno et al., 2009a). This is because reduced levels of tissue plasminogen activator (tPA) and plasmin, the two key enzymes required for the processing of proNGF, have been detected in the brains of patients with mild cognitive impairments (Bruno et al., 2009a). These patients also had increased levels of MMP, an enzyme that degrades NGF (Bruno et al., 2009b). If we are to develop an NGF-based therapeutic strategy for AD, it is important that we strive to understand the mechanisms that are responsible for the deregulation of proNGF/NGF processing, particularly with regard to the reduction of tPA or plasmin.

In this study, we demonstrate that the elevation of miR-144-3p in the hippocampi and prefrontal cortex can directly inhibit the translation of its target, tPA. The loss of tPA results in an increase in the proNGF/NGF ratio, which then promotes cholinergic degeneration in a mouse model of AD. The artificial upregulation of miR-144-3p in wild-type mice fully simulated these cholinergic degeneration and synaptic/memory impairments. Finally, administration of the antagomir of miR-144-3p partially rescued the cholinergic degeneration and synaptic/memory impairments in AD mice by rebalancing the proNGF/NGF ratio.

MATERIALS AND METHODS

Animals

APPswe/PS1dE9 mice (APP/PS1 mice) were purchased from the Jackson Laboratory (Bar Harbor, ME, United States, stock #034829) and conserved in the Experimental Animal Central of Tongji Medical College at Huazhong University of Science and Technology. The genotyping protocol was performed according to the manufacturer's instructions, and wild-type littermates were used as control. The animals were bred at room temperature with food and water *ad libitum* on a 12-h light/dark cycle. All animal experiments were approved by the Animal Care and Use Committee of Tongji Medical College and under its guidelines.

Cell Culture

The mouse neuroblastoma N2a cell line was maintained in DMEM supplemented with 10% fetal bovine serum (FBS) at 37°C in a 5% carbon dioxide (CO_2) condition. The culture medium was replaced every 3 days. Cell transfection was performed by Lipofectamine 2000 (Invitrogen, Carlsbad, CA, United States) according to the manufacturer's instruction.

Context–Place Memory Test

Apparatus

The experimental device is two wooden boxes (30 × 50 × 50 cm), and their bottom and walls are, respectively, pasted paper with different patterns and colors to distinguish the two different contexts (1 and 2).

Procedure

Mice were familiarized to the experimental room for 30 min before the behavioral experiments and then were placed in context 1 for free exploration for 15 min. On the second day, the mice were habituated in context 2 for 15 min; the experimental process was the same as the first day. On the third day, the mice were habituated to explore contexts 1 and 2 for 5 min with a 1-h interval. Context 1 (2) was cleaned with 70% ethanol between each trial. On the fifth day, two objects with similar shape and color (A/B) were placed in contexts 1 and 2. Two of object A are placed on the left and north of context 1, and two of object B are placed on the right and north of context 2. Then the mice were placed in the center of contexts 1 and 2 for 2 min to explore the contexts and objects to learn the spatial arrangement of the objects that are associated with each context. On the test stage, two of object C are placed on the left and right of context 1 or 2, and the mice were allowed to explore context 1 or 2 for 2 min. Time spent exploring the novel object within familiar location (TF) and novel object within novel location (TN) was measured. The discrimination index was defined as follows: (TN − TF)/(TN + TF) × 100%. This behavioral paradigm was performed as previously reported (Lesburguères et al., 2017).

Quantitative RT-PCR

The total RNA was extracted by a TRIzol reagent (Invitrogen, CA, United States) following the manufacturer's instructions. One microgram of RNA was reversely transcripted for mRNA or miRNA by a First-Strand cDNA Synthesis Kit (TOYOBO, Osaka, Japan) or a miRcute Plus miRNA First-Strand cDNA Kit (Tiangen, Beijing, China), respectively. The standard qPCR was performed on an ABI StepOnePlus real-time quantitative PCR instrument using TB Green® Premix Ex Taq^{TM} II (Takara, Tokyo, Japan). The reaction was performed with pre-denaturation at 95°C for 3 min, followed by 40 cycles of denaturation at 95°C for 5 s and annealing at 60°C for 30 s. This cycle was followed by a melting curve analysis, ranging from 60 to 95°C with temperature increases by steps of 0.5°C every 10 s. The primers used for RT-PCR detection were listed in **Table 1**.

Western Blot

Mice were sacrificed, and their brains were immediately dissected. The tissues were extracted with RIPA Lysis Buffer (Beyotime, Shanghai, China) with a protease inhibitor cocktail (Roche) on ice. After boiling for 10 min, the protein samples were lysed by 20 pulses of sonication, and the concentration of proteins was measured by a BCA Protein Assay Reagent (Thermo Fisher Scientific, IL, United States). Proteins were separated by 10% SDS-PAGE gel and transferred to nitrocellulose membranes (GE Healthcare Life Sciences, Loughborough, United Kingdom). After blocking in 5% non-fat milk for 30 min, the membranes were incubated with primary antibodies (**Table 2**) overnight at 4°C, followed by washing with phosphate-buffered saline with Tween 20 (PBST). Then the membranes were incubated with anti-rabbit or anti-mouse IgG-conjugated secondary antibodies IRDye 800 (1:10,000; Rockland Immunochemicals) for 1 h at room temperature. The protein bands were visualized by using the Odyssey Imaging System (LI-COR, Lincoln, NE, United States).

Immunohistochemistry

The immunohistochemistry was performed according to the previously described protocol (Yan et al., 2018). Mice were anesthetized using a mixture of ketamine (100 mg/kg) and dexmedetomidine (0.5 mg/kg) with intraperitoneal injection. Then the mice were perfused with 0.9% normal saline followed by precooled 4% paraformaldehyde solution. The brains were carefully taken out of the cranial cavity and soaked in 4% paraformaldehyde solution overnight. After gradient dehydration of 30% sucrose solution, coronal slices were cut with a thickness of 30 μm in a freezing cryostat (SLEE, Mainz, Germany). Brain slices were rinsed with 1 × PBS for 10 min and incubated with 0.3% H_2O_2 and 0.5% Triton X-100 at room temperature for 30 min to break the membrane. After those section were rinsed with PBS solution thrice, the non-specific antigen was blocked by incubation with 5% bovine serum albumin (BSA) in 1 × PBS for 30 min at room temperature. The sections were then incubated with primary antibody goat-anti-ChAT (Merck Millipore, AB144P, 1:400) at 4°C overnight. The slices were rinsed with 1 × PBS thrice and incubated with the secondary antibody biotinylated anti-goat (Vector Laboratories, BA-9500, 1:300) diluted with PBS for 2 h at 37°C. They were washed in PBS thrice and added with streptomycin-labeled peroxidase working solution (ABC-kit, Vector Laboratories, PK-4500, 1:300) for 1 h at 37°C. After being washed in PBS, the brain slices were stained in 3,3′-diaminobenzidine (DAB) staining solution (D-8001, Sigma-Aldrich, Germany) for 5–10 min, and then PBS was added to stop the reaction. Then the brain slices were stuck on glass slides coated with gelatin. After being dried, they were dehydrated in a series of ethanol, 75, 80, 95, and 100% ethanol, for 10 min each. And they were made transparent in xylene and sealed. Digital images for all slices were taken with a Coolpix 5000 Nikon Camera.

Fluorescence *in situ* Hybridization (FISH)

FISH was performed as previously described (Su et al., 2019). Briefly, the mice were perfused with 0.9% NaCl and 4% PFA. The brain tissues were fixed in PFA at 4°C for 24 h and then

TABLE 1 | Primers.

Gene	ID	qPCR Primer (from 5′ to 3′)
mmu-miR-144-3p	MIMAT0000156	Forward Sequence: TACAGTATAGATGATGTACT Reverse Sequence: GCTGTCAACGATACGCTACG
U6	19862	Forward Sequence: GATGACACGCAAATTCGTGAA Reverse Sequence: GCTGTCAACGATACGCTACG
tPA	18791	Forward Sequence: GTTACACAGCGTGGAGGACCAA Reverse Sequence: CACGTCAGCTTTCGGTCCTTCA
NGF	18049	Forward Sequence: GTTTTGCCAAGGACGCAGCTTTC Reverse Sequence: GTTCTGCCTGTACGCCGATCAA
Plg	18815	Forward Sequence: CCTCATAGGCACAACAGGACAC Reverse Sequence: TGGCTGTCAGTGGTATAGCACC
β-Actin	11461	Forward Sequence: GAGACCTTCAACACCCCAGC Reverse Sequence: GGAGAGCATAGCCCTCGTAGAT

TABLE 2 | Antibodies.

Name	Source	Cat#	WB/IF/IHC	RRID
ChAT	Millipore	AB144P	1:100 for IHC	RRID:AB_2079751
NGF	Abcam	ab52918	1:500 for WB	RRID:AB_881254
tPA	ABclonal	A4210	1:200 for IF, 1:1,000 for WB	RRID:AB_2863209
Plg	ProteinTech	66399-1-Ig	1:1,000 for WB	RRID:AB_2881773
β-Actin	ProteinTech	60008-1-Ig	1:3,000 for WB	RRID:AB_2289225

dehydrated in 30% (w/v) sucrose in PFA at 4°C until complete dehydration. The brain slices were cut at 20-μm thickness on a cryostat. The probe for miR-144-3p was synthesized by TSINGKE (Wuhan, China), and FISH was performed according to the manufacturer's instruction. All images were obtained with a confocal microscope (ZEISS, LSM 800).

Administration of miR-144-3p Agomir and Antagomir

mmu-miR-144-3p agomir, antagomirs, and scrambled control were purchased from RiboBio (Guangzhou, China). Mice were anesthetized, and holes were made in the skull above the hippocampal CA3 (bregma: anterior/posterior −2.0 mm, medial/lateral ± 2.35 mm, and dorsal/ventral −2.35 mm). The concentration for miR-144-3p referenced previously published articles (Wang et al., 2018). About 1.5 μl of miR-144-3p antagomirs (50 μM) was stereotactically injected into the hippocampi of 11-months-old APP/PS1 mice every 2 weeks. The needle was left in the animal brain for 10 min, and it was then slowly withdrawn. Subsequently, the wound was sutured, and mice were allowed to recover.

Enzyme-Linked Immunosorbent Assay (ELISA)

The NGF ELISA was performed by mouse an NGF ELISA kit (MBS702384, MyBioSource, Inc., United States) according to the manufacturer's instructions. Briefly, 100 mg of tissue was homogenized in 1 ml of 1 × PBS. After two freeze–thaw cycles were performed to break the cell membranes, the homogenates were centrifuged at 5,000 g, 4°C for 5 min. The supernate was removed and assayed immediately. A 100 μl sample was added into a plate well and incubated for 2 h at 37°C. NGF was captured using NGF antibody-coated plates, followed by detection with biotinylated antibody. Samples were incubated with the secondary antibody and then with avidin horseradish peroxidase (HRP). Plates were developed using tetramethylbenzidine (TMB) as a substrate. After the reaction stopped, optical density was read at 450 nm. Raw data were converted to nanograms per gram of wet tissue by comparison to a standard curve of synthetic A.

ChAT Activity Analysis

ChAT activity was determined by using a ChAT assay kit (Jiancheng Bioengineering Institute, Nanjing, China), following the manufacturer's protocol. The tissue was removed from mice and homogenated in saline according to a weight–volume ratio of 5% (g/ml). The mixed solution was prepared at 37°C for 5 min according to the instructions, and a 25 μl of the sample was then added into the mixed solution at 37°C for 20 min. Subsequently, those samples were boiled at 100°C for 2 min to terminate the reaction, and 425 μl of double-distilled water was added. Then, samples were centrifuged at 4,000 rpm for 10 min, and 10 μl of solution 7 was added into 500 μl of supernatant for 15 min. Finally, optical density was measured at 324 nm. The ChAT activity (U/g tissue) was calculated according to the manufacturer's instructions.

Long-Term Potentiation (LTP) Recording

Mice were sacrificed, and the brains were quickly immersed in ice-cold artificial cerebrospinal fluid (ACSF) (in mM: 3.0 KCl, 2.5 $CaCl_2$, 125 NaCl, 1.25 KH_2PO_4, 26 $NaHCO_3$, 1.2 $MgSO_4$, and 10 glucose), which was saturated with 95% oxygen and 5% carbon dioxide. Coronal brain slices of 300 μm were prepared with a vibratome (VT1000S, Leica, Germany). Brain sections were recovered in the oxygenated ACSF at 32°C for 30 min and then at room temperature for 1 h constantly immersed in ACSF. Then, brain sections were recorded by a planar multielectrode recording setup (MED64, Alpha Med Sciences, Japan). An electrophysiological recording method and statistical analysis were performed as previously reported (Wang et al., 2018).

Luciferase Activity Assay

The wild-type or mutant tPA 3′-untranslated region (UTR) plasmid was cloned and inserted into psiCHECK-2 within *Xho*I and *Not*I restriction sites located downstream of the *Renilla* luciferase gene. All primers for cloning are provided as follows: wild-type tPA 3′-UTR (forward primer: 5′-CAA AGAAAGCCCAGCTCCTTC-3′, reverse primer: 5′-TTG GAAAAGTGTGAAAAATACCTC-3′); mutant tPA 3′-UTR (forward primer: 5′-GTATGTAATATCTCTTAAATAATAAATT CAGAGGTATTTTTCACA-3′, reverse primer: 5′-TAAGAGA TATTACATACAAAGTTATAGTAACAAAGTAAAAACTAAAA TAG-3′). Site-directed mutation of tPA 3′-UTR was performed by using Mut Express II Fast Mutagenesis Kit V2 (Vazyme, Nanjing, China). These plasmids were cotransfected into N2a cells with the miR-144-3p or the scramble agomir at a final concentration of 100 nM. After 48 h, cells were harvested, and lysates were used for firefly and *Renilla* luciferase activities using the dual-luciferase reporter assay kit (Promega) according to the manufacturer's instruction. The normalized values (*Renilla*/firefly activity) were used for analysis. Experiments were performed in triplicate.

Statistical Analysis

All data were shown as the mean ± SEM and analyzed using GraphPad Prism software (version 8). A two-tailed unpaired Student's *t*-test was used to assess the variance between two groups, and the difference among multiple groups was analyzed by one-way ANOVA adjusted with Tukey's multiple comparisons. Value with $p < 0.05$ are considered statistically significant. Both $^{**}p < 0.01$ and $^{***}p < 0.001$ represent extremely significant difference. All the statistical analysis data are supplied in **Supplementary Table 2**.

RESULTS

Degeneration of the Cholinergic System Was Accompanied by Synaptic and Memory Impairments in APP/PS1 Mice

To investigate cholinergic dysfunction in a mouse model of AD, we first performed immunohistochemistry with an anti-ChAT antibody to identify cholinergic fibers in the hippocampi and the medial prefrontal cortex (mPFC), the two major regions of the brain that were projected from BFCNs (Ballinger et al., 2016). We found that the intensity of ChAT immunostaining was dramatically reduced in the hippocampi of 12-months-old AD mice when compared to that in the age-matched C57 controls (**Figures 1A,B**), thus indicating the loss of cholinergic fibers in AD. Specifically, the densities of cholinergic fibers had decreased to 74, 71, and 63% in the CA1, CA3, and DG areas of AD mice, respectively, when compared with wild-type controls (**Figures 1C–E**). In addition, the expression of ChAT protein and the levels of ChAT enzyme activity in the hippocampi were also significantly reduced in AD mice (**Figures 1F,G**). Similar results were also found in the mPFC region (**Supplementary Figures 1A–C**). Importantly, we observed some dystrophic neurites in the hippocampi and

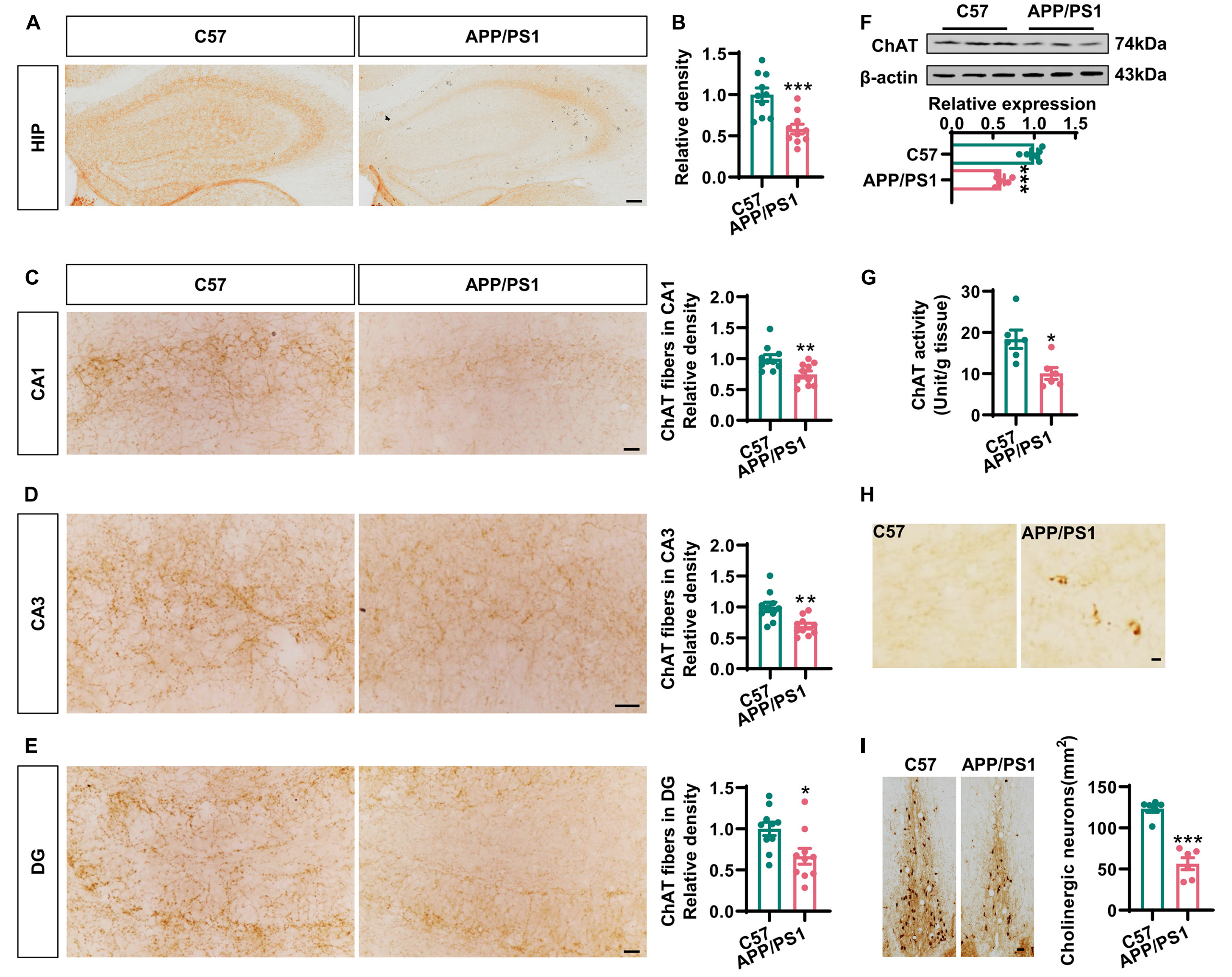

FIGURE 1 | The cholinergic dysfunction was impaired in the hippocampi of AD mice. **(A)** Representative immunohistochemical images in the hippocampi stained with anti-ChAT antibody from APP/PS1 mice and age-matched C57 mice. Bar = 100 μm. **(B)** The relative density of ChAT fibers was analyzed by ImageJ. Unpaired Student's *t*-test, *n* = 10 from four to five mice for each group, $^{***}p < 0.001$. **(C–E)** Representative immunohistochemical images in CA1, CA3, and DG stained with anti-ChAT antibody; the relative density of ChAT fibers was analyzed in CA1 **(C)**, CA3 **(D)**, and DG **(E)**. Bar = 20 μm. Unpaired Student's *t*-test, *n* = 10 from six mice for each group, $^{**}p < 0.01$ and $^{*}p < 0.05$. **(F)** The protein level of ChAT in the hippocampi was measured by western blotting, and the quantitative analysis was performed in the lower panel. Unpaired Student's *t*-test, *n* = 6 mice for each group, $^{***}p < 0.001$. **(G)** The ChAT enzyme activity in the hippocampi was measured by an ELISA kit. Unpaired Student's *t*-test, *n* = 6 mice for each group, $^{*}p < 0.05$. **(H)** Representative immunohistochemical images of dystrophic neurites in the hippocampi stained with anti-ChAT antibody from APP/PS1 mice and age-matched C57 mice. Bar = 10 μm. **(I)** Representative immunohistochemical images of ChAT-positive neurons in the basal nucleus of Meynert stained with anti-ChAT antibody. The quantitative analysis was performed and shown in the right panel. Bar = 50 μm. Unpaired Student's *t*-test, *n* = 6 mice for each group, $^{***}p < 0.001$.

the mPFC of AD mice but not in control mice (**Figure 1H** and **Supplementary Figure 1D**). As expected, the loss of ChAT-positive neurons was obvious in the basal nucleus of Meynert (**Figure 1I**), which was consistent with previous report (Foidl et al., 2016). Collectively, these data strongly suggested that the degeneration of the cholinergic system occurs in the forebrain of AD mice.

The cholinergic system plays an important role in hippocampal synaptic plasticity and memory (Haam and Yakel, 2017). Next, we examined LTP in the CA3–CA1 synapses. We found that the input–output curve of the CA3–CA1 circuit was lower in the AD mice when compared to that in wild-type mice (**Figure 2A**). Following HFS stimulation, the normalized fEPSP was also reduced in the AD mice (**Figures 2B,C**). We also evaluated context–place memory by applying the where–which task (**Figure 2D**); this is a test that is known to rely on normal cholinergic functions (Easton et al., 2011). We found that wild-type mice exhibited exploration scores that were significantly greater than chance, while the AD mice did not (**Figure 2E**). These data suggested that synaptic plasticity and memory that were dependent on the cholinergic system were impaired in AD mice.

Disturbance of the proNGF/NGF Ratio in AD Mice Was Caused by the Reduction of tPA and Plasmin

It has been established that mature NGF plays an important role in maintaining the normal function of the cholinergic system (Cuello et al., 2019). Therefore, we first examined the expression of NGF in the hippocampi by Q-PCR, ELISA, and western blotting. In line with previous studies (Fahnestock et al., 1996), the levels of mRNA encoding NGF did not change although the total level of NGF increased dramatically in AD mice (**Figures 3A,B**). This raised the question as to whether NGF deregulation is involved in the cholinergic degeneration of AD mice. We noted that the levels of proNGF, but not mature NGF, were increased in AD mice (**Figures 3C,D**), thus suggesting the disturbance of the proNGF/NGF ratio, an occurrence that has been validated in the brain of AD patients (Peng et al., 2004). Next, we investigated how the proNGF/NGF imbalance

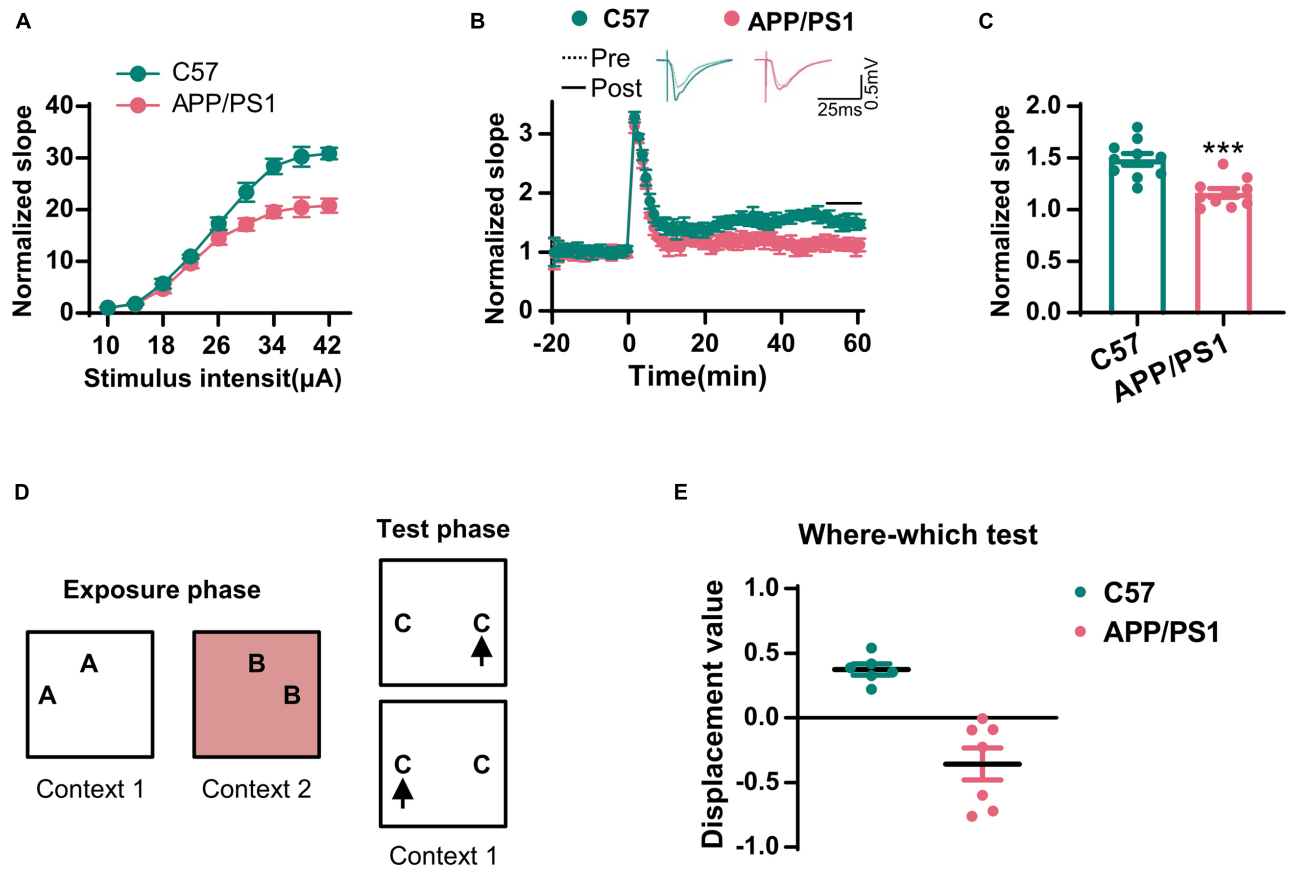

FIGURE 2 | The synaptic transmission and context–place memory were derogated in AD mice. **(A)** The input–output curve of the CA3–CA1 LTP was shown. **(B)** The electrophysiological recording to detect the fEPSP slope was used to evaluate the CA3–CA1 LTP. The representative fEPSP traces were shown in the upper panel, and the relative fEPSP slopes were shown in the lower panel. **(C)** The fEPSP slope of the last 5 min was statistically analyzed. Unpaired Student's *t*-test; $n = 10$ slices from three mice for each group, $^{***}p < 0.001$. **(D)** A schematic diagram of the where–which test was used to examine the context–place memory. **(E)** The displacement value in the where–which test was evaluated. Unpaired Student's *t*-test, $n = 6–7$ mice for each group, $^{***}p < 0.001$.

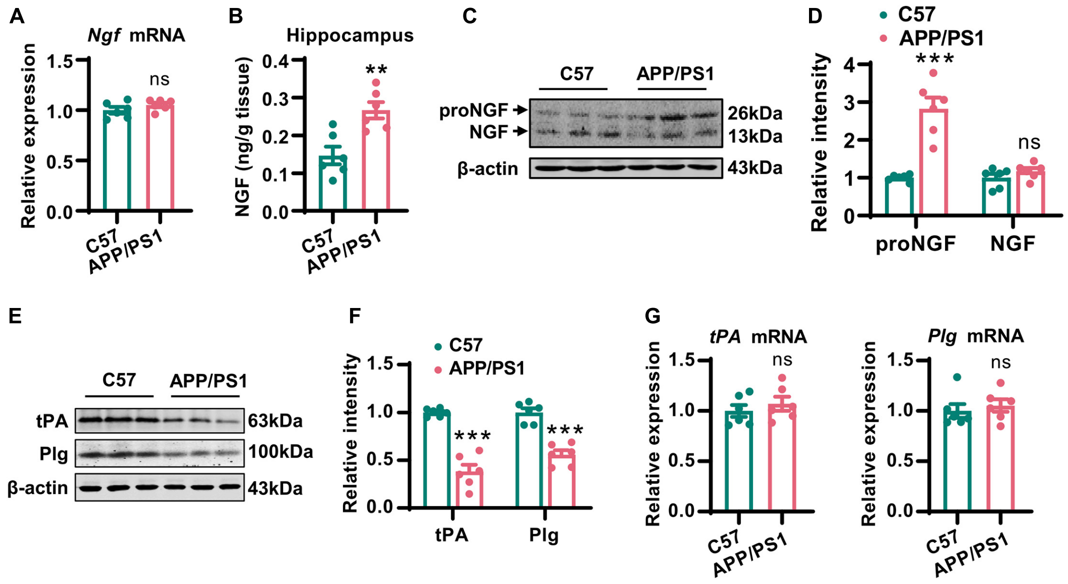

FIGURE 3 | Disturbance of the proNGF/NGF ratio in AD mice was caused by the reduction of tPA and plasmin. **(A)** The NGF mRNA in hippocampi of 12-months-old APP/PS1 mice and C57 mice was examined by Q-PCR. Unpaired two-tailed Student's t-test, $n = 6$ mice for each group; ns, no significance. **(B)** The total NGF in hippocampi of 12-months-old APP/PS1 mice and C57 mice was measured by an ELISA kit. Unpaired two-tailed Student's t-test, $n = 6$ mice for each group, $^{**}p < 0.01$. **(C,D)** The protein level of mature NGF in the hippocampi of 12-months-old APP/PS1 mice and C57 mice was detected by western blotting. The representative images were shown in **(C)**, and quantitative analysis was shown in **(D)**. Multiple t-test adjusted with the Holm-Šidák method, $n = 6$ mice for each group, $^{***}p < 0.001$. **(E,F)** The protein levels of tPA and plasminogen (Plg) were examined in the hippocampi of 12-months-old APP/PS1 mice and C57 mice. The representative images were shown in **(E)**, and quantitative analysis was shown in **(F)**. Multiple t-test adjusted with the Holm–Šidák method, $n = 6$ for each group, $^{***}p < 0.001$. **(G)** The mRNA levels of tPA and Plg in the hippocampi of 12-months-old APP/PS1 mice and C57 mice were examined by Q-PCR. Unpaired two-tailed Student's t-test, $n = 6$ mice for each group; ns, no significance.

was induced. Considering these data, we predicted that an impairment of NGF maturation might be involved. As tPA and plasmin are the two most critical enzymes required for the maturation of NGF (Bruno and Cuello, 2006), we then examined the mRNA and protein levels of these two molecules. We found that the protein levels of tPA and plasmin were significantly lower in the hippocampi of AD mice than in the wild-type mice (**Figures 3E,F**); however, the levels of mRNA encoding tPA and plasmin remained unchanged (**Figure 3G**). Thus, the loss of tPA and plasmin might be crucial for disturbance in the proNGF/NGF ratio.

Increased Expression of miR-144-3p Led to the Translational Repression of tPA

Considering that the loss of tPA was not due to the suppression of transcription, we next investigated whether posttranscriptional regulation might be involved. It is known that miRNAs are able to control gene expression at the posttranscriptional level by hybridizing to target mRNAs and thereby regulating their translation or stability (Jonas and Izaurralde, 2015). Previous researchers have reported alterations in a range of miRNAs in the AD brain (Wang et al., 2019). Therefore, we attempted to investigate whether any of these miRNAs may play an important role in the posttranscriptional repression of tPA. By using three online prediction tools (TargetScan, miRDB, and miRcode), we found that miR-144-3p may represent a key regulatory miRNA for tPA and plasmin (**Figure 4A**, **Supplementary Figure 2**, and **Supplementary Table 1**). Next, we investigated the levels of miR-144-3p in the hippocampi and found that levels of this miRNA were increased in AD mice (**Figure 4B**). By using a luciferase reporter system, we identified that miR-144-3p is able to bind with the wild-type 3′-UTR of tPA. However, when the seed-region binding site in the 3′-UTR of tPA was mutated, miR-144-3p cannot bind with it (**Figure 4C**). Furthermore, the binding site for miR-144-3p in the 3′-UTR of tPA is conserved in mammalian species (**Figure 4D**). In N2a cells, the application of the agomir or antagomir of miR-144-3p was able to downregulate or upregulate the protein levels but not the mRNA levels of tPA (**Figures 4E,F** and **Supplementary Figure 3**). In the hippocampi of AD mice, we observed a negative correlation between the levels of miR-144-3p and those of tPA (**Figures 4G,H**). Moreover, in the mPFC of AD mice, the levels of miR-144-3p were also increased and negatively correlated with the levels of tPA (**Supplementary Figures 4A–C**). Collectively, these data suggested that miR-144-3p regulates the levels of tPA in a direct manner.

The Administration of miR-144-3p Induced Cholinergic Degeneration and Synaptic/Memory Impairments

Next, we investigated whether the artificial upregulation of miR-144-3p could induce an imbalance of the proNGF/NGF ratio in the hippocampi and then lead to cholinergic degeneration

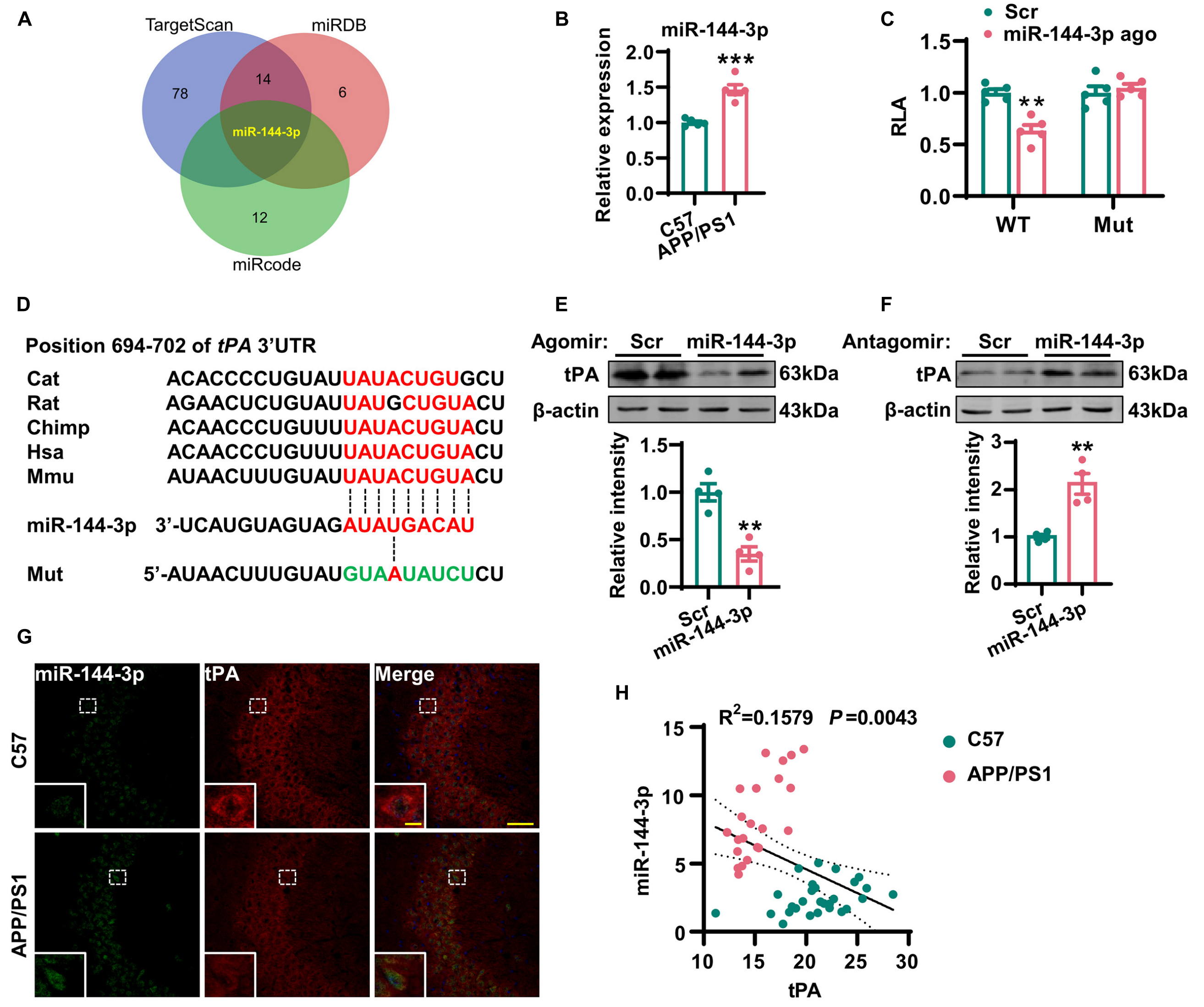

FIGURE 4 | Increased expression of miR-144-3p led to the translational repression of tPA. **(A)** The miRNAs potentially regulating the tPA translation were shown in a Venn diagram by three different online tools as indicated. **(B)** The expression profiles of this candidate miRNA in the hippocampi of 12-months-old APP/PS1 mice and C57 mice were evaluated by Q-PCR. Unpaired Student's *t*-test was used, $n = 5$ mice for each group, $^{***}p < 0.001$. **(C)** The wild-type (WT) or mutant (Mut) 3′-UTR of tPA in psiCHECK-2 vector was co-transfected into N2a cells with miR-144-3p agomir or scrambled control (Scr). The luciferase activity was determined at 48 h after the transfection. Multiple *t*-test adjusted with the Holm–Šidák method, $n = 5$ for each group, $^{**}p < 0.01$. **(D)** Diagram to display the conserved binding site in tPA 3′-UTR to the miR-144-3p. The mutant sequence in 3′-UTR of tPA for luciferase analysis was provided at the bottom. **(E)** N2a cells were transfected with miR-144-3p agomir or Scr. The cell lysates were collected, and the protein levels of tPA were then detected 48 h later by western blotting. The quantitative analysis was shown in the lower panel. Unpaired Student's *t*-test was used, $n = 4$ for each group, $^{**}p < 0.01$. **(F)** N2a cells were transfected with miR-144-3p antagomir (miR-144 anta) or Scr. The protein levels of tPA were detected 48 h later by western blotting. The quantitative analysis was shown in the lower panel. Unpaired Student's *t*-test, $n = 4$ for each group, $^{**}p < 0.01$. **(G)** The staining of fluorescence *in situ* by using the probe of miR-144-3p (green) and immunofluorescence of anti-tPA (red) antibody was performed in the hippocampi of APP/PS1 mice and C57 mice at 12 months. Bar = 50 μm. The representative image of an amplified neuron was shown in the southwest corner. Bar = 5 μm. **(H)** The correlation analysis between the intensities of miR-144-3p and tPA in **(G)**. $n = 22$ or 28 from the APP/PS1 mice or C57 mice.

and synaptic/memory impairment. To this end, we injected the agomir of miR-144-3p or the scrambled control into the hippocampi of wild-type mice at 3 months old (**Figures 5A,B**). Two weeks later, we subjected the mice to the where–which task. We found that the discrimination index was reduced in the mice treated with miR-144-3p (**Figure 5C**). Electrophysiological recordings suggested that the LTP of the CA3–CA1 circuit was also reduced in the mice treated with miR-144-3p (**Figures 5D,E**). We also noted that the upregulation of miR-144-3p induced a lower intensity of ChAT immunostaining in the hippocampi (**Figure 5F**) and decreased the expression of ChAT protein (**Figure 5G**). Furthermore, the levels of tPA and plasmin were decreased in the hippocampi of mice treated with miR-144-3p (**Figure 5H**). Importantly, the proNGF/NGF ratio was

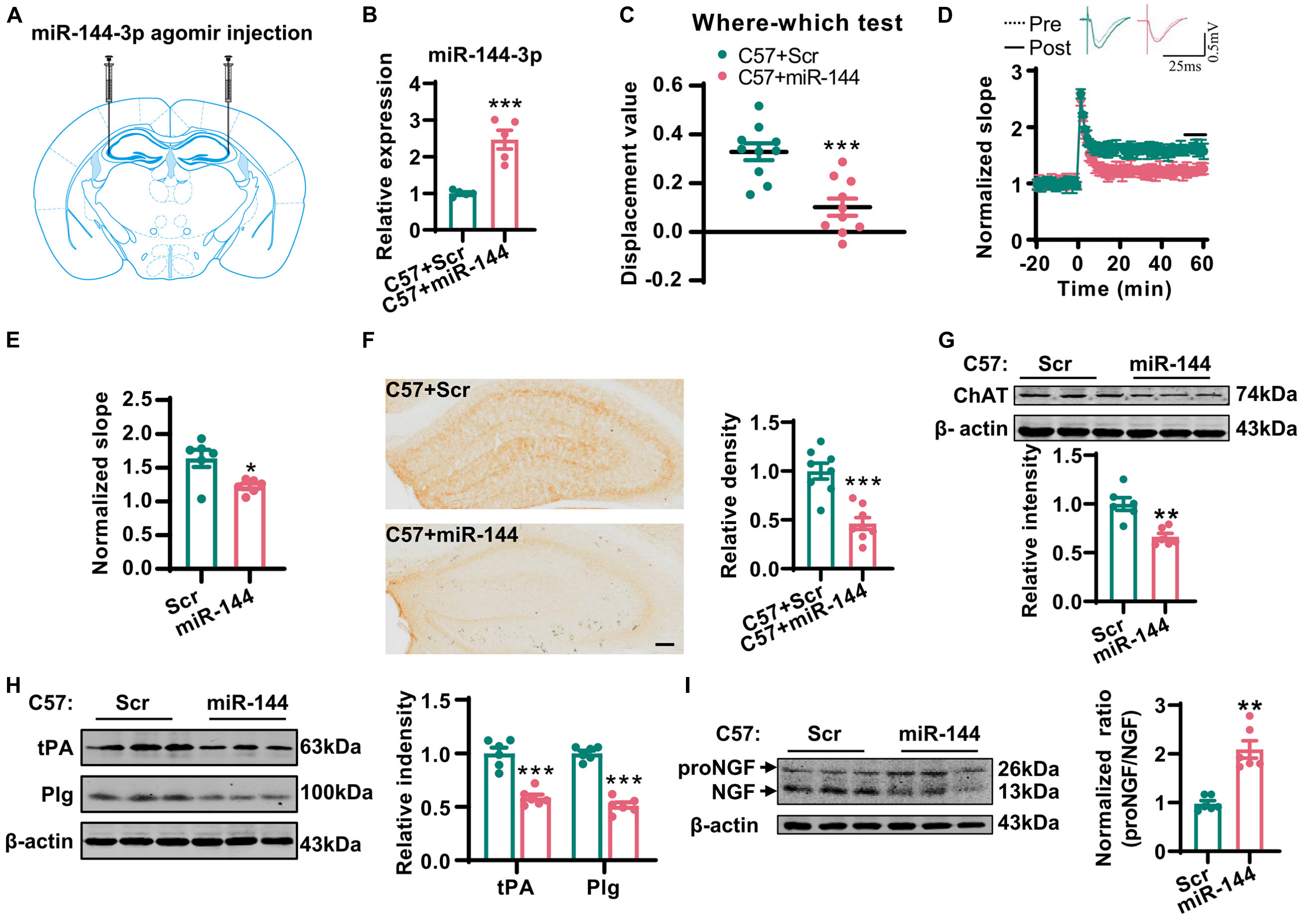

FIGURE 5 | Overexpression of miR-144-3p induced cholinergic degeneration and synaptic/memory impairments. **(A)** The diagram for the stereotactic injection experiment was shown. **(B)** The expression of miR-144-3p was evaluated in 3-months-old C57 mice after injection of miR-144-3p agomir 2 weeks later. Unpaired Student's *t*-test, $n = 5$ mice for each group, $^{**}p < 0.01$. **(C)** The where–which test was used to assess the context memory after administration of miR-144-3p agomir. Unpaired Student's *t*-test, $n = 10$ mice for each group, $^{***}p < 0.001$. **(D)** The electrophysiological recording to detect the fEPSP slope was used to evaluate CA3–CA1 LTP after administration of miR-144-3p agomir. The representative fEPSP traces were shown in the upper panel, and the relative fEPSP slopes were shown in the lower panel. $n = 4$–6 slices from three mice for each group. **(E)** The fEPSP slope of the last 5 min was statistically analyzed. Unpaired Student's *t*-test, $n = 6$ from three mice for each group, $^{*}p < 0.05$. **(F)** Representative immunohistochemical images in the hippocampi in C57 mice with miR-144-3p agomir treatment. And the quantitative analysis was shown in the right panel. Bar = 100 μm. Unpaired Student's *t*-test, $n = 8$ from four mice for each group, $^{***}p < 0.001$. **(G)** Hippocampal tissue lysates from the mice above were collected, and the protein level of ChAT was detected by western blotting. Unpaired Student's *t*-test, $n = 6$ mice for each group, $^{**}p < 0.01$. **(H)** The protein levels of tPA and Plg were also detected in those mice by western blotting, and the quantitative analysis was shown in the right panel. Unpaired Student's *t*-test, $n = 6$ mice for each group, $^{***}p < 0.001$. **(I)** The protein level of NGF was examined by western blotting in the left panel, and the normalized proNGF/NGF ratio was shown in the right panel. Unpaired Student's *t*-test, $n = 6$ mice for each group, $^{**}p < 0.01$.

increased in the mice treated with miR-144-3p (**Figure 5I**). These data suggested that the artificial administration of miR-144-3p could induce cholinergic degeneration and synaptic/memory impairments by elevating the proNGF/NGF ratio.

The Inhibition of miR-144-3p Rescued Cholinergic Degeneration and Synaptic/Memory Impairments in a Mouse Model of AD

Finally, we investigated whether the inhibition of miR-144-3p could rescue cholinergic degeneration and synaptic/memory impairments in a mouse model of AD. We injected the antagomir of miR-144-3p into the hippocampi of 11-months-old APP/PS1 mice every 2 weeks. One month later, the high levels of miR-144-3p in APP/PS1 mice were significantly reduced by the inhibition of miR-144-3p (**Supplementary Figure 5**). Subsequently, we found that the inhibition of miR-144-3p (**Figure 6A**) significantly restored the discrimination index derived from the where–which task in the APP/PS1 mice (**Figure 6B**). We also observed that the LTP in the CA3–CA1 circuit was also rescued by the inhibition of miR-144-3p (**Figures 6C,D**). ChAT immunoreactivity in the hippocampi, along with neuronal loss in the basal nucleus of Meynert, was also restored (**Figures 6E,F**). Furthermore, the loss of tPA was restored, and the proNGF/NGF ratio was suppressed in mice treated with the miR-144-3p antagomir

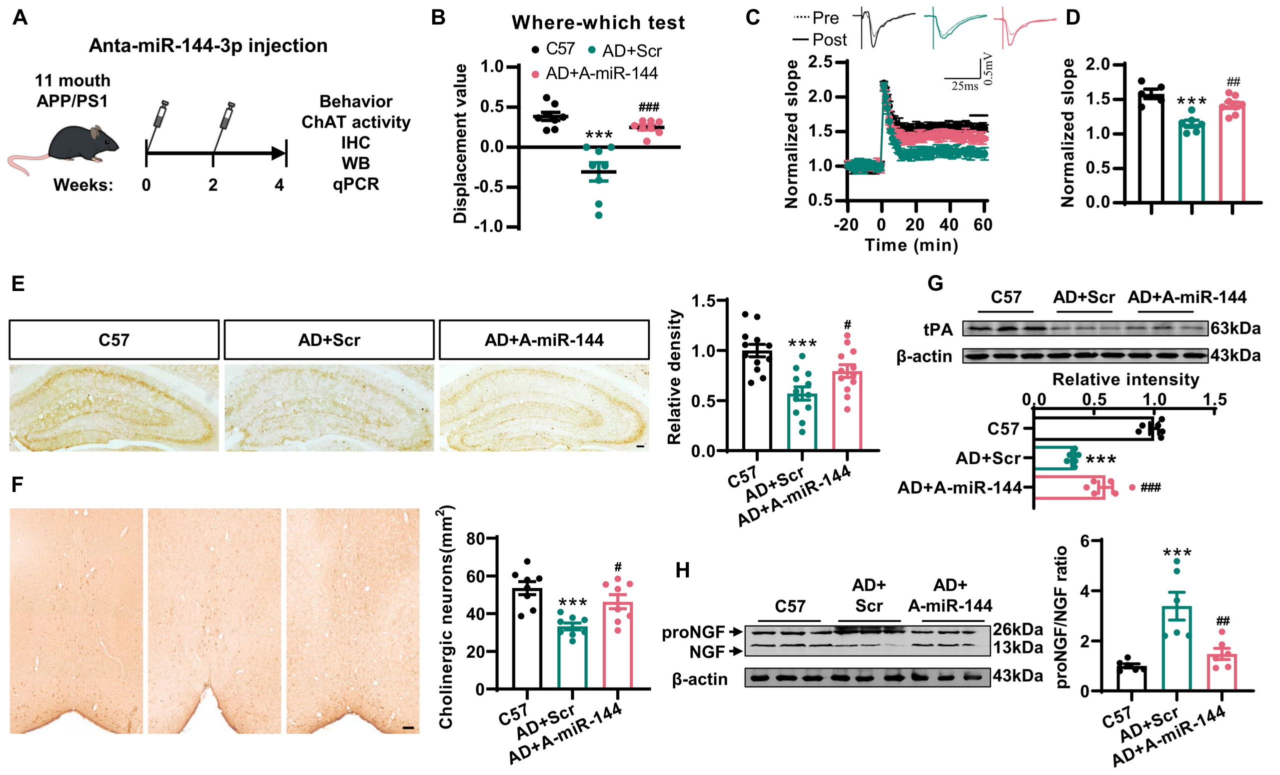

FIGURE 6 | The inhibition of miR-144-3p rescued cholinergic degeneration and synaptic/memory impairments in APP/PS1 mice. **(A)** The flow diagram of administration of miR-144-3p antagomir. The miR-144-3p antagomir was injected into the hippocampal CA3 of 11-months-old APP/PS1 mice that were used for subsequent experiments. **(B)** The where–which test was used to assess the context memory in C57, APP/PS1 + Scr (AD + Scr) and APP/PS1 + A-miR-144 (AD + A-miR-144) groups. Ordinary one-way ANOVA with Tukey's multiple comparisons, *n* = 8 mice for each group, $^{***}p < 0.001$ for AD + Scr vs. C57 and $^{\#\#\#}p < 0.001$ for AD + A-miR-144 vs. AD + Scr. **(C)** The electrophysiological recording to detect the fEPSP slope was used to evaluate the CA3–CA1 LTP of those three groups. The representative fEPSP traces were shown in the upper panel, and the relative fEPSP slopes were shown in the lower panel. *n* = 5–8 slices from three mice for each group. **(D)** The fEPSP slope of the last 5 min was statistically analyzed. *n* = 5–8 from three mice for each group, $^{***}p < 0.001$ for AD + Scr vs. C57 and $^{\#\#}p < 0.01$ for AD + A-miR-144 vs. AD + Scr. **(E)** Representative immunohistochemical images in the hippocampi from mice in those three groups were shown in the left panel, and the quantitative analysis was shown in the right panel. Bar = 100 μm. Ordinary one-way ANOVA with Tukey's multiple comparisons, *n* = 12 from four mice for each group, $^{***}p < 0.001$ for AD + Scr vs. C57 and $^{\#}p < 0.05$ for AD + A-miR-144 vs. AD + Scr. **(F)** Representative immunohistochemical images of ChAT-positive neurons in the basal nucleus of Meynert were shown. Bar = 100 μm. The quantitative analysis was indicated in the right panel. Ordinary one-way ANOVA with Tukey's multiple comparisons, *n* = 8 from four mice for each group, $^{***}p < 0.001$ for AD + Scr vs. C57 and $^{\#}p < 0.05$ for AD + A-miR-144 vs. AD + Scr. **(G)** The protein level of tPA was detected in those mice by western blotting, and the quantitative analysis was shown. Ordinary one-way ANOVA with Tukey's multiple comparisons, *n* = 6 mice for each group, $^{***}p < 0.001$ for AD + Scr vs. C57 and $^{\#\#\#}p < 0.001$ for AD + A-miR-144 vs. AD + Scr. **(H)** The protein level of tPA was detected in the left panel, and the quantitative analysis was shown in the right panel. Ordinary one-way ANOVA with Tukey's multiple comparisons, *n* = 6 mice for each group, $^{***}p < 0.001$ for AD + Scr vs. C57 and $^{\#\#}p < 0.01$ for AD + A-miR-144 vs. AD + Scr.

(**Figures 6G,H**). Thus, the inhibition of miR-144-3p was able to rescue cholinergic degeneration and synaptic/memory impairments in the mouse model of AD.

DISCUSSION

In this study, we demonstrated that cholinergic degeneration is accompanied by synaptic disorders in the hippocampi and memory impairments in AD mice. One of the most prominent clinical symptoms of AD patients is the progressive decline in spatial memory. More specifically, these patients persistently forget where they are or how they arrived at particular locations (Alzheimer's Disease Facts and Figures, 2020). A previous clinical study recruited 31 patients with AD and 35 healthy aged-matched controls; a context memory task revealed that the AD patients exhibited difficulties in remembering information related to "who," "where," and "when" (El Haj and Antoine, 2018). Previous studies suggested that compromised function in the hippocampi and prefrontal cortex may contribute to contextual memory errors in patients with AD (Mitchell et al., 2006). Here, we demonstrated cholinergic degeneration, such as the loss of cholinergic fibers, the formation of dystrophic neurites, and the reduction of ChAT activity, in the hippocampi and mPFC of AD mice with contextual memory impairments. It is known that the hippocampi and mPFC are the two key brain regions that receive cholinergic projections from the BFCN. Previous research showed that the impairment of cholinergic neurons in the medial septum of rats led to a worse performance in where–which memory (Easton et al., 2011). In addition, acetylcholine

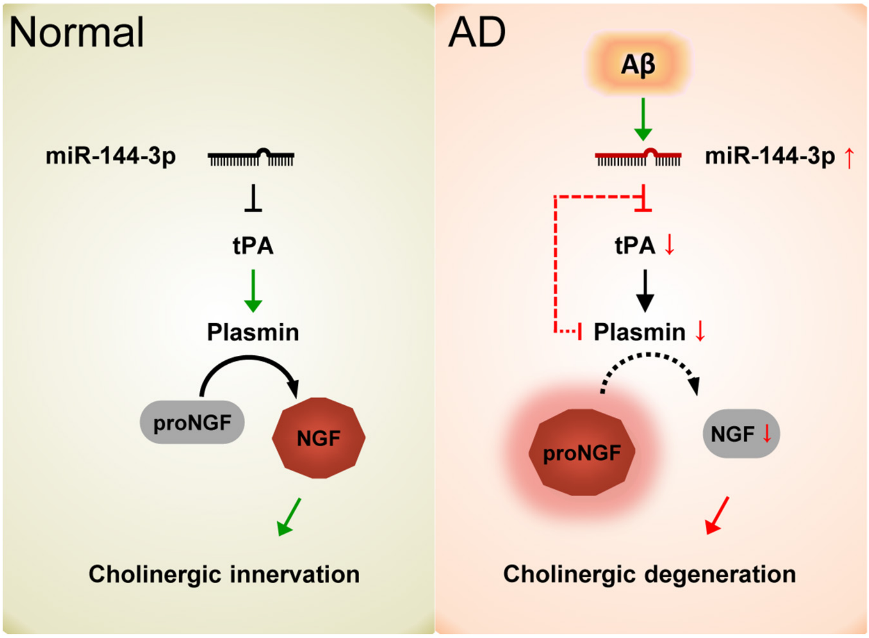

FIGURE 7 | Schematic diagram of the current study. In normal conditions, the proper levels of tPA and plasmin play an important role in the maturation of NGF and maintain the function of the cholinergic system. In AD, the elevation of miR-144-3p leads to the downregulation of tPA and plasmin, which in turn inhibits the maturation of NGF and impairs the plasticity of cholinergic neurons.

in the hippocampi is able to encode novel contexts into a higher priority by controlling sensory inputs from proactive inhibition (Maurer and Williams, 2017). Therefore, cholinergic degenerations in the hippocampi might play an important role in the contextual memory impairments in AD mice. By reversing the cholinergic degeneration induced by the suppression of miR-144-3p, we found that we were able to rescue the contextual memory impairment.

The deregulation of miRNAs has been well validated in AD (Liu et al., 2017; Wang et al., 2018; Tang et al., 2019; Xie et al., 2019; Hou et al., 2020). In the present study, we found that miR-144-3p was upregulated in the hippocampi and mPFC of mice with AD. The injection of the agomir of miR-144-3p into the hippocampi led to cholinergic degeneration, hippocampal synaptic disorders, an imbalance of the proNGF/NGF ratio, and contextual memory deficits, as seen in patients with AD. In line with our current data, previous work showed that miR-144-3p can be stimulated by Aβ and then suppress the expression of A disintegrin and metalloprotease 10 (ADAM10) (Cheng et al., 2013). The reduction of ADAM10 promoted the generation of Aβ and formed a vicious cycle. And this report also indicated that transcription factor AP-1 promoted the expression of miR-144 through the AP-1 binding sites located upstream of the miR-144 precursor. Previous research has also reported increased expression levels of miR-144-3p in the plasma of patients with traumatic brain injury (TBI) and rat models of TBI. The inhibition of miR-144-3p exerts protective effects on the rat model of TBI, including the reduction of lesion volume and brain edema, and also recovered cognitive deficits (Sun et al., 2017). miR-144-3p has also been implicated in many other neurological disorders. For example, miR-144-3p was shown to be an extinction-specific regulated miRNA due to the fact that the expression of miR-144-3p was increased in the amygdala of both extinction-intact BL6 mice and extinction-rescued 129S1/SvlmJ mice (Murphy et al., 2017). Researchers have also discovered that the plasma levels of miR-144-3p were reduced in patients suffering from depression. Interestingly, after 8 weeks of psychotherapy, the expression levels of miR-144-5p were restored to normal, as seen in healthy controls (Wang et al., 2015). A genome-wide study suggested that miR-144-3p plays a crucial role in brain aging and the pathogenesis of spinocerebellar ataxia (Persengiev et al., 2011). We also identified that the increased levels of miR-144-3p inhibit the translation of tPA and subsequently lead to an imbalance of the proNGF/NGF ratio in AD mice. Indeed, a number of validated targets for miR-144-3p have been associated with signals related to synaptic plasticity, including the PI3K/AKT (Jiang et al., 2015), MAPK/ERK (Li et al., 2014), and Notch signaling pathways (Sureban et al., 2011). Interestingly, NGF has been linked with the PI3K/AKT (Sang et al., 2018), MAPK/ERK (Karmarkar et al., 2011), and Notch signaling pathways (Salama-Cohen et al., 2006) and can independently stimulate neuronal projections, neuroprotection, and synaptic inputs. Thus, maintaining the appropriate expression levels of miR-144-3p might be very important with regard to NGF and related signaling pathways.

NGF is a neurotrophin that is highly conserved across vertebrates (Ullrich et al., 1983). The maturation of NGF results from the cleavage of the NGF precursor and forms a biologically active dimer (Iulita and Cuello, 2014). Its mRNA has been shown to exist in the neocortex and hippocampi, while relatively high NGF protein levels have been detected in the cell body of neurons in the basal forebrain and septum (Korsching et al., 1985). Cholinergic neurons in the basal forebrain require NGF in order to maintain functional capability; NGF can be transported in a retrograde manner from the fibers to innervate cholinergic neurons (Hamburger and Levi-Montalcini, 1949). Research has shown that the expression of NGF was positively correlated with the levels of ChAT and AChE during postnatal development (Isaev et al., 2017). Furthermore, cholinergic neurons were shown to be impaired in NGF-knockout mice ($NGF^{+/-}$); this was accompanied by memory and learning deficits (Chen et al., 1997). Furthermore, the number of cholinergic neurons was dramatically reduced in AD (Yan et al., 2018), while the application of NGF in AD mice prevented cholinergic deficit, β-amyloid accumulation, and memory loss (Eyjolfsdottir et al., 2016; Yan et al., 2018). Collectively, these reports were consistent with our findings in that the indirect restoration of NGF by the injection of an antagomir of miR-144-3p could rescue cholinergic metabolic dysfunction and contextual memory in AD mice.

Collectively, our data demonstrated that the elevation of miR-144-3p may play an important role in the imbalance of the proNGF/NGF ratio and that this event subsequently leads to cholinergic degeneration and synaptic/memory impairments in AD (**Figure 7**).

DATA AVAILABILITY STATEMENT

The raw data supporting the conclusions of this article are included in the article/**Supplementary Material**, without undue reservation.

ETHICS STATEMENT

The animal study was reviewed and approved by the Huazhong University of Science and Technology.

AUTHOR CONTRIBUTIONS

DL initiated and designed the study. L-QZ, DL, and CY supervised the study. L-TZ, JZ, LT, H-ZH, YZ, and Z-QL performed the molecular biological experiments and animal experiments. L-TZ, JZ, and LT analyzed the data. DL and L-TZ wrote the manuscript. All authors contributed to the article and approved the submitted version.

FUNDING

This study was supported partially by grants from the National Key Research and Development Program of China (Grant no. 2019YFE0121200), the National Natural Science Foundation of China (Grant nos. 82030032, 81801204, 81829002, 81871108, and 31721002), Top-Notch Young Talents Program of China of 2014, and Academic Frontier Youth Team of Huazhong University of Science and Technology to L-QZ.

ACKNOWLEDGMENTS

We thank all the members of our research team for their help and support from the School of Basic Medicine, Tongji Medical College, Huazhong University of Science and Technology.

SUPPLEMENTARY MATERIAL

The Supplementary Material for this article can be found online at: https://www.frontiersin.org/articles/10.3389/fcell.2021.667412/full#supplementary-material

REFERENCES

Alzheimer's Disease Facts and Figures (2020). Alzheimer's disease facts and figures. *Alzheimers Dement.* 16, 391–460.

Apelt, J., Kumar, A., and Schliebs, R. (2002). Impairment of cholinergic neurotransmission in adult and aged transgenic Tg2576 mouse brain expressing the Swedish mutation of human beta-amyloid precursor protein. *Brain Res.* 953, 17–30. doi: 10.1016/s0006-8993(02)03262-6

Ballinger, E. C., Ananth, M., Talmage, D. A., and Role, L. W. (2016). Basal forebrain cholinergic circuits and signaling in cognition and cognitive decline. *Neuron* 91, 1199–1218. doi: 10.1016/j.neuron.2016.09.006

Bell, K. F., Ducatenzeiler, A., Ribeiro-da-Silva, A., Duff, K., Bennett, D. A., and Cuello, A. C. (2006). The amyloid pathology progresses in a neurotransmitter-specific manner. *Neurobiol. Aging* 27, 1644–1657. doi: 10.1016/j.neurobiolaging.2005.09.034

Bruno, M. A., and Cuello, A. C. (2006). Activity-dependent release of precursor nerve growth factor, conversion to mature nerve growth factor, and its degradation by a protease cascade. *Proc. Natl. Acad. Sci. U.S.A.* 103, 6735–6740. doi: 10.1073/pnas.0510645103

Bruno, M. A., Leon, W. C., Fragoso, G., Mushynski, W. E., Almazan, G., and Cuello, A. C. (2009a). Amyloid beta-induced nerve growth factor dysmetabolism in Alzheimer disease. *J. Neuropathol. Exp. Neurol.* 68, 857–869. doi: 10.1097/nen.0b013e3181aed9e6

Bruno, M. A., Mufson, E. J., Wuu, J., and Cuello, A. C. (2009b). Increased matrix metalloproteinase 9 activity in mild cognitive impairment. *J. Neuropathol. Exp. Neurol.* 68, 1309–1318. doi: 10.1097/nen.0b013e3181c22569

Chen, K. S., Nishimura, M. C., Armanini, M. P., Crowley, C., Spencer, S. D., and Phillips, H. S. (1997). Disruption of a single allele of the nerve growth factor gene results in atrophy of basal forebrain cholinergic neurons and memory deficits. *J. Neurosci.* 17, 7288–7296. doi: 10.1523/jneurosci.17-19-07288.1997

Cheng, C., Li, W., Zhang, Z., Yoshimura, S., Hao, Q., Zhang, C., et al. (2013). MicroRNA-144 is regulated by activator protein-1 (AP-1) and decreases expression of Alzheimer disease-related a disintegrin and metalloprotease 10 (ADAM10). *J. Biol. Chem.* 288, 13748–13761. doi: 10.1074/jbc.m112.381392

Conner, J. M., Franks, K. M., Titterness, A. K., Russell, K., Merrill, D. A., Christie, B. R., et al. (2009). NGF is essential for hippocampal plasticity and learning. *J. Neurosci.* 29, 10883–10889. doi: 10.1523/jneurosci.2594-09.2009

Cuello, A. C., and Bruno, M. A. (2007). The failure in NGF maturation and its increased degradation as the probable cause for the vulnerability of cholinergic neurons in Alzheimer's disease. *Neurochem. Res.* 32, 1041–1045. doi: 10.1007/s11064-006-9270-0

Cuello, A. C., Pentz, R., and Hall, H. (2019). The brain NGF metabolic pathway in health and in Alzheimer's pathology. *Front. Neurosci.* 13:62.

Easton, A., Fitchett, A. E., Eacott, M. J., and Baxter, M. G. (2011). Medial septal cholinergic neurons are necessary for context-place memory but not episodic-like memory. *Hippocampus* 21, 1021–1027.

El Haj, M., and Antoine, P. (2018). Context memory in Alzheimer's disease: the "Who, Where, and When". *Arch. Clin. Neuropsychol.* 33, 158–167. doi: 10.1093/arclin/acx062

Eyjolfsdottir, H., Eriksdotter, M., Linderoth, B., Lind, G., Juliusson, B., Kusk, P., et al. (2016). Targeted delivery of nerve growth factor to the cholinergic basal forebrain of Alzheimer's disease patients: application of a second-generation encapsulated cell biodelivery device. *Alzheimers Res. Ther.* 8:30.

Fahnestock, M., Scott, S. A., Jette, N., Weingartner, J. A., and Crutcher, K. A. (1996). Nerve growth factor mRNA and protein levels measured in the same tissue from normal and Alzheimer's disease parietal cortex. *Brain Res. Mol. Brain Res.* 42, 175–178. doi: 10.1016/s0169-328x(96)00193-3

Foidl, B. M., Do-Dinh, P., Hutter-Schmid, B., Bliem, H. R., and Humpel, C. (2016). Cholinergic neurodegeneration in an Alzheimer mouse model overexpressing amyloid-precursor protein with the Swedish-Dutch-Iowa mutations. *Neurobiol. Learn. Mem.* 136, 86–96. doi: 10.1016/j.nlm.2016.09.014

Haam, J., and Yakel, J. L. (2017). Cholinergic modulation of the hippocampal region and memory function. *J. Neurochem.* 142(Suppl. 2), 111–121. doi: 10.1111/jnc.14052

Hamburger, V., and Levi-Montalcini, R. (1949). Proliferation, differentiation and degeneration in the spinal ganglia of the chick embryo under normal and experimental conditions. *J. Exp. Zool.* 111, 457–501. doi: 10.1002/jez.1401110308

Hou, T. Y., Zhou, Y., Zhu, L. S., Wang, X., Pang, P., Wang, D. Q., et al. (2020). Correcting abnormalities in miR-124/PTPN1 signaling rescues tau pathology in Alzheimer's disease. *J. Neurochem.* 154, 441–457. doi: 10.1111/jnc.14961

Ioannou, M. S., and Fahnestock, M. (2017). ProNGF, but Not NGF, switches from neurotrophic to apoptotic activity in response to reductions in TrkA receptor levels. *Int. J. Mol. Sci.* 18:599. doi: 10.3390/ijms18030599

Isaev, N. K., Stelmashook, E. V., and Genrikhs, E. E. (2017). Role of nerve growth factor in plasticity of forebrain cholinergic neurons. *Biochemistry* 82, 291–300. doi: 10.1134/s0006297917030075

Iulita, M. F., and Cuello, A. C. (2014). Nerve growth factor metabolic dysfunction in Alzheimer's disease and down syndrome. *Trends Pharmacol Sci* 35, 338–348. doi: 10.1016/j.tips.2014.04.010

Jiang, X., Shan, A., Su, Y., Cheng, Y., Gu, W., Wang, W., et al. (2015). miR-144/451 promote cell proliferation via targeting PTEN/AKT pathway in Insulinomas. *Endocrinology* 156, 2429–2439. doi: 10.1210/en.2014-1966

Johnston, M. V., Rutkowski, J. L., Wainer, B. H., Long, J. B., and Mobley, W. C. (1987). NGF effects on developing forebrain cholinergic neurons are regionally specific. *Neurochem. Res.* 12, 985–994. doi: 10.1007/bf00970927

Jonas, S., and Izaurralde, E. (2015). Towards a molecular understanding of microRNA-mediated gene silencing. *Nat. Rev. Genet.* 16, 421–433. doi: 10.1038/nrg3965

Karmarkar, S. W., Bottum, K. M., Krager, S. L., and Tischkau, S. A. (2011). ERK/MAPK is essential for endogenous neuroprotection in SCN2.2 cells. *PLoS One* 6:e23493. doi: 10.1371/journal.pone.0023493

Knowles, J. K., Rajadas, J., Nguyen, T. V., Yang, T., LeMieux, M. C., Vander Griend, L., et al. (2009). The p75 neurotrophin receptor promotes amyloid-beta(1-42)-induced neuritic dystrophy in vitro and in vivo. *J. Neurosci.* 29, 10627–10637. doi: 10.1523/jneurosci.0620-09.2009

Koliatsos, V. E., Nauta, H. J., Clatterbuck, R. E., Holtzman, D. M., Mobley, W. C., and Price, D. L. (1990). Mouse nerve growth factor prevents degeneration of axotomized basal forebrain cholinergic neurons in the monkey. *J. Neurosci.* 10, 3801–3813. doi: 10.1523/jneurosci.10-12-03801.1990

Korsching, S., Auburger, G., Heumann, R., Scott, J., and Thoenen, H. (1985). Levels of nerve growth factor and its mRNA in the central nervous system of the rat correlate with cholinergic innervation. *EMBO J.* 4, 1389–1393. doi: 10.1002/j.1460-2075.1985.tb03791.x

Lesburguères, E., Tsokas, P., Sacktor, T. C., and Fenton, A. A. (2017). The object context-place-location paradigm for testing spatial memory in mice. *Bio. Protoc.* 7:e2231.

Li, J., Rohailla, S., Gelber, N., Rutka, J., Sabah, N., Gladstone, R. A., et al. (2014). MicroRNA-144 is a circulating effector of remote ischemic preconditioning. *Basic Res. Cardiol.* 109:423.

Liu, D., Tang, H., Li, X. Y., Deng, M. F., Wei, N., Wang, X., et al. (2017). Targeting the HDAC2/HNF-4A/miR-101b/AMPK pathway rescues tauopathy and dendritic abnormalities in Alzheimer's disease. *Mol. Ther.* 25, 752–764. doi: 10.1016/j.ymthe.2017.01.018

Maurer, S. V., and Williams, C. L. (2017). The cholinergic system modulates memory and hippocampal plasticity via its interactions with non-neuronal cells. *Front. Immunol.* 8:1489.

Mitchell, J. P., Sullivan, A. L., Schacter, D. L., and Budson, A. E. (2006). Mis-attribution errors in Alzheimer's disease: the illusory truth effect. *Neuropsychology* 20, 185–192. doi: 10.1037/0894-4105.20.2.185

Murphy, C. P., Li, X., Maurer, V., Oberhauser, M., Gstir, R., Wearick-Silva, L. E., et al. (2017). MicroRNA-mediated rescue of fear extinction memory by mir-144-3p in extinction-impaired mice. *Biol. Psychiatry* 81, 979–989. doi: 10.1016/j.biopsych.2016.12.021

Niewiadomska, G., Mietelska-Porowska, A., and Mazurkiewicz, M. (2011). The cholinergic system, nerve growth factor and the cytoskeleton. *Behav. Brain Res.* 221, 515–526. doi: 10.1016/j.bbr.2010.02.024

Oda, Y. (1999). Choline acetyltransferase: the structure, distribution and pathologic changes in the central nervous system. *Pathol. Int.* 49, 921–937. doi: 10.1046/j.1440-1827.1999.00977.x

Oosawa, H., Fujii, T., and Kawashima, K. (1999). Nerve growth factor increases the synthesis and release of acetylcholine and the expression of vesicular acetylcholine transporter in primary cultured rat embryonic septal cells. *J. Neurosci. Res.* 57, 381–387. doi: 10.1002/(sici)1097-4547(19990801)57:3<381::aid-jnr10>3.0.co;2-c

Ovsepian, S. V., Antyborzec, I., O'Leary, V. B., Zaborszky, L., Herms, J., and Oliver Dolly, J. (2014). Neurotrophin receptor p75 mediates the uptake of the amyloid beta (Abeta) peptide, guiding it to lysosomes for degradation in basal forebrain cholinergic neurons. *Brain Struct. Funct.* 219, 1527–1541. doi: 10.1007/s00429-013-0583-x

Peng, S., Wuu, J., Mufson, E. J., and Fahnestock, M. (2004). Increased proNGF levels in subjects with mild cognitive impairment and mild Alzheimer disease. *J. Neuropathol. Exp. Neurol.* 63, 641–649. doi: 10.1093/jnen/63.6.641

Persengiev, S., Kondova, I., Otting, N., Koeppen, A. H., and Bontrop, R. E. (2011). Genome-wide analysis of miRNA expression reveals a potential role for miR-144 in brain aging and spinocerebellar ataxia pathogenesis. *Neurobiol. Aging* 32:2316.e17-e27.

Pongrac, J. L., and Rylett, R. J. (1998). Molecular mechanisms regulating NGF-mediated enhancement of cholinergic neuronal phenotype: c-fos trans-activation of the choline acetyltransferase gene. *J. Mol. Neurosci.* 11, 79–93. doi: 10.1385/jmn:11:1:79

Salama-Cohen, P., Arévalo, M. A., Grantyn, R., and Rodríguez-Tébar, A. (2006). Notch and NGF/p75NTR control dendrite morphology and the balance of excitatory/inhibitory synaptic input to hippocampal neurones through Neurogenin 3. *J. Neurochem.* 97, 1269–1278. doi: 10.1111/j.1471-4159.2006.03783.x

Sang, Q., Sun, D., Chen, Z., and Zhao, W. (2018). NGF and PI3K/Akt signaling participate in the ventral motor neuronal protection of curcumin in sciatic nerve injury rat models. *Biomed. Pharmacother.* 103, 1146–1153. doi: 10.1016/j.biopha.2018.04.116

Sotthibundhu, A., Sykes, A. M., Fox, B., Underwood, C. K., Thangnipon, W., and Coulson, E. J. (2008). Beta-amyloid(1-42) induces neuronal death through the p75 neurotrophin receptor. *J. Neurosci.* 28, 3941–3946. doi: 10.1523/jneurosci.0350-08.2008

Su, Y., Deng, M. F., Xiong, W., Xie, A. J., Guo, J., Liang, Z. H., et al. (2019). MicroRNA-26a/death-associated protein Kinase 1 signaling induces synucleinopathy and dopaminergic neuron degeneration in parkinson's disease. *Biol. Psychiatry* 85, 769–781. doi: 10.1016/j.biopsych.2018.12.008

Sun, L., Zhao, M., Zhang, J., Liu, A., Ji, W., Li, Y., et al. (2017). MiR-144 promotes β-amyloid accumulation-induced cognitive impairments by targeting ADAM10 following traumatic brain injury. *Oncotarget* 8, 59181–59203. doi: 10.18632/oncotarget.19469

Sureban, S. M., May, R., Lightfoot, S. A., Hoskins, A. B., Lerner, M., Brackett, D. J., et al. (2011). DCAMKL-1 regulates epithelial-mesenchymal transition in human pancreatic cells through a miR-200a-dependent mechanism. *Cancer Res.* 71, 2328–2338. doi: 10.1158/0008-5472.can-10-2738

Tang, H., Ma, M., Wu, Y., Deng, M. F., Hu, F., Almansoub, H., et al. (2019). Activation of MT2 receptor ameliorates dendritic abnormalities in Alzheimer's disease via C/EBPα/miR-125b pathway. *Aging Cell* 18:e12902. doi: 10.1111/acel.12902

Ullrich, A., Gray, A., Berman, C., and Dull, T. J. (1983). Human beta-nerve growth factor gene sequence highly homologous to that of mouse. *Nature* 303, 821–825. doi: 10.1038/303821a0

Wang, M., Qin, L., and Tang, B. (2019). MicroRNAs in Alzheimer's disease. *Front. Genet.* 10:153.

Wang, X., Liu, D., Huang, H. Z., Wang, Z. H., Hou, T. Y., Yang, X., et al. (2018). A novel microRNA-124/PTPN1 signal pathway mediates synaptic and memory deficits in Alzheimer's disease. *Biol. Psychiatry* 83, 395–405. doi: 10.1016/j.biopsych.2017.07.023

Wang, X., Sundquist, K., Hedelius, A., Palmér, K., Memon, A. A., and Sundquist, J. (2015). Circulating microRNA-144-5p is associated with depressive disorders. *Clin. Epigenetics* 7:69.

Whitehouse, P. J., Price, D. L., Clark, A. W., Coyle, J. T., and DeLong, M. R. (1981). Alzheimer disease: evidence for selective loss of cholinergic neurons in the nucleus basalis. *Ann. Neurol.* 10, 122–126. doi: 10.1002/ana.410100203

Wilcock, G. K., Esiri, M. M., Bowen, D. M., and Smith, C. C. (1982). Alzheimer's disease. correlation of cortical choline acetyltransferase activity with the severity of dementia and histological abnormalities. *J. Neurol. Sci.* 57, 407–417.

Wong, T. P., Debeir, T., Duff, K., and Cuello, A. C. (1999). Reorganization of cholinergic terminals in the cerebral cortex and hippocampus in transgenic mice carrying mutated presenilin-1 and amyloid precursor protein transgenes. *J. Neurosci.* 19, 2706–2716. doi: 10.1523/jneurosci.19-07-02706.1999

Xie, A. J., Hou, T. Y., Xiong, W., Huang, H. Z., Zheng, J., Li, K., et al. (2019). Tau overexpression impairs neuronal endocytosis by decreasing the GTPase dynamin 1 through the miR-132/MeCP2 pathway. *Aging Cell* 18:e12929. doi: 10.1111/acel.12929

Yan, H., Pang, P., Chen, W., Zhu, H., Henok, K. A., Li, H., et al. (2018). The lesion analysis of cholinergic neurons in 5XFAD mouse model in the three-dimensional level of whole brain. *Mol. Neurobiol.* 55, 4115–4125.

Zhang, H., Petit, G. H., Gaughwin, P. M., Hansen, C., Ranganathan, S., and Zuo, X. (2013). NGF rescues hippocampal cholinergic neuronal markers, restores neurogenesis, and improves the spatial working memory in a mouse model of Huntington's Disease. *J. Huntingtons Dis.* 2, 69–82. doi: 10.3233/jhd-120026

Conflict of Interest: The authors declare that the research was conducted in the absence of any commercial or financial relationships that could be construed as a potential conflict of interest.

frontiers
in Cell and Developmental Biology

ORIGINAL RESEARCH
published: 15 April 2021
doi: 10.3389/fcell.2021.650167

Hyperglycemia-Induced Dysregulated Fusion Intermediates in Insulin-Secreting Cells Visualized by Super-Resolution Microscopy

Guoyi Yang[1], Liuju Li[1], Yanmei Liu[1,2], Kuo Liang[3], Lisi Wei[1]* and Liangyi Chen[1,4,5,6]*

[1] State Key Laboratory of Membrane Biology, Beijing Key Laboratory of Cardiometabolic Molecular Medicine, Institute of Molecular Medicine, School of Future Technology, Peking University, Beijing, China, [2] Institute for Brain Research and Rehabilitation, Key Laboratory of Brain, Cognition and Education Science, South China Normal University, Guangzhou, China, [3] Department of General Surgery, Xuanwu Hospital, Capital Medical University, Beijing, China, [4] PKU-IDG/McGovern Institute for Brain Research, Beijing, China, [5] Beijing Academy of Artificial Intelligence, Beijing, China, [6] Shenzhen Bay Laboratory, Shenzhen, China

OPEN ACCESS

Edited by:
Wei Liu,
Shenzhen PKU-HKUST Medical Center, China

Reviewed by:
Jernej Jorgaèevski,
University in Ljubljana, Slovenia
Herbert Gaisano,
University of Toronto, Canada

Correspondence:
Liangyi Chen
lychen@pku.edu.cn
Lisi Wei
lisi_wei@pku.edu.cn

Specialty section:
This article was submitted to Membrane Traffic, a section of the journal Frontiers in Cell and Developmental Biology

Received: *06 January 2021*
Accepted: *15 March 2021*
Published: *15 April 2021*

Citation:
Yang G, Li L, Liu Y, Liang K, Wei L and Chen L (2021) Hyperglycemia-Induced Dysregulated Fusion Intermediates in Insulin-Secreting Cells Visualized by Super-Resolution Microscopy. Front. Cell Dev. Biol. 9:650167. doi: 10.3389/fcell.2021.650167

Impaired insulin release is a hallmark of type 2 diabetes and is closely related to chronically elevated glucose concentrations, known as "glucotoxicity." However, the molecular mechanisms by which glucotoxicity impairs insulin secretion remain poorly understood. In addition to known kiss-and-run and kiss-and-stay fusion events in INS-1 cells, ultrafast Hessian structured illumination microscopy (Hessian SIM) enables full fusion to be categorized according to the newly identified structures, such as ring fusion (those with enlarged pores) or dot fusion (those without apparent pores). In addition, we identified four fusion intermediates during insulin exocytosis: initial pore opening, vesicle collapse, enlarged pore formation, and final pore dilation. Long-term incubation in supraphysiological doses of glucose reduced exocytosis in general and increased the occurrence of kiss-and-run events at the expense of reduced full fusion. In addition, hyperglycemia delayed pore opening, vesicle collapse, and enlarged pore formation in full fusion events. It also reduced the size of apparently enlarged pores, all of which contributed to the compromised insulin secretion. These phenotypes were mostly due to the hyperglycemia-induced reduction in syntaxin-1A (Stx-1A) and SNAP-25 protein, since they could be recapitulated by the knockdown of endogenous Stx-1A and SNAP-25. These findings suggest essential roles for the vesicle fusion type and intermediates in regulating insulin secretion from pancreatic beta cells in normal and disease conditions.

Keywords: fusion pore, exocytosis, SNARE, secretory vesicle, insulin, glucotoxicity, structured illumination microscopy

INTRODUCTION

Insulin is a physiological hormone released from pancreatic beta cells and plays a vital role in regulating blood glucose levels. In mammalian cells, an increase in glucose blocks ATP-dependent potassium channels, leading to membrane depolarization and the influx of calcium that triggers insulin granule exocytosis (Flatt et al., 1980). Glucose-stimulated insulin secretion (GSIS) is compromised in diabetes, which, in part, leads to the long-term hyperglycemia condition first proposed by Unger et al. in the 1980s as "glucotoxicity" (Unger and Grundy, 1985; Ostenson and Efendic, 2007; Bensellam et al., 2012). The molecular mechanisms underlying glucotoxicity, however, have not been fully explored. In addition to enhanced ER stress (Lemaire and Schuit, 2012), cell apoptosis (Tomita, 2016), altered Ca^{2+} signaling (Klec et al., 2019), and reduced insulin secretion ability are associated with decreased SNARE proteins (Gaisano et al., 2002; Zhang et al., 2002). Interestingly, insulin granules are released from fusion pore intermediate structures, as demonstrated indirectly by optical imaging (Takahashi et al., 2002) and directly by electrophysiological methods (MacDonald et al., 2006), which could help more selectively release of neurotransmitters over insulin from the granules. It has been suggested that *SOX4*, which is overexpressed in diabetes, may reduce insulin secretion by impairing fusion pore expansion (Collins et al., 2016). These data indicate a possible link between fusion intermediate dysregulation and defective insulin secretion in diabetes, although a systematic investigation is needed.

Fusion pores were first detected by the electrochemistry method (Chow et al., 1992). Hormone release from granules oxidized by a carbon fiber electrode (CFE) was detected as an electric current with "foot signals," which are thought to arise from the restricted diffusion of molecules by narrow pores (Wightman et al., 1991; Zhou et al., 1996). In combination with membrane capacitance recording (Albillos et al., 1997), the opening and reversible flickering of a small pore in some fusion events was established as "kiss-and-run" (MacDonald et al., 2006; Hanna et al., 2009). Additionally, methods based on real-time fluorescence imaging have also been used to detect the regulation of vesicle secretion and to probe the spatial profiles of vesicle exocytosis (Anantharam et al., 2010; Zhao et al., 2013; Bendahmane et al., 2018). However, with a limited spatiotemporal resolution, these imaging methods mainly indirectly classify different types of exocytosis based on fluorescently tagged proteins' kinetics after fusion (Guček et al., 2019). Recently, we developed ultrasensitive Hessian structured light illumination microscopy (Hessian-SIM) (Huang et al., 2018). Meanwhile, we labeled VAMP2 (vesicle-associated membrane protein-2/synaptobrevin) with the pH-sensitive variant of GFP (pHluorin) to visualize single exocytotic vesicles. The pHluroin attached to the lumenal side of VAMP2 is quenched before exocytosis. During exocytosis, the vesicle fuses with the plasma membrane and exposes its lumen. The dequenching of luminal pH from 5.5 to 7.3 leads to an increase in the pHluorin fluorescence, which marks vesicle fusion (Miesenböck et al., 1998). Thus, this technique enables enlarged fusion pores and other millisecond fusion intermediates labeled with VAMP2-pHluorin to be observed in live INS-1 cells.

In the current study, Hessian SIM imaging in INS-1 cells cultured in different glucose concentrations demonstrated that long-term hyperglycemia reduced secretion events and switched the vesicle fusion mode from full fusion to kiss-and-run fusion. Besides, hyperglycemia also delayed fusion pore opening and vesicle collapse, reduced the size of enlarged fusion pores, and hindered full fusion pore expansion. Overall, we demonstrate possible mechanisms underlying insulin secretion that are compromised by different levels of sustained glucose exposure.

RESULTS

INS-1 Cell Exocytosis Mainly Exhibited Full-Fusion and Kiss-and-Run Fusion Modes

Insulin granule exocytosis was evoked by a depolarizing solution containing high K^+ (70 mM KCl and 20 mM glucose), and was continuously recorded in real-time for 10 min at a frame rate of 291 Hz using the TIRF-SIM microscope. The fusion events were characterized by a transient fluorescence increase at the center of the VAMP2-pHluorin molecule intensity, followed by a decay to baseline (**Figures 1A–D**).

Regarding the pHluorin-labeled events, we observed four categories of fusion modes according to their fluorescence intensity profile and diffusion pattern: ring fusion (full fusion with a "ring" structure, **Figure 1A**), dot fusion (full fusion with puncta, **Figure 1B**), kiss-and-run (K&R, **Figure 1C**) and kiss-and-stay (K&S, **Figure 1D**) according to their fluorescence intensity profile and diffusion pattern. In full fusion events (ring and dot fusion), corresponding to spreading or discharge, a robust fluorescence increase occurred both at the center and in the annular area of VAMP2-pHluorin molecules (**Figures 1A,B,E**), indicating the full collapse of a vesicle's one-time diffusion to the plasma membrane and a dilated fusion pore. In contrast, confined events (kiss-and-run and kiss-and-stay) showed a brightening of the central intensity but no or a limited fluorescence increase in the annular area (**Figures 1C–E**), representing transient opening and reclosure of a restricted fusion pore that limits vesicle collapse.

Markedly, 80% of the total vesicle exocytotic events were full fusion (**Figure 1F**), including ring fusion (25%, FWHM ~202 ± 27 nm in diameter, **Figures 1F,G**) and dot fusion (55%, FWHM ~92 ± 19 nm in diameter, **Figures 1F,G**), when depolarizing stimulation using high K^+ solution were applied to INS-1 cells. The percentages of kiss-and-run and kiss-and-stay events were 15 and 5%, respectively (**Figure 1F**). Collectively, the data indicate that after stimulation by membrane depolarization, full fusion and Kiss-and-run fusion are the dominant release modes in INS-1 cell exocytosis.

Next, we characterized the kinetics of single fusion events. A previous study showed that for the ring and dot fusions, with an improved frame rate of 291 Hz [via a "rolling" SIM reconstruction (Huang et al., 2018), four kinetically distinct steps could be dissected (Huang et al., 2018)]: (1) an initial rapid increase in the fluorescence intensity (fast rise, duration $\mathbf{t}_1$), which appeared to represent the initial pore opening when vesicular H^+ efflux occurred; (2) a slower increase (slow rise, duration $\mathbf{t}_2$) due to the movement of the fusing vesicle toward the plasma membrane; and (3) a stage in which the fluorescence remained elevated (plateau phase, duration $\mathbf{t}_3$) and during which the enlarged fusion pore formed; and (4) the final return of fluorescence to the baseline value (decay phase, the time constant τ), which refers to

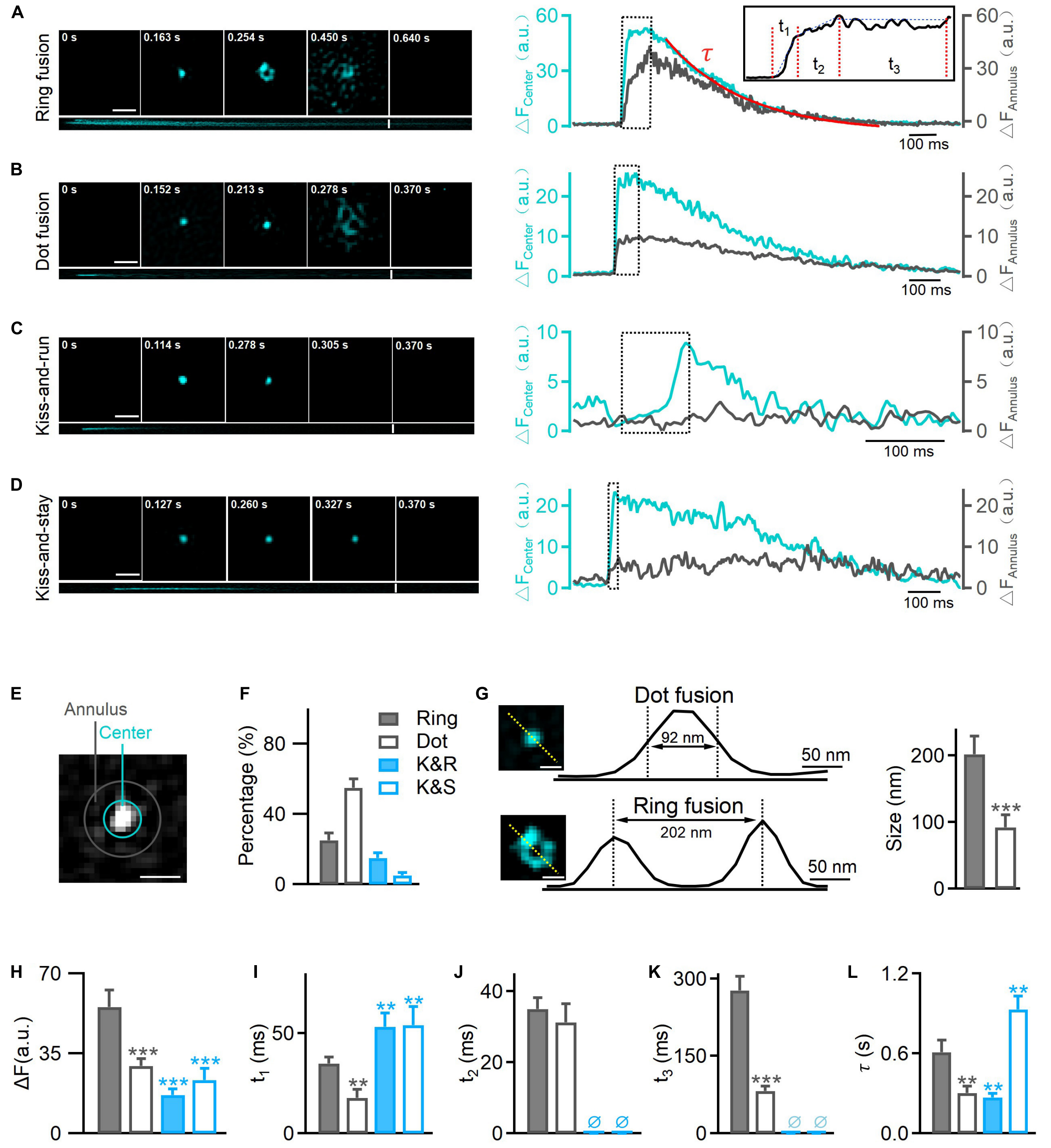

FIGURE 1 | Hessian-TIRF-SIM reveals four types of exocytosis. INS-1 cells were transfected with VAMP2-pHluorin and stimulated with 70 mM KCl and 20 mM glucose. **(A)** Left: representative SIM images showing ring fusion events. Montages (upper) and kymographs (lower) of a ring fusion event in vesicles labeled with VAMP2-pHluorin (cyan). Scale bar, 300 nm; frame rate, 291 Hz [with the "rolling" procedure (Huang et al., 2018)]. Right: changes in fluorescence intensities of annulus (gray) and center (cyan) regions of the fusion event shown in **(E)**. Inset: a high magnification of the trace. Durations $\mathbf{t_1}$, $\mathbf{t_2}$, and $\mathbf{t_3}$ and the decay constant τ (fitted with a single exponential function) describe the durations of different intermediates: the initiation of fusion pore opening, collapse of the vesicle with the plasma membrane, formation of enlarged pores, and final dilation, respectively. **(B–D)** The montages, kymographs, and time-dependent fluorescence traces of a representative dot fusion **(B)**, a kiss-and-run event **(C)**, or a kiss-and-stay event **(D)**. Notably, the fluorescence intensities at the annulus region surrounding the exocytotic site exhibited either no change under kiss-and-run fusion (gray, **C**, right) or a small and delayed increase under kiss-and-stay fusion (gray, **D**, right). **(E)** The annulus (gray) represents the diffusion area between the inner (10 pixels in diameter) and outer (16 pixels in diameter) circles; the center (cyan) represents the inner circle of the fusion pore area. Scale bar, 200 nm. **(F)** Percentages of ring fusion, dot fusion, kiss-and-run exocytosis, and kiss-and-stay exocytosis evoked by 70 mM KCl and 20 mM glucose (n = 150 fusion events from 10 cells). **(G)** The fluorescence intensity profiles for the dotted lines across the enlarged pore (lower) and fluorescence puncta (upper). Diameters were measured as the full width at half maximum (FWHM) of the fluorescence valley (lower, pore size) and peak (upper, puncta size), which gave sizes of 202 ± 27 nm (n = 35 fusion events) and 92 ± 19 nm (n = 40 fusion events) for the pore and puncta, respectively. Scale bar, 100 nm. **(H–L)** Averaged calculations of $\mathbf{t_1}$, $\mathbf{t_2}$, $\mathbf{t_3}$, τ, and the amplitude change of different types of exocytosis (n = 300 fusion events from 6 cells). $^*p < 0.05$, $^{**}p < 0.01$, $^{***}p < 0.001$.

the final dilation of the vesicle (**Figure 1A**, higher magnification inset, **Figure 5**). Meanwhile, for kiss-and-run and kiss-and-stay events, the fusion of single vesicles exhibited only the fast rise phase $\mathbf{t}_1$ and the decay phase (time constant τ); the slow-rise and plateau phases were absent (**Figures 1C,D**). The rising phase probably represents fusion pore opening, and the decay phase may depict the vesicle resealed and reacidification of the vesicle lumen at the kiss-and-run events (**Figure 5**).

Further, we found that the average $\mathbf{t}_1$, $\mathbf{t}_3$, and τ values for ring fusion were 1.5–3.5-fold longer than those for dot fusion events. Given the rate of change in fluorescence was the same in the two populations according to a previous study (Huang et al., 2018), more time is needed for the dequenching or diffusion of VAMP2 in vesicles undergoing ring events. Simultaneously, the mean peak intensity of ring events was 1.5-fold higher than that of dot events, suggesting that ring events involve vesicles with larger membrane surfaces (**Figure 1H**). Among the confined events, the rise times are similar between kiss-and-run (∼60 ms) and kiss-and-stay (∼64 ms) events (**Figure 1I**), but were markedly slower than full fusion events, in agreement with smaller fusion pores. In contrast, the vesicle collapse times of full fusion were quite similar (**Figure 1J**). In addition, ring events remained in the enlarged fusion pore intermediate phase ($\mathbf{t}_3$) for more extended periods (**Figure 1K**). Finally, the decay time (τ) of kiss-and-stay events was 3.5-fold longer than that of kiss-and-run events, suggesting very slow diffusion of vesicular proteins on the plasma membrane (**Figure 1L**).

Sustained Exposure of INS-1 Cells to High Glucose Concentrations Decreased the Full Fusion Frequency and Evoked More Liss-and-Run Events

To better explore the mechanism by which chronic hyperglycemia impairs GSIS, we established a glucose toxicity model in INS-1 cells. Briefly, glucotoxicity conditions were created by exposing INS-1 cells to RPMI 1640 full culture medium containing 20 or 30 mM glucose for 120 h. The cells were then used to detect cell function under GSIS conditions. Using ELISA experiments to detect insulin secretion, we showed that (1) for INS-1 cells cultured in the presence of basal (5 mM) glucose, stimulation with 16.7 mM glucose produced a threefold enhancement of insulin secretion; and (2) with increasing concentrations of glucose in the medium, the secretory response to 16.7 mM glucose was reduced by 40–68% in cells cultured under high glucose ($p < 0.01$) (**Supplementary Figure 1**).

Next, to determine whether high glucose treatment inhibits vesicle synthesis, we counted the number of vesicles labeled with VAMP2-pHluorin after NH_4Cl incubation (50 mM, 2 min) under control (11 mM glucose) and hyperglycemic conditions (high glucose: 20 and 30 mM) (**Figure 2A**). Although diameters of granules in cells cultured in 20 and 30 mM glucose remained unchanged (**Figure 2H** and **Supplementary Figure 3**), hyperglycemia significantly reduced the number of secretory vesicles (**Figure 2C**). This result agreed with the reduced insulin granules immunofluorescently labeled in INS-1 cells cultured under elevated glucose concentrations (**Supplementary Figure 2**). Meanwhile, the hyperglycemic conditions severely reduced the fusion frequency (**Figures 2B,D**) and the probability of vesicle release (**Figure 2E**), confirming the reduced exocytosis in cells after long-term incubation in high glucose concentrations (**Supplementary Figure 1**).

Thus, we examined the fusion mode. Surprisingly, long-term exposure to high glucose concentrations reduced the full fusion percentage (**Figure 2F**, ring fusion: ∼25–5%; dot fusion: ∼55–30%) and triggered more kiss-and-run events (∼15–60%), while the percentage of kiss-and-stay events remained unchanged (∼5%) (**Figure 2G**). Regarding whether high glucose treatment altered the kinetics of the confined events, the results showed a slower rise time for kiss-and-run events, which reflected a longer brightening time for the pHluorin molecules and a smaller fusion pore (**Figure 2I**). In contrast, kiss-and-stay events showed more tolerance to glucotoxicity since the rise and decay times showed no significant differences compared to the events under control glucose concentrations (**Figure 2J**).

Restricted Fusion Pore, Delayed Opening, Vesicle Collapse, and Enlarged Pore Formation of Full Fusion Events Under Long-Term Hyperglycemia Conditions

Next, we investigated spatiotemporal kinetics of full fusion events revealed by the Hessian SIM, and compared the fusion pore sizes at $\mathbf{t}_2$ (vesicle collapse) and $\mathbf{t}_3$ (enlarged pore formation) under normal (11 mM glucose) and long-term hyperglycemia (20 mM and 30 mM glucose, 120 h) conditions. The results showed that glucotoxicity reduced the fusion pore size (**Figures 3A,B**), from 198 ± 15 nm (Control, $n = 30$) to 153 ± 11 nm (20 mM, $n = 25$) and 120 ± 9 nm (30 mM, $n = 35$) at the $\mathbf{t}_2$ stage, and from 230 ± 12 nm (Control, $n = 30$) to 168 ± 12 nm (20 mM, $n = 30$) and 132 ± 10 nm (30 mM, $n = 20$) at the $\mathbf{t}_3$ stage. Correspondingly, long-term exposure to glucose also delayed ring fusions. A longer period of time was needed to observe the first appearance of pore structures (**Figure 3C**), along with delayed initial fusion pore opening (**Figure 3D**, $\mathbf{t}_1$), vesicle collapse, and extended large pore formation (**Figure 3D**, $\mathbf{t}_2$, $\mathbf{t}_3$). The final dilation and diffusion of the vesicular membrane, however, was not affected. Similarly, $\mathbf{t}_1$, $\mathbf{t}_2$, and $\mathbf{t}_3$ were all slowed in dot fusion events from cells been treated with high glucose for 120 h (**Figure 3E**).

Hyperglycemia-Induced Reduction in SNARE Protein Expressions Contributes to the Altered Fusion Dynamics

To better explore the underlying mechanisms, we further determined whether glucotoxicity altered expressions of key regulators in vesicle fusion, SNARE proteins. Surprisingly, we found that core SNARE complex expression was significantly reduced at higher glucose concentrations (**Figure 4A** and **Supplementary Figure 4**). Correspondingly, knocking down syntaxin-1A and SNAP-25 in INS-1 cells decreased the fusion frequency (**Figure 4B**), triggered more kiss-and-run events

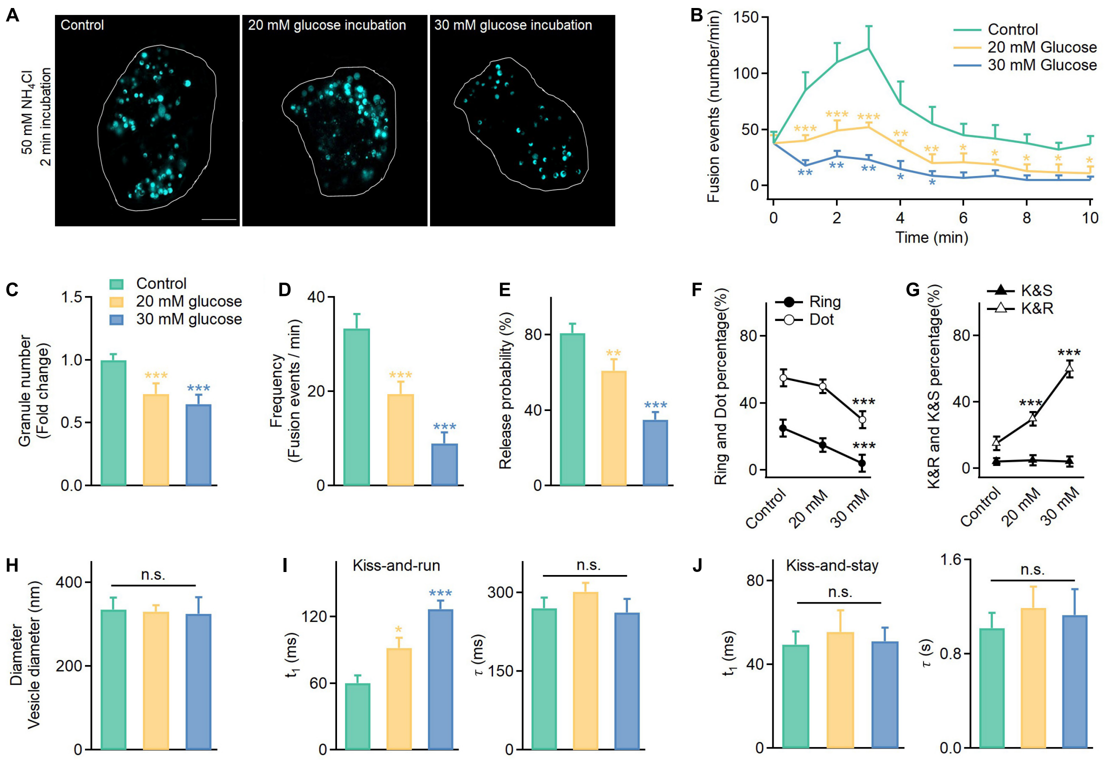

FIGURE 2 | In addition to reduced exocytosis, hyperglycemia leads to more kiss-and-run events at the expense of full fusion events in INS-1 cells. **(A)** Vesicles labeled with VAMP2-pHluorin after NH_4Cl incubation (50 mM, 2 min) observed in control cells cultured in normal glucose (11 mM) or supraphysiological glucose (20 and 30 mM) for 120 h. Scale bar: 3 μm. **(B)** Time-dependent exocytosis triggered by 20 mM glucose and 70 mM KCl in INS-1 cells cultured under different glucose concentrations. **(C–E)** Normalized total vesicle numbers (**C**, Control: n = 180 vesicles; 20 mM: n = 186 vesicles; 30 mM: n = 182 vesicles), release frequency **(D)**, and release probability (normalized to the total vesicle number, **E**). **(F,G)** The percentage of ring fusion, dot fusion **(F)**, kiss-and-run, and kiss-and-stay events **(G)** under different glucose concentrations. **(H)** Vesicle diameters in INS-1 cells cultured under different glucose concentrations (control: n = 180 vesicles; 20 mM: n = 186 vesicles; 30 mM: n = 182 vesicles). **(I,J)** The $\mathbf{t_1}$ and τ of kiss-and-run (**I**, n = 80) and kiss-and-stay events (**J**, n = 60 fusion events) under different glucose concentrations. $^*p < 0.05$, $^{**}p < 0.01$, $^{***}p < 0.001$.

(**Figure 4C**), and restricted the fusion pore size (**Figure 4D**), which were similar to the effects of hyperglycemia.

Next, we determined how the fusion pore dynamics changed when interfering with syntaxin-1A and SNAP-25. For ring fusion, decreased syntaxin-1A expression slowed early pore opening and inhibited vesicle collapse to the plasma membrane (**Figure 4E**), while decreased SNAP-25 expression slowed early pore opening, inhibited vesicle collapse, and hindered the enlarged pore formation process (**Figure 4F**). Similar results occurred in dot fusion (**Supplementary Figures 5A,B**). In addition, decreased SNARE expression also inhibited the initial pore opening of kiss-and-run events (**Figure 4G**) but had no significant effect on kiss-and-stay events (**Supplementary Figure 5C**), phenocopied the effects of long-term exposure to high glucose in INS-1 cells.

Proposed Working Model: Long-Term Exposure to High Glucose Changed the Fusion Mode and Inhibited Fusion Pore Dynamics

Hessian SIM microscopy enabled the direct visualization of the insulin fusion process and led us to the following conclusions:

1. Glucotoxicity triggers more kiss-and-run events while decreasing full fusion events, which may reduce insulin secretion.
2. For full fusion events, glucotoxicity changes the fusion pore dynamics by restricting the fusion pore size, hindering fusion pore opening, delaying vesicle collapse, and inhibiting the pore expansion process. For kiss-and-run events, glucotoxicity only inhibits fusion pore opening (**Figure 5**).
3. Glucotoxicity regulates fusion pore dynamics by decreasing SNARE complexes, which may be the potential mechanism leading to defective insulin secretion in diabetes.

DISCUSSION

Here, we revealed that glucotoxicity impacts insulin secretion at three different levels. While the reduction in glucose-stimulated fusion events agrees, in general, with previous studies (Kawahito et al., 2009), the increase in the relative ratio of kiss-and-run fusion came at the cost of reduced full fusion.

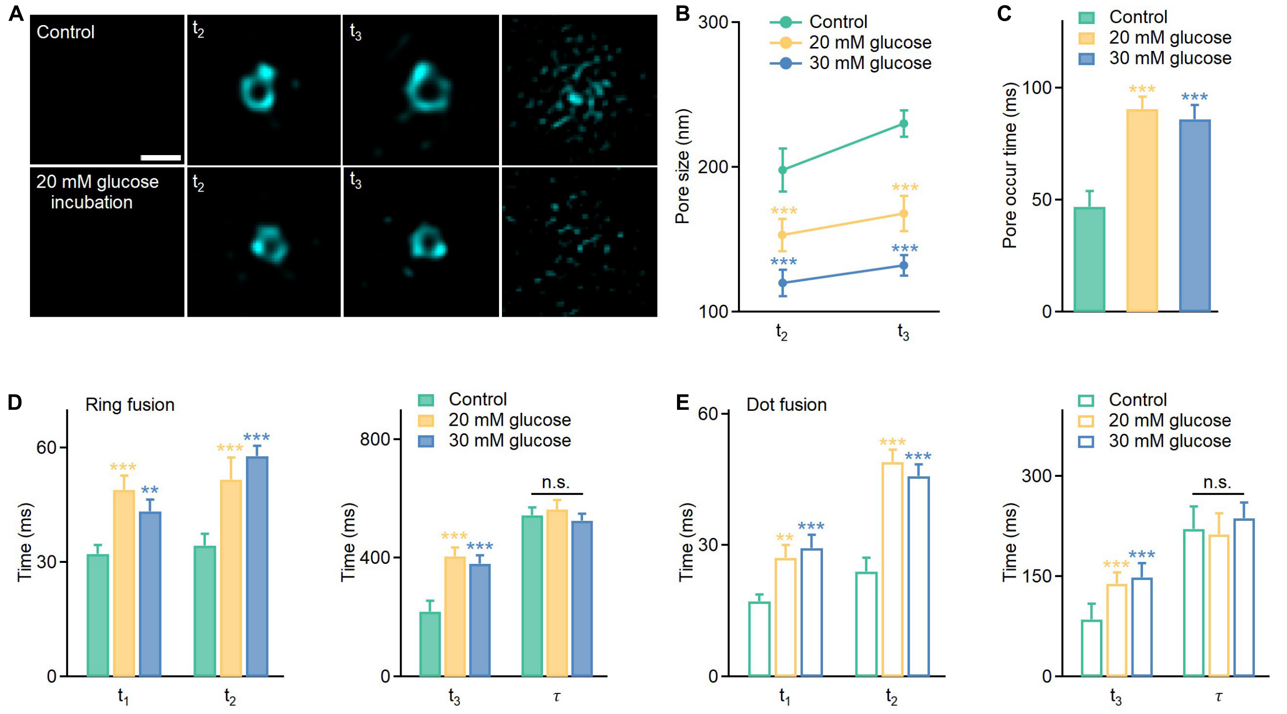

FIGURE 3 | Hyperglycemia delays the opening of the fusion pore, vesicle collapse, and enlarged pore formation in full fusion events and reduces the size of apparently enlarged pores. **(A)** Representative images of enlarged pores at the $\mathbf{t_2}$ and $\mathbf{t_3}$ stages under different conditions. Scale bar: 200 nm. **(B,C)** Average pore sizes and pore occur times under different conditions (Control: $n = 80$ fusion events from 25 cells; 20 mM glucose: $n = 120$ fusion events from 20 cells; 30 mM glucose: $n = 90$ fusion events from 20 cells). **(D,E)** Effects of long-term hyperglycemia on fusion intermediates of ring fusion and dot fusion (ring fusion: $n = 50$ fusion events from 10 cells; dot fusion: $n = 60$ fusion events from 8 cells). $^{*}p < 0.05$, $^{**}p < 0.01$, $^{***}p < 0.001$.

The relative occurrence of kiss-and-run in insulin-secreting cells varies widely, from completely absent (Ma et al., 2004) to the vast majority of events (Tsuboi and Rutter, 2003). Exogenously overexpressing VAMP2-pHlourin may perturb the intrinsic secretion properties of insulin granules. Fusion dynamics may differ upon different vesicular labeling strategies (Rutter et al., 2006; Caromile et al., 2010). However, both the numbers of insulin granules detected by the immunofluorescence microscope (**Supplementary Figure 2**) and the secretion detected by the ELISA experiments (**Supplementary Figure 1**) agreed nicely with experiments conducted with VAMP2-pHlourin (**Figures 2A–D**). Therefore, we believe that the exogenously expressed VAMP2-pHlourin does not significantly affect the exocytosis of insulin granules. By defining fusion events with no diffusion of VAMP2-pHluorin from the release sites as kiss-and-run events (**Figure 1C**), the percentage of these events increased from 15 to 60% in cells cultured with 30 mM glucose, suggesting an important role of insulin release regulated by the fusion mode.

By applying Hessian SIM, we identified enlarged pore formation in some fusion events, which led to the separation of full fusion into subcategories of ring fusion and dot fusion. These enlarged pores resembled similar structures observed under stimulated emission depletion (STED) microscopy (Shin et al., 2018). However, because of the intense phototoxicity and photobleaching associated with STED, long time-lapse live-cell imaging of hundreds of fusion events for statistical analysis was not possible previously. These enlarged pores are different in size from pores several nanometers in diameter detected either by electrochemical or electrophysiological methods (Alvarez de Toledo et al., 1993; MacDonald et al., 2006) and thus may not function to prioritize the release of small over large cargoes. However, these greater than ∼100 nm pores are similar to those in images captured with a rapid-freezing electron microscope more than 30 years ago (Ornberg and Reese, 1981). Hessian SIM enabled hundreds of events to be recognized in live INS-1 cells, thus further validating the general relevance of this phenomenon. Moreover, millisecond temporal resolution enabled intricate dynamics that last only ∼30 ms to be resolved, such as the initial abrupt increase in pHluorin intensity resembling vesicular H^{+} efflux via opened pores and the slow increase in pHluorin intensity resembling movement of the fusing vesicle toward the plasma membrane, which could not be separated by super-resolution microscopy, even when operating at the video frame rate. Having characterized these four intermediates, we were able to show that hyperglycemia inhibited the initial opening, delayed vesicle collapse, reduced enlarged pore sizes, and prolonged the pore duration (**Figure 3**). These data suggest possible delayed and reduced insulin release even in full fusion events, which represents the final layer of glucotoxic effects.

Chronic incubation of INS-1 cells or beta cells in high glucose for 72 h, 96 h, and 5-days' have been tested previously (Unger and Grundy, 1985; Ostenson and Efendic, 2007;

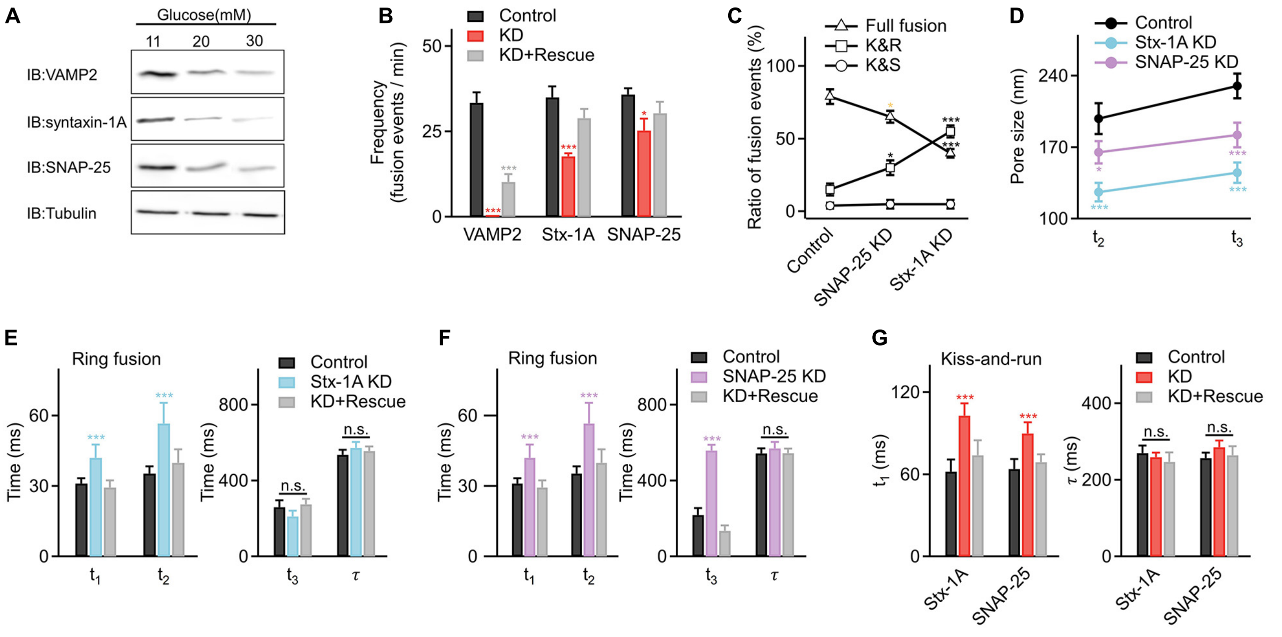

FIGURE 4 | Hyperglycemia alters fusion kinetics by decreasing the expression of the core SNARE complex in INS-1 cells. **(A)** Representative examples of reduced expression of SNARE proteins in INS-1 cells cultured at elevated glucose concentrations. Tubulin was used as a control (four repeats in each condition). **(B)** Fusion frequencies in control INS-1 cells (*n* = 25 cells); cells with knockdown (KD) of VAMP2 (*n* = 10 cells), syntaxin-1A (Stx-1A) (*n* = 16 cells), or SNAP-25 (*n* = 18 cells), and KD cells overexpressing designated SNARE proteins as the rescue (KD+ Rescue) (VAMP2: *n* = 10 cells; syntaxin-1A: *n* = 16 cells; SNAP-25: *n* = 18 cells). **(C)** Percentage of full fusion, kiss-and-run and kiss-and-stay events upon KD of SNARE proteins (Control: *n* = 90 fusion events from 7 cells; Stx-1A KD: *n* = 60 fusion events from 8 cells; SNAP-25 KD: *n* = 85 fusion events from 9 cells). **(D)** Average sizes of enlarged fusion pores during the **t2** and **t3** stages upon KD of SNARE proteins (Control: *n* = 35 fusion events from 6 cells; Stx-1A KD: *n* = 25 fusion events from 10 cells; SNAP-25 KD: *n* = 30 fusion events from 10 cells). **(E,F)** Fusion pore intermediates of ring fusion upon KD of syntaxin-1A **(E)**, SNAP-25 **(F)** (Control: *n* = 35 fusion events from 6 cells; Stx-1A KD: *n* = 25 fusion events from 10 cells; SNAP-25 KD: *n* = 30 fusion events from 10 cells) and SNARE proteins KD+ Rescue (Stx-1A: *n* = 30 fusion events from 7 cells; SNAP-25: *n* = 26 fusion events from 10 cells). **(G)** Dynamics of kiss-and-run events in INS-1 cells with KD of syntaxin-1A, SNAP-25 (Control: *n* = 25 fusion events from 6 cells; Stx-1A KD: *n* = 20 fusion events from 7 cells; SNAP-25 KD: *n* = 30 fusion events from 7 cells) and SNARE proteins KD+ Rescue (Stx-1A: *n* = 25 fusion events from 5 cells; SNAP-25: *n* = 30 fusion events from 8 cells). $^*p < 0.05$, $^{**}p < 0.01$, $^{***}p < 0.001$.

Bensellam et al., 2012). In our case, we employed a high-glucose incubation period of 120 h (5 days) to simulate similar clinical hyperglycemia conditions. Indeed, decreased expression of exocytotic SNARE proteins in pancreatic islets is a postulated mechanism behind impaired insulin release, demonstrated by significantly reduced mRNA and protein levels in both rodent models of type 2 diabetes (Nagamatsu et al., 1999; Gaisano et al., 2002; Zhang et al., 2002) and islets of type 2 diabetic patients (Ostenson and Efendic, 2007). We also showed that long-term hyperglycemia led to reduced SNAP-25 and syntaxin-1A expression (**Figure 4A** and **Supplementary Figure 4**), which may constitute the major factor for reshaping vesicle fusion dynamics. Interestingly, we found different effects when reducing endogenous syntaxin-1A compared to SNAP-25. Interfering with either syntaxin-1A or SNAP-25 slowed the initial pore opening and inhibited vesicle collapse to the plasma membrane (**Figure 4E**) while reducing only SNAP-25 prolonged the formation of enlarged pores (**Figure 4F**). Thus, different components of the SNARE complex may have different regulatory effects on the opening-to-expansion process of the fusion pores. Another possible explanation is that BoNT/C α51 depletes syntaxin-1A predominantly but may not affect syntaxin-3 and syntaxin-4, which mediate newcomer granule fusion (Zhu et al., 2013; Xie et al., 2015). These remaining syntaxins may be able to assist the expansion of the fusion pore.

We also noticed that the kiss-and-stay granules were not significantly affected by reducing SNARE protein levels (**Figure 2J**). Because the proportion of kiss-and-stay fusion to total fusion is around 5%, it may use only a small portion of all SNARE complexes in the INS-1 cell. Thus, decreased number of SNARE complex may have mild effects on this kind of fusion event.

Besides, from the perspective of fusion kinetics, we found that the initial pore opening (**t**$_1$) and pore formation time (**t**$_3$) in dot fusion are much faster than that in the large fusion pore ring structure (**Figures 1I,K**). This may indicate that the dot fusion may require fewer SNARE proteins and is more likely to be initiated than ring fusion. In contrast, large vesicles may require more SNARE complexes to maintain the pore opening and subsequent fusion (Weber et al., 1998; Shi et al., 2012; Bao et al., 2018).

In addition to the core SNARE proteins, many other accessory proteins interact with the SNARE complex (e.g., NSF/SNAPs, Rab family members, Sec1/Munc18, synaptotagmin, Munc13, and complexin) during the fusion process to jointly regulate the secretion process. For example, Munc18 is often considered to

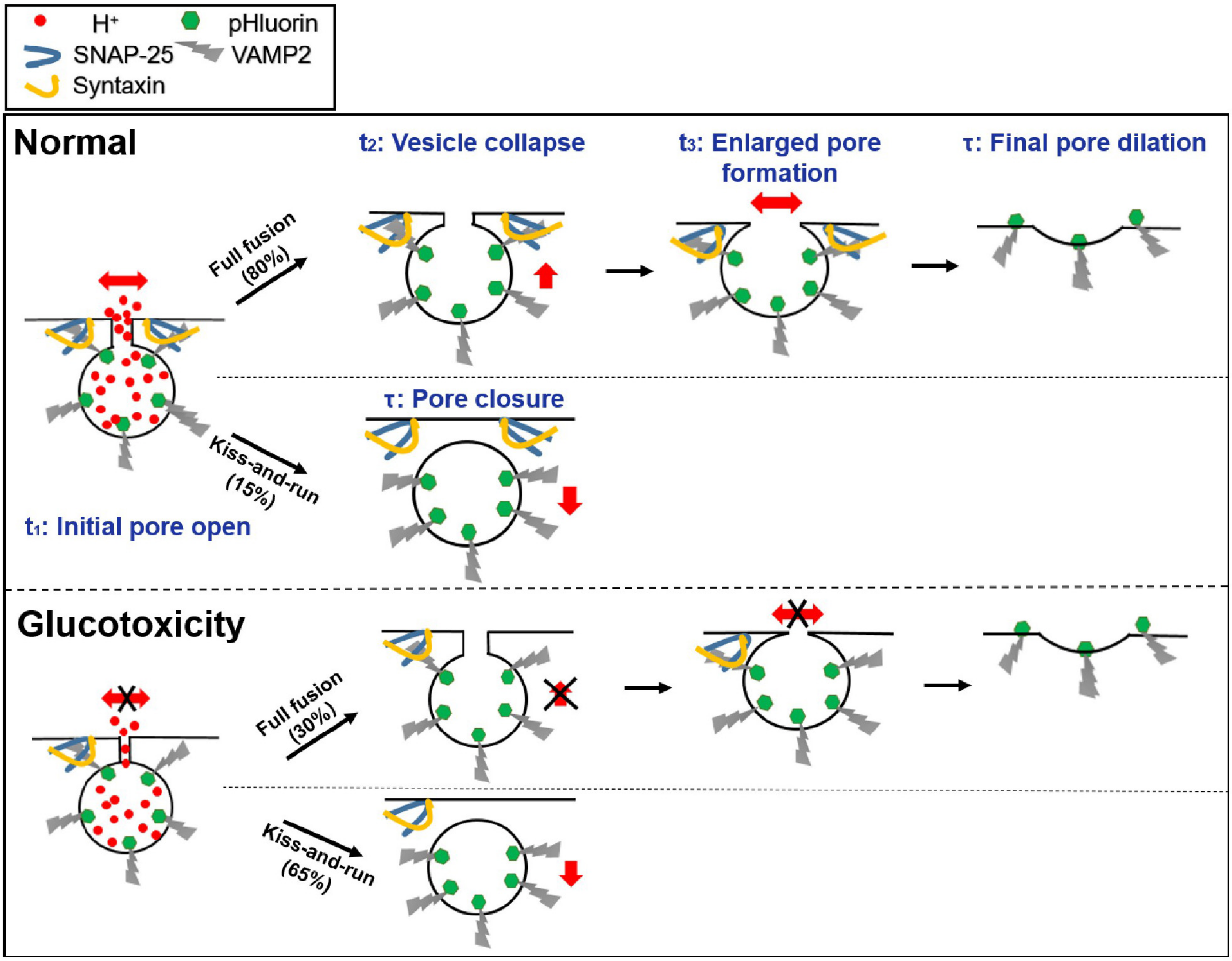

FIGURE 5 | Proposed model of exocytosis under normal and glucotoxicity conditions.

be the protein most closely related to the assembly of SNARE proteins (Rizo and Südhof, 2002), while synaptotagmin acts as a Ca^{2+} sensor for regulated secretion (Sudhof, 2004). Further work is needed to clarify the function of these proteins in fusion pore regulation.

Although this study was carried out in INS-1 cells, the glucotoxicity model may simulate the hyperglycemic environment in primary beta cells to some extent. Furthermore, the functions of the involved proteins are conserved in primary beta cells. Thus, the mechanisms found here may be extrapolated to defective insulin secretion in diabetes.

RESEARCH DESIGN AND METHODS

Plasmid Expression

To study the fusion pore dynamics, INS-1 cells were transfected with VAMP2-pHluorin using Lipofectamine 2000 reagent (Thermo Fisher Scientific, 11668019) and plated onto polylysine-coated coverslips. The experiments were conducted after 16–24 h of culturing in an incubator at 37°C. For the knockdown and rescue experiments, cells were transfected with BoNT/C α51, BoNT/E, syntaxin1A-EGFP, and SNAP-25-EGFP.

INS-1 Cell Culture and Preparation

The rat insulinoma β-cell line INS-1 was cultured as previously described (Zhou and Misler, 1996). The cells were maintained at 37°C in a humidified incubator supplemented with 5% CO_2 and were subcultured twice per week. The cells were maintained in RPMI 1640 medium containing 11 mM D-glucose supplemented with 10% FBS (fetal bovine serum), 100 mg/ml penicillin-streptomycin, 10 mM HEPES, 1 mM sodium pyruvate, 2 mM L-glutamine, and 50 μM beta-mercaptoethanol (Invitrogen, Saint Aubin, France).

All experiments were performed at 37°C. INS-1 cells were plated on glass coverslips and incubated with bath solution containing the following (in mM): 136 NaCl, 4.2 KCl, 2.4 $CaCl_2$, 1.2 KH_2PO_4, 1.2 $MgSO_4$, 5 glucose, 10 HEPES, and 1 L-glutamine (pH 7.4). Individual coverslips were then placed in a metal chamber mounted on a heated stage. The INS-1 cells were stimulated with a solution containing the following (in mM): 70 NaCl, 70 KCl, 2.4 $CaCl_2$, 1.2 KH_2PO_4, 1.2 $MgSO_4$, 20 glucose, 10 HEPES, and 1 L-glutamine (pH 7.4) to trigger insulin granule exocytosis under the TIRF-SIM microscope.

Glucotoxicity conditions were obtained by exposing INS-1 cells to 20 mM and 30 mM glucose (high glucose) for 120 h. The control cells were INS-1 cells exposed to standard culture medium containing 11 mM glucose (Control) for 120 h. Each respective culture medium was changed after 48 h and replaced with the same culture medium until 120 h.

Antibodies

The following primary antibodies were used for immunofluorescence and western blot analysis: polyclonal guinea pig anti-insulin antibody (1:200, Dako, Carpentaria, CA, United States); mouse monoclonal anti-syntaxin-1A (1:1000, SySy); mouse monoclonal anti-SNAP-25 (1:1000, SySy); rabbit monoclonal anti-VAMP2 (1:1000, Abcam); rabbit monoclonal anti-tubulin (1:1000, Abcam). The secondary antibody was DyLight 488 goat anti-guinea pig IgG (1:500, Thermo); IRDye 800CW goat anti-rabbit IgG (1:1000, LI-COR Biosciences); and IRDye 680CW goat anti-mouse IgG (1:1000, LI-COR Biosciences).

ELISA Detection of Insulin Secretion

INS-1 cells cultured in control or high glucose conditions were washed with 1 ml of KRBB buffer (125 mM NaCl, 5.9 mM KCl, 2.56 mM $CaCl_2$, 1.2 mM $MgCl_2$, 1 mM L-glutamine, 25 mM HEPES, and 1 g/L BSA) containing 5 mM glucose, preincubated for 1 h at 37°C and then transferred to KRBB containing 16.7 mM glucose for 20 min at 37°C. The incubation solution was then collected, cell lysates were prepared by incubating for 30 min in RIPA buffer at 4°C, and the insulin levels were quantified using a rat/mouse insulin ELISA kit according to the manufacturer's instructions (EZRMI-13K, Millipore). Insulin secretion was normalized to the total insulin content determined from the cell lysates, and the values shown in **Supplementary Figure 1** were detected by normalizing 4×10^5 cells.

RNA Extraction and Real-Time Quantitative RT-PCR

Total RNA was extracted from INS-1 cells using the RNeasy Mini Kit (74104, QIAGEN). First-strand complementary DNA was synthesized from total RNA using TransScript One-Step gDNA Removal and cDNA Synthesis SuperMix (AT311-03, TransGenBiotech). Real-time PCR was performed on an Eppendorf RealPlex2 system using TransStart Top Green qPCR SuperMix (AQ131-03, TransGenBiotech). The qPCR primers used to detect *VAMP2, syntaxin-1A, and SNAP-25* expression were VAMP2-F (5′-GGGAGTCTGGACTTTTGGGG-3′), VAMP2-R (5′-GAAACGGGGTAAGGGAAG-3′), syntaxin-1A-F (5′-CATGGACTCCAGCATCTCGAA-3′), syntaxin-1A-R (5′-TCCATGAACATGTCGTGCAGC-3′), SNAP-25-F (5′-TCGGGAACCTCCGTCAC-3′), and SNAP-25-R (5′-AATTCTGGTTTTGTTGGAATCAG-3′). RNA transcript levels were quantified using the $2^{-\Delta\Delta Ct}$ method.

Immunofluorescence

For immunofluorescence labeling, cell samples were fixed with 4% paraformaldehyde in PBS for 15 min, followed by permeabilization in PBS containing 0.5% Triton X-100 (MERCK, Billerica, MA, United States) for 10 min and blocking in PBS containing 5% bovine serum for 60 min. The samples were incubated for 60 min in PBS containing primary antibodies and 2.5% bovine serum and then exposed to fluorescent dye-conjugated secondary antibodies for 60 min at 37°C. The cell samples were scanned with an Olympus IX81 (Olympus, Tokyo, Japan).

Insulin granules of INS-1 cells were labeled with anti-insulin antibodies. Besides, we performed the Z-series analysis of the whole-cell and calculated the averaged insulin vesicle number by normalizing per cell size. The insulin granule density in **Supplementary Figure 2** was defined as the number of insulin puncta per cell volume (number/μm^3). All the Immunofluorescence images were shown as maximum intensity projection throughout the cell and were determined by ImageJ (National Institutes of Health[1]).

Western Blot Assay

The cell samples were washed with PBS and homogenized on ice with lysate buffer [150 mM NaCl, 1% NP-40, 0.5% deoxycholic acid, 0.1% SDS, 50 mM Tris, pH 8.0, 1 mM PMSF, and 2% proteinase inhibitor (539134, Calbiochem)]. The homogenates were centrifuged at 16,000 *g* for 15 min at 4°C, and the centrifuged supernatant was adjusted to same total protein concentration following protein quantification by a standard BCA method. Proteins were electrophoresed and transferred to nitrocellulose filter membranes. Each membrane was blocked by incubation for 1 h with PBS containing 0.1% Tween-20 (v/v) and 5% non-fat dried milk (w/v). After washing with 0.1% Tween-20 containing PBS (PBST), the blots were incubated with primary antibodies at 4°C overnight in PBST containing 2% bovine serum albumin (BSA). Secondary antibodies were then applied at room temperature for 1 h. Blots were scanned with an Odyssey infrared imaging system (LI-COR Biosciences) and quantified with ImageJ. At least three independent western blots were conducted, and one typical blot is presented.

Fluorescence Imaging

All confocal microscope images in **Supplementary Figure 2** were generated using an inverted fluorescence microscope (Olympus, IX81) and a Laser Scanning Confocal system (Yokogawa, CSU-X1) with a 100×, 1.30 numerical aperture (NA) oil objective lens. The confocal settings used for image capture were held constant when samples were being compared. Images were quantified and analyzed using ImageJ software (National Institutes of Health).

TIRF-SIM imaging. The imaging system has been schematically illustrated (Huang et al., 2018). Briefly, it was

---

[1] https://imagej.nih.gov/ij/

based on a commercially available inverted fluorescence microscope (IX83, Olympus) equipped with a TIRF objective (Apo N 100×/1.7 HI Oil, Olympus), and images were captured by a sCMOS camera (Flash 4.0 V2, Hamamatsu, Japan). For TIRF-SIM, nine raw images are required to reconstruct one super-resolved image. Reaching a frame rate of 873 Hz, the temporal resolution for the non-overlapping reconstruction of SR images was 97 Hz. Because the three images in one orientation were independent of the images in the other two orientations, we proposed the reconstruction of time-lapse SIM images using overlapping raw image sequences ("rolling") (Huang et al., 2018). By implementing this algorithm, we further increased the temporal resolvability to 291 Hz. All the images were obtained at a frame rate of 291 Hz except for **Figure 2A** and **Supplementary Figure 2**.

A 488-nm laser was used to excite GFP/pHluorin. To visualize VAMP2-pHluorin-labeled granule numbers (**Figure 2A**), the TIRF illumination was adjusted to 2D-SIM. Each pixel from the camera was 32.5 nm × 32.5 nm. The release probability in **Figure 2E** was defined to describe the chances of vesicles to fuse to the plasma membrane, which can be calculated as (number of fusion events) / (granule number per cell).

Data Analysis and Statistics

Image processing was primarily performed using ImageJ software. The reconstruction of the images acquired by TIRF-SIM or 2D-SIM was accomplished using customized MATLAB software (2016a). The data analysis and curve fitting were performed using Igor Pro software (6.11, WaveMetrics, Lake Oswego, OR, United States) and GraphPad 7.0 software. To analyze different stages of vesicle fusion, we determined the time interval between the initiation of the fast rise in fluorescence intensity (the intersection of the stable linear fit at the bottom and the fitted fast rise) to the initiation of slow rise (the intersection of the fitted fast rise slope and the fitted slow rise) as the $\mathbf{t}_1$; the time interval between the initiation of the slow rise in fluorescence intensity to the time point of the initiation of stable fluorescence (the intersection of the fitted slow rise and the stable linear fit at the top) as the $\mathbf{t}_2$; the time interval between the initiation of stable fluorescence to the time point of the initiation of fluorescence decay (the intersection of the stable linear fit at the top and the fitted exponential decay) as the $\mathbf{t}_3$.

The results are presented as the mean ± SEM. Statistical significance was evaluated using Student's *t*-test for single Gaussian-distributed datasets or the Mann–Whitney rank sum test for non-single Gaussian-distributed datasets. The asterisks *, **, and *** denote statistical significance at $p < 0.05$, $p < 0.01$, and $p < 0.001$, respectively.

DATA AVAILABILITY STATEMENT

All relevant data is contained within the article. The raw data supporting the conclusions of this article will be made available by the authors, without undue reservation.

AUTHOR CONTRIBUTIONS

LC and LW conceived and supervised the research. GY designed and performed the experiments, and data analysis and prepared the figures. GY and LW wrote the manuscript. All authors participated in discussions and data interpretation. All authors contributed to the article and approved the submitted version.

FUNDING

This work was supported by grants from the National Natural Science Foundation of China (92054301, 81925022, 91854112, 91750203, and 31821091), the National Science and Technology Major Project Program (2016YFA0500400), the Beijing Natural Science Foundation (Z200017, Z201100008420005, and 7182063), and the High-performance Computing Platform of Peking University.

SUPPLEMENTARY MATERIAL

The Supplementary Material for this article can be found online at: https://www.frontiersin.org/articles/10.3389/fcell.2021.650167/full#supplementary-material

Supplementary Figure 1 | Reduced glucose-stimulated insulin secretion in INS-1 cells cultured under hyperglycemic conditions. Insulin secretion of INS-1 cells under control (11 mM) and high glucose culture medium (20 and 30 mM glucose) ($n = 4$ repeats per condition). *$p < 0.05$, **$p < 0.01$, ***$p < 0.001$.

Supplementary Figure 2 | Hyperglycemia leads to the decreased insulin granule density in INS-1 cells. Immunofluorescence analysis of vesicles content (labeled with insulin antibody), showing **(A)** subcellular distribution and **(B)** granule density under normal glucose (11 mM, $n = 20$ cells) and supraphysiological glucose (20 mM: $n = 25$ cells; 30 mM: $n = 18$ cells). Scale bar: 5 μm. *$p < 0.05$, **$p < 0.01$, ***$p < 0.001$.

Supplementary Figure 3 | Unaltered vesicle diameters after long-term exposure to high glucose culture conditions. **(A–C)** We applied 2 min of 50 mM NH_4Cl incubation to neutralize the acidic pH within the vesicles and then estimated the diameters of VAMP2-pHluorin vesicles in INS-1 cells cultured in control and high glucose conditions. **(A)** Control, 11 mM glucose; **(B)** 20 mM glucose; **(C)** 30 mM glucose ($n = 120$ vesicles per condition). *$p < 0.05$, **$p < 0.01$, ***$p < 0.001$.

Supplementary Figure 4 | Hyperglycemia decreases the expression of core SNARE complex in INS-1 cells. Quantification of mRNA expression **(A)** and protein expression of SNARE complex proteins **(B)** in INS-1cells. Values were normalized to intensities of control (11 mM glucose). *$p < 0.05$, **$p < 0.01$, ***$p < 0.001$.

Supplementary Figure 5 | Decreased SNARE proteins altered the fusion kinetics of dot fusion and kiss-and-stay events. **(A,B)** Dot fusion intermediates upon KD of syntaxin-1A **(A)**, SNAP-25 **(B)**, (Control: $n = 40$ fusion events from 8 cells; Stx-1A KD: $n = 25$ fusion events from 10 cells; SNAP-25 KD: $n = 30$ fusion events from 10 cells) and SNARE proteins KD+ Rescue (Stx-1A: $n = 45$ fusion events from 7 cells; SNAP-25: $n = 30$ fusion events from 6 cells). **(C)** Dynamics of kiss-and-stay events in INS-1 cells with KD of syntaxin-1A, SNAP-25 (Control: $n = 10$ fusion events from 5 cells; Stx-1A KD: $n = 15$ fusion events from 4 cells; SNAP-25 KD: $n = 14$ fusion events from 5 cells) and SNARE proteins KD+ Rescue (Stx-1A: $n = 18$ fusion events from 5 cells; SNAP-25: $n = 15$ fusion events from 4 cells). *$p < 0.05$, **$p < 0.01$, ***$p < 0.001$.

REFERENCES

Albillos, A., Dernick, G., Horstmann, H., Almers, W., Alvarez, de Toledo, G., et al. (1997). The exocytotic event in chromaffin cells revealed by patch amperometry. *Nature* 389, 509–512. doi: 10.1038/39081

Alvarez, de Toledo, G., Fernández-Chacón, R., and Fernández, J. M. (1993). Release of secretory products during transient vesicle fusion. *Nature* 363, 554–558. doi: 10.1038/363554a0

Anantharam, A., Onoa, B., Edwards, R. H., Holz, R. W., and Axelrod, D. (2010). Localized topological changes of the plasma membrane upon exocytosis visualized by polarized TIRFM. *J. Cell Biol.* 188, 415–428. doi: 10.1083/jcb.200908010

Bao, H., Das, D., Courtney, N. A., Jiang, Y., Briguglio, J. S., Lou, X., et al. (2018). Dynamics and number of trans-SNARE complexes determine nascent fusion pore properties. *Nature* 554, 260–263. doi: 10.1038/nature25481

Bendahmane, M., Bohannon, K. P., Bradberry, M. M., Rao, T. C., Schmidtke, M. W., Abbineni, P. S., et al. (2018). The synaptotagmin C2B domain calcium-binding loops modulate the rate of fusion pore expansion. *Mol. Biol. Cell* 29, 834–845. doi: 10.1091/mbc.E17-11-0623

Bensellam, M., Laybutt, D. R., and Jonas, J.-C. (2012). The molecular mechanisms of pancreatic β-cell glucotoxicity: recent findings and future research directions. *Mol. Cell. Endocrinol.* 364, 1–27. doi: 10.1016/j.mce.2012.08.003

Caromile, L. A., Oganesian, A., Coats, S. A., Seifert, R. A., and Bowen-Pope, D. F. (2010). The neurosecretory vesicle protein phogrin functions as a phosphatidylinositol phosphatase to regulate insulin secretion. *J. Biol. Chem.* 285, 10487–10496. doi: 10.1074/jbc.M109.066563

Chow, R. H., von Rüden, L., and Neher, E. (1992). Delay in vesicle fusion revealed by electrochemical monitoring of single secretory events in adrenal chromaffin cells. *Nature* 356, 60–63. doi: 10.1038/356060a0

Collins, S. C., Do, H. W., Hastoy, B., Hugill, A., Adam, J., Chibalina, M. V., et al. (2016). Increased expression of the diabetes gene SOX4 reduces insulin secretion by impaired fusion pore expansion. *Diabetes* 65, 1952–1961. doi: 10.2337/db15-1489

Flatt, P. R., Boquist, L., and Hellman, B. (1980). Calcium and pancreatic β-cell function. The mechanism of insulin secretion studied with the aid of lanthanum. *Biochem. J.* 190, 361–372. doi: 10.1042/bj1900361

Gaisano, H. Y., Ostenson, C.-G., Sheu, L., Wheeler, M. B., and Efendic, S. (2002). Abnormal expression of pancreatic islet exocytotic soluble N-ethylmaleimide-sensitive factor attachment protein receptors in Goto-Kakizaki rats is partially restored by phlorizin treatment and accentuated by high glucose treatment. *Endocrinology* 143, 4218–4226. doi: 10.1210/en.2002-220237

Guček, A., Gandasi, N. R., Omar-Hmeadi, M., Bakke, M., Døskeland, S. O., Tengholm, A., et al. (2019). Fusion pore regulation by cAMP/Epac2 controls cargo release during insulin exocytosis. *eLife* 8:e41711. doi: 10.7554/eLife.41711

Hanna, S. T., Pigeau, G. M., Galvanovskis, J., Clark, A., Rorsman, P., and MacDonald, P. E. (2009). Kiss-and-run exocytosis and fusion pores of secretory vesicles in human beta-cells. *Pflugers Arch. Eur. J. Physiol.* 457, 1343–1350. doi: 10.1007/s00424-008-0588-0

Huang, X., Fan, J., Li, L., Liu, H., Wu, R., Wu, Y., et al. (2018). Fast, long-term, super-resolution imaging with Hessian structured illumination microscopy. *Nat. Biotechnol.* 36, 451–459. doi: 10.1038/nbt.4115

Kawahito, S., Kitahata, H., and Oshita, S. (2009). Problems associated with glucose toxicity: role of hyperglycemia-induced oxidative stress. *World J. Gastroenterol.* 15, 4137–4142. doi: 10.3748/wjg.15.4137

Klec, C., Ziomek, G., Pichler, M., Malli, R., and Graier, W. F. (2019). Calcium signaling in ß-cell physiology and pathology: a revisit. *Int. J. Mol. Sci.* 20:6110. doi: 10.3390/ijms20246110

Lemaire, K., and Schuit, F. (2012). Integrating insulin secretion and ER stress in pancreatic β-cells. *Nat. Cell Biol.* 14, 979–981. doi: 10.1038/ncb2594

Ma, L., Bindokas, V. P., Kuznetsov, A., Rhodes, C., Hays, L., Edwardson, J. M., et al. (2004). Direct imaging shows that insulin granule exocytosis occurs by complete vesicle fusion. *Proc. Natl. Acad. Sci. U S A.* 101, 9266–9271. doi: 10.1073/pnas.0403201101

MacDonald, P. E., Braun, M., Galvanovskis, J., and Rorsman, P. (2006). Release of small transmitters through kiss-and-run fusion pores in rat pancreatic beta cells. *Cell Metab.* 4, 283–290. doi: 10.1016/j.cmet.2006.08.011

Miesenböck, G., De Angelis, D. A., and Rothman, J. E. (1998). Visualizing secretion and synaptic transmission with pH-sensitive green fluorescent proteins. *Nature* 394, 192–195. doi: 10.1038/28190

Nagamatsu, S., Nakamichi, Y., Yamamura, C., Matsushima, S., Watanabe, T., Ozawa, S., et al. (1999). Decreased expression of t-SNARE, syntaxin 1, and SNAP-25 in pancreatic beta-cells is involved in impaired insulin secretion from diabetic GK rat islets: restoration of decreased t-SNARE proteins improves impaired insulin secretion. *Diabetes* 48, 2367–2373. doi: 10.2337/diabetes.48.12.2367

Ornberg, R. L., and Reese, T. S. (1981). Beginning of exocytosis captured by rapid-freezing of Limulus amebocytes. *J. Cell Biol.* 90, 40–54. doi: 10.1083/jcb.90.1.40

Ostenson, C.-G., and Efendic, S. (2007). Islet gene expression and function in type 2 diabetes; studies in the Goto-Kakizaki rat and humans. *Diabetes Obesity Metab.* 9(Suppl. 2), 180–186. doi: 10.1111/j.1463-1326.2007.00787.x

Rizo, J., and Südhof, T. C. (2002). Snares and Munc18 in synaptic vesicle fusion. *Nat. Rev. Neurosci.* 3, 641–653. doi: 10.1038/nrn898

Rutter, G. A., Loder, M. K., and Ravier, M. A. (2006). Rapid three-dimensional imaging of individual insulin release events by Nipkow disc confocal microscopy. *Biochem. Soc. Trans.* 34(Pt 5), 675–678. doi: 10.1042/BST0340675

Shi, L., Shen, Q.-T., Kiel, A., Wang, J., Wang, H.-W., Melia, T. J., et al. (2012). SNARE proteins: one to fuse and three to keep the nascent fusion pore open. *Science* 335, 1355–1359. doi: 10.1126/science.1214984

Shin, W., Ge, L., Arpino, G., Villarreal, S. A., Hamid, E., Liu, H., et al. (2018). Visualization of membrane pore in live cells reveals a dynamic-pore theory governing fusion and endocytosis. *Cell* 173, 934–945.e12. doi: 10.1016/j.cell.2018.02.062

Sudhof, T. C. (2004). The synaptic vesicle cycle. *Ann. Rev. Neurosci.* 27, 509–547. doi: 10.1146/annurev.neuro.26.041002.131412

Takahashi, N., Kishimoto, T., Nemoto, T., Kadowaki, T., and Kasai, H. (2002). Fusion pore dynamics and insulin granule exocytosis in the pancreatic islet. *Science* 297, 1349–1352. doi: 10.1126/science.1073806

Tomita, T. (2016). Apoptosis in pancreatic β-islet cells in Type 2 diabetes. *Bosnian J. Basic Med. Sci.* 16, 162–179. doi: 10.17305/bjbms.2016.919

Tsuboi, T., and Rutter, G. A. (2003). Multiple forms of "kiss-and-run" exocytosis revealed by evanescent wave microscopy. *Curr. Biol. CB* 13, 563–567. doi: 10.1016/s0960-9822(03)00176-3

Unger, R. H., and Grundy, S. (1985). Hyperglycaemia as an inducer as well as a consequence of impaired islet cell function and insulin resistance: implications for the management of diabetes. *Diabetologia* 28, 119–121. doi: 10.1007/BF00273856

Weber, T., Zemelman, B. V., McNew, J. A., Westermann, B., Gmachl, M., Parlati, F., et al. (1998). SNAREpins: minimal machinery for membrane fusion. *Cell* 92, 759–772. doi: 10.1016/s0092-8674(00)81404-x

Wightman, R. M., Jankowski, J. A., Kennedy, R. T., Kawagoe, K. T., Schroeder, T. J., Leszczyszyn, D. J., et al. (1991). Temporally resolved catecholamine spikes correspond to single vesicle release from individual chromaffin cells. *Proc. Natl. Acad. Sci. U S A.* 88, 10754–10758. doi: 10.1073/pnas.88.23.10754

Xie, L., Zhu, D., Dolai, S., Liang, T., Qin, T., Kang, Y., et al. (2015). Syntaxin-4 mediates exocytosis of pre-docked and newcomer insulin granules underlying biphasic glucose-stimulated insulin secretion in human pancreatic beta cells. *Diabetologia* 58, 1250–1259. doi: 10.1007/s00125-015-3545-4

Zhang, W., Khan, A., Ostenson, C.-G., Berggren, P.-O., Efendic, S., and Meister, B. (2002). Down-regulated expression of exocytotic proteins in pancreatic islets of diabetic GK rats. *Biochem. Biophys. Res. Commun.* 291, 1038–1044. doi: 10.1006/bbrc.2002.6555

Zhao, Y., Fang, Q., Herbst, A. D., Berberian, K. N., Almers, W., and Lindau, M. (2013). Rapid structural change in synaptosomal-associated protein 25 (SNAP25) precedes the fusion of single vesicles with the plasma membrane in live chromaffin cells. *Proc. Natl. Acad. Sci. U S A.* 110, 14249–14254. doi: 10.1073/pnas.1306699110

Zhou, Z., and Misler, S. (1996). Amperometric detection of quantal secretion from patch-clamped rat pancreatic beta-cells. *J. Biol. Chem.* 271, 270–277. doi: 10.1074/jbc.271.1.270

Zhou, Z., Misler, S., and Chow, R. H. (1996). Rapid fluctuations in transmitter release from single vesicles in bovine adrenal chromaffin cells. *Biophys. J.* 70, 1543–1552. doi: 10.1016/S0006-3495(96)79718-7

Zhu, D., Koo, E., Kwan, E., Kang, Y., Park, S., Xie, H., et al. (2013). Syntaxin-3 regulates newcomer insulin granule exocytosis and compound fusion in pancreatic beta cells. *Diabetologia* 56, 359–369. doi: 10.1007/s00125-012-2757-0

Conflict of Interest: LC was employed by Shenzhen Bay Laboratory.

The remaining authors declare that the research was conducted in the absence of any commercial or financial relationships that could be construed as a potential conflict of interest.

frontiers
in Cell and Developmental Biology

REVIEW
published: 10 May 2021
doi: 10.3389/fcell.2021.611443

Multiple GPCR Functional Assays Based on Resonance Energy Transfer Sensors

Yiwei Zhou[1], Jiyong Meng[1], Chanjuan Xu[1,2] and Jianfeng Liu[1,2]**

[1] *Cellular Signaling Laboratory, Key Laboratory of Molecular Biophysics of Ministry of Education, College of Life Science and Technology, Huazhong University of Science and Technology, Wuhan, China,* [2] *Bioland Laboratory, Guangzhou Regenerative Medicine and Health Guangdong Laboratory, Guangzhou, China*

G protein-coupled receptors (GPCRs) represent one of the largest membrane protein families that participate in various physiological and pathological activities. Accumulating structural evidences have revealed how GPCR activation induces conformational changes to accommodate the downstream G protein or β-arrestin. Multiple GPCR functional assays have been developed based on Förster resonance energy transfer (FRET) and bioluminescence resonance energy transfer (BRET) sensors to monitor the conformational changes in GPCRs, GPCR/G proteins, or GPCR/β-arrestin, especially over the past two decades. Here, we will summarize how these sensors have been optimized to increase the sensitivity and compatibility for application in different GPCR classes using various labeling strategies, meanwhile provide multiple solutions in functional assays for high-throughput drug screening.

Keywords: GPCR, functional assay, G-protein, β-arrestin, dimerization, BRET, TR-FRET

Edited by:
Wei Liu,
Shenzhen Peking University
Hong Kong University of Science and Technology Medical Center,
China

Reviewed by:
Takeaki Ozawa,
The University of Tokyo, Japan
Mohammed Akli Ayoub,
United Arab Emirates University,
United Arab Emirates

***Correspondence:**
Chanjuan Xu
chanjuanxu@hust.edu.cn
Jianfeng Liu
jfliu@mail.hust.edu.cn

Specialty section:
This article was submitted to Membrane Traffic,
a section of the journal Frontiers in Cell and Developmental Biology

Received: *29 September 2020*
Accepted: *05 February 2021*
Published: *10 May 2021*

Citation:
Zhou Y, Meng J, Xu C and Liu J (2021) Multiple GPCR Functional Assays Based on Resonance Energy Transfer Sensors.
Front. Cell Dev. Biol. 9:611443.
doi: 10.3389/fcell.2021.611443

INTRODUCTION

G protein-coupled receptors (GPCRs) represent one of the largest membrane receptor superfamily, which is encoded by approximately 3% of human genes and over 800 members (Klabunde and Hessler, 2002; Fredriksson et al., 2003; Pin et al., 2019). They are widely expressed in all cells and organs from brain tissue to blood vessels, and are responsible for sensing a variety of external stimuli, ranging from light and temperature to neurotransmitters, peptides, and lipids (Lagerstrom and Schioth, 2008). GPCRs are involved in diverse physiological activities and play critical roles in pathogenesis, making them important drug targets (Sriram and Insel, 2018).

Members of the GPCR superfamily share a common seven-transmembrane (7TM) topology, and are classified into classes A, B, C, and F according to sequence similarity (Fredriksson et al., 2003; Fredriksson and Schioth, 2005). Generally, class A GPCRs possess a short extracellular

---

Abbreviations: β_2AR, β_2-Adrenergic receptor; α_{2A} AR, α2A adrenergic receptor; A_{2A}R, A_{2A}-adenosine receptor; AT_1R, angiotensin II receptor type 1A; BRET, bioluminescence resonance energy transfer; FRET, förster resonance energy transfer; $GABA_B$ receptor, metabotropic γ-aminobutyric acid receptors; GFP, green fluorescent protein; GPCRs, G protein-coupled receptors; HTS, high-throughput screening; ICL, intracellular loop; KOR, κ opioid receptor; LH, luteinizing hormone receptor; mGluR, metabotropic glutamate receptor; $P2Y_2$R, Purinergic receptor; PTHR, Parathyroid hormone 1 receptor; Rluc, Renilla Luciferase; TM, Transmembrane helix; TR-FRET, time-resolved FRET; VFT, Venus fly-trap; YFP, yellow fluorescent protein; 7TM, seven-transmembrane.

domain (ECD), while class C GPCRs have a large ECD called Venus Flytrap domain (VFT). Ligand binding induces conformational changes from the extracellular ligand-binding site to the intracellular side of the receptor. The outward movement of the cytoplasmic end of transmembrane domain (TM) 6 in class A GPCRs opens up an intracellular cavity to accommodate the Gα subunit and activate G protein; in class B GPCRs, TM6 shows a disruption of the helical fold and the formation of a sharp kink to bind Gα subunits (Hilger et al., 2020). In contrast to Class A and B GPCRs, which are reported to function as monomers, class C GPCRs are reported as obligatory dimers (Kniazeff et al., 2011). Ligand binding to class C GPCR leads to the closure of VFT, triggering the conformational change in the cysteine-rich domain or stalk domain, further rearranging the TMs from inactive interface to TM6/TM6 active interface, which is similar in class C GPCR homodimers such as metabotropic glutamate receptor type 2 (mGlu2) (Xue et al., 2015), mGlu5 (Koehl et al., 2019), and calcium sensing receptor (CaSR) (Liu et al., 2020), or heterodimer, like metabotropic γ-aminobutyric acid receptors ($GABA_B$ receptor) (Xue et al., 2019; Mao et al., 2020; Papasergi-Scott et al., 2020; Park et al., 2020; Shaye et al., 2020). Hence, monitoring the conformational changes of GPCRs provide a structural basis to evaluate GPCR activation.

The classical functional assays used to measure the activity of GPCRs are mainly based on downstream messengers, such as Ca^{2+} release, 1, 4, 5-inositol phosphate (IP3)/IP1 accumulation, cyclic adenosine monophosphate (cAMP) production, or reporter gene expression (Thomsen et al., 2005). Most of them have been successfully developed into high-throughput screening (HTS) and robust assays, and widely applied in the pharmaceutical industry and academic research (**Figure 1A**). Furthermore, with the discovery of G protein-independent β-arrestin signaling, functional assays have been developed by detecting β-arrestin recruitment to GPCRs or β-arrestin-induced GPCR internalization (Zhang and Xie, 2012; **Figure 1B**), while the first GPCR biased drug have been approved by FAD recently (Mullard, 2020). In addition to these classical assays, multiple functional assays based on resonance energy transfer (RET), which is a technology to detect the protein-protein interaction, have been developed in recent years for directly monitoring conformational changes in GPCRs, G proteins, and β-arrestins (**Figure 1C**). Using these sensors, the GPCR signaling profiles and GPCR activation process have been investigated at multiple scales.

RET sensors have been well-reviewed to illustrate GPCR activation and signaling previously (Lohse et al., 2012; Kauk and Hoffmann, 2018; El et al., 2019; Haider et al., 2019; Quast and Margeat, 2019). In this review, we have summarized the FRET and BRET sensors, which contributed to G protein and β-arrestin signaling, intra-GPCR rearrangement, and inter-GPCR movement investigations, especially in recent years. Meanwhile, we will focus on how these sensors are optimized to better investigate GPCR signaling and adapted to HTS in functional assays, as well as what new mechanism have been identified based on these sensors.

THE PRINCIPLES OF RET

RET is a photo physical process, in which the energy of a fluorescent donor is transferred to a suitable fluorescent energy acceptor (Förster, 1948; **Figure 2**). The efficiency of RET depends on three parameters: (1) the emission spectrum of the donor overlaps with the excitation spectrum of the acceptor; (2) the distance between the fluorophores is within 100 Å; (3) the relative orientation of their dipole moments toward each other (the parallel dipole orientation gets highest RET) (Stryer, 1978). According to the fluorescent labels, RET sensors can be normally classified into FRET and BRET. The excitation of FRET donor fluorophores needs an extra excitation laser, while BRET is based on the use of light-emitting enzymes-luciferase and other different variations. RET is a good approach to measure the GPCR activation and signaling in a living system (Cottet et al., 2012; Lohse et al., 2012; Kauk and Hoffmann, 2018).

GPCR/G PROTEIN SIGNALING FUNCTIONAL ASSAYS

Sensors for GPCR/G Protein Interaction

G protein heterotrimer activity is initiated by exchange of GDP with GTP, when ligand binding to GPCR triggers the G protein coupling to the receptor (Neubig, 1994). Though some RET-based sensors have used to detect the dynamic interaction of G proteins to GPCRs upon stimulation (**Table 1**; Azpiazu and Gautam, 2004; Gales et al., 2005; Hein et al., 2005; Nobles et al., 2005; Philip et al., 2007; Audet et al., 2008), agonist-induced G protein recruitment represents high diversity and specificity among different G protein subtypes and GPCRs (Du et al., 2019) and dynamic GPCRs and G proteins interactions cannot always easily be detected. MiniG proteins are used to improve the stability of the GPCR-G protein complex (Nehme et al., 2017). They are modified by deleting membrane anchor domains and the Gβγ binding surface in wild-type Gα proteins, and mutated in many positions to increase GPCR/G protein complex stabilization (Nehme et al., 2017; Wan et al., 2018). MiniG BRET sensors used energy pair of *Renilla* luciferase (Rluc) and Venus fused in GPCR and miniG protein, respectively (**Figure 3A**), which can effectively recognize different families of GPCRs, even class F GPCRs (Wright et al., 2019). MiniG BRET sensors can be used to investigate the dynamic interactions of GPCRs with almost all G protein families, including $G\alpha_{i/o}$, Gαs, $G\alpha_{12/13}$, and $G\alpha_{q/11}$ (Wan et al., 2018). And then, the $miniG_q$ sensor is successfully applied in HTS compare of 5-HT_{2A} serotonin receptor hallucinogen agonists (Kim et al., 2020). Further optimization of miniG BRET sensors by replacing the BRET donor Rluc with NanoLuc (Nluc), which has stronger brightness and smaller size (Hall et al., 2012), or replacing the BRET donor and acceptor with NanoLuc Binary Technology (NanoBiT) pairs, which is based on the Nluc complementation system consisting of LgBiT (18 kDa) and SmBiT (1.3 kDa) proteins (Dixon et al., 2016), can further increase the sensitivity. The optimized miniG sensors can be used to detect GPCR

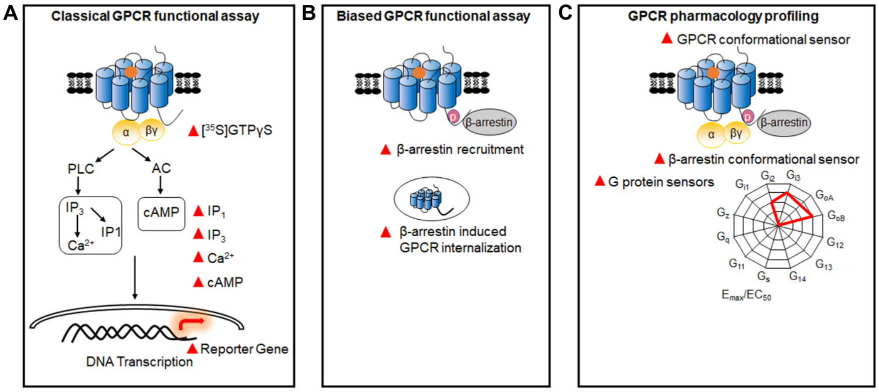

FIGURE 1 | GPCR functional assays. **(A)** Classical GPCR functional assays based on the measurement of GTPγS, and Ca^{2+}, IP1, IP3, cAMP, and reporter gene. **(B)** Biased GPCR functional assays. Assays were used to identify the biased signals between G proteins and β-arrestins, through detecting β-arrestin recruitment and GPCR internalization. **(C)** Multiple GPCR pharmacology profiling. GPCR sensors based on the conformational changes of different G protein subtypes, β-arrestins, and GPCRs.

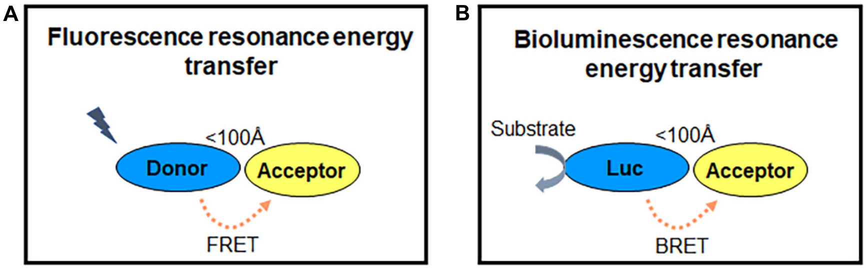

FIGURE 2 | RET principle. **(A,B)** FRET and BRET detect energy transfer between two proteins within 100 Å, while one fluorophore is excited by laser as energy donor in FRET **(A)** and enzymes (luciferase) reacting with substrate (coelenterazine) to emit light as the energy donor in BRET **(B)**. The energy acceptor is another fluorophore in both FRET and BRET.

activation in intracellular compartments, such as the Golgi apparatus (Wan et al., 2018).

Sensors for G Protein Heterotrimer

As G protein can pre-associate to some GPCRs in the absence of ligand (Gales et al., 2005; Nobles et al., 2005; Philip et al., 2007; Audet et al., 2008), detecting G protein heterotrimer activity provides a more general way to evaluate GPCR activation. Measuring the proximity change between Gα and Gβγ subunits through BRET assay (**Figure 3B**), can reflect the G protein heterotrimer states and activation of GPCRs (Galés et al., 2006). Three flexible regions in Gα_i around amino acid numbers 91, 122, and 60 were reported to be accessible for BRET sensors insertion, according to Gα subunit structure. Interestingly, the BRET ratio between Gα_{i1}-91Rluc or Gα_{i1}-122Rluc and green fluorescent protein (GFP) 10-Gγ decreased significantly, whereas Gα_{i1}-60Rluc and GFP10-Gγ exhibited an increase of BRET ratio during α_{2A} AR activation (Galés et al., 2006). This indicates that small rearrangements have occurred in the Gαβγ heterotrimer, which can be detected using BRET assay. Rluc can be replaced by Rluc8 and other enhanced luciferases (Rluc II) to increased brightness and quantum yield in BRET (Loening et al., 2006; Sauliere et al., 2012). Based on optimized BRET sensors, activation of different G protein subtypes can be measured, such as Gα_i, Gα_o, Gα_s, Gα_q, Gα_{12}, and Gα_{13}. GPCR ligand such as S II, which was previous known as β-arrestin-biased agonist of angiotensin II receptor type 1A (AT$_1$R) using classical functional assays, is considered as partial agonist, as it can induce ∼20% BRET ratio change in G$_{i/o}$, G$_q$, and G$_{13}$ compared with the full agonist Ang II (Sauliere et al., 2012). It indicated the advantage and the necessity to combine BRET sensor in GPCR functional assays and proved the HTS application of BRET sensors in G protein signaling.

The G protein BRET sensors can be useful tools to evaluate the activity of individual G protein subtypes and many sensors have been reported as summarized in **Table 1**. However, not all the subtypes can be detected with good sensitivity. The new BRET Gαβγ biosensors TRUPATH have systematically optimized the insertion positions of the donor in Gα and the best combination of Gβ and Gγ subtypes. 14 optimized sensors have been developed, including the first Gα_{15} and G$\alpha_{Gustducin}$ sensors (Olsen et al., 2020). TRUPATH biosensors extremely increase the sensitivity of G protein BRET functional assays, contributing to the development of a powerful platform to investigate most G proteins activation in an array of GPCRs agonists, antagonists, inverse agonists and biased ligands. Meanwhile, NanoBiT system

TABLE 1 | The typical sensors for GPCR and modulators.

Targetedmodulators	Donor-acceptor pairs	Comments	Receptor/ modulator	References
Gprotein				
GPCR-G protein	CFP-YFP	The FRET sensor illustrated M2R and G_o protein form the exclusive complex after agonist stimulation at membrane.	M2R/$G\alpha_o$-$G\beta$.	Azpiazu and Gautam, 2004
	Rluc-GFP	BRET sensor measuredthe direct and kinetic interaction of $G\alpha_s\beta_1\gamma_2$ proteins and β_2AR in living cells, and supported the precoupling of $G\alpha_s\beta_1\gamma_2$-β_2AR by basal BRET signal.	β_2AR/$G\alpha_s\beta_1\gamma_2$	Gales et al., 2005
	CFP-YFP	The FRET sensor detected the fast agonist-induced α_{2A}AR- $G\alpha_{i1}\beta_1\gamma_2$ interactionkinetic in single living cell (<100 ms).	α_{2A}AR/$G\alpha_{i1}\beta_1\gamma_2$	Hein et al., 2005
	CFP-YFP	The FRET sensor identified α_{2A}AR pre-coupled to G_o protein but not G_s,while IP pre-coupled to G proteins in opposite way, indicating the specific interaction between GPCRs and G proteins.	α_{2A}AR/$G\alpha_o$/$G\alpha_s$ IP/$G\alpha_o$/$G\alpha_s$	Nobles et al., 2005
	eCFP-eGFP	The FRET sensorobserved B_2R pre-coupled to $G\alpha_q\beta\gamma$protein in the resting statewhich allowed for a rapid and directed cell response.	B_2R/$G\alpha_q$	Philip et al., 2007
	Rluc8-Venus/ Nluc-Venus	The miniG BRET sensor is modified from native G protein,obtained higher stability and selectivity. The miniG BRET sensors can recognize and stabilize the active states of β_2AR and several Frizzled paralogs.	β_2AR/miniGα_s β_2AR/miniGα_{12} Frizzled receptors/miniGα	Wan et al., 2018; Wright et al., 2019
$G\beta\gamma$protein-GRK	Nluc-Venus	These sensors can quantitatively detectthe magnitudes and kinetics of GPCRs general $G\beta\gamma$-GRK interaction allowed the fingerprinting to be profiled of individual GPCR.	$G\beta\gamma$-masGRK3ct	Masuho et al., 2015
Gprotein-specific unimolecules	Nluc-YFP	Membrane-anchored unimolecular BRET sensor specifically binds to GTP-$G\alpha$protein and produce the BRET signal to indicate the activity of endogenous GPCRs/G proteins without any modifications.	α_{2A}AR/$G\alpha_i$ M3R/$G\alpha_q$ PAR1/$G\alpha_{13}$	Maziarz et al., 2020
$G\alpha\beta\gamma$ heterotrimer rearrangement	CFP-YFP	The G protein heterotrimer FRET sensor measured α_{2A}AR ligand-induced G protein activity, indicating the rearrangement occurred in $G\alpha_i\beta_1\gamma_2$ heterotrimer instead of dissociation, and detecting activation of G protein in 1-2s, slower than receptors activation.	α_{2A}AR/$G\alpha_i\beta_1\gamma_2$	Bunemann et al., 2003
	Rluc-GFP10	The multiple sites inserted BRET sensorscan monitor conformational rearrangementsat $G\alpha_{i1}\beta_1\gamma_2$subunits interfaces after α_{2A}AR stimulation, supporting the open interface of $G\alpha_{i1}\beta_1\gamma_2$ rather than totally dissociation.	α_{2A}AR/$G\alpha_{i1}\beta_1\gamma_2$	Galés et al., 2006
	Rluc8-GFP10	With high sensitivity, the BRET sensors re-defined the SII as the partial agonist of AT_1R rather than β-arrestins biased agonist by detecting multiple G protein heterotrimersactivities.	AT_1R/$G\alpha\beta\gamma$	Sauliere et al., 2012
	Rluc8-GFP	The study generated through exhaustive protein engineering and empirical testing, building the TRUPATH suite of $G\alpha\beta\gamma$ biosensors includes the first $G\alpha_{15}$ and $G\alpha_{Gustducin}$ probes.	β_2AR/$G\alpha\beta\gamma$ κOR/$G\alpha\beta\gamma$ CB_1R/$G\alpha\beta\gamma$ μOR/$G\alpha\beta\gamma$ NT_1R/$G\alpha\beta\gamma$	Olsen et al., 2020
	Nluc	The NanoBiT system is used for monitoring the most G protein heterotrimers kinetics in real-time with highly reproducible signals under most GPCRs, such as AT_1R, D2R, Prostanoid receptors.	Prostanoid receptors/$G\alpha\beta\gamma$ AT_1R/$G\alpha\beta\gamma$ β_2AR/$G\alpha\beta\gamma$ D2R/$G\alpha\beta\gamma$	Inoue et al., 2019
	CFP-YFP	FRET sensor of $G\alpha_s$ protein heterotrimer exhibited the decrease in ratiometric FRET after 100 μM adenosine stimulation of A_{2A}R, indicating α and $\beta\gamma$ subunits of G_s dissociated or at least reoriented.	A_{2A}R/$G\alpha_s\beta_1\gamma_2$	Hein et al., 2006
	CFP-YFP	Using FRET-based assay developed the direct sensors in mammalian to measure multiple G protein subtypes heterotrimer changes, it is indicated that $G\alpha_i$ and $G\alpha_z$ undergo rearrangement rather than dissociation, whereas $G\alpha_o$ dissociate or rearrange in distinct manner after α_{2A}AR activation.	α_{2A}AR/$G\alpha_{o/i/z}\beta_1\gamma_2$	Frank et al., 2005
	YFP-mTurquoise	The improved G_qFRET sensor (with the best CFP variant) firstly allowed the detection of K_{on} of G_q and the FRET sensor indicated the dissociation of $G_q$from G protein heterotrimer after stimulation of H1R.	H1R/$G\alpha_q\beta_1\gamma_2$	Adjobo-Hermans et al., 2011

(Continued)

TABLE 1 | Continued

Targeted modulators	Donor-acceptor pairs	Comments	Receptor/modulator	References
	Venus-mTurquoise2	The $G\alpha_{13}$ FRET sensor can be used to detect heterotrimeric Gproteinsactivity in HeLa and primary HUVECs,and the sensor confirmed the dissociation of $G\alpha_{13}$ from $G\alpha\beta\gamma$ complex under LPA2 receptor and PARs stimulation.	LPA2 receptor/$G\alpha_{13}\beta_1\gamma_2$ PARs/$G\alpha_{13}\beta_1\gamma_2$	Mastop et al., 2018
β-arrestins				
GPCR/β-arrestins	Rluc-YFP	The BRET sensor detected the β-arrestin2 interaction with β_2AR after agonist addition with high sensitivity.	β_2AR/β-arrestin2	Angers et al., 2000
	Rluc-eYFP	These BRET sensors were used to identify the interaction of β-arrestins with TRHRs, and then revealed TRHR1 interacted equally β-arrestin1 and 2 while TRHR2 only interacted with β-arrestin2 that correlated with β-arrestins promoted internalization of TRHRs.	TRHRs/β-arrestins	Kroeger et al., 2001; Hanyaloglu et al., 2002
	Rluc-YFP	Using OTR/β-arrestin BRET sensor obtained the result that the BERT signal started at 10s and achieved the peak at 35s, indicated the delay and slow course of β-arrestin recruitment may be limited by receptors phosphorylation via GRK.	OTR/β-arrestin2	Hasbi et al., 2004
	RlucII-rGFP	Enhanced bystander(Eb) BRET sensor monitored compartmental trafficking of β-arrestins/AT_1R complex and compartmentalβ-arrestin recruitment induced by AT_1R agonist with high spatial-temporal resolution in living cells, providing the clear imaging BRET signal.	AT_1R/β-arrestin2	Namkung et al., 2016
	CFP-YFP	The FRET sensor was used to detect the dynamic GPCR/β-arrestins interaction and provided the evidence oftime delay compared to the activation of PTHR.	PTHR/β-arrestin2	Vilardaga et al., 2002, 2003
	CFP-GFP/YFP	The study used FRET sensors to classify the $P2Y_2$ receptor as a class A receptor when stimulated with ATP or as a class B receptor when stimulated with UTP, according to the interaction manners with β-arrestins.	$P2Y_2$R/β-arrestins	Hoffmann et al., 2008
	FlAsH/ReAsH	Double site-specific and orthogonal labeled FRET sensor was proposed in PTHR/β-arrestin2interaction investigation with minimal disturbance of their function proved the method may be widely applied.	PTHR/β-arrestin2	Zurn et al., 2010
β-arrestins conformational changes	Rluc-YFP/GFP	The double-brilliance β-arrestin intramolecular BRET sensor firstly allowed the real-time monitoring of conformational changes of β-arrestin2 after both classA (β_2AR) and class B (V2R) receptors activation in intact cells.	β_2AR/V2R β-arrestin2	Charest and Bouvier, 2003; Charest et al., 2005
	Rluc-YFP	The intramolecular BRET sensor observed the different conformational changes of β-arrestin2 upon stimulations of biased ligands or unbiased ligands under AT_1R, β_2AR and PTH1R.	β_2AR/β-arrestin2 AT_1R/β-arrestin2 PTH1R/β-arrestin2	Shukla et al., 2008
	Nluc-CyOFP1	The optimized BRET sensorsdetected β-arrestin2 partial active state under AT_1R stimulations with increased brightness and wider spectral separation, and the sensors can be applied with a wide panel of class A and B receptors even orphan receptors.	AT_1R/β-arrestin2	Oishi et al., 2020
	CFP-FlAsH	The FlAsH-FRET sensorshave advantages of the small size and robust fluorescence signal. The multiple sites inserted FlAsH-FRET sensors detected different conformational changes in β-arrestin2 under β_2AR and M_2AChR after agonist stimulation, and supportedreceptor-specific patterns of conformational changes in β-arrestin2.	β_2AR/β-arrestin2 M_2AChR/β-arrestin2	Nuber et al., 2016
	Rluc-FlAsH	A series of intramolecular FlAsH-BRET sensors were designed todetect different conformational changes in β-arrestins under multiple GPCRs, such as PTH_1R, β_2AR and AT_1R, supporting that specific ligand-receptors could invoke different conformational changes in β-arrestins and provide the insight into mechanism of GPCRs generating diverse functions.	PTH_1R/β-arrestin2 β_2AR/β-arrestin2 AT_1R/β-arrestin2	Lee et al., 2016

TRHR, Thyrotropin-releasing hormone receptors; OTR, Oxytocin receptor; V2R, V2 vasopressin receptor; PTH1R, Parathyroid hormone 1 receptor; α_{2A} AR, α2A adrenergic receptor; β_2AR, β_2-Adrenergic receptor; $P2Y_2$R, purinergic receptor; A_{2A}R, A_{2A} adenosine receptor; mTurquoise, Monomeric Turquoise; H1R, Histamine H1 receptor; PARs, protease activated receptors; IP, prostacyclin receptor; κOR, κ-opioid receptor; μOR, μ-opioid receptor; CB_1R, cannabinoid-1 receptor; NT_1R, Neurotensin-1 receptor; D2R, Dopamine D2 receptor; B_2R, B2-Bradykinin receptor; M3R, M3 muscarinic acetylcholine receptor; M2R, M2 muscarinic acetylcholine receptor.

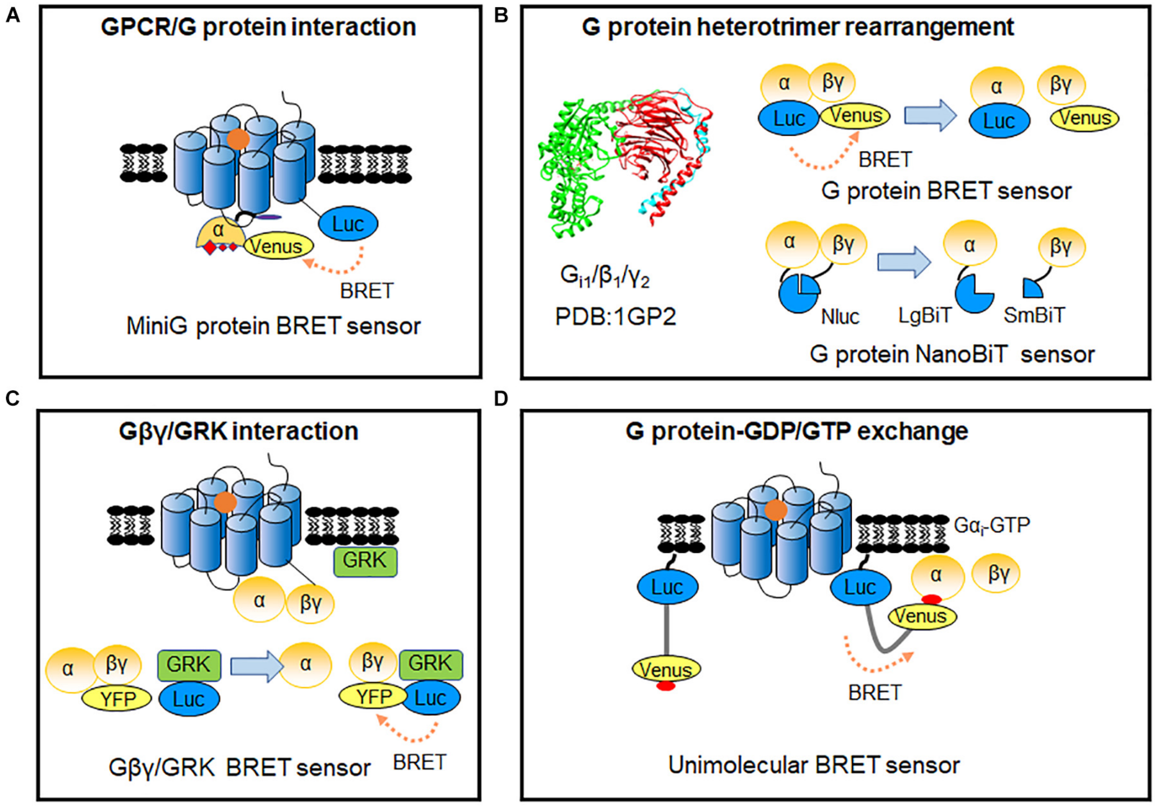

FIGURE 3 | RET-sensors for GPCR/G protein interaction. **(A)** MiniG protein BRET sensor. MiniG protein was introduced into BRET sensors for G protein recruitment detection. **(B)** G protein heterotrimer-based sensor. Luciferase and YFP-tagged Gα-Gβγ constitute the G protein intermolecular BRET sensor for detecting the rearrangements of G protein heterotrimers (upper). G protein heterotrimer NanoBiT sensor based on Nluc complementation system was applied to monitor G protein heterotrimer rearrangements (lower). **(C)** Gβγ-GRK BRET sensor. The BRET signal was produced between the Gβγ and GRK after GPCR activation. **(D)** Unimolecular BRET sensor, BERKY biosensor (BRET biosensor with ER/K linker and YFP). After G protein activation, the detector module YFP-KB-1753 binds to active G-protein $G\alpha_i$-GTP on membranes, and the BRET signal produced between N-terminus Nluc and YFP.

has been used to modify the G protein sensors (**Figure 3B**). The advantages of the smaller size and strong signal can avoid possible steric hindrance induced by large proteins such as Rluc, GFP or Venus, and enable the stable detection in hours (Dixon et al., 2016; Inoue et al., 2019).

To further compare the activation efficacy between different G protein subtypes, Gβγ-GRK NanoBRET sensor has been developed based on the Gβγ subunit and lipid-modified reporter peptide GRK3ct (masGRK3ct) (Hollins et al., 2009; Masuho et al., 2015; **Figure 3C**). The NanoBRET strategy was achieved by fusing Nluc to the GRK3ct and Venus to Gβγ (Masuho et al., 2015). It can determine both the kinetics and extent of G protein activation to independently analyze the catalytic activities of GPCRs and their signaling efficacy toward various targeted Gα protein subtypes (Masuho et al., 2015; Hauser et al., 2018).

Up to now, tools that are suitable for primary cells or native tissues of endogenous GPCRs remain limited. Very recently, Maziarz et al. (2020) developed a type of BRET biosensor with ER/K linker and YFP, called BERKY biosensor to capture the GTP form of the Gα protein (**Figure 3D**). The membrane-anchoring sequence-fused Nluc was used as the BRET donor, and the YFP-fused synthetic peptide KB-1753 served as the acceptor (Johnston et al., 2006). This unimolecular biosensor can specifically and sensitively bind to $G\alpha_i$-GTP, and causes an increased BRET signal. It allows endogenous Gα-GTP and free Gβγ to be detected in primary living cells, and record the activation of G proteins in native, physiological environments. BERKY biosensors have been developed for endogenous $G\alpha_q$-GTP, $G\alpha_{13}$-GTP, free Gβγ, and Rho-GTP in cells via a similar strategy (Maziarz et al., 2020).

GPCR/β-ARRESTIN SIGNALING FUNCTIONAL ASSAYS

β-arrestins are considered to be prominent mediators of GPCR internalization, facilitating GPCR desensitization and the negative regulating G proteins (Lefkowitz, 1998). β-arrestins also act as key modulators of GPCRs to initiate G protein-independent signaling pathways (Lefkowitz and Shenoy, 2005). Based on the interaction with β-arrestins, GPCRs can be classified into class A and B. Class A GPCRs interact with β-arrestins rapidly and transiently, whereas class B GPCRs stably associate with β-arrestins with a higher affinity (Oakley et al., 2000; Hasbi et al., 2004). β-arrestins can adopt different conformational

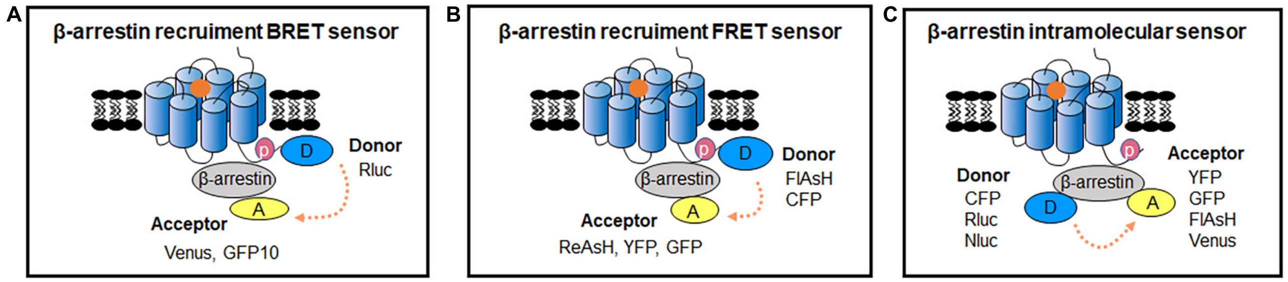

FIGURE 4 | RET-sensors for GPCR/β-arrestin interaction and intramolecular β-arrestin conformational change. **(A)** Schematic representation of the BRET sensor for β-arrestin recruitment to GPCRs. Luciferase and YFP were introduced between β-arrestin and GPCRs, the BRET signal increased after GPCR activation. **(B)** β-arrestin recruitment FRET sensor. Different fluorophore pairs are introduced into FRET assay to better monitor β-arrestins dynamic recruitment to receptors in living cells. Donor-acceptor: FlAsH-ReAsH CFP-YFP CFP-GFP. **(C)** β-arrestin intramolecular sensor. The FRET-based and BRET-based intramolecular sensors are introduced in living cells to detect β-arrestins conformational changes, and multiple fluorophore pairs are applied. Donor-acceptor: CFP-FlAsH CFP-YFP CFP-GFP Rluc-YFP Rluc-GFP Rluc-Venus Nluc-Venus Nluc-YFP.

changes while interacting with phosphorylated GPCRs (Shukla et al., 2008). The dynamic of β-arrestin conformational rearrangement can be longer than GPCR/β-arrestins interaction (Nuber et al., 2016). Accordingly, there are two main types of biosensors for studying the kinetics of GPCR/β-arrestin signal based on BRET and FRET: intermolecular sensors used for monitoring GPCR/β-arrestin dynamic interactions and intramolecular sensors used for measuring β-arrestin conformational rearrangement (**Table 1**; Bertrand et al., 2002; Charest and Bouvier, 2003; Krasel et al., 2005).

Sensors for GPCR/β-Arrestin Interaction

BRET sensors detecting recruitment of β-arrestins to active GPCRs in living cells was firstly reported by Angers et al. (2000). They used Rluc and GFP as BRET donor and acceptor, which were fused to the C terminus of β2 Adrenergic receptor (β_2AR) and β-arrestin2, respectively (**Figure 4A**). The results showed a large increase in BRET ratio following β_2AR stimulation, and represented an agonist concentration-dependent manner. Subsequently, many similar studies investigated the recruitment of β-arrestins to GPCRs (**Table 1**). Furthermore, this kind of BRET sensors were successfully applied in HTS for GPCRs antagonists, which show compatibility and sensitivity as a functional assay (Hamdan et al., 2005).

While the conventional BRET sensors use the non-natural combination of donor and acceptor from different species such as Rluc from *Renilla reniformis* and GFP from *Aequorea Victoria* to limit non-specific signals from random interaction, enhanced bystander BRET (EbBRET) sensor is composed with BRET energy pairs both from *Renilla reniformis*. It possesses moderate affinity, optimally transferred energy, and improved signal, which shows the advantage in investigation of compartmental and ligand-biased β-arrestin trafficking in the plasma membrane and endosomal membrane in real time (Molinari et al., 2008; Namkung et al., 2016). EbBRET sensors can work in real time image recording up to 20 min, greatly facilitating the studies of β-arrestin and GPCR trafficking at high spatial and temporal resolutions (Lan et al., 2012; Namkung et al., 2016; Cao et al., 2019).

Compared to BRET sensors, FRET sensors are more suitable for visualizing the kinetics of GPCRs and β-arrestins with high temporal resolution in cells (Lohse et al., 2012; **Figure 4B**). Using the FRET sensor, which consists of the CFP-labeled parathyroid hormone 1 receptor (PTH1R) and YFP-labeled β-arrestin2, has shown a time delay of β-arrestin2 recruitment to PTHR after receptor activation (Vilardaga et al., 2002, 2003). Through comparing the recruiting rate of β-arrestin2 to β_2AR, repeated short-term stimulation promoted β_2ARs phosphorylation and showed very rapid increase of FRET with $t_{0.5}$ at 2.1 s, while the first stimulation caused fairly slow FRET change ($t_{0.5}$ of 19.6 s), which indicate the GPCR phosphorylation is the rate-limiting step for β-arrestin recruitment (Krasel et al., 2005). Furthermore, β-arrestin subtypes: β-arrestin1 and β-arrestin2 can exist different recruitment manner to the same GPCR when stimulated with different ligand, such as P2Y$_2$R (a Purine receptor subtype) agonist UTP induced both β-arrestin1 and β-arrestin2 interacted with P2Y$_2$R, whereas ATP caused stronger interaction of β-arrestin1 than β-arrestin2 with P2Y$_2$R (Hoffmann et al., 2008).

To reduce the size of FRET acceptor, a smaller fluorescent probe fluorescein arsenical hairpin binder (FlAsH) was introduced as FlAsH-FRET sensors (**Figure 4B**). A short peptide of 6 amino acids containing tetracysteine was inserted into the targeted protein, which can specifically bind to FlAsH dyes that produce FRET signal between proximate fluorophore pairs. The CFP/FlAsH FRET sensors showed almost five times the signal amplitude compared to the CFP/GFP FRET sensors (Hoffmann et al., 2005). And then, the double site-specific and orthogonal labeling FRET sensor such as FlAsH/ReAsH (a red arsenical hairpin binder) can also be introduced to investigate GPCR/β-arrestin dynamic interaction (Zurn et al., 2010).

β-Arrestin Intramolecular Sensors

β-arrestin conformational change occurs following recruitment to the receptor (Charest et al., 2005; Nuber et al., 2016). β-arrestin intramolecular BRET biosensor is based on the proximity change between the N- and C-terminus of β-arrestin (**Figure 4C**). Intramolecular BRET sensors (Luc-β-arrestin-YFP) indicated that β-arrestin can adopt multiple active conformations with different ligands treatment (Shukla et al., 2008). It can be optimized by using Nluc and red-shifted fluorescent protein (CyOFP1) to increase brightness and wider spectral separation (Oishi et al., 2020). This sensor can monitor the early conformational changes of β-arrestin 2 in complex with GPCRs, with a wide panel of different class A and class B GPCRs upon agonist activation, and with orphan GPCRs known to spontaneously recruit β-arrestin2. After the R170E mutation was introduced, the sensor was able to detect the partial active state of β-arrestin2. It permits the monitoring of β-arrestin change in different stage during the GPCR activation (Oishi et al., 2020). Additionally, intramolecular FlAsH-BRET sensors using Rluc and FlAsH pair or intramolecular FlAsH-FRET sensors using CFP and FlAsH pair have also been developed (**Figure 4C**). They confirmed distinct conformational changes in β-arrestins induced by different ligands and GPCRs (Lee et al., 2016; Nuber et al., 2016; Strungs et al., 2019).

INTRAMOLECULAR CONFORMATIONAL GPCR SENSORS

Though GPCR intramolecular RET sensors have already been developed in 1995 in purified GPCRs (Gether et al., 1995), Vilardaga et al. firstly reported a FRET sensor to detect GPCR conformational changes in living cells, which inserts CFP at the ICL3 and YFP at the C-terminus (**Figure 5A**) in PTHR and α_{2A} AR (Vilardaga et al., 2003, 2005). Using this sensor, the authors presented different FRET signals induced by full agonists (a strong decrease) and partial agonists (a weak decrease) or inverse agonists (a significant increase) of α_{2A} AR, indicating the dynamic activation process and distinct receptor conformation rearrangements specific to different ligands. Then, many similar intramolecular conformational GPCR sensors have been developed, such as β_1AR (Rochais et al., 2007), β_2AR (Reiner et al., 2010), A_{2A}-adenosine receptor (A_2AR) (Hoffmann et al., 2005), and B_2-Bradykinin receptor (B_2R) (Chachisvilis et al., 2006) as shown in **Table 2**. FlAsH labeling provided an alternative choice to replace CFP or YFP (**Figure 5A**). The FlAsH labeling (∼1 kDa) can be induced into the ICL3 of GPCRs as the energy acceptor, while inserting CFP as donor at the C-terminus. This FlAsH-FRET sensor confirmed the similar fast kinetics of GPCR activation and also showed a fivefold improvement in signal-to-noise ratio (Hoffmann et al., 2005).

Similar intramolecular BRET sensors of GPCRs were also used to monitor the conformational rearrangement promoted by diverse ligands (Sleno et al., 2016, 2017; Bourque et al., 2017; Devost et al., 2017). Intramolecular FlAsH-BRET sensors are modified the C-tail with Rluc II, and introduced FlAsH labeling in the ICL3 (**Figure 5B**). In the case of the F prostanoid receptor, AT1R, and β_2AR, although three FlAsH-BRET sensors were constructed in a similar way, the BRET signals exhibited receptor-specific behavior, indicating that different GPCRs have unique conformational profile (Bourque et al., 2017). Furthermore, distinct patterns of conformational changes can be observed by biased ligand. Multiple positioned FlAsH-BRET sensors of AT_1R showed rapid, sustained and robust BRET signals to allow the comparison of the full agonist and biased ligands stimulation (Devost et al., 2017). Moreover, intramolecular BRET sensors can be used to investigate the allosteric interactions between two receptors, such as the heterodimeric AT1R and prostaglandin F2α receptors (Sleno et al., 2017).

Alternatively, BRET assay with Nluc and YFP or GFP10 can be used to detect the GPCR conformational rearrangements (**Figure 5B**), which can be induced by various compounds or mutation in the receptor as well as the impact of interacting proteins (Picard et al., 2018). Schihada et al. (2018) screened the efficacy of different fluorescent proteins or dyes as acceptors, combined with Nluc as a BRET-based α_{2A} AR biosensor, NanoBRET 618 (Nluc and Halo Tag dye pair) showed the highest amplitude upon agonist stimulation. It is a powerful approach to distinguish slight differences induced by partial agonist in the BRET signal instead of the full agonist effect identified by classical cAMP assay. These BRET sensors are also adaptable for micro-liter plate assays with HTS formats.

A novel assay for detecting conformational changes in GPCRs, based on nanobodies recognizing specific conformations, has been reported in recent years. Several conformation-specific nanobodies for GPCRs have been developed, including κ opioid receptor (KOR) (Che et al., 2018), μ opioid receptor (Huang et al., 2015), M2-muscarinic receptors (Kruse et al., 2013), β_2AR (Rasmussen et al., 2011), AT_1R (Szalai et al., 2012), and mGlu2 (Scholler et al., 2017b). For example, two conformation-sensitive nanobodies of KOR, Nb39 and Nb6, recognize the active and inactive states, respectively (Che et al., 2018). Combined with the BRET approach, it can be used to detect KOR activity. For the Nb6 sensor, a strong BRET ratio decreased upon KOR activation induced by agonist, in which Nb6 dissociated from activated receptors and recovered after the antagonist addition, while the Nb39 sensor had the opposite effect (**Figure 5C**). Moreover, the conservative binding of Nb6 in the region provides a compatible tool for ligand-induced active conformational changes of other class A GPCRs, when replace their ICL3 by KOR ICL3 (Che et al., 2020). Nanobody-based GPCR conformational sensors also have the advantage of investigating the transactivation induced by other receptors. For example, Nb80, an active β2AR sensitive nanobody, was used to analyze the effect of vascular endothelial growth factor receptor 2 on β_2AR activation (Kilpatrick et al., 2019). Nanobody application reduced the modification in GPCRs. However, as there are only a few nanobodies available for GPCRs and the intellectual property protection, the application of nanobodies in GPCR functional assays remains limited.

Regarding to the application in native cells or animals *in vivo* model, genetically encoded sensors based on GPCR conformational changes have incorporated circularly permuted fluorescent protein (cpGFP) to optical visualize the neurotransmitter release in brain (Sun et al., 2018; Peng et al., 2020). The cpGFP is modified from original GFP, in which the amino and carboxyl portions have been interchanged and reconnected by a short spacer between the original terminus. It is more flexible and accessible than original protein, and the fluorescence intensity of cpGFP is related to its conformation (Baird et al., 1999). Thus, cpGFP offered a suitable strategy for

TABLE 2 | Multiple RET-sensors for detection of GPCR conformational changes.

Type of sensors	Fluorescent probe	Receptors	Comments	References
RET-sensors applied in purified protein				
Polarity sensitive fluorescent dyes	IANBD	β_2AR	The first direct evidence for ligand specific conformational changes occurring in a GPCR.	Gether et al., 1995
Fluorescence quenching	Fluorescein maleimide (FM) and oxyl-N-hydroxysuccinimide as quencher	β_2AR	Showed the relative movements of the two labeled amino acid and 20 s activation kinetics through the fluorescent change after ligand addition.	Ghanouni et al., 2001a,b
Intramolecular RET-sensors in cells				
FRET	CFP/YFP	PTHR; α_{2A} AR; β1AR; β_2AR; A_2AR; B_2R	The first generation of FRET sensor to detect GPCR conformational changes in living cells, and showed a fast activation kinetic induced by various ligands in single cell assay using microscopy.	Vilardaga et al., 2003, 2005; Hoffmann et al., 2005; Chachisvilis et al., 2006; Rochais et al., 2007; Reiner et al., 2010
FRET	CFP/FlAsH	A_2AR; α_{2A} AR	The smaller FlAsH tag avoided to disturb G protein signaling and provided a better signal-to-noise ratio compared with CFP/YFP FRET sensor.	Hoffmann et al., 2005
BRET	Rluc II/FlAsH	F prostanoid receptor; *AT1R;*β_2AR	The BRET sensors allow microplate assay to probe the conformational rearrangement promoted by diverse ligands but require exogenous labeling and extensive washing.	Sleno et al., 2016; Bourque et al., 2017; Devost et al., 2017; Sleno et al., 2017
nanoBRET	Nluc/Halo-618	PTHR; α_{2A} AR; β_2AR	These BRET sensors are directly translatable to other class A and B GPCRs and the high amplitude induced by agonist suitable for microtiter plate assays with HTS formats.	Schihada et al., 2018
nanoBRET	Nluc/YFP	β_2AR	The genetically encoded biosensors don't need dyes labeling and can be a tool to evaluate ligands with different intrinsic efficacy by BRET changes in HTS formats.	Picard et al., 2018
BRET	Rluc8/mVenus fused with conformation sensitive nanobody	KOR	Two KOR state specific nanobodies can be used as real time reporters for monitoring both ligand-dependent and independent conformational states in cells.	Che et al., 2020
nanoBRET	Nluc/NB80-GFP	β_2AR	NanoBRET sensor based on NB80-GFP confirmed the activation of β_2AR in VEGFR2-β_2AR complexes was not influenced by VEGFR.	Kilpatrick et al., 2019
TR-FRET	SNAP (BG-green) /ACP17 (CoA–Lumi4-Tb)	LH receptor; $GABA_B$R	Two cases illustrated how to use the TR-FRET toolbox construct intramolecular conformational change sensors.	Scholler et al., 2017a
Intermolecular RET-sensors				
FRET	CFP/YFP	mGlu1 homodimer	Observed the intermolecular FRET change between protomers and showed 10 ms of mGlu1 receptor activation kinetics between two subunits after agonist addition in real-time.	Tateyama and Kubo, 2006; Marcaggi et al., 2009
FRET	4-azido-L-phenylalanine (site specifically labeling Cy3 and Cy5 fluorophores)	mGlu2 homodimer	Used the unnatural amino acid-incorporation strategy to successfully constructed mGlu2 intermolecular sensor in living cells. And revealed new conformational states during receptor activation.	Liauw et al., 2021
BRET	Rluc/YFP	MT1/MT2 heterodimer	The specific interaction of ligands with the MT1/MT2 heterodimer was studied by this sensor.	Ayoub et al., 2004
TR-FRET	SNAP (BG -Green and BG-Lumi4-Tb)	mGlu2 homodimer	Inter-subunit FRET change induced by series ligands demonstrated that a reorientation of the ECDs is associated with receptor activation in mGlu receptor.	Doumazane et al., 2013; Scholler et al., 2017a

IANBD, the cysteine-reactive fluorescent probe N,N-dimethyl-N-(iodoacetyl)- N*-(7-nitrobenz2-oxa-1,3-diazol-4-yl) ethylenediamine; BG, O^6-benzyl-guanines; metabotropic glutamate receptor (mGlu receptor); metabotropic γ-aminobutyric acid receptors ($GABA_B$ receptor); luteinizing hormone (LH) receptor; β_2AR, β_2-Adrenergic receptor; B_2R, B_2-Bradykinin receptor; Parathyroid hormone 1 receptor (PTHR); α_2A AR, α_2A adrenergic receptor; A_{2A}R, A_{2A}-adenosine receptor; F prostanoid (FP) receptor; KOR, κ opioid receptor; D_2R, D_2-dopamine receptor; MT1, MT1 melatoninreceptor; MT2, MT2 melatonin receptor.*

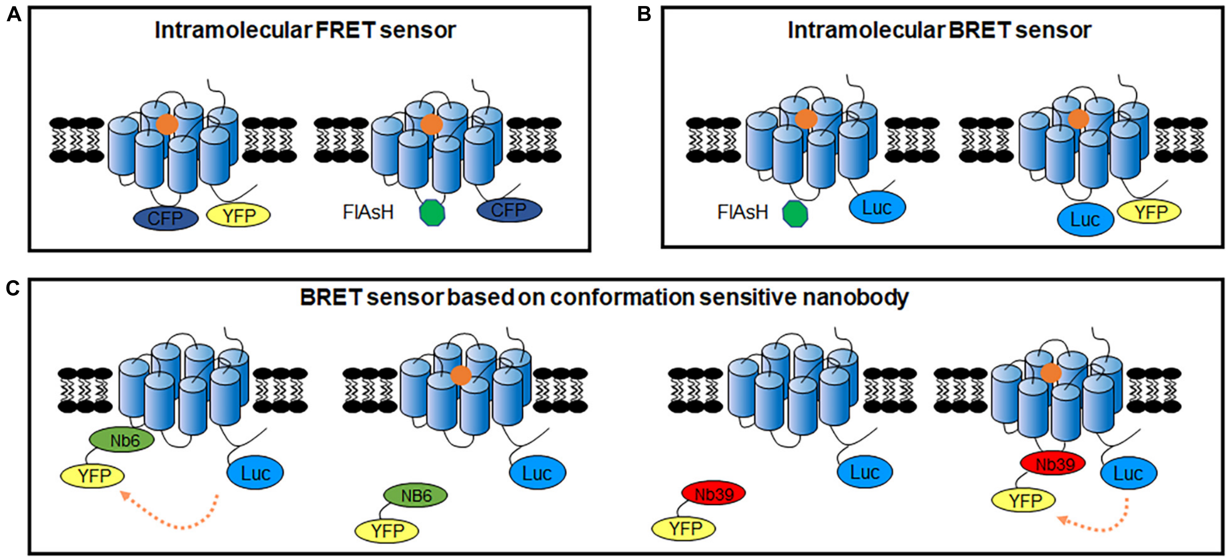

FIGURE 5 | GPCR intracellular conformational changes sensors. **(A)** GPCR intracellular conformational changes sensors based on FRET between fluorescent protein (left) or FRET between CFP and FlAsH dye (right). **(B)** GPCR intracellular conformational changes sensors based on BRET between Rluc II and FlAsH dye (left) or BRET between Nluc and fluorescent protein (right). **(C)** GPCR intracellular conformational changes BRET sensors based on conformation sensitive nanobody. Nb6-YFP only binds to GPCR in inactivated state, while Nb39-YFP only binds to GPCR in activated state.

conformation-sensitive sensors. As similar movements between TM5 and TM6 occurred during class A GPCRs activation (Weis and Kobilka, 2018; Hilger et al., 2020), fusing cpGFP at the ICL3 would allow significant fluorescence signal changes of cpGFP following GPCR activation upon ligand binding (Doi and Yanagawa, 1999; Sun et al., 2018). Mutation to abolish the G protein coupling in these sensors is required to not change the physiological GPCR function when expressed in the animals. The advantage of genetically encoded sensors is the rapid and high resolution in two-photon imaging systems for spatial neurotransmitters detecting in living animal (Sun et al., 2018; Peng et al., 2020). However, to obtain sensors with high sensitivity, large number of screening has been done for the cpEGFP insertion and linker residues (Sun et al., 2018). The experience in developing the sensor of one neurotransmitter is not always well adapted to another. Neuromodulator sensors are available for dopamine, serotonin, norepinephrine, acetylcholine, endocannabinoid, adenosine and gastrin-releasing peptide, but for glutamate and γ-aminobutyric acid remains difficult (Labouesse and Patriarchi, 2021).

INTERMOLECULAR CONFORMATIONAL GPCR DIMERIZATION SENSORS

Intermolecular FRET sensors are considered as good approaches for investigating the dimerization/oligomerization of GPCRs, especially in class C GPCRs (Milligan and Bouvier, 2005; Kniazeff et al., 2011). The classical CFP/YFP FRET sensor can detect the inter-subunit conformational change. When inserting the fluorescent protein in ICL2 of mGlu1 receptor, it showed an increased FRET signal indicating the relative movement of two mGlu1 subunits (Tateyama and Kubo, 2006). Subsequently, through measuring the FRET between two mGlu1 subunits in real-time; a fast increased inter-subunit FRET signal between protomers was detected within 10 ms after glutamate application (Marcaggi et al., 2009). However, difficulties remain in these classical CFP/YFP FRET sensor applications due to low sensitivity, photobleaching and limitations of inserting position.

Time-resolved FRET (TR-FRET) use long-fluorescence lifetime fluorophore, such as lanthanide cryptate instead of fluorescent protein. The fluorescence lifetimes of these molecules are very long, ranging from 100 to 1,000 μs, which leads the efficiency of FRET is not affected by the orientation of dipole moments between donor and acceptor, and becomes truly dependent on their distance (Mathis, 1995; Selvin, 2002). Taking a fixed delay time before acquiring the signal allows the removal of most of the fluorescent background provided by biological media and instrument, which largely improves the signal-to-noise ratio, compared with classical FRET sensors (Maurel et al., 2008; Scholler et al., 2017a). TR-FRET sensors can be adapted in multi-well plates format from 96 well to 384 well for drug HTS (Scholler et al., 2017a; Liu et al., 2020).

Antibodies labeled with long-lifetime lanthanide-based cryptate fluorophores were used in the first-generation TR-FRET sensors, which target small tags fused in GPCRs, such as HA, Flag, or c-Myc (**Figure 6A**). It was used to prove the protein interactions and indicate the interface (Kniazeff et al., 2004; Liu et al., 2004). However, it failed to monitor the dynamic changes between the GPCR subunits, might because of the large size of the antibodies.

The SNAP tag is two-thirds the size of GFP, derived from the O^6-guanine nucleotide alkyltransferase that covalently reacts

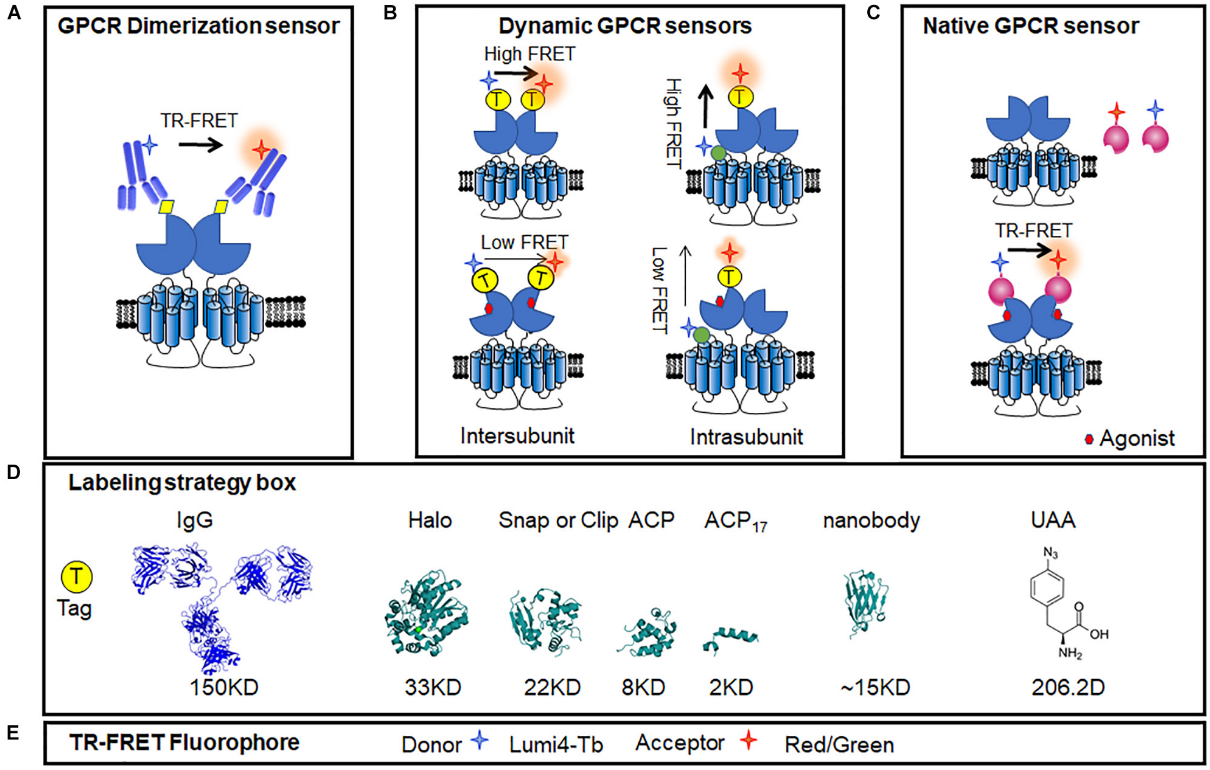

FIGURE 6 | Intermolecular GPCR dimerization sensors. Fluorescent donors and acceptors were introduced using antibodies or tags allowing for the FRET measurement of GPCR dimerization and activation in membrane and living cells, even in the acutely isolated cells. **(A)** GPCR dimer TR-FRET sensor based on anti-HA/flag/c-Myc antibody. **(B)** Conformational changes in TR-FRET sensor of dimeric GPCR using different tags, including N-terminal labeling and the intra-subunit conformational TR-FRET sensor. **(C)** Conformational changes in TR-FRET sensor of GPCRs based on active conformation-binding nanobodies. **(D)** Ribbon model structures of the different tags used to label receptors: IgG (PDB ID: 1IGT), Halo tag (PDB ID: 5UY1), SNAP tag (PDB ID: 3KZZ), and ACP tag (PDB ID: 2MLB), UAA (4-Azido-L-phenylalanine, CAS No.: 33173-53-4). **(E)** Common TR-FRET compatible dyes. Lumi4-Tb was used as donor, and red or green dyes were used as acceptors.

with benzyl-guanines (BG). The SNAP tag can be specifically and covalently labeled with any fluorophore carried by the BG benzyl group. By using non-permeant BG derivatives compatible with TR-FRET measurements, it allows to identify the dimer of GPCRs (**Figure 6B**). Using SNAP and CLIP labeling TR-FRET sensors, the mGluRs, which are considered strict homodimers, have been found to be heterodimers between different sub-groups (Doumazane et al., 2011). Meanwhile, SNAP labeling sensors can be used to identify oligomers, such as the GABA$_B$ receptor, which was previously considered to be heterodimers (Maurel et al., 2008; Comps-Agrar et al., 2011).

Furthermore, a N-terminal SNAP tag strategy combined with TR-FRET technology was developed to monitor the dynamic changes between two subunits in class C GPCR dimer. The mGlu receptors are dimeric entities with a large ECD, and during activation, a large conformational change results from the rotation of almost 70° of one ECD relative to the other (Huang et al., 2011). According to the available structures of mGlu receptor ECDs (Kunishima et al., 2000; Tsuchiya et al., 2002; Muto et al., 2007; Koehl et al., 2019), the distance between the N terminus varies from 2.8 nm in the inactive conformation to 3.3 nm in the active conformation. Consistently, in the TR-FRET measurement, inactive mGlu2 receptors were found to have a high FRET signal, while a low FRET signal was obtained in the active state (**Figure 6B**). The agonist-induced decrease in inter-subunit FRET efficiency was caused by a large change in the distance between the separated fluorophores (Doumazane et al., 2013). Such a movement is closely related to receptor activation, as agonist potencies presented by TR-FRET are perfectly correlated with those determined in cell-based functional assays (including IP1, cAMP, and Ca^{2+} release), indicating the efficiency and accuracy of the conformational change-sensitive TR-FRET sensor. The N-terminal SNAP strategy is feasible for most class C GPCRs, including all mGlu family members (mGlu1-8) and CaSR (Scholler et al., 2017a; Liu et al., 2020; **Figure 6B**). SNAP-tagged TR-FRET sensor of the mGlu5 receptor based on ECD conformation showed enhanced basal activation in the presence of D1R (Sebastianutto et al., 2020).

To increase the compatibility of SNAP-tagged TR-FRET sensor to different GPCRs, several modifications are required to obtain a large signal-to-noise ratio, including the insertion position, labeling strategies, and methods to quantify signals. For example, the N-terminal SNAP strategy does not work for the GABA$_B$ receptor because GABA$_B$ receptors do not undergo a strong conformational change similar to that of the mGlu receptors during activation (Geng et al., 2012; Lecat-Guillet et al., 2017). To detect the conformational change of this receptor, researchers kept the SNAP tag on the N-terminal of the GABA$_{B1}$ subunit and introduced a short version of the acyl carrier protein (ACP)-tag (ACP$_{17}$) within extracellular lobe 2 of the same subunit based on the knowledge of the activation of the GABA$_B$ receptor (**Figure 6B**). A high TR-FRET signal was largely decreased upon GABA$_B$ receptor activation and was suppressed by the competitive antagonist CGP54626 (Lecat-Guillet et al., 2017; Scholler et al., 2017a). Different sizes of tags, such as ACP (8 kDa) and ACP$_{17}$ (2 kDa) (George et al., 2004; Yin et al., 2005) or the O^6-alkylguanine-DNA alkyl transferase derivatives, SNAP (Keppler et al., 2003), CLIP (23 kDa) (Gautier et al., 2008), and Halo Tag (33 kDa) (Encell et al., 2012), combined with compatible fluorophore pairs build a toolbox for TR-FRET sensors optimization (**Figures 6D,E**). Another representative application of intra-subunit sensor is the luteinizing hormone (LH) receptor from the class A family, which has a large extracellular domain. After the addition of agonist, TR-FRET signals increased while the ACP$_{17}$ and SNAP tags were constructed at the loop and N terminus, respectively, revealing an important conformational change within the extracellular domain of the LH receptor. The strategy of the extracellular intra-subunit sensor is feasible for these kinds of monomeric GPCRs, in which the extracellular domain undergoes a large conformational change during activation (Scholler et al., 2017a).

In addition to class C GPCR, some classes A and B GPCRs were found to form dimer or oligomer (Carrillo et al., 2003; Berthouze et al., 2005; Harding et al., 2009; Kasai et al., 2018). These heterodimers showed distinct functions and related to pathogenesis. For example, AT$_1$R and B$_2$R heteromerization was found to occur in human placental biopsies from pregnancies complicated by preeclampsia, and the aberrant heteromerization of AT$_1$R-B$_2$R was found to result in exaggerated calcium signaling and high vascular smooth muscle mechanosensitivity (Quitterer et al., 2019). TR-FRET sensors are also adaptable to other GPCR dimers, such as class A relaxin family peptide receptor 3 (RXFP3) and the LH receptor, class B PTHR, corticotropin-releasing factor receptor 1 (CRF1R), and pituitary-activating cAMP polypeptide (PACAP) receptor 1 (PAC1). The potency of a series of agonists obtained from measurements of the TR-FRET assay correlated with those obtained in functional assays (Scholler et al., 2017a). On the other side, BRET approaches using Rluc and YFP pair can be used to identify the formations of GPCR dimers (Ayoub and Pfleger, 2010; Johnstone and Pfleger, 2012; El et al., 2019). But few intermolecular BRET conformational change sensors have been reported. Though ligand-induced BRET changes have been presented in MT1/MT2 melatonin receptor heterodimers (Ayoub et al., 2002, 2004), conformational changes in other dimers such as F prostanoid receptor, were not robust enough for investigation (Sleno et al., 2016).

The unnatural amino acid (UAA) site-directed modification strategy is considered to be a potential way to build flexible RET sensors that minimize the labeling tag size into one residue. The UAA technology can be used to investigate the interaction sites between two proteins, such as β-arrestin binding to AT$_1$R (Gagnon et al., 2019). Then, with an optimization in UAA incorporation strategy, it can measure FRET signal between two specific labeling sites of GPCR at the living cell level and the single-molecule level (Liauw et al., 2021). This UAA incorporation strategy in living cells provide a good protocol to apply UAA instead of other tags in GPCR sensors, which may have higher sensitivity to monitor more differential conformational change.

CONCLUSION AND PERSPECTIVES

In this review, we summarized four types of conformational sensors for GPCR signaling and activation based on FRET and BRET. These sensors have identified new mechanisms of GPCRs activation process and also lead to significant breakthroughs in high-throughput drug screening toolboxes. Generally, most FRET sensors show strong intensity and microscopy compatibility, which possess better spatial and temporal resolution for imaging purposes. The TR-FRET sensor can also be applied in HTS. BRET sensors have more sustainable signals, higher signal-to-noise ratios and HTS applications. These sensors have been optimized using various labeling strategies to increase the sensitivity and compatibility, from heterogeneous systems to endogenous conditions. Using these assays, GPCR signaling and activation have been investigated on a large scale and at multiple levels. However, the introduction of BRET and FRET sensors without breaking normal expression and function remains challenging. The UAA site-directed modification strategy for FRET sensors may be a promising approach (Liauw et al., 2021). BERKY biosensors for endogenous G proteins will be a good choice to investigate endogenous GPCR activation (Maziarz et al., 2020).

Meanwhile, although smaller and smaller tags can be preferred to minimize the extra influence, a few FRET sensors based on traditional antibodies (Liu et al., 2004; Comps-Agrar et al., 2011) or labeled small molecule ligands (Albizu et al., 2010) have shown advantages in the detection of GPCR in native samples. However, due to the excessive molecular weight of antibodies or insufficient specificity of some antibodies and small molecule ligands, it is difficult to detect GPCR complexes in native tissue. Nanobodies, which have a smaller size, higher affinity, and conformation specificity, may provide breakthroughs in native GPCR functional assays and signaling (Scholler et al., 2017b; **Figure 6C**). As the hetero-complexes of GPCRs have received increasing attention for their connection with diseases (Prinster et al., 2005; Gomes et al., 2016), nanobody-based assays will provide useful tools for investigating roles of GPCR heteromers in physiological and pathological processes in the future.

AUTHOR CONTRIBUTIONS

All authors listed have made a substantial, direct and intellectual contribution to the work, and approved it for publication.

FUNDING

JL was supported by the Ministry of Science and Technology (grant no. 2018YFA0507003), the National Natural Science Foundation of China (NSFC) (grant nos. 81720108031, 81872945, and 31721002), the Program for Introducing Talents of Discipline to the Universities of the Ministry of Education (grant no. B08029), and Key Program of Natural Science Foundation of Hubei Province (grant no. 2019ACA128) and Wuhan (2019020701011481).

REFERENCES

Adjobo-Hermans, M. J., Goedhart, J., van Weeren, L., Nijmeijer, S., Manders, E. M., Offermanns, S., et al. (2011). Real-time visualization of heterotrimeric G protein Gq activation in living cells. *BMC Biol.* 9:32. doi: 10.1186/1741-7007-9-32

Albizu, L., Cottet, M., Kralikova, M., Stoev, S., Seyer, R., Brabet, I., et al. (2010). Time-resolved FRET between GPCR ligands reveals oligomers in native tissues. *Nat. Chem. Biol.* 6, 587–594. doi: 10.1038/nchembio.396

Angers, S., Salahpour, A., Joly, E., Hilairet, S., Chelsky, D., Dennis, M., et al. (2000). Detection of beta 2-adrenergic receptor dimerization in living cells using bioluminescence resonance energy transfer (BRET). *Proc. Natl. Acad. Sci. U.S.A.* 97, 3684–3689. doi: 10.1073/pnas.060590697

Audet, N., Gales, C., Archer-Lahlou, E., Vallieres, M., Schiller, P. W., Bouvier, M., et al. (2008). Bioluminescence resonance energy transfer assays revealed ligand-specific conformational changes within preformed signaling complexes containing delta-opioid receptors and heterotrimeric G proteins. *J. Biol. Chem.* 283, 15078–15088. doi: 10.1074/jbc.M707941200

Ayoub, M. A., and Pfleger, K. D. (2010). Recent advances in bioluminescence resonance energy transfer technologies to study GPCR heteromerization. *Curr. Opin. Pharmacol.* 10, 44–52. doi: 10.1016/j.coph.2009.09.012

Ayoub, M. A., Couturier, C., Lucas-Meunier, E., Angers, S., Fossier, P., Ayoub, M. A., et al. (2002). Monitoring of ligand-independent dimerization and ligand-induced conformational changes in melatonin receptors in living cells by bioluminescence resonance energy transfer. *J. Biol. Chem.* 277, 21522–21528. doi: 10.1074/jbc.M200729200

Ayoub, M. A., Levoye, A., Delagrange, P., and Jockers, R. (2004). Preferential formation of MT1/MT2 melatonin receptor heterodimers with distinct ligand interaction properties compared with MT2 homodimers. *Mol. Pharmacol.* 66, 312–321. doi: 10.1124/mol.104.000398

Azpiazu, I., and Gautam, N. (2004). A fluorescence resonance energy transfer-based sensor indicates that receptor access to a G protein is unrestricted in living mammalian cells. *J. Biol. Chem.* 279, 27709–27718. doi: 10.1074/jbc.M403712200

Baird, G. S., Zacharias, D. A., and Tsien, R. Y. (1999). Circular permutation and receptor insertion within green fluorescent proteins. *Proc. Natl. Acad. Sci. U.S.A.* 96, 11241–11246. doi: 10.1073/pnas.96.20.11241

Berthouze, M., Ayoub, M., Russo, O., Rivail, L., Sicsic, S., Fischmeister, R., et al. (2005). Constitutive dimerization of human serotonin 5-HT4 receptors in living cells. *FEBS Lett.* 579, 2973–2980. doi: 10.1016/j.febslet.2005.04.040

Bertrand, L., Parent, S., Caron, M., Legault, M., Joly, E., Angers, S., et al. (2002). BRET2/arrestin assay in stable recombinant cells: a platform to screen for compounds that interact with G protein-coupled receptors (GPCRS). *J. Recept. Signal Transduct. Res.* 22, 533–541. doi: 10.1081/rrs-120014619

Bourque, K., Petrin, D., Sleno, R., Devost, D., Zhang, A., and Hebert, T. E. (2017). Distinct conformational dynamics of three G protein-coupled receptors were measured using FlAsH-BRET biosensors. *Front. Endocrinol. (Lausanne)* 8:61. doi: 10.3389/fendo.2017.00061

Bunemann, M., Frank, M., and Lohse, M. J. (2003). Gi protein activation in intact cells involves subunit rearrangement rather than dissociation. *Proc. Natl. Acad. Sci. U.S.A.* 100, 16077–16082. doi: 10.1073/pnas.2536719100

Cao, Y., Namkung, Y., and Laporte, S. A. (2019). Methods to monitor the trafficking of beta-arrestin/G protein-coupled receptor complexes using enhanced bystander BRET. *Methods Mol. Biol.* 1957, 59–68. doi: 10.1007/978-1-4939-9158-7_3

Carrillo, J. J., Pediani, J., and Milligan, G. (2003). Dimers of class A G protein-coupled receptors function via agonist-mediated trans-activation of associated G proteins. *J. Biol. Chem.* 278, 42578–42587. doi: 10.1074/jbc.M306165200

Chachisvilis, M., Zhang, Y. L., and Frangos, J. A. (2006). G protein-coupled receptors sense fluid shear stress in endothelial cells. *Proc. Natl. Acad. Sci. U.S.A.* 103, 15463–15468. doi: 10.1073/pnas.0607224103

Charest, P. G., and Bouvier, M. (2003). Palmitoylation of the V2 vasopressin receptor carboxyl tail enhances beta-arrestin recruitment, leading to efficient receptor endocytosis and ERK1/2 activation. *J. Biol. Chem.* 278, 41541–41551. doi: 10.1074/jbc.M306589200

Charest, P. G., Terrillon, S., and Bouvier, M. (2005). Monitoring agonist-promoted conformational changes of β-arrestin in living cells by intramolecular BRET. *EMBO Rep.* 6, 334–340. doi: 10.1038/sj.embor.7400373

Che, T., English, J., Krumm, B. E., Kim, K., Pardon, E., Olsen, R., et al. (2020). Nanobody-enabled monitoring of the kappa opioid receptor states. *Nat. Commun.* 11:1145. doi: 10.1038/s41467-020-14889-7

Che, T., Majumdar, S., Zaidi, S. A., Ondachi, P., McCorvy, J. D., Wang, S., et al. (2018). Structure of the nanobody-stabilized active state of the kappa opioid receptor. *Cell* 172, 55–67. doi: 10.1016/j.cell.2017.12.011

Comps-Agrar, L., Kniazeff, J., Norskov-Lauritsen, L., Maurel, D., Gassmann, M., Gregor, N., et al. (2011). The oligomeric state sets the GABA(B) receptor signaling efficacy. *EMBO J.* 30, 2336–2349. doi: 10.1038/emboj.2011.143

Cottet, M., Faklaris, O., Maurel, D., Scholler, P., Doumazane, E., Trinquet, E., et al. (2012). BRET and Time-resolved FRET strategy to study GPCR oligomerization: from cell lines toward native tissues. *Front. Endocrinol. (Lausanne)* 3:92. doi: 10.3389/fendo.2012.00092

Devost, D., Sleno, R., Petrin, D., Zhang, A., Shinjo, Y., Okde, R., et al. (2017). Conformational profiling of the AT1 angiotensin II receptor reflected biased agonist, G protein coupling, and cellular context. *J. Biol. Chem.* 292, 5443–5456. doi: 10.1074/jbc.M116.763854

Dixon, A. S., Schwinn, M. K., Hall, M. P., Zimmerman, K., Otto, P., Lubben, T. H., et al. (2016). NanoLuc complementation reporter optimized for the accurate measurement of protein interactions in cells. *ACS Chem. Biol.* 11, 400–408. doi: 10.1021/acschembio.5b00753

Doi, N., and Yanagawa, H. (1999). Design of generic biosensors based on green fluorescent proteins with allosteric sites by directed evolution. *FEBS Lett.* 453, 305–307. doi: 10.1016/s0014-5793(99)00732-2

Doumazane, E., Scholler, P., Fabre, L., Zwier, J. M., Trinquet, E., Pin, J. P., et al. (2013). Illuminating the activation mechanisms and allosteric properties of metabotropic glutamate receptors. *Proc. Natl. Acad. Sci. U.S.A.* 110, E1416–E1425. doi: 10.1073/pnas.1215615110

Doumazane, E., Scholler, P., Zwier, J. M., Trinquet, E., Rondard, P., and Pin, J. P. (2011). A new approach to analyze cell surface protein complexes reveals specific heterodimeric metabotropic glutamate receptors. *FASEB J.* 25, 66–77. doi: 10.1096/fj.10-163147

Du, Y., Duc, N. M., Rasmussen, S., Hilger, D., Kubiak, X., Wang, L., et al. (2019). Assembly of the GPCR-G protein complex. *Cell* 177, 1232–1242. doi: 10.1016/j.cell.2019.04.022

El, K. C., Reverchon-Assadi, F., Hervouet-Coste, N., Blot, L., Reiter, E., and Morisset-Lopez, S. (2019). Bioluminescence resonance energy transfer as a method to study protein-protein interactions: application to G protein-coupled receptor biology. *Molecules* 24:537. doi: 10.3390/molecules24030537

Encell, L. P., Friedman, O. R., Zimmerman, K., Otto, P., Vidugiris, G., Wood, M. G., et al. (2012). Development of a dehalogenase-based protein fusion tag capable of rapid, selective, and covalent attachment to customizable ligands. *Curr. Chem. Genom.* 6, 55–71. doi: 10.2174/1875397301206010055

Förster, T. (1948). Zwischenmolekulare energiewanderung und fluoreszenz. *Ann. Phys. (Leipzig)* 2, 55–75.

Frank, M., Thumer, L., Lohse, M. J., and Bunemann, M. (2005). G Protein activation without subunit dissociation depends on the G{alpha}(i)-specific region. *J. Biol. Chem.* 280, 24584–24590. doi: 10.1074/jbc.M414630200

Fredriksson, R., and Schioth, H. B. (2005). The repertoire of G-protein-coupled receptors in fully sequenced genomes. *Mol. Pharmacol.* 67, 1414–1425. doi: 10.1124/mol.104.009001

Fredriksson, R., Lagerstrom, M. C., Lundin, L. G., and Schioth, H. B. (2003). G-protein-coupled receptors in the human genome form five main families.

Phylogenetic analysis, paralogon groups, and fingerprints. *Mol. Pharmacol.* 63, 1256–1272. doi: 10.1124/mol.63.6.1256

Gagnon, L., Cao, Y., Cho, A., Sedki, D., Huber, T., Sakmar, T. P., et al. (2019). Genetic code expansion and photocross-linking identify different beta-arrestin binding modes to the angiotensin II type 1 receptor. *J. Biol. Chem.* 294, 17409–17420. doi: 10.1074/jbc.RA119.010324

Gales, C., Rebois, R. V., Hogue, M., Trieu, P., Breit, A., Hebert, T. E., et al. (2005). Real-time monitoring of receptor and G-protein interactions in living cells. *Nat. Methods* 2, 177–184. doi: 10.1038/nmeth743

Galés, C., Van Durm, J. J. J., Schaak, S., Pontier, S., Percherancier, Y., Audet, M., et al. (2006). Probing activation-promoted structural rearrangements in preassembled receptor–G protein complexes. *Nat. Struct. Mol. Biol.* 13, 778–786. doi: 10.1038/nsmb1134

Gautier, A., Juillerat, A., Heinis, C., Correa, I. J., Kindermann, M., Beaufils, F., et al. (2008). An engineered protein tag for multiprotein labeling in living cells. *Chem Biol* 15, 128–136. doi: 10.1016/j.chembiol.2008.01.007

Geng, Y., Xiong, D., Mosyak, L., Malito, D. L., Kniazeff, J., Chen, Y., et al. (2012). Structure and functional interaction of the extracellular domain of the human GABA(B) receptor GBR2. *Nat. Neurosci.* 15, 970–978. doi: 10.1038/nn.3133

George, N., Pick, H., Vogel, H., Johnsson, N., and Johnsson, K. (2004). Specific labeling of cell surface proteins with chemically diverse compounds. *J. Am. Chem. Soc.* 126, 8896–8897. doi: 10.1021/ja048396s

Gether, U., Lin, S., and Kobilka, B. K. (1995). Fluorescent labeling of purified beta 2 adrenergic receptors. Evidence for ligand-specific conformational changes. *J. Biol. Chem.* 270, 28268–28275. doi: 10.1074/jbc.270.47.28268

Ghanouni, P., Gryczynski, Z., Steenhuis, J. J., Lee, T. W., Farrens, D. L., Lakowicz, J. R., et al. (2001a). Functionally different agonists induce distinct conformations in the G protein coupling domain of the β_2 adrenergic receptor. *J. Biol. Chem.* 276, 24433–24436. doi: 10.1074/jbc.C100162200

Ghanouni, P., Steenhuis, J. J., Farrens, D. L., and Kobilka, B. K. (2001b). Agonist-induced conformational changes in the G-protein-coupling domain of the β_2 adrenergic receptor. *Proc. Natl. Acad. Sci. USA.* 98, 5997–6002. doi: 10.1073/pnas.101126198

Gomes, I., Ayoub, M. A., Fujita, W., Jaeger, W. C., Pfleger, K. D., and Devi, L. A. (2016). G protein-coupled receptor heteromers. *Annu. Rev. Pharmacol. Toxicol.* 56, 403–425. doi: 10.1146/annurev-pharmtox-011613-135952

Haider, R. S., Godbole, A., and Hoffmann, C. (2019). To sense or not sense new insights from GPCR-based and arrestin-based biosensors. *Curr. Opin. Cell Biol.* 57, 16–24. doi: 10.1016/j.ceb.2018.10.005

Hall, M. P., Unch, J., Binkowski, B. F., Valley, M. P., Butler, B. L., Wood, M. G., et al. (2012). Engineered luciferase reporter from a deep sea shrimp utilizing a novel imidazopyrazinone substrate. *ACS Chem. Biol.* 7, 1848–1857. doi: 10.1021/cb3002478

Hamdan, F. F., Audet, M., Garneau, P., Pelletier, J., and Bouvier, M. (2005). High-throughput screening of G protein-coupled receptor antagonists using a bioluminescence resonance energy transfer 1-based beta-arrestin2 recruitment assay. *J. Biomol. Screen.* 10, 463–475. doi: 10.1177/1087057105275344

Hanyaloglu, A. C., Seeber, R. M., Kohout, T. A., Lefkowitz, R. J., and Eidne, K. A. (2002). Homo- and hetero-oligomerization of thyrotropin-releasing hormone (TRH) receptor subtypes Differential regulation of β-arrestin 1 and 2. *J. Biol. Chem.* 277, 50422–50430. doi: 10.1074/jbc.M209340200

Harding, P. J., Attrill, H., Boehringer, J., Ross, S., Wadhams, G. H., Smith, E., et al. (2009). Constitutive dimerization of the G-protein coupled receptor, neurotensin receptor 1, reconstituted into phospholipid bilayers. *Biophys. J.* 96, 964–973. doi: 10.1016/j.bpj.2008.09.054

Hasbi, A., Devost, D., Laporte, S. A., and Zingg, H. H. (2004). Real-time detection of interactions between the human oxytocin receptor and G protein-coupled receptor kinase-2. *Mol. Endocrinol.* 18, 1277–1286. doi: 10.1210/me.2003-0440

Hauser, A. S., Chavali, S., Masuho, I., Jahn, L. J., Martemyanov, K. A., Gloriam, D. E., et al. (2018). Pharmacogenomics of GPCR drug targets. *Cell* 172, 41–54. doi: 10.1016/j.cell.2017.11.033

Hein, P., Frank, M., Hoffmann, C., Lohse, M. J., and Bunemann, M. (2005). Dynamics of receptor/G protein coupling in living cells. *EMBO J.* 24, 4106–4114. doi: 10.1038/sj.emboj.7600870

Hein, P., Rochais, F., Hoffmann, C., Dorsch, S., Nikolaev, V. O., Engelhardt, S., et al. (2006). Gs activation is time limiting in initiating receptor-mediated signaling. *J. Biol. Chem.* 281, 33345–33351. doi: 10.1074/jbc.M606713200

Hilger, D., Kumar, K. K., Hu, H., Pedersen, M. F., O'Brien, E. S., Giehm, L., et al. (2020). Structural insights into differences in G protein activation by family A and B GPCRs. *Science* 369:3373. doi: 10.1126/science.aba3373

Hoffmann, C., Gaietta, G., Bunemann, M., Adams, S. R., Oberdorff-Maass, S., Behr, B., et al. (2005). A FlAsH-based FRET approach to determine G protein-coupled receptor activation in living cells. *Nat. Methods* 2, 171–176. doi: 10.1038/nmeth742

Hoffmann, C., Ziegler, N., Reiner, S., Krasel, C., and Lohse, M. J. (2008). Agonist-selective, receptor-specific interactions of human P2Y receptors with beta-arrestin-1 and -2. *J. Biol. Chem.* 283, 30933–30941. doi: 10.1074/jbc.M801472200

Hollins, B., Kuravi, S., Digby, G. J., and Lambert, N. A. (2009). The c-terminus of GRK3 indicates rapid dissociation of G protein heterotrimers. *Cell. Signal.* 21, 1015–1021. doi: 10.1016/j.cellsig.2009.02.017

Huang, S., Cao, J., Jiang, M., Labesse, G., Liu, J., Pin, J. P., et al. (2011). Interdomain movement in metabotropic glutamate receptor activation. *Proc. Natl. Acad. Sci. U.S.A.* 108, 15480–15485. doi: 10.1073/pnas.1107775108

Huang, W., Manglik, A., Venkatakrishnan, A. J., Laeremans, T., Feinberg, E. N., Sanborn, A. L., et al. (2015). Structural insights into μ-opioid receptor activation. *Nature* 524, 315–321. doi: 10.1038/nature14886

Inoue, A., Raimondi, F., Kadji, F., Singh, G., Kishi, T., Uwamizu, A., et al. (2019). Illuminating G-protein-coupled selectivity of GPCRs. *Cell* 177, 1933–1947. doi: 10.1016/j.cell.2019.04.044

Johnston, C. A., Lobanova, E. S., Shavkunov, A. S., Low, J., Ramer, J. K., Blaesius, R., et al. (2006). Minimal determinants for binding activated Gα from the structure of a Gαi1- peptide dimer. *Biochemistry U. S.* 45, 11390–11400. doi: 10.1021/bi0613832

Johnstone, E. K. M., and Pfleger, K. D. G. (2012). Receptor-heteromer investigation technology and its application using BRET. *Front. Endocrinol.* 3:101. doi: 10.3389/fendo.2012.00101

Kasai, R. S., Ito, S. V., Awane, R. M., Fujiwara, T. K., and Kusumi, A. (2018). The Class-A GPCR dopamine D2 receptor forms transient dimers stabilized by agonists: detection by single-molecule tracking. *Cell Biochem. Biophys.* 76, 29–37. doi: 10.1007/s12013-017-0829-y

Kauk, M., and Hoffmann, C. (2018). Intramolecular and intermolecular FRET sensors for GPCRs monitoring conformational changes and beyond. *Trends Pharmacol. Sci.* 39, 123–135. doi: 10.1016/j.tips.2017.10.011

Keppler, A., Gendreizig, S., Gronemeyer, T., Pick, H., Vogel, H., and Johnsson, K. (2003). A general method for covalent labeling of fusion proteins with small molecules in vivo. *Nat. Biotechnol.* 21, 86–89. doi: 10.1038/nbt765

Kilpatrick, L. E., Alcobia, D. C., White, C. W., Peach, C. J., Glenn, J. R., Zimmerman, K., et al. (2019). Complex formation between VEGFR2 and beta2-Adrenoceptor. *Cell Chem. Biol.* 26, 830–841. doi: 10.1016/j.chembiol.2019.02.014

Kim, K., Che, T., Panova, O., DiBerto, J. F., Lyu, J., Krumm, B. E., et al. (2020). Structure of a Hallucinogen-activated Gq-coupled 5-HT2A serotonin receptor. *Cell* 182, 1574–1588. doi: 10.1016/j.cell.2020.08.024

Klabunde, T., and Hessler, G. (2002). Drug design strategies for targeting G-protein-coupled receptors. *Chembiochem* 3, 928–944. doi: 10.1002/1439-7633(20021004)3:10<928::AID-CBIC928<3.0.CO;2-5

Kniazeff, J., Bessis, A. S., Maurel, D., Ansanay, H., Prezeau, L., and Pin, J. P. (2004). The closed state of both binding domains of homodimeric mGlu receptors is required for full activity. *Nat. Struct. Mol. Biol.* 11, 706–713. doi: 10.1038/nsmb794

Kniazeff, J., Prezeau, L., Rondard, P., Pin, J. P., and Goudet, C. (2011). Dimers and beyond: functional puzzles of class C GPCRs. *Pharmacol Ther.* 130, 9–25. doi: 10.1016/j.pharmthera.2011.01.006

Koehl, A., Hu, H., Feng, D., Sun, B., Zhang, Y., Robertson, M. J., et al. (2019). Structural insights into the activation of metabotropic glutamate receptors. *Nature* 566, 79–84. doi: 10.1038/s41586-019-0881-4

Krasel, C., Bunemann, M., Lorenz, K., and Lohse, M. J. (2005). Beta-arrestin binding to the beta2-adrenergic receptor requires both receptor phosphorylation and activation. *J. Biol. Chem.* 280, 9528–9535. doi: 10.1074/jbc.M413078200

Kroeger, K. M., Hanyaloglu, A. C., Seeber, R. M., Miles, L. E., and Eidne, K. A. (2001). Constitutive and agonist-dependent homo-oligomerization of thyrotropin-releasing hormone receptor Detection in living cells using bioluminescence resonance energy transfer. *J. Biol. Chem.* 276, 12736–12743. doi: 10.1074/jbc.M011311200

Kruse, A. C., Ring, A. M., Manglik, A., Hu, J., Hu, K., Eitel, K., et al. (2013). Activation and allosteric modulation of the muscarinic acetylcholine receptor. *Nature* 504, 101–106. doi: 10.1038/nature12735

Kunishima, N., Shimada, Y., Tsuji, Y., Sato, T., Yamamoto, M., Kumasaka, T., et al. (2000). Structural basis of glutamate recognition by a dimeric metabotropic glutamate receptor. *Nature* 407, 971–977. doi: 10.1038/35039564

Labouesse, M. A., and Patriarchi, T. (2021). A versatile GPCR toolkit to track in vivo neuromodulation: not a one-size-fits-all sensor. *Neuropsychopharmacology* doi: 10.1038/s41386-021-00982-y [Epub ahead of print].

Lagerstrom, M. C., and Schioth, H. B. (2008). Structural diversity of G protein-coupled receptors and their significance in drug discovery. *Nat. Rev. Drug Discov.* 7, 339–357. doi: 10.1038/nrd2518

Lan, T. H., Liu, Q., Li, C., Wu, G., and Lambert, N. A. (2012). Sensitive and high-resolution localization and tracking of membrane proteins in live cells using BRET. *Traffic* 13, 1450–1456. doi: 10.1111/j.1600-0854.2012.01401.x

Lecat-Guillet, N., Monnier, C., Rovira, X., Kniazeff, J., Lamarque, L., Zwier, J. M., et al. (2017). FRET-based sensors reveal activation and allosteric modulation of the GABA$_B$ receptor. *Cell Chem. Biol.* 24, 360–370. doi: 10.1016/j.chembiol.2017.02.011

Lee, M. H., Appleton, K. M., Strungs, E. G., Kwon, J. Y., Morinelli, T. A., Peterson, Y. K., et al. (2016). The conformational signature of beta-arrestin2 predicts its trafficking and signaling functions. *Nature* 531, 665–668. doi: 10.1038/nature17154

Lefkowitz, R. J. (1998). G protein-coupled receptor III. New roles for receptor kinases and beta-arrestins in receptor signaling and desensitization. *J. Biol. Chem.* 273, 18677–18680. doi: 10.1074/jbc.273.30.18677

Lefkowitz, R. J., and Shenoy, S. K. (2005). Transduction of receptor signals by beta-arrestins. *Science* 308, 512–517. doi: 10.1126/science.1109237

Liauw, B. W., Afsari, H. S., and Vafabakhsh, R. (2021). Conformational rearrangement during the activation of a metabotropic glutamate receptor. *Nat. Chem. Biol.* 17, 291–297. doi: 10.1038/s41589-020-00702-5

Liu, H., Yi, P., Zhao, W., Wu, Y., Acher, F., Pin, J. P., et al. (2020). Illuminating allosteric modulation of calcium-sensing receptors. *Proc. Natl. Acad. Sci. U.S.A.* 117, 21711–21722. doi: 10.1073/pnas.1922231117

Liu, J., Maurel, D., Etzol, S., Brabet, I., Ansanay, H., Pin, J. P., et al. (2004). Molecular determinants involved in allosteric control of agonist affinity in the GABA$_B$ receptor by the GABA$_{B2}$ subunit. *J. Biol. Chem.* 279, 15824–15830. doi: 10.1074/jbc.M313639200

Loening, A. M., Fenn, T. D., Wu, A. M., and Gambhir, S. S. (2006). Consensus-guided mutagenesis of *Renilla luciferase* yielded enhanced stability and light output. *Protein Eng. Des. Sel.* 19, 391–400. doi: 10.1093/protein/gzl023

Lohse, M. J., Nuber, S., and Hoffmann, C. (2012). Fluorescence/bioluminescence resonance energy transfer techniques to study G-protein-coupled receptor activation and signaling. *Pharmacol. Rev.* 64, 299–336. doi: 10.1124/pr.110.004309

Mao, C., Shen, C., Li, C., Shen, D. D., Xu, C., Zhang, S., et al. (2020). Cryo-EM structures of inactive and active GABA$_B$ receptors. *Cell Res.* 30, 564–573. doi: 10.1038/s41422-020-0350-5

Marcaggi, P., Mutoh, H., Dimitrov, D., Beato, M., and Knopfel, T. (2009). Optical measurement of mGluR1 conformational changes revealed fast activation, slow deactivation, and sensitization. *Proc. Natl. Acad. Sci. U.S.A.* 106, 11388–11393. doi: 10.1073/pnas.0901290106

Mastop, M., Reinhard, N. R., Zuconelli, C. R., Terwey, F., Gadella, T. J., van Unen, J., et al. (2018). FRET-based biosensor for measuring Galpha13 activation in single cells. *PLoS One* 13:e0193705. doi: 10.1371/journal.pone.0193705

Masuho, I., Ostrovskaya, O., Kramer, G. M., Jones, C. D., Xie, K., and Martemyanov, K. A. (2015). Distinct profiles of functional discrimination among G proteins determine the actions of G protein-coupled receptors. *Sci. Signal.* 8:ra123. doi: 10.1126/scisignal.aab4068

Mathis, G. (1995). Probing molecular interactions using homogeneous techniques based on rare-earth cryptates and fluorescence energy transfer. *Clin. Chem.* 41, 1391–1397.

Maurel, D., Comps-Agrar, L., Brock, C., Rives, M. L., Bourrier, E., Ayoub, M. A., et al. (2008). Cell-surface protein-protein interaction analysis with time-resolved FRET and snap-tag technologies: Application to GPCR oligomerization. *Nat. Methods* 5, 561–567. doi: 10.1038/nmeth.1213

Maziarz, M., Park, J., Leyme, A., Marivin, A., Garcia-Lopez, A., Patel, P. P., et al. (2020). Revealing the activity of trimeric G-proteins in live cells using a versatile biosensor design. *Cell* 182, 770.–785.

Milligan, G., and Bouvier, M. (2005). Methods for monitoring the quaternary structure of G protein-coupled receptors. *FEBS J.* 272, 2914–2925. doi: 10.1111/j.1742-4658.2005.04731.x

Molinari, P., Casella, I., and Costa, T. (2008). Functional complementation of high-efficiency resonance energy transfer: A new tool for the study of protein-binding interactions in living cells. *Biochem. J.* 409, 251–261. doi: 10.1042/BJ20070803

Mullard, A. (2020). FDA approves first BCMA-targeted therapeutic. *Nat. Rev. Drug Discov.* 19:659. doi: 10.1038/d41573-020-00157-2

Muto, T., Tsuchiya, D., Morikawa, K., and Jingami, H. (2007). Structures of the extracellular regions of group II/III metabotropic glutamate receptors. *Proc. Natl. Acad. Sci. U.S.A.* 104, 3759–3764. doi: 10.1073/pnas.0611577104

Namkung, Y., Le Gouill, C., Lukashova, V., Kobayashi, H., Hogue, M., Khoury, E., et al. (2016). Monitoring G protein-coupled receptor and beta-arrestin trafficking in live cells using enhanced bystander BRET. *Nat. Commun.* 7:12178. doi: 10.1038/ncomms12178

Nehme, R., Carpenter, B., Singhal, A., Strege, A., Edwards, P. C., White, C. F., et al. (2017). Mini-G proteins: Novel tools for studying GPCRs in their active conformation. *PLoS One* 12:e0175642. doi: 10.1371/journal.pone.0175642

Neubig, R. R. (1994). Membrane organization in G-protein mechanisms. *FASEB J.* 8, 939–946. doi: 10.1096/fasebj.8.12.8088459

Nobles, M., Benians, A., Tinker, A., and Jan, L. Y. (2005). Heterotrimeric G proteins couple with G protein-coupled receptors in living cells. *Proc. Natl. Acad. Sci. U.S.A.* 102, 18706–18711. doi: 10.1073/pnas.0504778102

Nuber, S., Zabel, U., Lorenz, K., Nuber, A., Milligan, G., Tobin, A. B., et al. (2016). Beta-arrestin biosensors exhibit a rapid, receptor-dependent activation/deactivation cycle. *Nature* 531, 661–664. doi: 10.1038/nature17198

Oakley, R. H., Laporte, S. A., Holt, J. A., Caron, M. G., and Barak, L. S. (2000). The differential affinities of visual arrestin, beta arrestin1, and beta arrestin2 for G protein-coupled receptors delineate two major classes of receptors. *J. Biol. Chem.* 275, 17201–17210. doi: 10.1074/jbc.M910348199

Oishi, A., Dam, J., and Jockers, R. (2020). beta-arrestin-2 BRET biosensors detect different beta-arrestin-2 conformations in interaction with GPCRs. *ACS Sens* 5, 57–64. doi: 10.1021/acssensors.9b01414

Olsen, R., DiBerto, J. F., English, J. G., Glaudin, A. M., Krumm, B. E., Slocum, S. T., et al. (2020). TRUPATH is an open-source biosensor platform for interrogating the GPCR transducerome. *Nat. Chem. Biol.* 16, 841–849. doi: 10.1038/s41589-020-0535-8

Papasergi-Scott, M. M., Robertson, M. J., Seven, A. B., Panova, O., Mathiesen, J. M., and Skiniotis, G. (2020). Structures of metabotropic GABAB receptor. *Nature* 584, 310–314. doi: 10.1038/s41586-020-2469-4

Park, J., Fu, Z., Frangaj, A., Liu, J., Mosyak, L., Shen, T., et al. (2020). Structure of the human GABAB receptor in an inactive state. *Nature* 584, 304–309. doi: 10.1038/s41586-020-2452-0

Peng, W., Wu, Z., Song, K., Zhang, S., Li, Y., and Xu, M. (2020). Regulation of the sleep homeostasis mediator adenosine by basal forebrain glutamatergic neurons. *Science* 369:556. doi: 10.1126/science.abb0556

Philip, F., Sengupta, P., and Scarlata, S. (2007). Signaling through a G protein-coupled receptor and its corresponding G protein follows a stoichiometrically limited model. *J. Biol. Chem.* 282, 19203–19216. doi: 10.1074/jbc.M701558200

Picard, L., Schönegge, A. M., Lohse, M. J., and Bouvier, M. (2018). Bioluminescence resonance energy transfer-based biosensors allow the monitoring of ligand- and transducer-mediated conformational changes in GPCRs. *Commun. Biol.* 1:101. doi: 10.1038/s42003-018-0101-z

Pin, J. P., Kniazeff, J., Prezeau, L., Liu, J. F., and Rondard, P. (2019). GPCR interaction is a possible method for allosteric control between receptors. *Mol. Cell. Endocrinol.* 486, 89–95. doi: 10.1016/j.mce.2019.02.019

Prinster, S. C., Hague, C., and Hall, R. A. (2005). Heterodimerization of G protein-coupled receptors: specificity and functional significance. *Pharmacol. Rev.* 57, 289–298. doi: 10.1124/pr.57.3.1

Quast, R. B., and Margeat, E. (2019). Studying GPCR conformational dynamics using single-molecule fluorescence. *Mol. Cell. Endocrinol.* 493:110469. doi: 10.1016/j.mce.2019.110469

Quitterer, U., Fu, X., Pohl, A., Bayoumy, K. M., Langer, A., and Abdalla, S. (2019). Beta-arrestin1 prevents preeclampsia by downregulating mechanosensitive AT1-B2 receptor heteromers. *Cell* 176, 318–333. doi: 10.1016/j.cell.2018.10.050

Rasmussen, S. G. F., Choi, H., Fung, J. J., Pardon, E., Casarosa, P., Chae, P. S., et al. (2011). Structure of a nanobody-stabilized active state of β2 adrenoceptor. *Nature* 469, 175–180. doi: 10.1038/nature09648

Reiner, S., Ambrosio, M., Hoffmann, C., and Lohse, M. J. (2010). Differential signaling of the endogenous agonists at the beta2-adrenergic receptor. *J. Biol. Chem.* 285, 36188–36198. doi: 10.1074/jbc.M110.175604

Rochais, F., Vilardaga, J. P., Nikolaev, V. O., Bunemann, M., Lohse, M. J., and Engelhardt, S. (2007). Real-time optical recording of beta1-adrenergic receptor activation revealed the supersensitivity of the Arg389 variant to carvedilol. *J. Clin. Invest.* 117, 229–235. doi: 10.1172/JCI30012

Sauliere, A., Bellot, M., Paris, H., Denis, C., Finana, F., Hansen, J. T., et al. (2012). Deciphering the complexity of biased-agonism reveals a new active AT1 receptor entity. *Nat. Chem. Biol.* 8, 622–630. doi: 10.1038/nchembio.961

Schihada, H., Vandenabeele, S., Zabel, U., Frank, M., Lohse, M. J., and Maiellaro, I. (2018). A universal bioluminescence resonance energy transfer sensor design enables high-sensitivity screening of the GPCR activation dynamics. *Commun. Biol.* 1:72. doi: 10.1038/s42003-018-0072-0

Scholler, P., Moreno-Delgado, D., Lecat-Guillet, N., Doumazane, E., Monnier, C., Charrier-Savournin, F., et al. (2017a). HTS-compatible FRET-based conformational sensors clarify membrane receptor activation. *Nat. Chem. Biol.* 13, 372–380. doi: 10.1038/nchembio.2286

Scholler, P., Nevoltris, D., de Bundel, D., Bossi, S., Moreno-Delgado, D., Rovira, X., et al. (2017b). Allosteric nanobodies uncover the role of hippocampal mGlu2 receptor homodimers in contextual fear consolidation. *Nat. Commun.* 8:1038. doi: 10.1038/s41467-017-01489-1

Sebastianutto, I., Goyet, E., Andreoli, L., Font-Ingles, J., Moreno-Delgado, D., Bouquier, N., et al. (2020). D1-mGlu5 heteromers mediate non-canonical dopamine signaling in Parkinson's disease. *J. Clin. Invest.* 130, 1168–1184. doi: 10.1172/JCI126361

Selvin, P. R. (2002). Principles and biophysical applications of lanthanide-based probes. *Annu. Rev. Biophys. Biomol. Struct.* 31, 275–302. doi: 10.1146/annurev.biophys.31.101101.140927

Shaye, H., Ishchenko, A., Lam, J. H., Han, G. W., Xue, L., Rondard, P., et al. (2020). Structural basis for the activation of a metabotropic GABA receptor. *Nature* 584, 298–303. doi: 10.1038/s41586-020-2408-4

Shukla, A. K., Violin, J. D., Whalen, E. J., Gesty-Palmer, D., Shenoy, S. K., and Lefkowitz, R. J. (2008). Distinct conformational changes in beta-arrestin result in biased agonism at the seven-transmembrane receptors. *Proc. Natl. Acad. Sci. U.S.A.* 105, 9988–9993. doi: 10.1073/pnas.0804246105

Sleno, R., Devost, D., Pétrin, D., Zhang, A., Bourque, K., Shinjo, Y., et al. (2017). Conformational biosensors reveal allosteric interactions between the heterodimeric AT1 angiotensin and prostaglandin Fα receptors. *J. Biol. Chem.* 292, 12139–12152. doi: 10.1074/jbc.M117.793877

Sleno, R., Pétrin, D., Devost, D., Goupil, E., Zhang, A., and Hébert, T. E. (2016). Designing BRET-based conformational biosensors for G protein-coupled receptors. *Methods* 92, 11–18. doi: 10.1016/j.ymeth.2015.05.003

Sriram, K., and Insel, P. A. (2018). G Protein-coupled receptors as targets for approved drugs: How many targets and the number of drugs? *Mol. Pharmacol.* 93, 251–258. doi: 10.1124/mol.117.111062

Strungs, E. G., Luttrell, L. M., and Lee, M. H. (2019). Probing arrestin function using intramolecular FlAsH-BRET biosensors. *Methods Mol Biol* 1957, 309–322. doi: 10.1007/978-1-4939-9158-7_19

Stryer, L. (1978). Fluorescence energy transfer as a spectroscopic ruler. *Annu. Rev. Biochem.* 47, 819–846. doi: 10.1146/annurev.bi.47.070178.004131

Sun, F., Zeng, J., Jing, M., Zhou, J., Feng, J., Owen, S. F., et al. (2018). A genetically encoded fluorescent sensor enables rapid and specific detection of dopamine in flies, fish, and mice. *Cell* 174, 481–496. doi: 10.1016/j.cell.2018.06.042

Szalai, B., Barkai, L., Turu, G., Szidonya, L., Várnai, P., and Hunyady, L. (2012). Allosteric interactions within the AT1 angiotensin receptor homodimer: Role of the conserved DRY motif. *Biochem. Pharmacol.* 84, 477–485. doi: 10.1016/j.bcp.2012.04.014

Tateyama, M. and Kubo, Y. (2006). Dual signaling is differentially activated by different active states of the metabotropic glutamate receptor 1α. *Proc. Natl. Acad. Sci. USA.* 103, 1124–1128. doi: 10.1073/pnas.0505925103

Thomsen, W., Frazer, J., and Unett, D. (2005). Functional assays for screening GPCR targets. *Curr. Opin. Biotechnol.* 16, 655–665. doi: 10.1016/j.copbio.2005.10.008

Tsuchiya, D., Kunishima, N., Kamiya, N., Jingami, H., and Morikawa, K. (2002). Structural views of the ligand-binding cores of a metabotropic glutamate receptor complexed with an antagonist and both glutamate and Gd3+. *Proc. Natl. Acad. Sci. U.S.A.* 99, 2660–2665. doi: 10.1073/pnas.052708599

Vilardaga, J. P., Bunemann, M., Krasel, C., Castro, M., and Lohse, M. J. (2003). Measurement of the millisecond activation switch of G protein-coupled receptors in living cells. *Nat. Biotechnol.* 21, 807–812. doi: 10.1038/nbt838

Vilardaga, J. P., Krasel, C., Chauvin, S., Bambino, T., Lohse, M. J., and Nissenson, R. A. (2002). Internalization determinants of the parathyroid hormone receptor differentially regulate beta-arrestin/receptor association. *J. Biol. Chem.* 277, 8121–8129. doi: 10.1074/jbc.M110433200

Vilardaga, J. P., Steinmeyer, R., Harms, G. S., and Lohse, M. J. (2005). Molecular basis of inverse agonism in G protein-coupled receptors. *Nat. Chem. Biol.* 1, 25–28. doi: 10.1038/nchembio705

Wan, Q., Okashah, N., Inoue, A., Nehme, R., Carpenter, B., Tate, C. G., et al. (2018). Mini G protein probes for active G protein-coupled receptors (GPCRs) in live cells. *J. Biol. Chem.* 293, 7466–7473. doi: 10.1074/jbc.RA118.001975

Weis, W. I., and Kobilka, B. K. (2018). The molecular basis of G protein-coupled receptor activation. *Annu. Rev. Biochem.* 87, 897–919. doi: 10.1146/annurev-biochem-060614-033910

Wright, S. C., Kozielewicz, P., Kowalski-Jahn, M., Petersen, J., Bowin, C. F., Slodkowicz, G., et al. (2019). A conserved molecular switch in class F receptors regulates receptor activation and pathway selection. *Nat. Commun.* 10:667. doi: 10.1038/s41467-019-08630-2

Xue, L., Rovira, X., Scholler, P., Zhao, H., Liu, J., Pin, J. P., et al. (2015). Major ligand-induced rearrangement of the heptahelical domain interface in a GPCR dimer. *Nat. Chem. Biol.* 11, 134–140. doi: 10.1038/nchembio.1711

Xue, L., Sun, Q., Zhao, H., Rovira, X., Gai, S., He, Q., et al. (2019). Rearrangement of the transmembrane domain interfaces associated with the activation of a GPCR hetero-oligomer. *Nat. Commun.* 10:2765. doi: 10.1038/s41467-019-10834-5

Yin, J., Straight, P. D., McLoughlin, S. M., Zhou, Z., Lin, A. J., Golan, D. E., et al. (2005). Genetically encoded short peptide tag for versatile protein labeling by Sfp phosphopantetheinyl transferase. *Proc. Natl. Acad. Sci. U.S.A.* 102, 15815–15820. doi: 10.1073/pnas.0507705102

Zhang, R., and Xie, X. (2012). Tools for GPCR drug discovery. *Acta Pharmacol. Sin.* 33, 372–384. doi: 10.1038/aps.2011.173

Zurn, A., Klenk, C., Zabel, U., Reiner, S., Lohse, M. J., and Hoffmann, C. (2010). Site-specific orthogonal labeling of proteins in intact cells with two small biarsenical fluorophores. *Bioconjug. Chem.* 21, 853–859. doi: 10.1021/bc900394j

Conflict of Interest: The authors declare that the research was conducted in the absence of any commercial or financial relationships that could be construed as a potential conflict of interest.

frontiers
in Cell and Developmental Biology

ORIGINAL RESEARCH
published: 19 July 2021
doi: 10.3389/fcell.2021.663431

Membrane Binding of α-Synuclein Stimulates Expansion of SNARE-Dependent Fusion Pore

Ryan Khounlo[1], Brenden J. D. Hawk[1], Tung-Mei Khu[1], Gyeongji Yoo[2], Nam Ki Lee[3], Josh Pierson[1] and Yeon-Kyun Shin[1]*

[1] Yeon-Kyun Shin Lab, Roy J. Carver Department of Biochemistry, Biophysics & Molecular Biology, Iowa State University, Ames, IA, United States, [2] School of Interdisciplinary Bioscience and Bioengineering, Pohang University of Science and Technology, Pohang, South Korea, [3] Department of Chemistry, Seoul National University, Seoul, South Korea

SNARE-dependent membrane fusion is essential for neurotransmitter release at the synapse. Recently, α-synuclein has emerged as an important regulator for membrane fusion. Misfolded α-synuclein oligomers are potent fusion inhibitors. However, the function of normal α-synuclein has been elusive. Here, we use the single vesicle-to-supported bilayer fusion assay to dissect the role of α-synuclein in membrane fusion. The assay employs 10 kD Rhodamine B-dextran as the content probe that can detect fusion pores larger than ∼6 nm. We find that the SNARE complex alone is inefficient at dilating fusion pores. However, α-synuclein dramatically increases the probability as well as the duration of large pores. When the SNARE-interacting C-terminal region of α-synuclein was truncated, the mutant behaves the same as the wild-type. However, the double proline mutants compromising membrane-binding show significantly reduced effects on fusion pore expansion. Thus, our results suggest that α-synuclein stimulates fusion pore expansion specifically through its membrane binding.

Keywords: SNARE, single-molecule, fusion pore, α-synuclein, TIRF

****Correspondence:***
Yeon-Kyun Shin
colishin@iastate.edu

Specialty section:
This article was submitted to Membrane Traffic, a section of the journal Frontiers in Cell and Developmental Biology

Received: *02 February 2021*
Accepted: *28 June 2021*
Published: *19 July 2021*

Citation:
Khounlo R, Hawk BJD, Khu T-M, Yoo G, Lee NK, Pierson J and Shin Y-K (2021) Membrane Binding of α-Synuclein Stimulates Expansion of SNARE-Dependent Fusion Pore. Front. Cell Dev. Biol. 9:663431. doi: 10.3389/fcell.2021.663431

INTRODUCTION

Communication between neurons, which underlies cognition, memory, and motor movement, is built upon neurotransmitter release at the synapse. In the neuron, cargo vesicles undergo membrane fusion with the plasma membrane, which releases the neurotransmitters into the synaptic cleft. It is established that the widely conserved SNARE (soluble N-ethylmaleimide sensitive factor attachment protein receptor) complex is the minimal machinery that drives membrane fusion (Sollner et al., 1993; Weber et al., 1998). SNARE motifs from vesicle-associated v-SNARE VAMP2 (or synaptobrevin 2) and those from target plasma membrane t-SNAREs, syntaxin-1A and SNAP-25, form a highly stable parallel coiled-coil (Poirier et al., 1998; Sutton et al., 1998). There is evidence that the SNARE complex zippers from the membrane distal region to the membrane-proximal region, culminating the folding energy toward apposition and merger of two membranes (Gao et al., 2012; Min et al., 2013; Shin et al., 2014).

The membrane fusion process transits through distinct multiple stages (**Figure 1**). Hemifusion, in which outer leaflets of two bilayers are merged but inner leaflets are not (Lu et al., 2005;

Xu et al., 2005), is followed by formation of a small aqueous fusion pore through which neurotransmitters are allowed to pass (Breckenridge and Almers, 1987; Han et al., 2004). The small pore then dilates to a large pore that could ultimately lead to a complete merger of two membranes into a single bilayer (Chernomordik and Kozlov, 2003). Alternatively, after a brief release, the fusion pore may close and the vesicle might then disengage from the plasma membrane without complete fusion, termed kiss-and-run (Alabi and Tsien, 2013). It is unknown what protein factors control the bias between two pathways.

α-synuclein (αS) is one of the most prevalent presynaptic proteins. But, when misfolded or aggregated, those aberrant forms are known to have close ties to the Parkinson's disease and Lewy body dementia (Baba et al., 1998). Despite its abundance, its regular functions in the neuron have been elusive. Recently, there has been evidence that αS controls the size of the vesicle pool (Nemani et al., 2010), vesicle clustering (Diao et al., 2013), as well as vesicle docking to the plasma membrane (Lou et al., 2017). In addition, αS may stabilize SNARE complexes by interacting with VAMP2 (Sun et al., 2019).

Recently, Edwards and coworkers have proposed that αS plays a role in the dilation of the fusion pore, potentially biasing vesicle recycling toward the complete fusion pathway (Logan et al., 2017). They found that overexpressed αS promotes the release of the large cargo in chromaffin cells. However, it is unknown if αS also functions as a fusion pore dilator in the neuron and if it is the result of direct interaction with SNAREs or an indirect consequence of a multiprotein pathway.

On a molecular level, there are two well-known interactions for αS. The first is the interaction between its acidic C-terminal region and vesicle-attached VAMP2 (Burre et al., 2010). This specific interaction has been shown to be responsible for vesicle clustering (Diao et al., 2013), vesicle docking, as well as inhibition of vesicle fusion (Choi et al., 2013). The second is the membrane binding due to its affinity of the amphipathic N-terminal region toward negatively charged lipids (Jo et al., 2000). Despite extensive investigations, the physiological function of αS's membrane binding is not fully understood (Snead and Eliezer, 2014).

In this work, we monitor the real-time dynamics of the fusion pore induced exclusively by SNARE proteins with the *in vitro* single vesicle-to-supported bilayer fusion assay (Liu et al., 2005; Kiessling et al., 2017; Kim and Shin, 2017; Kreutzberger et al., 2019). With this well-defined system, we intend to pinpoint the exact role that αS plays in the fusion pore dynamics. By encapsulating a fluorescent polymer probe of approximately 6 nm in diameter (Arrio-Dupont et al., 1996), we are able to observe the transient opening and contraction of the large fusion pore. We find that SNAREs alone are inefficient at generating a large fusion pore. When we include αS, however, we observe a dramatic increase in the number of vesicles that have the ability to open the large pore. In addition, we observe a significant increase of the duration of the large pore. Meanwhile, when the double proline mutants (A11P/V70P and T44P/A89P) of αS—which have reduced membrane binding—were used, the stimulating effects on fusion pore expansion were significantly diminished. In contrast, the truncation mutant in which VAMP2-interacting C-terminal region is deleted (αS 1-95), behaved the same as the wild-type.

RESULTS

Single Vesicle-to-Supported Bilayer Fusion Assay to Monitor a Large Fusion Pore

To probe the SNARE-induced large fusion pore, we monitor single vesicle-to-supported bilayer fusion utilizing total internal reflection fluorescence microscopy (TIRFM) (**Figure 2A**). The supported bilayer contains 5 mole% polyethylene glycol (PEG)-PE that creates a PEG-pillared aqueous gap between the bilayer and the quartz support through which a fluorescent reporter could diffuse. We use Rhodamine B conjugated to 10 kD dextran (RB-dextran) as the fluorescent reporter for the fusion pore. The rationale for using RB-dextran is two-fold. Firstly, the hydrodynamic diameter of the molecules is estimated to be ∼6 nm. Thus, unlike small fluorescent probes, its 2D diffusion within the aqueous gap is predicted to be sufficiently slow to be readily visible with TIRFM, which captures data with millisecond time resolutions. Secondly, RB-dextran is allowed to escape from the vesicle when the fusion pore opens larger than ∼6 nm in diameter, enabling the detection of a large fusion pore.

The supported bilayer is prepared by spontaneous fusion of proteoliposomes, reconstituted with t-SNAREs (lipid-to-protein ratio (L/P) = 2000), onto a clean, hydroxylated quartz surface in the flow cell. The quality and the homogeneity of the supported bilayer are visually inspected under a microscope with a small amount (0.5 ppm) of the lipid dye DiD (1,1′-Dioctadecyl-3,3,3′,3′- Tetramethylindodicarbocyanine). Separately, v-SNAREs are reconstituted into liposomes that encapsulate RB-dextran as the internal content (v-vesicle).

To monitor the large fusion pore, the v-vesicles are injected into the flow cell containing the preformed supported bilayer. The formation of the SNARE complexes mediates vesicle docking and fusion. When a v-vesicle docks to the bilayer, a fluorescent spot appears on the imaging surface (red spike in **Figure 2B**). Subsequently, if a fusion pore greater than 6 nm in diameter is induced, we observe 2D diffusion of fluorophores as RB-dextran is dispersed underneath the supported bilayer (green trace in **Figure 2B**). The large pore often contracts prior to complete fusion. Pore contraction results in a solid fluorescence spot with a reduced intensity that gradually fades to dark (blue trace in **Figure 2B**). The slow decrease of fluorescence in this phase most likely indicates the slow leakage of the polymer content via a small fusion pore (please see somewhat different interpretation of the data in Kreutzberger et al., 2019). In fact, Chapman and coworkers recently shown that SNARE complexes alone can sustain prolonged opening of a small fusion pore (Bao et al., 2018).

Surprisingly, in the time trace, we observe that content release causes the initial increase and then, the subsequent decrease of the fluorescence intensity (green trace in **Figure 2B**). Since

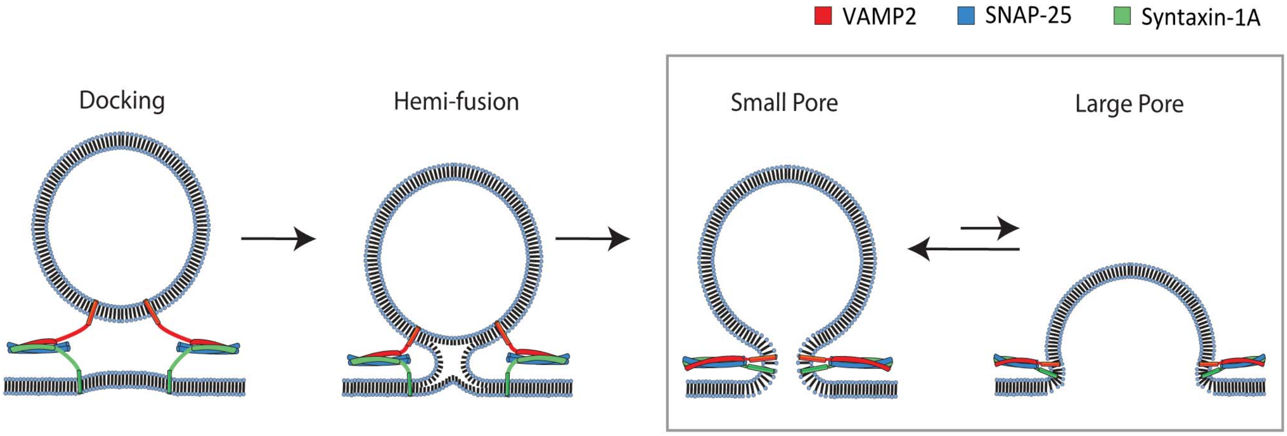

FIGURE 1 | Pathway of SNARE-mediated membrane fusion. The v-SNARE VAMP2 located on the incoming vesicle initiates binding to the t-SNAREs syntaxin-1A and SNAP-25 on the plasma membrane. The v-and t-SNAREs begin to zipper into a coiled-coil that docks the vesicle to the plasma membrane. Continued zippering drives the outer leaflets of the two membranes to merge into a hemifusion state. Complete zippering drives the merger of the inner leaflets of two bilayers, which creates a small fusion pore. The small pore expands to a large pore, resulting in complete merger of the vesicle to the plasma membrane. The box shows the transition to which our single vesicle fusion assay is designed to be sensitive.

the entrapped fluorophore concentration (90 μM) is lower than the critical concentration for self-dequenching, we rule out the possibility that the initial increase of fluorescence is due to self-dequenching. A likely scenario for the increase of the fluorescence intensity is that the internal content of the vesicle moves into the region of the stronger evanescent wave during formation of the large pore (**Figure 2C**). A similar increase of the fluorescence intensity was observed by Tamm and coworkers during the late stage of fusion of dense core vesicles to the planner bilayer employing the mRuby dye tagged to 36-residue neuropeptide Y (Kreutzberger et al., 2019). They interpreted the data similarly. The data suggests that the larger the size of the fusion pore, the more the vesicle would collapse to the surface, and the higher the fluorescence intensity increase in this phase would be. Thus, the increase of the fluorescence intensity here is likely to reflect the size of the fusion pore. We note, however, that the fluorescence steps from fusion of dense core vesicles are not entirely identical to those from our experiment. In particular, Tamm and coworkers observed a decrease of the fluorescence intensity after the docking plateau between red and green traces in **Figure 2B**. Such a decrease is not present in our time traces. The difference is most likely due to the fast kinetics in our vesicle-to-supported bilayer fusion.

As controls, to confirm that content release is SNARE-dependent, individual SNARE proteins are omitted or replaced with a disabled mutant in separate assays (**Figure 2D**). The v-SNARE dependence is tested using v-vesicles without VAMP2. When these vesicles are flowed over the bilayer, there are virtually no content release events. The t-SNARE dependence is evaluated using a SNAP-25 truncation mutant, SNAP-25E that is derived from the product of Botulinum toxin E cleavage that removes 26 residues from the C-terminal SNARE motif. SNAP-25E, which has been shown to impair vesicle docking (Arrio-Dupont et al., 1996), supports no content release events. In both controls, there are non-release events displaying vesicles that transiently dwell on the bilayer, without content release, followed by disengagement from the membrane (**Figure 2E**). Events with such a fluorescent trace pattern are excluded in the analysis.

SNAREs Are Not Effective in Driving Formation of the Fusion Pore Larger Than 6 nm

With SNAREs alone, a majority of the vesicles that dock to the surface of the bilayer via SNARE zippering do not open a large pore. Out of the 285 events analyzed, 177 vesicles (62%) do not show a sharp change of fluorescence nor 2D diffusion of fluorophores, indicating that the large fusion pore was not formed. A prototypical fluorescence time trace representing this group shows a spike in fluorescence due to docking, but it is followed by a slow decay of fluorescence to the baseline over several seconds (**Figure 3A** left).

A minor population was able to open the large pore briefly before contracting. This led to a trace with an initial sharp increase and decrease of fluorescence prior to the slow leakage phase (**Figure 3A** right). More precisely, 108 out of 285 (38%) vesicles analyzed show the sharp increase then decrease of fluorescence and concurrent 2D diffusion of the fluorophores, reminiscent of the large fusion pore (**Figure 3B**). We also note that for a small percentage of the docked vesicles (5%), we observe two discrete release events from a single docked vesicle. These events are separated and are not included in the analysis of 285 total events. Thus, with SNAREs only, the probability of the large fusion pore for a single docked vesicle is 38%, indicating that SNARE complex alone is not an efficient driver of fusion pore expansion.

Besides the probability, other important parameters such as the duration and the qualitative pore size can be estimated from the data. For the majority of large pore fusion events, the large pore contracts after the partial release, rarely reaching

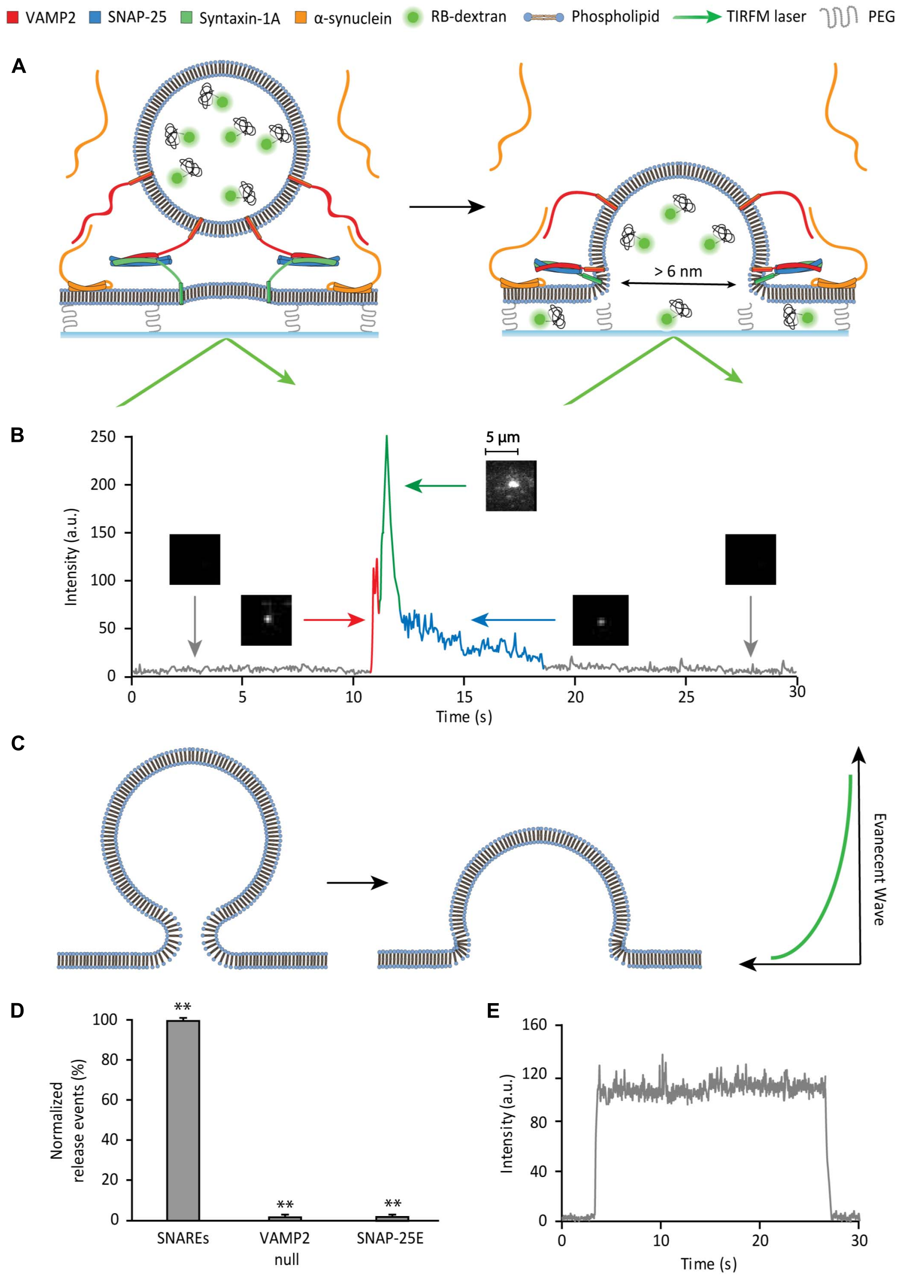

FIGURE 2 | Single vesicle-to-supported bilayer fusion assay to monitor a large fusion pore. **(A)** Schematic of the content release assay. **(B)** Detection of large pore fusion event. Before the injection of vesicles, there is a black background (gray trace). As vesicles are injected and dock to the surface, there is a spike in the fluorescence intensity (red trace) visualized by a fluorescent spot. After a short plateau (red trace), the vesicle develops a large fusion pore, where the fluorescence intensity increases sharply and declines sharply thereafter (green trace). During this period of increase and decline, the vesicle discharges content, which can be visualized by 2D diffusion of fluorophores. As the large pore contracts in size, the internal content escapes slowly, producing a slow decay (blue trace). The 2D diffusion of fluorophores is the criterion that divides the green trace and the blue trace. During the blue trace, 2D diffusion of fluorophores is not observed. This is visualized by a gradual dimming of the fluorescent spot to the black background. **(C)** Hypothetical model of membrane deformation in vesicle fusion. Here, SNARE complexes are not shown for clarity. **(D)** Controls for the SNARE dependence of the large fusion pore. The data are shown as means ± SD. $**p < 0.01$ by Student's *t*-test; $n = 3$ independent experiments. **(E)** Fluorescence trace of a non-release event. There is no decay in fluorescence over the span of over 20 s, indicating photobleaching is negligible.

the full release. The duration of the large fusion pore is defined as the time lapse of the green trace in **Figure 2B**. The duration distributes between 0.02 s and 1.00 s with an average of 0.28 ± 0.18 s (**Figure 3C**). On the other hand, the intensity increases due to the flattening (or collapse) of the vesicle during large pore formation provides qualitative estimation of

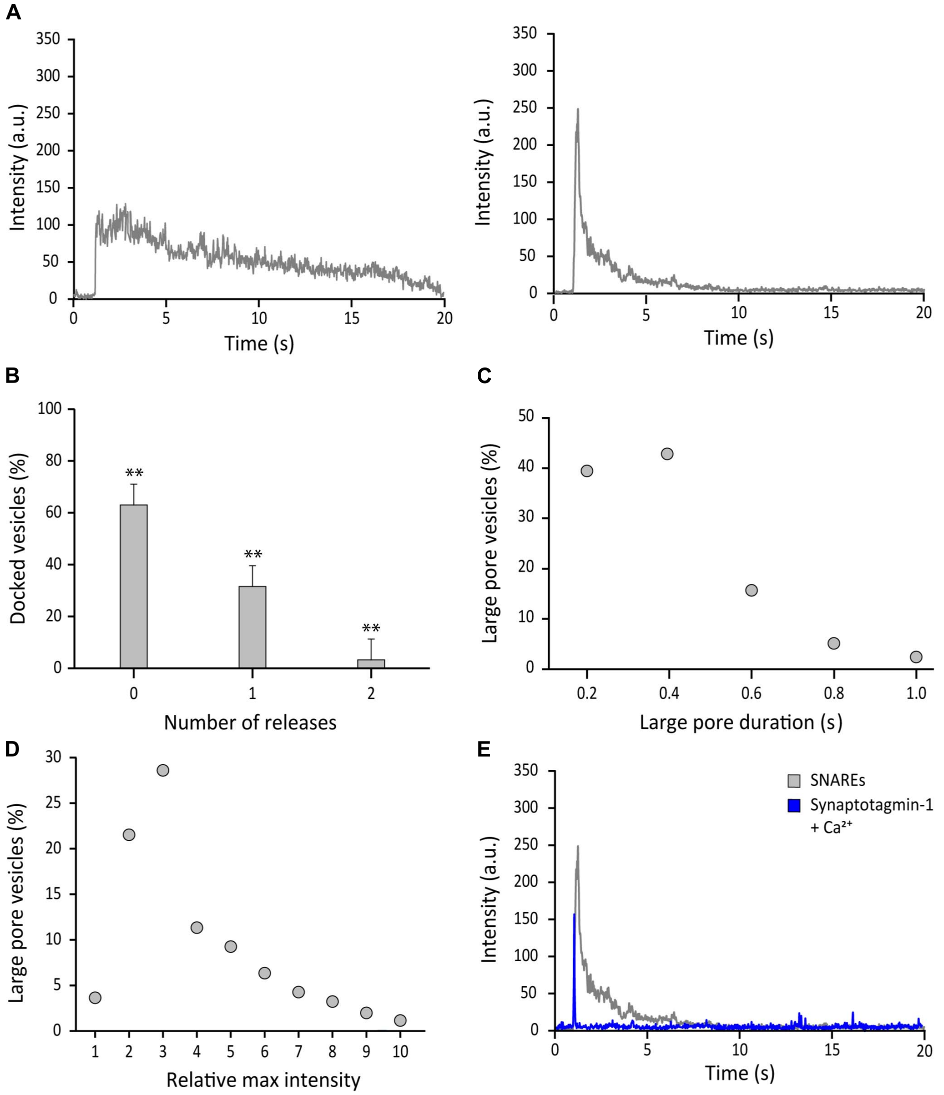

FIGURE 3 | SNAREs are inefficient at driving formation of the fusion pore larger than 6 nm. **(A)** Representative fluorescence time-traces of SNARE mediated fusion. Docked vesicles without apparent release (left) and with release (right) determined by 2D diffusion of fluorophores are shown. **(B)** Distribution of the number of large pore fusion events for individual docked vesicles. Total 4 independent measurements were analyzed for B–D. Error bars represent standard deviations from means. The data are shown as means ± SD. $**p < 0.01$ by Student's *t*-test; $n = 3$ independent experiments. **(C)** Distribution of duration of the large fusion pore, which is measured by the green part in **Figure 2B**. **(D)** Distribution of the relative maximum fluorescence intensity. The relative maximum fluorescence intensity of each event is calculated by dividing the maximum intensity caused by fusion pore expansion by the fluorescence intensity at the moment of vesicle docking. This is necessary because every vesicle has different number of content dyes. **(E)** Representative time traces of the content release event with SNAREs alone (gray) and with synaptotagmin-1 and 500 μM Ca^{2+} (blue). Synaptotagmin 1 and Ca^{2+} were premixed before injection (Kim and Shin, 2017). The molar ratio of VAMP-2 vs. synaptotagmin 1 in the vesicle is 1:1. More than 100 time traces are collected and they all show the similar pattern.

the fusion pore size. The fluorescence intensity increases as much as 10 times with the median at 3 times (**Figure 3D**), indicating significant flattening (or collapsing) of the vesicle during the large pore fusion event.

It was previously shown that synaptotagmin-1 promotes dilation of the fusion pore (Lai et al., 2013). Thus, as a positive control, we added synaptotagmin-1 together with 500 μM Ca^{2+} concentration (Kim and Shin, 2017). In contrast to the case with SNAREs only, most vesicles show the full content release in a short time span (∼0.02 s) producing a sharply spiked time trace (**Figure 3E**). Thus, the results show that synaptotagmin-1 with Ca^{2+} is a major stimulator for fusion pore dilation, consistent with previous findings (Lai et al., 2013; Wu et al., 2019).

αS Promotes the Probability, the Duration, but Not the Size of the Large Fusion Pore

The vesicle-to-supported bilayer fusion assay employing a large polymer cargo provides an opportunity to dissect the effect of the fusion modulators on the formation of the large fusion pore. In **Figure 3**, we demonstrate that the analysis of individual single vesicle fusion can yield probability, duration, and relative size of the large fusion pore. To uncover the effect of αS on the formation of SNARE-induced large pore, we included 5 μM αS, a typical cellular concentration, in our membrane fusion assay (Hawk et al., 2019). The vesicles are premixed with αS and after 10 min incubation, the mixture is injected into the flow chamber. The flow chamber also was incubated with 5 μM αS before injection.

Firstly, out of 691 events analyzed, we found that αS drastically increases the probability of a docked vesicle to form a large fusion pore. As much as 97% of docked vesicles showed the release of RB-dextran, which is in sharp contrast with 38% for SNAREs only (**Figure 4A**). However, even in the presence αS, vesicles struggled to reach complete release through a large pore prior to contraction. Secondly, with αS, the duration of the large pore is 1.15 ± 0.67 s on average, which is an increase by about factors of 4 compared with the average duration with SNAREs only (**Figure 4B**). Thirdly, we found that with αS, there is no further increase of the fluorescence intensity at the initial phase of formation of the large fusion pore, indicating that sizes of the large fusion pore remain approximately the same as those of SNAREs only (**Figure 4C**). This resulted in αS displaying a trace with a longer release phase than the trace of SNAREs alone (**Figure 4D**). Thus, the results show that αS increases the probability and the duration of the large fusion pore significantly, while the size of the large fusion pore is largely unaffected.

The SNARE Interaction With αS Does Not Affect Fusion Pore Expansion

Structurally, αS is composed of distinct two parts, the membrane-binding amphipathic region of N-terminal 100 residues and the acidic C-terminal region of 40 residues. The soluble C-terminal region may be functionally important because it interacts with the N-terminal region of v- SNARE, VAMP2. Previously, we have shown that αS can cross-bridge a vesicle to the lipid bilayer by utilizing these two interactions (Lou et al., 2017). It is unclear if such cross-bridging can affect the fusion pore. To test this idea, we generated the truncation mutant αS 1-95 by removing the final 45 amino acids from the C-terminal of αS (Lai et al., 2014; Lou et al., 2017).

This time, we used 200 nM for both wild-type αS and αS 1-95 due to the aggregation of αS 1-95 at the μM concentration range under our experimental conditions. Out of 403 events analyzed, we found that the probability of the large fusion pore for αS 1-95 is similar to that for wild-type αS (99% vs. 97%, respectively) (**Figure 5A**). However, the average duration of the large pore for αS 1-95 is slightly shorter than that for wild-type αS (0.86 ± 0.50 s vs. 1.15 ± 0.67 s, respectively) (**Figure 5B**). With αS 1-95, the

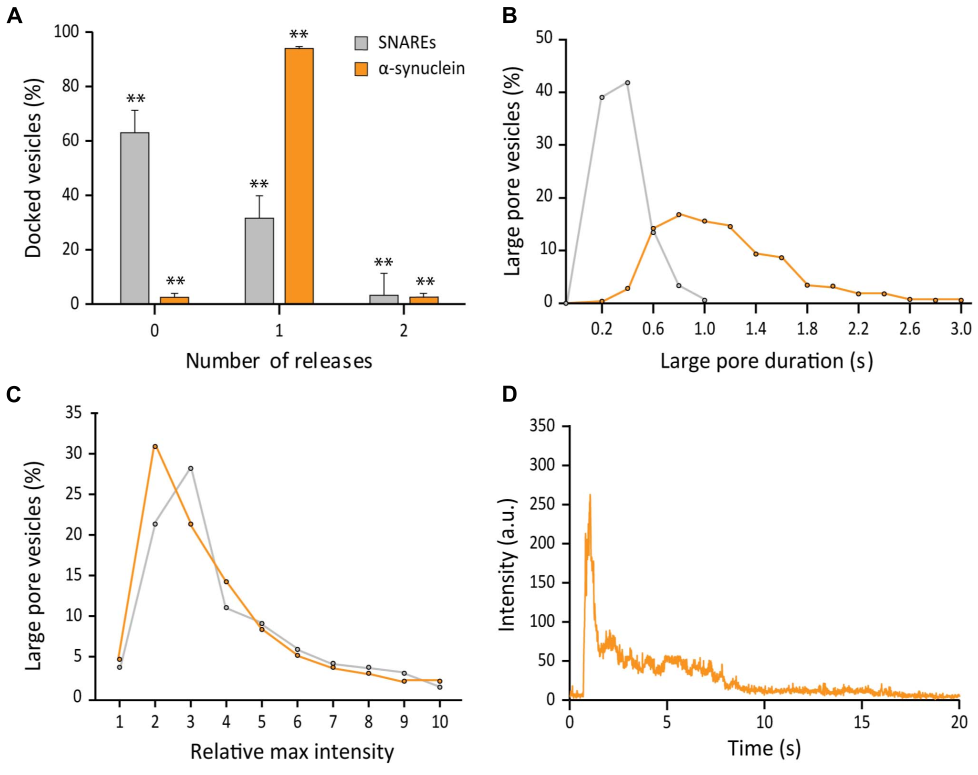

FIGURE 4 | αS promotes probability, duration, but not the size of the large fusion pore. **(A)** Distribution of number of large pore fusion events for individual docked vesicles. For αS, events from 7 independent measurements were analyzed for **A–C**. Error bars represent standard deviations from means. The data are shown as means ± SD. ∗∗ $p < 0.01$ by Student's *t*-test; $n = 3$ independent experiments. **(B)** Distribution of the duration of the large fusion pore. **(C)** Distribution of relative maximum intensities of large pore fusion events. **(D)** Representative fluorescence time trace of a large pore fusion event with αS.

increase of the fluorescence intensity at the initial phase of large pore formation was somewhat less (2.86 ± 1.53) than the increase for the wild-type (3.38 ± 2.20) (**Figure 5C**). Thus, although there are some minor variations, our results show that the C-terminal of αS and possibly, its interaction with VAMP2 is not much to do with the stimulation of large fusion pore formation.

Membrane Binding of αS Plays a Role in Stimulating Fusion Pore Expansion

After learning that the interaction between αS and v-SNARE VAMP2 has minimal effects on the parameters of fusion pore expansion, we asked if membrane binding of αS is the factor that governs its stimulatory role in fusion pore expansion. Recently, Sudhof and coworkers isolated and characterized double proline mutants of αS A11P/V70P and T44P/A89P whose membrane binding activity is significantly impaired (Burré et al., 2015). In parallel to their impaired membrane-binding activity, both double proline mutants showed significantly reduced stimulation of fusion pore expansion compared to that by the wild-type. In the presence of the mutants, the probability to open a large pore reaches only 50%, which is slightly higher than that of SNAREs only, but much lower than 97% in the presence of wild-type αS (**Figure 6A**). Similarly, the durations of the large fusion pore are longer than those with SNAREs only, but shorter than those in the presence of the wild-type (**Figure 6B**). Interestingly, it appears that the rank order of the durations follows the rank order of the membrane affinity (Lai et al., 2014), where the wild-type is the first, T44P/A89 the second, and A11P/V70P the third for the both parameters. There was no significant different in pore sizes between the wild-type and the mutations (**Figure 6C**). Thus, our results show that membrane binding of αS is the major factor that determines its activity of stimulating fusion pore expansion.

Familial Mutations A30P and A53T of αS Moderately Reduce the Duration of the Large Fusion Pore

Studies of families with a history of Parkinson's disease have resulted in the identification of several familial mutations (αS A30P, E46K, and A53T) involved in early-onset forms of the disease (Wong and Krainc, 2017). Of those mutations, Edwards and coworkers have shown that A30P and A53T abolish promotion of large cargo release by αS in chromaffin cells (Logan et al., 2017).

To test if their findings are applicable for neuronal SNAREs, we examined three αS point mutants with our single vesicle-to-supported bilayer assay. When compared to wild-type αS, all three mutants have nearly identical capacities to increase the probability of large fusion pore formation with probabilities >90% (**Figure 7A**). Interestingly, the duration of the large pore is somewhat reduced to 0.61 ± 0.20 s for A30P and 0.69 ± 0.37 s for A53T compared to 1.15 ± 0.67 s for the wild-type (**Figure 7B**). Meanwhile, the duration for E46K is 1.05 ± 0.42 s, which is similar to that for the wild-type within experimental uncertainty. For the increase of the fluorescence intensity at the initial phase of the release, all familial mutants and the wild-type are statistically similar to each other (**Figure 7C**). Thus, the results suggest that for all αS familial mutations, the fusion pore can grow as large as the size of the wild-type, but for A30P and A53T, the enlarged pore is not as stable as that of the wild-type.

DISCUSSION

In this work, we have found, using an *in vitro* single vesicle fusion assay that αS has the capacity to promote the formation of the large fusion pore in SNARE-dependent membrane fusion. Our results are consistent with the findings by Edwards and coworkers (Logan et al., 2017), that αS enhances the release of a large protein cargo in chromaffin cells. For neuronal SNAREs, our data shows that αS increases the probability of individual vesicles to advance to the large fusion pore (diameter larger than 6 nm). Moreover, our results show that the duration of the large fusion pore is also increased by αS significantly. Consistently in neurons, Edwards and coworkers have found that αS delays the closing of the fusion pore for the release of small neurotransmitter, therefore, most likely the small fusion pore. Thus, the results together support the conclusion that αS has the tendency to keep the fusion pore open longer than it is without αS, regardless of the size of the fusion pore. Our results show that SNARE complex alone is only capable of expanding the fusion pore larger than 6 nm in diameter for less than 40% of the docked vesicles. More than 60% of them are not able to reach a pore size sufficiently large to allow release of 6 nm-diameter RB-dextran. Interestingly, we find that the SNARE-induced large pore is transient. In the presence of αS, the probability of large fusion pore formation is increased to nearly 100%.

Regardless of the presence of αS, after some release, the fusion pore contracts back to a very slow release state, which is most likely a small pore stage. Such incomplete dilation leaves residual RB-dextran in the vesicle. This suggests that although SNARE complexes can generate a transient large fusion pore, they are not fully sufficient to drive the complete dilation of the fusion pore. In sharp contrast, fusion pore expansion is fast and ends up with complete decantation of the content in the presence of synaptotagmin-1 and Ca^{2+}. Thus, we speculate that synaptotagmin-1 and Ca^{2+} are the determining factors that drive fusion pore expansion into completion.

We speculate that the stimulating effects of synaptotagmin-1 and Ca^{2+} and that of αS are additive because synaptotagmin-1 and αS would not likely compete with each other for membrane binding. Ideally, this prediction could be tested with a similar *in vitro* vesicle fusion assay to the current one, but with a faster time resolution. The current method is limited with the time resolution of 20 msec, which is too slow to resolve the kinetics of fusion pore expansion in the presence of synaptotagmin-1 and Ca^{2+}.

On a molecular level, αS is known for the interaction with v-SNARE VAMP2 as well as its interaction with the negatively charged membrane. The former is mediated by the binding between the C-terminal end of αS and the N-terminal region of VAMP2. However, our results show that this specific interaction has little to do with the probability, the duration, and the size of the large fusion pore. When the VAMP2-binding C-terminal

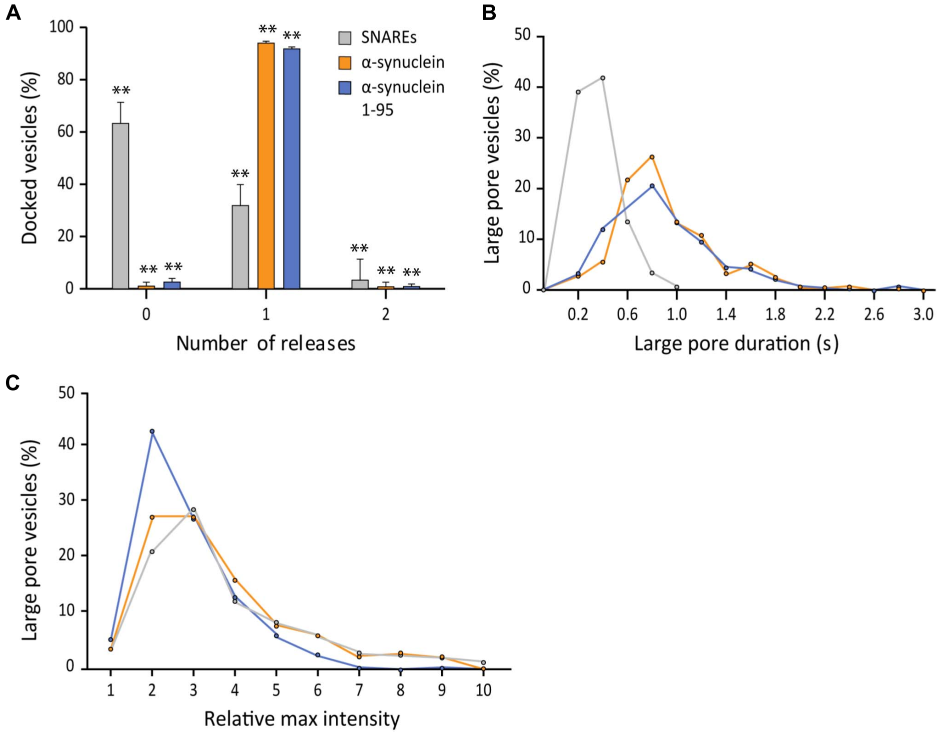

FIGURE 5 | The SNARE interaction with αS does not affect fusion pore expansion. **(A)** Distribution of number of large pore fusion events for individual docked vesicles. For αS 1-95, events from 5 independent measurements were analyzed for **A–C**. Error bars represent standard deviations from means. The data are shown as means ± SD. $** \; p < 0.01$ by Student's *t*-test; $n = 3$ independent experiments. **(B)** Distribution of the duration of the large fusion pore. **(C)** Distribution of relative maximum intensities of large pore fusion events.

region of αS was eliminated the three parameters remain virtually the same as that of the wild-type. Alternatively, the latter is mediated by the affinity of the N-terminal amphipathic region to the acidic lipids. Our data unambiguously finds that αS's membrane-binding property plays a major role in fusion pore dilation. We speculate that αS binds to the membrane and adapts to the diverse architecture of the fusion pore, which stabilizes the membrane curvature (Trexler and Rhoades, 2009). For example, Trexler and Rhoades have shown that αS has preferential binding to the positive membrane curvature. The positive curvature surrounding the fusion pore could be stabilized by αS binding.

In chromaffin cells, Edwards and coworkers found that the familial mutations A30P and A53T abolish the ability of αS to promote large cargo release. Intriguingly, we find that, although the differences are small, these same familial mutations are not as efficient as the wild-type in providing the stability of the enlarged fusion pore (**Figure 7B**). However, it is not clear if such a small effect is relevant to the early onset of the Parkinson's disease, warranting further investigation.

In this work, we have demonstrated that the single vesicle to supported bilayer fusion method is highly effective in dissecting the regulation of fusion pore expansion by αS. However, there are some weaknesses of the method. Although we add certain amounts of proteins, we have no way of estimating the exact number of molecules at the fusion site. We point out the new nanodisc approach, developed by other groups (Bao et al., 2018; Wu et al., 2019), with which one can control the number of proteins. We believe that the two methods will serve complimentarily.

In summary, elucidating the mechanism by which αS regulates SNARE-dependent membrane fusion is of great general interest. In this work, using the *in vitro* single vesicle-to-supported bilayer fusion assay employing 10 kD RB-dextran, we demonstrate that the SNARE complex could drive the enlargement of the fusion pore greater than 6 nm in diameter, but it collapses without progressing toward full dilation. However, in the presence of αS, more vesicles reach states of the sustained large fusion pore. Our results suggest that membrane binding of αS is responsible for the stimulating activity of fusion pore expansion.

MATERIALS AND METHODS

Plasmid Constructs and Site-Directed Mutagenesis

DNA sequences encoding SNAP-25 (amino acids 1-206), SNAP-25E (amino acids 1-180), syntaxin-1A (amino acids 1-288), VAMP2 (1-116), αS (amino acids 1-140) including all mutations, and αS 1-95 (amino acids 1-95) are inserted into the pGEX-KG vector as N-terminal glutathione S-transferase (GST) fusion proteins. Native cysteines are replaced by alanines for all the

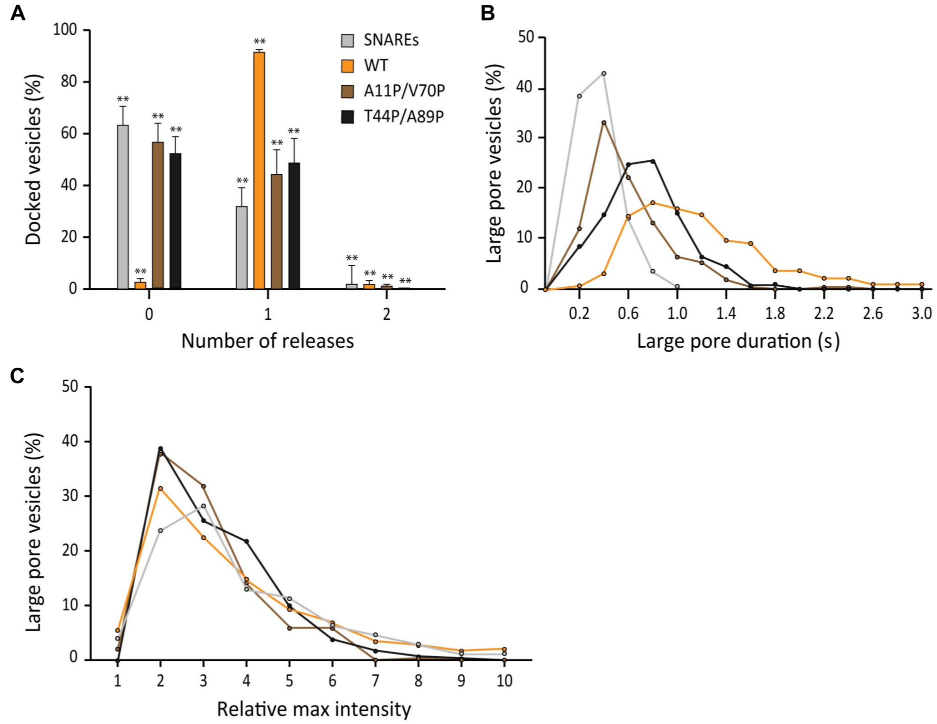

FIGURE 6 | Membrane binding of αS plays a role in stimulating fusion pore expansion. **(A)** Distribution of number of large pore fusion events for individual docked vesicles. For αS A11P/V70P, 124 release events were detected out of 289 total events from 18 independent measurements. For αS T44P/A89P, 98 large pore fusion events were detected out of 209 total events from 19 independent measurements. Error bars represent standard deviations from means. The data are shown as means ± SD. $** p < 0.01$ by Student's *t*-test; $n = 3$ independent experiments. **(B)** Distribution of the duration of the large fusion pore. **(C)** Distribution of relative maximum intensities of large pore fusion events.

sequences. DNA sequences are confirmed by the Iowa State University DNA Sequencing Facility.

Protein Expression and Purification

N-terminal SNARE GST fusion proteins (SNAP-25, SNAP-25E, syntaxin-1A, and VAMP2) are expressed in *Escherichia coli* BL21 (DE3) competent cells. Cells are grown at 37°C in LB medium with ampicillin (100 μg/mL) until the absorbance at 600 nm reaches 0.6–0.8, and induced by the addition of IPTG (isopropyl β-D-thiogalactopyranoside, 0.3 mM final concentration) to express the protein overnight at 16°C. Cells are pelleted and resuspended in a wash solution [497 mM NaCl, 2.7 mM KCl, 10 mM Na_2HPO_4, 1.8 mM KH_2PO_4, pH 7.4, (4 g/L Triton-X 100 added for the membrane proteins, VAMP2 and syntaxin-1A)] with final concentrations of 1 mM AEBSF [4-(2-aminoethyl) benzenesulfonyl fluoride and 4 mM DTT. Cells are lysed by homogenization and centrifuged to separate the supernatant from the pellet. The supernatant is collected and mixed with reduced glutathione resin in a batch purification method. After incubation, the protein is purified by washing the resin with wash solution. After washing, the resin is equilibrated into an elution buffer [137 mM NaCl, 2.7 mM KCl, 10 mM Na_2HPO_4, 1.8 mM KH_2PO_4, pH 7.4, (0.8% octyl-beta-glucoside (OG) was added for the membrane proteins)]. Proteins were eluted by cleavage with 30 U of thrombin at 4°C for 16 h. The protein was stored at −80°C with 15% glycerol. αS (wild type, mutants, and truncated variants) are expressed and purified in the same manner as detailed above, but have an additional step.

The elution was further purified using FPLC employing a home-made size exclusion column packed with toyopearl HW-50F in a 2.5 cm × 60 cm Chromaflex column. PBS (137 mM NaCl, 2.7 mM KCl, 10 mM Na_2HPO_4, 1.8 mM KH_2PO_4, pH 7.4) was used as the mobile phase. 5 mL fractions were collected and samples of each fraction were run on a 15%-SDS-PAGE gel to identify fractions that lacked higher molecular weight species. Pure fractions were combined, concentrated, and stored at −80°C with 15% glycerol.

Lipid Preparation

The lipids used to form the supported-bilayer (t-lipids) are made using a mixture of POPC (1-palmitoyl-2-dioleoyl-sn-glycero-3-phosphatidylcholine), DOPS (1,2-dioleoyl -sn-glycero-3-phosphatidylserine), PIP2 (phosphatidylinositol 4,5-bisphosphate), and PEG2000-PE {1,2-dipalmitoyl-sn-glycero-3-phosphoethanolamine-N-[methoxy(polyethylene glycol)-2000]} in chloroform at a molar ratio of 78:15:2:5. The lipid mixture is first dried under an air stream, then dried further in a vacuum overnight. The t-lipids are resuspended in HEPES-OG buffer (25 mM HEPES/KOH, 150 mM KCl, 1% β-OG, pH 7.4).

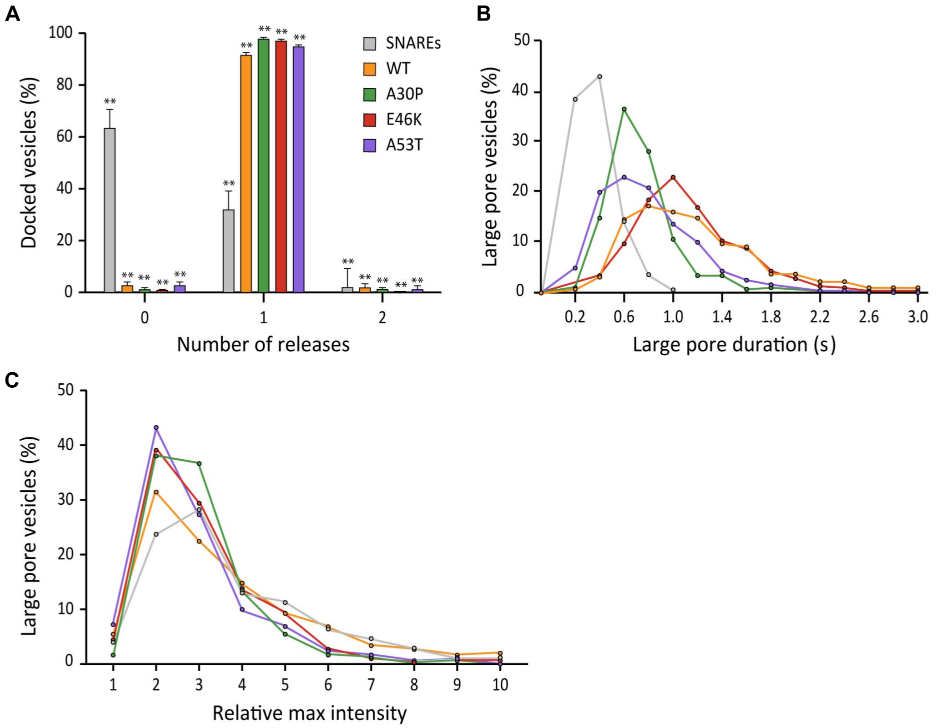

FIGURE 7 | Familial mutations A30P and A53T of αS moderately reduce the duration of the large fusion pore. **(A)** Distribution of docked vesicles vs. number of large pore fusion events. In total for αS A30P, 288 large pore fusion events were detected from 290 total events from 4 independent measurements. For αS E46K, 326 large pore fusion events were detected from 331 total events from 5 independent measurements. For αS A53T, 322 large pore fusion events were detected from 337 total events from 7 independent measurements. Error bars represent standard deviations from means. The data are shown as means ± SD. $** p < 0.01$ by Student's *t*-test; $n = 3$ independent experiments. **(B)** Distribution of the duration of the large fusion pore. **(C)** Distribution of relative maximum intensities of large pore fusion events.

The lipids used to form liposome for v-SNARE VAMP2 reconstitution (v-lipids) are made using a mixture of POPC, DOPS, and cholesterol in chloroform at a molar ratio of 75:5:20. The v-lipids are resuspended in HEPES with 90 μM Rhodamine B conjugated to 10 kD dextran (RB-dextran) before 10 flash freeze-thaw cycles, alternating between liquid nitrogen and boiling water. Unilamellar vesicles were prepared by extrusion through 100 nm diameter polycarbonate filters to make v-liposomes.

SNARE Reconstitution

For the supported bilayer, syntaxin-1A and SNAP-25 are premixed in a molar ratio of 1:1.5, and the mixture incubated at room temperature to form the t-SNARE complex. The t-lipids are added to the t-SNARE complex at a lipid:syntaxin-1A ratio of 2000:1. The mixture is diluted 3-fold using HEPES buffer to reduce detergent concentration and insert the t-SNARE complex into the t-lipids. The mixture is then dialyzed overnight at 4°C in 2L of HEPES containing Bio-Beads^{TM} SM-2 Resin to remove all detergent.

For v-vesicles, v-liposomes are mixed with VAMP2 at a lipid-to-protein ratio of 200:1. The mixture is diluted and dialyzed in the same manner as described above while ensuring that concentration of RB-dextran is constant at ∼90 μM. Vesicles prepared with this method were found to be ∼ 90 nm ± 10 nm in diameter with few small unilamellar vesicles (SUV) when examined with transmission electron microscopy (Yoon et al., 2006).

Vesicle-to-Supported Bilayer Fusion Content-Release Assay

A quartz slide and a glass cover slip are cleaned and hydroxylated by boiling in a piranha solution (1:1 mixture of concentrated sulfuric acid and 30% hydrogen peroxide) for 15 min. Afterward, the slide and cover slip are thoroughly rinsed with deionized H_2O and placed in a cleaning sonicator for 30 min to remove residual acid. The slide and coverslip are then dried and assembled to generate several microfluidic chambers separated by double sided Scotch tape. The chambers are filled with t-bilayer prepared from the overnight dialysis. The t-bilayer formed on the quartz surface for 2 h at 37°C. The excess liposomes/protein mixture was washed out with HEPES and replaced with 5 μM αS.

The microfluidic chambers are then placed on the imaging stand of our microscope. Imaging oil was put on the prism of our prism-type TIRFM, and then the prism was lowered onto the quartz slide. The incident angle of the exciting laser (532 nm) was adjusted and we initiated real-time movie acquisition with an imaging area of 110 × 110 μm using 20 ms time resolution.

The viewing area is divided into the 512 × 512 pixels and the data is stored in the 512 × 512 arrays. To perform the fusion assay, we injected the v-vesicles from dialysis with 5 μM αS into the microfluidic chamber at a rate of 50 μl/min. The sample to be injected into the flow cell has 250 nM of v-vesicles (total lipid concentration) encapsulating ∼90 μM of RB-dextran. The sample contains 3.75 nM of RB-dextran in the bulk solution which does not affect our measurements. We collected 60 s videos for each microfluidic chamber and analyzed fusion events using our custom-built analysis software.

Data Analysis

Fluorescence of RB-dextran from the content vesicles is monitored to determine content release from fusion events using in-house MATLAB® 2019 (a) analysis software. Each recording is analyzed frame by frame based on both visual determination and fluorescence trace pattern analysis.

The fluorescence intensities shown in **Figure 2** are calculated by summing up those in 5 × 5 pixels surrounding the central pixel with the brightest light intensity.

Large pore content release is indicated when a vesicle immobilized and fused on the surface displays 2D diffusion of the fluorophore. The corresponding fluorescence trace shows a large spike in fluorescence followed by a sharp decrease within less than 2 s. Events that did not form a large pore are indicated when a vesicle immobilized on the bilayer with no visible 2D diffusion of the fluorophore. The corresponding fluorescence trace shows a large spike in fluorescence followed by a slow decay to baseline over several seconds. Non-release events are when a vesicle became immobilized on the surface and disengaged after several seconds without any visible release. The fluorescence trace of a non-release event that contained a sharp increase in fluorescence, did not decay over several seconds during a plateau period, and then sharply declined to baseline. Non-release events were not included in the data analysis. This lack of fluorescence decay also indicates that photobleaching is not observable in the time scales we are measuring.

The selected traces corresponding to large pore content release events are background-corrected by fitting the minimum baseline for all traces from a single recording with a polynomial and then subtracting the polynomial from all the traces. The number of content release events are manually counted. The duration of release was quantified as the time from the beginning to end of large pore content release which is determined by the period of apparent 2D diffusion of the fluorophore.

DATA AVAILABILITY STATEMENT

The raw data supporting the conclusions of this article will be made available by the authors, without undue reservation.

AUTHOR CONTRIBUTIONS

RK contributed to the protein purification, data collection, and analysis of the experiments along with drafting the manuscript. BH contributed to developing the data analysis program. T-MK and JP contributed to the protein purification and data collection. GY and NL provided the plasmids for the αS truncation studies. Y-KS was responsible for the directing the research and manuscript drafting. All authors contributed to the article and approved the submitted version.

FUNDING

This work was supported by the grant from the National Institute of Health R01 GM051290.

REFERENCES

Alabi, A. A., and Tsien, R. W. (2013). Perspectives on kiss-and-run: role in exocytosis, endocytosis, and neurotransmission. *Annu. Rev. Physiol.* 75, 393–422. doi: 10.1146/annurev-physiol-020911-153305

Arrio-Dupont, M., Cribier, S., Foucault, G., Devaux, P. F., and d'Albis, A. (1996). Diffusion of fluorescently labeled macromolecules in cultured muscle cells. *Biophys. J.* 70, 2327–2332. doi: 10.1016/s0006-3495(96)79798-9

Baba, M., Nakajo, S., Tu, P. H., Tomita, T., Nakaya, K., Lee, V. M., et al. (1998). Aggregation of alpha-synuclein in Lewy bodies of sporadic Parkinson's disease and dementia with Lewy bodies. *Am. J. Pathol.* 152, 879–884.

Bao, H., Das, D., Courtney, N. A., Jiang, Y., Briguglio, J. S., Lou, X., et al. (2018). Dynamics and number of trans-SNARE complexes determine nascent fusion pore properties. *Nature* 554, 260–263. doi: 10.1038/nature25481

Breckenridge, L. J., and Almers, W. (1987). Currents through the fusion pore that forms during exocytosis of a secretory vesicle. *Nature* 328, 814–817. doi: 10.1038/328814a0

Burré, J., Sharma, M., and Südhof, T. C. (2015). Definition of a molecular pathway mediating α-synuclein neurotoxicity. *J. Neurosci.* 35, 5221–5232. doi: 10.1523/jneurosci.4650-14.2015

Burre, J., Sharma, M., Tsetsenis, T., Buchman, V., Etherton, M. R., and Sudhof, T. C. (2010). Alpha-synuclein promotes SNARE-complex assembly in vivo and in vitro. *Science* 329, 1663–1667. doi: 10.1126/science.1195227

Chernomordik, L. V., and Kozlov, M. M. (2003). Protein-lipid interplay in fusion and fission of biological membranes. *Annu. Rev. Biochem.* 72, 175–207. doi: 10.1146/annurev.biochem.72.121801.161504

Choi, B. K., Choi, M. G., Kim, J. Y., Yang, Y., Lai, Y., Kweon, D. H., et al. (2013). Large alpha-synuclein oligomers inhibit neuronal SNARE-mediated vesicle docking. *Proc. Natl. Acad. Sci. U. S. A.* 110, 4087–4092. doi: 10.1073/pnas.1218424110

Diao, J., Burré, J., Vivona, S., Cipriano, D. J., Sharma, M., Kyoung, M., et al. (2013). Native α-synuclein induces clustering of synaptic-vesicle mimics via binding to phospholipids and synaptobrevin-2/VAMP2. *Elife* 2:e00592. doi: 10.7554/eLife.00592

Gao, Y., Zorman, S., Gundersen, G., Xi, Z., Ma, L., Sirinakis, G., et al. (2012). Single reconstituted neuronal SNARE complexes zipper in three distinct stages. *Science* 337, 1340–1343. doi: 10.1126/science.1224492

Han, X., Wang, C. T., Bai, J., Chapman, E. R., and Jackson, M. B. (2004). Transmembrane segments of syntaxin line the fusion pore of Ca2+-triggered exocytosis. *Science* 304, 289–292. doi: 10.1126/science.1095801

Hawk, B. J. D., Khounlo, R., and Shin, Y. K. (2019). Alpha-synuclein continues to enhance SNARE-dependent vesicle docking at exorbitant concentrations. *Front. Neurosci.* 13:216. doi: 10.3389/fnins.2019.00216

Jo, E., McLaurin, J., Yip, C. M., St George-Hyslop, P., and Fraser, P. E. (2000). Alpha-synuclein membrane interactions and lipid specificity. *J. Biol. Chem.* 275, 34328–34334. doi: 10.1074/jbc.M004345200

Kiessling, V., Liang, B., Kreutzberger, A. J., and Tamm, L. K. (2017). Planar supported membranes with mobile SNARE proteins and quantitative fluorescence microscopy assays to study synaptic vesicle fusion. *Front. Mol. Neurosci.* 10:72. doi: 10.3389/fnmol.2017.00072

Kim, J., and Shin, Y. K. (2017). Productive and non-productive pathways for synaptotagmin 1 to support Ca(2+)-triggered fast exocytosis. *Front. Mol. Neurosci.* 10:380. doi: 10.3389/fnmol.2017.00380

Kreutzberger, A. J. B., Kiessling, V., Stroupe, C., Liang, B., Preobraschenski, J., Ganzella, M., et al. (2019). In vitro fusion of single synaptic and dense core vesicles reproduces key physiological properties. *Nat. Commun.* 10:3904. doi: 10.1038/s41467-019-11873-8

Lai, Y., Diao, J., Liu, Y., Ishitsuka, Y., Su, Z., Schulten, K., et al. (2013). Fusion pore formation and expansion induced by Ca2+ and synaptotagmin 1. *Proc. Natl. Acad. Sci. U. S. A.* 110, 1333–1338. doi: 10.1073/pnas.1218818110

Lai, Y., Kim, S., Varkey, J., Lou, X., Song, J. K., Diao, J., et al. (2014). Nonaggregated α-synuclein influences SNARE-dependent vesicle docking via membrane binding. *Biochemistry* 53, 3889–3896. doi: 10.1021/bi5002536

Liu, T., Tucker, W. C., Bhalla, A., Chapman, E. R., and Weisshaar, J. C. (2005). SNARE-driven, 25-millisecond vesicle fusion in vitro. *Biophys. J.* 89, 2458–2472. doi: 10.1529/biophysj.105.062539

Logan, T., Bendor, J., Toupin, C., Thorn, K., and Edwards, R. H. (2017). Alpha-synuclein promotes dilation of the exocytotic fusion pore. *Nat. Neurosci.* 20, 681–689. doi: 10.1038/nn.4529

Lou, X., Kim, J., Hawk, B. J., and Shin, Y. K. (2017). α-Synuclein may cross-bridge v-SNARE and acidic phospholipids to facilitate SNARE-dependent vesicle docking. *Biochem. J.* 474, 2039–2049. doi: 10.1042/bcj20170200

Lu, X., Zhang, F., McNew, J. A., and Shin, Y. K. (2005). Membrane fusion induced by neuronal SNAREs transits through hemifusion. *J. Biol. Chem.* 280, 30538–30541. doi: 10.1074/jbc.M506862200

Min, D., Kim, K., Hyeon, C., Cho, Y. H., Shin, Y. K., and Yoon, T. Y. (2013). Mechanical unzipping and rezipping of a single SNARE complex reveals hysteresis as a force-generating mechanism. *Nat. Commun.* 4:1705. doi: 10.1038/ncomms2692

Nemani, V. M., Lu, W., Berge, V., Nakamura, K., Onoa, B., Lee, M. K., et al. (2010). Increased expression of alpha-synuclein reduces neurotransmitter release by inhibiting synaptic vesicle reclustering after endocytosis. *Neuron* 65, 66–79. doi: 10.1016/j.neuron.2009.12.023

Poirier, M. A., Xiao, W., Macosko, J. C., Chan, C., Shin, Y. K., and Bennett, M. K. (1998). The synaptic SNARE complex is a parallel four-stranded helical bundle. *Nat. Struct. Biol.* 5, 765–769. doi: 10.1038/1799

Shin, J., Lou, X., Kweon, D. H., and Shin, Y. K. (2014). Multiple conformations of a single SNAREpin between two nanodisc membranes reveal diverse pre-fusion states. *Biochem. J.* 459, 95–102. doi: 10.1042/bj20131668

Snead, D., and Eliezer, D. (2014). Alpha-synuclein function and dysfunction on cellular membranes. *Exp. Neurobiol.* 23, 292–313. doi: 10.5607/en.2014.23.4.292

Sollner, T., Whiteheart, S. W., Brunner, M., Erdjument-Bromage, H., Geromanos, S., Tempst, P., et al. (1993). SNAP receptors implicated in vesicle targeting and fusion. *Nature* 362, 318–324. doi: 10.1038/362318a0

Sun, J., Wang, L., Bao, H., Premi, S., Das, U., Chapman, E. R., et al. (2019). Functional cooperation of α-synuclein and VAMP2 in synaptic vesicle recycling. *Proc. Natl. Acad. Sci. U. S. A.* 116, 11113–11115. doi: 10.1073/pnas.1903049116

Sutton, R. B., Fasshauer, D., Jahn, R., and Brunger, A. T. (1998). Crystal structure of a SNARE complex involved in synaptic exocytosis at 2.4 A resolution. *Nature* 395, 347–353. doi: 10.1038/26412

Trexler, A. J., and Rhoades, E. (2009). Alpha-synuclein binds large unilamellar vesicles as an extended helix. *Biochemistry* 48, 2304–2306. doi: 10.1021/bi900114z

Weber, T., Zemelman, B. V., McNew, J. A., Westermann, B., Gmachl, M., Parlati, F., et al. (1998). SNAREpins: minimal machinery for membrane fusion. *Cell* 92, 759–772.

Wong, Y. C., and Krainc, D. (2017). α-synuclein toxicity in neurodegeneration: mechanism and therapeutic strategies. *Nat. Med.* 23, 1–13. doi: 10.1038/nm.4269

Wu, Z., Dharan, N., McDargh, Z. A., Thiyagarajan, S., O'Shaughnessy, B., and Karatekin, E. (2019). The neuronal calcium sensor Synaptotagmin-1 and SNARE proteins cooperate to dilate fusion pores mechanically. *bioRxiv* [Preprint]. https://www.biorxiv.org/content/10.1101/623827v1.full

Xu, Y., Zhang, F., Su, Z., McNew, J. A., and Shin, Y. K. (2005). Hemifusion in SNARE-mediated membrane fusion. *Nat. Struct. Mol. Biol.* 12, 417–422. doi: 10.1038/nsmb921

Yoon, T. Y., Okumus, B., Zhang, F., Shin, Y. K., and Ha, T. (2006). Multiple intermediates in SNARE-induced membrane fusion. *Proc. Natl. Acad. Sci. U. S. A.* 103, 19731–19736. doi: 10.1073/pnas.0606032103

Conflict of Interest: The authors declare that the research was conducted in the absence of any commercial or financial relationships that could be construed as a potential conflict of interest.

Advantages of publishing in Frontiers

OPEN ACCESS
Articles are free to read
for greatest visibility
and readership

FAST PUBLICATION
Around 90 days
from submission
to decision

HIGH QUALITY PEER-REVIEW
Rigorous, collaborative,
and constructive
peer-review

TRANSPARENT PEER-REVIEW
Editors and reviewers
acknowledged by name
on published articles

Frontiers
Avenue du Tribunal-Fédéral 34
1005 Lausanne | Switzerland

Visit us: www.frontiersin.org
Contact us: frontiersin.org/about/contact

REPRODUCIBILITY OF RESEARCH
Support open data
and methods to enhance
research reproducibility

DIGITAL PUBLISHING
Articles designed
for optimal readership
across devices

FOLLOW US
@frontiersin

IMPACT METRICS
Advanced article metrics
track visibility across
digital media

EXTENSIVE PROMOTION
Marketing
and promotion
of impactful research

LOOP RESEARCH NETWORK
Our network
increases your
article's readership